

Lecture Notes in Mechanical Engineering

Chander Prakash
Sunpreet Singh
Grzegorz Krolczyk *Editors*

Advances in Functional and Smart Materials


Select Proceedings of ICFMMP 2021

 Springer

Lecture Notes in Mechanical Engineering


Series Editors

Fakher Chaari, National School of Engineers, University of Sfax, Sfax, Tunisia

Francesco Gherardini , Dipartimento di Ingegneria “Enzo Ferrari”, Università di Modena e Reggio Emilia, Modena, Italy

Vitalii Ivanov, Department of Manufacturing Engineering, Machines and Tools, Sumy State University, Sumy, Ukraine

Editorial Board

Francisco Cavas-Martínez , Departamento de Estructuras, Construcción y Expresión Gráfica Universidad Politécnica de Cartagena, Cartagena, Murcia, Spain

Francesca di Mare, Institute of Energy Technology, Ruhr-Universität Bochum, Bochum, Nordrhein-Westfalen, Germany

Mohamed Haddar, National School of Engineers of Sfax (ENIS), Sfax, Tunisia

Young W. Kwon, Department of Manufacturing Engineering and Aerospace Engineering, Graduate School of Engineering and Applied Science, Monterey, CA, USA

Justyna Trojanowska, Poznan University of Technology, Poznan, Poland

Lecture Notes in Mechanical Engineering (LNME) publishes the latest developments in Mechanical Engineering—quickly, informally and with high quality. Original research reported in proceedings and post-proceedings represents the core of LNME. Volumes published in LNME embrace all aspects, subfields and new challenges of mechanical engineering. Topics in the series include:

- Engineering Design
- Machinery and Machine Elements
- Mechanical Structures and Stress Analysis
- Automotive Engineering
- Engine Technology
- Aerospace Technology and Astronautics
- Nanotechnology and Microengineering
- Control, Robotics, Mechatronics
- MEMS
- Theoretical and Applied Mechanics
- Dynamical Systems, Control
- Fluid Mechanics
- Engineering Thermodynamics, Heat and Mass Transfer
- Manufacturing
- Precision Engineering, Instrumentation, Measurement
- Materials Engineering
- Tribology and Surface Technology

To submit a proposal or request further information, please contact the Springer Editor of your location:

China: Ms. Ella Zhang at ella.zhang@springer.com

India: Priya Vyas at priya.vyas@springer.com

Rest of Asia, Australia, New Zealand: Swati Meherishi at swati.meherishi@springer.com

All other countries: Dr. Leontina Di Cecco at Leontina.dicecco@springer.com

To submit a proposal for a monograph, please check our Springer Tracts in Mechanical Engineering at <https://link.springer.com/bookseries/11693> or contact Leontina.dicecco@springer.com

Indexed by SCOPUS. All books published in the series are submitted for consideration in Web of Science.

Chander Prakash · Sunpreet Singh ·
Grzegorz Krolczyk
Editors

Advances in Functional and Smart Materials

Select Proceedings of ICFMMP 2021

 Springer

Editors

Chander Prakash
School of Mechanical Engineering
Lovely Professional University
Phagwara, India

Sunpreet Singh
Centre for Nanofibers and Nanotechnology
National University of Singapore
Singapore, Singapore

Grzegorz Krolczyk
Department of Mechanical Engineering
Opole University of Technology
Opole, Poland

ISSN 2195-4356

ISSN 2195-4364 (electronic)

Lecture Notes in Mechanical Engineering

ISBN 978-981-19-4146-7

ISBN 978-981-19-4147-4 (eBook)

<https://doi.org/10.1007/978-981-19-4147-4>

© The Editor(s) (if applicable) and The Author(s), under exclusive license to Springer Nature Singapore Pte Ltd. 2023, corrected publication 2023

This work is subject to copyright. All rights are solely and exclusively licensed by the Publisher, whether the whole or part of the material is concerned, specifically the rights of translation, reprinting, reuse of illustrations, recitation, broadcasting, reproduction on microfilms or in any other physical way, and transmission or information storage and retrieval, electronic adaptation, computer software, or by similar or dissimilar methodology now known or hereafter developed.

The use of general descriptive names, registered names, trademarks, service marks, etc. in this publication does not imply, even in the absence of a specific statement, that such names are exempt from the relevant protective laws and regulations and therefore free for general use.

The publisher, the authors, and the editors are safe to assume that the advice and information in this book are believed to be true and accurate at the date of publication. Neither the publisher nor the authors or the editors give a warranty, expressed or implied, with respect to the material contained herein or for any errors or omissions that may have been made. The publisher remains neutral with regard to jurisdictional claims in published maps and institutional affiliations.

This Springer imprint is published by the registered company Springer Nature Singapore Pte Ltd.

The registered company address is: 152 Beach Road, #21-01/04 Gateway East, Singapore 189721, Singapore

Preface

This book Volume I entitled *Advances in Functional and Smart Materials*, presents select proceedings of International Conference on Functional Material, Manufacturing and Performances (ICFMMP 2021) and aims to a comprehensive and broad-spectrum picture of the state-of-the-art research, development and commercial prospective of various discoveries conducted in the real-world materials science applications. The book also presents the various synthesis and fabrication route of functional and smart materials for universal applications such as material science, mechanical engineering, manufacturing, metrology, nanotechnology, physics, chemical, biology, chemistry, civil engineering, and food science. Here, the authors provide graduate, postgraduate, doctorate students, faculty, and scientists with an in-depth account of the evolutionary behaviour of material science and engineering for industrial applications. The book can be a valuable reference for beginners, researchers, and professionals interested in sustainable construction and allied fields.

Phagwara, India
Singapore
Opole, Poland

Chander Prakash
Sunpreet Singh
Grzegorz Krolczyk

Contents

Sustainable Lean and Green Manufacturing: An Empirical Review of Their Strategies	1
Arun Arora, Vijay Kumar Singh, and Rajeev Rathi	
An Extensive Review Owing to the Influence of Surface Coating on the Technical Performance of Solar Cells	13
Gobinath Velu Kaliyannan, Rajasekar Rathanasamy, Santhosh Sivaraj, Moganapriya Chinnasamy, and Suganeswaran Kandasamy	
First Principle Investigations of $\text{AgBr}_{1-x}\text{I}_x$ Ternary Alloys	25
Neha Munjal, Barun Dhanna, P. Padmakumar, and Pavas	
Phycoremediation of Dairy Wastewater and Biodiesel Production Using <i>Mairne Microalage Tetraselmis Indica</i>	35
Amit, Uttam Kumar Ghosh, Rahul Gautam, Amit Jaiswal, and Siddhartha Pandey	
RETRACTED CHAPTER: On Parametric Optimization of TSE for PVDF-Graphene-MnZnO Composite Based Filament Fabrication for 3D/4D Printing Applications	43
Vinay Kumar, Rupinder Singh, and Inderpreet Singh Ahuja	
Characteristic Analysis of Nylon Fiber Reinforced Epoxy Composite Materials	59
A. Saravanan, R. Naveen Kumar, and A. S. Tharun Sankar	
Effect of Annealing Temperature on Phase Transformation of NiCr_2O_4 Nanoparticles and Evaluated Its Structural and Magnetic Properties	71
Jarnail Singh, Pankaj Bhardwaj, Ravi Kumar, Kaushal Kumar, Saurav Dixit, and Vikram Verma	

Comparative Study of Concrete Cylinders Confined Using Natural and Artificial Fibre Reinforced Polymers	79
Priyanka Singh, Saurav Dixit, Margel Taso, Kaushal Kumar, Jarnail Singh, Krystyna Araszkiwicz, Nikolai Ivanovich Vatin, and Chander Prakash	
Experimental Evaluation of Moringa and Amaranth Oil as Bio-Nanolubricant for Light Gear Application	93
Sagar Galgat and Ankit Kotia	
Application of Life Cycle Analysis in Sustainable Machining of Aluminium 6061 Alloy Under Different Lubricating Conditions	103
Kamal Hassan, Amardeep Singh Kang, Gurraj Singh, and Chander Prakash	
Improving Mechanical Properties of Hot Rolled Coil Using Micro Alloy	111
Vijay Kumar Singh	
Synthesis and Characterization of Highly Transparent and Superhydrophobic Zinc Oxide (ZnO) Film	119
Ashish Jaswal, Kamal Kishore, Amarjit Singh, Jarnail Singh, Saurav Dixit, Kaushal Kumar, and Manoj Kumar Sinha	
Titania Reinforced Hydroxyapatite Thin Film Coatings for Orthopedic Applications	129
Ravinder Pal Singh, Anoop Aggarwal, Gurdyal Singh, and Mayukh Sarkar	
Different Materials Used for Leachate Management—A Review	135
Saurabh Sunil Naik, Shantanu N. Pawar, Siddhartha Pandey, and Bhushan H. Shinde	
Study of Thermoelectrical Behavior of BaXO₃ Perovskites (X = Pu, Am, Cm)	143
Preeti Kumari and Vipul Srivastava	
Optical Behavior of Polyvinylchloride–Polyamide Blend	155
Jiltan Roy and Kawaljeet Singh Samra	
Research and Development of Biomass Production in India: A Bibliometric Study	161
Shiv Singh, Kirti Singh, Jamil Ahmed, Vijay Mohan Soni, and Neha Munjal	
A First Principle Study of Structural Properties of KX_xI_{1-x} (X = Cl, Br and X= 0.00, 0.25, 0.50, 0.75, and 1.00)	175
Agnibha Das Majumdar, Puneet Kaur, and Neha Munjal	

First Principle Study on Structural Properties of Boron Compounds . . .	187
Agnibha Das Majumdar, P. Padmakumar, Rajni, Neha Munjal, and Uma Kamboj	
On Techno-economic Aspect of Dental Crown Fabrication by DMLS and Investment Casting for Veterinary Application	193
Smruti Ranjan Pradhan, Rupinder Singh, and Sukhwant Singh Banwait	
A Critical Study of Structural and Electronic Properties of Co₂TiN Full-Heusler Alloy	203
Navdeep kaur and Vipul Srivastava	
Effect of Additive on Flowability and Compressibility of Fly Ash	211
Kaushal Kumar, Rishabh Arora, Jarnail Singh, Sarah Khan, Lavesh Mishra, Prabhakar Bhandari, Saurav Dixit, and Chander Prakash	
First Principle Investigations of Half-Metallicity in Co₂YZ (Y = Sc, Y; Z = P, As, Sb, Bi)	219
Ananya Shankar, Preetisha Goswami, Archana Tripathi, Ruby Jindal, Rajni Gautam, Neeraj Kumari, Himani Yadav, and Sheetal Tyagi	
Future of Indian Manufacturing: Lean and Green Manufacturing System (LGMS)	225
Arun Arora and Vijay Kumar Singh	
Experimental and Computational Wear Studies of Alumina and Zirconia Versus SS316L for Hip Prosthesis	235
S. Shankar, R. Nithyaprakash, and R. Naveen Kumar	
An Outlook on Self-healing Materials	245
Nitin Kumar Gupta, Nalin Somani, Tushar Panwar, Nishant Ranaa, Faisal Ahmeda, and Abhinav Dimri	
On Some Convective Mechanisms of Nanofluids	255
Monika Arora and Avinash Rana	
Study of Erosion Behavior of Al₂O₃ Coatings Deposited by Plasma Spray on SS-304	265
Gaurav Prashar and Hitesh Vasudev	
Erosion Behaviour of Al₂O₃ Coatings Deposited by Plasma Spray on AISI-316 Substrate	273
Gaurav Prashar and Hitesh Vasudev	
A Detailed Investigation of Structural and Optical Properties of CTAB-Assisted Cr₂O₃ Nanoparticles	281
Jarnail Singh, Mayank Dotiyal, Pankaj Bhardwaj, Prabhakar Bhandari, Kaushal Kumar, Saurav Dixit, and Vikram Verma	

Effect of Glazing Materials and Shading Position on the Energy Consumption Pattern and Indoor Visual Comfort of Office Building . . .	291
Ramkishore Singh, Ian J. Lazarus, and Dharam Buddhi	
Sn-Based Perovskites for Photovoltaic Applications	303
Amit Kumar Sharma and Deepak Kumar	
Phase Transformation Analysis of Fe-Substituted Cr₂O₃ Nanoparticles Using Rietveld Refinement	311
Jarnail Singh, Pankaj Bhardwaj, Ravi Kumar, Saurav Dixit, Kaushal Kumar, and Vikram Verma	
A Review Study on Advancement and Development of First Generation to Next Generation Optical Fibers	323
Puja Acharya, Vivek Singh Tanwar, and Bhavesh Vyas	
Review on the Mechanical Properties and Performance of Permeable Concrete	341
Priyanka Singh, Tejasvi Bishnoi, Saurav Dixit, Kaushal Kumar, Nikolai Ivanovich Vatin, and Jarnail Singh	
Effect of Machining Parameters on Surface Roughness and Material Removal Rate in Dry Turning of AISI 1080 Mild Steel Using HSS Tools	353
Job M. Wambua, Celestine K. Kinyua, Royston K. Mwikathi, Ayub O. Owino, Martin M. Kirimi, Fredrick M. Mwema, and T. C. Jen	
Garnet: Structural and Optical Properties	365
Anu Bala and Suman Rani	
Molecular Interaction Study of PEGs in Butyl p-hydroxybenzoate and Methanol Mixtures at 303.15 K and 308.15 K Temperatures Using Acoustic Method	373
Ashima Prince Kumar and K. C. Juglan	
Application of Efficient Naturally Occurring Clay Mineral for Fuchsin Basic Dye Removal	381
Chandra Mohan, Neeraj Kumari, Ruby Jindal, and Rajni Gautam	
Prevention of Reversal Blood Flow Phenomenon into Intravenous Line with the Aid of Smart Device	391
Rajasekar Rathanasamy, Yogeswaran Baskar, Vinith Ravichandran, Rohit Kannan, and Santhosh Sivaraj	
Thermodynamic and Acoustic Investigation of D-Panthenol in Homologous Series of Polyethylene Glycol at Different Temperatures	403
Prachi Patnaik, Nabaparna Chakraborty, Parminder Kaur, K. C. Juglan, and Harsh Kumar	

A Feasibility Investigation of Photo Voltaic Cell-Assisted Linke Hofmann Busch Coach Used in Indian Railways: A Case Study in Context to Present Scenario 425
 Abhishek Barua, Dilip Kumar Bagal, Siddharth Jeet, Swastik Pradhan, Asini Kumar Baliarsingh, and Deepak Kumar Bagal

Drilling Simulation of AA7075 T351 Graded Aluminium Alloy Using Deform-3D 439
 Dilip Kumar Bagal, Siddharth Jeet, Abhishek Barua, Swastik Pradhan, Arati Rath, and Surya Narayan Panda

Numerical Modeling of Explosive Welded Ti/Al7075-T6 Bimetal Composite Plate Using Smoothed Particle Hydrodynamics 461
 Abhishek Barua, Swastik Pradhan, Siddharth Jeet, Dilip Kumar Bagal, Kanchan Kumari, Saujanya Kumar Sahu, and Arati Rath

Parametric Investigation of Injection Moulding for LDPE using Capuchin Search Algorithm and Honey Badger Algorithm 481
 Siddharth Jeet, Abhishek Barua, Dilip Kumar Bagal, Swastik Pradhan, Surya Narayan Panda, and Siba Sankar Mahapatra

Bibliometric Analysis of Friction Stir Spot Welded Joints using SCOPUS Database 499
 Dilip Kumar Bagal, Siddharth Jeet, Abhishek Barua, Swastik Pradhan, Surya Narayan Panda, and Saujanya Kumar Sahu

Multi Parametric Optimization of Dry Turning of Titanium Alloy (Ti6Al4V Graded 5) using Coated Carbide Insert: A Novel Hybrid RSM-Artificial Gorilla Troop Optimization and Dingo Optimization Algorithm 515
 Dilip Kumar Bagal, Siddharth Jeet, Abhishek Barua, Swastik Pradhan, Arati Rath, and Saujanya Kumar Sahu

Retraction Note to: On Parametric Optimization of TSE for PVDF-Graphene-MnZnO Composite Based Filament Fabrication for 3D/4D Printing Applications C1
 Vinay Kumar, Rupinder Singh, and Inderpreet Singh Ahuja

Editors and Contributors

About the Editors

Dr. Chander Prakash is Professor in the School of Mechanical Engineering, Lovely Professional University, Jalandhar, India. He has received Ph.D. in mechanical engineering from Panjab University, Chandigarh, India. His areas of research are biomaterials, rapid prototyping and 3-D printing, advanced manufacturing, modeling, simulation, and optimization. He has more than 14 years of teaching experience. He has contributed extensively to the world in the titanium and magnesium based implant literature with publications appearing in *Surface and Coating Technology*, *Materials and Manufacturing Processes*, *Journal of Materials Engineering and Performance*, *Journal of Mechanical Science and Technology*, *Nanoscience and Nanotechnology Letters*, *Proceedings of the Institution of Mechanical Engineers, Part B: Journal of Engineering Manufacture*. He has authored 60 research papers and 10 book chapters. He is also editor of 3 books: *Current Trends in Bio-manufacturing*; *3D Printing in Biomedical Engineering*; and *Biomaterials in Orthopaedics and Bone Regeneration—Design and Synthesis*. He is also guest editor of 3 journals: Special issue of *Functional Materials and Advanced Manufacturing*, *Facta Universitatis*, Series: Mechanical Engineering (Scopus Indexed), Materials Science Forum (Scopus Indexed), and special issue on *Metrology in Materials and Advanced Manufacturing*, Measurement and Control (SCI indexed).

Dr. Sunpreet Singh is researcher in NUS Nanoscience and Nanotechnology Initiative (NUSNNI). He has received Ph.D. in Mechanical Engineering from Guru Nanak Dev Engineering College, Ludhiana, India. His area of research is additive manufacturing and application of 3D printing for development of new biomaterials for clinical applications. He has contributed extensively in additive manufacturing literature with publications appearing in *Journal of Manufacturing Processes*, *Composite Part: B*, *Rapid Prototyping Journal*, *Journal of Mechanical Science and Technology*, *Measurement*, *International Journal of Advance Manufacturing Technology*,

and *Journal of Cleaner Production*. He has authored 10 book chapters and monographs. He is working in joint collaboration with Prof. Seeram Ramakrishna, NUS Nanoscience and Nanotechnology Initiative and Prof. Rupinder Singh, manufacturing research lab, GNDEC, Ludhiana. He is also editor of 3 books—*Current Trends in Bio-manufacturing*, *3D Printing in Biomedical Engineering*, and *Biomaterials in Orthopaedics and Bone Regeneration—Design and Synthesis*. He is also guest editor of 3 journals—special issue of *Functional Materials and Advanced Manufacturing*, *Facta Universitatis*, series: Mechanical Engineering (Scopus Indexed), Materials Science Forum (Scopus Indexed), and special issue on *Metrology in Materials and Advanced Manufacturing*, Measurement and Control (SCI indexed).

Prof. Grzegorz Krolczyk is Professor in the Opole University of Technology. He is an originator and a Project Manager of OUTEch's new Surface Integrity Laboratory. In his career he held positions such as: Head of Unit Design and Technology, Product Engineer, Production Manager, Product Development Engineer and Production Director. Co-author and Project Leader of a project Innovative, energy-efficient diaphragm flow device of a new generation. He is connected with the mechanical industry, where he managed teams from a few to over a hundred people. His industrial engineering experience was gained while working in an European holding company involved in machining of construction materials and plastic injection, where he was responsible for contacts with companies on technical issues such as quotation and implementation of new products. In professional career he was responsible for the implementation to production products such as peristaltic pumps, ecological sprayers to spray organic pesticides and many pressure equipment operating e.g. in chemical plants. As a production manager, he was responsible for implementation to production and launching the assembly line for innovative sprayer Ultra-Low Volume Spraying System. Author and co-author of over 80 scientific publications and nearly 20 studies and implementation of industry. The main directions of scientific activity is surface metrology, optimization of geometrical and physical parameters of surface integrity, optimization of production and cutting tool wear analyze in dry machining process of difficult-to-cut materials. He is also Editor of various Journals and Books.

Contributors

Acharya Puja K.R. Mangalam University, Gurgaon, Haryana, India

Aggarwal Anoop Chitkara University Institute of Engineering and Technology, Chitkara University, Chitkara, Punjab, India

Ahmed Jamil Bennett University (Times of India Group), Greater Noida, Uttar Pradesh, India

Ahmeda Faisal Department of Mechanical Engineering, DIT University Dehradun, Dehradun, India

Ahuja Inderpreet Singh Department of Mechanical Engineering, Punjabi University, Patiala, Punjab, India

Amit Department of Polymer and Process Engineering, Indian Institute of Technology, Roorkee, India

Araszkievicz Krystyna Faculty of Civil and Environmental Engineering, West Pomeranian University of Technology, Szczecin, Poland

Arora Arun School of Mechanical Engineering, Lovely Professional University, Phagwara, Punjab, India

Arora Monika Department of Mathematics, Lovely Professional University, Phagwara, India

Arora Rishabh School of Engineering and Technology, K.R. Mangalam University, Gurgaon, India

Bagal Deepak Kumar Department of Electrical Engineering, Veer Surendra Sai University of Technology, Burla, Odisha, India

Bagal Dilip Kumar Department of Mechanical Engineering, Government College of Engineering, Kalahandi, Bhawanipatna, Odisha, India

Bala Anu Department of Physics, School of Chemical Engineering and Physical Sciences, Lovely Professional University, Phagwara, Punjab, India

Baliarsingh Asini Kumar Department of Electrical Engineering, Government College of Engineering, Kalahandi, Bhawanipatna, Odisha, India

Banwait Sukhwant Singh National Institute of Technical Teachers Training and Research, Chandigarh, India

Barua Abhishek Department of Mechanical Engineering, Centre for Advanced Post Graduate Studies, BPUT, Rourkela, Odisha, India

Baskar Yogeswaran Department of Mechanical Engineering, Kongu Engineering College, Perundurai, TamilNadu, India

Bhandari Prabhakar Department of Mechanical Engineering, School of Engineering and Technology, K.R. Mangalam University, Gurgaon, India

Bhardwaj Pankaj Department of Material Science and Engineering, National Institute of Technology Hamirpur, Hamirpur, India

Bishnoi Tejasvi Department of Civil Engineering, Amity University Noida, Noida, India

Buddhi Dharam Uttaranchal University, Arcadia Grant, Chandanwari Dehradun, Uttarakhand, India

Chakraborty Nabaparna Department of Physics, Lovely Professional University, Phagwara, Punjab, India

Chinnasamy Moganapriya Department of Mechanical Engineering, Kongu Engineering College, Perundurai, Tamilnadu, India;
Department of Mining Engineering, Indian Institute of Technology, Kharagpur, West Bengal, India

Das Majumdar Agnibha Lovely Professional University, Phagwara, Punjab, India;
Department of Physics, Lovely Faculty of Science & Technology, Phagwara, Punjab, India

Dhanna Barun Lovely Professional University, Phagwara, Punjab, India

Dimri Abhinav Department of Mechanical Engineering, DIT University Dehradun, Dehradun, India

Dixit Saurav Department of Mechanical Engineering, K.R. Mangalam University, Gurgaon, India;
Division of Research and Innovation, Uttaranchal University, Dehradun, India;
Peter the Great St. Petersburg Polytechnic University, Saint Petersburg, Russia;
School of Management and Commerce, K.R. Mangalam University, Gurgaon, India;
SOMC, National Institute of Technology Hamirpur, Hamirpur, India

Dotiyal Mayank Department of Mechanical Engineering, K.R. Mangalam University, Gurgaon, India

Galgat Sagar Lubrication and Sustainable Technologies, Bangalore, India

Gautam Rahul Department of Polymer and Process Engineering, Indian Institute of Technology, Roorkee, India

Gautam Rajni School of Basic and Applied Sciences, K.R. Mangalam University, Gurugram, Haryana, India

Ghosh Uttam Kumar Department of Polymer and Process Engineering, Indian Institute of Technology, Roorkee, India

Goswami Preetisha Department of Physics, Gargi College, University of Delhi, Delhi, New Delhi, India

Gupta Nitin Kumar Department of Mechanical Engineering, DIT University Dehradun, Dehradun, India

Hassan Kamal Department of Mechanical Engineering, Lovely Professional University, Phagwara, Punjab, India

Ivanovich Vatin Nikolai Peter the Great St. Petersburg Polytechnic University, Saint Petersburg, Russia

Jaiswal Amit School of Food Science and Environmental Health, College of Sciences and Health, Technological University Dublin, Grangegorman, Dublin 7, Ireland;

Environmental Sustainability and Health Institute, Technological University Dublin, Grangegorman, Dublin 7, Ireland

Jaswal Ashish Department of Material Science and Engineering, National Institute of Technology Hamirpur, Hamirpur, India

Jeet Siddharth Department of Mechanical Engineering, Centre for Advanced Post Graduate Studies, BPUT, Rourkela, Odisha, India

Jen T. C. Department of Mechanical Engineering Science, University of Johannesburg, Auckland Park, South Africa

Jindal Ruby School of Basic and Applied Sciences, K.R. Mangalam University, Gurugram, Haryana, India

Juglan K. C. Department of Physics, Lovely Professional University, Phagwara, Punjab, India

Kaliyannan Gobinath Velu Department of Mechatronics Engineering, Kongu Engineering College, Perundurai, Tamilnadu, India

Kamboj Uma Department of Physics, Lovely Faculty of Science & Technology, Phagwara, Punjab, India

Kandasamy Suganeswaran Department of Mechatronics Engineering, Kongu Engineering College, Perundurai, Tamilnadu, India

Kang Amardeep Singh Department of Mechanical Engineering, Lovely Professional University, Phagwara, Punjab, India

Kannan Rohit Department of Mechanical Engineering, Kongu Engineering College, Perundurai, TamilNadu, India

Kaur Parminder Department of Physics, Lovely Professional University, Phagwara, Punjab, India

Kaur Puneet CGC Technical Campus, Jhanjheri, Mohali, Punjab, India

kaur Navdeep Department of Physics, School of Chemical Engineering and Physical Sciences, Lovely Professional University, Phagwara, Punjab, India

Khan Sarah School of Engineering and Technology, K.R. Mangalam University, Gurgaon, India

Kinyua Celestine K. Department of Mechanical Engineering, Dedan Kimathi University of Technology, Nyeri, Kenya

Kirimi Martin M. Department of Mechanical Engineering, Dedan Kimathi University of Technology, Nyeri, Kenya

Kishore Kamal Department of Material Science and Engineering, National Institute of Technology Hamirpur, Hamirpur, India

Kotia Ankit Lubrication and Sustainable Technologies, Bangalore, India;
Division of Research and Innovation, Uttaranchal University, Dehradun, India

Kumar Ashima Prince Department of Physics & Astronomical Sciences, Central
University of Jammu, Samba, Jammu and Kashmir, India

Kumar Deepak Department of Physics, Lovely Professional University, Phagwara,
Punjab, India

Kumar Harsh Department of Chemistry, Jalandhar, Punjab, India

Kumar Kaushal Department of Mechanical Engineering, K.R. Mangalam Univer-
sity, Gurgaon, India;

School of Engineering and Technology, K.R. Mangalam University, Gurgaon, India

Kumar R. Naveen Department of Mechanical Engineering, Kongu Engineering
College, Erode, Tamilnadu, India

Kumar Ravi Department of Material Science and Engineering, National Institute
of Technology Hamirpur, Hamirpur, India

Kumar Vinay Department of Production Engineering, Guru Nanak Dev Engi-
neering College, Ludhiana, Punjab, India

Kumari Kanchan Department of Mechanical Engineering, Parala Maharaja Engi-
neering College, Berhampur, Odisha, India

Kumari Neeraj School of Basic and Applied Sciences, K.R. Mangalam University,
Gurugram, Haryana, India

Kumari Preeti Department of Physics, School of Chemical Engineering and
Physical Sciences, Lovely Professional University, Phagwara, India

Lazarus Ian J. Department of Physics, Durban University of Technology, Durban,
South Africa;

KZN Industrial Energy Efficient Training and Resource Centre (IEETR), Durban
University of Technology, Durban, South Africa

Mahapatra Siba Sankar Department of Mechanical Engineering, National Insti-
tute of Technology, Rourkela, Odisha, India

Mishra Lavesh School of Management and Commerce, K.R. Mangalam Univer-
sity, Gurgaon, India

Mohan Chandra School of Basic and Applied Science, K.R. Mangalam University,
Gurugram, India

Munjal Neha Lovely Professional University, Phagwara, Punjab, India;
Department of Physics, Lovely Faculty of Science & Technology, Phagwara, Punjab,
India

Mwema Fredrick M. Department of Mechanical Engineering, Dedan Kimathi
University of Technology, Nyeri, Kenya;

Department of Mechanical Engineering Science, University of Johannesburg, Auckland Park, South Africa

Mwikathi Royston K. Department of Mechanical Engineering, Dedan Kimathi University of Technology, Nyeri, Kenya

Naik Saurabh Sunil Department of Civil Engineering, G. H. Rasoni University Amravati, Amravati, India;

Department of Civil Engineering, G H Rasoni Institute of Business Management Jalgaon, Jalgaon, India

Naveen Kumar R. Department of Mechanical Engineering, Kongu Engineering College, Perundurai, Erode, India

Nithyaprakash R. Department of Mechatronics Engineering, Kongu Engineering College, Erode, India

Owino Ayub O. Department of Mechanical Engineering, Dedan Kimathi University of Technology, Nyeri, Kenya

Padmakumar P. Lovely Professional University, Phagwara, Punjab, India; Department of Physics, Lovely Faculty of Science & Technology, Phagwara, Punjab, India

Panda Surya Narayan Department of Production Engineering, Birsa Institute of Technology, Sindri, Dhanbad, Jharkhand, India

Pandey Siddhartha Department of Operations Management, Indian Institute of Management, Ranchi, India; Division of Research and Innovation, Uttaranchal University, Dehradun, India

Panwar Tushar Department of Mechanical Engineering, DIT University Dehradun, Dehradun, India

Patnaik Prachi Department of Physics, Lovely Professional University, Phagwara, Punjab, India

Pavas Lovely Professional University, Phagwara, Punjab, India

Pawar Shantanu N. Department of Civil Engineering, G H Rasoni Institute of Business Management Jalgaon, Jalgaon, India

Pradhan Smruti Ranjan National Institute of Technical Teachers Training and Research, Chandigarh, India

Pradhan Swastik School of Mechanical Engineering, Lovely Professional University, Phagwara, Punjab, India

Prakash Chander Department of Mechanical Engineering, Lovely Professional University, Phagwara, Punjab, India; School of Mechanical Engineering, Lovely Professional University, Phagwara, India

Prashar Gaurav School of Mechanical Engineering, Lovely Professional University, Phagwara, Punjab, India

Rajni Department of Physics, Lovely Faculty of Science & Technology, Phagwara, Punjab, India

Rana Avinash Department of Marketing, Lovely Professional University, Phagwara, India

Ranaa Nishant Department of Mechanical Engineering, DIT University Dehradun, Dehradun, India

Rani Suman Department of Physics, School of Chemical Engineering and Physical Sciences, Lovely Professional University, Phagwara, Punjab, India

Rath Arati School of Computer Engineering, Kalinga Institute of Industrial Technology, Bhubaneswar, Odisha, India

Rathanasamy Rajasekar Department of Mechanical Engineering, Kongu Engineering College, Perundurai, TamilNadu, India

Rathi Rajeev School of Mechanical Engineering, Lovely Professional University, Phagwara, Punjab, India

Ravichandran Vinith Department of Mechanical Engineering, Kongu Engineering College, Perundurai, TamilNadu, India

Roy Jiltan Department of Physics, Lovely Professional University, Phagwara, Punjab, India

Sahu Saujanya Kumar Department of Civil Engineering, Government College of Engineering, Kalahandi, Bhawanipatna, Odisha, India

Samra Kawaljeet Singh Department of Physics, Lovely Professional University, Phagwara, Punjab, India

Sankar A. S. Tharun Department of Mechanical Engineering, Kongu Engineering College, Erode, Tamilnadu, India

Saravanan A. Department of Mechanical Engineering, Kongu Engineering College, Erode, Tamilnadu, India

Sarkar Mayukh School of Mechanical Engineering, Lovely Professional University, Phagwara, Punjab, India

Shankar Ananya Department of Physics, Gargi College, University of Delhi, Delhi, New Delhi, India

Shankar S. Department of Mechatronics Engineering, Kongu Engineering College, Erode, India

Sharma Amit Kumar Department of Physics, Maharana Pratap Govt. College Amb, Una, H.P, India

Shinde Bhushan H. Department of Civil Engineering, G. H. Rasoni University Amravati, Amravati, India

Singh Amarjit Department of Material Science and Engineering, National Institute of Technology Hamirpur, Hamirpur, India

Singh Gurdyal Chitkara University Institute of Engineering and Technology, Chitkara University, Chitkara, Punjab, India

Singh Gurraj Department of Industrial and Production, Dr. B.R Ambedakar National Institute of Technology, Jalandhar, Punjab, India

Singh Jarnail Department of Mechanical Engineering, K.R. Mangalam University, Gurgaon, India;
School of Engineering and Technology, K.R. Mangalam University, Gurgaon, India

Singh Kirti Dr. D P Rastogi Central Research Institute of Homeopathy, Noida, Utter Pradesh, India

Singh Priyanka Department of Civil Engineering, Amity University Noida, Noida, India

Singh Ramkishore School of Chemical Engineering and Physical Sciences, Lovely Professional University, Phagwara, India

Singh Ravinder Pal School of Mechanical Engineering, Lovely Professional University, Phagwara, Punjab, India

Singh Rupinder Department of Mechanical Engineering, National Institute of Technical Teacher Training and Research, Chandigarh, India

Singh Shiv Bennett University (Times of India Group), Greater Noida, Utter Pradesh, India

Singh Vijay Kumar School of Mechanical Engineering, Lovely Professional University, Phagwara, India;
School of Mechanical Engineering, Lovely Professional University, Phagwara, Punjab, India

Sinha Manoj Kumar Department of Mechanical Engineering, K.R. Mangalam University, Gurgaon, India

Sivaraj Santhosh Department of Mechanical Engineering, Kongu Engineering College, Perundurai, TamilNadu, India

Somani Nalin Department of Mechanical Engineering, DIT University Dehradun, Dehradun, India

Soni Vijay Mohan Lovely Professional University, Phagwara, Punjab, India

Srivastava Vipul Department of Physics, School of Chemical Engineering and Physical Sciences, Lovely Professional University, Phagwara, Punjab, India

Tanwar Vivek Singh K.R. Mangalam University, Gurgaon, Haryana, India

Taso Margel Civil Engineering Department, Amity University Uttar Pradesh, Noida, India

Tripathi Archana Department of Physics, Gargi College, University of Delhi, Delhi, New Delhi, India

Tyagi Sheetal School of Basic and Applied Sciences, K.R. Mangalam University, Gurugram, Haryana, India

Vasudev Hitesh School of Mechanical Engineering, Lovely Professional University, Phagwara, Punjab, India

Verma Vikram Department of Material Science and Engineering, National Institute of Technology Hamirpur, Hamirpur, India;
Department of Mechanical Engineering, K.R. Mangalam University, Gurgaon, India

Vyas Bhavesh K.R. Mangalam University, Gurgaon, Haryana, India

Wambua Job M. Department of Mechanical Engineering, Dedan Kimathi University of Technology, Nyeri, Kenya

Yadav Himani School of Basic and Applied Sciences, K.R. Mangalam University, Gurugram, Haryana, India

Sustainable Lean and Green Manufacturing: An Empirical Review of Their Strategies



Arun Arora, Vijay Kumar Singh, and Rajeev Rathi

Abstract Sustainable lean green manufacturing research is the primary emphasis of this study (SLGM). Manufacturing Organizations can benefit from a combination of lean practices and environmental practices, according to this paper. Despite countless studies, there is no definitive definition of lean and green. In terms of social, economic, and environmental concerns, studies have linked lean manufacturing to green manufacturing. A review of previous research is undertaken in this study to assess the manufacturing industry's shortcomings. Research papers from well-known databases were analyzed to identify the gaps in sustainable lean and green manufacturing practices. After a thorough analysis, it is recommended that sustainable lean and green manufacturing be further developed. Reduced implementation gaps for lean and green manufacturing will increase industrial sustainability. The essay also discusses lean and green manufacturing, as well as lean waste, lean processes, and lean green implementation. Finally, the research closes with a literature survey in order to better understand the present state of lean manufacturing and its varied approaches.

Keywords Sustainability · Lean manufacturing · Green manufacturing · Systematic review

1 Introduction

Organizations of all kinds are using the term “sustainability” as a marketing gimmick. Previous research has suggested links between environmental sustainability and lean and green practices. Reducing the amount of resources used to manufacture something while also improving the environment is central to the lean philosophy. Literature reviews reveal that economic development and societal well-being are inextricably linked to environmental sustainability (Fig. 1). According to Dombrowski and Mielke [1], lean and green refer to the effective use of resources, pollution

A. Arora (✉) · V. K. Singh · R. Rathi
School of Mechanical Engineering, Lovely Professional University, Phagwara, Punjab, India
e-mail: arun13arora@gmail.com

reduction, and waste optimization. Environmental sustainability and lean and green operations, according to [2], go hand in hand. Lean and green manufacturing methods require both technological and financial support in order to achieve long-term profitability while also improving the environmental performance of industrial processes. In spite of the fact that lean and green concepts are enticing instruments for waste reduction, most industrial organizations have difficulty sustaining long-term success with these concepts. Based on socio-technical processes, the lean manufacturing process is a decision-making technique designed to reduce waste in the manufacturing process. In order to get the best results, use a problem solving and training of staff to handle numerous tasks, and vendor management, customer satisfaction, and continuous improvement are all aspects of lean manufacturing. As a result, customer needs and environmental conditions drive the sustainability system. As a result of the environmental concerns in today's production systems, management should focus on reducing waste and increasing profitability through lean manufacturing. With the support of employee devotion and lean manufacturing, firms may achieve world-class production [3]. When lean management systems were not considered as a human resource management activity in the past, manufacturing performance was negatively affected. Communication of goals, training progress, ideas for development, awards and recognition, and employee health and safety are all part of good human resource management. Lean manufacturing relies on the most up-to-date technological expertise and clean manufacturing methods, all of which help to minimize manufacturing costs and, as a result, the final product's retail price [4]. Increasing the value of resources and ensuring that customers are happy are two key components of a productive and efficient manufacturing process [5]. Because of the intense competition in today's market, it is critical for businesses to embrace lean manufacturing practices in order to provide high-quality products at low cost. As a result, a lean workplace encourages people to use their natural abilities for process improvement and product quality control while also providing them with the tools to do so. For those looking for a production method that uses the fewest resources while also producing the least amount of waste, consider implementing the lean manufacturing technique [6]. Following the successful implementation of the Toyota Production System (TPS), the concept of lean manufacturing was introduced to reduce any non-value-added operations in a production process [7]. Green, on the other hand, refers to environmental sustainability, which includes waste creation and recycling, as well as pollution of the air, water, and land, as well as energy consumption and efficiency. As a result of green applications, such as the green economy, there is an increase in value while using a smaller amount of resources. While simultaneously decreasing environmental risk and ecological scarcity, the green economy, which propels economic growth while also encouraging new low-carbon technology innovation, would enhance human well-being and social fairness. Sustainability has become the new lean in the green industry, which was formerly known as the new lean. Reactive and proactive environmentally friendly solutions are the core of a business strategy known as "green manufacturing." When a company uses clean technology and renewable energy to reduce pollution and waste while reducing the use of resources, it is known as "Green" production, as



Fig. 1. Relationship between Environmental stability , Economic and Social development

defined by Andrew [8]. Lean and green manufacturing can work together to increase operational efficiency by creating value and reducing waste. Many researchers are intrigued by the idea that working together can improve the productivity of both groups. A new era of eco-innovation ushered in the term “green manufacturing” in the early 1990s. Using an environmentally friendly production process reduces the environmental impact and another detrimental impact on resources. Environmentally friendly manufacturing is known as “green manufacturing,” and it is a way to reduce waste while boosting the economy without having to sacrifice the environment. Green manufacturing, according to Sezen and Cankaya [9], has the potential to spur economic development while also improving environmental and social conditions. A company’s environmental performance can be improved while also meeting customer needs through green management and innovation. To remain competitive, the manufacturing industry is looking for ways to integrate lean production with traditional manufacturing practices. Additionally, the companies are looking into ways to boost output while maintaining a healthy environmental footprint.

2 Methodology

Previous studies on lean and green manufacturing have been reviewed for this study. For this review, we used databases from well-known lean and green publishers such

as Springer, Elsevier, Wiley, and Taylor and Francis, as well as Emerald and Sage. The approaches and answers were discovered as a result of the literature review. The review also included the ideas, enablers, and challenges of lean and green manufacturing. The study excluded gray literature, such as book chapters, unpublished articles, and research papers written before 2000. To gain a better grasp of lean and green manufacturing practices and methods, this article was written.

The objectives of this study are:

1. Understanding the concept of lean and green strategies through literature review
2. Effect of lean and green implementation on business metrics
3. Integration of sustainable lean manufacturing (SLM) in socioeconomic and environmental indicators.

3 Literature Review

Using lean manufacturing, which has been popular since the Industrial Revolution, means reducing unnecessary steps in the production process [10]. The seven (7) wastes of lean manufacturing are based on the early breakthroughs that sparked the idea of waste removal. Early in 1910, Henry Ford's Model T assembly line, which created the first mass-produced automobile, achieved a manufacturing breakthrough when it featured interchangeable standard workpieces. FPS was the foundation for Toyota's TPS idea, which was based on Jidoka and Just in Time (JIT). Using Jidoka, or "automation with a human touch," TPS produces and meets demand without the need for additional production or inventory, whereas JIT utilizes JIT [11]. The quality circle and the importance of inventories were also recognized by Toyota. Both the Toyota Production System and lean manufacturing emphasize continual improvement and the Toyota principles, according to Kochnev. The lean technique has the potential to eliminate overproduction, waiting, transportation, overprocessing, inventory, motion, and faults. A basic premise of lean manufacturing is to identify which parts of a process flow contribute to the overall value of the product. A number of lean tools are used in lean manufacturing to assist detect and eliminate waste [12]. It has been proposed that every organization, regardless of the type of product they generate, can apply lean tools. However, if lean manufacturing technologies are used incorrectly, this can lead to extra waste of resources. It is a problem that has been addressed by Pavnaskar and colleagues in 2003, when they presented a classification method for lean tools that fits the waste to be avoided. According to Simona and Cristina [13], an organization must have a lot of expertise with lean manufacturing processes in order to get meaningful outcomes from the use of these fifteen lean tools. A combination of lean tools, such as Sig-Sigma and Agile systems, is often used by lean practitioners when conditions are optimal. With the use of DMAIC cycle, [14] built a conceptual model for integrating lean, Six Sigma, and Green ideas. According to study, a company's culture has a significant impact on the effectiveness of lean manufacturing initiatives. Lean manufacturing demands an organization's leadership to influence the behavior and attitudes of their

employees. The human factors play a critical role in the effective implementation of a lean manufacturing strategy. This requires a systematic approach from the top-down that empowers people to ensure the effective adoption of lean manufacturing in an organization. Green manufacturing is just as important as mean manufacturing because both approaches focus on reducing waste and implementing environmentally friendly production techniques. There were no environmental considerations because of the lean manufacturing system's only focus on waste reduction. As a result, businesses began placing an emphasis on environmental safety. An ecologically friendly manufacturing method known as "green manufacturing" can be used to increase profitability while reducing negative impacts on human health and the environment [15]. When eco-innovation emerged in the 1990s, the concept of green manufacturing was born [9]. Environmental risk and other negative effects of production can be reduced by eco-innovation methods. Green manufacturing is a waste reduction strategy based on environmentally friendly and cost-effective processes, products, and materials [16]. Green manufacturing was defined by Mittal and Sangwan [17] as a strategy to improve the economy without hurting the environment. All activities that reduce waste are considered green production, according to Mohanty and Deshmukh [18]. To bridge the Lean-Green divide, [19] recommended aligning green and lean waste. Verrier et al. [20] proposed that combining lean waste and green trash could increase operational efficiency. Green wastes include GHG (greenhouse gas emissions), eutrophication, overconsumption of natural resources, and pollution, according to the report's authors. Both lean and green approaches have established similar targets for reducing non-value-added commodities and improving operational performance. According to [14], Lean and Green is referred to as the lean environment rather than the green environment, which is incorrect. Lean manufacturing and green manufacturing are significant tools for increasing production efficiency and global competition, and they demonstrate a strong commitment to waste-free practices. When it comes to improving operational and environmental outcomes, both green manufacturing and lean manufacturing have a lot in common [21]. Green manufacturing has a positive impact and generates a synergy between environmental management and operational success. There is a strong correlation between Lean and Green in industrial businesses. The two methods complement each other and are mutually beneficial. Both lean and green manufacturing have the same goals, which are to improve performance, product quality, and time to minimize operation and to provide value for stakeholders. As a result, the manufacturing system's Lean-Green link is formed [2]. According to the study, lean manufacturing is focused on reducing costs while green manufacturing is focused on reducing environmental risks. This shows a symbiotic relationship between the two systems.

3.1 Green and Lean Integration

According to the study, there is a strong connection between green and lean principles [22]. According to the research, combining green and lean projects has significant

synergistic impacts [21]. In light of the natural synergy between green and lean because they complement each other, it makes sense for businesses to implement strategic initiatives such as changing company culture and implementing continuous improvement and waste elimination as well as resource optimization to achieve the desired result [23]. As a result of this integration, the environmental impact of the production process is minimized to the greatest extent. As a result of initiatives like value stream mapping and Kaizen events, a new approach of controlling industrial operations is adopted. Lean and Green practices can be combined to manage supply chains, according to [24], for example. Lean and green approaches may be combined into a single model to improve energy flow in production environments. To find any flaws, [14] uses Six Sigma to examine the link between the green and lean paradigms. Green and lean practices have generated encouraging results, but organizations with limited resources might benefit from incorporating them. According to Garza-Reyes, there are a number of drawbacks to integrating a green and lean approach (2015). Johansson and Winroth [25], stated that an understanding of the relationship between green and lean methods is needed. The assessment approach of [26] is likely to help resolve this issue (Fig. 2).

The literature review analysis of lean and green manufacturing systems can be diagrammatically represented as shown in the Fig. 3:

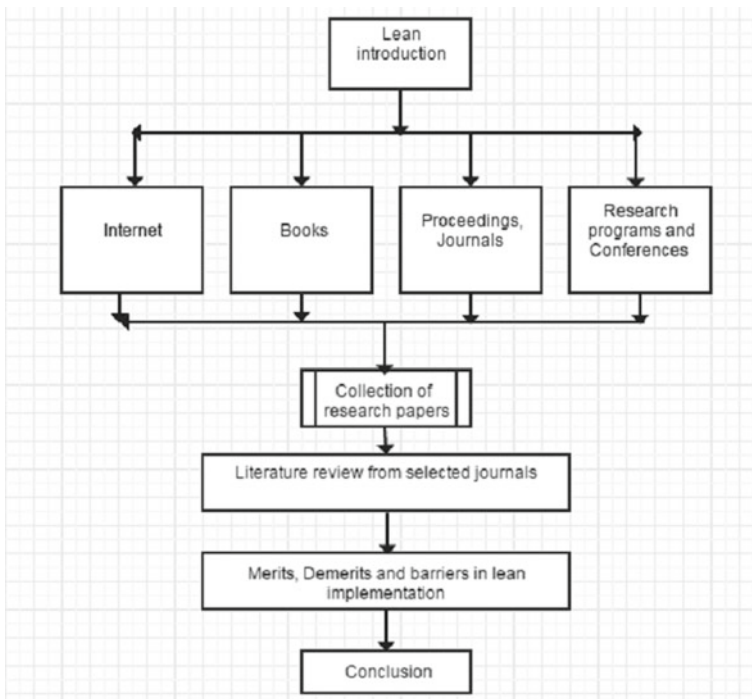
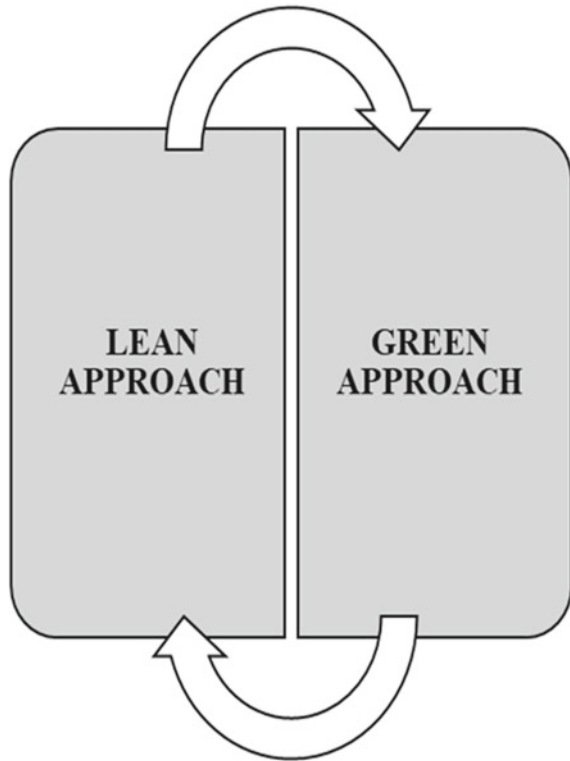


Fig. 2 Lean and green manufacturing cycle for collected literature review

Fig. 3 Relationship between lean and green approaches



4 Lean and Green Maturity Model

Progress in performance enhancement methods has been made possible in part thanks to the Lean and Green Maturity models [27]. The Capability Maturity Model Integration (CMMI) is one of the best and most widely used models, which has five phases and serves as a framework for assessing an organization's deployment maturity. Manufacturing companies have a wide range of needs and approaches, and this model seeks to satisfy those differences. This concept has been incorporated into the Lean and Green strategy in order to improve the practical evaluation and deployment. Models of Lean and Green synergies are proposed based on the prior literature review. Lean and Green best practices improve the proposed maturity model (Fig. 4).

The Lean and Green maturity model suggests five levels which have been discussed below as follows:

Level 1, Initial: The organizations have limited understanding of Lean and Green issues and the knowledge that they both can co-exist. At this level, there is no supervision or controls regarding environmental indicators from the top management. The organization is not aware of the competitors move with regard to lean and green strategies.

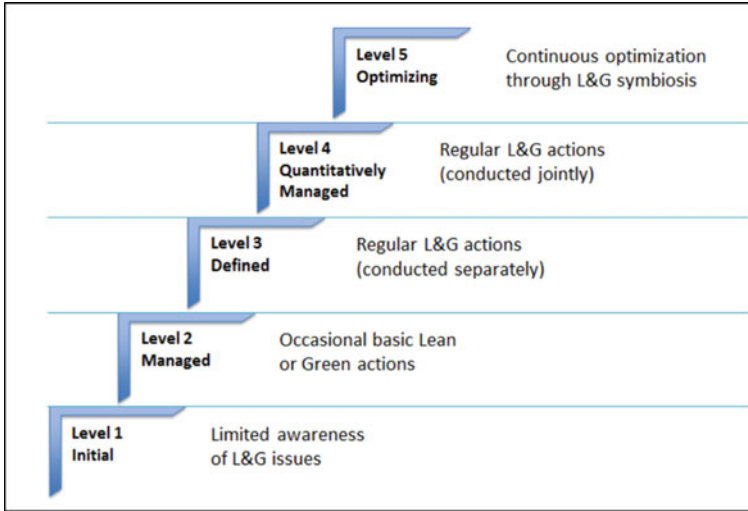


Fig. 4 Lean and Green maturity model (inputs taken from the model proposed by Verrier et al. [20])

Level 2, Managed: An organization's basic Lean or Green initiatives are carried out at level 2. There is a realization that the companies are losing money because of the amount of non-value-added waste that occurs. Major environmental indicators such as water use and trash output are managed at the organizational level. EPA Organizations shift their focus to managing production space at this level (5S). The organization recognizes that in order to succeed in today's competitive marketplace, Lean and Green practices must be adopted.

Level 3, Defined: Lean and Green environmental practices are implemented on a daily basis, and enterprises realize that they can offer value to the company. Top management is now compelled to implement modern lean and green techniques as soon as possible as a result of this new understanding. Organizations are making waste reduction their main goal. The most important environmental indicators are reduced at operational levels to serve as process-related indicators. The most important thing to the company's top executives is to improve the system. Internal communication on Lean and Green topics is limited, and monitoring is carried out. Continuous feedback is collected to determine the impact of lean and environmentally friendly activities.

Level 4, Quantitatively managed: Organizations at this level consider Lean and Green techniques essential to their growth. At this level, there is strong top-down and bottom-up management in place to guarantee that the action is quantified and monitored on a regular basis. Waste reduction is tracked to improve Lean and Green performance. Critical indicators are put up and monitored in accordance with those objectives in order to meet the company's demands. Employee meetings are organized on a regular basis to encourage involvement and request suggestions

for improvement. It is common practice to include workers in the process of improving the business.

Level 5, Optimizing: Lean and Green approaches come together at this last stage. Process improvement and waste reduction are mutually reinforcing at this level. The plan is developed in tandem with the lean and green initiatives. With an understanding of both good and negative repercussions of combining Lean with Green, the organization has taken steps to strengthen the positive ones. A proactive approach is taken by the organizations to ensure that they are always improving. An efficient Lean and Green strategy sustainability is achieved at this level. All Lean and Green strategies are closely monitored by the organization to ensure maximum advantages are realized at all levels. Lean and Green philosophy is fully implemented at this level of the organization.

5 Conclusion and Discussion

Lean and Green techniques appear to be challenging to implement in firms with a wide range of processes and specificities. The goal of this research is to make it easier for people to understand and put into practice Lean and eco-friendly practices by identifying the most effective methods (such as TPS and FPS). For lean and green initiatives to succeed, there must be a strong link between top-down and bottom-up management. To maximize formalization and deployment of Lean and Green in manufacturing businesses, a Lean and Green maturity model was developed, which analyzes the organization's philosophy at every level to promote the synergistic adoption of Lean and Green in manufacturing firms. A motivated workforce is important to achieving Lean and Green efficiency. Waste optimization, process orientation, staff involvement, and top management commitment and review were the main points of the study. Results can be evaluated on the basis of competition, strategic planning, and economic sustainability as a result of lean and green implementation. Everyone participating in the project has made it a priority to learn the fundamentals of lean and green. The integration of Lean and Green practices improves an organization's operational and environmental performance. This article discusses some of the barriers and challenges that lean and green implementation has to deal with. The organization's top-down dedication to Lean and Green adoption is largely responsible for its success. An influential theory, lean manufacturing, has also been discovered to be applied as a guiding principle in the manufacturing industry. Lean manufacturing is becoming more widely accepted as the most profitable method for both manufacturers and their customers. Lean techniques were addressed either explicitly or implicitly by academics for this study. As stated in the report, lean manufacturing is crucial in all areas of innovation, but the industry has yet to implement it. Incorporating lean and green practices can decrease waste, save money, limit excess production and inventory, remove delays, encourage systematization, raise staff dedication, and improve customer satisfaction. Businesses and their customers will be able to achieve better success with lean as its base. Using the lean and green maturity model conceptual,

it is possible to measure the performance effects of each lean and green practice. To improve our understanding of Lean and Green, further research is needed on the relationship between Lean tools and their impact on Green performance. An additional focus for future research might be the extension and adaptation of Lean and Green techniques to various phases of the product life cycle.

References

1. Dombrowski U, Mielke T (2013) Lean leadership—fundamental principles and their application. *Procedia cirp* 7:569–574
2. Bergmiller GG, McCright PR (2009) Parallel models for lean and green operations. In: *Proceedings of the 2009 industrial engineering research conference*, vol. 1, No. 1. The University of South Florida and Zero Waste Operations Research and Consulting, pp 22–26
3. Ramesh N, Ravi A (2017) Determinants of total employee involvement: a case study of a cutting tool company. *Int J Bus Excell* 11(2):221–240
4. Kumar R, Kumar V (2015) Lean manufacturing in Indian context: a survey. *Manag Sci Lett* 5(4):321–330
5. Wright C (2015) ShadowBox™: flexible training to impart the expert mindset. *Procedia Manuf* 3:1574–1579
6. Pettersen J (2009) Defining lean production: some conceptual and practical issues. *TQM J*
7. Maynard M (2013) How Eiji Toyoda created the modern version of Toyota <www.forbes.com/sites/MichelineMaynard/2013/09/17/how-Eiji-toyoda-created-the-modern-version-of-Toyota/>
8. Andrew (2012) Green manufacturing: what is it? [online] *Clean Technica*. Available at: <https://cleantechnica.com/2012/04/15/green-manufacturing/>
9. Sezen B, Cankaya SY (2013) Effects of green manufacturing and eco-innovation on sustainability performance. *Procedia Soc Behav Sci* 99:154–163
10. Nawaniir G, Lim KT, Othman SN, Adeleke AQ (2018) Developing and validating lean manufacturing constructs: an SEM approach. *Benchmarking Int J*
11. Rouse SV (2015) Reliability analysis of mechanical Turk data. *Comput Hum Behav* 43:304–307
12. Liker JK (2004) *Toyota way: 14 management principles from the world's greatest manufacturer*. McGraw-Hill Education
13. Simona U, Cristina D (2015) Review on Lean tools used in manufacturing process improvement (I). *Ovidius Univ Annals, Econ Sci Ser* 15(1):642–647
14. Garza-Reyes JA (2015) Lean and green—a systematic review of the state-of-the-art literature. *J Clean Prod* 102:18–29
15. Abdul-Rashid SH, Sakundarini N, Ghazilla RAR, Thurasamy R (2017) The impact of sustainable manufacturing practices on sustainability performance: empirical evidence from Malaysia. *Int J Oper Prod Manage*
16. Maruthi GD, Rashmi R (2015) Green manufacturing: It's tools and techniques that can be implemented in manufacturing sectors. *Mater Today Proc* 2(4–5):3350–3355
17. Mittal VK, Sangwan KS (2014) Prioritizing barriers to green manufacturing: environmental, social and economic perspectives. *Procedia Cirp* 17:559–564
18. Mohanty RP, Deshmukh SG (1998) Advanced manufacturing technology selection: a strategic model for learning and evaluation. *Int J Prod Econ* 55(3):295–307
19. Hines P (2009) *Lean and green. Source the Home of Lean Thinking*
20. Verrier B, Rose B, Caillaud E (2016) Lean and green strategy: the lean and green house and maturity deployment model. *J Clean Prod* 116:150–156
21. Galeazzo A, Furlan A, Vinelli A (2014) Lean and green in action: interdependencies and performance of pollution prevention projects. *J Clean Prod* 85:191–200

22. Ng R, Low JSC, Song B (2015) Integrating and implementing lean and green practices based on the proposition of Carbon-Value efficiency metric. *J Clean Prod* 95:242–255
23. Govindan K, Soleimani H, Kannan D (2015) Reverse logistics and closed-loop supply chain: a comprehensive review to explore the future. *Eur J Oper Res* 240(3):603–626
24. Mollenkopf D, Stolze H, Tate WL, Ueltschy M (2010) Green, lean, and global supply chains. *Int J Phys Distrib Logistics Manag*
25. Johansson G, Winroth M (2009) Lean versus green manufacturing: similarities and differences. In: *Proceedings of the 16th international annual EurOMA conference, implementation realizing operations management knowledge*. Göteborg, Sweden
26. Duarte S, Cruz-Machado V (2013) Modelling lean and green: a review from business models. *Int J Lean Six Sigma*
27. Estampe D, Lamouri S, Paris JL, Brahim-Djelloul S (2013) A framework for analyzing supply chain performance evaluation models. *Int J Prod Econ* 142(2):247–258

An Extensive Review Owing to the Influence of Surface Coating on the Technical Performance of Solar Cells



Gobinath Velu Kaliyannan, Rajasekar Rathanasamy, Santhosh Sivaraj, Moganapriya Chinnasamy, and Suganeswaran Kandasamy

Abstract Global energy consumption rate is getting higher and higher day by day due to industrialization, urbanization, increased population, etc. Hence, conventional non-renewable energy sources were been draining at faster rate due to excessive utilization. In the future, global energy needs might fully rely on the renewable energy sources. Solar energy is one among the renewable energy sources. Solar photovoltaic technology transforms solar energy into electrical energy by means of solar cells. Various photovoltaic cells were been engineered for obtaining stability and higher efficiency. But performance of solar cells was been hindered by various factors such as reflection, temperature, current–voltage, battery, and inverter efficiency. In this review article, we are focusing on reducing the reflection losses through the application of Anti-Reflection Coatings (ARCs) which may result in enhancing solar cell efficiency. ARCs through various deposition techniques were been discussed in this article. The most common coating technique preferred for ARC especially in the perspective of reducing reflectance is sputter deposition technique. Through this technique, a transparent coating can be achieved easily. In this technique, the material from the target is coated over the substrate in an inert gas environment, preferably argon. The operating pressure is quite low, and high-quality coated films can be achieved through this technique. This in turn reduces reflection losses and ensures better power conversion efficiency (PCE).

Keywords Renewable energy · Solar cell · Anti-reflection coatings (ARCs) · Thin films · Sputter coating · Power conversion efficiency

G. V. Kaliyannan · S. Kandasamy
Department of Mechatronics Engineering, Kongu Engineering College, Perundurai,
Tamilnadu 638060, India

R. Rathanasamy (✉) · S. Sivaraj · M. Chinnasamy
Department of Mechanical Engineering, Kongu Engineering College, Perundurai,
Tamilnadu 638060, India
e-mail: rajasekar.cr@gmail.com

M. Chinnasamy
Department of Mining Engineering, Indian Institute of Technology, Kharagpur, West
Bengal 721302, India

1 Introduction

With growing demands for electricity, the available energy sources could face a severe shortage in the upcoming decades. There is a necessity to opt for alternate sources of energy like solar energy, ocean, geothermal, biomass, and wind energy which cause no harm to the environment. Out of these, one of the most viable choices for energy generation is solar energy as it could support humanity for another billion years [1, 2].

The photovoltaic solar cell is a stationary and the least complicated device that makes use of the sun's energy to generate electricity. With the increasing price and demands, conventional fuels like coal and petroleum along with the alarming consequences to the environment need a much quicker implementation of these renewable sources. Silicon solar cell wafers tend to absorb the photons from the sunrays. The solar cells are doped with boron and germanium to produce the average PCE of 18%. Then electrical contacts are developed in solar cells. This consists of an emitter and junction as the functioning part of the cell. The emitters absorb the maximum amount of the light and create an electron-hole pair and also produce minority carriers into the junction.

The majority and minority carrier current differ based on the selection of semiconductor material such as intrinsic and extrinsic semiconductors. The p-type semiconductor has a large number of holes, while the n-type possess more number of electrons in the conduction band. The most commonly used Si solar cells are categorized mainly based on crystallinity such as amorphous and crystalline types. Based on the number of crystals, the crystalline solar cells are further classified into monocrystalline and polycrystalline cells. Polycrystalline type is preferred mostly, as it is economically suitable for larger utilization and easier adaptation for varying climatic conditions. The efficiency of this type is around 15% and can be analyzed based on the I-V characteristic curve of the cell. Recent advancements paved way for newer materials such as Copper Indium Gallium Selenides (CIGS), Copper indium sulfide (CuInS_2), Copper Zinc Tin Selenide (CZTSe), and Cadmium Telluride (CdTe) for solar cell preparation. Moreover, CuInS_2 solar cells can be produced by a non-conventional process like ink rolling.

1.1 Monocrystalline Solar Cell

Monocrystalline solar cell is generally a single-crystalline cell with pure silicon used for converting light energy to electrical energy. Figure 1a clearly displays the assembled structure of Monocrystalline solar cells.

The texturing is done to reduce incident light reflection and enhance light absorption. Soon after the formation of $p-n$ junction, metallization is done which is quite expensive process. Then, the metal contacts were prepared most commonly through

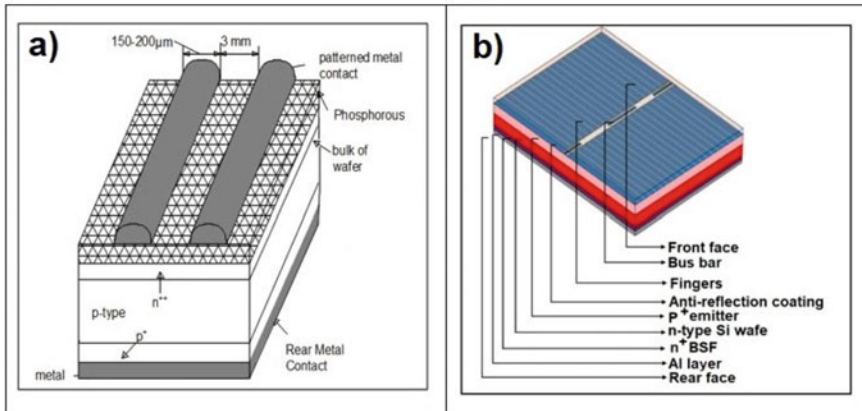


Fig. 1 a Monocrystalline silicon solar cell and b Structure of polycrystalline silicon solar cell

screen printing technique. The metal contact especially made of aluminum (Al) helps us to retrieve the generated electrons through bus bars and fingers.

1.2 Polycrystalline Solar Cell

Polycrystalline solar cells are generally composed of many smaller crystallites. The structure of polycrystalline silicon solar cell is shown in Fig. 1b. The silicon solar cell with boron-doped $p +$ type emitter mainly depends on Al_2O_3 surface passivation layer. The front surface emitter ($P +$) was developed in tube furnace by heating boron tribromide (BBr_3) to the diffusion temperature of $870\text{ }^\circ\text{C}$ along with optimal operating conditions. The prepared emitter is then passivized with Al_2O_3 layer deposited by means of Atomic Layer Deposition (ALD) technique. The back surface field (BSF) of phosphorus-doped $n +$ layer is obtained by diffusion of phosphorus oxychloride ($POCl_3$) at higher temperatures ranging from 800 to $900\text{ }^\circ\text{C}$. The silicon solar cell with screen printed metal strips of silver (Ag) paste on the front surface of solar cells called a bus bar is seen in the figure and while Al paste is applied to entire surface as back contact. Thin grid finger-like structures run perpendicular to the bus bar to improve the current conductivity of solar cell.

1.3 Anti-Reflection Coating (ARC)

The ARCs were been employed over the surface of solar cells especially for absorbing more amount of incident light. Light reflection is a major concern in solar cells which hinders the cell efficiency. In real time, reduced efficiency is mainly due to

the optical loss which leads to reduction in short-circuit current (I_{sc}). The optical losses could be minimized by using ARCs, light trapping, and surface texturing. Here, surface texturing involves roughening the surface which reduces the reflection to the surrounding air, as the texturing causes the light reflection to return onto the solar cell surface.

In ARC, the minimum reflectivity of the solar cell increases light absorbance, thereby increasing the PCE of the solar cell. The ARC can be distinguished as a single layer, double layer, and multi-layer ARCs depending on number of coating layers. In light trapping process, the optical path length which is a product of path length of light traveled and refractive index is much higher than the actual device thickness. This causes the un-absorbed photon to travel within the device for a longer time before it escapes the device. Generally, the significance of the ARC on the front surface of solar cell can vary based on the thickness of the coating and surface texturing. This cause effective trapping of the incident light by reducing the reflection rate. Other than conventional deposition techniques, the ARC depositions were also made on silicon solar cell by electrostatic attraction which reduces the reflection rate by 0.1%.

Based on the composition, ARCs could be classified as homogeneous and heterogeneous ARCs. Further on the fabrication methods, they are classified as conventional and unconventional ARC techniques. Conventional coating methods involve spin coating, dip coating, meniscus coating, glancing angle deposition, chemical vapor deposition, and etching. The etching process is categorized into wet etching (chemical, electrochemical) and dry etching. The unconventional method involves lithography, micro-replication technique, and miscellaneous techniques. Moreover, it has been said that double and triple-junction structures tend to increase conversion efficiency. An overview of the ARC materials incorporated over solar cell surface were been discussed in forthcoming sections.

2 Different Coating Techniques

Thin-film technology is booming day by day because of their lesser weight, better stability and good mechanical strength. Thin-film deposition technologies can be broadly classified into physical and chemical methods [3]. Figure 2 depicts the different types of thin-film coating techniques. The benefits and adaptability of thin films could be accomplished using reasonable practice for the precipitation formation. Generally, thin-film deposition techniques were preferred for coating anti-reflection films on the solar cell surface. During the chemical method of deposition, the liquid precursors enhance adherence of films with substrates [4, 5].

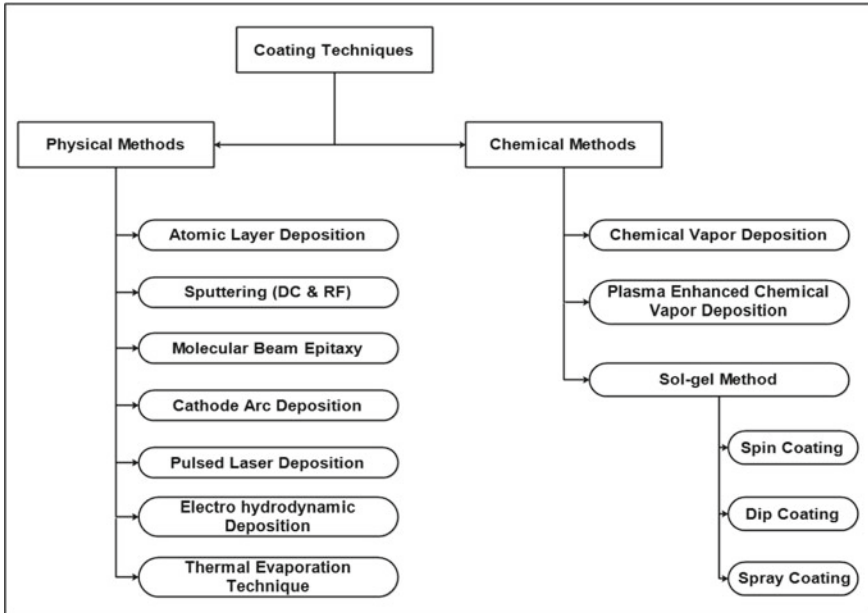


Fig. 2 Different types of thin-film coating techniques

2.1 Sputter Deposition

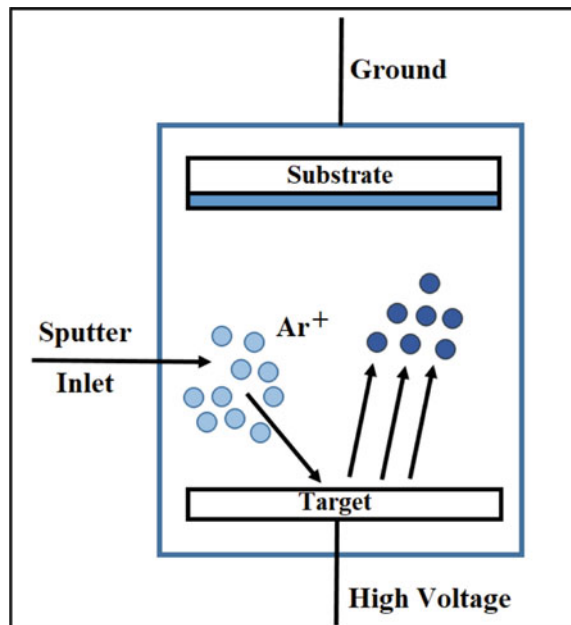
Out of these physical and chemical methods based on their uniform deposition rates, properties, and other necessary parameters, a suggestion is provided for sputter coating by considering their better deposition rate, minimum thickness, and higher anti-reflection rates [6, 7]. The target might be either in solid or powdered state which is the most convenient feature. Sputtering is one of the physical deposition processes, in which argon gas at a pressurized domain dislodges the particles from the objective material and then deposits it as a layer of thin film over the substrate. The objective material is held at low temperatures. The thickness of coated film will be in the range of some nanometers [8].

Sputtering is a method by which particles are ejected from a powerful target material and then gets deposited over the mounted substrate in the presence of gaseous atmosphere. In this operation, the critical disintegration of materials was in the particle form such as ions, atoms, or molecules. In photovoltaic technology, the coating materials with higher melting point temperatures can be easily coated through sputter deposition technique than other evaporation techniques. The major issue that hinders the photovoltaic performance of solar cell is higher reflectance which can be overcome through AR coating over cell surface. Thus, AR coatings might be effective with sputter deposition technique under optimal operating conditions. For instance, Copper Indium Gallium Selenide (CIGS) layer is used in acquiring the effectiveness of 18% by sputtering process.

Figure 3 depicts the sputtering deposition method. Sputtering is performed either with DC voltage (DC magnetron sputtering) or using AC voltage (RF sputtering). In DC sputtering, the voltage of 3–5 kV is set as a reference voltage and in RF sputtering, the control supply is set to the frequency of 14 MHz along with corresponding operating parameters results in deposition of ejected target materials. The most commonly used sputter deposition technique is magnetron sputter deposition technique. Here, DC diodes were just parallel plates controlled by a few kVA power supply in presence of working pressure ranges from 10 to 100 mTorr. The cathode is the negative plate from which the particles get disintegrated and then travel between the DC diodes resulting in deposition of cathodic particles over the affixed substrate material for developing thin films. DC diodes play an important role in sputter coating technique which regulates the coating process. The advancement of sputtering deposition technique was to replace the DC control supply with an RF supply for obtaining fine deposited thin films. This change wiped out the arcing issues of dielectrics that improved the deposition rates. There are different types of sputter deposition process. They are gas flow sputtering, magnetron sputtering, Ion-beam sputtering, High-target-utilization sputtering, Ion-assisted deposition, Reactive sputtering, and High-power impulse magnetron sputtering.

In this section, the basic working of various sputter deposition and their drawbacks which were noticed in recent years were been discussed. Now, a discussion is to be made on testing methods and characterization techniques that are undergone after the sputter deposition process.

Fig. 3 Sputter deposition technique



3 Results and Discussion

The deposited thin films through sputtering techniques were been examined through various characterization techniques. The characterization techniques help us to have a clear picture based on electrical, optical, structural, and chemical studies. The quality of deposited film, composition of film, surface topography, thickness of deposited films, grain size, surface roughness, resistivity of film, and grain development can be easily revealed through characterization techniques. Also, the inference of deposited films over the solar cell substrates can be evaluated through these techniques. The characterization techniques include X-Ray Diffraction (XRD), Atomic Force Microscope (AFM), Field Emission Scanning Electron Microscope (FE-SEM), High Resolution Transmission Electron Microscope (HR-TEM), X-ray Spectroscopy (XPS), and Four probe method for resistivity analysis. In addition to these, the optical properties are analyzed through UV–Vis spectrometry. The electrical properties like mobility, carrier density, and hall coefficients are estimated by hall effect estimation device, while electrical resistivity can be found through Four probe method.

3.1 XRD Analysis

X-Ray Diffraction(XRD) technique is one of the non-destructive evaluation techniques used to inspect and analyze the crystallinity of materials subjected to this inspection technique [9]. Thereby, chemical composition of the coated film material can be identified easily. The phases of various rudiments have to be studied such as crystalline and quantitative phases. These findings lead to the resolution of the characteristics of the substance. These are very much necessary as the property relies upon its crystal structure. Moreover, even if the cell is polycrystalline, the orientation of dopant concentration may be preferred over any of the axis. Diffraction is primarily based on the equation framed by Bragg. The average crystallite size of the crystal structures thus obtained can be determined using the Debye–Scherrer equation.

Gobinath VK et.al utilized ZnS-Al₂O₃ blends for ARC over Si cell through RF sputtering technique [10]. The average crystallite size of homogenous blended particles was 15.83 nm which then coated over Si cell delivers the photo current with maximum PCE of 19.38%. Sang-Hun Jeong et al. have experimented the ARC-coated SiO₂ and TiO₂ materials over the glass substrate through RF sputter coating. The XRD patterns reveal that in the room temperature, the bare silicon experiences maximum crystallinity than other heated Si substrates.

The novel AR material coated over Si cell substrate was subjected for chemical composition analysis through EDX and XRD technique which confirms the presence of crystalline phased ZnAl₂O₃ experimented by Gobinath et al. [10]. Khuram Ali et al. have opened up a field of AR coating of silicon cell through RF sputtering deposition. Here, the SiO₂ and SiO₂/TiO₂ sputter coated over p-type Si solar cell were subjected to EDX and XRD techniques. From EDX analysis, the individual

constituents were appear as peaks and the diffraction patterns reveal the level of crystallinity of coated material.

3.2 SEM Analysis

Surface morphology of coated solar cell specimen is investigated through Field Emission Transmission Electron Microscope (FE-SEM) analysis. Rahmane et al. [11] reported about transparent conductive oxides (TCO) of polycrystalline Si cells. AZO films were efficiently developed by the RF magnetron sputtering method at room temperature on glass and silicon substrates. Figure 4 demonstrates the structural characterization of ZnO thin films deposited with different thickness such as 20 nm (a), 80 nm (b), 265 nm (c), 755 nm (d), and 1500 nm (e) at room temperature using SEM analysis. The analysis shows that the surface morphological characteristics of coated films are void-free and display a tightly packed structure with uniform particle size. It is noted that surface morphology of film differs with film thickness. The films are in thick granular structure, except for the 20 nm thick sample that occurs as smooth surface. The volume of grain on film surface increases with increase in density of coated film.

3.3 Current–Voltage Analysis

Current–Voltage (I–V) characteristic curve is plotted with current density against the corresponding voltage obtained. From the I–V characteristics, the ability of solar cell to generate electricity from the sun light can be clearly represented. Current–Voltage (I–V) characteristics are studied through Keithley 2450 source meter for solar cells [12, 13]. It is seen that the increase in ARC thickness may increase or decrease the I_{sc} of coated cell as compared with uncoated solar cell. But the increased I_{sc} obtained with optimal AR coating thickness which varies from material to material results in enhanced photovoltaic performance of solar cell. Beyond the optimal coating thickness, due to the hindrance of light penetration into the cell, there occurs a decrease in photovoltaic performance than actual uncoated cell. But I_{sc} and open circuit voltage have direct influence on overall photovoltaic performance.

Table. 1 and Fig. 5 clearly show that for the simple Si solar cell, PCE is very low due to the increased reflectance and lower refractive index. I–V characteristics for silicon solar cell with single layer (with SiO_2) and double layer (with SiO_2 and TiO_2) as their anti-reflective coating are studied. From the obtained results, it is been clear that AR-coated solar cell possess lower reflectance; hence, power generation is increased. Also, the increase in the AR-coated layers here seemed to be consistent increase in transmittance [15]. The solar cells' current and voltage characteristics with Single Layer Anti-Reflective (SLAR) and Double Layer Anti-Reflective (DLAR) coatings were shown in Fig. 5. From the figure, it was clear that when the solar cells are

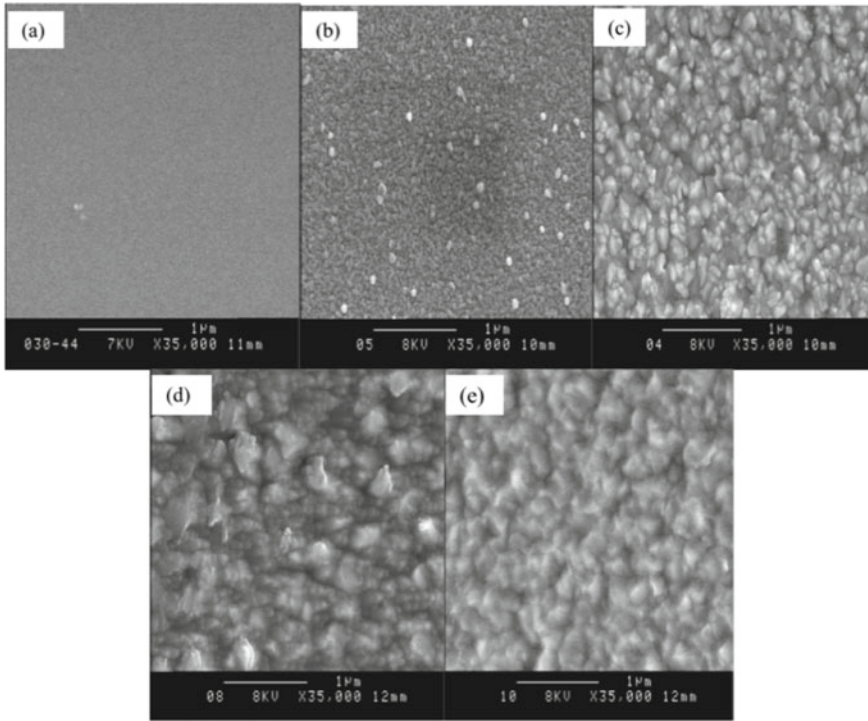


Fig. 4 FE-SEM pictures of ZnO thin film deposited at different thicknesses: **a** 20 nm, **b** 80 nm, **c** 265 nm, **d** 755 nm, and **e**1500 nm [11]

Table 1 I–V characteristics of coated and uncoated solar cell [14]

S. No	Samples	V_{oc} (V)	I_{sc} (A)	Fill Factor	Efficiency η (%)
1	Pure cell	0.441	0.00924	0.69	2.8
2	Single layer ARC	0.504	0.01235	0.72	4.5
3	Double layer ARC	0.520	0.01613	0.75	6.2

characterized under 100 mW/cm^2 illumination condition. The short-circuit current was increased up to 6.9 mA/cm^2 when compared with Si solar cell.

4 Areas to Focus in Future Works

The areas that have to be improved in sputtering are the pressure levels and adhesion property of coatings with the non-conducting substrate like glass. It takes hours to create a high vacuum in the sputtering chamber. This would be beneficial only if an

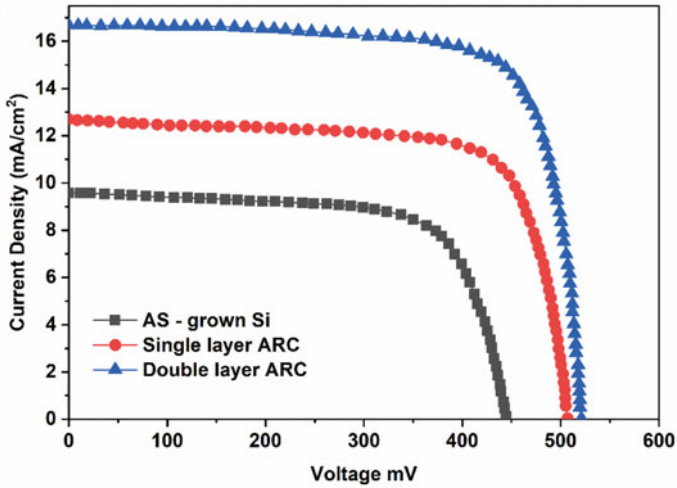


Fig. 5 I-V characteristics of SLAR and DLAR coatings with the as-grown silicon solar cell [14]

alternate gas for argon which assists the sputter deposition at much lower pressure. Moreover, the coating chamber with the target and substrate seemed to be small.

This is because only much smaller substrates are coated using this process. Hence, it is used only for research purposes and is difficult for bringing it into commercialization. Some materials remain unused, even if they possess anti-reflection property because of the working pressure, not compatible with this technique and other environmental conditions required in this process. Thus, if these common problems were solved in the near future, then it would be beneficial for the researchers especially for efficiency enhancement of commercial Si cells in large scale through this technique.

5 Conclusion

As suggestion is made for the sputter deposition technique compared to other deposition methods for the preparation of thin-film solar cells. The sputter deposition technique is preferred especially for obtaining uniform thin films, even for the materials having higher melting point temperatures. This is not possible in evaporation-based deposition techniques. The efficiency is calculated using the I-V characteristics curve, and the surface morphology is studied using XRD, FE-SEM, UV-Vis spectroscopy, and AFM. The morphological studies of coated surface reveal grain growth, thickness of coated layer, and composition of target materials. The efficiency of cell internally depends on the thickness of coated film. The results revealed that the overall PCE of the thin-film solar cell can be enhanced 18 to 22% at the maximum. In the present study, different materials with better anti-reflection property such as CaTiO_3 ,

TiO₂, ZnO, Al: ZnO, SiO₂, and their deposition methods are reviewed. Thus, sputter deposition technique can probably preferred at most of times as coating strength is independent of melting point temperature of coating materials. Also, sputter deposition technique for the thin-film coatings on surface of solar cell seemed to be more economical than other deposition techniques.

References

1. Khattak YH, Baig F, Toura H, Beg S, Soucase BM (2019) Efficiency enhancement of Cu 2 BaSnS 4 experimental thin-film solar cell by device modeling. *J Mater Sci* 54(24):14787–14796
2. Kaliyannan GV, Palanisamy SV, Rathanasamy R, Palanisamy M, Palaniappan SK, Chinnasamy M (2020) Influence of ultrathin gahnite anti-reflection coating on the power conversion efficiency of polycrystalline silicon solar cell. *J Mater Sci Mater Electron* 31(3):2308–2319
3. Bouhafs D, Moussi A, Chikouche A, Ruiz J (1998) Design and simulation of antireflection coating systems for optoelectronic devices: application to silicon solar cells. *Sol Energy Mater Sol Cells* 52(1–2):79–93
4. Jaganathan SK, Mani MP, Ayyar M, Rathanasamy R (2019) Biomimetic electrospun polyurethane matrix composites with tailor made properties for bone tissue engineering scaffolds. *Polym Test* 78:105955
5. Nayak GC, Sahoo S, Rajasekar R, Das CK (2012) Novel approach for the selective dispersion of MWCNTs in the Nylon/SAN blend system. *Compos A Appl Sci Manuf* 43(8):1242–1251
6. Rajasekar R, Nayak G, Malas A, Das C (2012) Development of compatibilized SBR and EPR nanocomposites containing dual filler system. *Mater Des* 35:878–885
7. Ayyar M, Mani MP, Jaganathan SK, Rathanasamy R (2018) Preparation, characterization and blood compatibility assessment of a novel electrospun nanocomposite comprising polyurethane and ayurvedic-indhulekha oil for tissue engineering applications. *Biomed Eng/Biomed Tech* 63(3):245–253 (2018)
8. Gruber D, Ponath N, Müller J, Lindstaedt F (2005) Sputter-deposited ultra-low catalyst loadings for PEM fuel cells. *J Power Sources* 150:67–72
9. Gobinath V, Rajasekar R, Moganapriya C, Sri AM, Raja G, Kumar PS, Jaganathan S (2021) Surface engineering of zinc sulphide film for augmenting the performance of polycrystalline silicon solar cells. *Chalcogenide Lett* 18(7)
10. Kaliyannan GV, Palanisamy SV, Rathanasamy R, Palanisamy M, Nagarajan N, Sivaraj S, Anbupalani MS (2020) An extended approach on power conversion efficiency enhancement through deposition of ZnS-Al 2 S 3 blends on silicon solar cells. *J Electron Mater* 49(10):5937–5946
11. Rahmane S, Aida MS, Djouadi MA, Barreau N (2015) Effects of thickness variation on properties of ZnO: Al thin films grown by RF magnetron sputtering deposition. *Superlattices Microstruc* 79:148–155
12. Kaliyannan GV, Palanisamy SV, Palanisamy M, Chinnasamy M, Somasundaram S, Nagarajan N, Rathanasamy R (2019) Utilization of 2D gahnite nanosheets as highly conductive, transparent and light trapping front contact for silicon solar cells. *Appl Nanosci* 7:1427–1437
13. Kaliyannan GV, Palanisamy SV, Palanisamy M, Subramanian M, Paramasivam P, Rathanasamy R (2019) Development of sol-gel derived gahnite anti-reflection coating for augmenting the power conversion efficiency of polycrystalline silicon solar cells. *Mater Sci-Pol* 37(3):465–472
14. Ali K, Khan SA, Jafri MM (2014) Effect of double layer (SiO₂/TiO₂) anti-reflective coating on silicon solar cells. *Int J Electrochem Sci* 9(12):7865–7874
15. Santhosh S, Rajasekar R, Gobinath V, Moganapriya C, Arun Kumar S, Manju Sri A (2021) Influence of electrospayed MoSe₂ antireflective surface coatings on performance of multicrystalline silicon solar cell. *Silicon* 1–13

First Principle Investigations of $\text{AgBr}_{1-x}\text{I}_x$ Ternary Alloys



Neha Munjal, Barun Dhanna, P. Padmakumar, and Pavas

Abstract In the current research article, by using density functional theory (DFT) the structural parameters of $\text{AgBr}_{1-x}\text{I}_x$ where x is concentration of doping at 0.0, 0.25, 0.50, 0.75, and 1.0 ternary alloy compound been systematically accomplished. The doping of iodine (I) in AgBr causes the decrease in bulk modulus and increase in lattice constant. The result is compared with Vegard's law which is in good agreement with the previous investigation.

Keywords First principle study · LCAO · Lattice constant · Bulk modulus · Elastic properties

1 Introduction

The work is about to solve many body problem which is observed in first-level approximation which make it much simpler but still too difficult to solve. Several methods are applied to make it simpler with more accuracy and one of historic method that was used is Hartree–Fock method (HF) but for solids it is not that much accurate and still it is plausible to apply it in quantum chemistry. Method other than this method which is used and gives much accurate result is APW method, LAPW method, and PAW method. The density functional theory (DFT) which is more powerful method is used and gives probably more accurate results, and here, DFT method is used through CRYSTAL software in which KH equation is inbuilt and is used to calculate the lattice constant and bulk modulus by coding and we get the data. It is observed that Vegard's law for lattice constant goes with the data that is observed in this research work with only little variation. In this research work, rock salt of silver halide is being used with different concentration of iodine in it, $\text{AgBr}_{1-x}\text{I}_x$, where x represents the concentration of iodine in silver bromide at different concentration of doping of iodine in AgBr, silver halide is taken into consideration because it shows some photographic process.

N. Munjal (✉) · B. Dhanna · P. Padmakumar · Pavas
Lovely Professional University, Phagwara, Punjab PIN-144411, India
e-mail: neha.18869@lpu.co.in

The reason of choosing silver halide over which this research work is done because its structural property is important to study because silver halides are sensitive toward light; due to this reason, it is used in photographic process, it is also been used as electrolyte and also as liquid semiconductors [1–3]. Under the normal atmospheric condition, it is observed experimentally that structure of silver bromide is B1 structure which is face-centered cubic. To calculate the elastic properties, structural properties, and optical properties of silver halide, many theoretical and experimental results are being observed, also for the intermediate structure at different doping concentrations such as that of $\text{AgBr}_{1-x}\text{I}_x$ where x represents the concentration doping at 0%, 25%, 50%, 75%, and 100% [4–11]. By using both EXAFS and single crystal X-ray diffraction, the local structural of B1 phase of $\text{AgBr}_{1-x}\text{I}_x$ solid solution is known to best knowledge; no theoretical work was done previously so far as is done experimentally by Yoshioka et al. [11]. Full—potential linear muffin—tin orbital method is used for density of state of $\text{AgBr}_{1-x}\text{I}_x$ alloy and presently in this research paper structural properties of $\text{AgBr}_{1-x}\text{I}_x$ alloy such as bulk modulus and lattice constant at various concentration of Iodine in silver bromide in B1 structure (face-centered) are investigated thoroughly. On using data of lattice constant and bulk modulus, elastic properties of these ternary alloys such as elastic properties, Young's modulus, Poisson's ratio, and shear modulus are all reported for the B1 (face-centered cubic) structure of silver halide alloys and also for the intermediate alloys which is observed at different concentration of iodine doped in given structure of silver bromide. Many optical properties such as refractive index, absorption coefficient, optical conductivity, dielectric functions, and optical reflectivity in terms of incident photon energy up to 13.5 eV are calculated by using the density functional theory, and the results that are observed are same as that of theoretical and experimental results.

Ab-initio calculation of optoelectronic and structural properties of silver halide is calculated by theoretical study. In this approach, total local density approximation (LDA) and generalized gradient approximation (GGA) are being used as exchange correlation potential. Total energy allowed to investigate several structural properties and these results which are obtained by this computational solving of many body program give the same results as is being observed experimentally or theoretically. It is observed by using first principle investigation of silver halide ternary alloy that by increasing concentration of iodine in silver bromide there is increase in lattice constant and increase in bulk modulus. The magnesium-based biodegradable alloys are very efficient to design the orthopedic inserts. Electric discharge machining (EDM) has been used efficiently in a wide manner to fabricate in such an accurate way along with in-situ surface modification technique to produce nanohydroxyparticle coating on the alloy biomaterial. This is very time and cost-effective method [12]. During the development of material science and technology, composite materials have secured a leading place. Those materials have several industrial applications in so many fields like bio-medical, aerospace, automotive, sports, etc. Those materials can be characterized in three categories that is based on matrix phase, based on reinforcement, and based on scale. Different studies have been carried out to study composite material structure and properties. Although many composite materials have been taken into the research, but biodegradable composite materials have a special acceptance because of their eco-friendly nature [13]. For the

efficient transportation, cooling of the car engine is much more needed. Two-layer nano-particle-enhanced phase change materials have been used to achieve this [14].

2 Materials and Method

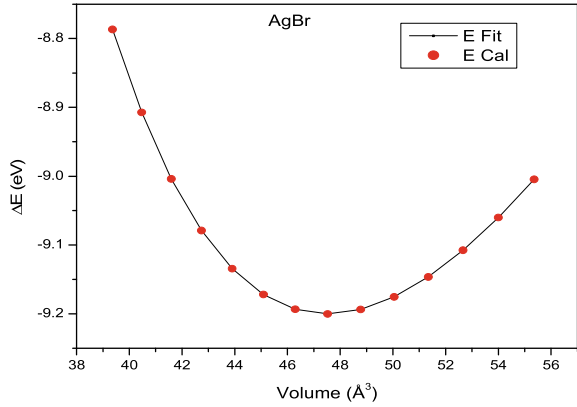
2.1 FGM Material Models

In present calculation, the first principle Linear Combination of Atomic Orbitals (LCAO) method has been applied for determination of structural parameters of $\text{AgBr}_{1-x}\text{I}_x$ ternary alloy, where x is the doping concentration and is taken at 0%, 25%, 50%, and 75%, respectively. This method has proved the effective results of many semiconductors compound [15–21]. The coding for the calculation has been done by performing KH equation which is inbuilt on CRYSTAL software, on doping silver bromide (AgBr) with iodine (I), and on increasing the doping concentration, there is increase in lattice constant for a unit cell formed after doping and there is decrease in bulk modulus of alloy which is being observed. Optimization of the energy values with unit cell volume of crystal has been performed to calculate the lattice parameters. The reading had taken at the minimum energy value where the unit cell is perfectly stable. The values of bulk modulus have been studied with utilization of Birch–Mrughman equation. Mathematically, this equation states that

$$E(V) = E_0 + \frac{9V_0B_0}{16} \left\{ \left[\left(\frac{V_0}{V} \right)^{\frac{2}{3}} - 1 \right]^3 B'_0 + \left[\left(\frac{V_0}{V} \right) - 1 \right]^2 \left[6 - 4 \left(\frac{V_0}{V} \right)^{\frac{2}{3}} \right] \right\}$$

where $E(V)$ represents the energy corresponding to particular volume, here E_0 as equilibrium energy, bulk modulus (B_0), and equilibrium volume (V_0). The calculations were comparable with results which theoretically being observed. This Birch–Mrughman equation gives us the relation between energy at different volume of unit cell, the equation which is used above is useful in finding the lattice constant, and this corresponding lattice constant is calculated when we observe the graph with the minima of the graph have volume of unit cell and corresponding energy that we get is the lowest energy which shows that at the minima of graph we get the unit cell with minimum energy which is more stable among them, and KH equation is being used to calculate the bulk modulus (B_0) which is put in above equation and for different volume of unit cell which is formed as intermediate we observed the corresponding value of energy of that particular intermediate unit cell at particular doping level of iodine in silver bromide which exactly overlaps the E fit graph which is for silver halide semiconductors by using the origin software. And Vegard's law also has the same results for the intermediate results of different concentration of iodine in silver bromide, and it is to be noted that Vegard's law is only for intermediate states and graph shows the same match for Vegard's laws which show that this method of finding

Fig. 1 Energy(eV) versus volume plot for AgBr



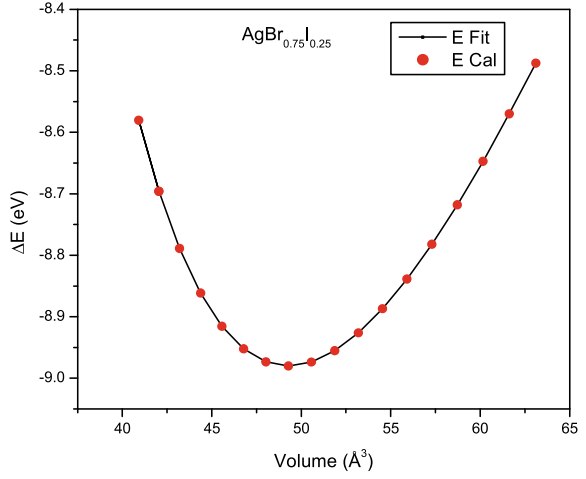
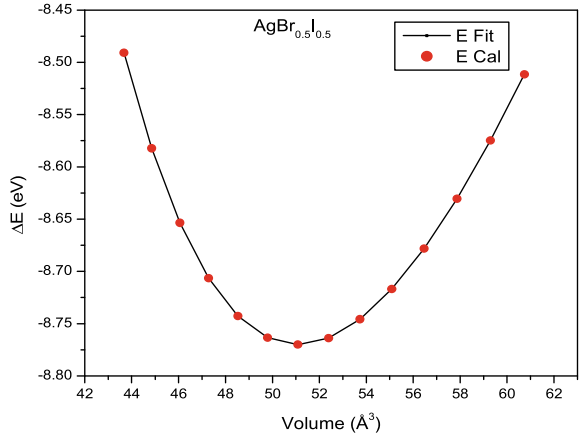
lattice constant gives the much accurate results as it follows this law. By changing concentration of doping of iodine in silver halide, there is increase in lattice constant and decrease in bulk modulus as is observed in the table given below.

3 Results and Discussion

The elastic constant is important to measure the stability and stiffness of material which is formed during process and at different doping concentration of iodine in silver bromide elastic constant C_{11} , C_{12} , and C_{44} is shown in table shown below calculated elastic constants C_{ij} (GPa), bulk modulus B (GPa), Voigt shear modulus G_V (GPa), Reuss shear modulus G_R (GPa), Hill shear modulus G_H (GPa), Young’s modulus E (GPa), Poisson’s ratio ν , and anisotropy factor A (Table 1 and Figs. 1, 2, 3, 4, 5, 6, 7).

	AgBr	AgBr _{0.75} I _{0.25}	AgBr _{0.5} I _{0.5}	AgBr _{0.25} I _{0.75}	AgI
C_{11}	91.676	90.23	88.97	87.53	86.253
C_{12}	32.179	31.02	29.98	28.34	27.892
C_{44}	6.674	7.84	8.89	9.43	10.498
B	52.011	50.75	49.64	48.07	47.34
G_V	15.90	16.54	17.13	17.49	17.97
G_R	9.67	11.105	12.337	12.963	14.112
G_H	12.785	13.845	14.73	15.22	16.041
ν	11,012.25	10,344.39	9774.81	9069.17	8688.45
E	35.45	38.072	40.212	41.301	43.239
A	0.224	0.264	0.301	0.318	0.359

where,

Fig. 2 Energy(eV) versus volume for $\text{AgBr}_{0.75}\text{I}_{0.25}$ **Fig. 3** Energy(eV) versus volume plot for $\text{AgBr}_{0.5}\text{I}_{0.5}$ 

$$G_H = (G_V + G_R)/2. \quad (2)$$

$$B = (C_{11} + 2C_{12})/3 \quad (3)$$

$$E = 9BG_H/(G_H + 3B) \quad (4)$$

$$G_V = (C_{11} - C_{12} + 3C_{44})/5 \quad (5)$$

Fig. 4 Energy versus(eV) volume plot for AgBr_{0.25}I_{0.75}

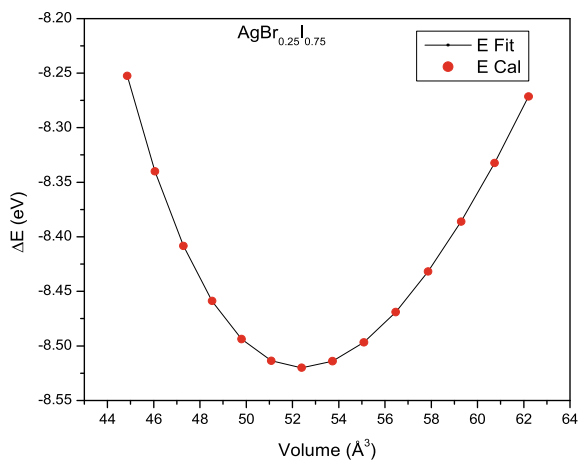


Fig. 5 Energy(eV) versus volume diagram plot AgI

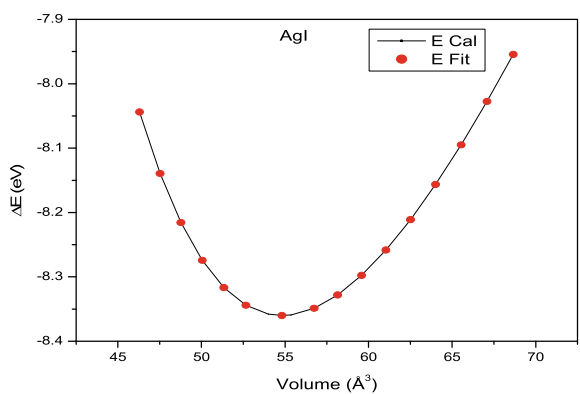


Fig. 6 Bulk modulus (GPa) and concentration (x)

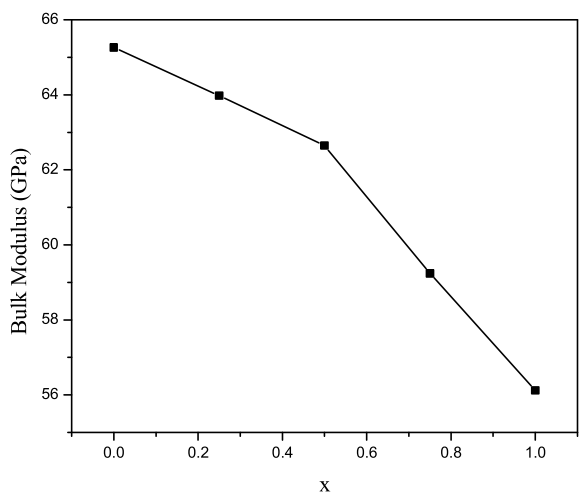


Fig. 7 Lattice constant(10–10 m) and concentration(x) plot

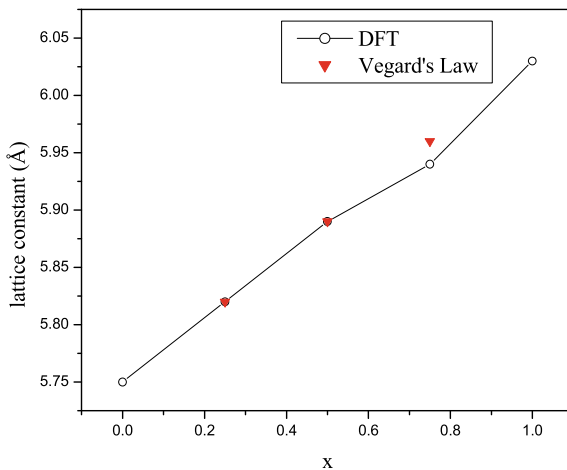


Table 1 Presented and other values of the silver halide compounds

X Concentration (%)		a (Å)			B (GPa)		Vegards law (Å)
		This work	Expt	Other cal	This work	Other cal	
0	AgBr	5.75	5.75 ^a	5.58 ^c	65.26	63.499 ^g	
25	AgBr _{0.75} I _{0.25}	5.82	5.815 ^l		63.98		5.82
50	AgBr _{0.5} I _{0.5}	5.89	6.034 ^b	6.169 ^m	62.65		5.89
75	AgBr _{0.25} I _{0.75}	5.94	6.034 ^b	6.169 ^m	59.24		5.96
100	AgI	6.03	6.034 ^b	6.169 ^m	56.12		

^a Ref. [Cain (1977)]

^b Ref. [Hamilton (1988)]

^c Ref. [Weber (1976)]

^g Ref. [Benmessabih et al. (2007)]

^l Ref. [Yoshiasa et al. (1986)]

^mRef. [Mellander (1982)]

$$\nu = (3B - 2G_H)/2(3B + G_H) \quad (6)$$

$$G_R = (5C_{44}(C_{11}-C_{12}))/4(C_{44} + 3(C_{11}-C_{12})) \quad (7)$$

$$A = 2C_{44}/(C_{11}-C_{12}) \quad (8)$$

4 Conclusion

It is concluded that as the concentration x varies from 0 to 100%, the lattice constant changes from 5.75 to 6.03. With doping concentration, the bulk modulus decreases from 65.26 to 56.12 GPA. It is observed that there is increase in lattice constant and decrease in bulk modulus. The Vegard's law exactly fits for $x = 0.25, 0.50$, and small deviation is observed at concentration of 75%. The calculated values are in good agreement with theoretical and experimental results.

References

1. Hamilton JF (1988) The silver halide photographic process. *Adv Phys* 37:359
2. Mellander BE (1982) Electrical conductivity and activation volume of the solid electrolyte phase α -AgI and the high-pressure phase fcc AgI. *Phys Rev B* 26:5886
3. Hull S, Keen D (1999) Pressure-induced phase transitions in AgCl, AgBr, and AgI. *Phys Rev B* 59:750
4. Cain L (1977) The elastic constants and their temperature and pressure derivatives of AgBr-AgCl mixed crystals. *Phys Chem Solids* 38:73
5. Weber J (1976) Indirect near edge emission in pure AgBr. *Phys Status Sol (b)*, 78:699
6. Li Y, Zhang L, Cui T, Ma Y, Zou G, Klug D (2006) Phonon instabilities in rocksalt AgCl and AgBr under pressure studied within density functional theory. *Phys Rev B* 74:054102
7. Amrani BT, Hassan B, Hamdache FEH, F. and Zoaeter M (2007) Computational study of AgCl and AgBr semiconductors. *Phys B Condens Matter* 392:309
8. Bootz B, Von Der Osten, Uhle N (1974) Long wavelength optical phonons of $\text{AgBr}_x\text{Cl}_{1-x}$ mixed crystals. *Phys Status Solidi (b)*, 66:169
9. Fujii A, Stolz H, Von W, Osten J (1983) Excitons and phonons in mixed silver halides studied by resonant Raman scattering. *Phys C Solid State Phys* 16:1713
10. Rekab-Djabri H, Louhibi-Fasla S, Amari S, Bahlouli S, Elchikh E (2017) Structural and electronic properties of $\text{Cu}_x\text{Ag}_{1-x}\text{Cl}$: first-principles study. *Phys J Plus* 132:471
11. Koto YK, Emura S, Kanamaru F (1986) *J Phys Coll* 47:C8
12. Prakash C, Singh S, Pabla BS, Uddin MS (2018) Synthesis, characterization, corrosion and bioactivity investigation of nano-HA coating deposited on biodegradable Mg-Zn-Mn alloy. *Surf Coat Technol* 346:9–18
13. Rajak DK, Pagar DD, Kumar R, Pruncu CI (2019) Recent progress of reinforcement materials: a comprehensive overview of composite materials. *J Market Res* 8(6):6354–6374
14. Jilte R, Afzal A, Panchal S (2021) A novel battery thermal management system using nano-enhanced phase change materials. *Energy* 219:119564
15. Majumdar AD et al (2020) Investigation of structural and electronic properties of BaX ($X = \text{S, Se, and Te}$): a DFT Study. *Adv Mater Sci Eng*. Springer, Singapore, pp 281–289
16. Majumdar AD, Gopal R, Munjal N (2020) Structural and electronic properties of III-nitride semiconductor alloys: a first principle study. *Eur J Mol Clin Med* 7(7):3475–3480
17. Munjal N, Majumdar AD, Kamboj U, Kumar A (2020) Structural properties of scandium chalcogenides via first principle calculations. *J Phys Conf Ser* 1531(1):(2020)
18. Munjal N (2019) A first principle study of structural and electronic properties of INN and BN. *J Gujarat Res Soc* 21(6):660–664
19. Munjal N, Bhambhani P, Sharma G, Vyas V, Sharma BK (2012) Study of phase transition and cohesive energy in MgO. *J Phys Conf Ser* 377(1), IOP Publishing

20. Kumar R, Munjal N, Sharma G, Vyas V, Dhaka MS, Sharma BK (2012) Electron momentum density and phase transition in SrO. *Phase Transitions* 85(12):1098–1108
21. Majumdar AD, Munjal N (2022) High-pressure structural phase transition of Alkali hydride compounds: an ab initio study. In: *Advanced functional materials and devices*. Springer, Singapore, pp 139–148

Phycoremediation of Dairy Wastewater and Biodiesel Production Using Mairne Microalgae *Tetraselmis Indica*



Amit, Uttam Kumar Ghosh, Rahul Gautam, Amit Jaiswal,
and Siddhartha Pandey

Abstract The aspire to carry out this study is Phycoremediation of dairy wastewater for microalgal biomass production to attain the clean and renewable biofuel production and simultaneous removal of nutrients (micronutrient and macronutrients) from dairy wastewater. The microalgae *T. indica* reported to reduce nitrate, phosphate and ammoniacal nitrogen in 72.7%, 63.97% and 78.96% respectively in dairy wastewater. The corresponding value for *T. indica* biomass in terms of productivity was 0.032 g L⁻¹ d⁻¹ in 50% of dairy wastewater. After remediation of dairy wastewater, lipids were extracted from the microalgal cells using modified Bligh and Dyer methods. The FAME (Fatty acids methyl ester) analysis substantiate the such as pentadecylic acid, palmitic acid, oleic acid, linoleic acid and eicosanoic acid in *T. indica* biomass. This study expresses and confirms the role of microalgae, *T. indica* for biomass production for clean and sustainable biodiesel production through algal biomass and removal of nutrients.

Keywords Biomass · Dairy wastewater · Lipid productivity · Biodiesel production

Amit (✉) · U. K. Ghosh · R. Gautam
Department of Polymer and Process Engineering, Indian Institute of Technology, Roorkee, India
e-mail: amit@pe.iitr.ac.in

A. Jaiswal
School of Food Science and Environmental Health, College of Sciences and Health,
Technological University Dublin, City Campus, Grangegorman, Dublin 7, Ireland

Environmental Sustainability and Health Institute, Technological University Dublin, City
Campus, Grangegorman, Dublin 7, Ireland

S. Pandey
Department of Operations Management, Indian Institute of Management, Ranchi,
Jharkhand, India

Division of Research and Innovation, Uttaranchal University, Dehradun, India

1 Introduction

Currently, fossil fuels has major stake in the total energy production and account for roughly 80% energy worldwide. This has lead to fill serious environmental issues like Green House Gas Emissions, climate change, increased CO₂ concentration, related health concerns etc. [1, 2]. Thus, Carbon neutral energy sources are sought. Biofuels are the most valuable in global energy arrangement, and expected to play and contribute significantly in future. Biodiesel, perhaps the most regularly utilized biofuel, is perceived as an optimal recyclable energy transporter, and consequently as an essential primary energy source [3]. Marketable biodiesel is now made from waste frying oil, animal fat and vegetable oils [4], and its rivalry for horticultural land with consumable vegetable oil is still a contentious subject [5]. Microalgae has unicellular organism that grow rapidly and are capable to convert sunlight based energy to substance energy through CO₂ fixation, making it a considerable oil source for the production of biodiesel [6]. Under the appropriate culture conditions, few microalgae species (freshwater and marine) are able to store up to 70% of lipid per dry weight [3]. The FAME profile of microalgae species is found appropriate for the biodiesel production [7]. In any case, bulk production of microalgal based fuel various specialized difficulties that reduce the current advancement of the algal fuel based industry commercially unviable. Furthermore, developing cost-effective technology for biomass harvesting and oil extraction is required, but it is extremely difficult. However, as microalgae production is seen as a realistic way to reduce global warming, also have significant benefits beyond the fuel. As a result, microalgae is now commonly used as a feedstock for third-generation biofuels [8]. Wastewater has become one of the important issues across the world due to increasing population, urbanization and change in modern lifestyle. It contains both inorganic and organic nutrients in high concentration with high biological oxygen demand (BOD) and chemical oxygen demand (COD) and poses threat to environment if discharged without any treatment. Previous research works demonstrated that microalgae can grow in different wastewaters leading to simultaneously wastewater treatment and biomass production. Additionally, microalgae have the ability for CO₂ fixation, which causes reduction of greenhouse emissions [9]. Thus, microalgae may be the most promising feedstock for producing biodiesel to replace conventional diesel fuel. Cultivation of *T. indica* in secondary treated domestic sewage was done in previous research work [10]. It has been reported by the previous studies that the reduction of nutrients from the wastewater using microalgae [11–13]. Moazami et al. [14] reported that maximum biomass growth 46 g L⁻¹ was achieved with *Nannochloropsis*. Mahapatra et al. [15] showed 122 mg L⁻¹ d⁻¹ maximum biomass productivity and 32 mg L⁻¹ d⁻¹ lipid productivity were obtained. Malla et al. [16] reported 0.75 g L⁻¹ dry biomass concentration in IARI wastewater. Komolafe et al. [17] reported 0.58 g L⁻¹ higher maximum biomass concentration with *Desmodesmuss* in untreated wastewater. Most appropriate method is the selection of microalgae strain on the basis of high lipid content and biomass productivity. Mata et al. [6] reported that in comparison of freshwater microalgae, mostly

marine water microalgae contain high lipid content. Current research study focus on the phycoremediation of dairy wastewater for the nutrients removal and biodiesel production.

2 Material and Methods

A marine microalga *Tetraselmis indica* (*T. indica*), was ordered from NFMC, Bharathidasan University Tamil Nadu, India. The microalgal cell culture was maintained in synthetic medium (F2). Dairy wastewater was collected from local dairy and stored at 4 °C in refrigerator. Wastewater was sterile and filtered through membrane filter before the use for the cultivation. Nitrate and phosphate were measured by Ion exchange chromatography (850 professional IC, Metrohm). APHA (APHA, 1992) methods was used for the ammonical nitrogen measurement. Characterization of dairy wastewater was done before and after the cultivation of microalgae. Micronutrients were characterized using the ICP-OES. Total organic carbon was evaluated using TOC Instrument.

2.1 Experimental Setup

250 ml of Erlenmeyer conical flask was used as artificial photobioreactor to perform all the experiments at 25 ± 1 °C for 20 days of cultivation periods. *T. indica* was grown on 250 ml conical flask in different concentrations (25–100%) of DW under (16L: 08D) hr with $94.5 \mu\text{mol m}^{-2} \text{s}^{-1}$ light intensity at 25 ± 2 °C. All the experiments were performed in triplicates as shown in Fig. 1.

a. Extraction of lipid and FAME analysis

To drive lipid out of the algal biomass, the modified Bligh and Dyer method was performed (Bligh and Dyer 1959). For the analysis of FAME, GC–MS (Agilent, Santa Clara, CA, USA) was used. The samples were injected through splitless injection mode (1 μL at 250 °C), helium as the carrier gas.

3 Results and Discussion

3.1 Biomass Production and Nutrient Removal

Microalgal growth depends upon presence of macro or micro nutrients on growth medium. The growth of microalgal cell starts growing from first day of cultivation with 4 days of exponential phase and followed by the decline phase of microalga. The



Fig. 1 Experimental setup for the cultivation of *T. Indica*

exponential phase shifted to stationary phase on 16th day of growth period, where the difference between growth phase and death phase became zero in F2 Fig. 2. Though, the lowest concentration dairy wastewater did not support the microalgal cells growth due to the lower concentration of macro or micro nutrients. After the observation, dairy wastewater was mixed with equal amount of distilled water (50:50) for cultivation of microalgae. *T. indica* shows $0.032 \text{ g L}^{-1} \text{ d}^{-1}$ highest biomass productivity and 0.52 g L^{-1} biomass concentration in 50% of DW as shown in Fig. 3. Reyimu et al. [18] reported the $(12.75 \times 10^6 \text{ cells/ml})$ maximum biomass cell density was reached on 7th day of cultivations period, in 75% concentration of wastewater. *T. indica* show 1.05 g/L biomass yield in F2 medium Fig. 2. Chakraborty et al. [19] reported 1.93 g L^{-1} maximum biomass yield by *Chlorella minutissima* in airlift reactor. *S. abundans* showed 0.79 g L^{-1} maximum biomass concentration in municipal wastewater [19]. The largest source of carbon in wastewater is organic carbon, which is responsible for development of microalgae. Michels et al. [20] reported *Tetraselmis suecica* showed the 0.50 g L^{-1} maximum biomass yield, when fish farm wastewater used as growth medium in tubular photobioreactor. From the Fig. 4, it can be seen that *T. indica* eliminated 63.97% phosphate, 72.7% nitrate, 78.96% ammoniacal nitrogen, and 91.56 TOC. Delgadillo-Mirquez et al. [21] reported the removal about 100% of phosphorus and 75–90% of nitrogen from municipal wastewater using the consortium of microalgae and bacteria. *B. braunii* showed maximum 1.84 g L^{-1} biomass concentration, simultaneously removal of 100% phosphorus and 79.63% of nitrogen from treated domestic wastewater was recorded by Sydney et al. [22]. Nayak et al. [23] reported that *scenedesmus abundans* shows the 0.97 g/L of

maximum biomass yield in pharmaceutical wastewater. The removal of the different parameters has been summarised in the Table 1.

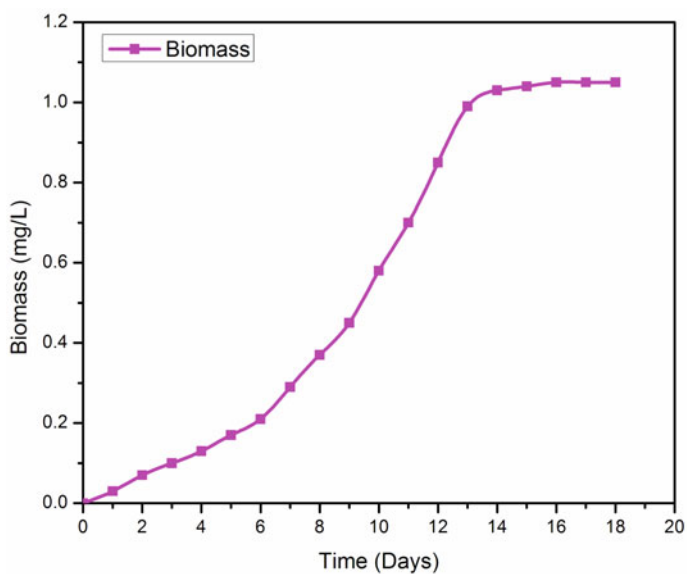


Fig. 2 Biomass yield on F2 medium

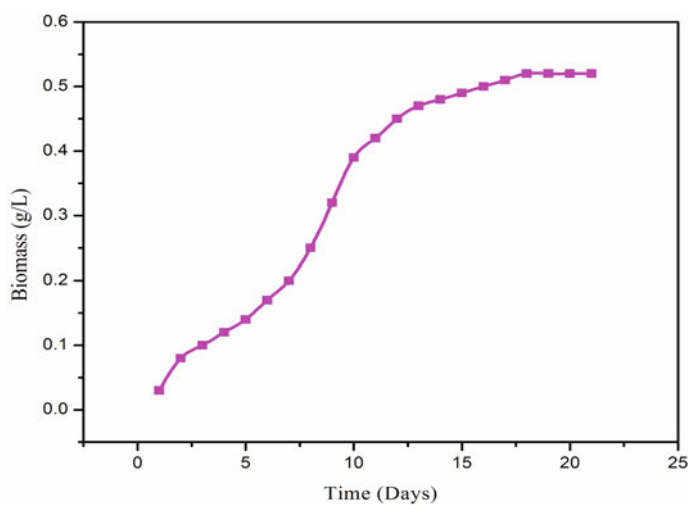


Fig. 3 Biomass growth on dairy wastewater

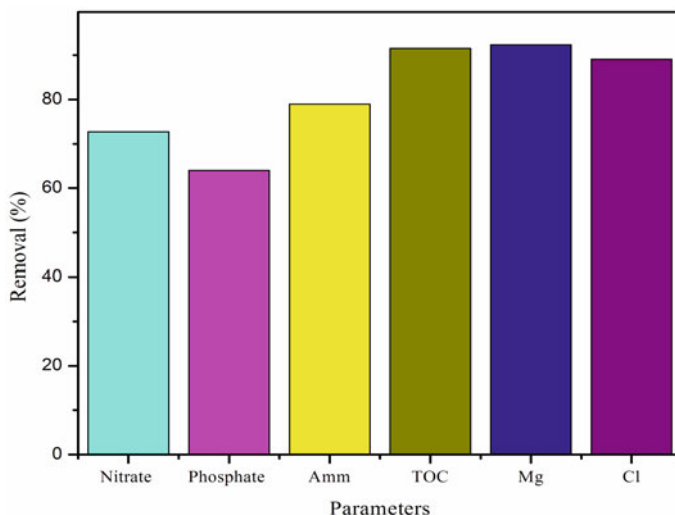


Fig. 4 Removal of pollution load in dairy wastewater

Table 1 Removal of parameters

Parameters	Removal in percentage
Nitrate	72.7
Phosphate	63.97
Ammonical nitrogen	78.96
Total organic carbon	91.57
Magnesium	52
Calcium	65
Iron	69
Aluminum	95

3.2 FAME Analysis

The FAME analysis of *T. indica* lipid samples confirms the presence of pentadecylic acid, linoleic acid, palmitic acid, oleic acid and eicosanoic acid in DW. *T. indica* achieved $0.032 \text{ g L}^{-1} \text{ d}^{-1}$ and $18.44 \text{ mg L}^{-1} \text{ d}^{-1}$, of biomass productivity and lipid productivity respectively, in DW. Kim et al. 2016, reported FAME profile of *Tetraselmis* sp. were palmitic acid, oleic acid and linolenic acid at different salinity environment/conditions [24].

4 Conclusion

The outcome of current study concluded that *T. indica* is one of the major microalga that can be utilized for biodiesel production and also has capability to remove the nutrients from dairy wastewater. *T. indica* reduced the concentration of nitrate, phosphate and ammoniacal nitrogen by 72.7, 63.97 and 78.96%. *T. indica* shows the biomass yield of 0.032 g L⁻¹ d⁻¹ in 50% of dairy wastewater. The major acid such as pentadecylic acid, palmitic acid, oleic acid, linoleic acid and eicosanoic acid were present in *T. indica*, which makes it a suitable choice for bio-diesel production.

References

1. Benemann JR (2003) Bio-fixation of CO₂ and greenhouse gas abatement with microalgae-technology roadmap. Final Report to the US Department of Energy. National Energy Technology Laboratory 30
2. Gautam R, Nayak JK, Talapatra KN, Amit, Ghosh UK (2021) Assessment of different organic substrates for Bio-electricity and Bio-hydrogen generation in an integrated bio-electrochemical system. Mater Today Proc xxx:6–10. <https://doi.org/10.1016/j.matpr.2021.06.223>
3. Gautam R, Nayak JK, Daverey A, Ghosh UK (2022) Emerging sustainable opportunities for waste to bioenergy: an overview. In: waste-to-energy approaches toward zero waste, pp 1–55. <https://doi.org/10.1016/B978-0-323-85387-3.00001-X>
4. Barnwal BK, Sharma MP (2005) Prospects of biodiesel production from vegetable oils in India. Renew Sustain Energy Rev 9(4):363–378
5. Branco-Vieira M, Costa D, Mata TM, Martins AA, Freitas MAV, Caetano NS (2020) A life cycle inventory of microalgae-based biofuels production in an industrial plant concept. Energy Rep 6:397–402
6. Mata TM, Martins AA, Caetano NS, Renew M (2010) Sustain Energy Rev 14(2010):217–232. <https://doi.org/10.1016/J.RSER.2009.07.020>
7. Branco-Vieira M, Mata TM, Martins AA, Freitas MAV, Caetano NS (2020) Economic analysis of microalgae biodiesel production in a small-scale facility. Energy Rep 6:325–332
8. Oliveira VB, Simões M, Melo LF, Pinto AMFR (2013) Overview on the developments of microbial fuel cells. Biochem Eng J 73:53–64
9. Chisti Y (2007) Biodiesel from microalgae. Biotechnol Adv 25(3):294–306
10. Van Den Hende S, Vervaeren H, Boon N (2012) Flue gas compounds and microalgae: (Bio-)chemical interactions leading to biotechnological opportunities. Biotechnol Adv 30(6):1405–1424
11. Chandra R, Ghosh UK, Nayak JK (2017) Phycoremediation potential of marine microalga Tetraselmis indica on secondary treated domestic sewage for nutrient removal and biodiesel production. Environ Sci Pollut Res 24(26):20868–20875
12. Lu W, Wang Z, Wang X, Yuan Z (2015) Cultivation of Chlorella sp. using raw dairy wastewater for nutrient removal and biodiesel production: characteristics comparison of indoor bench-scale and outdoor pilot-scale cultures. Biores Technol 192:382–388
13. Cai T, Park SY, Li Y (2013) Nutrient recovery from wastewater streams by microalgae: status and prospects. Renew Sustain Energy Rev 19:360–369
14. Moazami N, Ashori A, Ranjbar R, Tangestani M, Egtesadi R, Nejad AS (2012) Biomass Bioenergy. 39:449–453. <https://doi.org/10.1016/j.biombioe.2012.01.046>
15. Mahapatra DM, Chanakya HN, Ramachandra TV (2014) Bioremediation and lipid synthesis through mixotrophic algal consortia in municipal wastewater. Biores Technol 168:142–150

16. Malla FA, Khan SA, Sharma GK, Gupta N, Abraham GJEE (2015) Phycoremediation potential of *Chlorella minutissima* on primary and tertiary treated wastewater for nutrient removal and biodiesel production. *Ecol Eng* 75:343–349
17. Komolafe O, Orta SBV, Monje-Ramirez I, Noguez IY, Harvey AP, Ledesma MTO (2014) Biodiesel production from indigenous microalgae grown in wastewater. *Biores Technol* 154:297–304
18. Reyimu Z, Özçimen D (2017) Batch cultivation of marine microalgae *Nannochloropsis oculata* and *Tetraselmis suecica* in treated municipal wastewater toward bioethanol production. *J Clean Prod* 150:40–46
19. Chakraborty S, Mohanty D, Ghosh S, Das D (2016) Improvement of lipid content of *Chlorella minutissima* MCC 5 for biodiesel production. *J Biosci Bioeng* 122(3):294–300
20. Michels MH, Vaskoska M, Vermuë MH, Wijffels RH (2014) Growth of *Tetraselmis suecica* in a tubular photobioreactor on wastewater from a fish farm. *Water Res* 65:290–296
21. Delgadillo-Mirquez L, Lopes F, Taidi B, Pareau D (2016) Nitrogen and phosphate removal from wastewater with a mixed microalgae and bacteria culture. *Biotechnol Rep* 11:18–26
22. Sydney ED, Da Silva TE, Tokarski A, Novak, AD, De Carvalho JC, Woiciechowski AL, Soccol CR (2011) Screening of microalgae with potential for biodiesel production and nutrient removal from treated domestic sewage. *Appl Energ* 88(10):3291–3294
23. Nayak JK, Ghosh UK (2020) Microalgae cultivation for pretreatment of pharmaceutical wastewater associated with microbial fuel cell and biomass feed stock production. In: 2nd water-energy-nexus – international conference microalgae cultivation for pretreatment of pharmaceutical wastewater, pp 3–6. <https://doi.org/10.1007/978-3-030-13068-8>
24. Kim G, Lee CH, Lee K (2016) *Korean J Chem Eng* 33:230–237. <https://doi.org/10.1007/s11814-015-0089-8>
25. APHA (1992) *Water Environ Fed* 18th 9–45
26. Sharma GK, Khan SA, Fayaz MA, Gupta N (2014) Nutrient sequestration and phycoremediation of sewage waste water by selective microalgae. *Green Farming* 5:623–626

RETRACTED CHAPTER: On Parametric Optimization of TSE for PVDF-Graphene-MnZnO Composite Based Filament Fabrication for 3D/4D Printing Applications



Vinay Kumar, Rupinder Singh, and Inderpreet Singh Ahuja

1 Introduction

In contrast to commercial manufacturing processes, fused deposition modeling (FDM) based additive manufacturing (AM) process has deeper roots in utilization of polymers for 3D printing applications. Polymer 3D printing is economical and useful due to its low cost, large area of application and good build quality. Fused filament fabrication (FFF) setup/3D printer in which thermoplastic materials are used has been modified by some researchers to investigate the mechanical and electrical properties in one of the highly reported smart plastic material Polyvinylidene fluoride (PVDF). The reported study on 3D printed sheets of PVDF showed $d_{31} = 1.19$ pm/V [1]. The composite having reinforcement of functionalized graphene (F-Gr) in PVDF matrix has shown good dielectric properties for developing better 3D printing based sensors. For preparation of such composites and to functionalize the graphene nanoparticle, AgNO_3 catalyst has been used. Ethanol and de-ionized water has been incorporated in the blend of PVDF-F-Gr for cleaning functionalized graphene [2]. A lot of studies reported on PVDF blends in which varieties of material (like: lithium carbonate, meso-porous silicate nano-particles, barium titanate and

The original version of this chapter was retracted. The retraction note to this chapter is available at https://doi.org/10.1007/978-981-19-4147-4_48.

V. Kumar (✉)
Department of Production Engineering, Guru Nanak Dev Engineering College, Ludhiana, Punjab, India
e-mail: vinaykumr6192@gmail.com

I. S. Ahuja
Department of Mechanical Engineering, Punjabi University, Patiala, Punjab, India

R. Singh
Department of Mechanical Engineering, National Institute of Technical Teacher Training and Research, Chandigarh, India
e-mail: rupindersingh@nitttrchd.ac.in

© The Author(s), under exclusive license to Springer Nature Singapore Pte Ltd. 2023, corrected publication 2023

C. Prakash et al. (eds.), *Advances in Functional and Smart Materials*, Lecture Notes in Mechanical Engineering, https://doi.org/10.1007/978-981-19-4147-4_5

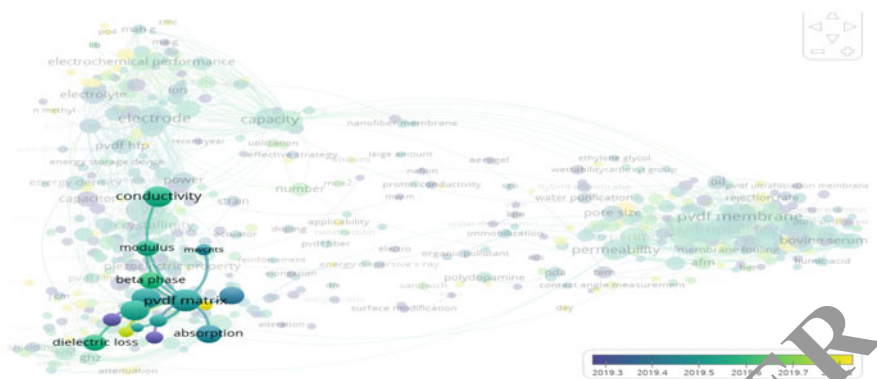


Fig. 2 The research gap in cluster of PVDF based device application highlighting lack in the area of 3D printing application

But, the combined effect of reinforcing Mn-ZnO and Gr in PVDF matrix composite is not reported for 3D printing application.

The recent studies on 3D printing related applications of polymer matrices mainly thermoplastic polyurethane (TPU), PVDF, polyamide (PA-6), acrylonitrile butadiene styrene (ABS) and poly-lactic acid (PLA) highlighted that filament preparation using TSE is effective to obtain a low cost but mechanically acceptable composite for 3D/4D printing [4, 15–18]. As an extension to the previously reported work in which PVDF was mechanically blended with 3% Mn-ZnO nano particles and 6% Graphene nano particles (GNP named PGMZ) for investigating 4D characteristics like self-assembly, the present work targets the development of PGMZ feedstock filament using TSE setup and its parametric optimization for fabrication of 3D printing wire filament with best properties.

2 Material and Method

The PVDF polymer was procured (from: ThermoFisher scientific: Alfa Aesar) and a pilot work was performed to distinguish the PVDF and PGMZ composite by performing material characterization i.e. rheological (based on melt flow index (MFI) testing), thermal (i.e. differential scanning calorimetry (DSC)) and mechanical strength (universal testing machine (UTM)) testing. Figure 3 shows methodology of the experimental work performed. On the basis of pilot experimentation, three input parameters of TSE with three levels were selected experimentally to design Taguchi L9 OA. Wire filament specimens were investigated for best mechanical properties, shore D hardness and morphological characteristics. Taguchi design was analyzed for parametric optimization of TSE input parameters for best settings.

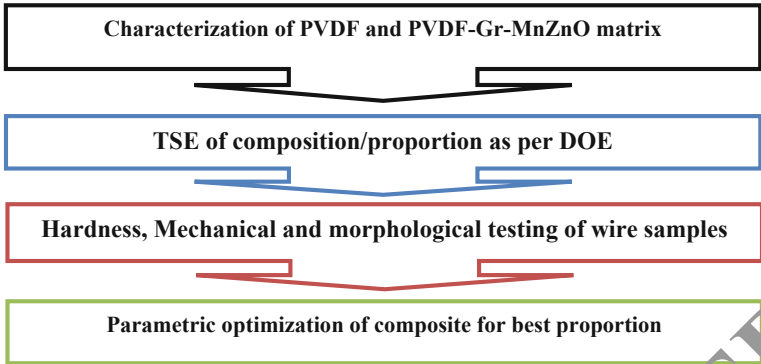


Fig. 3 Process flow for investigating optimum processing parameters of proposed composite

3 Experimentation

3.1 Pilot Experimentation

3.1.1 Rheological and Thermal Characterization

For characterization of flow property, MFI meter was used as per ASTM D1238. The MFI of PVDF and PGMZ matrix was obtained 3.7 g/(10 min) and 2.71 g/(10 min) respectively. The MFI of PGMZ decreased from the virgin PVDF grade but this MFI value was suitable for 3D printing process. After rheological testing, DSC analysis of both samples was performed. Figure 4 shows the results obtained for DSC of PVDF and PGMZ. The axis-X of graph shows the increment and decrement in temperature with respect to time and axis-Y shows heat capacity of tested specimens. Heat capacity of PVDF increased from -24.63 to -64.42 Jg^{-1} (as PGMZ composite) in first heating cycle and -27.68 to 78.25 Jg^{-1} in second heating cycle. The PGMZ was found more thermally stable than PVDF for further studies on the basis of DSC test.

3.1.2 Mechanical Characterization

The wire samples of PVDF and PGMZ were tested on UTM for calculating mechanical properties (like: modulus of toughness (MoT) and Young's modulus (YM)). The UTM results for PVDF and PGMZ wire is shown in Table 1 whereas Fig. 5 shows stress strain graph for comparison between PVDF and the composition. It was observed that mechanical properties of PVDF increased with reinforcement of nano-particles.

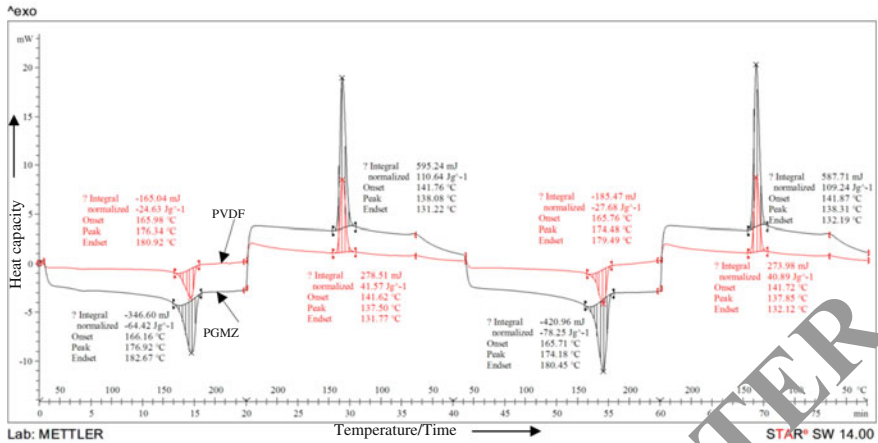


Fig. 4 Graphs showing DSC results for PVDF and PGMZ composite

3.2 Final Experimentation

3.3 TSE

On the basis of pilot study outcomes, PGMZ composite was processed through TSE at different processing conditions. The parametric conditions and their levels are listed in Table 2. The input parameters from Table 2 were used in Minitab software to obtain set of experiments shown in Table 3.

The design of experiment for processing PGMZ composite according to the set of parameters (Table 3) was followed to wire specimens to investigate mechanical, hardness and morphological characteristics. Figure 6a shows the TSE setup and Fig. 6b, c and d shows different temperature and torque conditions of PGMZ composite.

For every single set of operation, TSE was run for 5–6 min and graphical observations were recorded for discussion. In Fig. 6b, c and d TS1 and TS2 shows the temperature of screw 1 and screw 2 respectively that varied from 170 to 190 °C; n shows the rotations per minute (rpm) of screws at particular value of torque (M) in Nm. The graph shows the change in speed (rpm)/torque (Nm) of screws (along Y-axis) with the passage of time (min) (along X-axis). Once the TSE initiates, the mechanical blend of composite matrix is poured into the opening of extruder unit. After the application of applied load on the compounder, the speed of screws decreases quickly to adjust the set value of torque. As soon as the TSE reached its desired torque level, it automatically controls the outflow of material from the compounder. This way the uniformity of wire specimens is controlled. When the material leaves the compound zone and came out from the nozzle end, the speed of screws gradually increases to greater extent indicating the vacant chamber for pouring more material into this chamber.

Table 1 UTM results for PVDF and PGMZ composite

Material	PL (N)	BL (N)	PE (mm)	BE (mm)	PS (N/mm^2)	BS (N/mm^2)	SaB (mm)	SaP (mm)	MoT (N)	YM (MPa)
PVDF	121.61	109.40	2.28	2.28	38.73	34.85	0.038095	0.038462	0.66381	1019.2
PGMZ	145.10	130.52	2.58	3.42	46.21	41.59	0.057143	0.043077	1.18828	1074.6

Here, *PL* Peak load, *PE* Peak elongation, *BL* Break load, *BE* Break elongation, *PS* Peak strength, *BS* Break strength, *SaB* Strain at break, *SaP* strain at peak, *MoT* Modulus of toughness, *YM* Young's Modulus

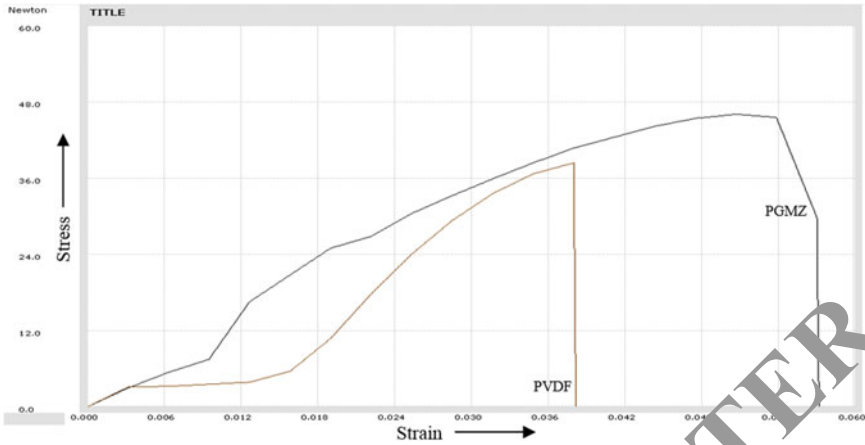


Fig. 5 Stress versus strain graph for PVDF and PGMZ composite

Table 2 Selected parameters and their levels

S. No	Screw temperature (°C)	Torque (Nm)	Dead weight (kg)
1	170	0.1	5
2	180	0.2	10
3	190	0.3	15

Table 3 DOE as per Taguchi L9 OA

S. No.	Screw temperature (°C)	Torque (Nm)	Dead weight (kg)
1	170	0.1	5
2	170	0.2	10
3	170	0.3	15
4	180	0.1	10
5	180	0.2	15
6	180	0.3	5
7	190	0.1	15
8	190	0.2	5
9	190	0.3	10



Figure 6. a Twin screw extruder setup, b, c and d graphical output showing effect of temperature and torque on processing of filament wire

4 Results and Discussion

4.1 UTM Testing

The UTM test results obtained for each wire specimen (with cross section are 3.92 mm² and grip separation of 60 mm during tensile test) are listed in Table 4. A significant improvement was observed in mechanical properties like peak strength, break strength and YM of PGMZ composite. Graph obtained stress–strain analysis is shown in Fig. 7.

It may be considered that processing temperature greatly affected the mechanical properties of PGMZ as consistent increment in peak strength and YM was recorded in stress strain graph (Fig. 7) as the screw temperature increased from 170 to 190 °C.

4.2 Optimization of Young's Modulus

Taguchi L9 OA was analyzed for optimization of TSE processing parameters using Minitab to investigate best processing conditions that can provide better mechanical property in form of YM. The signal to noise (SN) ratio for YM of tested samples (as per Table 3) is listed in Table 5.

After processing the SN ratio (obtained in Table 5), main effect plot shown in Fig. 8 was recorded. It indicated that 190 °C screw temperature, 0.3 Nm torque and 10 kg applied weight are the best settings at which good mechanical strength can be achieved in PGMZ filament wire.

Analysis of variance (ANOVA) obtained in Table 6 shows that the proposed experimental model was accurate as one parameter i.e. screw temperature has P value less than 0.05. Table 7 shows the rank table for each input parameter. Processing temperature was ranked 1, torque was ranked 2 and weight was ranked 3; which indicated that weight is the least important process parameter for the TSE process.

4.2.1 Prediction for Young's Modulus

For prediction of YM, the equation used for calculation is:

$$\eta_{\text{opt}} = Y + (Y_{A2} - Y) + (Y_{B3} - Y) + (Y_{C1} - Y)$$

Here, η_{opt} is the optimum value of SN ratio for YM, Y (mean SN ratio for YM) = 59.58 (from Table 5), Y_{A2} (maximum temperature) = 59.77, Y_{B3} (maximum torque) = 59.90 and Y_{C1} (maximum weight) = 61.63 as per Table 7.

$$\text{So, } \eta_{\text{opt}} = 62.14 \text{ dB}$$

Table 4 UTM results of PVDF-Gr-MnZnO wire samples

S. No.	PL (N)	BL (N)	PS (N/mm ²)	BS (N/mm ²)	PE (mm)	BE (mm)	SaB (mm)	SaP (mm)	MoT (N)	YM (MPa)
1	79.968	71.736	20.45	18.33	1.68	2.34	0.039	0.028	0.35685	728.5714
2	93.688	82.712	23.93	21.19	1.04	2.58	0.043	0.034	0.45365	702.9412
3	87.808	77.616	22.42	19.82	1.74	7.86	0.131	0.029	1.2969	772.4138
4	141.904	127.008	36.26	32.44	2.2	6.31	0.105	0.037	1.701	978.3784
5	139.16	124.264	35.57	31.74	2.34	7.26	0.121	0.039	1.91785	910.2564
6	151.704	135.24	38.74	34.53	2.22	8.04	0.134	0.037	2.3115	1045.946
7	182.672	165.032	46.63	42.18	2.16	6.72	0.112	0.036	2.3576	1294.444
8	121.128	103.096	30.91	26.36	1.92	9.9	0.165	0.032	2.16975	965.625
9	170.755	159.152	43.56	40.65	1.86	13.86	0.231	0.031	4.6893	1405.161

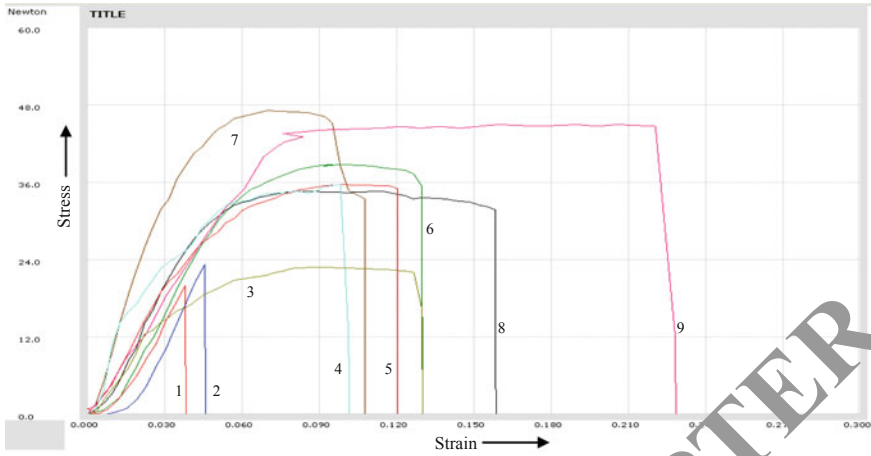


Fig. 7 Graphical results for stress versus strain based UTM test of TSE wire samples

Table 5 Signal to noise ratio for Young's modulus of tested wires

S. No.	Young's Modulus (MPa)	SN ratio
1	728.5714	57.2494
2	702.9012	56.9384
3	724.4138	57.7570
4	973.3784	59.8101
5	910.2564	59.1833
6	1045.946	60.3902
7	1294.444	62.2417
8	965.625	59.6962
9	1405.161	62.9545

For larger is better condition statement, Optimum value (y_{opt}),

$$y_{opt}^2 = (1/10)^{-n_{opt}/10}$$

$$y_{opt} = 1279.41 \text{ Mpa}$$

Therefore, predicted YM = 1279.41 Mpa.

The observed value for YM 1294.4 Mpa (Table 5, S. No. 7) was found closer to the value predicted by the model ensured that valid results are achieved with 95% confidence level.

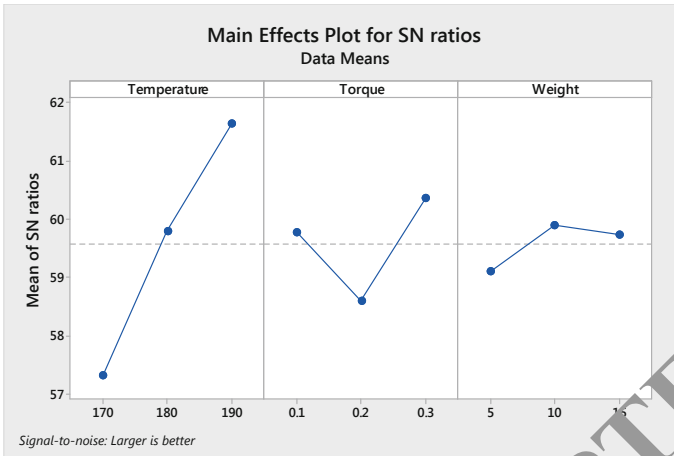


Fig. 8 Mean effect plot showing best processing conditions (Obtained from signal to noise ratio for YM)

Table 6 Analysis of variance for SN ratios

Source	DF	MS	Seq SS	Adj SS	Adj	F	P	%C
Temperature	2		28.147	28.147	1.43734	25.67	0.037	80.22
Torque	2		4.811	4.811	2.4053	4.39	0.186	13.71
Weight	2		1.032	1.032	0.5158	0.94	0.515	3.19
Residual error	2		1.006	1.006	0.5481			2.86
Total	8		35.016					

Table 7 Response table for signal to noise ratios

Level	Temperature	Torque	Weight
1	57.31	59.77	59.11
2	59.79	58.61	59.90
3	61.63	60.37	59.73
Delta	4.32	1.76	0.79
Rank	1	2	3

4.3 Shore D Hardness

The shore D hardness of wire samples along the radial and longitudinal axis is shown in Table 8. The maximum shore D hardness of 55.8 HD along the radial axis was obtained in sample 9 whereas sample 8 shows hardness of 41.6 HD along longitudinal axis.

Table 8 Shore D hardness of TSE wires along radial and longitudinal axis

S. No	Average shore D hardness (HD) (along radial axis)	Average shore D hardness (HD) (along longitudinal axis)
1	42.5	32.5
2	45.1	35.1
3	44.5	34.6
4	48.5	36.7
5	51.8	37.5
6	50.5	36.4
7	54.5	39.5
8	52.7	41.6
9	55.8	38.5

4.4 Morphological Analysis

The metallurgical microscopic images were observed at $\times 30$ magnification to investigate the porosity in wire samples along the radial axis. Figure 9 shows the microscopic images taken from the spot at which wire sample, broken during UTM testing. The porosity percentage of each specimen is listed in Fig. 10.

The porosity percentage shows that lower temperature conditions are very poor for morphological characteristics of PGMZ composite. The cross-section of filament wire is more uniform and less porous at higher processing temperature and torque conditions i.e. 190 °C and 0.3 Nm respectively.

5 Conclusion

The conclusions that can be drawn from the present research article are as follows:

1. The pilot experimentation shows that PGMZ based composite possess acceptable rheological, better heat capacity and mechanical properties as compared to PVDF polymer matrix. PGMZ shows MFI of 2.7 g/(10 min), maximum heat capacity of -18.25Jg^{-1} and YM 1074.6 MPa.
2. As regards to mechanical properties for selected composition of PGMZ is concerned, maximum MoT of 4.68 N and YM of 1405.16 MPa was observed for feedstock filament when prepared with TSE at screw temperature 190 °C with 0.3 Nm torque and 10 kg applied load.
3. The feed stock samples prepared possess good shore D hardness = 55.8HD (along radial axis) and 38.5 HD (along longitudinal axis) at best settings. These settings were counter verified by performing morphological analysis which outlined that porosity for PGMZ was 6.43% for cross-surface (i.e. along radial axis).

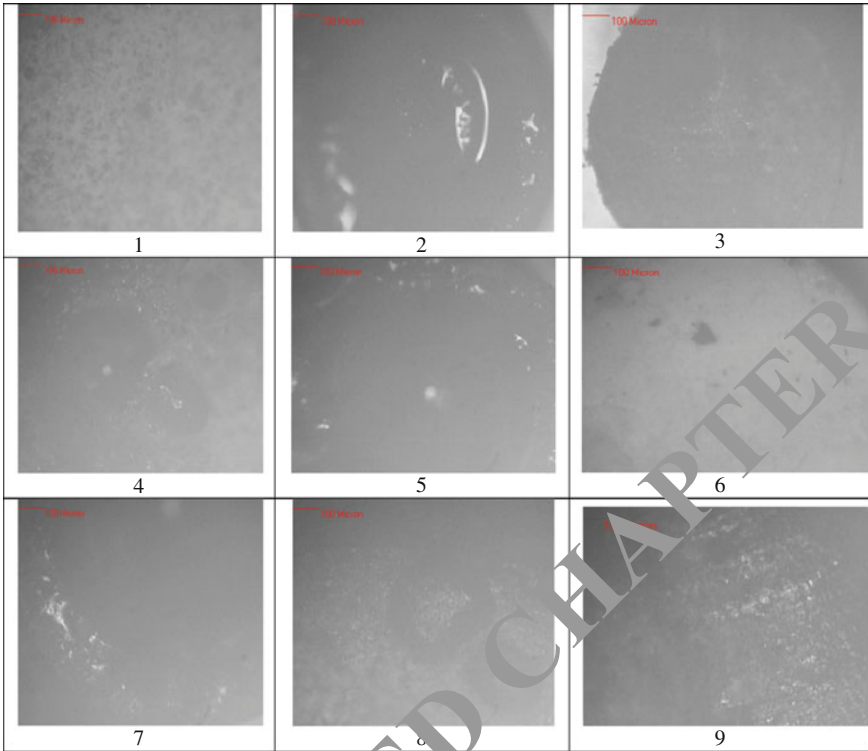


Fig. 9 Metallurgical microscope images of cross-sectional surface of wire samples captured at $\times 15$ magnification

4. The parametric optimization of twin screw extrusion process resulted in providing useful processing conditions to fabricate the filament wire (with acceptable/good mechanical properties) for open source 3D printers.

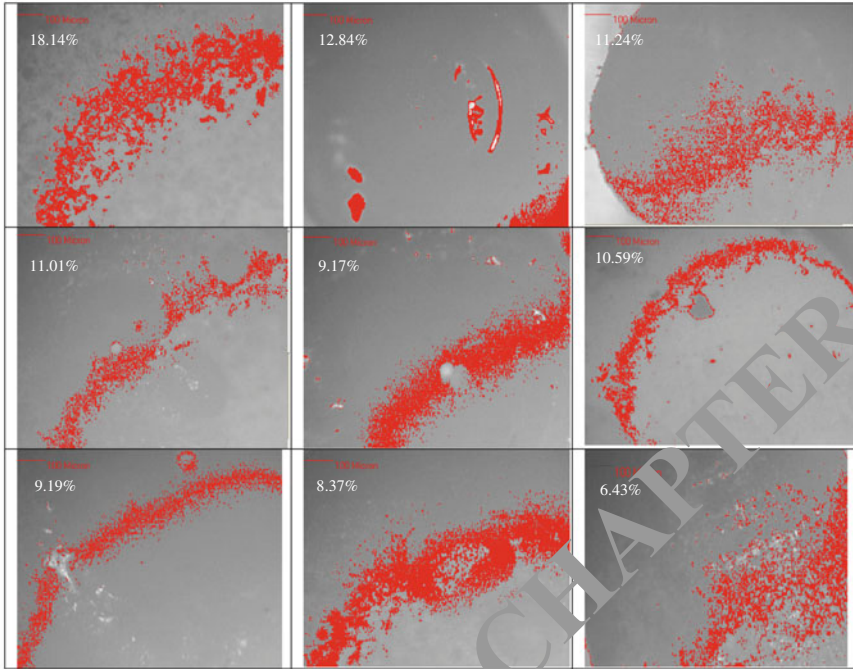


Fig. 10 Porosity percentage obtained for filament fiber samples along the cross-sectional surface

Acknowledgements The authors are thankful to Manufacturing Research Lab, GNDEC, Ludhiana (Punjab, India), Department of Mechanical Engineering, NITTTR, Chandigarh and Department of Mechanical Engineering, Punjabi University, Patiala (Punjab, India) for providing their kind support during testing in lab.

The authors received financial support from Department of Science and Technology (DST), Govt. of India (GoI), under project file no. DST/TDT/SHRI-35/2018.

References

1. Porter DA, Hoang TV, Berfield TA (2017) Effects of in-situ poling and process parameters on fused filament fabrication printed PVDF sheet mechanical and electrical properties. *Addit Manuf* 13:81–92
2. Zheng X, Yu H, Yue S, Xing R, Zhang Q, Liu Y, Zhang B (2018) Functionalization of graphene and dielectric property relationships in PVDF/graphene nanosheets composites. *Int J Electrochem Sci* 13:1–13
3. Mohseni MSAAR, Shirazi FH, Nemati NH (2020) Preparation and characterization of self-electrical stimuli conductive gellan based nano scaffold for nerve regeneration containing chopped short spun nano-fibers of PVDF/MCM41 and polyaniline/graphene nanoparticles: Physical, mechanical and morphological studies. *Int J Biol Macromol*

4. Wang H, Lin C, Yan X, Wu A, Shen S, Wei G, Zhang J (2020) Mechanical property-reinforced PEO/PVDF/LiClO₄/SN blend all solid polymer electrolyte for lithium ion batteries. *J Electroanal Chem* 869:114156
5. Wu L, Jing M, Liu Y, Ning H, Liu X, Liu S, Lin L, Hu N, Liu L (2019) Power generation by PVDF-TrFE/graphene nanocomposite films. *Compos B Eng* 164:703–709
6. Xu P, Cui Z, Chen H, Ding Y (2019) Synergistic enhanced dielectric properties of PVDF nanocomposites containing γ -oxo-pyrenebutyric acid functionalized graphene and BaTiO₃ nanofillers. *Compos Commun* 13:63–69
7. Chiu FC, Chen YJ (2015) Evaluation of thermal, mechanical, and electrical properties of PVDF/GNP binary and PVDF/PMMA/GNP ternary nanocomposites. *Compos A Appl Sci Manuf* 68:62–71
8. Chiu FC, Chuang YC, Liao SJ, Chang YH (2018) Comparison of PVDF/PVAc/GNP and PVDF/PVAc/CNT ternary nanocomposites: enhanced thermal/electrical properties and rigidity. *Polym Test* 65:197–205
9. Raja M, Ryu SH, Shanmugaraj AM (2014) Influence of surface modified multi-walled carbon nanotubes on the mechanical and electroactive shape memory properties of polyurethane (PU)/poly (vinylidenedifluoride) (PVDF) composites. *Colloids Surf A* 450:57–66
10. Kumar V, Singh R, Ahuja IPS (2020) Effect of extrusion parameters on primary recycled ABS: mechanical, rheological, morphological and thermal properties. *Mater Res Express* 7(1):015208
11. Petersmann S, Spoerk M, Van De Steene W, Üçal M, Wiesner J, Pinner G, Arbeiter F (2020) Mechanical properties of polymeric implant materials produced by extrusion-based additive manufacturing. *J Mech Behav Biomed Mater* 104:10361
12. Kumar V, Singh R, Ahuja IPS, Davim JP (2021) On nano-graphene-reinforced polyvinylidene fluoride composite matrix for 4D applications. *J Mater Eng Perform*. <https://doi.org/10.1007/s11665-021-05459-z>(b)
13. Sharma R, Singh R (2018) Optimizing tensile strength of biocompatible FDM feedstock filament developed through twin screw extruder. *Reference modules in material science and engineering*
14. Sharma R, Singh R, Batish A (2020) On mechanical and surface properties of electro-active polymer matrix-based 3D printed functionally graded prototypes. *J Thermoplast Compos Mater* 0892705720907677
15. Poomathi N, Singh S, Prakash C, Subramanian A, Sahay R, Cinappan A, Ramakrishna S (2020) 3D printing in tissue engineering: a state of the art review of technologies and biomaterials. *Rapid Prototyping J* 26(7):1313–1334
16. Prakash C, Singh G, Singh S, Linda WL, Zheng HY, Ramakrishna S, Narayan R (2021) Mechanical reliability and in vitro bioactivity of 3D-printed porous polylactic acid-hydroxyapatite scaffold. *J Mater Eng Perform* 30(7):4946–4956
17. Singh R, Singh R (2020) Twin Screw extrusion for recycling of thermoplastics. *Reference modules in material science and engineering*
18. Pandey A, Singh G, Singh S, Jha K, Prakash C (2020) 3D printed biodegradable functional temperature-stimuli shape memory polymer for customized scaffoldings. *J Mech Behav Biomed Mater* 108:103781

Characteristic Analysis of Nylon Fiber Reinforced Epoxy Composite Materials



A. Saravanan, R. Naveen Kumar, and A. S. Tharun Sankar

Abstract This study deals with the manufacture of composites (NRC) of synthetic fibre. Nylon acts as a reinforcement material in this type of composite, while epoxy resin acts as the matrix. A simple manual lay-up process followed by the compression moulding procedure was used to prepare the woven matted Nylon fibre epoxy laminated composite (NFMRLC). The composites consisted of matt woven nylon fibre and resin epoxy. Three plates (25% Nylonfiber + 75% Epoxy-resin + Hardener), (30% Nylon Fiber + 70% Epoxy-resin + Hardener) have been made (35% NY + 65% Epoxy-resin + Hardener). Three plates have been made. The tensile, flexural and impact mechanical properties were tested according to the ASTM standards. The experimental results of the three mechanical properties were taken. The plate of 35% has obtained higher values comparing to remaining two plates.

Keywords Composite material · Nylon fibre epoxy · Epoxy-resin · Hardener · Laminated composite · Mechanical properties

1 Introduction

Composites of carbon fiber/epoxide (CF/EP) were found in numerous technical applications, offering significant reduction of weight and improved corrosion and resistance to fatigue in comparison with their metals. Composites are one of engineering materials most sophisticated and adaptable. Composite materials have long been used for solving technological problems, but these materials were only used in the 1960s when polymer-based composites became the focus of industry [1, 2]. Characterizing polymers is an important step in polymerization. Such efforts are normally aimed at a particular purpose. In the end, macromolecular structure and organization determine the mechanical, physical and chemical properties of polymers. Special attention has been paid to particulate reinforced thermoplastic composites over many years. Excellent efforts to design composites have been made unique and low-cost properties [3,

A. Saravanan (✉) · R. N. Kumar · A. S. T. Sankar
Department of Mechanical Engineering, Kongu Engineering College, Erode, Tamilnadu, India
e-mail: saro88.mech@kongu.edu

4]. Conventional tightening methods involving the dispersal of the rubber phase into the resin matrix have improved the tolerance to damage compressive performance sacrifice hot/wet parts. These fascinating and wonderful materials were born in the field of materials science and technology [5, 6]. Composites are heterogeneous, made up of two or more fillers or compactable matrix. The matrix can be made from metal, ceramic or polymer. The composite form, appearance of the surface, environmental tolerance and overall hot springs [7, 8]. Composites play a crucial role in aerospace at present. The industry, the car industry and other engineering applications are exceptional weight-to-weight ratio of strength and module to weight [9, 10]. Stiff composites made of high performance polymeric materials were studied with glass, graphite, kevlar, nylon or silicon carbide fibres much due to their application in the technology of aerospace and space vehicles. The particles also share the load with the matrix but are not as large as a fibre. Particulate strengthening increases rigidity but generally does not strengthen.

2 Materials

The nylon mat was made from high pressure, heated, carbon-based chemicals found in coal and oil. The extracted nylon fibre was used to prepare the nylon fibre yarn by hand spinning process. The hand weaving method was used to fabricate the nylon fibre yarn mat with linear density 6 yarns per square centimetre in warp and weft directions. The thickness of the mat is approximately 3 mm thickness. It shows the nylon fibre yarn woven mat for preparing the laminate epoxy composites. Epoxy resin is widely used for fabricating fibre reinforced polymer composites because of its less shrinkage and better stability resistance. It is a form of epichlorohydrin and bi-s-phenol. The good adhesion, mechanical properties, are excellent properties of epoxy resin, processing ease, very less shrinkage, which makes it a good choice of selection when compared to other resin. Hardener is the curing agent as shown in Fig. 1. Epoxy resin belongs to the category called thermosetting polymer where it cures on mixing the resin with hardener due to polymerization and cross-links. The ratio of resin to hardener was 100:10 that is, 10 ml of hardener is mixed with every 100 ml of resin.

3 Methodology

- Apply grease to the mould as well as the compressor mould.
- Depending on the size of the mould, paste the OHP sheets above the grease applied area (Fig. 2).
- Maintaining uniform thickness over the plates by keeping the 3 mm metal parts in the four corners of the mould (Figs. 3 and 4).



Fig. 1 Hardener



Fig. 2 OHP sheet fix

- Pour the resin mixture over the nylon fibres in the mould. The resin is applied to the mould with a brush.
- To remove air bubbles from the mould surface, a roller was rolled over the mat.
- Repeat the steps above for the next two to three layers of nylon mat.
- After that, the mould was sealed and placed in a hydraulic press for 6 h at 35 bar pressure and room temperature to solidify. Totally three plates were manufactured.

4 Experimental Investigation

4.1 Tensile Testing

The elastic examples were cut with a crisscross shaper after the composite plate was set up as indicated by ASTM D638 norms. The examples are canine bone molded, estimating 165 mm long, 19 mm in width and 7 mm in thickness. The tractable test was performed with a 25 kN heap cell on the Universal Test Machine (UTM), and the elastic stress, stress and shape were resolved with regard to the load against the estimation of removal. The test was carried out with a crosshead of 2 mm/min at room



Fig. 3 Clamp



Fig. 4 Manufacturing setup

temperature. The example's measure length and width at check length were 50 mm and 13 mm, individually. Absolutely nine examples were tried for three composite plates.

The following equation can be used to measure the composites' tensile stress, strain, and tensile modulus (Fig. 5),



Fig. 5 Tensile test fractured specimen

$$\sigma_t = \frac{P}{b \times d}$$

where

σ_t Stress of the traction (MPa)

P charging (N)

b Specimen Breadth

d Specimen Thickness

$$e_t = \frac{E}{l}$$

where

e_t Tensile strain (%)

E Elongation of specimen

L Gauge length of specimen

$$E_t = \frac{\sigma_t}{e_t}$$

where

E_t Tensile modulus (GPa)

4.2 Flexural Testing

The flexural test tests were cut from the composite plate utilizing a crisscross shaper as per ASTM D790. The examples are rectangular fit as a fiddle and have a thickness



Fig. 6 Flexural test fractured specimen

of 7 mm. The proportion of length to profundity was 16:1. The flexural test was performed with a 25 kN load cell at a crosshead speed of 1.5 mm/min on the Universal testing machine (UTM) and the flexural stress strain and modulus. Absolutely eight examples tests are tried for four composite plates. The following equation can be used to measure the composites' flexural stress, strain, and flexural modulus (Fig. 6),

$$\sigma_f = \frac{3PL}{2bd^2}$$

where

- σ_f Flexural stress (MPa)
- P Charging (N)
- L Support span length of specimen
- b Specimen width
- d Specimen thickness

$$e_f = \frac{6Dd}{L^2}$$

where

- e_f Flexural strain (%)
- D Deflection caused by the applied load

$$E_f = \frac{mL^3}{4bd^3}$$



Fig. 7 Impact test fractured specimen

where

E_f Flexural modulus (MPa)

m slope value of load on the specimen and its deflection (N/m).

4.3 Impact Testing

The effect test tests were eliminated from the composite plate utilizing a crisscross shaper, and the test was performed by ASTM D-256, with the exploration tests estimating 6412.77 mm³. IZOD TESTC-R and Deepak poly-plast Pvt. Ltd. are the model and maker of the effect testing machine. The accuracy of the down weight hammer and the unit is 25 J and 0.001 J, separately. The V score on the example was made utilizing a physically worked bit shaper before testing (Fig. 7).

5 Results and Discussion

5.1 Tensile Properties

The modulus of flexibility, versatile cutoff, prolongation, corresponding breaking point, and decrease in territory, elasticity, yield point, yield strength and other ductile properties are totally dictated by deciding the malleable properties. The test is finished utilizing widespread malleable machine. Peak load is in kgf (Table 1).

5.1.1 25% Nylon Fibre with 75% Epoxy Resin

See Fig. 8.

Table 1 Result of tensile test

Sample No.	CSArea (mm ²)	Peak load (N)	%Elongation	UTS (N/mm ²)
1	39.000	962.135	7.090	24.672
2	39.000	1012.314	7.360	25.957
3	39.000	665.344	3.760	17.060
4	39.000	561.858	4.330	14.411
5	39.000	939.808	8.950	24.093
6	39.000	747.846	5.290	19.179
7	39.000	1504.393	12.180	38.573
8	39.000	939.808	5.130	24.074
9	39.000	1051.534	7.070	26.958

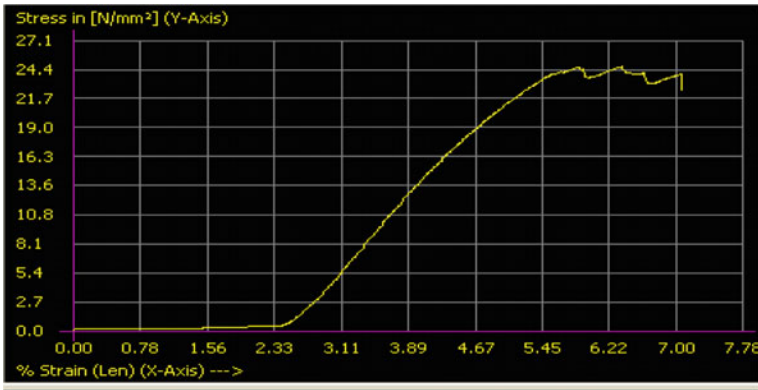


Fig. 8 Stress versus strain for nylon fibre sample 1

5.1.2 30% Nylon Fibre with 70% Epoxy Resin

See Fig. 9.

5.1.3 35% Nylon Fibre with 65% Epoxy Resin

See Fig. 10.

5.2 Flexural Properties

The flexural test decides how much power is expected to twist a shaft under three-point stacking. The data is regularly used to pick materials for parts that can withstand

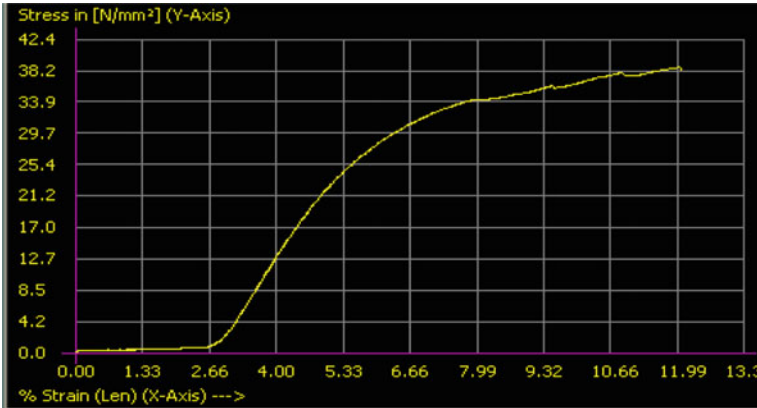


Fig. 9 Stress versus strain for nylon fibre sample 4

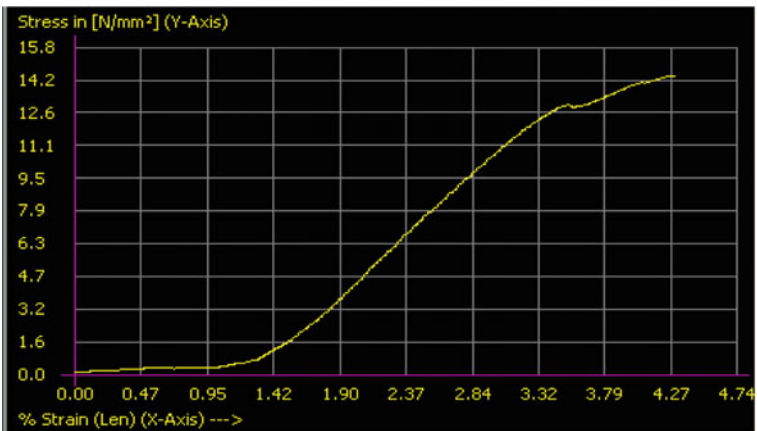


Fig. 10 Stress versus strain for nylon fibre sample 7

loads without flexing. The flexural modulus of a material is an estimation of its solidness when flexed. The test is finished utilizing all inclusive elastic machine. Peak load is in kgf (Table 2).

5.2.1 25% Nylon Fibre with 75% Epoxy Resin

See Fig. 11.

Table 2 Results of flexural test

Sample No.	CS Area (mm) ²	Peak load (N)	Flexural strength (MPa)
1	39.000	89.271	57.225
2	39.000	108.813	69.751
3	39.000	72.682	46.594
4	39.000	104.388	66.919
5	39.000	87.044	55.801
6	39.000	116.141	69.833
7	39.000	108.940	74.154
8	39.000	115.680	74.449
9	39.000	118.985	76.276

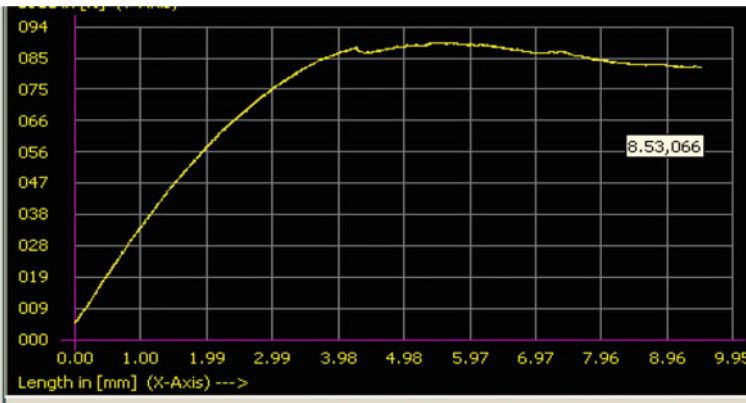


Fig. 11 Length versus load for nylon fibre sample1

5.2.2 30% Nylon Fibre with 70% Epoxy Resin

See Fig. 12.

5.2.3 35% Nylon Fibre with 65% Epoxy Resin

See Fig. 13.

5.3 Impact Properties

The measure of energy devoured by a material during breaking is controlled by an effect assessment. This assimilated energy is an estimation of a material’s hardness

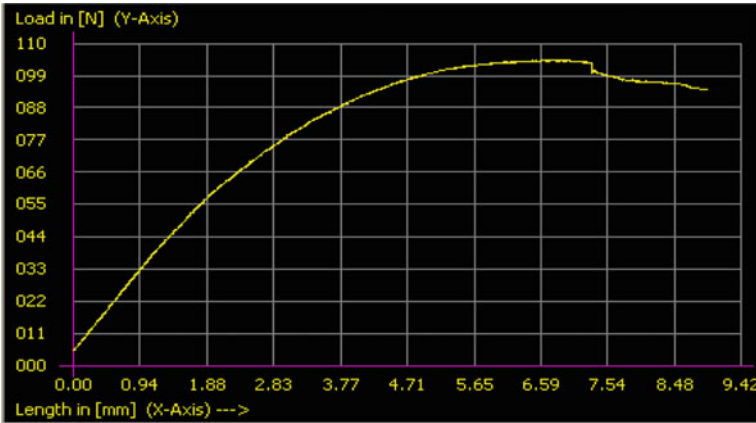


Fig. 12 Length versus load for nylon fibre sample 4

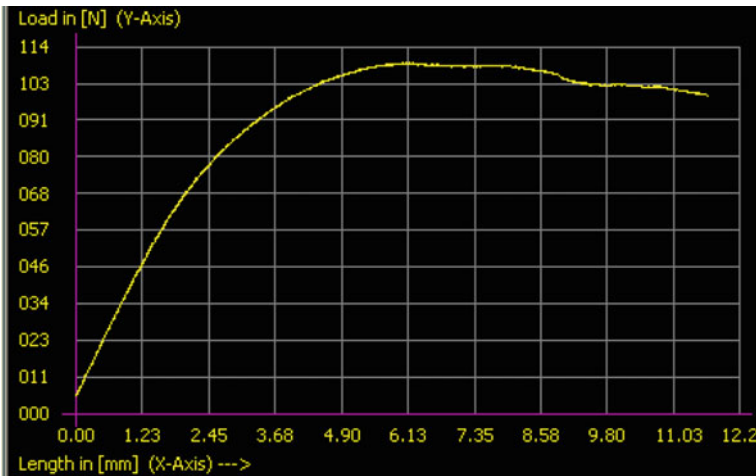


Fig. 13 Length versus load for nylon fibre sample

and can be utilized to explore the temperature-subordinate fragile bendable progress. Effect test is finished utilizing Izod testing techniques. The work done is appeared in Joule (Table 3).

6 Conclusion

Pressure shaping was utilized to make the jute fibre framework built up cover composites, which were then laid up by hand utilizing a nylon fibre mesh of (25% Nylon

Table 3 Impact test results

Sample No.	Izod Impact value in J for 3 mm thickness	Sample No.	Izod Impact value in J for 3 mm thickness
1	1.50	6	2.10
2	1.55	7	2.90
3	1.65	8	3.15
4	1.90	9	3.50
5	2.10	–	–

fibre + 75% Epoxy – resin + hardener), (30% nylon fibre + 70% Epoxy – 65% Epoxy – resin + hardener). The semi static resin + hardener), (35% Nylon fibre + and weariness execution of nylon fibre built up composites hybridized are researched in this investigation. The investigation tracked down that expanding the substance of composites builds the crossover composite's static malleable properties while diminishing the voids 'fraction. Notwithstanding the way that glass composites have a more extended weariness life than nylon and cross breed composites, they have the most elevated exhaustion affectability, as estimated by firmness degradation after some time.

References

1. Anand A, Kumar N, Harshe R, Joshi M (2017) Glass/epoxy structural composites with interleaved nylon6/6 nanofibers. *J Compos Mater* (2017)
2. Beylergi IB, Tanoglu M, Aktas E (2020) Experimental and statistical analysis of carbon fibre/epoxy composites interleaved with nylon6, 6 nonwoven fabric interlayers. *J Compos Mater*
3. Charles J, Rmakrishnan GR, Si A, Gunasekaran S (2009) FTIR and thermal studies on nylon-66 and 30% glass fibre reinforced nylon-66. *E-J Chem* (2009)
4. Unal H, Findik F, Mimaroglu A (2002) Mechanical behavior of nylon composites containing Talc and Kaolin. *J Appl Polym* (2002)
5. Frigione ME, Mascia L, Acierno D (1995) Oligomeric and polymeric modifiers for toughening of epoxy resins. *Eur Polym J* (1995)
6. Park BY, Kim SC, Jung B (1997) Interlaminar fracture toughness of carbon fiber/epoxy composites using short kevlar fiber and/or nylon-6 powder reinforcement. *Polym Adv Technol* (1997)
7. Gorton BS (1964) Interaction of nylon polymers with epoxy resin in adhesive blends. *J Appl Polym Sci*
8. Cheng F, Li H, Jiang W, Chen D (2006) Properties of compatibilized nylon 6/ABS polymer blends. *J Macromolecular Sci*
9. Gupta MK, Srivastava RK (2017) Mechanical, thermal and dynamic mechanical analysis of jute fibre reinforced epoxy composite. *Indian J Fibre Textile Res (IJFTR)*
10. Liu L, Yu J, Cheng L, Qu W (2009) Mechanical properties of poly (butylene succinate)(PBS) biocomposites reinforced with surface modified jute fibre. *Compos Part A Appl Sci Manufac*

Effect of Annealing Temperature on Phase Transformation of NiCr₂O₄ Nanoparticles and Evaluated Its Structural and Magnetic Properties



Jarnail Singh , Pankaj Bhardwaj, Ravi Kumar, Kaushal Kumar, Saurav Dixit, and Vikram Verma

Abstract Tetragonal nickel chromite (NiCr₂O₄) nanoparticles were synthesized using the wet chemical method and investigated their structural and magnetic properties at different annealing temperatures. Structural properties of as-prepared were determined using X-ray diffraction (XRD), Fourier-transform infra-red (FTIR) spectroscopy, and Raman spectroscopy technique. XRD results demonstrated that NiCr₂O₄ nanoparticles annealed at 800 and 900 °C led to the multi-phase compound formation of rhombohedral chromium oxide (Cr₂O₃) and tetragonal NiCr₂O₄ phase. However, a complete transformation of multi-phase to single NiCr₂O₄ tetragonal phase was achieved at 1000 °C. Raman and FTIR spectra also confirmed the formation of a single nickel chromite phase at an annealing temperature of 1000 °C. Some weak traces of characteristics modes of Cr₂O₃ phase were demonstrated at the lower annealing temperature. Magnetic properties of NiCr₂O₄ nanoparticles at different annealing temperatures were determined using a vibrating sample magnetometer (VSM). Multi-phase compound nanoparticles exhibited a mixed antiferromagnetic and paramagnetic behavior, whereas single-phase compound was ascribed to paramagnetic ones only.

Keywords Phase transformation · Nanoparticles · Chromite · Paramagnetic · Multi-phase compound · Spinel structure

J. Singh (✉) · K. Kumar

Department of Mechanical Engineering, K.R. Mangalam University, Gurugram 122103, India
e-mail: jarnail.singh@krmangalam.edu.in

P. Bhardwaj · R. Kumar · V. Verma

Department of Material Science and Engineering, National Institute of Technology Hamirpur, Hamirpur 177005, India

S. Dixit

School of Management and Commerce, K.R. Mangalam University, Gurugram 122103, India

Division of Research and Innovation, Uttaranchal University, Dehradun, India

1 Introduction

Spinel chromites based on transition metal with a general composition formula of $M\text{Cr}_2\text{O}_4$ (where $M = \text{Mn}^{2+}, \text{Fe}^{2+}, \text{Co}^{2+}, \text{Ni}^{2+}, \text{and } \text{Zn}^{2+}$) have received enormous interest owing to their magnetic properties and their remarkable technological expansion as ceramic pigment [1]. Pigment industries use transition metal oxides materials as ceramic dyeing due to their high thermal stability, surface area, and chemical resistance [2]. These spinel chromites are also used as an absorbent material to eradicate the sulfur-containing materials from refractory and hot-coal gas by utilizing their optical properties [3–5]. Therefore, spinel compounds have been extensively investigated due to their high structural stability, low optical band gap, high melting point, and exceptional catalytic and corrosion resistance properties [6–8]. Generally, spinel compounds (AB_2O_4) comprise the binary transition metal oxides having three different types of cation distribution patterns between the octahedral and tetrahedral sites, i.e., normal, inverse, and random. Considering the normal spinel structure, A cations are located at the tetrahedral sites, while B ions occupy the octahedral sites. On the contrary, in inverse spinel, half of the B cations are incorporated at the tetrahedral sites, and all the A cations relocate to the octahedral ones [9, 10]. Hence, the structural, optical, electrical, and catalytic properties of spinels can be tailored by the distribution and oxidation state of cations. Considering the spinel chromites, nickel chromite (NiCr_2O_4) has been explored by various researchers, so that it paved the way to render applications in the field of electronic and chemical industry [11]. However, NiCr_2O_4 is also recognized as a potential catalytic material. Therefore, the synthesization of nickel chromite nanoparticles with a large surface area is highly desirable from the application point of view [12–14]. Various methods have been used to synthesize NiCr_2O_4 materials such as microemulsion, sol–gel, polymeric gel, hydrothermal processes, citrate–nitrate gel combustion, sol spray processes, and solid-state reaction [2]. But, the lack of homogeneity, stoichiometry, and low surface area are the main disadvantages of the solid-state route [15]. All these drawbacks can overcome by using the solution-based technique, i.e., the wet chemical method. Therefore, we have used a wet chemical technique to synthesize the NiCr_2O_4 nanoparticles, providing better control over stoichiometry, homogeneity, and purity. It also offers several advantages like its flexibility, repeatability, swift process, novel, and cost-effective.

In this present report, we have synthesized nickel chromite nanoparticles using wet chemical method at different annealing temperatures and demonstrated the modification in its structural and magnetic properties.

2 Experimental Details

The chromium nitrate nonahydrate ($\text{Cr}(\text{NO}_3)_3 \cdot 9\text{H}_2\text{O}$) and nickel nitrate hexahydrate ($\text{Ni}(\text{NO}_3)_2 \cdot 6\text{H}_2\text{O}$) purchased from Sigma Aldrich with a purity of 99.99% was used

as a metal precursor without further purification. The 0.5 M solution of chromium precursor was prepared with double deionized water and continuously stirred for 30 min. Subsequently, nickel precursor solution was prepared with double deionized water and mixed with the former solution according to the stoichiometric amount under constant stirring for uniform mixing. Initially, the solution is acidic in nature. Therefore, ammonium hydroxide (NH_4OH) was introduced dropwise to form the dark green precipitates in the mother liquid by increasing the pH value to 7. After that, formed precipitates were allowed to settle down and washed many times with double deionized water to remove the soluble impurities. Later, precipitates were dried on a heating mantle at $90\text{ }^\circ\text{C}$ to evaporate the solvent gently and finally, annealed at 800, 900 and $1000\text{ }^\circ\text{C}$ in a muffle furnace under ambient environment for 4 h.

3 Results and Discussion

3.1 XRD Analysis

Figure 1 shows the XRD patterns of NiCr_2O_4 nanoparticles at different annealing temperatures. All the diffraction peaks observed at an annealing temperature of 800 and $900\text{ }^\circ\text{C}$ corresponds to Cr_2O_3 and NiCr_2O_4 phase. But, at an annealing temperature of $1000\text{ }^\circ\text{C}$, the weak characteristics peaks of the Cr_2O_3 phase are no longer observed. The multi-phase compound consists of NiCr_2O_4 and Cr_2O_3 phase transformed into single-phase nickel chromite (NiCr_2O_4) phase only [16]. All peaks reflected in the XRD pattern at $1000\text{ }^\circ\text{C}$ corresponds to the tetragonal crystal structure of NiCr_2O_4 having space group $I4_1/amd$, which is well in agreement with JCPDS card no. 89-6616 [17]. Apart from that, intensities of peaks are increasing with annealing temperature, indicating the improvement in the crystallinity of as-synthesized nanoparticles. Variation of lattice parameters of NiCr_2O_4 phase with annealing temperature is summarized in Table 1. It is clearly evident from Table 1 that lattice parameters and cell volume are decreasing with an increase in annealing temperature due to the strain induced in the crystal lattice. Average crystallite sizes of as-prepared nanoparticles are also determined using the Scherrer's equation [16]:

$$D = \frac{K\lambda}{\beta \cos \theta} \quad (1)$$

where, D is the average crystallite size, λ is the wavelength of incident X-rays, β is the full width at half maximum (FWHM) of diffraction peak (in radians), and θ is the diffraction angle at which FWHM is being determined. The highly intense peaks were used to calculate the average crystallite sizes of prepared nanoparticles annealed at various temperatures. The crystallite sizes of all the nanopowders are in nano-range, as depicted in Table 1. Similar to structural parameters, average crystallite size decreases as the multi-phase compound transforms into a single NiCr_2O_4 phase.

Fig. 1 XRD patterns of NiCr₂O₄ nanoparticles at different annealing temperatures. The symbol (*) corresponds to Cr₂O₃ phase and symbol (#) corresponds to NiCr₂O₄ phase

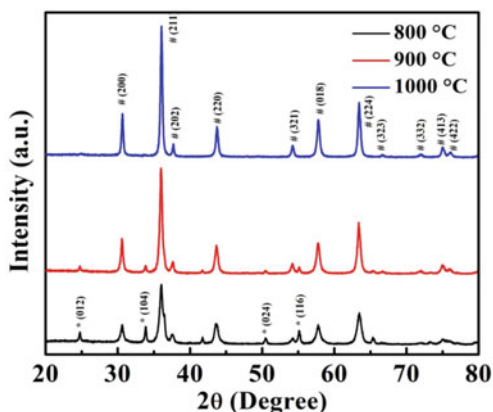


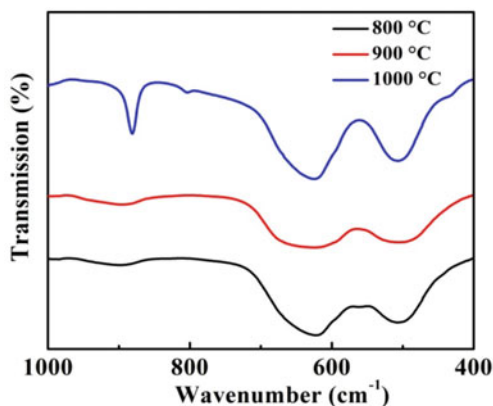
Table 1 Variation of lattice parameters, cell volume and crystallite size of NiCr₂O₄ nanoparticles with annealing temperature

Sample ID (°C)	Lattice parameter, a (Å)	Lattice parameter, c (Å)	Volume (Å) ³	Crystallite size, D (nm)
800	5.844	8.415	287.392	28.2
900	5.832	8.295	282.131	22.3
1000	5.828	8.287	281.473	21.7

3.2 FTIR Analysis

The FTIR spectra of synthesized NiCr₂O₄ nanoparticles at different annealing temperatures are depicted in Fig. 2. Two broad absorption bands centered at 508 and 623 cm⁻¹ have been observed in every sample. These bands confirmed the formation of NiCr₂O₄ phase. The first band seen at 508 cm⁻¹ is attributed to vibrational mode of Cr–O, while second band observed at 623 cm⁻¹ corresponds to Ni–O vibration in the tetrahedral environment [17]. The narrowing of 623 cm⁻¹ band is illustrated in Fig. 2. Because some traces of Cr₂O₃ phase are also present in prepared nanoparticles annealed at 800 and 900 °C (as discussed in XRD results). And, the absorption band of Cr₂O₃ phase is expected to be observed at 640 cm⁻¹ [16], which is responsible for the broadening of 623 cm⁻¹ band at an annealing temperature of 800 and 900 °C. Furthermore, intensity is also increasing with annealing temperature, indicating the fine crystallinity of the sample. These results are well consistent with our XRD results. Apart from the above-mentioned absorption band, another peak is reflected in FTIR spectra at 882 cm⁻¹, ascribed to the Ni–Cr vibration mode.

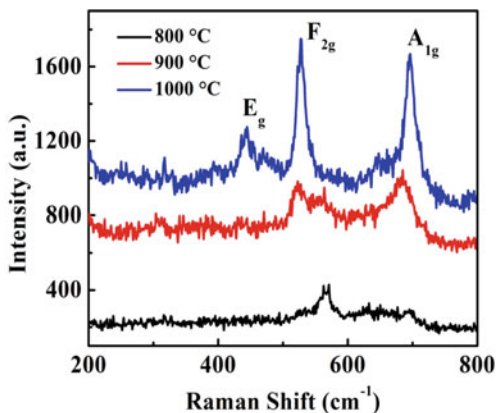
Fig. 2 FTIR spectra of NiCr_2O_4 nanoparticles at different annealing temperature



3.3 Raman Analysis

The room temperature Raman spectra of nickel chromite nanoparticles were performed within the range of 200–800 cm^{-1} . Four symmetry modes have been demonstrated in Fig. 3. The modes observed at 437, 528, and 686 cm^{-1} corresponds to the tetragonal NiCr_2O_4 phase having E_g , F_{2g} , and A_{1g} symmetry, respectively [18]. All peaks attributed to the nickel chromite phase become highly intense with annealing temperature. That's why peaks become most prominent due to structural transformation from multi-phase to single NiCr_2O_4 phase with increasing annealing temperature.

Fig. 3 Raman spectra of nickel chromite nanoparticles



3.4 Magnetic Analysis

Figure 4 shows the field dependence magnetization at room temperature annealed at 800 °C, 900 °C, and 1000 °C. The coercivity (H_c), retentivity (M_r), and saturation magnetization (M_s) values were determined from the M–H curve, as shown in Table 2. The as-prepared nanoparticles M–H curve shows the dominated linear nature with an applied magnetic field of 1.8 T confirming the mixed paramagnetic and antiferromagnetic behavior. The M–H curves observed at annealing temperatures of 800 °C and 900 °C are constituted of the mixed-phase of Cr_2O_3 and NiCr_2O_4 , while prepared nanoparticles annealed at 1000 °C were transformed into a single NiCr_2O_4 phase as confirmed by structural analysis. From Table 2, it is seen that with an increase in annealing temperature from 800 °C to 1000 °C, the H_c decreases from 131.74 to 18.72 Oe.

The decrease in coercivity value can be explained by change in crystallite size of as-prepared nanoparticles. The reduction in crystallite size induces an increase in the multi-domain region, which increases the coercivity up to its critical diameter only (surface spin effects). After further reduction in crystallite size, system moves to a single domain region, responsible for decrease in coercivity value [11, 19]. Furthermore, as-prepared nanoparticles annealed at 800 °C have a higher antiferromagnetic

Fig. 4 M–H plots of NiCr_2O_4 nanoparticles at various annealing temperatures. The inset illustrated the enlarged view of M–H curve

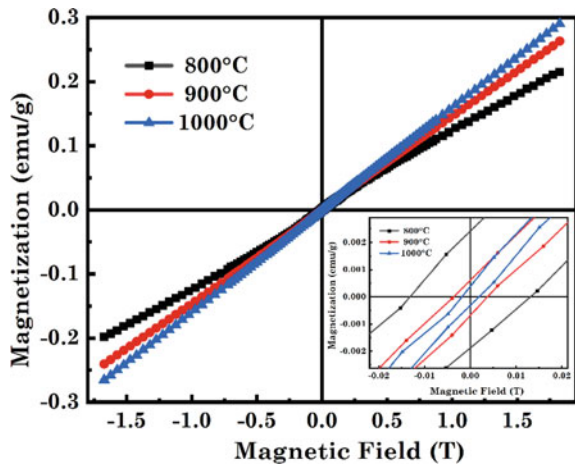


Table 2 Variation of coercivity (H_c), retentivity (M_r), and saturation magnetization (M_s) of NiCr_2O_4 nanoparticles at different annealing temperatures

Sample ID (°C)	Saturation magnetization, M_s (emu/g)	Coercivity, H_c (Oe)	Retentivity, M_r (emu/g)
800	0.277	131.74	1.77×10^{-3}
900	0.252	36.95	2.62×10^{-4}
1000	0.206	18.72	6.48×10^{-4}

Cr_2O_3 ($T_n = 310 \text{ K}$ [20]) impurities containing Ni^{2+} and Cr^{3+} spins, increasing interfacial superexchange interaction, which is responsible for enhanced hysteresis. At 1000°C annealing temperature, the M – H curve shows a very narrow loop with negligible M_r and H_c and magnetization linearly dependent on the applied magnetic field depicts the paramagnetic phase of NiCr_2O_4 nanoparticles as they exhibit ferrimagnetic ordering below 74 K [16]. This magnetic study implies a clear transition from mixed AFM Cr_2O_3 phase to paramagnetic NiCr_2O_4 phase with increasing annealing temperature.

4 Conclusion

Single-phase nickel chromite (NiCr_2O_4) has been successfully synthesized using wet chemical method by varying the thermal treatment. XRD results confirmed the formation of single-phase nickel chromite from multi-phase at an annealing temperature of 1000°C . Lattice parameters and crystallite size were found to be diminishing with the increase in annealing temperature. This is due to the strain induced by the weak traces of Cr_2O_3 phase. Raman and FTIR spectra also revealed the successful formation of a single NiCr_2O_4 phase. The coercivity, retentivity value, and saturation magnetization value was found to be diminishing as crystal structure transforms into single-phase NiCr_2O_4 phase, which is paramagnetic.

References

1. Barman J, Bora T, Ravi S (2015) *J Magn Magn Mater* 385:93–98
2. Fairouz NY, Imran AR (2013) *J Appl Chem* 2:129–136
3. Khalil N, Hassan MB, Ewais EM, Saleh FA (2010) *J Alloy Comp* 496:600–607
4. Ying WC, Bonk RR, Tucker ME (1988) precipitation-treatment of spent electroless nickel plating pass. *J Hazard Mater* 18:69–89
5. Ayala R, Marsh DW (1991) *Ind Eng Chem Res* 30:30–55
6. Lv W, Liu B, Qiu Q, Wang F, Luo Z, Zhang P, Wei S (2009) *J Alloy Comp* 479:480–483
7. Yan JY, Gang LJ, Ling NG (2006) *J Chin Ceram Soc* 34:1084–1807
8. Patdeshi SK, Pawar RY (2010) *Mater Res Bull* 45:609–615
9. Theophil Anand G, John Kennedy L, Judith Vijaya J (2013) *J Alloy Compd* 581:558–566
10. Ziemniak SE, Gaddipati AR, Sander PC (2005) *J Phys Chem Solids* 66:1112–1121
11. Zhuiykov S, Nakano T, Kunimoto A (2001) *Norio Miura. Electrochem Commun* 3:97
12. Li N, Chen YH, Hu C, Hsieh CH, Lo SL (2011) *J Hazard Mater* 198:356–361
13. Klemme S, Van Miltenburg J (2002) *Phys Chem Miner* 29:663–667
14. El-Sheikh SM, Rabbah M (2013) *Thermochim Acta* 568:13–19
15. Niasari MS, Davar A, Farhadi M (2009) *J Chem Mater Sci* 51:48–52
16. Singh J, Kumar R, Verma V, Kumar R (2020) *Ceram Int* 46:24071–24082
17. Ptak M, Maczka M, Ґagor A, Pikul A, Macalik L, Hanuza J (2013) *J Solid State Chem* 201:270–279

18. Karmakar S, Parey V, Mistari CD, Thapa R, More MA, Behera D (2020) *Phys Status Solidi A* 217:1900741
19. Devi EC, Singh SD (2021) *J Supercond Novel Magn* 34:617–622
20. Bhardwaj P, Singh J, Kumar R, Kumar R, Verma V (2021) *Solid State Sci* 115:106581

Comparative Study of Concrete Cylinders Confined Using Natural and Artificial Fibre Reinforced Polymers



Priyanka Singh, Saurav Dixit, Margel Taso, Kaushal Kumar, Jarnail Singh, Krystyna Araszkiwicz, Nikolai Ivanovich Vatin, and Chander Prakash

Abstract Fibre reinforced polymers are light, corrosion resistant, and resilient, thereby creating a boom for the future technical knowhow in means of transportation ranging from roadways, railways, and airways. Use of natural fibre by mankind can be dated back since ages ago like building materials. Polymers' invention in the early nineteenth century opened new doors for a researcher to use natural fibre. Synthetic fibre, for example, glass fibre, usage has skyrocketed fibre. More usage of synthetic fibre leads to pollution during its manufacture and recycling shifting the need to use from synthetic to natural fibre. This generated newfound interest in the new ways of natural fibre and to be neck-to-neck of the synthetic fibres. Nowadays, it is being used in aerospace and building industry. Here, the testing has been done to calculate confinement modulus and strength, thereby plotting load vs deflection and axial stress versus axial strain. Comparison has been carried out between confinement modulus and strength when they are fully and partially warped.

Keyword Fibre reinforcement polymers · Concrete · Construction management · Buildings

P. Singh · M. Taso

Civil Engineering Department, Amity University Uttar Pradesh, Noida 201313, India

S. Dixit (✉) · N. Ivanovich Vatin

Peter the Great St. Petersburg Polytechnic University, 195251 Saint Petersburg, Russia

e-mail: sauravarambol@gmail.com

S. Dixit

Division of Research & Innovation, Uttarakhand University, Uttarakhand 248007, India

K. Kumar · J. Singh

School of Engineering and Technology, K.R. Mangalam University, Gurgaon 122103, India

K. Araszkiwicz

Faculty of Civil and Environmental Engineering, West Pomeranian University of Technology, Szczecin, Poland

C. Prakash

School of Mechanical Engineering, Lovely Professional University, Phagwara, India

1 Introduction

1.1 Confinement

Confinement helps to reinforce building columns. Reinforced concrete confinement, steel confinement, fibre reinforced polymer composite confinement, and confinement using high tension materials such as carbon fibre and glass fibre are the most common forms. Confinement is used to increase concrete confinement by using transverse fibre or reinforcement, especially for circular cross-sectional columns, and to boost flexural strength by using longitudinal fibre or reinforcement, provided they are properly anchored at crucial portions [1–4] Table 1.

1.2 Confinement of Concrete

Confinement refers to the process of restricting concrete by utilising closely spaced unique transverse reinforcing in perpendicular directions to the applied load. These are spaced closely together. Small-diameter ties in columns and stirrups in beams are examples. Proper confinement is especially important at the joints between beams and columns. Tension must be transmitted from the top of the beam on one side of the joint to the bottom of the beam on the other at these points, when both building inter-storey drifts and joint rotations are high [5–8]. Simultaneously, tension must be transmitted from one side of the column to the other through the same section of the joint known as the panel zone, resulting in strong shear forces in the panel zone Table 1. Vertical and horizontal transverse reinforcing, as well as longitudinal reinforcing, is all crammed into the joints of concrete [9–14].

1.3 FRP

Fibres themselves and resin matrix are the two physical phases of fibre reinforced polymers. Carbon, glass, and aramid are most generally used as fibre materials. Glass fibre provides less stiffness to composite material than carbon and aramid. Polyester, epoxy, vinyl ester, and phenolic types are resins commonly used for matrices. Selecting the electrical and adhesive characteristic, service temperature capabilities, and chemical resistance properties of the composite depends on type of resin [15–20].

Table 1 Different types of natural fibres along with their applications

Fibre name	Source	Major producing states	Production in India (Mt/year)	Application in building material
Rice husk (<i>Oryza sativa</i>)	Rice mills	Orissa, Punjab, etc.	20	As a source of energy for the production of building materials and goods such as rice husk binder, fibrous building panels, bricks, and acid-resistant cement
Banana leaves/stalk (<i>Musa acuminata</i>)	Banana plants	Southern Indian states and Gujarat	0.20	Fire-resistant fibre board is being used in the construction of high-rise materials
Coconut husk (<i>Cocos nucifera</i>)	Coir fibre industry	Kerala, Tamil Nadu, etc.	1.60	As a lightweight aggregate, coir fibre reinforced composite, cement board, geo-textile, rubberised coir, construction boards, roofing sheets, insulation boards, and building panels
Groundnut shell (<i>Arachis hypogaea</i>)	Groundnut oil mills	Andhra Pradesh, Maharashtra, Madhya Pradesh, etc.	11.00	In the production of building panels and building blocks, as well as chipboards, roofing sheets, and particle boards
Coconut husk (<i>Cocos nucifera</i>)	Coir fibre industry	Kerala, Tamil Nadu, etc.	1.60	As a lightweight aggregate, coir fibre reinforced composite, cement board, geo-textile, rubberised coir, construction boards, roofing sheets, insulation boards, and building panels

(continued)

Table 1 (continued)

Fibre name	Source	Major producing states	Production in India (Mt/year)	Application in building material
Groundnut shell (<i>Arachis hypogaea</i>)	Groundnut oil mills	Andhra Pradesh, Maharashtra, Madhya Pradesh, etc.	11.00	In the production of building panels and building blocks, as well as chipboards, roofing sheets, and particle boards
Jute fibre (<i>Corchorus capsularis</i>) or (<i>Corchorus olitorius</i>)	Jute industry	West Bengal, North-Eastern states, etc.	1.44	For the production of chipboards, roofing sheets, and door shutters
Rice/wheat straw	Agricultural farm	North India, North-East, Karnataka, West Bengal, and Bihar	12.00	Fabrication of roofing panels and wall panels/boards
Saw mill waste	Saw mills/wood	Most part of India	2.00	Cement-bonded wood chips, blocks, boards, particle boards, insulation boards, and briquettes are manufactured
Sisal fibres (<i>Agave sisalana</i>)	Sisal plantation	Andhra Pradesh, Bihar, Orissa, Karnataka, Maharashtra, and West Bengal	0.023 (Asia)	Plastering walls and creating roofing sheets, rice husk composite board, cement roofing sheet, roofing tiles, and paper and pulp manufacture
Cotton stalk (<i>Gossypium hirsutum</i>)	Cotton plantation	Gujarat, Maharashtra, and Andhra Pradesh,	1.10	Fibre boards, panelling, door shutters, roofing sheets, autoclaved cement composite, paper, and wall plastering

1.4 Function of Various Constituents of FRP

The fibres used have a significant impact on the composite. They are used to boost the composite material's load-carrying capacity, and they have a very high tensile strength. They only have tensile qualities over the length of the fibre, similar to rope

fibres [21]. A woven fibre is frequently used to reinforce the composite, giving it good strength in all directions. Oriented fibres give a composite a lot of strength in the direction of the fibres. All fibres are linear elastic till failure and have a higher stress capacity than conventional steel [22–27].

Schematic illustration of the modified ORC–VCR system with recuperator and reheater is shown in the Fig. 1a. In system, we have two cycles, first is power cycle (1-2-3-4-5-6-7-8-9-1), and the other is refrigeration cycle (7-10-11-12-7); both cycles share same refrigerant as a working fluid. This modified system has a recuperator and two expanders which are operating at same shaft speed, and compressor is also directly coupled to this shaft. At outlet of the boiler, working fluid is in vapour phase which enters in first expander and pressure decreases up to intermediate pressure; then, again it is sent to the boiler for reheating. After reheating, working fluid expands into second expander up to condenser pressure. Now, working fluid enters in the recuperator which is a counter flow energy recovery heat exchanger. Recuperator is placed between the second expander exit and the condenser inlet or between the pump exit and boiler inlet for heat recovery. In the recuperator, liquid is preheated before entering into the boiler by absorbing heat from the working fluid coming out from the second expander.

Figure 1b shows the T–S diagram of the improved ORC–VCR system. 12 real expansion through the high pressure expander is one of the processes that describe the system. 34% real expansion through the low pressure expander; 45% constant pressure cooling of low pressure expander vapour by mixing with compressor discharge vapour; 23% reheating at constant pressure; 34% actual expansion through the low pressure expander; 56%: The expander exhaust is used to warm the working fluid leaving the pump. 7: real pumping work; 6: isobaric heat rejection (condensation); 6: isobaric heat rejection (condensation); 6: isobaric heat rejection (con 89%: The expander exhaust pre-heats the working fluid.

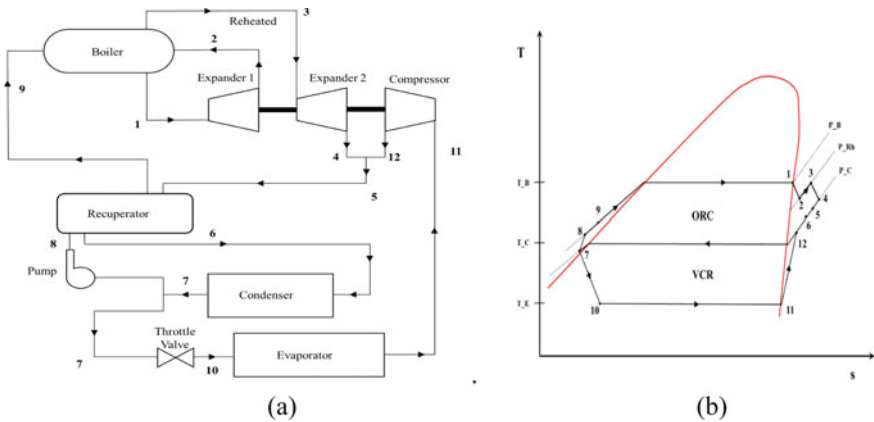


Fig. 1 a Schematic illustration of modified ORC–VCR system b T–S diagram of the modified ORC–VCR System

11: isobaric heat absorption (evaporation) in the VCR cycle; 10: isenthalpic expansion through the throttle valve in the VCR cycle; 12: actual compression through the compressor.

2 Thermodynamics Analysis

In the present work, thermodynamic analysis of modified ORC–VCR system has been carried out by considering all components are in steady-state conditions and there are no heat and friction losses. The thermophysical properties of the working fluids for different states have been calculated using a software package Energy Equation Solver (EES). Software EES is a vital tool for thermodynamic calculations of refrigeration and cryogenic systems [17, 18]

Work obtained by the first expander

$$\dot{w}_{E1} = \dot{w}_{1-2} = \dot{m}_{\text{ORC}}(h_1 - h_{2s})\eta_{\text{exp}1} \quad (1)$$

$$\dot{w}_{E1} = \dot{m}_{\text{ORC}}(h_1 - h_2) \quad (2)$$

Heat supplied in the reheater

$$\dot{Q}_{\text{Re}} = \dot{m}_{\text{ORC}}(h_3 - h_2) \quad (3)$$

Work obtained by the second expander

$$\dot{w}_{E2} = \dot{w}_{3-4} = \dot{m}_{\text{ORC}}(h_3 - h_{4s})\eta_{\text{exp}2} \quad (4)$$

$$\dot{w}_{E2} = \dot{m}_{\text{ORC}}(h_3 - h_4) \quad (5)$$

Recuperator

$$(\dot{m}_{\text{ORC}} + \dot{m}_{\text{VCR}})(h_5 - h_6) = \dot{m}_{\text{ORC}}(h_9 - h_8) \quad (6)$$

The effectiveness (ε) is the ratio of the actual to maximum possible heat transfer rates and is expressed as

$$\varepsilon = \frac{T_5 - T_6}{T_5 - T_8} \quad (7)$$

Heat rejected in condenser

$$\dot{Q}_C = (\dot{m}_{\text{ORC}} + \dot{m}_{\text{VCR}})(h_6 - h_7) \quad (8)$$

Work supplied in pump

$$\dot{w}_P = \dot{w}_{7-8} = \dot{m}_{\text{ORC}}(h_{8s} - h_7)/\eta_{\text{pump}} \quad (9)$$

$$\dot{w}_P = \dot{m}_{\text{ORC}}(h_8 - h_7)$$

Heat supplied in boiler

$$\dot{Q}_{\text{Boiler}} = \dot{m}_{\text{ORC}}(h_1 - h_9) \quad (10)$$

Net work obtained from the ORC

$$\dot{w}_{\text{net}} = \dot{w}_{E1} + \dot{w}_{E2} - \dot{w}_P \quad (11)$$

Total heat supplied to ORC

$$\dot{Q}_{\text{Supply}} = \dot{Q}_{\text{Boiler}} + \dot{Q}_{\text{Re}} \quad (12)$$

Efficiency of ORC

$$\eta_{\text{ORC}} = \frac{\dot{w}_{\text{net}}}{\dot{Q}_{\text{Supply}}} \quad (13)$$

Heat absorbed in the evaporator

$$\dot{Q}_E = \dot{m}_{\text{VCR}}(h_{11} - h_{10}) \quad (14)$$

Work supplied to the compressor

$$\dot{w}_C = \dot{w}_{11-12} = \dot{m}_{\text{VCR}}(h_{12s} - h_{11})/\eta_{\text{comp}} \quad (15)$$

$$\dot{w}_C = \dot{m}_{\text{VCR}}(h_{12} - h_{11})$$

$$\text{COP}_{\text{VCR}} = \frac{\dot{Q}_E}{\dot{w}_{\text{net}}} \quad (16)$$

Work supplied to the compressor of VCR = Net work obtained from ORC

$$\dot{w}_C = \dot{w}_{\text{net}} \quad (17)$$

$$\text{COP}_{\text{system}} = \text{COP}_{\text{VCR}} \times \eta_{\text{ORC}} \quad (18)$$

Table 2 The input parameters and boundary conditions

Parameters	Boundary	Range
Boiler exit temperature (T_b)	80 °C	60–90 °C
Condenser temperature (T_c)	40 °C	30–55 °C
Constant subcooling in condenser	3 °C	
Evaporator temperature (T_e)	5 °C	–15–15 °C
High pressure expander isentropic efficiency (η_{exp1})	0.80	–
Low pressure expander isentropic efficiency (η_{exp2})	0.80	–
Compressor isentropic efficiency (η_{comp})	0.80	–
Boiler feed pump isentropic efficiency η_{pump}	0.75	–
Effectiveness of recuperator (ε)	0.90	–
Working fluid mass flow rate in ORC (\dot{m})	1 kg/s	–
Reheat exit temperature (T_b)	–	60–90 °C
Reheat pressure	$(P_e * P_c)^{1/2}$	–

$$EPR = V_1/V_4 \quad (19)$$

$$CMR = P_{12}/P_{11} \quad (20)$$

Table 2 lists the input parameters as well as the boundary conditions. The maximum boiler exit temperature is set to 90 °C, which corresponds to a heat source temperature of around 100 °C. Flat-plate solar collectors or water-dominated geothermal energy can readily achieve this temperature level.

3 Results and Discussion

The effects of the boiler exit (BE) temperature on the COP system are shown in Fig. 2a. The redesigned ORC–VCR system's COP system increases with BE temperature, as can be seen. For R1270, R290, R600a, and R600, the COP system increases by 90.92%, 103.01%, 123.04%, and 125.8%, respectively, while the BE temperature rises from 60 to 90 °C. Due to the higher critical temperature of this fluid, R600 has the highest COP system. With the BE temperature at 90 °C, the COP system for the R600 case is 0.5542, which is around 6.6%, 26.3%, and 37.89% higher than the R600a, R290, and R1270 cases, respectively.

Figure 2b demonstrates how BE temperature affects the mQ0 (flow rate mass per kW refrigeration capacity). As the work generated by the expanders increases, mQ0 decreases with the increase in BE temperature for all working fluids. R600 has the lowest flow rate, which is followed by R600a, R290, and R1270. R1270 has the greatest mQ0 at 90 °C, with a value of 0.01869 kg/kW-s.

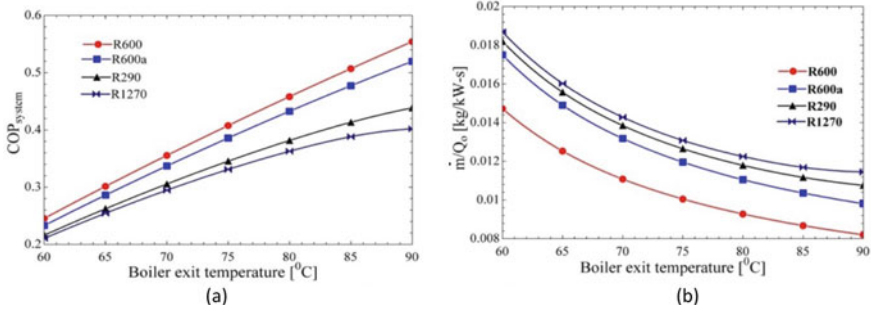


Fig. 2 Variation of **a** COP_{system} and **b** \dot{m}/Q_0 with BE temperature

Figure 3 shows the effect of BE temperature on the EPR (a). EPR in ORC increases when BE temperature rises but condenser temperature remains constant, since boiler temperature rises, so does saturation pressure. For wet refrigerants such as R290 and R1270, EPR at the BE temperature of 90 °C is approximately three times that at 60 °C, and for dry refrigerants such as R600 and R600a, it is two times. R1270 has the highest EPR, which is followed by R290, R600, and R600a. However, the changes in EPR for these hydrocarbons are initially extremely minor, with the highest appearing at about 37.86% between the R600 and R1270 cycles at a boiler exit temperature of 90 °C.

Figure 3 shows an example of this (b). The condenser in an ORC–VCR system is shared by both cycles and is also affected by the ambient temperature. A high condenser temperature is undesirable for fixed boiler and evaporator temperatures. When a result of the plot, it can be determined that as the condensation temperature rises, the COP system decreases. R600 is a better choice than R290, R600a, and R1270. At a condensation temperature of 55 °C, the COP system of the ORC–VCR systems utilising R1270, R290, R600a, and R600 as working fluids yields 0.1367, 0.1446, 0.1675, and 0.1821, respectively.

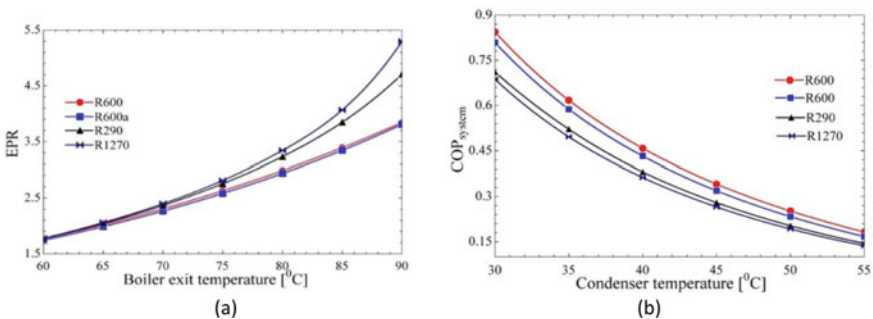


Fig. 3 **a** Variation of EPR with BE temperature. **b** Variation of COP_{system} with condenser temperature

The fluctuation of mass flow rate per kW cooling capacity with condenser temperature is seen in Fig. 4a. The mass flow rate per kW cooling capacity increases as the condenser temperature rises. The lowest mass flow rate per kW cooling capacity is obtained in the case of R600, with a value of 0.02113, under the same operating conditions, whereas the highest occurs for R1270 reaching to 0.03076 kg/kW-s.

The EPR in the ORC diminishes as the condenser temperature increases, as shown in Fig. 4b. This is self-evident when considering the thermophysical parameters of these working fluids. For condenser temperatures ranging from 30 to 55 °C, the differences in expander ratio values for the four hydrocarbons are roughly equal. When compared to the other fluids, the decrease in EPR in R1270 and R290a is more pronounced. It is worth noting that when the condenser temperature is above 50 °C, the differences in EPR for dry hydrocarbons, such as R600 and R600a, are fairly modest.

From Fig. 5a, it is observed that CMR value increases with condenser temperature as pressure ratio in the VCR cycle increases. However, the value of CMR significantly increases with condenser temperature for R600 and R600a.

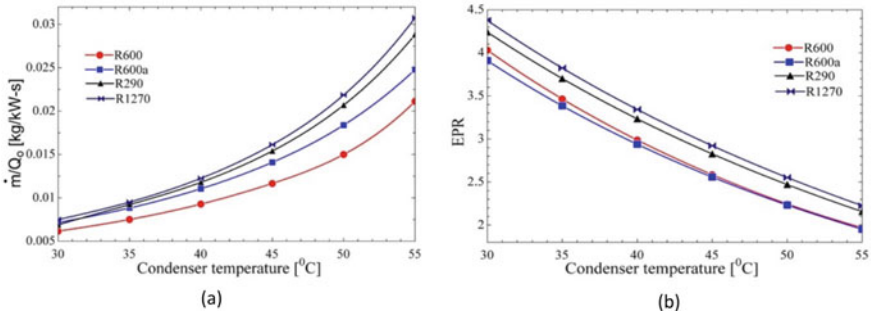


Fig. 4 a Variation of condenser temperature with \dot{m}/Q_c . b Variation of condenser temperature with EPR

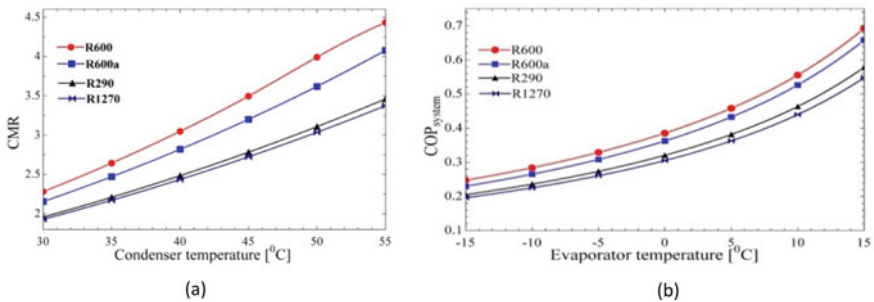


Fig. 5 a Variation of CMR with condenser temperature. b Variation of COP_{system} with evaporator temperature

In Fig. 5b, as the pressure ratio in the VCR cycle increases, the CMR value increases with condenser temperature. For R600 and R600a, however, the value of CMR increases dramatically as the condenser temperature rises. Because of the thermophysical qualities of the working fluids, this is clear.

The effect of the evaporation temperature on the COP system is seen in Fig. 5b. It can be shown that as the evaporation temperature rises, so does the COP system of the ORC–VCR system. When the evaporator temperature rises, the pressure ratio lowers, reducing compressor work. This enhances the overall system performance by increasing the COP of the VCR system. The COP system increases by around 179.7% for the four examples when the evaporation temperature varies from –15 to 15 °C. Furthermore, under similar operating conditions, the R600 case performs better. The COP system of the ORC–VCR system utilising R600, for example, is roughly 5.1% when the evaporation temperature is 15%, 19.76%, and 26.36% higher than the cases of R600a, R290, and R1270, respectively.

Figure 6a demonstrates how $m\dot{Q}_0$ changes as the evaporator temperature rises. The value of $m\dot{Q}_0$ grows as the evaporator temperature rises. The $m\dot{Q}_0$ declines as the evaporator temperature rises from –15 to 15 °C, and it is lowest for butane. Furthermore, R1270 a has the best mass flow rate per kW cooling capacity under similar operating conditions. $m\dot{Q}_0$ is approximately 17.8%, 24.79, and 29.43% lower than R600a, R290, and R1270, respectively.

The fluctuation of evaporator temperature with CMR is depicted in Fig. 6b. Because the evaporation temperature ranges from –15 to 15 °C, CMR decreases, and it is lowest for the propylene. Propane and propylene both are wet fluid refrigerants, and their CMR are almost similar. On increasing evaporator temperature at fixed condenser temperature, the pressure ratio decreases, and hence, the size of compressor reduces.

The performance of the modified ORC–VCR system with recuperator and reheater is also compared with simple ORC–VCR system with no additional component and ORC–VCR system with recuperator only. For the modified ORC–VCR cycle, at boiler exit temperature of 90 °C and condenser temperature 40 °C the system COP

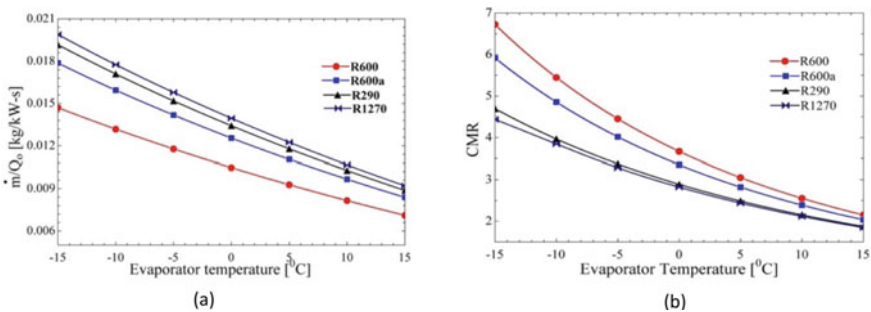


Fig. 6 a Variation of evaporator temperature with \dot{m}/Q_0 . b Variation of CMR with evaporator temperature

with butane is 0.5542 which is 7.1% and 18% higher than that of ORC–VCR cycle with recuperator only and simple ORC–VCR cycle, respectively.

4 Conclusion

In the work, modified ORC–VCR cycle integrated with recuperator and reheater has been investigated and R600a, R600, R290, and R1270 were proposed as working fluids. From the analysis, effect of various operating conditions, viz. evaporator temperature, condenser temperature, BE temperature on overall COP, mass flow rate per kW cooling capacity, and expansion ratio and compression ratio, is concluded here. The performance of modified ORC–VCR cycle with recuperator and reheater is seen good with R600 and R600a in comparison with R290 and R1270. Moreover, for same conditions, the performance of the modified ORC–VCR cycle is higher in comparison with simple ORC–VCR system and ORC–VCR cycle with recuperator.

References

1. Saleh B (2016) Parametric and working fluid analysis of a combined organic Rankine-vapor compression refrigeration system activated by low-grade thermal energy. *J Adv Res* 7(5):651–660
2. Thangavel S, Verma V, Tarodiya R, Kaliyaperumal P (2021) Comparative analysis and evaluation of different working fluids for the organic Rankine cycle performance. *Mater Today Proc*
3. Raghulnath D, Saravanan K, Mahendran J, Lakshmanan P (2020) Analysis and optimization of organic Rankine cycle for IC engine waste heat recovery system. *Mater Today Proc* 1(21):30–35
4. Rawat KS, Pratihari AK (2018) Numerical investigation of ice slurry flow in a horizontal pipe. *IOP Conf Ser Mater Sci Eng* 310(1):012095
5. Kim KH, Perez-Blanco H (2015) Performance analysis of a combined organic Rankine cycle and vapor compression cycle for power and refrigeration cogeneration. *Appl Therm Eng* 5(91):964–974
6. Saleh B (2018) Energy and exergy analysis of an integrated organic Rankine cycle-vapor compression refrigeration system. *Appl Therm Eng* 1(141):697–710
7. Li H, Bu X, Wang L, Long Z, Lian Y (2013) Hydrocarbon working fluids for a Rankine cycle powered vapor compression refrigeration system using low-grade thermal energy. *Energy Build* 1(65):167–172
8. Yue C, You F, Huang Y (2016) Thermal and economic analysis of an energy system of an ORC coupled with vehicle air conditioning. *Int J Refrig* 1(64):152–167
9. Rawat KS, Khulve H, Pratihari AK (2015) Thermodynamic analysis of combined ORC–VCR system using low grade thermal energy. *Int J Res Appl Sci Eng Technol* 3:515–522
10. Pektezel O, Acar HI (2019) Energy and exergy analysis of combined organic Rankine cycle-single and dual evaporator vapor compression refrigeration cycle. *Appl Sci* 9(23):5028
11. Nabati A, Saadat-Targhi M (2021) Use of solar radiation to produce cold water for hospital air conditioning system using the combined organic Rankine-vapor compression cycle. *Energy Equip Syst* 9(1):53–69
12. Rawat KS, Bisht VS, Pratihari AK (2015) Thermodynamic analysis and optimization CO₂ based transcritical cycle. *Int J Res Appl Sci Eng Technol* 3:287–293

13. Bisht VS, Pratihari AK, Vishnoi PK, Bhandari P (2018) R1234YF: an eco-friendly drop in replacement of R12 and R134A. *Asian J Appl Sci Technol* 2(4):36–46
14. Goyal A, Sherwani AF, Tiwari D (2021) Optimization of cyclic parameters for ORC system using response surface methodology (RSM). *Energy Sources Part A: Recovery, Utilization, and Environmental Effects* 43(8):993–1006
15. Salim MS, Kim MH (2019) Multi-objective thermo-economic optimization of a combined organic Rankine cycle and vapour compression refrigeration cycle. *Energy Convers Manage* 199:112054
16. Bademlioglu AH, Canbolat AS, Kaynakli O (2020) Multi-objective optimization of parameters affecting organic Rankine cycle performance characteristics with Taguchi-grey relational analysis. *Renew Sustain Energy Rev* 117:109483
17. Bisht VS, Pratihari AK (2014) Thermodynamic analysis of actual vapour compression system with R12 and its eco-friendly alternatives refrigerants. *Int J Eng Res Appl* 4(1):114–122
18. Bisht VS (2014) Thermodynamic analysis of Kapitza cycle based on nitrogen liquefaction. *IOSR J Eng* 4:38–44
19. Arora R, Kumar KI, Dixit S, Mishra L (2021) Analyze the outcome of waste material as cement replacement agent in basic concrete. *Mater Today Proc*
20. Kumar KI, Arora R, Khan S, Dixit S (2021) Characterization of fly ash for potential utilization in green concrete. *Mater Today Proc*
21. Dixit S, Stefańska A (2021) Digitisation of contemporary fabrication processes in the AEC sector. *Mater Today Proc*
22. Dixit S, Sharma K, Singh S (2020) Identifying and analysing key factors associated with risks in construction projects. In: *Emerging trends in civil engineering*, vol 61. Springer, Singapore, pp 25–32. https://doi.org/10.1007/978-981-15-1404-3_3
23. Dixit S, Stefańska A, Musiuk A (2021) Architectural form finding in arboreal supporting structure optimisation. *Ain Shams Eng J* 12(2):2321–2329
24. Dixit S (2021) Impact of management practices on construction productivity in Indian building construction projects: an empirical study. *Organ Technol Manage Constr* 13(1):2383–2390
25. Dixit S (2020) Study of factors affecting the performance of construction projects in AEC industry. *Organ Technol Manage Constr Int J* 12(1):2275–2282
26. Dixit S, Stefańska A (2022) Bio-logic a review on the biomimetic application in architectural and structural design. *Ain Shams Eng J* 101822. <https://doi.org/10.1016/j.asej.2022.101822>
27. Aghimien D, Ngcobo N, Aigbavboa C, Dixit S, Vatin NI, Kampani S, Khera GS (2022) Barriers to digital technology deployment in value management practice. *Buildings* 12(6):731. <https://doi.org/10.3390/buildings12060731>

Experimental Evaluation of Moringa and Amaranth Oil as Bio-Nanolubricant for Light Gear Application



Sagar Galgat and Ankit Kotia

Abstract Lubricating oil based on mineral oils put forward a challenge of water contamination and prolonged toxicity to environment due to non-degradable nature. Further continuous depletion of fossil resources and higher cost of conventional oil motivate to explore alternative of mineral oil-based lubricants. Recent approach is to identify plant and animal derived oil as bio-lubricant. In the present study, moringa and amaranth oils are used as base oil for bio-lubricant as both have high unsaturated fatty acid composition. The rheological analysis is experimentally investigated for the plain base oil and with nanoparticles. MWCNT and CeO₂ are used as nanoparticles for the development of bio-nanolubricants, both of which are dispersed in a 1% weight fraction with the base moringa and amaranth oil. The dispersion of MWCNT shows higher viscosity for the case of moringa oil, and CeO₂ shows higher increment with amaranth oil. All the sample displayed Newtonian behavior.

Keywords Bio-lubricant · Nanoparticles · MWCNT · CeO₂ · Rheological analysis · Bio-nanolubricants

1 Introduction

Conventional petroleum-based products are facing problems due to continuous depletion of fossil fuel resources and high cost. These petroleum-based products are harmful to the environment as they are non-degradable and highly toxic. It is also difficult to dispose of waste oil which can contaminate the air and soil. All these issues highlight the need for an alternative to petroleum-based products. Many researches are focused on developing a bio-lubricant which is a potential alternative of the conventional lubricating oil. Bio-lubricant is the lubricating oil obtained from plants or artificial ester produced by modifying the natural oil. The unsaturated fatty acid

S. Galgat · A. Kotia (✉)
Lubrication and Sustainable Technologies, Bangalore, India
e-mail: ankitkotia@gmail.com

A. Kotia
Division of Research and Innovation, Uttaranchal University, Dehradun, India

composition is one of the prominent factors for selecting a natural oil for bio-lubricant production. Bio-lubricant can be produced from oil that is either non-edible or edible. The utilization of consumable oil for the creation of bio-oil is not practicable on the grounds that they are in extraordinary inclination for satisfying the prerequisite of human food. As consumable plant is utilized in the natural pecking order, the utilization of consumable oil as lubricating oil can lead to the biological harm by utilizing their property. The work of non-consumable oil as lubricating oil has different benefits; for example, non-consumable plant can be developed in a brutal climate and does not cause eco-coherent harm, effectively realistic, low cost, biodegradable, and non-poisonous [1]. There are various latest researches which are focused on the production of bio-lubricant. But these studies did not presume that bio-oil acquired by using nanoparticles has more prominent tribological properties along with strength of oxidation and thermal. A new bio-lubricant must be developed which can work as an alternative for the petroleum-based lubricating oil, which possesses both good thermo-physical property and thermal and oxidative stability [2].

Moringa and amaranth oils are considered as base oil bio-lubricant in the present study as both have high unsaturated fatty acid composition. The composition percentage of unsaturated fatty acid in vegetable oil is responsible for better thermo-oxidative stability. Table 1 shows the composition of *Moringa oleifera* oil fatty acid. The percentage of oleic acid (unsaturated fatty acid) exist in moringa oil is observed to be 73.85%, and it owns more thermo-oxidative stability than other many vegetable oils [3]. *M. oleifera* plant is being developed and produced by direct seeding method because it has high yield and germination rate with which it takes 5–12 days after seeding and the depth of plantation in the soil is nearly 2 cm and cultivated from cutting with 1 m length and 4.5 cm in diameter. The *M. oleifera* is also known as the drumstick and horseradish tree, and it commonly grows in the subtropical and tropical region of the world, mostly grown in the India [4]. Moringa oil is gotten from the *M. oleifera* seeds as represented in Fig. 1.

M. oleifera has several uses such as alley cropping, animal forage, biogas from residual plants and leaves, domestic cleaning agents, fencing, foliar nutrients, blue dye of wood, fertilizers, green manure, gum from tree trunks, ornament planting,

Table 1 Composition of fatty acid [3]

Fatty acid	Composition (%)
Palmitic (C16:0)	6.65
Stearic (C18:0)	6.09
Arachidic (C20:0)	3.98
Behenic (C22:0)	5.85
Total saturated fatty acid	22.57
Oleic (C18:1)	73.85
Eicosenoic (C20:1)	1.99
Linoleic (C18:2)	0.99
Total unsaturated fatty acid	76.83



Fig. 1 Extraction of *Moringa oleifera* oil [2]

tannin for tanning hides, honey and sugarcane juice clarifiers, flower nectar honey, biopesticides, and water purification. *M. oleifera* Lam. is one of the endlessly utilized plants whose different parts (leaf, natural product, seeds, and so on) are remembered for standard eating routine for their various capacity of fighting a few medical problems [5]. The leaves of *M. oleifera* are an expected wellspring of regular antibacterial and cancer prevention agents [6, 7]. Solanki et al. [8] investigated the adequacy of *M. oleifera* and *Camellia sinensis* in blend to explore hostile to peritonitic action in rodent model. The leaves are harvested in the dry season of the year where there were very few vegetables seen [9, 10]. *M. oleifera* oil also has a great potential for biodiesel production, and it was analyzed by various investigations. Rashid et al. [11] prepared biodiesel from moringa oil by alkali-catalyzed transesterification. Da Silva et al. [12] verified physicochemical properties of the Moringa biodiesel and suggested that this oil can be consumed as diesel engine fuel. *Amaranthus* is a cosmopolitan variety of yearly or fleeting enduring plants on the whole known as amaranths. Species of some amaranth are grown as elaborate plants and leaf vegetables. Amaranth grain inhibits 5–8% oil, which basically included triacylglycerols (78–82%). The remarkable synthesis of amaranth seed oil makes it a helpful fixing in the food, drug, and furthermore cosmetic businesses [13–15]. Table 2 shows the fatty acid composition of Amaranth oil.

Amaranth oil is extricated from the seeds of two types of the sort *Amaranthus*, *Amaranthus cruentus* and *Amaranthus hypochondriacus* that are called altogether as amaranth grain. The extraction amaranth oil is shown in Fig. 2. Amaranth oil is a

Table 2 Fatty acid composition [14]

Fatty acid	Composition (%)
Palmitic (C16:0)	19
Stearic (C18:0)	3
Total saturated fatty acid	22
Oleic (C18:1)	23
Linoleic (C18:2)	50
Total unsaturated fatty acid	73

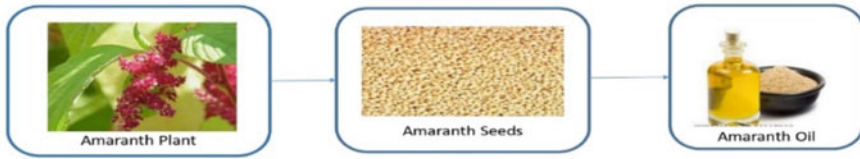


Fig. 2 Extraction of Amaranth oil

reasonable fluid with a light to medium color that is pourable at moderate temperatures. It is a wellspring of unsaturated fats, with the most elevated convergences of oleic acid, linoleic acid, and palmitic acid. The oil's capacity to add warm soundness at both high and low temperatures makes it important. Food varieties, beauty care products, shampoos, and intermediates for the development of greases, meds, elastic mixtures, aromatics, and surface dynamic specialists are among the business employments of amaranth oil [16].

2 Materials and Method

In the present work, two main materials are used to make a bio-lubricant, i.e., additives and base oil. The additives are used mostly less or equal to 10% in lubricants to maintain the properties like viscosity index, anti-friction, etc. For the base oil, *M. oleifera* and Amaranth are bought from the local suppliers; then, the extraction of oil from the seeds is being done which says to have 41% of the Moringa oil and 8% Amaranth oil.

Cerium oxide and MWCNT are considered and used as additives. Multi-wall carbon nanotube (MWCNT) is elongated as hallow cylinder nanoobject which consists of sp² carbon. Diameter of the nanoobject is (3–30) nm and can elongate several cm; variation can be seen in their expected ratio from 10 to 10 million. It is having a constant wall thickness along axis; their inner channel is straight, due to the perfect ends of MWCNTs; and perhaps the channel cannot be attainable directly from outside. The MWCNTs are capped by half fullerene sphere. However, it could enter by the nanotube opening, e.g., ion beam treatment, oxidation, or milling [17, 18]. CeO₂ is a metal oxide nanoparticle which can be used as additive for lubricating oil since it has high friction reduction, load-carrying capability, outstanding wear resistance, and moreover eco-friendly additive in environment. CeO₂ nanoparticles are a lubricating oil extreme pressure agent and exhibit excellent performance regarding reduction in friction with very less concentration (0.01 wt%). Anti-wear ability and the bearing capacity are directly proportional to the concentration of CeO₂ nanoparticles. CeO₂ nanoparticles makes a compact tribo-film and enhances load-carrying capacities [19].

Advanced Air Bearing Rheometer Bohlin Gemini 2 (Malvern Instruments, UK) is used for experimentation. Moringa and Amaranth oils are considered as base oil as



Fig. 3 Advanced air bearing rheometer Bohlin Gemini 2

shown in Fig. 3. Three samples each are prepared by considering both Moringa and Amaranth oil as base oil. Three samples are prepared from base oil and MWCNT and CeO₂ nanoparticles (additives), one of which contains base oil and MWCNT (98.62 gm + 1.38 gm), the other contains base oil and cerium oxide (98.62 gm + 1.38 gm), and the last one is a pure 100% base oil (100 gm). The mixtures are then added in the ultra-sonic machine to mix thoroughly for 30 min. Then, the two samples, i.e., base oil with MWCNT and base oil with cerium oxide, are left idle in room temperature for 24 h to see whether the nanoparticles are distracted from the oil (thin layer on the surface). The experiment is performed at 30 °C.

3 Results and Discussion

The rheological investigation of *M. oleifera* oil is evaluated experimentally in plain and with nanoparticles. Chemical modification of moringa oil is done by adding CeO₂ and MWCNT nanoparticles. Figure 4 shows the variation of viscosity (at 30 °C) and shear rate. From the graph, it is observed that mixture of moringa oil with 1 wt% of CeO₂ or MWCNT nanoparticles improves the lubrication properties. For plain moringa oil and mixture of moringa and CeO₂ nanoparticle, the change in viscosity with respect to shear rate is very less; on the other hand, at each value of shear rate the mixture with MWCNT nanoparticles shows higher viscosity than the other two samples and this viscosity continuously goes on decreasing with respect to shear rate, and hence, at higher shear rate the mixture with MWCNT nanoparticles shows shear thinning behavior. MWCNT/moringa oil has higher viscosity than the CeO₂/moringa oil. Figure 5 shows the variation of shear stress (at 30 °C) and shear rate. From the graph, it is observed that mixture of MWCNT and moringa oil has higher viscosity

of 13% and 47% than the mixture with CeO₂ and plain moringa oil, respectively. It can be observed that for normal Moringa oil, the shear stress is constant at the initial stage and with increase in the shear rate, there is a slight increase initially and then shear stress keeps on increasing till it ends.

The rheological investigation of Amaranth oil is evaluated experimentally in plain and with nanoparticles. Chemical modification of Amaranth oil is done by adding CeO₂ and MWCNT nanoparticles. Figure 6 shows the variation of viscosity (at 30 °C) and shear rate. From the graph, it is observed that mixture of Amaranth oil with 1% of CeO₂ or MWCNT nanoparticles improves the lubrication properties. For all the three samples, there is very less change in viscosity with respect to shear rate but

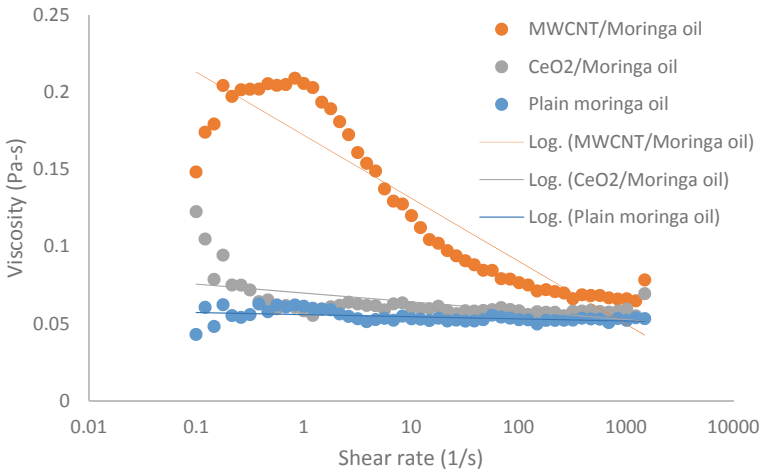


Fig. 4 Variation of viscosity with shear rate at 30 °C for moringa oil nano-bio-lubricant

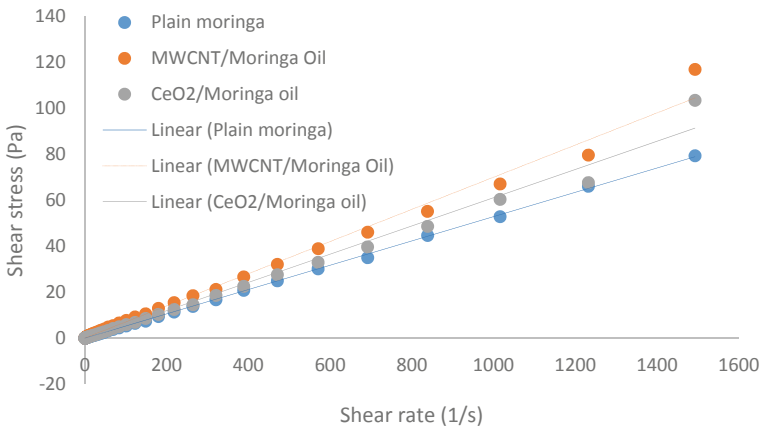


Fig. 5 Variation of shear stress with shear rate at 30 °C for moringa oil nano-bio-lubricant

for the mixture with CeO₂ nanoparticles at each value of shear rate, the viscosity is higher than the other two samples. Also, mixture of CeO₂ and Amaranth oil has higher viscosity of 10 and 25% than the mixture with MWCNT and plain Amaranth oil, respectively. Figure 7 shows the variation of shear stress (at 30 °C) and shear rate. From the graph, it is observed that there is similar trend line for each sample, all the three samples are Newtonian, and the lubrication properties are increased by adding CeO₂/MWCNT nanoparticles.

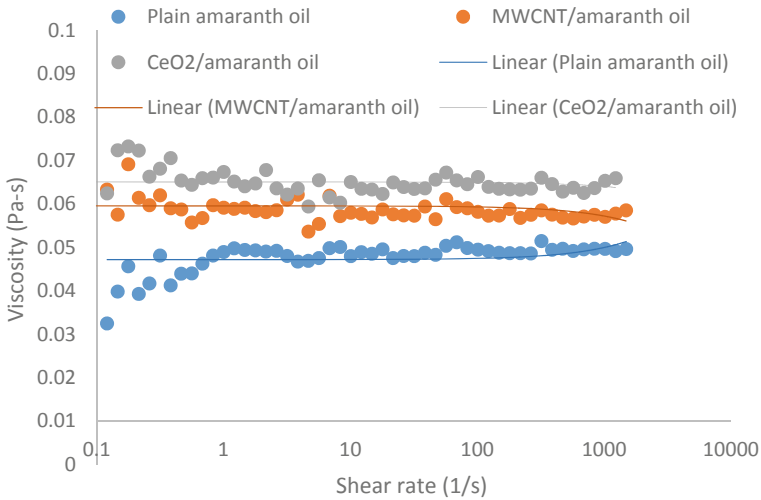


Fig. 6 Variation of viscosity with shear rate at 30 °C for amaranth oil bio-nanolubricant

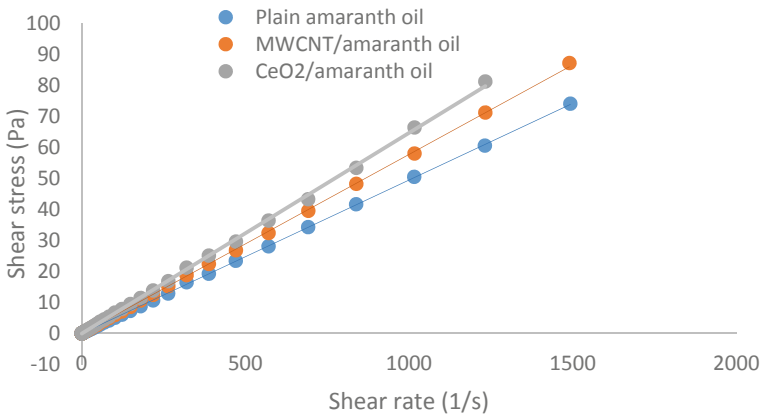


Fig. 7 Variation of shear stress with shear rate at 30 °C for amaranth oil nano-bio-lubricant

It is clear from rheological analysis that moringa and amaranth oils have good enhancement in tribological properties when mixed with the MWCNT or CeO₂ Nanoparticles.

4 Conclusion

This present study analyzes rheological properties of Moringa oil and Amaranth oil to provide an alternative lubricant for light gear application. The two nanoparticles MWCNT and cerium oxide (CeO₂) are added to Moringa oil and Amaranth oil samples, and further tests are performed on the samples. Viscosity and shear tests have been conducted by varying shear rate and temperature to the samples. The rheological analysis shows that the mixture of MWCNT and moringa oil has higher viscosity of 14 and 46% than the mixture with CeO₂ and plain moringa oil; also, it has higher shear of 13 and 47% than the mixture with CeO₂ and plain moringa oil. By this, it clearly shows that the moringa oil with MWCNTs has shown better properties than remaining two samples. In the case of rheological analysis considering amaranth as base oil, mixture of CeO₂ and Amaranth oil shows higher viscosity of 10 and 25% than the mixture with MWCNT and plain Amaranth oil; also, it shows higher stress of 10 and 25% than the mixture with MWCNT and plain Amaranth oil. By this, it clearly shows that the amaranth oil with CeO₂ shown better properties than remaining two samples. In this present study, enhancement in lubrication properties is seen due to the addition of nanoparticles on the basis of only 1% weight concentration; from these results, further rheological analysis can be done by increasing the concentration of nanoparticles in the samples. From this study, it can be concluded that Moringa and Amaranth oil with nanoparticles shows better tribological properties and these oils can be considered further for the chemical modification through transesterification or epoxidation for producing bio-lubricant.

References

1. Singh Y, Sharma A, Singla A (2019) Non-edible vegetable oil-based feedstocks capable of bio-lubricant production for automotive sector application—a review. *Environ Sci Pollut J Res* 26:14867–14882
2. Galgat S, Kotia A (2021) Biolubricants based on non-edible oil: a review. In: Jha K, Gulati P, Tripathi UK (eds) Recent advances in sustainable technologies. Lecture notes in mechanical engineering. Springer, Singapore
3. Sharma BK, Rashid U, Anwar F, Erhan SZ (2009) Lubricant properties of Moringa oil using thermal and tribological techniques. *J Therm Anal Calorim* 96:999–1008
4. Gopalakrishnan L, Doriya K, Kumar DS (2016) *Moringa oleifera*: a review on nutritive importance and its medicinal application. *Food Sci Human Wellness* 5:49–56
5. Biswas D, Nandy S, Mukherjee A, Pandey DK, Dey A (2020) *Moringa oleifera* Lam. and derived phytochemicals as promising antiviral agents: a review. *S Afr J Bot* 129:272–282

6. Kumar V, Pandey N, Mohan N, Singh RP (2012) Antibacterial and antioxidant activity of different extract of *Moringa oleifera* leaves—an in vitro study. *Int J Pharm Sci Rev Res* 12(1):89–94
7. Farooq B, Koul B, Mahant D, Yadav D (2021) Phytochemical analyses, antioxidant and anticancer activities of Ethanolic leaf extracts of *Moringa oleifera* Lam. Varieties. *Plants* 10(11):2348
8. Solanki N, Jayaswal RP, Pankaj PP (2015) Therapeutic efficacy of *Moringa oleifera* and *Camellia sinensis* extracts in combination against peritonitis induced rat model. *Int J Toxicol Pharmacol Res* 7(3). ISSN 9755160
9. Gandji K, Chadare FJ, Idohou R, Salako VK, Assogbadjo AE, Glèlè Kaka RL (2018) Status and utilisation of *Moringa oleifera* Lam: a review. *Afr Crop Sci J* 26(1):137–156
10. Warra AA (2014) A review of *Moringa oleifera* Lam seed oil prospects in personal care formulations. *J Pharm Nanotechnol* 2(3):31–34
11. Rashid U, Anwar F, Moser BR, Knothe G (2008) *Moringa oleifera* oil: a possible source of biodiesel. *Biores Technol* 99:8175–8179
12. da Silva JPV, Serra TM, Gossmann M, Wolf CR, Meneghetti MR, Meneghetti SMP (2010) *Moringa oleifera* oil: studies of characterization and biodiesel production. *Biomass Bioenergy* 34:1527–1530
13. Nasirpour-Tabrizi P, Azadmard-Damirchi S, Hesari J, Piravi-Vanak Z (2020) Amaranth seed oil composition. In: Natural value of Amaranth. Intech open, February 2020
14. Bozorov SS, Berdiev NSh, Ishimov UJ, Olimjonov SS, Ziyaviddinov JF, Asrorov AMA, Salikhov SI (2018) Chemical composition and biological activity of seed oil of amaranth varieties. *Nova Biotechnol Chim* 17(1):66–73
15. León-Camacho M, García-González DL, Aparicio R (2001) A detailed and comprehensive study of amaranth (*Amaranthus cruentus* L.) oil fatty profile. *Eur Food Res Technol* 213:349–355
16. Amonovich MR, Halimovich MK, Bakaevna KM, Khayotovna TD, Xudoyshukurovna QN, Raupovna DD (2020) Study of amaranth seeds as the raw material for the extraction of biologically active additives. *Eur J Mol Clin Med* 7(03)
17. Arunkumar T, Karthikeyan R, Ram Subramani R, Viswanathan K, Anish M (2018) Synthesis and characterisation of multi-walled carbon nanotubes (MWCNTs). *Int J Ambient Energy*
18. Kukovec A, Kozma G, Kónya Z (2013) Multi-walled carbon nanotubes
19. Wu L, Lei X, Zhang Y, Zhang S, Yang G, Zhang P (2020) The tribological mechanism of cerium oxide nanoparticles as lubricant additive of poly- α olefin. *Tribol Lett* 68:101

Application of Life Cycle Analysis in Sustainable Machining of Aluminium 6061 Alloy Under Different Lubricating Conditions



Kamal Hassan, Amardeep Singh Kang, Gurraj Singh, and Chander Prakash

Abstract Aluminium is considered more precious than gold, most commonly used for different aerospace, automotive, and shipping industries. Boring is a critical machining method in assembly operations. This paper investigates the machining performance in machining aluminium 6061 alloy under different cutting conditions through a specially designed mixing nozzle for mist and flood lubrication. Experiments were performed with twenty-seven runs selected from Taguchi robust design and cutting parameters selected from the manufacturer's recommendation. Results revealed an improved machining characteristic while machining the component with near dry machining compared to dry and flood lubrication. Life cycle assessment of selected functional unit is to investigate the ecological impact using CML baseline method. LCA analysis concluded that dry machining is a more sustainable approach than near dry and flood machining approaches.

Keywords Machining time · Metal removal rate · Functional unit · Life cycle assessment

Abbreviations

v_c	Cutting speed
f_n	Feed rate
a_p	Depth of cut
FL	Flood lubrication
C_s	Cutting time (s)
S_t	Standby time (s)

K. Hassan · A. S. Kang · C. Prakash (✉)
Department of Mechanical Engineering, Lovely Professional University, Phagwara, Punjab, India
e-mail: chander.21503@lpu.co.in

G. Singh
Department of Industrial and Production, Dr. B.R Ambedkar National Institute of Technology,
Jalandhar, Punjab, India

T_r	Tool return time (s)
T_t	Total time (s)
MQL	Minimum quantity lubrication
LCA	Life cycle assessment
FU	Functional unit
AD	Abiotic depletion
ADFF	Abiotic depletion (fossil fuels)
GW	Global warming (GWP100a)
ODP	Ozone layer depletion
HT	Human toxicity
FWAE	Fresh water aquatic ecotoxicity
MAE	Marine aquatic ecotoxicity
TE	Terrestrial ecotoxicity
PO	Photochemical oxidation
AF	Acidification
EU	Eutrophication

1 Introduction

Machining productivity increases with the usage of lubricants and coolants by reducing wear and surface roughness. Lubricating fluids contain harmful chemical ingredients that cause environmental pollution. Persistent exposure while machining may lead to respiratory drawbacks in the operator's health. Disposal of cutting fluids is also a significant concern in flood lubrication. The high temperature established at the contact surface in internal turning operations is due to increased hardness and poor thermal conductivity. Traditional cooling has frequently been used to tackle heat production and development effectiveness issues, with extensive use of lubricants. It seems a viable elucidation to prominent levels of heat up, but it poses a severe health risk, endangering green production and long-term sustainability [1]. In the modern industrial sector, sustainable manufacturing is the most recent notion. Sustainable manufacturing, which includes three functional elements: sustainable products, processes, and systems, is a comparatively lesser-known but crucial component of sustainable development [2]. Mist lubrication systems reached a milestone in reducing the allergic effects of non-degradable lubricants on workshop floors [3]. The MQL approach decreases the concentration of lubricant without sacrificing the project's effectiveness.

Consequently, this technique can be acknowledged as a credible alternative for addressing non-degradable lubricant issues. Mist [4] lubrication utilizes aerosol through various channel systems, offering a reduction in environmental pollution. Fluids should be biodegradable and offer stability for a more extended period due to less quantity usage. Near dry machining [5] is superior to dry and wet machining while turning AISI4340 steel with an uncoated carbide insert to analyse the effect of

MQL on flank wear and surface roughness. Cutting forces increase prominently in dry conditions and decrease in flood lubrication [6]. Cutting enactment with MQL is far better than the dry turning process as it offers lower temperature reduction [7]. Machining with MQL proved to be better than dry and wet cooling, increasing cutting performance by reducing tool wear, cutting temperature, and forces between chip-tool interactions [8]. A bulk of reports focusing on how to make machining operations more sustainable are focused on dry or MQL machining [9].

This work investigates the effect of three different cutting conditions (dry, flood, and minimum quantity lubrication) on cutting time, rate of metal removal, and various environmental impact indicators.

2 Material and Methods

Boring trials were executed on 200 mm long aluminium 6061 alloy (internal diameter—69 mm, outer diameter—75 mm, and wall thickness—3 mm) as shown in Fig. 1 with carbide insert Kennametal through-hole boring bar on a conventional lathe at different cutting parameters under different cutting environments to evaluate the extensive machinability features as shown in Fig. 2. The material chemical composition and experimental details are given in Tables 1 and 2.

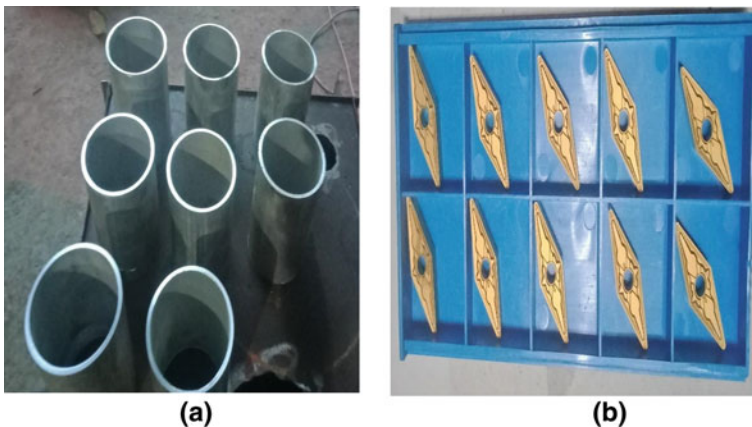


Fig. 1 a Aluminium alloy stocks. b Carbide inserts

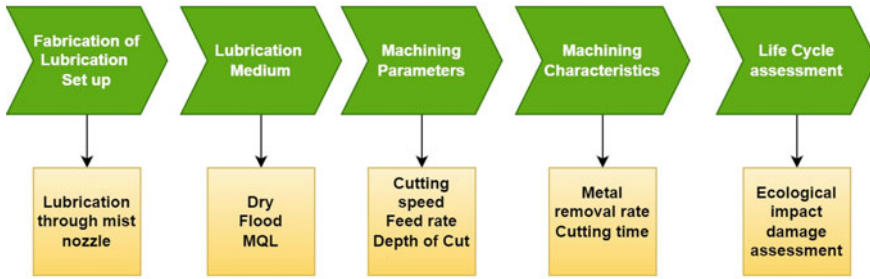


Fig. 2 Adopted research methodology

Table 1 Aluminium 6061 alloy chemical compositions [10]

Element	Mg	Si	Fe	Cu	Cr	Z	Ti	Mn	Al
Amount (wt %)	0.8–1.2	0.4–0.8	0.7	0.15–0.4	0.04–0.035	0.25	0.15	0.15	96.85

Table 2 Experimental conditions

Machine tool	Manual lathe machine 6 ft 14 × 12, HMT 6, 2 HP
Work material	Aluminium 6061 alloy (\varnothing 75 mm × 3 mm thickness)
Boring bar specifications	Kennametal A16T-SVUBR3NH2, diameter: 30 mm, length: 305 mm, L/D ratio: 10 mm, through-hole type
Cutting insert geometry	VNMG160408-QM wintech carbide, L : 16.6 mm, D : 9.525, S : 4.76, d_1 : 3.81, R : 0.8, positive rake
Process parameters	v_c : 185, 215, 245 mm/min, f_n : 0.15, 0.20, 0.25 mm/rev, a_p : 0.3, 0.5, 0.7 mm
Cutting condition	Dry, flood, and MQL
Air pressure and lubricant flow rate	6 bar, dry: 0 ml/h, flood: 120,000 ml/h, MQL: 100 ml/h through internal nozzle in boring bar

3 Results and Discussion

The efficacy, efficiency, and total cutting cost with specific inserts are primarily determined by the tool–work material machinability at required conditions under different cutting conditions as see in Table 3.

Metal removal rate and machining time are addressed in this study to compare machinability characteristics in different machining techniques. Due to the presence of lubricating layer and less heat generation during machining, less cutting time is observed in near dry machining, Fig. 3.

LCA (life cycle assessment) is a useful tool for estimating the potential environmental implications of products, processes, or services in order to help with product selection. Technical requirements must be assessed with environmental and economic

Table 3 Experimental results

Lubrication type	C _s	F	D _c	MRR	C _s (s)	S _t (s)	T _R (s)	T _t (s)
1	185	0.15	0.30	8.35	18.00	37.00	4.50	59.50
1	185	0.20	0.50	18.50	20.00	47.00	5.00	72.00
1	185	0.25	0.70	32.37	34.00	59.00	8.50	101.50
1	215	0.15	0.50	16.13	36.00	64.00	9.00	109.00
1	215	0.20	0.70	30.19	28.00	56.00	7.00	91.00
1	215	0.25	0.30	16.12	25.00	48.00	6.20	79.20
1	245	0.15	0.70	25.72	19.00	37.00	4.70	60.70
1	245	0.20	0.30	14.70	17.00	35.00	4.20	56.20
1	245	0.25	0.50	30.62	16.40	32.50	3.90	52.80
2	185	0.15	0.50	13.88	17.70	45.40	4.40	67.50
2	185	0.20	0.70	25.90	18.00	51.00	4.70	73.70
2	185	0.25	0.30	13.87	33.20	57.00	8.10	98.30
2	215	0.15	0.70	22.57	34.80	52.00	8.20	95.00
2	215	0.20	0.30	12.90	24.70	54.00	5.90	84.60
2	215	0.25	0.50	26.87	22.40	56.00	5.60	84.00
2	245	0.15	0.30	11.02	17.20	51.00	4.40	72.60
2	245	0.20	0.50	24.50	15.60	49.00	3.80	68.40
2	245	0.25	0.70	42.87	14.90	46.00	3.70	64.60
3	185	0.15	0.70	19.42	15.00	32.00	3.75	50.75
3	185	0.20	0.30	11.10	14.70	31.00	3.90	49.60
3	185	0.25	0.50	23.12	11.40	33.00	2.80	47.20
3	215	0.15	0.30	9.68	13.20	28.00	3.30	44.50
3	215	0.20	0.50	21.50	14.10	29.00	3.50	46.60
3	215	0.25	0.70	37.62	10.00	32.00	2.50	44.50
3	245	0.15	0.50	18.38	6.80	28.00	1.70	36.50
3	245	0.20	0.70	34.30	8.70	31.00	2.20	41.90
3	245	0.25	0.30	18.38	9.20	30.00	2.30	41.50

factors in order to create more sustainable process designs [11]. The goal of this research is to compare the environmental implications of three different cutting procedures for the internal turning of aluminium alloy: dry, flood, and MQL. LCA analysis was carried out using the CML Baseline LCIA methodology by ISO 14040:2006 and ISO 14044:2006 standards [12], as mentioned in Table 4.

The following process has been excluded while doing the inventory analysis for life cycle assessment:

- (a) The elements required to make the Al 6061 alloy and cutting tool and the manufacturing of workpiece which is used for three different cutting conditions.

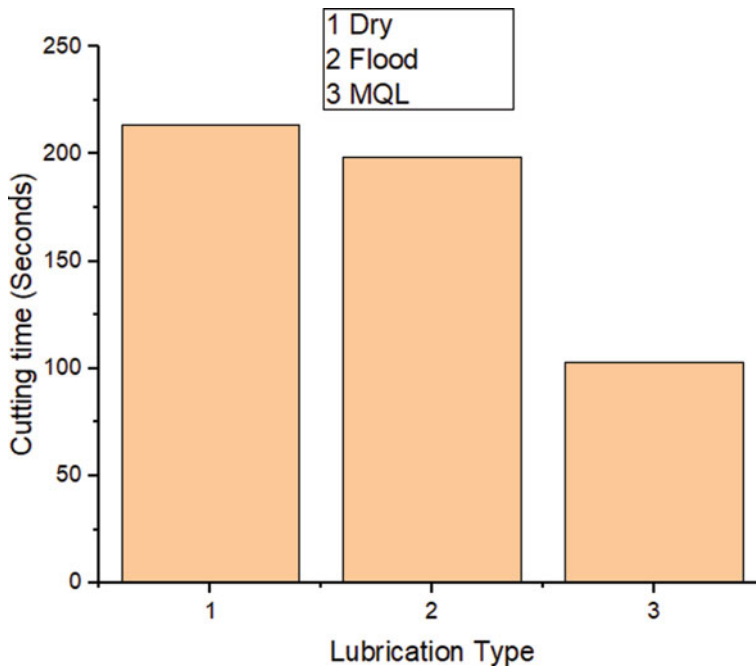


Fig. 3 Cutting time comparison in different cutting conditions

Table 4 Background process details for impact assessment

System input	Units	Description
Electricity	KWh	Electricity, high voltage {IN-Northern grid} market for electricity, high voltage Cut-off, U
Lubricants	Kg	Lubricating oil {RoW} production Cut-off, U
Compressed air	m ³	Compressed air, 600 kPa gauge {GLO} market for Cut-off, U

- (b) Manufacturing of coated carbide bit and its inability to enumerate the exact environmental impact of a coated carbide insert are inadequate due to a lack of appropriate datasets. This has an impact on the study's absoluteness and highlights the necessity for machining-specific datasets. This omission, however, has no significant impact on the outcomes of this study. According to a recent study, a thorough evaluation may still be done by factoring in power and coolant usage, which are important aspects of the life cycle assessment [13].
- (c) Transportation and its cost, cutting inserts, coolant, air compressor, and workpiece.
- (d) Carbon dioxide emission while machining the Al stock particularly in flood and mist lubrication. Due to the lack of adequate recorded data during experimentation, this parameter was also kept out of the assessment approach.

Table 5 Results of process inventories for ecological impact assessment

Impact category	Dry machining	Flood machining	MQL machining
AD	7.16E-05	1.15E-04	1.09E-04
ADFF	7.81E + 01	2.65E + 02	1.74E + 02
GW	8.26E + 00	1.41E + 01	1.34E + 01
ODP	2.37E-06	1.96E-06	9.25E-07
HT	4.84E + 00	7.99E + 00	7.62E + 00
FWAE	1.43E + 01	1.85E + 01	2.03E + 01
MAE	3.40E + 04	4.57E + 04	4.93E + 04
TE	2.38E-02	3.60E-02	3.59E-02
PO	2.62E-03	4.59E-03	4.19E-03
AF	4.14E-02	7.50E-02	6.80E-02
EU	1.54E-02	2.54E-02	2.47E-02

- (e) To conduct the inventory analysis, detailing of all three cutting conditions has been streamlined on similar aspects. Because the cutting parameters are having different subsets at all instances, the amount of material removed is different, and the finished product has variable material removal volume. As a result of the streamlining, the metal portion, the generated chips, and the finished product, all of which are made of aluminium alloy, are excluded from LCA calculations.

Regardless of the cutting fluid used, the machined part is expected to be used for the same purpose. As a result, the assessment does not include the use phase, end-of-life processing, or disposal.

Experimental data recorded during experimentation recorded on electricity consumption, lubricant quantity, and air compressor capacity. Total material removed from the machining trials in distinct cutting environments forms the calculation of impact assessment on hired method and damage assessment. Datasets used for analysis are given in Table 4, acquired from the Ecoinvent database (Table 5):

4 Conclusion

The outcome of lubrication conditions on metal removal rate in the boring of aluminium alloys 6061-T6 for various cutting speeds, feed rates, and depth of cut was investigated in this research study. Furthermore, life cycle assessment analysis indicates the ecological indications as per the given standard in the Ecoinvent database. Following conclusions can be drawn from the experimental studies:

- The mist produced by supplying aerosol internally through a boring bar proved an effective technique for better surface integrity than conventional and flood lubrication.

- MQL can be adopted as a permanent technique for boring operation, and it may be an economical approach compared to flood and dry machining.
- Cutting fluid with the least amount of lubrication reduces the negative aspects of cutting fluid during ecological aspects, such as friction reduction, cooling, and chip flushing.
- Human toxicity observed worst in case of flood machining due to abundant use of cutting fluid.

References

1. Gupta, MK, Pruncu CI, Mia M, Singh G, Singh S, Prakash C, Sood PK, Gill HS (2018) Machinability investigations of Inconel-800 super alloy under sustainable cooling conditions. *Materials* 11(11):2088
2. Pradhan S, Singh S, Prakash C, Królczyk G, Pramanik A, Pruncu CI (2019) Investigation of machining characteristics of hard-to-machine Ti-6Al-4V-ELI alloy for biomedical applications. *J Mater Res Technol* 8(5):4849–4862
3. Karim MR, Tariq JB, Morshed SM, Shawon SH, Hasan A, Prakash C, Singh S, Kumar R, Nirsanametla Y, Pruncu CI (2021) Environmental, economical and technological analysis of MQL-assisted machining of Al-Mg-Zr alloy using PCD tool. *Sustainability* 13(13):7321
4. Pramanik A, Basak AK, Littlefair G, Debnath S, Prakash C, Singh MA, Marla D, Singh RK (2020) Methods and variables in electrical discharge machining of titanium alloy—a review. *Heliyon* 6(12):05554
5. Zaman PB, Dhar NR (2019) Design and evaluation of an embedded double jet nozzle for MQL delivery intending machinability improvement in turning operation. *J Manuf Process* 44:179–196
6. Shahrookh Shakeel AD, Faizan Hasan Mohd. (2016) A review on study the methods and applications of MQL using natural oils. *IJSRD Int J Sci Res Dev* 4
7. Thakur A, Gangopadhyay S (2016) Dry machining of nickel-based super alloy as a sustainable alternative using TiN/TiAlN coated tool. *J Clean Prod* 129:256–268
8. Biermann D, Iovkov I (2015) Investigations on the thermal workpiece distortion in MQL deep hole drilling of an aluminium cast alloy. *CIRP Ann Manuf Technol* 64(1):85–88
9. Hassan K, Kang AS, Singh G (2020) Metamorphic developmental possibilities related to boring operation in the near future. *AIP Conf Proc* 2281
10. Aamir M, Tolouei-Rad M, Giasin K, Vafadar A (2020) Machinability of Al2024, Al6061, and Al5083 alloys using multi-hole simultaneous drilling approach. *J Mater Res Technol* 9(5):10991–11002
11. Gupta MK et al (2018) Machinability investigations of Inconel-800 super alloy under sustainable cooling conditions. *Materials (Basel)* 11(11)
12. Gupta MK et al (2021) Experimental characterisation of the performance of hybrid cryo-lubrication assisted turning of Ti-6Al-4V alloy. *Tribol Int* 153:106582
13. Shah P, Bhat P, Khanna N (2021) Life cycle assessment of drilling Inconel 718 using cryogenic cutting fluids while considering sustainability parameters. *Sustain Energy Technol Assess* 43:100950

Improving Mechanical Properties of Hot Rolled Coil Using Micro Alloy



Vijay Kumar Singh

Abstract Hot rolled coils are bulk product of a steel plant, the Ferro alloys (FeV and FeNb) are used as micro alloys. These micro alloys are very costly. In order to optimize the cost of alloys and maintain the desired mechanical properties, this study was done using Value Engineering steps.

Keywords Mechanical properties · Hot rolling · Micro alloy · Value Engineering

1 Introduction

Value Engineering is defined as “A step by step approach to achieve desired functions of product, process, service or system, at minimum cost, giving maximum value, maintaining performance, quality, reliability, maintainability and safety”. Value Engineering is a useful technique for refining the developed requirements of a product. It involves estimations and ultimately selection of less costly conditions. Value Engineering is a procedure to improve operations of products and their services. It also assists to reduce the cost of the product while maintaining the quality of the product. The procedure contains a multidisciplinary group of professionals such as Designer, Project Manager and Consultants. [1]. Fundamentally, VE is an organized way of thinking or looking at an item or a process through a functional approach [2]. Society of Japanese Value Engineering defines VE as: “A systematic approach to analyzing functional requirements of products or services for the purposes of achieving the essential functions at the lowest total cost” [3].

V. K. Singh (✉)

School of Mechanical Engineering, Lovely Professional University, Phagwara 144411, India
e-mail: vijay.24694@lpu.co.in

Nowadays, manufacturers in this global competitive market are competing for maximizing their product value and mitigating the overall cost of the product [4–6]. Value Engineering is objectively upgrading the functions performed by parts, components, products and procedure related to cost of the product [7, 8]. The sole purpose of this technical approach is to provide a skillful and efficient means for controlling the total cost of the product. This cost control procedure is comprehensively conducted in a systematic way by formulating alternative ways of achieving functions which are essential only. The purpose of Value Engineering is only then fulfilled when individual is able to define the necessary functions properly and remove the unnecessary functions to control cost. Therefore Value Engineering is also defined as systemized process for identifying unnecessary cost [9, 10]. Figure 1 shows the Job Plan Steps to be adapted when VE in industries or organizations is implemented. Orientation Phase consists of training of team members, and selecting team leaders and team members. Similarly, information phase consists of flow chart of operations and data (technical and administrative). Further, the function phase comprises of cost-worth analysis and Function Analysis Systems Technique (FAST) Diagram. In addition, creation phase includes allowing flow of ideas and self-evaluation without fear. Later, the evaluation phase recommends evaluation and development. Detailed testing and implementation plan would be included in implementation phase. Lastly, technical and cost audits would be in audit phase.

In present work, HR' Coils of grades, BSK-46, ASTM A 572 Gr. 50, and IS: 10787 Grade A are produced at a Hot Strip Mill in a steel plant (see Table 1). All the grades have micro alloy (Ferro alloy) additions. The purpose of micro alloying is to enhance strength along with ductility. The mechanical property of HR coils with existing level of micro alloying was resulting in Yield Stress and Ultimate tensile stress toward higher side of the specified limits and % elongation toward lower side.

The advantages of using FeNb cored wire replacing FeV is given in Table 2. Both the materials are used for improved mechanical properties/strength/toughness. But mechanism as well as temperature for achieving improved properties is different. However, in general, requirement of Nb will be around 50% that of V in a particular grade. For example if for a particular grade V is 0.04/0.05%, then it can be replaced by 0.02/0.03% Nb. But because of different strengthening mechanism, beyond 0.05% V requirement for a particular grade, generally both the elements are to be considered during alloy design keeping in view the application as well as rolling mill load condition for a particular shop/plant. A VE project was taken to explore the possibility of optimizing mechanical properties with reduction in micro alloying and control over operating parameters, to exceed customer's expectation.

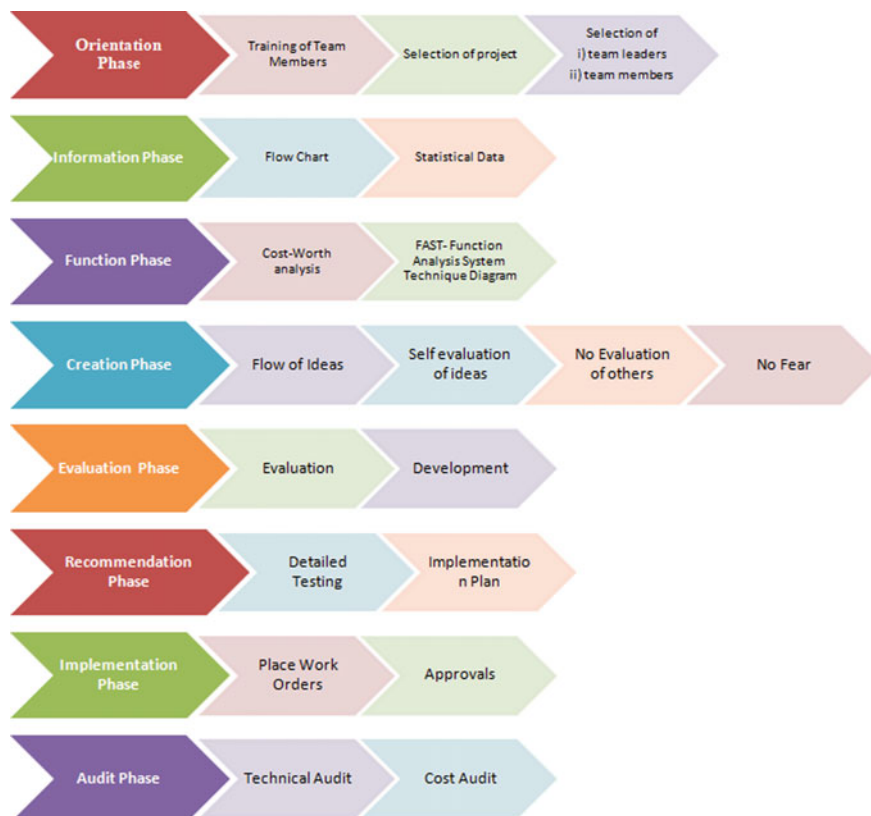


Fig. 1 Job plan steps in value engineering

Table 1 Grade and processing parameters

Details of grade and processing parameters

S. No.	Grade	Existing chemistry			Mechanical properties			Ferro alloy addition (kg/heat)
		C (%)	Mn (%)	MA (Nb/V)	YS (MPa)	UTS (MPa)	%EL	
1	IS:10787	0.06	0.55	0.005	270/320	365/410	30/38	35
2	BSK-46	0.06	1.25	0.05	470/560	540/620	22/28	125
3	ASTM A572	0.08	0.85	0.015	405/460	490/540	26/34	50

C carbon; Mn manganese; MA micro alloy; Nb niobium; V vanadium; FRT finish rolling temperature; CT coiling temperature; ROT run out table; YS yield strength; TS tensile strength or UTS ultimate tensile strength; % EL % elongation

Table 2 Function details

S. No.	Component/process	Function verb	Function noun	Basic (B)/secondary (S)
1	FeNb/FeV addition	Meet	Specification	B
		Improve	Mech. properties	B
		Produce	Fine grain	S
		Improve	YS/UTS ratio	S
		Reduce	Carbon equiv	S
2	Rolling parameters			
	FRT	Achieve	Mech. properties	B
		Control	Roll force	S
		Control	Scaling	S
	CT	Control	Mech. properties	B
		Control	Scaling	S
		Control	Coil shape	S
	ROT	Control	Mech. properties	B
		Dissipate	Heat	S

2 Information Phase

2.1 Function Phase

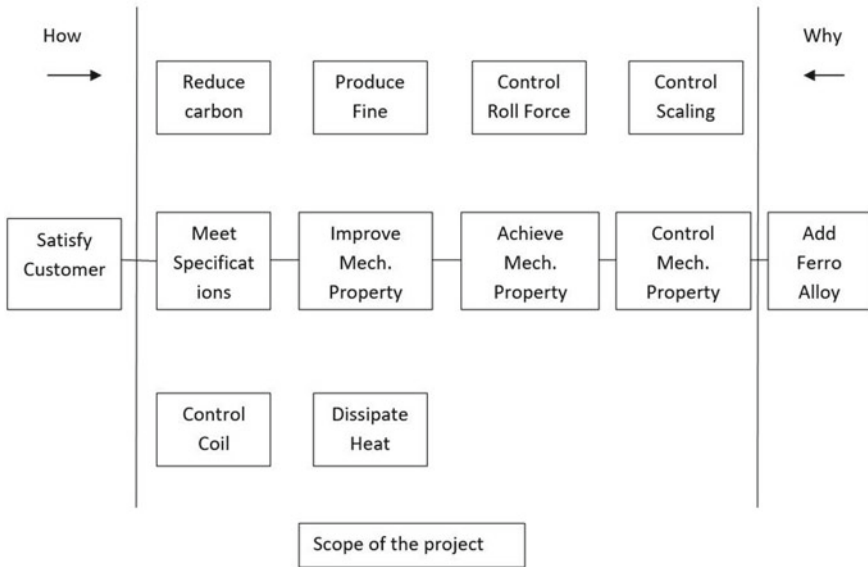
2.2 Function—Cost—Worth—Analysis

This analysis was done to find value gap and value index (Table 3).

Table 3 Cost analysis

S. No.	Function improve Mech. properties	Cost (C) Rs/t	Worth (W) Rs/t	Basis for worth	Value gap (C-W)	Value index (C/W)
1	IS:10787	100	15	Reduce FeV	85	6.6
2	BSK-46	500	300	Reduce FeNb	200	1.6
3	ASTM A572	200	100	Reduce FeNb	100	2.0

2.3 FAST Diagram



2.4 Creative Phase

Under this phase the brain storming technique is used to find the alternatives to achieve the desired function at lower cost. Around 23 ideas were generated. Out of which three ideas were taken for evaluation.

2.5 Evaluation Phase

The paired comparison method was used to evaluate the ideas. In this two matrices are used, criteria matrix and evaluation matrix.

The following criteria were selected for comparison, i.e. to give hierarchy to criteria. A scale of 1–10 was used.

Table 4 Criteria score and the ranking

Identifier	Criteria	Score	Rank
A	Reliability	6	2
B	Quality	4	3
C	Feasibility	1	5
D	Cost	2	4
E	Customer satisfaction	7	1

2.6 Criteria Matrix

	B	C	D	E	Score
A	A 1	A 3	A 1	E 1	5+1=6
B	B 2	B 1	E 1		3+1=4
C		D 1	E 2		0+1=1
D			E 2		1+1=2
E				E	6+1=7

The criteria score and the ranking is given in Table 4.

2.7 Decision Matrix

The decision was made using the score scale between 1 and 5 and giving weightage as the criteria given in Table 5.

2.8 Recommendation Phase

The recommendations on additions of Ferro Alloys grade wise is indicated in Table 6.

Table 5 Decision matrix

Criteria	Reliability	Quality	Feasibility	Cost	Customer satisfaction	Total score
Weightage	A = 6	B = 4	C = 1	D = 2	E = 7	
1. Reduce FeNb/FeV	5/30	3/12	3/3	3/6	4/28	79
2. Increase carbon equiv	3/18	2/8	3/3	2/4	2/14	47

Scale: Excellent = 5; Very Good = 4; Good = 3; Fair = 2; Poor = 1.

Table 6 Processing parameters

Details of grade and processing parameters								
S. No.	Grade	Existing chemistry			Mechanical properties			Ferro alloy addition (kg/heat)
		C (%)	Mn (%)	MA (Nb/V)	YS (MPa)	UTS (MPa)	%EL	
1	IS:10787	0.06	0.55	0.005	270/320	365/410	30/38	5
2	BSK-46	0.06	1.25	0.05	470/560	540/620	22/28	75
3	ASTM A572	0.08	0.85	0.015	405/460	490/540	26/34	25

C carbon; Mn manganese; MA micro alloy; Nb niobium; V vanadium; FRT finish rolling temperature; CT coiling temperature; ROT run out table; YS yield strength; TS tensile strength or UTS ultimate tensile strength; %EL %elongation

A plan was made to implement the recommendations.

3 Conclusion

A recurring savings of around 50% reduction in Ferro Alloy consumption was achieved.


References

- Fichte R (2000) Ferroalloys. In: Ullmann's encyclopedia of industrial chemistry. Wiley-VCH, Weinheim. https://doi.org/10.1002/14356007.a10_305
- Lisa A et al (2010) Ferroalloys. US Geol Surv 25.1–25.14. <https://doi.org/10.3133/mybvi>. Retrieved 18 Oct 2019
- www.kpitcummins.com. Value engineering white paper. [Online]
- Pimpamount P, Chutima P (2016) Applications of value engineering in head stack assembly process: a case study. Int J Mater Mech Manuf 4(1):46–51
- Behncke GH, Maisenbachera (2014) Extended model for integrated value engineering. In: Conference proceeding on systems engineering research, pp 781–787
- Nallusamy S (2016) Frequency analysis of lean manufacturing system by different critical issues in Indian automotive industries. Int J Eng Res Afr 23:181–187

7. Achawakorn K, Jearsiripongkul, Suksawat, Chaeng F (2013) The effect of pivot bearing assembly process on natural frequency of actuator arm. *J Energy Power Eng* 7:301–305
8. Annappa CM, Pandit Rao KS (2013) Optimization of furniture product in furniture industry by using value engineering with function analysis, function evaluation and decision matrix-A case study. *Int J Appl Innov Eng Manage* 2:55–64
9. Sharma A, Belokar (2012) Implementation of value engineering—a case study. *Int J Mark Fin Serv Manage Res* 1(3):64–70
10. Singh P, Singh J (2016) Application of value engineering in Chasis component for HCV—a case study. *Int J Knowl Eng* 2(1):43–49

Synthesis and Characterization of Highly Transparent and Superhydrophobic Zinc Oxide (ZnO) Film



Ashish Jaswal, Kamal Kishore, Amarjit Singh, Jarnail Singh , Saurav Dixit, Kaushal Kumar, and Manoj Kumar Sinha

Abstract This work represents the synthesization and functionalization of zinc oxide (ZnO) nanoparticles/films and investigated its superhydrophobic and optical properties. ZnO nanoparticles were prepared by precipitation method using sodium hydroxide (NaOH) as a precipitating agent. The functionalization of the ZnO nanoparticles was carried out to tailor its hydrophilic nature to hydrophobic. Mercapto-trimethoxysilane (MPMS) was also used for further modification of ZnO nanoparticles. Functionalized ZnO nanoparticles then mixed with polystyrene were passed through the rolling machine at a temperature of 200 °C. The required thin film was achieved after pressing the rolled thick film at 150 °C and 90 MPa. A scanning electron microscope was used to study the morphology of superhydrophobic film (SHF). The contact angle of the SHF was measured with the help of a tensiometer. Evaluation of optical properties of the prepared ZnO film was carried out using UV–visible spectrophotometry. An atomic force microscopy technique was used to illustrate the roughness of the film. Characterizations of SHF revealed that the film possesses the high optical transparency in visible range, which is almost similar to the bare glass. The antireflective film has provided an average transparency of 91.5%, comparable to the bare glass substrate 92% at a wavelength range of 320–750 nm. Moreover, this transparent and superhydrophobic film shows an average roughness of 27 nm with the highest water contact angle of 157°. The weight percentage of ZnO and MPMS found to significantly influence the contact angle, which governs the thin film's superhydrophobicity.

J. Singh (✉) · K. Kumar · M. K. Sinha
Department of Mechanical Engineering, K.R. Mangalam University, Gurgaon 122103, India
e-mail: jarnail.singh@kr.mangalam.edu.in

A. Jaswal · K. Kishore · A. Singh
Department of Material Science and Engineering, National Institute of Technology Hamirpur,
Hamirpur 177005, India

S. Dixit
SOMC, National Institute of Technology Hamirpur, Hamirpur 177005, India

Division of Research & Innovation, Uttaranchal University, Dehradun, India

Keywords Superhydrophobic · Contact angle · Transmission · Surface roughness · Nanoparticles · Zinc oxide

1 Introduction

Solar energy is one of the abundantly available sources of renewable energies on our planet earth. Various researchers are performing different types of study on photovoltaic (PV) devices to improve the cell's performance, which is primarily affected by the settling of dust and dirt on the surface of the PV panel. In the existence of dirt and dust, scattering and reflection of solar irradiance occur, which further leads to declination in the efficiency of a solar cell. Therefore, to contest against the above problem, the self-cleaning superhydrophobic film is required [1–3]. The preparation of superhydrophobic material has evolved from the structure and composition of the lotus leaf. In this fast-growing era, superhydrophobic (contact angle > 150°) surfaces are extensively used in industrial applications like resistance to icing, fogging, solar cells, self-cleaning, etc. Deposition techniques like chemical vapor deposition (CVD), spin coating, dip-coating, and spraying are mainly used to fabricate hydrophobic thin films [4, 5]. It is not an easy task to achieve superhydrophobicity and transparency simultaneously during the fabrication of thin films. This will enable the film to scatter the solar radiation incident on it, which in turn diminishes the transparency of the film [6]. Various researchers have extensively explored ZnO material due to its chemical and thermal stability, low cost, and environmental friendliness. It also falls in the wide band gap semiconductor category, which can be used in photochemical and catalytic applications [7]. To deposit a superhydrophobic film on the glass substrate is costly and challenging as well. The modified sol–gel method using the Torque Rheometer device turned out to be one of the best methods used for thin-film fabrication. Some critical parameters need to be considered when preparing ZnO nanoparticles, like chemical composition, particle size, morphology, and crystalline structure [8]. Tripathi et al. [9] analyzed the performance of the PV module against dust particles of limestone and red soil agglomerate on its surface. They found that the power output of the PV module decreases in the case of red soil compared to limestone dust. Das et al. [5] studied various methods to fabricate superhydrophobic coating for the solar PV panels. In addition to this, they also provided information about future advancements in superhydrophobic film synthesis and its applications. It is [10] investigated that high and low is the contact and roll-off angle of water can be obtained on the surface of the superhydrophobic film. The authors also observed that the recovery ratio is significantly high for the self-cleaning superhydrophobic film compared to the uncoated glass. Darband et al. [11] described various methods for preparing superhydrophobic surfaces (SHS). Description regarding mechanical stability, chemical stability, and corrosion resistance was also explained. The study found that providing roughness to the surface of material would lead to resistance in the corrosion and ultimately affects the contact angle of water. Bai et al. [12] investigated the superhydrophobic coating with self-recovering properties. It was reported

that the damage recovery of film structure is possible with spraying a mixture of zinc acetate, stearic acid, and polymethylmethacrylate on the coating. It was also found that the trapping of air between the bumpy spikes of the surface was replaced by continuous contact with water for 2–3 days. The coating still exhibited a contact angle up to 155° and a sliding angle of less than 10° . Thus, it demonstrated good water durability. Jiang and Li [13] proposed an easy method to prepare micro-structured cobalt tetraoxide (Co_3O_4) film on the glass substrate through a solvothermal process. The film was found to have ice-repellent, antireflective, and self-cleansing properties. It was concluded that an angle of 169° and sliding angle less than 3° would benefit various industrial applications. Mahadik et al. [14] presented the most straightforward method of fabricating highly superhydrophobic film with the help of MPMS. A significant change in substrate morphology and reduction in surface free energy of silane coating on glass substrate fabricated using spraying method were reported.

It can be observed that free surface energy is similar to surface tension, and it also helps to capture the interaction between solid and liquid. Moreover, surface tension is a sum of the intermolecular forces of matter. By measuring the contact angle of water, we can calculate the surface free energy of a solid. If the surface tension of the solid is significant, it means it consists of a larger adhesive force compared to cohesive forces, whereas if surface tension is low, then we can say it consists of low surface free energy and has larger cohesive forces than adhesive forces. So, to prepare superhydrophobic surfaces, we need low surface free energy so that water does not stick to the surface [7, 15–19]. The film's surface should also be stable at higher temperatures to render practical applications in various fields.

A thorough literature survey revealed that a significant amount of work had been carried out on the fabrication and characterization of superhydrophobic films using various materials and methods. In addition to the material and methods, selection cost is found as main culminating point. Hence, the present work explores a low-cost and easy process to fabricate superhydrophobic film using ZnO nanoparticles. A two-roll mill, an extruder, and a mixture machine were used for obtaining a highly transparent and superhydrophobic film.

2 Experimental Details

2.1 Preparation of ZnO Nanoparticles

A mixture of zinc acetate dehydrate (precursor, 10 g) was dissolved in 50 ml deionized water, and 2 g of NaOH was dissolved in 50 ml deionized water as well. These two solutions were mixed in a beaker under constant magnetic stirring for 2 h at a temperature of 70°C . Subsequently, the solution was filtered, and the white precipitates were washed several times with deionized water in order to remove the soluble

impurities. After that, the solution was centrifuged at 1400 rpm for 5 min to separate the precipitates from solvent and then dried in the muffle furnace overnight at 180 °C.

2.2 Functionalization of ZnO

It is well known that ZnO is hydrophilic, but it can be converted to a hydrophobic nature by the functionalization process. Functionalization means that modifying the surface properties by changing the surface chemistry of the material. It is a basic technique often used in biological engineering, nanotechnology, and material science. A solution of ZnO (2 g), chloro-trimethyl silane (TMCS, 0.05 mol), and ethanol (100 ml) was prepared in a beaker. The prepared mixture was stirred using a magnetic stirrer for 20 min at 65 °C. After that, filtration of the mixture was carried out with the help of a filter paper and then dried in an oven at 30 °C for 24 h. Thereafter, the above-functionalized ZnO was modified with the help of 3-MPMS (mercaptoptrimethoxysilane). In doing this, a mixture of MPMS (5 g), ZnO (2 g), and methanol (50 ml) was prepared and dispersed using ultra-sonication for 20 min. The ultra-sonicated mixture was stirred using a magnetic stirrer at reflux temperature for 8 h and then diluted and cooled with *n*-propanol. Eventually, the solution was filtered with filter paper and dried in an electric oven for 24 h. Hence, dual functionalized ZnO nanoparticles were prepared.

2.3 Preparation of Transparent ZnO Film

First of all, the functionalized ZnO and the polystyrene have been mixed in a mixture machine. Then, this mixture is cooled to the ambient temperature, which converts the mixture into a solid form. This solid has been broken into small pieces and placed over the two-roll milling machine at 200 °C, as shown in Fig. 2. After that, pull over the sheet from the two-roll milling machine and place it at the ambient temperature for drying. After drying, the prepared sheet has been cut into small pieces and put in between the hydraulic press plates. Furthermore, the temperature of the plates was kept at 150 °C and pressure up to 90 MPa (Fig. 1).

2.4 Characterization

Scanning electron microscope (SEM) operated at 30 kV was used to study the morphology of the ZnO nanoparticles and SHF. The contact angle of the SHF was characterized by the instrument known as a tensiometer, in which a water droplet (5 μ L) was used. Different samples were prepared by adding the variegated amount of



Fig. 1 Pictorial view of **a** hydraulic press, **b** two-roll milling machines, and **c** prepared transparent ZnO film

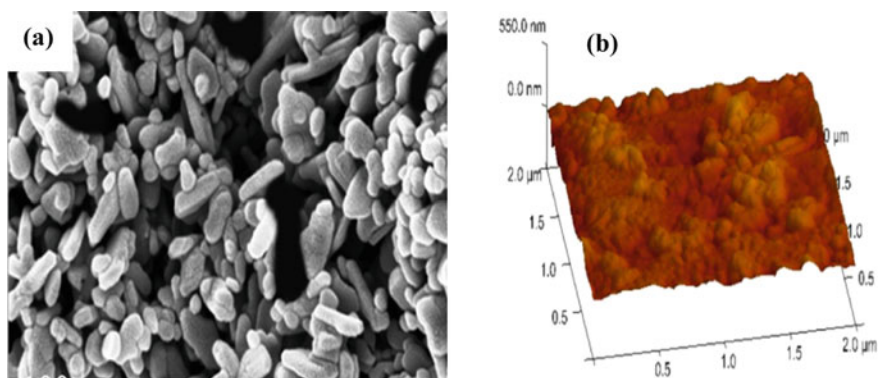


Fig. 2 **a** SEM image of functionalized ZnO nanoparticles and **b** AFM of functionalized ZnO film

functionalized ZnO with polystyrene based on their weight %. The superhydrophobic film's optical transmissivity was recorded by UV–visible spectrophotometry within the wavelength range of 200–800 nm. Atomic force microscopy (AFM) was used to demonstrate the surface roughness of superhydrophobic thin film.

3 Results and Discussion

3.1 Microstructural Analysis

Scanning electron microscopy (SEM) technique was performed to determine the morphology of the prepared nanoparticles. Figure 2a shows that functionalized ZnO nanoparticles consist of a round spherical wheat-like structure with non-uniform

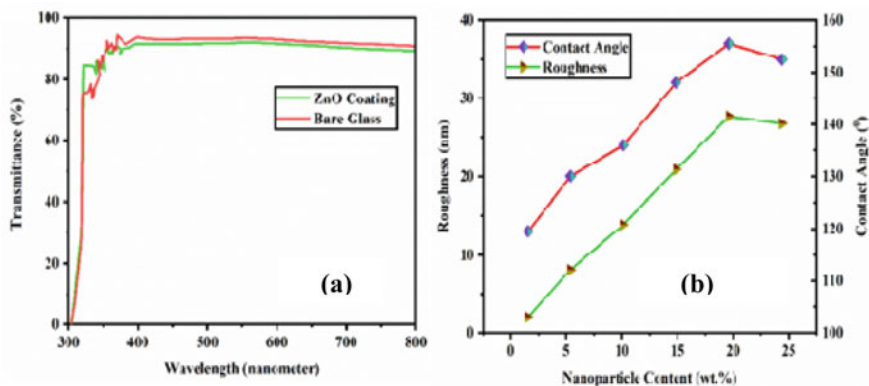


Fig. 3 **a** Optical transmittance spectra of ZnO film and bare glass and **b** effect of ZnO nanoparticles and MPMS content on the roughness and water contact angle of the thin film

size distribution. This type of microstructure results in creating roughness on the surface of the film. The AFM image of the superhydrophobic thin film is also shown in Fig. 2b. AFM micrograph illustrates that the size distribution is uniform and the sharp bumps on the surface are responsible for the roughness of ZnO film, which is found to be 27 nm.







3.2 Optical Analysis

Optical transmittance spectra of ZnO thin film and bare glass were recorded in the visible range, as illustrated in Fig. 3a. It was observed that ZnO thin film is highly transparent in the visible spectrum with average transparency of more than 90%. The optical transparency obtained for bare glass is very similar to ZnO thin film, which means it hardly affects the optical properties of bare glass, which is advantageous for photovoltaic (PV) panel applications. It is well known that ZnO is highly transparent in the visible region due to its wide optical band gap. Hence, it can be inferred that functionalizing of ZnO nanomaterial did not hamper its optical properties [7, 8].

3.3 Water Contact Angle Measurement Analysis

The effect of ZnO nanoparticles and MPMS content on ZnO thin film's roughness and contact angle has been studied. The average value of the roughness and the contact angle of water is first increasing up to 20 wt% use of ZnO nanoparticles and decreasing slightly beyond this limit because of the non-uniform mixing of nanoparticles with the polymer, as summarized in Table 1. From Table 1, the variation

Table 1 Effect of ZnO nanoparticles and MPMS contents on the water contact angles

Polystyrene (wt%)	Zinc oxide (wt%)	MPMS (wt%)	Contact angle (°)	Observation
50	1	49	120	
50	5	45	130	
50	10	40	135	
50	15	35	150	
50	20	30	157	
50	25	25	152	

of contact angle of water droplets has been depicted as a function of the amount of ZnO nanoparticles and polystyrene. The highest value of water contact angle of 157° has been recorded at 20 wt%, 50 wt%, and 30 wt% of ZnO nanoparticles, polystyrene, and MPMS, respectively. This optimum contact angle shows that increasing the weight percentage of ZnO nanoparticles leads to a uniform distribution within the polymer, but with an increase in the amount of ZnO nanoparticles beyond 20 wt% resulted in a decrease in the water contact angle and non-uniform distribution of nanoparticles within the polymer [20–24].

4 Conclusion

From the present work, the following significant conclusions can be drawn:

- i. This antireflective film provides 91.5% of transmittance compared to the bare glass substrate having 92% of transmittance within the wavelength range of 320–750 nm.
- ii. The prepared transparent and superhydrophobic film has shown an average roughness of 36 nm with a contact angle of 157°. This average roughness seems to be a vital function of nanoparticle weight percentage.
- iii. The average value of roughness and the contact angle of water increases up to 20 weight percentage use of nanoparticles and after that decreases slightly beyond this limit because of the non-uniform mixing of nanoparticles with the polymer.
- iv. This proposed method is appropriate in producing a transparent superhydrophobic antireflective film that can be further explored for different industrial applications.

References

1. Bach LG, Islam MR, Kim YH, Seo SD, Park C, Kim HG, Lim KT (2013) A facile route towards the synthesis of polystyrene/zinc oxide nanocomposites. *J Nanosci Nanotechnol* 13(1):694–697
2. Danial EN, Yousef JM (2014) Comparative studies between zinc oxide and manganese oxide nano-particle for their antimicrobial activities. *J Pure Appl Microbiol* 8(1):293–300
3. Cohen N, Dotan A, Dodiuk H, Kenig S (2016) Superhydrophobic coatings and their durability. *Mater Manuf Process* 31(9):1143–1155
4. Xu L, Geng Z, He J, Zhou G (2014) Mechanically robust, thermally stable, broadband antireflective, and superhydrophobic thin films on glass substrates. *ACS Appl Mater Interfaces* 6(12):9029–9035
5. Das S, Kumar S, Samal SK, Mohanty S, Nayak SK (2018) A review on superhydrophobic polymer nanocoatings: recent development and applications. *Ind Eng Chem Res* 57(8):2727–2745
6. Drelich J, Marmur A (2014) Physics and applications of superhydrophobic and superhydrophilic surfaces and coatings. *Surf Innov* 2(4):211–227
7. Sun RD, Nakajima A, Fujishima A, Watanabe T, Hashimoto K (2001) Photoinduced surface wettability conversion of ZnO and TiO₂ thin films. *J Phys Chem B* 105(10):1984–1990
8. Talam S, Karumuri SR, Gunnam N (2012) Synthesis, characterization, and spectroscopic properties of ZnO nanoparticles. *ISRN Nanotechnol* 2012:1–6
9. Tripathi AK, Aruna M, Murthy CSN (2018) Performance degradation of PV module due to different types of dust pollutants 10–13
10. Roslizar A, Dottermusch S, Vüllers F, Kavalenka MN, Guttman M, Schneider M, Paetzold UW, Hölscher H, Richards BS, Klampaftis E (2019) Self-cleaning performance of superhydrophobic hot-embossed fluoropolymer films for photovoltaic modules. *Sol Energy Mater Sol Cells* 189:188–196
11. Barati Darband G, Aliofkhaezrai M, Khorsand S, Sokhanvar S, Kaboli A (2018) Science and engineering of superhydrophobic surfaces: review of corrosion resistance, chemical and mechanical stability. *Arab J Chem*
12. Bai N, Li Q, Dong H, Tan C, Cai P, Xu L (2016) A versatile approach for preparing self-recovering superhydrophobic coatings. *Chem Eng J* 293:75–81
13. Jiang C, Li W (2014) A facile method for preparations of micro-nanotextured Co₃O₄ films with the excellent superhydrophobic and anti-icing behavior. *Mater Lett* 122(3):133–138
14. Mahadik SA, Mahadik DB, Kavale MS, Parale VG, Wagh PB, Barshilia HC, Gupta SC, Hegde ND, Rao AV (2012) Thermally stable and transparent superhydrophobic sol-gel coatings by spray method. *J Sol-Gel Sci Technol* 63(3):580–586

15. Maharjan S, Liao K-S, Wang AJ, Barton K, Haldar A, Alley NJ, Byrne HJ, Curran SA (2020) Self-cleaning hydrophobic nanocoating on glass: a scalable manufacturing process. *Mater Chem Phys* 239:122000
16. Galvan RF, Barranco V, Galvan JC, Batlle S, Fajardo SSF, García (2016) Introductory chapter: superhydrophobic surfaces—introduction and applications. *Intech, i(tourism)*, p 13
17. Kulinich SA, Farhadi S, Nose K, Du XW (2011) Superhydrophobic surfaces: are they really ice-repellent? *Langmuir* 27(1):25–29
18. Fathi M, Abderrezek M, Friedrich M (2017) Reducing dust effects on photovoltaic panels by hydrophobic coating. *Clean Technol Environ Policy* 19(2):577–585
19. Milionis A, Loth E, Bayer IS (2016) Recent advances in the mechanical durability of superhydrophobic materials. *Adv Colloid Interface Sci* 229:57–79
20. Kazem HA, Chaichan MT (2019) The effect of dust accumulation and cleaning methods on PV panels' outcomes based on an experimental study of six locations in Northern Oman. *Sol Energy* 187:30–38
21. Arianpour F (2010) Water and ice-repellent properties of nanocomposite coatings based on silicone rubber. In: *Water ice-repellent properties of nanocomposite coatings based silicone rubber*
22. Al-Housani M, Bicer Y, Koç M (2019) Assessment of various dry photovoltaic cleaning techniques and frequencies on the power output of CdTe-type modules in dusty environments. *Sustainability* 11(10)
23. Liu LQ, Wang XL, Jing M, Zhang SG, Zhang GY, Dou SX, Wang G (2012) Broadband and omnidirectional, nearly zero reflective photovoltaic glass. *Adv Mater* 24(47):6318–6322
24. Xu L, He J (2013) A novel precursor-derived one-step growth approach to fabrication of highly antireflective, mechanically robust and self-healing nanoporous silica thin films. *J Mater Chem C* 1(31):4655–4662

Titania Reinforced Hydroxyapatite Thin Film Coatings for Orthopedic Applications



Ravinder Pal Singh, Anoop Aggarwal, Gurdial Singh, and Mayukh Sarkar

Abstract The titania reinforced hydroxyapatite (THAP) thin films were deposited on Ti6Al4V substrates using a dip-coating technique. The concentration of titania in the HAP matrix was fixed at 10 wt%. The as-prepared THAP coatings were sintered at 800 °C before characterization. The coatings were analyzed for their phase and morphological structures. The corrosion resistance of the coatings was investigated using potentiostatic and potentiodynamic tools. The results revealed that the coatings were composed of the HAP phase with other secondary phases, including CaCO₃ and CaO. The coatings were uniformly spread across the substrates. The deposition of coatings enhanced the corrosion resistance of the substrates. The preliminary examination confirmed that the THAP coatings can enhance orthopedic alloys' corrosion resistance, making them suitable for orthopedic implant applications.

Keywords Hydroxyapatite · Titania · Thin films · Corrosion resistance · Orthopedic implants

1 Introduction

Hydroxyapatite (HAP) has been a widely accepted biomaterial for artificial bone grafts [1, 2] and bioactive coatings applications for orthopedic implants [3]. After interaction with body tissues, it has been observed that the HAP-coated orthopedic implants exhibit the formation of the secondary phases. The formation of such secondary phases depends on the material's chemical composition, structure, and morphological properties [4]. Consequently, metallic reinforcement may tailor the several attributes of HAP-based coatings. On the other hand, the reinforcement of HAP with zirconia [5, 6], alumina [7, 8], and titania (TiO₂) [9–13] produced coatings

R. P. Singh (✉) · M. Sarkar
School of Mechanical Engineering, Lovely Professional University, Phagwara, Punjab, India
e-mail: ravinder.25060@lpu.co.in

A. Aggarwal · G. Singh
Chitkara University Institute of Engineering and Technology, Chitkara University, Chitkara, Punjab, India

having superior mechanical properties suitable for load-bearing implant applications [10–13]. Although several articles are available discussing the effects of TiO₂ reinforcement on the physicochemical, structural, and mechanical properties of titania reinforced HAP (THAP) coatings. However, a dearth of reports explained the in-vitro corrosion resistance of THAP coatings, which is the motivation of this investigation.

In this investigation, the THAP coatings were developed with a 10 wt% concentration of TiO₂ mixed in HAP matrix in solvent form. The coatings were deposited on Ti6Al4V substrates using the dip-coating method. Before the characterization, coatings were sintered at 800 °C. The XRD and SEM tools were used for phase and morphological evaluations of the coatings. In addition, the potentiostatic and potentiodynamic techniques were used to measure the corrosion resistance of the coatings in simulated body fluid (SBF) media.

2 Materials and Method

Calcium nitrate tetrahydrate (CNT, Merck, 99%), diammonium hydrogen phosphate (DAHP, Merck, 99%), and titanium dioxide (TiO₂, Merck, 99%) reagents were used for Ca, P, and Ti ion sources, respectively. Ammonium hydroxide (Merck, 25%) was used to improve the gelation.

Briefly, 0.58 M hydrous DAHP precursor was drop-wise added into 1 M hydrous CNT precursor and formed HAP solution. Later, 1 M TiO₂ hydrous precursor was added drop-wise into the HAP solution and formed THAP solid solution. Thereafter, NH₄OH was added into THAP solid solution till its pH increased to 11. This THAP sol was aged at 80 ± 2 °C for 24 h in a hot air oven. After aging, the Ti6Al4V substrates (Ø5 mm) were immersed into THAP sol using a dip coater and withdrawn gently at 1 mm/s. Each substrate was dipped five times. The substrate was dried at 100 °C ± 2 °C after each coating. Finally, the coated samples were sintered at 800 °C ± 4 °C for one hour in a muffle furnace.

2.1 Characterization

X-ray Diffraction (XRD, X'Pert 1710) was performed using CuK α radiations. Crystallographic information was obtained using the full-pattern Rietveld refinement technique. The crystallographic and microstructural parameters were refined using MAUD software. Refinement was carried out until a close fit between observed and calculated patterns was observed. The JCPDS database, i.e., 09-0432 for HAP, β -tricalcium phosphate (β -TCP; 09-0169), CaCO₃ (5-586), CaO (37-1497), anatase (21-1272), and rutile (21-1276) phases were simulated for refinement purposes. The coating morphology was examined using SEM (JEOL) operated at 20 kV. The electrochemical evaluation of coated samples using polarization studies was performed in SBF to assess their corrosion resistance.

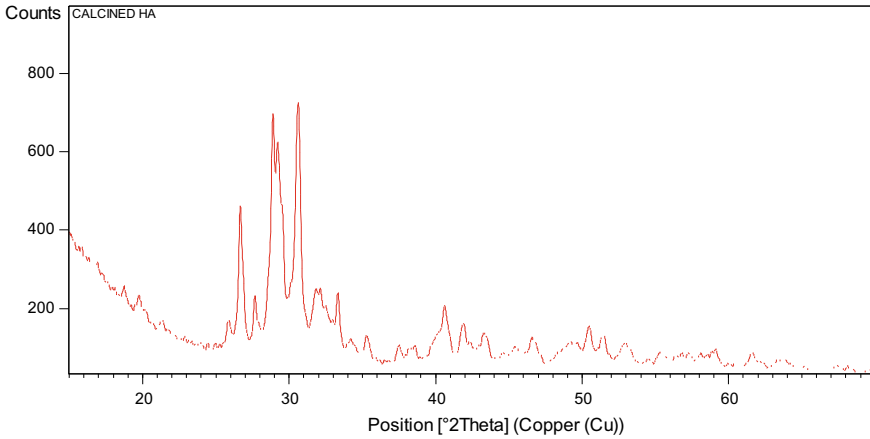


Fig. 1 XRD pattern of THAP coatings on Ti6Al4V substrate

3 Results and Discussion

3.1 Phase Composition

The XRD pattern of THAP coatings has been shown in Fig. 1. Rietveld refinement confirmed the triphasic structure of THAP coatings composed of HAP, CaCO_3 , and rutile phases. The quantitative analysis suggested that the THAP coatings were composed of 73% of HAP, 12% of CaCO_3 , and 15% for the rutile TiO_2 phase. According to the Scherrer formula and Rietveld algorithms, the apatitic crystals were 52 ± 6 nm and 58 ± 3 nm in size, respectively. Furthermore, the HAP crystals exhibited the tensile strain of 0.000485.

3.2 Morphological Composition

The SEM micrograph of THAP coatings is shown in Fig. 2. The morphology of THAP coatings confirmed the deposition of THAP films on Ti6Al4V. The coatings were unevenly distributed across the substrate. Furthermore, coatings were observed to be porous owing to the presence of voids, pores, and channel-like passages on them. It has been established that porous coatings are beneficial for the proliferation and differentiation of bone-forming cells. The particle size of coatings could not be calculated due to its agglomerated structure.

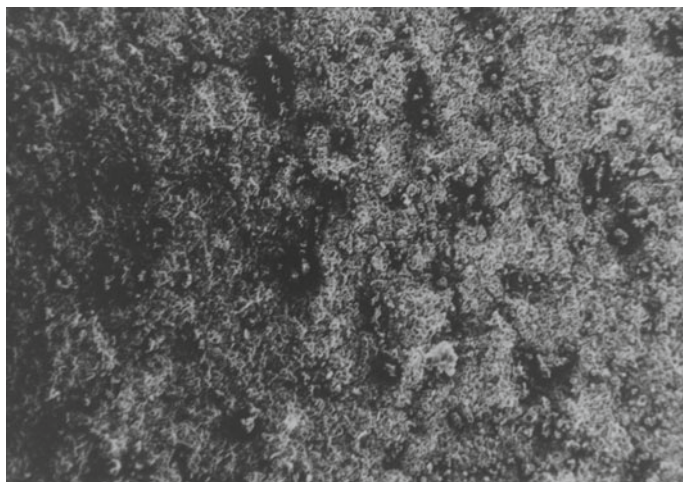


Fig. 2 SEM micrograph of THAP coatings

3.3 Electrochemical Evaluation

The potentiostatic and potentiodynamic results of THAP coatings are shown in Figs. 3 and 4. The potentiostatic test (Fig. 3) indicated that the THAP-coated sample reached equilibrium after 15 min at open circuit potential (OCP) of -0.10511 V. On the other hand, the potentiodynamic test (Fig. 4) exhibited the breakdown potential of 1.0 V at a current density of 1.4952×10^{-3} A/cm². Prakash et al. [14] reported corrosion resistance of TiO₂-loaded HAP layer deposited on β -Ti alloy at a current density of $8.18 \mu\text{A}/\text{cm}^2$ [14]. The comparison with uncoated substrates indicated that the THAP coatings enhanced the corrosion resistance of the substrates. Some corrosion reactions reach a steady state in a few minutes, while others may need several hours.

4 Conclusion

The THAP coatings were successfully deposited on Ti6Al4V substrates using the dip-coating route. Multi-layer depositions can quickly increase the film thickness of coatings. The THAP coatings were multiphasic composed of HAP, CaCO₃, and rutile phases. The sintering process nucleated the secondary phases in the coatings. The coatings were unevenly deposited, which needs to be overcome. Furthermore, the electrochemical testing assured that the corrosion resistance of substrates was

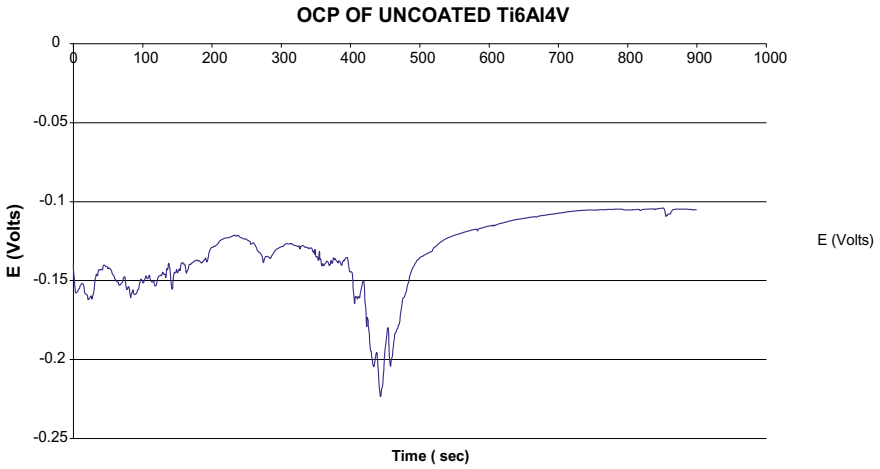


Fig. 3 Potentiostatic curve of THAP coatings

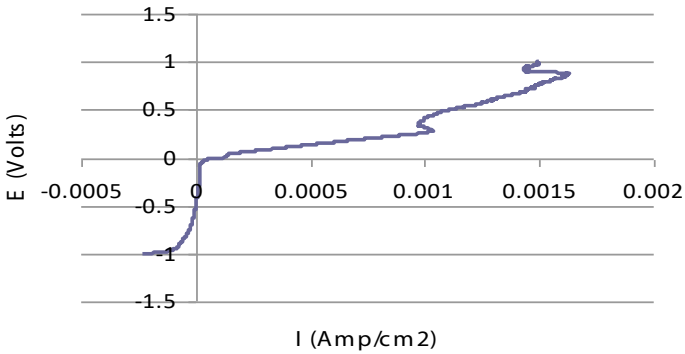


Fig. 4 Potentiodynamic curve of THAP coatings

enhanced after the deposition of THAP coatings. Thus, THAP coatings can suitably be used for therapeutic orthopedic applications, including tissue regeneration implants.

References

1. Singh H, Prakash C, Singh S (2020) Plasma spray deposition of HA-TiO₂ on β -phase Ti-35Nb-7Ta-5Zr alloy for hip stem: characterization of bio-mechanical properties, wettability, and wear resistance. *J Bionic Eng* 17(5):1029–1044
2. Singh S, Prakash C, Singh H (2020) Deposition of HA-TiO₂ by plasma spray on β -phase Ti-35Nb-7Ta-5Zr alloy for hip stem: characterization, mechanical properties, corrosion, and in-vitro bioactivity. *Surf Coat Technol* 398:126072
3. Ahmadi S, Mohammadi I, Sadrnezhaad SK (2016) Hydroxyapatite based and anodic titania nanotube biocomposite coatings: fabrication, characterization and electrochemical behavior. *Surf Coat Technol* 287:67–75
4. Mackovic M, Hoppe A, Detsch R, Mohn D, Stark WJ, Spiecker E, Boccaccini AR (2012) Bioactive glass (type 45S5) nanoparticles: in vitro reactivity on nanoscale and biocompatibility. *J Nanopart Res* 14(7):1–22
5. Kong YM, Bae CJ, Lee SH, Kim HW, Kim HE (2005) Improvement in biocompatibility of ZrO₂-Al₂O₃ nano-composite by addition of HA. *Biomaterials* 26(5):509–517
6. Sung YM, Kim DH (2003) Crystallization characteristics of yttria stabilized zirconia/hydroxyapatite composite nanopowder. *J Cryst Growth* 254(3):411–417
7. Li J, Fartash B, Hermansson L (1995) Hydroxyapatite-alumina composites and bone-bonding. *Biomaterials* 16(5):417–422
8. Gautier S, Champion E, Bernache-Assollant D (1999) Toughening characterization in alumina platelet-hydroxyapatite matrix composites. *J Mater Sci Mater Med* 10(9):533–540
9. Ramires PA, Romito A, Cosentino F, Milella E (2001) The influence of titania/hydroxyapatite composite coatings on in vitro osteoblasts behaviour. *Biomaterials* 22(12):1467–1474
10. Ramires PA, Cosentino F, Milella E, Torricelli P, Giavaresi G, Giardino R (2002) In vitro response of primary rat osteoblasts to titania/hydroxyapatite coatings compared with transformed human osteoblast-like cells. *J Mater Sci Mater Med* 13(8):797–801
11. Chu C, Lin P, Dong Y, Xue X, Zhu J, Yin Z (2002) Fabrication and characterization of hydroxyapatite reinforced with 20 vol% Ti particles for use as hard tissue replacement. *J Mater Sci Mater Med* 13(10):985–992
12. Chu C, Xue X, Zhu J, Yin Z (2006) Fabrication and characterization of titanium-matrix composite with 20 vol% hydroxyapatite for use as heavy load-bearing hard tissue replacement. *J Mater Sci Mater Med* 17(3):245–251
13. Ji S, Murakami S, Kamitakahara M, Ioku K (2009) Fabrication of titania/hydroxyapatite composite granules for photo-catalyst. *Mater Res Bull* 44(4):768–774
14. Prakash C, Wandra R, Singh S, Pramanik A, Basak A, Aggarwal A, Yadaiah N (2021) Synthesis of functionalized TiO₂-loaded HAp-coating by ball-burnishing assisted electric discharge cladding process. *Mater Lett* 301:130282

Different Materials Used for Leachate Management—A Review



Saurabh Sunil Naik, Shantanu N. Pawar, Siddhartha Pandey,
and Bhushan H. Shinde

Abstract Solid waste generation and its proper disposal are neglected issue in most of the countries across the globe. Sorting of the waste is the biggest challenge, and its effectiveness is the key issue in treatment. The inorganic, incombustible and non-recyclable fraction from solid waste is used for landfilling. Landfill using solid waste has advantage, but the fractions of organic non-separated waste lead to generation of leachate and other disadvantages also. In this paper, different materials to be used for controlling the leachate percolation are discussed with their effects on detection of heavy metals, filtration efficacy for the leachate. The materials are bentonite, geotextile, activated carbon, fly ash, etc. By using these materials at landfill sites either as a single or combination of both with different techniques to trap heavy metals which are present in leachate like Mn, Fe, Zn, Cu, Al, Pb, Cd. Also, these materials affect the groundwater characteristics and composition.

Keywords Land filling · Materials · Heavy metals · Leachate control

1 Introduction

Urban India produces approximately 54 Million Tons of municipal solid waste annually. Waste generation in metro cities varies from 0.20 kg to 0.60 kg per day depending upon population. The municipal solid waste (hereafter abbreviated as MSW) is classified according to:

S. S. Naik (✉) · B. H. Shinde
Department of Civil Engineering, G. H. Raisoni University Amravati, Amravati, India
e-mail: saurabhnaik603@gmail.com

S. S. Naik · S. N. Pawar
Department of Civil Engineering, G H Raisoni Institute of Business Management Jalgaon,
Jalgaon, India

S. Pandey
Department of Operations Management, Indian Institute of Management Ranchi, Suchana
Bhawan Meur's Road, Ranchi 834008, India

Division of Research and Innovation, Uttaranchal University, Dehradun, India

- Hotel, kitchen, vegetable waste or leaves, etc., i.e., biodegradable.
- Reusable materials, i.e., waste paper, glass, bottles, certain plastics, etc.
- Construction waste such as bricks and debris.
- Composite wastes as clothing, tetra packs, etc.
- Domestic waste and toxic waste: medical equipments, chemicals, bulb, spray cans, fertilizer and pesticide containers [1, 2].

After collecting the MSW at treatment plant, it is sorted in order of reusable and recyclable. There after it undergoes various processes and finally disposed of. Different methods of disposal of MSW are incineration, landfills and composting pits, etc. Landfill sites have gaseous emissions as well as leachate generation problems.

1.1 Landfills

Mostly landfills are situated at outskirts of urban areas where a large amount of municipal waste is generated and has dumped at one place. An open pit is dug on the ground, then the garbage is dumped, and the pit is covered by soil. At the end of the day, a layer of soil is scattered to compress and cover the garbage. Landfill is mainly used for disposal of MSW, due to cost effectiveness and the large size waste accommodation.

Throughout the world, landfill disposal is common and best suited method for especially solid wastes [3, 4]. Landfill is the major issue for groundwater pollution [5, 6].

There are varieties of materials used to reduce and control leachate percolation like geo-textiles, fibers, paper mill sludge, bottom ash, slag, etc., with various methods to characterize the same. A great deal of research work all over the world is going on to explore the feasibility of different materials for controlling leachate percolation. It is evident from the references summarized at the end. The present paper reviews some of the materials used for controlling the leachate percolation to groundwater.

1.2 Leachate

In rainy season, dumped solid waste in landfills gets watery, and the decomposed products of waste move with water. The liquid containing various organic and inorganic compounds is known as 'leachate'. The leachate gets collected beneath the landfill area, it percolates to the subsoil, and at the end, it reaches up to groundwater table level [7, 8].

Mostly, the residential areas near to landfills site get affected due to groundwater pollution because of leachate percolation which is generated from landfill site [9, 10]. The pollution of surface water and groundwater by the leachate creates unhygienic condition. The unhygienic condition in the periphery of cities, lead the people to

fear about their health condition because of spreading the diseases such as dengue, malaria, etc. [1, 2] There are many materials and technologies that can be used to assess and control groundwater pollution.

1.3 Properties of Leachate

Characteristics of leachate generated from landfill sites basically depend on age of landfill, landfill type, pH of leachate, BOD5/COD ratio, etc. Leachate can be classified according to age, i.e., young and stabilized (mature) [11, 12].

In case of fresh leachate, it has low pH value (less than 6.5), with a high COD (greater than 15,000 mg/L) which contains biodegradable matters and heavy metals greater than 2 mg/L, whereas, on the other side, stabilized leachate has usually high pH with low COD (less than 3000 mg/L) and heavy metals less than 2 mg/L [13–15]. Properties of leachate according to the classification of landfill depending on age are enlisted in Table 1 [16, 17].

If leachate is not collected properly or discharges carefully, then it becomes a pollution source for groundwater as well as soil [18–20]. The tolerance limits discharging leachate into surface water and other are mentioned in Table 2.

Table 1 According to age of landfill and their leachate properties, respectively

Parameters	Landfill type		
	Young	Intermediate	Old (stabilized)
Age of landfill in years	< 5	5–10	> 10
pH value	< 6.5	6.5–7.5	> 7.5
Quantity of organic compounds	Approx. 80% of fatty acids	Up to 30% humic and fulvic acid	Humic and fulvic acids completely
Chemical oxygen demand	> 10,000	4000–10,000	< 4000
TOC/COD	< 0.3	0.3–0.5	> 0.5
BOD5/COD	0.5–1.0	0.1–0.5	< 0.1
Heavy metals range (mg/L)	Low to medium	Low	Low
Biodegradability of landfill according to waste	Important	Medium	Low

Table 2 Range of parameters for discharging wastewater or leachate

S. No.	Parameters	Allowable limits			
		Surface water like river	Sewage system	Marine area	Agricultural land
1	Suspended solids present in leachate	100	600	100	200
2	Dissolved solids in leachate	2100	2100	–	2100
3	pH	5.5–9.0	5.5–9.0	5.5–9.0	5.5–9.0
4	Biological oxygen demand	30	350	100	100
5	Chemical oxygen demand	250	–	250	–
6	Chloride content	1000	1000	–	1000
7	Heavy metal—quantity of sulfate	1000	1000	1000	1000
8	Heavy metal—quantity of cadmium	2.0	1.0	2.0	1.0
9	Heavy metal—quantity of copper	3.0	3.0	3.0	3.0

2 Literature Review

There are various materials like fly ash, bentonite, saw dust, bottom ash as well as geotextile, geopolymers, etc., used for leachate management on landfill dumping site. The materials are used with respect to their local availability, cost effectiveness, purpose of material used, hydraulic properties, etc.

Literature review based on the following different materials

2.1 Palm Shell-Activated Carbon

Palm shell-activated carbon is a ground material having a size varies from 0.6 to 1.18 mm. To remove the impurities, wash the sample with distilled water. Afterward the palm shell-activated carbon was dried at a temperature of 103 °C then cooled in it and store in desiccators. It is used for determining landfill leachate flow pattern. This technology gives leachate profile through adsorption onto media in terms of chemical oxygen demand (COD). After considering the conditions, dispersion modeling study

and fixed bed adsorption study are used. This gives the result for the COD removal up to 50% [17].

2.2 Zeolitised Fly Ash

Synthetic zeolite is a byproduct of coal power plants. There are various methods used to develop synthesise zeolite from fly ash. Synthetic zeolite fly ash having high surface area is used to determine the removal percentage of heavy metal in leachate contaminated groundwater. In this case, two experimental setups were established for diluted landfill leachate and other one for recirculated effluent and sludge of the plant. By using the Zeolitised fly ash, COD is reduced to approximately 40% [21].

2.3 Lignite Fly Ash

Lignite fly ash is highly effective in reducing the leaching losses up to 2%. Fly ash contains various types of heavy metal like Pb, Cu and Cr, but they cannot be found in leachate. In case of intact subsoil, comparatively, the approximate flow of water in repacked soil column blended with Lignite Fly ash affects the chemical flow in the field. The leachate control process depends upon various proportions of fly ash dose composed with soil [22].

2.4 Geotextile

Generally geotextile is used as filter material because they are economical and easy to install. For pre-treatment of leachate generated from landfill, geotextile is generally used as a filter material. Geotextile reduces the leachate parameter like chemical oxygen demand to nearly 42%. Also, toxicity of leachate was reduced to some extent due to geotextile [23].

The usefulness of geonet geotextile is determined through the use of mathematical formulae along with a system dynamics modeling and validated by STELLA 9.1.4 software. The geotextile has the highest retention capability for the leachate volume. This perhaps is linkable to the fact that it has been reported to possess the lowest water absorption rate [24].

2.5 *Fly Ash*

Bentonite and fly ash combination is used for landfill liner. Perform various tests with different proportion of bentonite and fly ash like standard proctor test, hydraulic conductivity test, XRD, SEM, etc., for proportion 5, 10, 15 and greater than 15 if necessary of fly ash. From experimental studies it has been found that, the mixture that has 15% or greater than 15% of soil replaced by fly ash and combined with bentonite may have the value of hydraulic conductivity which satisfies it as bottom liner material [25–27].

Coal-based power house generates the waste by product commonly known as fly ash. Experimental investigation made according to properties of hydraulic barrier, chemical barrier and pH. Under the landfill condition, heavy metal is detected under the constant pH 6. So, fly ash is effective chemical barrier for landfill leachate [28, 29].

Adsorption of heavy metals which are present in leachate can be done by using fly ash. Various experimental tests performed like batch sorption test, kinetic study, etc. In batch sorption study, series of different bottles contains bottles containing different quantity of fly ash in leachate sample of 200 mL. The removal efficiencies of Cu, Mn and Zn are to be achieved with concentration of fly ash of 2 g/L. The low cost effective adsorbent to remove the heavy metal fly ash is the better solution [30–32].

2.6 *Summary of Review*

With reference to above literature, it can be summarized that there are varieties of materials that are used to control the leachate penetration which are generated from municipal solid waste dumping site. Some different materials are reviewed here with two distinct forms, viz. the first one is powder form material like fly ash with different ingredients, bentonite, etc., having good hydraulic property, adsorbent property, etc. [33, 34], on the other hand, some materials like geomembrane, geotextile, etc., having a good filtration property, impact resistance, etc. In some cases, there are combinations of two materials such as fly ash with bentonite.

3 **Concluding Remarks**

This paper reviews the different materials used for control of leachate produced from municipal waste landfill site.

1. To prevent the percolation of leachate, selection of material is basically dependent on the adsorbent property and hydraulic barrier property.

2. Leachate percolation in groundwater is hazardous to living beings for consumption as well as the soil fertility that percolated the leachate because it contained the heavy metals like Mn, Fe, Zn, Cu, Al, Pb, Cd, etc., which are harmful.
3. For controlling the leachate, researchers have tried different materials like activated carbon, bentonite, geotextile, fly ash, etc., with good hydraulic and adsorbent property. Generally geotextile or geomembrane is used as a filter material, and bentonite, activated carbon, fly ash, etc., are used for adsorbent material in landfill site where leachate is percolate.
4. By using these materials either single or combination of two with different techniques, the heavy metal present in leachate like Mn, Fe, Zn, Cu, Al, Pb and Cd can be controlled or removed. Also, it affects chemical oxygen demand, biological oxygen demand, pH, etc., of groundwater.

Hence, present paper indicates the different materials that are used for controlling leachate percolation in ground.

References

1. International Energy Agency (IEA) (2017)
2. Ministry of Urban Development of India (2013)
3. Li W, Zhou Q, Hua T (2010) Removal of organic matter from landfill leachate by advanced oxidation processes: a review. *Int J Chem Eng* 2010(2010):1–10
4. Shou-liang H, Bei-dou X, Hai-chan Y, Shi-lei F, Jing S, Hong-liang L (2008) In situ simultaneous organics and nitrogen removal from recycled landfill leachate using an anaerobic–aerobic process. *Bioresour Technol* 99(14):6456–6463
5. Fatta D, Papadopoulos A, Loizidou M (1999) A study on the landfill leachate and its impact on the groundwater quality of the greater area. *Environ Geochem Health* 21(2):175–190
6. US EPA (2013) Method 1314, liquid-solid partitioning as a function of liquid-solid ratio for constituents in solid materials using an up-flow percolation column procedure
7. Kale SS, Kadam AK, Kumar S, Pawar NJ (2010) Evaluating pollution potential of leachate from landfill site, from the Pune metropolitan city and its impact on shallow basaltic aquifers. *Environ Monit Assess* 162:327–346
8. Mor S, Ravindra K, Dahiya RP, Chandra A (2006) Leachate characterization and assessment of groundwater pollution near municipal solid waste landfill site. *Environ Monit Assess* 118:435–456
9. Nagarajan R, Thirumalaisamy S, Lakshumanan E (2012) Impact of leachate on groundwater pollution due to non-engineered municipal solid waste landfill sites of erode city, Tamil Nadu, India. *Iran J Environ Health Sci Eng* 9:35
10. Saleem M, Bukhari AA, Akram MN (2011) Electrocoagulation for the treatment of wastewater for reuse in irrigation and plantation. *J Basic Appl Sci* 7(1):11–20
11. Papadopoulou MP, Karatzas GP, Bougioukou GG (2007) Numerical modeling of the environmental impact of landfill leachate leakage on ground water quality—a field application. *Environ Model Assess* 12:43–54
12. Saarela J (2003) Pilot investigations of surface parts of three closed landfills and factors affecting them. *Environ Monit Assess* 84:183–192
13. Nidheesh PV, Gandhimathi R (2014) Removal of Rhodamine B from aqueous solution using graphite–graphite electro-Fenton system *Desalin. Water Treat* 52:1872–1877. <https://doi.org/10.1080/19443994.2013.790321>

14. Gandhimathi R, Babu A, Nidheesh PV, Ramesh ST, Anantha Singh TS (2014) Laboratory study on leachate treatment by electrocoagulation using fly ash and bottom ash as supporting electrolytes. *Am Soc Civ Eng*
15. Gandhimathi R, Durai NJ, Nidheesh PV, Ramesh ST, Kanmani S (2013) Use of combined coagulation-adsorption process as pretreatment of landfill leachate. *Iran J Environ Health Sci Eng* 10:24
16. Kulikowska D, Klimiuk E (2008) The effect of landfill age on municipal leachate composition. *Bioresour Technol* 99(13):5981–5985
17. Lim YN, Shaaban MG, Yin CY (2009) Treatment of landfill leachate using palm shell-activated carbon column: axial dispersion modeling and treatment profile. *Chem Eng J* 146(1):86–89
18. Environmental Laws of India (2000) CPR environmental education centre. Chennai, India
19. Atmaca E (2009) Treatment of landfill leachate by using electro-Fenton method. *J Hazard Mater* 163(1):109–114
20. Umar M, Aziz HA, Yusoff MS (2010) Variability of parameters involved in leachate pollution index and determination of LPI from four landfills in Malaysia. *Int J Chem Eng* 2010. Article ID 747953, 6 pages
21. Luna Y, Otal E, Vilches LF, Vale J, Querol X, Fernández Pereira C (2006) Use of zeolitised coal fly ash for landfill leachate treatment: a pilot plant study. *Waste Manage* 27:1877–1883
22. Ghosh RK, Singh N (2012) Managing metolachlor and atrazine leaching losses using lignite fly ash. *J Ecotoxicol Environ Saf*. <https://doi.org/10.1016/j.ecoenv.2012.07.015>
23. Silva SA, Palmeira EM (2017) Leachate pre-treatment using non-woven geotextile filters. *Environ Geotech*
24. Ojoawo S, Dauda JA (2012) Geonets and geotextiles as leachate containment materials in landfills: system dynamics modeling perspective. *J Civ Eng Archit* 6(9)(serial no. 58):1252–1257
25. Hecht NL, Duvall DS (1975) Characterization and utilization of municipal and utility sludges and ashes, vol III. Environmental Protection Agency, Utility Coal Ash, National Environmental Research Center, U.S
26. de Carvalho Izidorio J, da Silva Miranda C, Guilhen SN, Fungaro DA, Wang S (2018) Treatment of coal ash landfill leachate using zeolitic materials from coal combustion by-products. *Adv Mater Technol Environ Appl* 2(1):177–186. ISSN: 2559–2637
27. Nguyen LC, Chu HL, Ho LS (2019) Soil treatment by bentonite and fly ash for liners of waste landfill: a case study in Vietnam. *Int J GEOMATE* 17(63):315–322
28. Nhan CT, Graydon JW, Kirk DW (1997) Utilizing coal fly ash as a landfill barrier material. *Waste Manage* 16(7):587–595
29. Tiwari MK, Bajpai S, Dewangan UK, Tamrakar RK (2015) Suitability of leaching test methods for fly ash and slag: a review. *J Radiat Res Appl Sci*
30. Li J-s, Xue Q, Wang P, Wang H-q, Zhang T-t (2016) Evaluation of leaching characteristics of heavy metals from municipal solid waste incineration fly ash by up-flow percolation column tests. *Environ Earth Sci* 75:714
31. Haarstad K, Mæhlum T (2013) Tracing solid waste leachate in groundwater using $\delta^{13}C$ from dissolved inorganic carbon. *Isotopes Environ Health Stud* 49(1):48–61
32. Mohan S, Gandhimathi R (2009) Removal of heavy metal ions from municipal solid waste leachate using coal fly ash as an adsorbent. *J Hazard Mater* 169(1–3):351–359
33. Smith RD, Campbell JA, Nielson KK (1979) Concentration dependence upon particle size of volatilized elements in fly ash. *Environ Sci Technol* 13:553–558
34. Singh S (2017) Fly ash in India: generation utilization and global perspective. *Int J Appl Chem* 13(1):29–52. ISSN 9073-1792

Study of Thermoelectrical Behavior of BaXO₃ Perovskites (X = Pu, Am, Cm)



Preeti Kumari and Vipul Srivastava

Abstract Barium oxide perovskites are inspected for first-principles calculations based on density functional theory and full-potential linearized augmented plane-wave method FPLAPW method inbuilt within the WIEN2K code. The thermoelectric behavior of BaXO₃ (X = Pu, Am, and Cm) compounds are calculated through semi-classical Boltzmann transport theory. BoltzTrap2 code is used for determining transport parameters such as Seebeck coefficient S , electronic thermal conductivity κ_e/τ , electrical conductivity σ/τ , and slack approach are used to compute the lattice thermal conductivity κ_l/τ for BaXO₃ perovskites. These parameters are considered for their variation with temperature from 50 to 1200 K for spin-up as well as spin-down and their combined study using the two-current model. This work also shows the power factor and figure of merit zT variation relative to temperature. Among them, the maximum obtained value of zT is 0.06 for BaAmO₃ in a spin-up channel.

Keywords Density functional theory · WIEN2K · Thermoelectric · Boltzmann transport theory

1 Introduction

High-performing thermoelectric materials are a requirement in materials science due to their contribution to the field of energy. Overconsumption of energy resources necessitates the need to search for new energy sources to meet the existing generation's requirements. New kind of novel materials with extraordinary characteristics has provided new dimensions in materials science. Therefore, the synthesis of materials with properties related to photovoltaic and energy conversion can be considered as a substitute for the source of power generation [1, 2]. Thermoelectric materials will be helpful in the generation of thermoelectric power generators that can be used as an alternative source of energy. Many compounds have been reported in the past for properties like structural, magnetic, thermodynamic, etc. [3–13]. Perovskite

P. Kumari · V. Srivastava (✉)

Department of Physics, School of Chemical Engineering and Physical Sciences, Lovely Professional University, Phagwara 144411, India

e-mail: vipsri27@gmail.com

is one of the candidates for fulfilling the prerequisite of thermoelectric materials. Perovskites are known for their multifunctional behavior in their properties such as ferromagnetism [14–16], half metallicity [4–6, 17, 18], colossal magnetoresistance [19], Para-magnetism [20, 21], optical and electronic [22–24], etc. Diversity in their properties landed up into applications such as spintronic, magnetoelectric memory devices, fuel cells, photovoltaic cells, light-emitting diode, Cathode ray tubes, etc. [25–30]. Perovskites are having the general formula ABX_3 with A being the rare earth elements, B being the transition elements while X can either be halide or oxide. $CH_3NH_3PbI_3$ perovskite has a record of having good thermoelectric performance, high charge mobility, and optoelectronic properties, and major applications in solar cells [31–35]. But these lead-based perovskites are having certain limitations due to their high toxic levels and instability in the structure [36, 37]. So, the search for leadless perovskites is the next option to move forward. Transuranic lead-free halide perovskite can contribute positively in this regard. Perovskites with second place occupied by transuranic elements like $BaCmO_3$, $BaPuO_3$, $BaAmO_3$, $SrAmO_3$, and $SrPuO_3$ have been worked for their electronic, structural, and thermophysical parameters [38–42]. We have studied the thermoelectric behavior of $BaPuO_3$, $BaAmO_3$, and $BaCmO_3$. In this regard, the figure of merit is the key parameter to look for estimation of the efficiency of thermoelectric materials. Its values should be nearly equal to or more than 1 for the attainment of the highest performance of the thermoelectric materials. The figure of merit depends on the electrical and ionic thermal conductivity of the materials as depicted in Eq. 1.

$$zT = S^2\sigma T/\kappa \quad (1)$$

where S , σ , κ are the Seebeck coefficient, electrical, and ionic thermal conductivity. Ionic thermal conductivity consists of a lattice κ_l and electronic κ_e thermal conductivity. For practical applications, materials should have a low value of thermal conductivity and a high value of Seebeck coefficient and electrical conductivity.

We have investigated the thermoelectric properties of $BaXO_3$ ($X = Pu, Am,$ and Cm) perovskites in their cubic phase using Boltzmann transport theory [43–45] via BoltzTrap code [46, 47] which are not explored yet. We have divided our paper into a few sections. Section 1 portrays the brief introduction about the compound, Sect. 2 portrays the methodology part, in Sect. 3 results are discussed, and ended with the conclusion in Sect. 4.

2 Methodology

Most efficient density functional theory [48] as incorporated in WIEN2K programming package with full-potential linearized augmented treatment [49] is applied for generating the crystal structures of $BaXO_3$ ($X = Pu, Cm,$ and Am). Optimized lattice parameter is obtained by providing compression around equilibrium volume. Exchange correlation potential, Generalized Gradient Approximation of Perdew

Burke Ernzerhof (GGA-PBE) [50] is induced for investigation of the thermoelectric properties of the perovskites. 50,000 k points are provided for integration of the first Brillouin zone (BZ) via the tetrahedron method [51]. FPLAPW method sectioned unit cell into two different regions: (1) atomic sphere (2) Interstitial region. Wave function inside the atomic sphere uses radial and spherical harmonics while inside the interstitial region uses plane-wave basis. Convergence criteria are fulfilled by setting K_{MAX} , R_{MT} , charge, and energy difference to 7, 0.001 e/a.u.³, and 0.001 Ry, respectively in which R_{MT} denotes the smallest radii within the unit cell and K_{MAX} denotes the largest size propagation vector. Within the atomic sphere, charge density is Fourier expanded up to G_{MAX} equal to 12 a.u.⁻¹, and the maximum value of angular momentum L_{MAX} is fixed to 10.

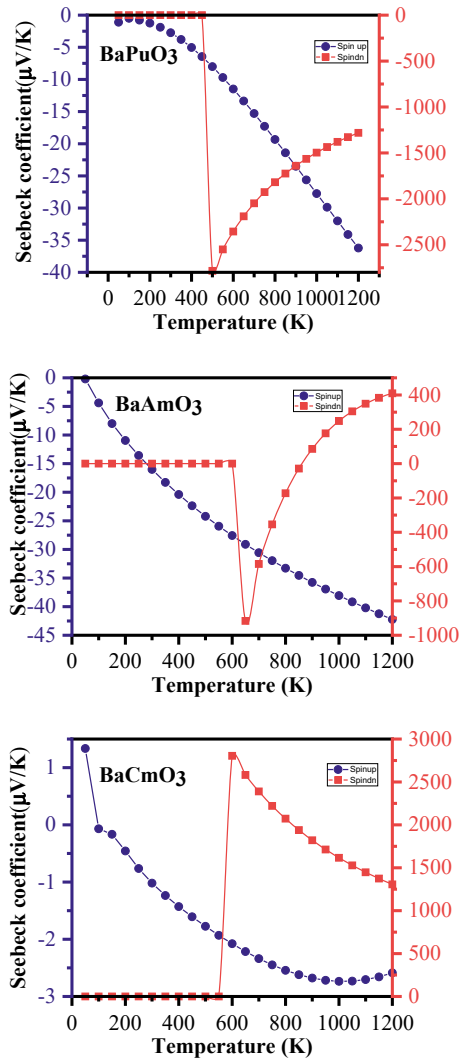
Self-consistent field equations have been solved for understanding the thermoelectric behavior for BaXO₃ (X = Pu, Am, and Cm) perovskites along with the Boltzmann transport phenomenon [43–45]. Boltztrap code [46, 47] interfaced with the WIEN2K package for investigation of transport properties of Barium oxide perovskites. The lattice part of the thermal conductivity is calculated using the slack equation [52].

3 Results and Discussion

Thermoelectric calculations have been performed with Boltzmann transport theory via BoltzTrap code interfaced to WIEN2K. These properties have been estimated for parameters such as Seebeck coefficient S , electrical conductivity σ/τ , power factor (PF) $S^2\sigma/\tau$, electronic thermal conductivity κ_e/τ , lattice thermal conductivity κ_l , total thermal conductivity κ and figure of merit zT for BaPuO₃, BaAmO₃, and BaCmO₃ within the temperature range 50–1200 K. BaPuO₃, BaAmO₃, and BaCmO₃ perovskite are reported to be half-metallic by Dar et al. [39, 40, 42]. Both spin states behave differently from each other. Band structure profile shows the spin-up state to be metallic while spin-down state to be semiconductor [39, 40, 42]. Spin polarization calculations with generalized gradient approximation GGA are used to investigate their thermoelectric profile for spin-up and spin-down states. Seebeck coefficient variation w.r.t temperature for Barium oxide perovskites BaXO₃ (X = Pu, Am, and Cm) are shown in Fig. 1. For BaPuO₃, S decreases for the spin-up state while for the spin-down state, it remains zero till 500 K after that sudden jump at 550 K and starts increasing with temperature. The same kind of trend can be easily observed for BaAmO₃, i.e., both spins' behavior is inverted of each other whereas increment in the spin-down state is more in BaAmO₃. The negative value represents electrons as majority charge carriers in the spin-up state. While in the case of BaCmO₃, S values decrease for both the spins. At room temperature, only the spin-up channel contributes to all Barium oxide perovskites.

The effects of temperature on electrical conductivity are shown in Fig. 2 for BaXO₃ compounds. Electrical conductivity behaves positively with temperature for the spin-up and down for BaPuO₃ and BaAmO₃ perovskite. It values increases from 1.30 (2.20) at 50 K to 1.41 (2.30) ($10^{20} \Omega^{-1} \text{ m}^{-1} \text{ s}^{-1}$) at 1200 K in BaPuO₃ (BaAmO₃) for

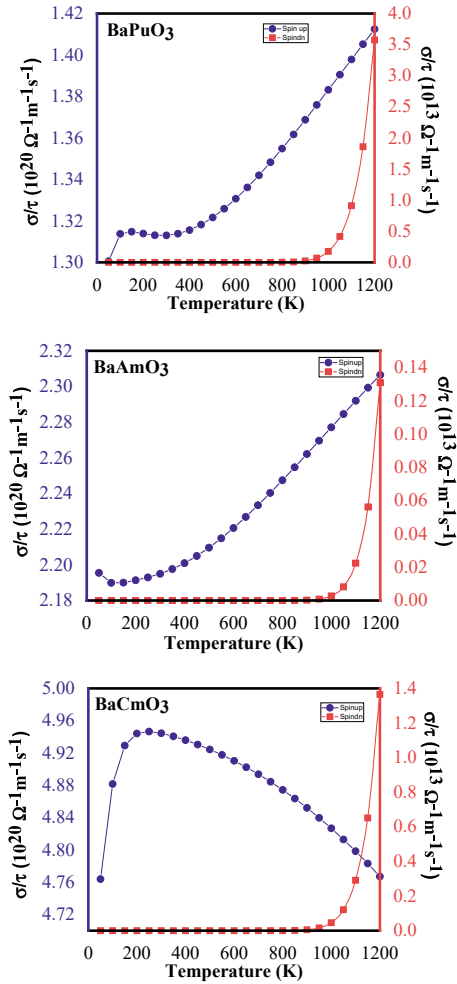
Fig. 1 Seebeck coefficient S versus temperature for $BaPuO_3$, $BaAmO_3$, and $BaCmO_3$ perovskites



spin-up state. In $BaCmO_3$ compound, we can observe that electrical conductivity for the spin-up state shows increment till 200 K beyond that it decreases as temperature's value increases whereas for spin-down state σ/τ increases after 1000 K. The value of electrical conductivity for the spin-up channel is 10^7 times more than the spin-down channel which indicates that spin-up channel is more conducting than spin-down. Spin-up shows the metallic nature of more conductance than the semiconducting nature of the spin-down channel.

The temperature-induced Power factor $PF S^2\sigma/\tau$ plot for both the spins are shown in Fig. 3. PF trend looks similar for $BaPuO_3$, $BaAmO_3$, and $BaCmO_3$. Its value is

Fig. 2 Electrical conductivity σ/τ versus temperature for BaPuO₃, BaAmO₃, and BaCmO₃ perovskites

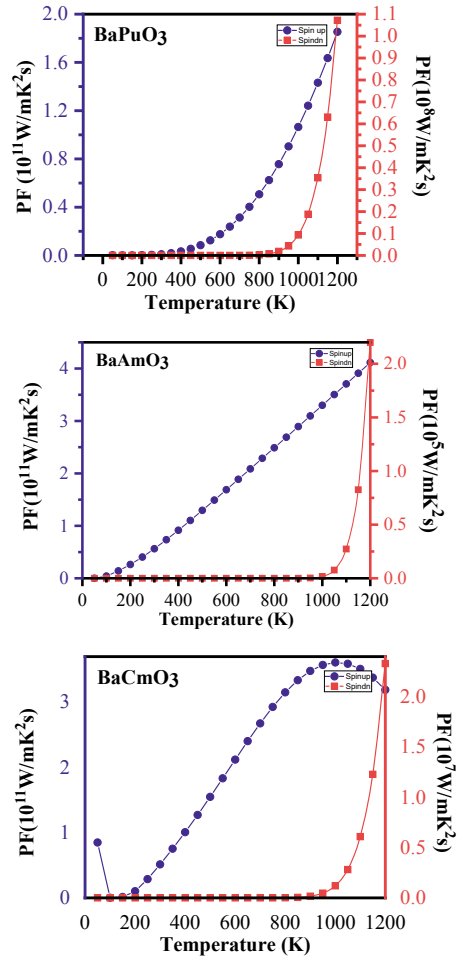


more in the case of spin-up state. For BaPuO₃ and BaAmO₃, in the spin-up channel, PF increases with temperature, and in the spin-down channel its increases only after 1000 K below that its value is zero. For BaCmO₃, PF increases till 900 K after that it shows decrement.

The figure of merit zT plot w.r.t temperature for BaPuO₃, BaAmO₃, and BaCmO₃ is presented in Fig. 4. It is found to increase with the increase in temperature. For all the considered compounds, zT is more in the case of spin-up. The maximum obtained values of zT are 0.04, 0.06, and 0.0003 for BaPuO₃, BaAmO₃, and BaCmO₃, respectively. zT for BaCmO₃ increases till 1100 beyond that it decreases.

A combined study of both the spins is required for understanding the collective behavior of the transport properties of these compounds. The nature of heat carriers is depicted using both spins correct model estimated in Eq. 2 [53].

Fig. 3 Power factor versus temperature for BaPuO₃, BaAmO₃, and BaCmO₃ perovskites



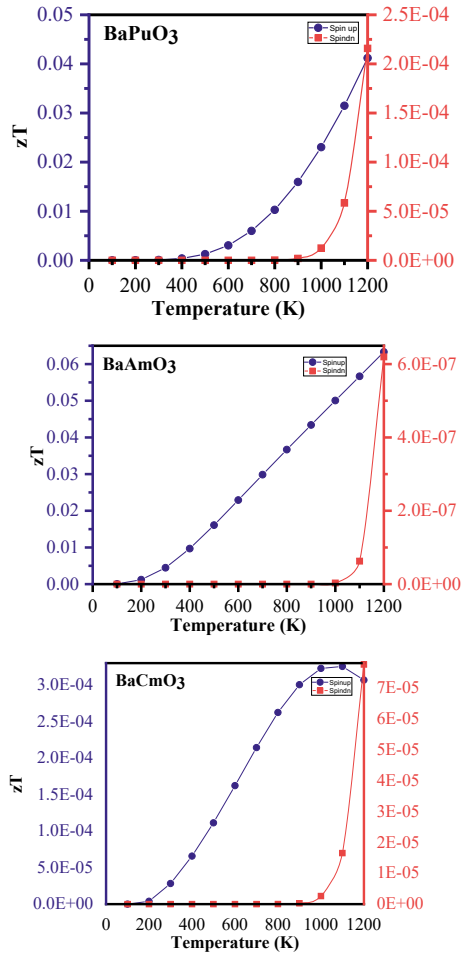
$$S = \frac{S(\uparrow)\sigma(\uparrow) + S(\downarrow)\sigma(\downarrow)}{\sigma(\uparrow) + \sigma(\downarrow)} \quad (2)$$

where $S(\uparrow)$, $\sigma(\uparrow)$, $S(\downarrow)$, and $\sigma(\downarrow)$ are the Seebeck coefficient and electrical conductivities in spin-up and spin-down states. Total electrical conductivity and total electronic thermal conductivity can be expressed as

$$\sigma = \sigma(\uparrow) + \sigma(\downarrow) \quad (3)$$

$$\kappa_e = \kappa_e(\uparrow) + \kappa_e(\downarrow) \quad (4)$$

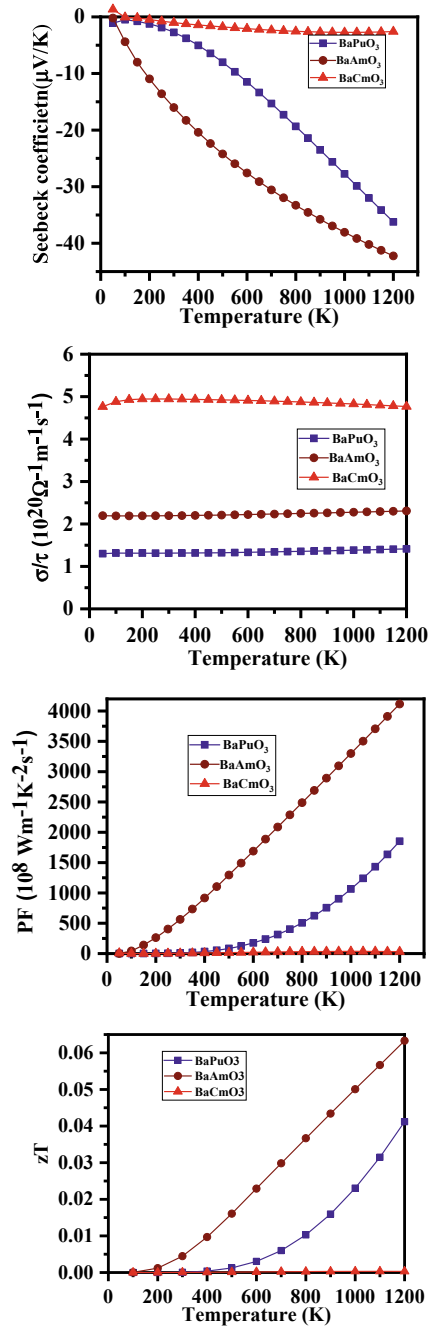
Fig. 4 Figure of merit versus temperature for BaPuO₃, BaAmO₃, and BaCmO₃ perovskites



where $\sigma(\uparrow)$ and $\sigma(\downarrow)$ are the electrical conductivity in spin-up and spin-down states while $\kappa_e(\uparrow)$ and $\kappa_e(\downarrow)$ are electronic thermal conductivity in spin-up and downstate. The combined S , σ/τ , PF, and zT effects with temperature for BaPuO₃, BaAmO₃, and BaCmO₃ are presented in Fig. 5. Seebeck coefficient is dominating for spin-up states $S(\uparrow)$ only. It is also observed that total S decreases with temperature interpreting that the negative charges are in majority. Sluggish increase in electrical conductivity σ/τ was found for BaXO₃ ($X = \text{Pu, Am}$) while decreases can be easily observed in BaCmO₃. Power factor and figure of merit increase with temperature. PF and zT increase with changing transition element in X as $\text{Cm} < \text{Pu} < \text{Am}$. zT is least for BaCmO₃ perovskite.

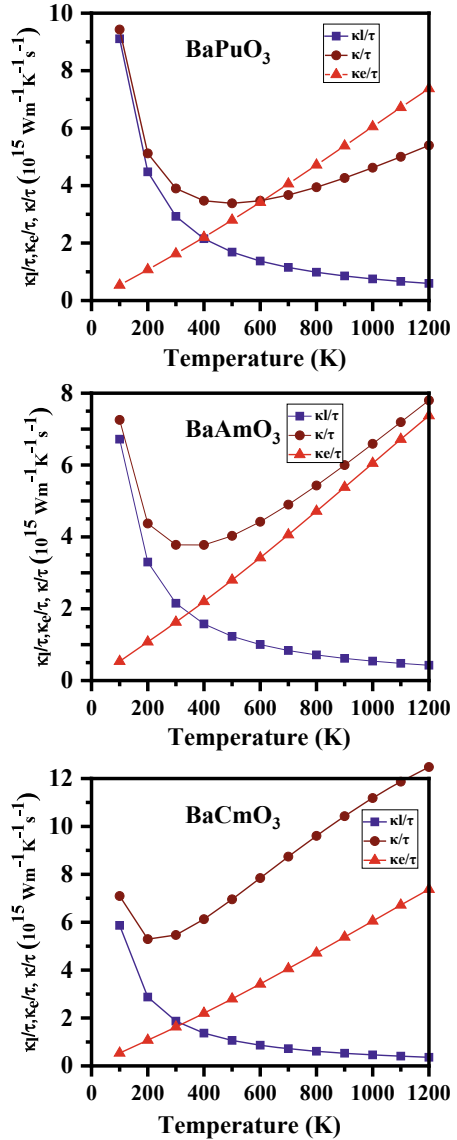
Total, electronic and lattice thermal conductivity effects with temperature are shown in Fig. 6. Figure 6 represents the individual effect of lattice and electronic conductivity and total thermal conductivity. Electronic thermal conductivity κ_e/τ

Fig. 5 Combined S , σ/τ , PF, and zT versus temperature for BaPuO₃, BaAmO₃, and BaCmO₃ perovskites



increases linearly with increasing temperature while lattice thermal conductivity κ_l/τ decays as temperature increases for BaXO₃. We can see that in the case of total thermal conductivity (κ), κ_e/τ is dominating at a lower temperature while κ_l/τ dominates at a higher temperature for all perovskites under study.

Fig. 6 Total, electronic, and lattice thermal conductivities plot versus temperature for BaPuO₃, BaAmO₃, and BaCmO₃ perovskites



4 Conclusion

BaXO₃ (X = Pu, Am, and Cm) perovskites are interrogated for the behavior of their thermoelectric properties at higher temperature values. We have looked for the temperature variations of Seebeck coefficient, electrical conductivity, power factor, and figure of merit for spin-up as well as spin-down channels. The combined effect of spin-up and down with temperature for Seebeck coefficient, electrical conductivity, lattice, electronic and total thermal conductivity, power factor, and figure of merit is also shown using the two-current model. κ_e/τ and κ_1/τ behave oppositely with increasing temperature. κ/τ is dominating with κ_1/τ at a lower temperature while κ_e/τ dominates at higher values of T . The maximum value of the figure of merit is decreasing in order as Am > Pu > Cm.

References

1. Sorrell S (2015) Reducing energy demand: a review of issues, challenges and approaches. *Renew Sustain Energy Rev* 47:74–82
2. Frederiks ER, Stenner K, Hobman EV (2015) Household energy use: applying behavioural economics to understand consumer decision-making and behaviour. *Renew Sustain Energy Rev* 41:1385–1394
3. Ahmad SD, Srivastava V, Sakalle UK, Rashid A, Pagare G (2018) First-principles investigation on electronic structure, magnetic, mechanical and thermodynamic properties of SrPuO₃ perovskite oxide. *Mater Res Express* 5(2):026106
4. Ahmad SD, Srivastava V, Sakalle UK, Parey V (2018) Ferromagnetic phase stability, magnetic, electronic, elasto-mechanical and thermodynamic properties of BaCmO₃ perovskite oxide. *J Electron Mater* 47(7):3809–3816
5. Ahmad SD, Srivastava V, Sakalle UK, Pagare G (2018) Insight into structural, electronic, magnetic, mechanical, and thermodynamic properties of actinide perovskite BaPuO₃. *J Supercond Novel Magn* 31(10):3201–3208
6. Ahmad SD, Srivastava V, Sakalle UK, Khandy SA, Gupta DC (2018) A DFT study on structural, electronic mechanical and thermodynamic properties of 5f-electron system BaAmO₃. *J Supercond Novel Magn* 31(1):141–149
7. Khandy SA, Gupta DC (2017) Structural, elastic and magneto-electronic properties of half-metallic BaNpO₃ perovskite. *Mater Chem Phys* 198:380–385
8. Parrey KA, Devi N, Khenata R, Khandy SA (2018) Investigating structure, magneto-electronic, elastic and thermoelectric properties of alkaline earth actinide perovskite oxide (BaBkO₃) from first principle calculations. *Comput Condens Matter* 17:e00340
9. Trukhanov SV, Trukhanov AV, Salem MM, Trukhanova EL, Panina LV, Kostishyn VG, Darwish MA, Trukhanov AV, Zubar TI, Tishkevich DI, Sivakov V (2018) Preparation and investigation of structure, magnetic and dielectric properties of (BaFe_{11.9}A_{10.1}O₁₉)_{1-x}-(BaTiO₃)_x biocomponent ceramics. *Ceram Int* 44(17):21295–21302
10. Dar SA, Sharma R, Srivastava V, Sakalle UK (2019) Investigation on the electronic structure, optical, elastic, mechanical, thermodynamic and thermoelectric properties of wide band gap semiconductor double perovskite Ba₂InTaO₆. *RSC Adv* 9(17):9522–9532
11. Dar SA, Srivastava V, Sakalle UK (2019) Structural, elastic, mechanical, electronic, magnetic, thermoelectric and thermodynamic investigation of half metallic double perovskite oxide Sr₂MnTaO₆. *J Magn Mater* 484:298–306

12. Dar SA, Srivastava V, Sakalle UK, Parey V, Pagare G (2018) A combined DFT, DFT + U and mBJ investigation on electronic structure, magnetic, mechanical and thermodynamics of double perovskite Ba₂ZnOsO₆. *Mater Sci Eng B* 236:217–224
13. Kumari P, Srivastava V, Khenata R, Dar SA, Naqib SH (2021) A first-principles prediction of thermophysical and thermoelectric performances of SrCeO₃ perovskite. *Int J Energy Res*
14. Atou T, Chiba H, Ohoyama K, Yamaguchi Y, Syono Y (1999) Structure determination of ferromagnetic perovskite BiMnO₃. *J Solid State Chem* 145(2):639–642
15. Jin CQ, Zhou JS, Goodenough JB, Liu QQ, Zhao JG, Yang LX, Yu Y et al (2008) High-pressure synthesis of the cubic perovskite BaRuO₃ and evolution of ferromagnetism in ARuO₃ (A = Ca, Sr, Ba) ruthenates. *Proc Natl Acad Sci* 105(20):7115–7119
16. Subramanian MA, Ramirez AP, Marshall WJ (1999) Structural tuning of ferromagnetism in a 3D cuprate perovskite. *Phys Rev Lett* 82(7):1558
17. Mir SA, Gupta DC (2020) New ferromagnetic half-metallic perovskites for spintronic applications: BaMO₃ (M = Mg and Ca). *RSC Adv* 10(60):36241–36252
18. Philipp JB, Majewski P, Alff L, Erb A, Gross R, Graf T, Brandt MS, Simon J, Walther T, Mader W, Topwal D (2003) Structural and doping effects in the half-metallic double perovskite A₂CrWO₆ (A = Sr, Ba, and Ca). *Phys Rev B* 68(14):144431
19. Gutierrez J, Barandiaran JM, Insausti M, Lezama L, Pena A, Blanco JJ, Rojo T (1998) Magnetic and transport properties of Pb perovskites and Fe containing giant magnetoresistance perovskites. *J Appl Phys* 83(11):7171–7173
20. Ali Z, Khan I, Ahmad I, Khan MS, Asadabadi SJ (2015) Theoretical studies of the paramagnetic perovskites MTaO₃ (M = Ca, Sr and Ba). *Mater Chem Phys* 162:308–315
21. Khandy SA, Gupta DC (2015) Structural, elastic and thermo-electronic properties of paramagnetic perovskite PbTaO₃. *RSC Adv* 6(53):48009–48015
22. Quan LN, Rand BP, Friend RH, Mhaisalkar SG, Lee TW, Sargent EH (2019) Perovskites for next-generation optical sources. *Chem Rev* 119(12):7444–7477
23. Liang J, Liu Z, Qiu L, Hawash Z, Meng L, Wu Z, Jiang Y, Ono LK, Qi Y (2018) Enhancing optical, electronic, crystalline, and morphological properties of cesium lead halide by Mn substitution for high-stability all-inorganic perovskite solar cells with carbon electrodes. *Adv Energy Mater* 8(20):1800504
24. Vargas B, Torres-Cadena R, Rodriguez-Hernandez J, Gembicky M, Xie H, Jimenez-Mier J, Liu YS, Menendez-Proupin E, Dunbar KR, Lopez N, Olalde-Velasco P (2018) Optical, electronic, and magnetic engineering of (111) layered halide perovskites. *Chem Mater* 30(15):5315–5321
25. Bibes M, Barthélémy A (2008) Towards a magnetoelectric memory. *Nat Mater* 7(6):425–426
26. Bristowe NC, Varignon J, Fontaine D, Bousquet E, Ghosez P (2015) Ferromagnetism induced by entangled charge and orbital orderings in ferroelectric titanate perovskites. *Nat Commun* 6(1):1–6
27. Scott JF (2007) Multiferroic memories. *Nat Mater* 6(4):256–257
28. Tokura Y, Naoito N (2000) Orbital physics in transition-metal oxides. *Science* 288(5465):462–468
29. Bonanos N, Knight KS, Ellis B (1995) Perovskite solid electrolytes: structure, transport properties and fuel cell applications. *Solid State Ionics* 79:161–170
30. Gao P, Grätzel M, Nazeeruddin MK (2014) Organohalide lead perovskites for photovoltaic applications. *Energy Environ Sci* 7(8):2448–2463
31. He Y, Galli G (2014) Perovskites for solar thermoelectric applications: a first principle study of CH₃NH₃AI₃ (A = Pb and Sn). *Chem Mater* 26(18):5394–5400
32. Shi D, Adinolfi V, Comin R, Yuan M, Alarousi E, Buin A, Chen Y, Hoogland S, Rothenberger A, Katsiev K, Losovyj Y (2015) Low trap-state density and long carrier diffusion in organolead trihalide perovskite single crystals. *Science* 347(6221):519–522
33. Mettan X, Pisoni R, Matus P, Pisoni A, Jaćimović J, Náfrádi B, Spina M, Pavuna D, Forró L, Horváth E (2015) Tuning of the thermoelectric figure of merit of CH₃NH₃MI₃ (M = Pb, Sn) photovoltaic perovskites. *J Phys Chem C* 119(21):11506–11510
34. Xing G, Mathews N, Sun S, Lim SS, Lam YM, Grätzel M, Mhaisalkar S, Sum TC (2013) Long-range balanced electron- and hole-transport lengths in organic-inorganic CH₃NH₃PbI₃. *Science* 342(6156):344–347

35. Stoumpos CC, Malliakas CD, Kanatzidis MG (2013) Semiconducting tin and lead iodide perovskites with organic cations: phase transitions, high mobilities, and near-infrared photoluminescent properties. *Inorg Chem* 52(15):9019–9038
36. Babayigit A, Ethirajan A, Muller M, Conings B (2016) Toxicity of organometal halide perovskite solar cells. *Nat Mater* 15(3):247–251
37. Chowdhury SA, Inzani K, Peña T, Dey A, Wu SM, Griffin SM, Askari H (2016) Mechanical properties and strain transfer behavior of molybdenum ditelluride (MoTe_2) thin films. *J Eng Mater Technol* 144(1)
38. Dar SA, Srivastava V, Sakalle UK (2017) A first-principles calculation on structural, electronic, magnetic, mechanical, and thermodynamic properties of SrAmO_3 . *J Supercond Novel Magn* 30(11):3055–3063
39. Dar SA, Srivastava V, Sakalle UK, Khandy SA, Gupta DC (2018) A DFT study on structural, electronic mechanical and thermodynamic properties of 5f-electron system BaAmO_3 . *J Supercond Novel Magn* 31(1):141–149
40. Dar SA, Srivastava V, Sakalle UK, Pagare G (2018) Insight into structural, electronic, magnetic, mechanical, and thermodynamic properties of actinide perovskite BaPuO_3 . *J Supercond Novel Magn* 31(10):3201–3208
41. Dar SA, Srivastava V, Sakalle UK, Rashid A, Pagare G (2018) First-principles investigation on electronic structure, magnetic, mechanical and thermodynamic properties of SrPuO_3 perovskite oxide. *Mater Res Express* 5(2):026106
42. Dar SA, Srivastava V, Sakalle UK, Parey V (2018) Ferromagnetic phase stability, magnetic, electronic, elasto-mechanical and thermodynamic properties of BaCmO_3 perovskite oxide. *J Electron Mater* 47(7):3809–3816
43. Allen P (1996) Boltzmann theory and resistivity of metals. In: *Kluwer international series in engineering and computer science*, pp 219–250
44. Ziman JM (2001) *Electrons and phonons: the theory of transport phenomena in solids*. Oxford University Press
45. Hurd C (1972) *The hall effect in metals and alloys*. Plenum Press
46. Madsen GK, Singh DJ (2006) BoltzTraP. A code for calculating band-structure dependent quantities. *Comput Phys Commun* 175(1):67–71
47. Madsen GK, Carrete J, Verstraete MJ (2018) BoltzTraP2, a program for interpolating band structures and calculating semi-classical transport coefficients. *Comput Phys Commun* 231:140–145
48. Hohenberg P, Kohn W (1964) Inhomogeneous electron gas. *Phys Rev* 136(3B):B864
49. Blaha P, Schwarz K, Madsen GK, Kvasnicka D, Luitz J, Laskowski R, Tran F, Marks L, Marks L (2001) WIEN2k: an augmented plane wave + local orbitals program for calculating crystal properties 60
50. Perdew JP, Burke K, Ernzerhof M (1997) Generalized gradient approximation made simple (vol 77, pg 3865, 1996). *Phys Rev Lett* 78(7):1396–1396
51. Blöchl PE, Jepsen O, Andersen OK (1994) Improved tetrahedron method for Brillouin-zone integrations. *Phys Rev B* 49(23):16223
52. Morelli DT, Slack GA (2006) High lattice thermal conductivity solids. In: *High thermal conductivity materials*. Springer, New York, pp 37–68
53. Bhat TM, Singh S, Gupta DC (2018) Electronic and transport properties of $\text{LaNi}_4\text{Sb}_{12}$ skutterudite: modified Becke-Johnson approach. *J Electron Mater* 47(8):4544–4549

Optical Behavior of Polyvinylchloride–Polyamide Blend



Jiltan Roy and Kawaljeet Singh Samra

Abstract The present investigation is about the synthesis and structural characterization of polyvinylchloride (PVC)–polyamide (PA) blend. PVC and PA were mixed in different proportion, i.e., 70:30 and 60:40, and final sample in the form of films of ~40 μm was peeled out from the dried dip-coated glass slides. Prepared films were characterized using Fourier transform infrared (FTIR) and UV–visible spectroscopy. Formation of new bands was observed in the FTIR spectrum of PVC with the increase of PA's percentage in composition, which confirms the presence of guest polymer in the prepared blend. UV–visible analysis indicated the change in optical band gap with variation of PA's composition in PVC/PA blend.

Keywords Polyvinylchloride · Polyamide · Fourier transform infrared spectroscopy · UV–visible spectroscopy · Structural behavior

1 Introduction

Polymer is a macromolecule which is commercially very important. At present one cannot think about life without polymers as all substances, which we are using in our daily life, are somewhere made up of polymer [1–3]. So, interest is developed in scientific community from last few decades to synthesize new polymers or to tailor the characteristics of existing ones [4–8]. As one polymer cannot have all the required characteristics, so doping or blending of polymers of different types can be an effective technique to develop a new material with required properties [9–11].

Polyvinyl chloride (PVC) is cheap, easy to synthesize, lightweight, flexible, and offers strong resistance to weather corrosion, and therefore, it is extensively used, to manufacture pipes, bottles, electrical insulations, etc. Simultaneously it has certain disadvantages such as it cannot be used at high temperature, intolerant to ultra-violet rays, prone to cracking due to its lightweight and contains volatile contents such as compounds associated with chlorine, which are harmful to environment [12–15]. On

J. Roy · K. S. Samra (✉)

Department of Physics, Lovely Professional University, Phagwara, Punjab 144411, India
e-mail: samraphy@gmail.com; kawaljeet.16468@lpu.co.in

the other hand, polyamide (PA) is used in cloth and automobile industries, utensils and sports goods due to their high durability, high temperature resistance, toughness, and strong resistance to abrasion, but at the same time, high moisture absorption with dimensional instability is its major drawback [16–18].

In the present work, an attempt has been made to incorporate the benefits and eradicate the disadvantages of both above-mentioned polymers by developing a PVC/PA blend and to characterize its structural behavior.

2 Materials and Method

PVC in the form of white powder and PA resin in the form of bright yellow solid crystal and N-Methyl-2-pyrrolidone (NMP) with 99.9% purity were purchased from Central Drug House (CDH) Pvt. Ltd., India. PVC/PA blends were prepared by mixing 70:30 and 60:40 weight percentages of PVC and PA, respectively, in NMP using magnetic stirring for 8 h. Glass slides were dipped in the prepared solutions and dried in the oven at 60 °C overnight. Finally, films (~40 μm) of prepared polymeric blend with different compositions were peeled off from the dried slides. FTIR spectra were recorded in transmittance mode using Shimadzu FTIR-8400S in the range 400–4000 cm⁻¹. Absorption spectra in UV and visible range were obtained from Shimadzu UV-2600 in the range 200–700 nm.

3 Results and Discussion

3.1 FTIR Analysis

The Fourier transform infrared spectra of untreated polyvinylchloride and polyamide are shown in Fig. 1. In FTIR spectrum of untreated PVC, absorption bands at 614 and 961 cm⁻¹ were assigned to *cis* and *trans* wagging of CH bonds, respectively. Rocking and stretching vibrations of the CH bonds were visible at 1250 and 2910 cm⁻¹, respectively. Deformation mode of CH₂ groups was observed at 1335 cm⁻¹, and a small absorption band 830 cm⁻¹ was indicating the presence of C–Cl stretching vibrations [19]. In Fig. 1, characteristics of absorption bands of polyamide are shown with red color. Symmetric and asymmetric stretching vibrations of C–O–C bonds were seen at 1060 and 1242 cm⁻¹, respectively. Aromatic stretching of CH bonds was assigned to the absorption band at 3080 cm⁻¹, C = O bonds of amide groups at 1654 cm⁻¹, stretching vibrations of N–H and CH₃C–H were observed at 3300 cm⁻¹ and 2853 and 2950 cm⁻¹, respectively [20].

In Fig. 2, Fourier transform infrared spectra of PVC/PA blends at different composition are presented. Drastic changes in the FTIR spectrum of PVC were observed

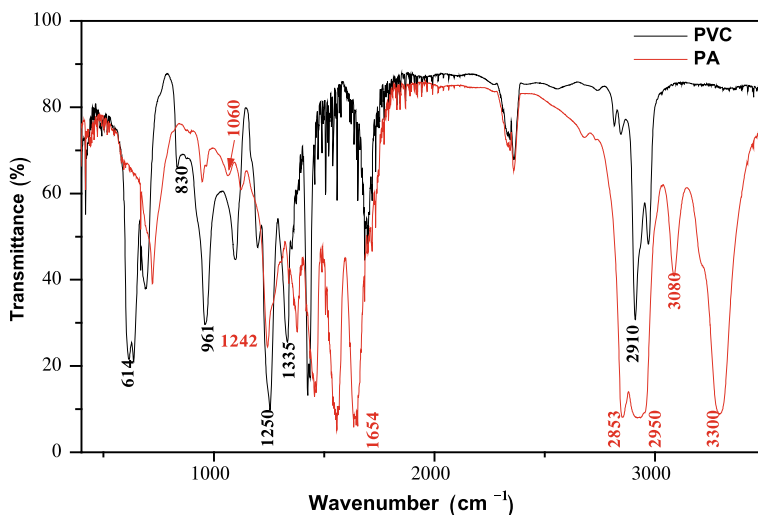


Fig. 1 Fourier transform infrared spectra of untreated polyvinylchloride and polyamide

as the composition of PA was increased in the blend. Even at the lowest incorporation of 30% PA by weight in the PVC/PA blend, characteristics bands such as 1060, 1242, 1654, 2853, 2950, 3080, and 3300 cm^{-1} of PA were clearly visible in the FTIR spectra, and consequently, it is expected that the resultant blend may have better strength and durability than untreated PVC. Intensity of prominent bands of PVC such as wagging and stretching vibrations of CH bonds and more importantly absorption bands associated with carbon-chlorine groups were decreased substantially, which revealed the decrease of volatile contents from the prepared polymeric blend.

3.2 UV–Visible Analysis

UV–visible absorption spectra of PVC, PA, and PVC/PA (60:40) blend are shown in Fig. 3. It is observed that the absorption edges of untreated PVC and PA were found at 229 and 340 nm, respectively, which were attributed to their respective optical band gaps. Further, it is noticeable from the same figure that the absorption behavior of the prepared PVC/PA blend with composition 60:40 was lying close to that of PA but with different slope, indicating the decrease of band gap of PVC after the incorporation of PA.

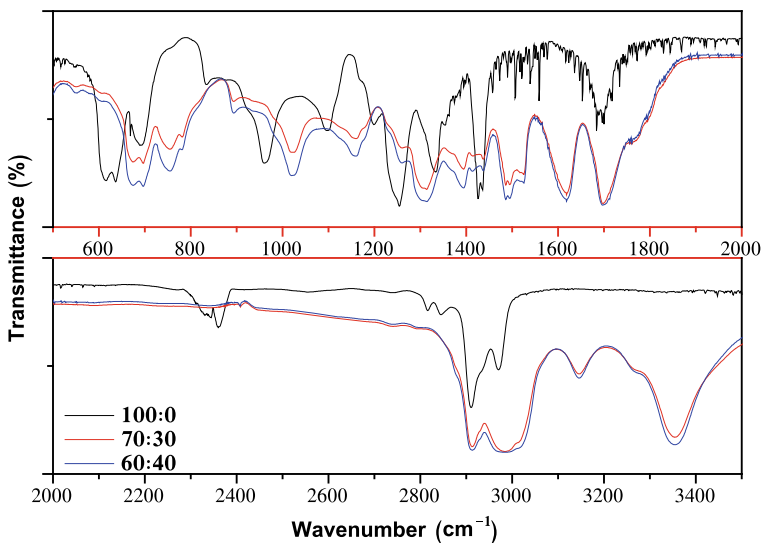


Fig. 2 Fourier transform infrared spectrum of PVC/PA blends at different composition

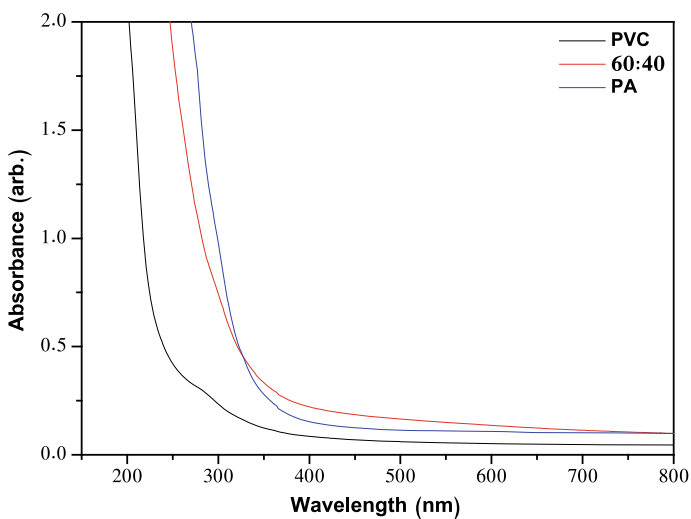


Fig. 3 UV-visible absorption spectra of PVC, PA, and PVC/PA blend

4 Conclusion

On the basis of the above-mentioned results and discussion, it can be concluded that the prepared PVC/PA polymeric blend is more inclined toward PA so possibly it

may have better strength, withstand high temperature applications, more durable, and have fewer volatile contents.

References

1. Huang J, Turner SR (2018) Hypercrosslinked polymers. *Polym Rev* 58:1–41
2. Luo SC (2013) Conducting polymers as biointerfaces and biomaterials. *Polym Rev* 53:303–310
3. Kamal MS, Sultan AS, Al-Mubaiyedh UA, Hussain IA (2015) Review on polymers flooding: rheology, adsorption, stability, and field applications of various polymer systems. *Polym Rev* 55:491–530
4. Safarpour M, Oskoui SA, Khataee A (2020) A review of two-dimensional metal oxide and metal-hydroxide nanosheets for modification of polymeric membranes. *J Ind Eng Chem* 82:31–41
5. John G, Nagarajan S, Vemula PK, Silverman JR, Pillai CK (2019) Natural monomers: a mine for functional and sustainable materials-occurrence, chemical modification and polymerization. *Prog Polym Sci* 92:158–209
6. Primo GA, Igarzabal CLA, Pino GA, Ferrero JC, Rossa M (2016) Surface morphological modification of crosslinked hydrophilic co-polymers by nanosecond pulsed laser irradiation. *Appl Surf Sci* 369:422–429
7. Liao Y, Loh CH, Tian M, Wong R, Fane AG (2019) Progress in electrospun nanofibrous membranes for water treatment: fabrication, modification and applications. *Prog Polym Sci* 77:69–94
8. Ferreira DP, Cruz J, Fangueiro R (2019) Chapter-1—Surface modification of natural fibers in polymer composites. In: *Green composites for automotive applications*, pp 3–41
9. Sangroniz L, Drongelen M, Cardinaels R, Santamaria A, Peters GWM, Muller AJ (2019) Effect of shear rate and pressure on the crystallization of PP nanocomposites and PP/PET polymer blend nanocomposites. *Polymers* 186:121950
10. Kaur M, Kaur R, Samra KS (2017) Luminescent behavior of semiconductor doped polyamide. *AIP Conf Proc* 1860:020004
11. Ren X, Meng N, Yan H, Bilotti E, Reece MJ (2019) Remarkably enhanced polarizability and breakdown strength in PVDF-based interactive polymer blends for advanced energy storage applications. *Polymers* 168:246–254
12. Liu Y, Zhou C, Li F, Liu H, Yang J (2020) Stocks and flows of polyvinyl chloride (PVC) in China: 1980–2050. *Resour Conserv Recycl* 154:104584
13. Taha TA, Azab AA (2019) Thermal, optical and dielectric investigations of PVC/La_{0.95}Bi_{0.05}FeO₃ nanocomposites. *J Mol Struct* 1178:39–44
14. Rajesh, Kaur D, Gaur MS, Goyal P, Tiwari RK, Rogachev AA, Rodachev AV (2019) Measurement of AC and DC relaxation properties in polyvinyl chloride (PVC) nanocomposites. *Measurements* 135:323–332
15. Cao Q, Yuan G, Yin L, Chen D, Wang H (2016) Morphological characteristics of polyvinyl chloride (PVC) dichlorination during pyrolysis process: influence of PVC content and heating rate. *Waste Manage* 58:241–249
16. Wang L, Zhu Q, Bai Y (2019) Synthesis and characterization of a series of water-soluble polyamides and their micellization behavior. *Polymer* 179:121634
17. Lu P, Zhao Z, Xu B, Li Y, Wang Y (2020) A novel inherently flame-retardant thermoplastic polyamide elastomer. *Chem Eng J* 379:122278
18. Nguyen PH, Spoljaric S, Seppala J (2018) Redefining polyamide property profiles via renewable long chain aliphatic segments: towards impact resistance and low water absorption. *Eur Polymer J* 109:16–25

19. Ramesh S, Leen KH, Kumutha K, Arof AK (2007) FTIR studies of PVC/PMMA blends based polymer electrolytes. *Spectrochimica Acta A* 66:1237–1242
20. Chang C, Liou G, Hsiao S (2006) Highly stable anodic green electrochromic aromatic polyamide: synthesis and electrochromic properties. *J Mater Chem* 17:1007–1015

Research and Development of Biomass Production in India: A Bibliometric Study



Shiv Singh, Kirti Singh, Jamil Ahmed, Vijay Mohan Soni, and Neha Munjal

Abstract Biomass is a renewable and sustainable energy source that may be used to generate electricity or other forms of power, which is the need of hour. Henceforth, in this paper, an attempt has been made to explore the growth of the research trends in biomass production in India. For this, the data has been extracted from the web of science (WOS). The extracted data has been analyzed on the most prolific authors, countries, journals, organizations, and keywords. In total 995 documents have been extracted from 369 sources, these articles have been contributed by 2274 authors. The most prominent organization is “Indian Council of Agricultural Research”. Singh G from Arid Forest Res Inst, Jodhpur, Rajasthan is the most prolific author. The majority of the publications belong to the “Biotechnology Applied microbiology” of the Web of Science Categories.

Keywords Biomass energy · Biomass production · Environment · Bibliometrics · Citation analysis · WOS

1 Introduction

Biomass is a renewable and sustainable energy source that may be used to generate electricity or other forms of power. It is made from organic materials. Wood and wood residues are the largest biomass energy source today. Other plants can also be used as fuel, for instance, corn, switchgrass, miscanthus, and bamboo. Biomass has acquired a ton of footing lately because of its capacity for inexhaustible power age, environmentally friendly power energy creation, biofuels, and nuclear power. Plants, a type of living biomass, are the most widely recognized kind of biomass that

S. Singh · J. Ahmed

Bennett University (Times of India Group), Greater Noida, Uttar Pradesh 201310, India

K. Singh

Dr. D P Rastogi Central Research Institute of Homeopathy, Noida, Uttar Pradesh, India

V. M. Soni · N. Munjal (✉)

Lovely Professional University, Phagwara, Punjab, India

e-mail: neha.18869@lpu.co.in

exists. They take in carbon dioxide as they develop and discharge it when they are utilized for energy. Biomass has been utilized as a wellspring of warmth energy since man previously found fire. The utilization of biofuels, for example, ethanol has been around for quite a while also. It was utilized as light fuel in the United States during the 1800s. The primary Model-T Fords utilized ethanol for fuel until 1908. As of late, biomass and biofuels have gotten famous as an option in contrast to petroleum derivatives like fuel [1]. About 32% of the all-out essential energy use in the nation is as yet gotten from biomass and over 70% of the country's populace relies on it for its energy needs. Ministry of New and Renewable Energy has understood the potential and job of biomass energy in the Indian setting and subsequently has started various projects for advancement of proficient innovations for its utilization in different areas of the economy to guarantee inference of greatest advantages. According to a recent study supported by MNRE, the current accessibility of biomass in India is assessed at around 750 million metric tons each year. The study demonstrated assessed surplus biomass accessibility at around 230 million metric tons for each annum covering agrarian deposits compared to a capability of around 28 GW [2].

2 Materials and Method

Bibliometric analysis is widely used technique for evaluating the research trends in various fields such as cataract [3], Ecology [4], Biomass energy [5, 6], Biophysics [7], and fuels [8–10]. To examine the publishing trends and patterns in biomass production, bibliometric data were retrieved from the Web of Science (WOS), the most authentic indexing and abstracting database in the world. In the WOS core collection, the following search query was run Topic (“Biomass production”) OR Topic: (“bio-based product”) Country = India, Timespan: 1989–2018. Indexes: SCI-Expanded, SSCI, A&HCI, ESCI. (14 Feb 2019 data of extract data).

3 Results and Discussion

The 995 publications were published in four document forms during the study period. A total of 925 literature published in articles with the 92.96% was the most frequently published document form. It was followed by review (61; 6.13%), note (8; 0.80) and meeting abstract (1; 0.10) (Fig. 1).

3.1 World and Indian Contribution on Biomass Production

The comparison between the India and rest of the world has been made in the term of publication contribution in biomass production. India contributed 995 publications

Fig. 1 Type of documents



Table 1 World and Indian contribution on biomass production

Year From-To	World publications	Indian publications
1989–1993	662	55
1994–1998	1367	81
1999–2003	1552	88
2004–2008	2239	138
2009–2013	4046	251
2014–2018	6236	382
Total	16,102	995

whereas 16,102 publications contributed by world. India’s and World’s continuous growth has been observed from 1989 to 2018. The analysis was carried out in a block period of five years and it was found that the maximum growth was during the period 2014–2018 (Table 1).

3.2 Top Countries

Table 2 illustrated the top 5 countries that contributed to biomass production along with their H-index, ACPP, citing articles, etc. USA dominated with 3544 publications published on biomass with 22.01% out of total publications. It is followed by China (1479), Germany (1266), and India stood on rank 4th with 995 publications. The USA has highest H-index, i.e., 140 followed by Germany (79). China is in second position in terms of publications output but Germany Scoring very well in ACPP, Citation, and without self-citation.

Table 2 Top contributed country on biomass production along with H-Index, ACPP, and citation and without self-citation

Country	NP	In %	H-index	ACA	TC	WSC	Citing articles	Without self-citations articles
USA	3544	22.01	140	31.88	112,980	107,500	84,131	82,386
Peoples R China	1479	9.185	62	15.76	23,310	22,134	19,495	18,875
Germany	1266	7.862	79	26.4	33,419	32,377	28,435	27,960
India	995	6.179	55	14.07	13,995	13,549	12,388	12,118
Brazil	939	5.832	44	11.63	10,920	10,419	9557	9272

NP No. of publications, ACA average citation per article, total citation, WSC without self-citations

3.3 Top Ranked Organization

This table presents the top 9 different organizations with contribution of more than 200 papers on biomass production in India. Indian Council of Agricultural Research is most productive organization contributed 226 papers followed by Council of Scientific Industrial Research CSIR with 123 papers and Indian Institute of Technology System with 92 papers. On parameters of citation impact, Indian Institute of Technology, Kharagpur had highest ACPP (21.77) followed by Indian Institute of Technology, Delhi, impact in terms of H-Index value, Indian Council of Agricultural Research has highest h-index value of 24 followed by Council of Scientific Industrial Research with h-index value 23 (Table 3).

3.4 Prolific Authors

Table 4 lists 7 prolific authors along the values of H-index and ACPP with sum of times cited for each author. The most prolific author G. Singh has contributed 24 papers on biomass production followed by A. Kumar and S. Kumar with contribution of 16 papers, respectively. D. Das has contributed only 11 papers but recorded highest ACPP with 36.36 among all the authors. Three authors have recorded h-index value 10, these are G. Singh, A. Malik, and A. Pandey.

3.5 Top Rank Journal

369 sources were produced in 995 articles. The top 10 journals contributed 216 papers on biomass production. Bioresour. Technol. Has contributed maximum no. of paper, i.e., 52 followed by Indian J. Agric. Sci. with 29, Biomass Bioenergy with

Table 3 Top rank contributed organization along with h-index and citation pattern

Rank	Name of organizations	NP ^a	% In	H-index	ACA
1	Indian Council of Agricultural Research ICAR	226	22.714	24	9.44
2	Council of Scientific Industrial Research CSIR, India	123	12.362	23	17.04
3	Indian Institute of Technology System IIT System	92	9.246	20	15.59
4	ICAR Indian Agricultural Research Institute	50	5.025	17	15.72
5	Indian Institute of Technology, Delhi	35	3.518	16	19.69
6	Indian Institute of Technology, Kharagpur	26	2.613	9	21.77
7	Arid Forest Research Institute	22	2.211	9	9.59
8	International Crops Research Institute for The Semi-Arid Tropics	21	2.111	10	16.05
9	Banaras Hindu University	20	2.01	10	14.7
9	ICAR Indian Grassland Fodder Research Institute	20	2.01	4	5.3

^aNP No. of publications average citations per article

21, and Indian J. Agron with 20 papers on Biomass. Bioresour Technol. has highest impact factor (6.669), the Biomass Bioenergy has 3.537 and on third position with 3.126 impact factor is For. Ecol. Manage with 13 papers contribution (Table 5 and Fig. 2).

3.6 Keywords

Table 6 provides the list of popular keywords used in biomass production study. This study highlighted that growth is widely used keyword in keyword plus, word from title, and word from abstract. The most popular words are Growth, Biomass, Production, Plants, Microalgae, biodiesel, etc. All these words focus on the growth of the biomass production as this is the need of hour. The scattering of the keywords indicates that biomass is an interdisciplinary field and ultimately all the research is toward biomass production (Figs. 3, 4, 5 and 6).

This list represents the top sources contributor in biomass production. The Biotechnology Applied Microbiology has contributed 224 records with 22.513% followed by Environmental Sciences with 156 records, Agronomy with 151 records, and Plant sciences with 127 records. The Biochemistry Molecular Biology has contributed only 45 records with 4523% (Table 7).

Table 4 Prolific authors with citation pattern

Rank	Authors	NP	% In	Affiliation	H-index	ACA	ACWSC	TCA	WSCA
1	Singh G	24	2.412	Arid Forest Res Inst, Jodhpur, Rajasthan	10	9.83	9.17	199	190
2	Kumar A	16	1.608	Govind Ballabh Pant Univ Agr & Technol, Uttar Pradesh	5	6.44	6.38	103	102
2	Kumar S	16	1.608	Indian Grassland & Fodder Res Inst, Jhansi	5	6.13	6.06	98	97
3	Singh B	15	1.508	Natl Bot Res Inst, Lucknow	7	9.73	9.73	146	146
4	Malik A	13	1.307	Indian Inst Technol Delhi, New Delhi	10	24.15	22.46	232	224
4	Pandey A	13	1.307	GB Pant Inst Himalayan Environment & Dev, Almora, UK	10	31.08	31.00	394	393
5	Sharma S	12	1.206	Indian Inst Technol Delhi, Ctr Rural Dev & Technol, New Delhi	4	8.5	8.42	101	100
6	Das D	11	1.106	Indian Inst Technol Kharagpur, West Bengal	6	36.36	35.82	379	374
6	Singh S	11	1.106	Cent Arid Zone Res Inst, Jodhpur	7	22.73	22.73	246	246
6	Srivastava AK	11	1.106	Indian Inst Technol Delhi, New Delhi	7	10.36	10.18	103	102
7	Mishra S	10	1.005	CSIR Cent Salt & Marine Chem Res Inst, Bhavnagar, Gujrat	5	11.9	11.50	117	113

NP No. of publications, ACA average citations per article, ACWSC average citations without self-citations, TCA total citing articles, WSCA without self-citation articles

Table 5 Top rank journal along with IF

Rank	Journal name	No. of articles	IF ^a
1	Bioresour. Technol	52	6.669
2	Indian J. Agric. Sci	29	0.253
3	Biomass Bioenerg	21	3.537
4	Indian J. Agron	20	–
5	Curr. Sci	19	0.756
6	Agrofor. Syst	18	1.792
7	J. Environ. Biol	16	0.555
8	Appl. Biochem. Biotechnol	14	2.140
8	Range Manag. Agrofor	14	0.103
9	For. Ecol. Manage	13	3.126

^aIF = Impact factor as per JCR 2018

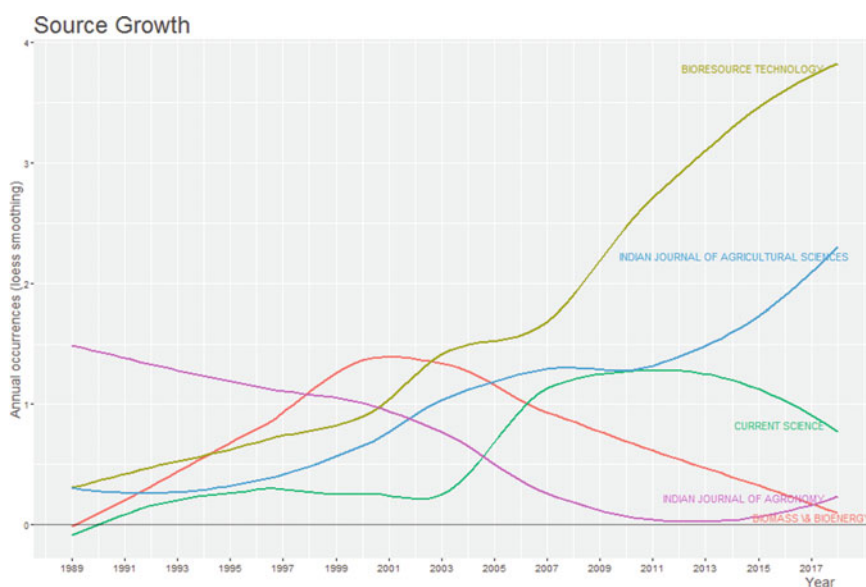


Fig. 2 Growth of top 5 sources

3.7 Country Collaboration

Biomass scholars collaborate with 60 countries, where USA is in top with 46 collaborations followed by Australia, China, England, and Germany with contribution of 28, 20, 17, and 16 accordingly. Figure 7 is highlighted countries (Fig. 8).

Table 6 Top rank keywords by authors, title, abstract

Keyword plus	Frequency	Author keywords	Frequency	Word from title	Frequency	Word from abstract	Frequency
Growth	164	Biomass	131	Production	333	Biomass	2120
Biomass production	82	Biomass production	59	Biomass	247	Production	1854
Plants	66	Microalgae	49	Growth	185	Growth	1029
Accumulation	57	Biodiesel	33	India	107	Soil	695
Soil	54	Growth	30	Soil	79	Higher	579
Nitrogen	48	Phytoremediation	23	Potential	73	Study	553
Biodiesel production	47	Biofuel	21	Carbon	67	Yield	551
Biomass	45	Lipid	20	Nutrient	67	Plant	521
Yield	45	Nitrogen	18	Species	57	Species	489
Cultivation	44	Production	17	Yield	57	Water	440

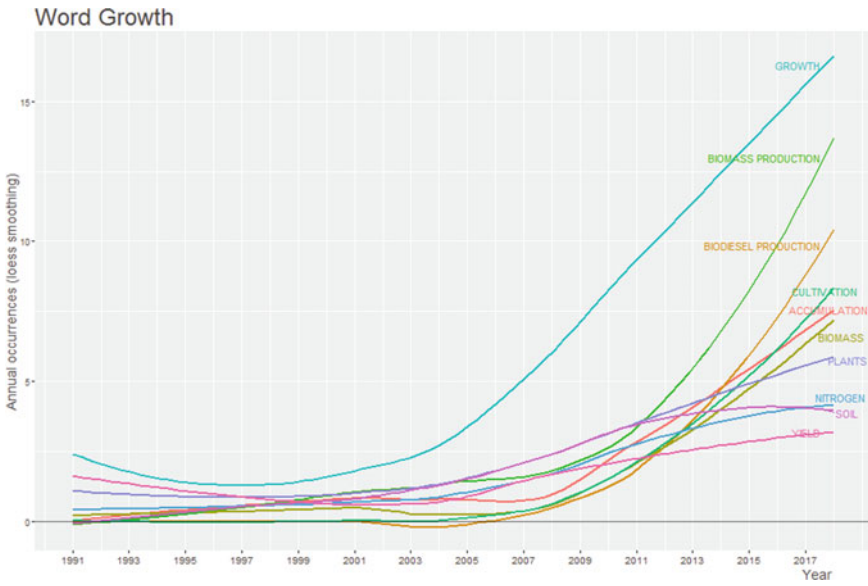


Fig. 3 Growth of keywords

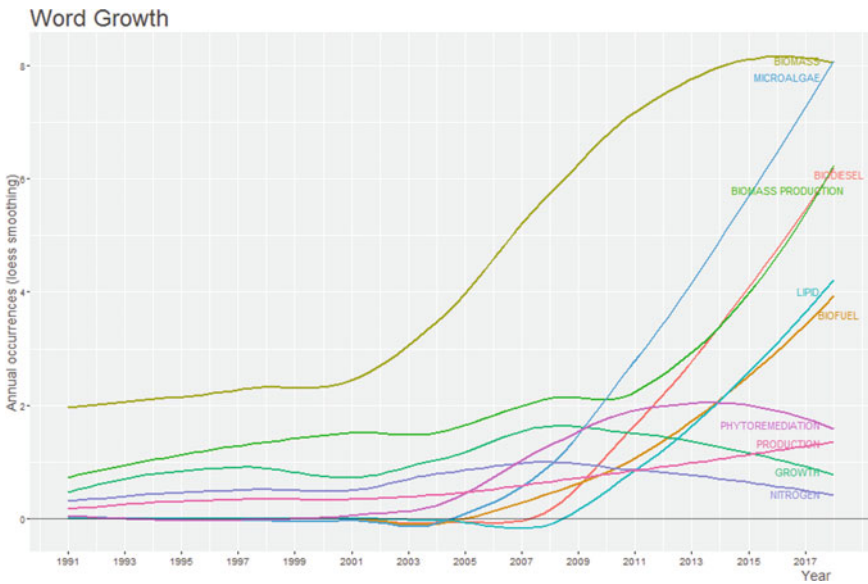


Fig. 4 Growth of author keywords

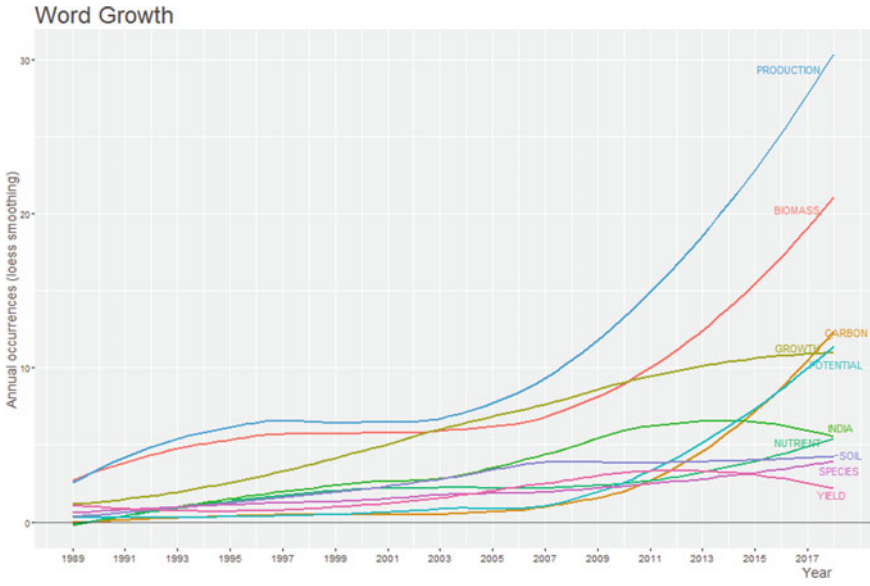


Fig. 5 Growth of keywords from title

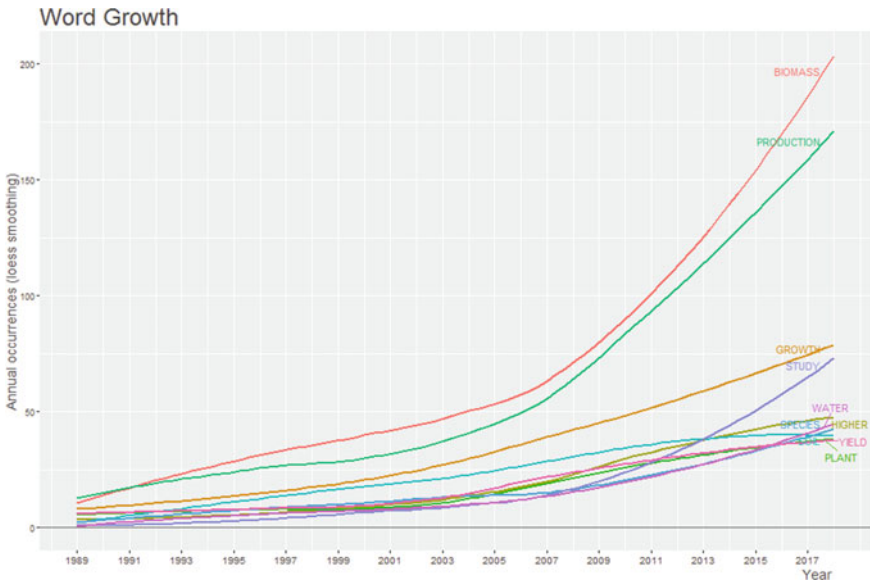


Fig. 6 Growth of keywords from abstract

Table 7 Top source contributor

Web of science categories	No. of publications	In %
Biotechnology applied microbiology	224	22.513
Environmental sciences	156	15.678
Agronomy	151	15.176
Plant sciences	127	12.764
Energy fuels	109	10.955
Agricultural engineering	83	8.342
Forestry	54	5.427
Agriculture multidisciplinary	50	5.025
Multidisciplinary sciences	49	4.925
Soil science	49	4.925
Ecology	47	4.724
Engineering chemical	46	4.623
Biochemistry molecular biology	45	4.523

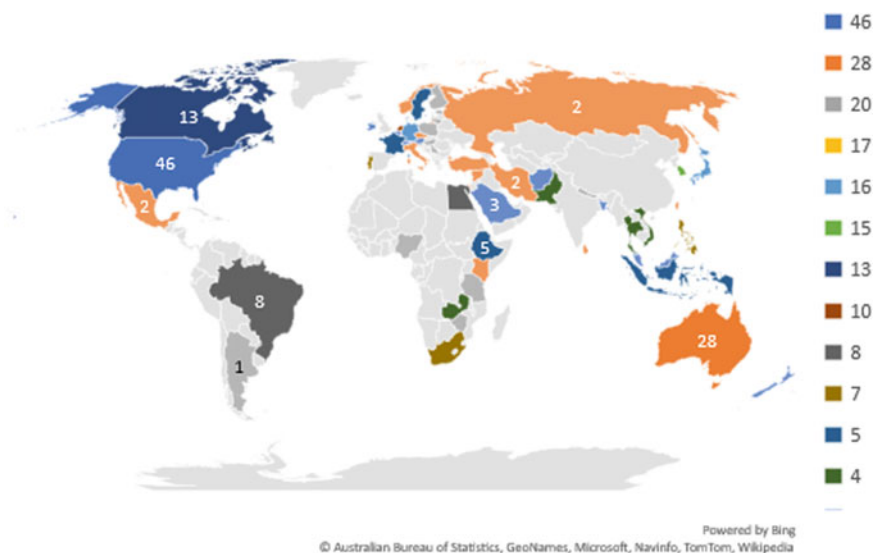


Fig.7 Biomass Indian scholars world collaborative map

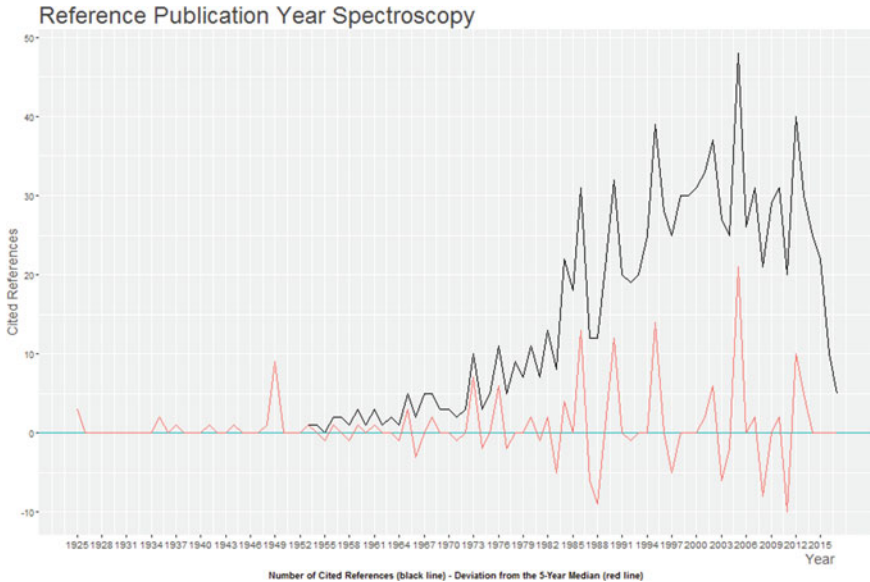


Fig. 8 Number of cited references and deviation from the 5 years

4 Conclusion

The present paper is focused to explore the research on the biomass in India. In total 995 papers were extracted from the WOS database to analyze the research trends on the basis of the top most countries, Journals, Organizations, Authors, and Keywords. These papers were contributed by 2274 authors. There are only 36 single-authored documents, thus reflecting that researchers are working in collaborative nature and the collaboration index is 2.83. Further approx. 3.82 co-authors were there per document. The continuous growth has been observed since 1989. India is on the fourth position worldwide. The most popular journal is “Bioresour. Technol.” having the IF of 6.669. The keyword distribution signifies that this area is interdisciplinary in nature. Henceforth it is hoped that this paper will help the researchers and policymakers to take decision for the advancement in this field.

References

1. Ferrari G, Pezzuolo A, Nizami AS, Marinello F (2020) Bibliometric analysis of trends in biomass for bioenergy research. *Energies* 13:3714. <https://doi.org/10.3390/en13143714>
2. Yu D, Meng S (2018) An overview of biomass energy research with bibliometric indicators. *Energy Environ* 29(4):576–590. <https://doi.org/10.1177/0958305X18756304>
3. Singh S, Kataria S (2020) Indian contribution status of the cataract research: a bibliometric analysis. *Libr Philos Pract* (e-journal) 4092. <https://digitalcommons.unl.edu/libphilprac/4092>

4. Houghton RA (2008) Biomass. In: Jorgensen SE, Fath BD (eds) Encyclopedia of ecology. Academic Press, pp 448–453
5. Guozhu M (2015) Past, current and future of biomass energy research: a bibliometric analysis. *Renew Sustain Energy Rev* 1823–1833. <https://doi.org/10.1016/j.rser.2015.07.141>
6. Yanyan D, Binmei G, Jiahui J (2014) Research and development situation of international biomass energy based on bibliometrics. *Meteorol Environ Res* 5(7):57–60
7. Munjal N, Singh S, Majumdar AD, Rizal G (2019) Biophysics research trends in India: special reference to Indian Universities. *Int J Innov Technol Explor Eng (IJITEE)* 9(1):508–511. <https://doi.org/10.35940/ijitee.E3078.119119>
8. Gavhane RS et al (2021) Influence of silica nano-additives on performance and emission characteristics of soybean biodiesel fuelled diesel engine. *Energies* 14(5):1489. <https://doi.org/10.3390/en14051489>
9. Mujtaba MA (2021) Development of empirical correlations for density and viscosity estimation of ternary biodiesel blends. *Renew Energy* 179:1447–1457. <https://doi.org/10.1016/j.renene.2021.07.121>
10. Devi DS, Kumar R, Rajak U (2021) Plastic waste as a biofuel feedstock—a conceptual study. *IOP Ser Conf Mater Sci Eng Bristol* 1116(1):012029. <https://doi.org/10.1088/1757-899X/1116/1/012029>

A First Principle Study of Structural Properties of KX_xI_{1-x} ($X = \text{Cl, Br}$ and $X = 0.00, 0.25, 0.50, 0.75,$ and 1.00)



Agnibha Das Majumdar, Puneet Kaur, and Neha Munjal

Abstract The present work focuses on the investigation of structural properties of alkali halides (KCl_xI_{1-x} , KBr_xI_{1-x}) using the first principle total energy calculations within linear combination of atomic orbital method. This work has been built up using density functional theory (DFT) with the use of CRYSTAL code. For the compounds KCl_xI_{1-x} and KBr_xI_{1-x} , the concentration of 0.00, 0.25, 0.50, 0.75, and 1.00 has been used. Some important parameters like bulk modulus and lattice constant have been calculated. The deviation for the calculated values for lattice constant is analyzed by Vegard's law also. All determined results are in good agreement with previous observational data.

Keywords First principle · Alkali halides · Vegard's law · CRYSTAL · DFT

1 Introduction

Alkali halides are the inorganic compounds. The chemical formula used for alkali halides is MX . In this formula, M is an alkali metal, and in place of X , the halogen is used [1–3]. Mostly used metal halide compound is in NaCl structure; these alkali halides are ionic crystals. They exist as the colorless crystalline solids in the white powder form [4]. The melting point of alkali halide is very high, and due to this, they reflect the high lattice energies. At the higher temperature, when they start melting the solid takes the form of liquid, and then, it gets evaporated in the form of gas, which is composed of diatomic molecules [5]. The alkali halides are soluble in the polar solvents and then give the ionic solutions, which contain the highly solvated cations and anions [6]. These compounds are widely used as the infrared prisms, window materials, infrared transmitters, and neutron monochromators. But the applications are limited due to the issue of mechanical properties. After doping, the alkali doped

A. Das Majumdar · N. Munjal (✉)
Lovely Professional University, Phagwara, Punjab, India
e-mail: neha.18869@lpu.co.in

P. Kaur
CGC Technical Campus, Jhanjheri, Mohali, Punjab 14007, India

crystals of alkali halides are harder so these are more useful in the mechanical applications [7, 8]. As alkali halides are having application in electronic and optoelectronic devices, it can be used in laser window application, neutron monochromators, and infrared transmitters also [4]. These compounds are used for making fertilizers called Potash, since many of the plants can grow with the ample presence of potassium. Also, as a chemical feedstock, we can use these compounds. After doing with some different concentrations, it is found that the impure doped crystals of alkali halides are harder in terms of physical strength and so they are more useful in these applications. The main scaling of properties of alkali halide compounds is mainly lattice constant, verified elastic constant, Debye's temperature, color center parameter, hardness, etc. [9]. Many theoreticians and experimental researchers have focused to do the determination of physical structure of the alkali halide crystals, because of its significant size and stable crystal structure. In some research, those alkali halide crystals are also being considered as the "model crystals." It has a wide application in the field of infrared optical windows, wave tunneling lasers, and many more. Those crystals have shown mainly two structures, that is NaCl and CsCl structure. Initially, those crystals have acquired NaCl structure, which is also known as B1 phase, but under some ambient conditions of pressure and temperature, it will transit from B1 phase to B2 phase. In B2 phase, it has shown CsCl crystal structure. So, both the structures are the basic structures of the alkali halide crystals. There is some basic structural information present about the alkali halide crystal in the B1 phase. The space group of those crystals is $Fm\bar{3}m$. The point groups are presented as $m\bar{3}m(O_h)$. The coordination number and number of molecules per unit cell can be depicted as 6 and 4, respectively. There is also a relation between inter ionic distance (r) and the lattice parameter (a). The relation can be expressed as

$$r = (1/2)a.$$

Reciprocal lattice for the alkali halide crystal in NaCl structure is bcc. And the different values of the Madelung constants are written as α_r and α_a . The values of these constants are 1.74756 and 3.49513, respectively [10].

In view of this, it becomes mandatory and also wrathful to determine the structural properties of alkali halide compounds; thus, in the present work the LCAO method as built in CRYSTAL [11] code has been used. This methodological approach has been initiated by some researchers [12–14]. All those above studies have been carried out with the help of computational study. Computational studies have its own importance in the field of material science. This approach is also known as first principle studies [15]. First principle studies have been carried out on the concept of density functional theory. Density functional theory is a quantum mechanical simulation process. And it is often used in the field of physics and chemistry [16]. For many-body condensed system, or any many-body atomic system, this method is efficiently used for calculating the structural and electronic properties. The concept of density functional theory for the many-body has been first introduced by two renowned scientists Professor Walter Kohn and John A Pople. Professor Kohn and Professor Pople are from University of California and North Western University, respectively. They

both have received the noble prize from the Royal Swedish academy of science in the year of 1998. Abovementioned works have been utilized with different methods. In this paper, linear combination of atomic orbital method has been taken into focus. Many researchers have used this method efficiently. This is efficiently used for the semiconductor method [17, 18]. A review article has been published on the different methods of the computational studies on the density functional theory approach. In this review article, authors have differentiated about the different DFT approaches such as CASTEP, LCAO, and FP-LAPW [19]. Phase transition is also important part of the study related to the structure of the crystals. As previously discussed, alkali metal halides have shown two different structures under some circumstances so the phase transition will take place. A transformation in the type of reversible and first order has been taken into consideration. The phase transition can be observed in the range of pressure values from 5 to 300 KBar for the alkali metal halides [5]. The magnesium-based biodegradable alloys are very efficient to design the orthopedic inserts. Electric discharge machining (EDM) has been used efficiently in a wide manner to fabricate in such a accurate way along with in situ surface modification technique to produce nano-hydroxyparticle coating on the alloy biomaterial. This is very time and cost-effective method [20]. During the development of material science and technology, composite materials have secured a leading place. Those materials several industrial applications in so many fields like bio-medical, aerospace, automotive, sports, etc. Those materials can be characterized in three categories, that is based on matrix phase, based on reinforcement, and based on scale. Different studies have been carried out to study composite material structure and properties. Although many composite materials have been taken into the research, biodegradable composite materials have an special acceptance because of their eco-friendly nature [21]. For the efficient transportation, cooling of the car engine is much more needed. Two-layer nano-particle enhanced phase change materials have been used to achieve this [22].

In this present study, we have used the computational tool to predict the different structural attribute that is lattice constant and bulk modulus. These parameters can depict the structure of the given compounds. Computational approach can be used as an alternative solution of the chemical methods initially, and it can reduce the rate of chemical wastage.

2 Materials and Method

The method that has been used to investigate the objectives is linear combination of atomic orbital method. The total energy values have been calculated using CRYSTAL code. Different authors have approached different methods [23]. The crystal structures have been coded with the basis set, and those atomic orbital basis set have been taken to solve Kohn–Sham Hamiltonian equations under DFT approach. In the current research, all the Gaussian basis set of K, Cl, Br, and I atoms have been used

(www.tcm.phy.cam.ac.uk). The Hamiltonian equation is formulated by undertaking the hybrid scheme B3LYP. To achieve self-consistency, 55% mixing of successive cycles is considered and self-consistency is achieved within 12 cycles. Using this method, the structural properties of $\text{KCl}_x\text{I}_{1-x}$ and $\text{KBr}_x\text{I}_{1-x}$ are explored. The properties are explored in terms of lattice constant and bulk modulus. The results of lattice constant obtained by DFT have been compared with results obtained through Vegard's law [24].

3 Results and Discussion

The physical (structural) parameters of the $\text{KCl}_x\text{I}_{1-x}$ and $\text{KBr}_x\text{I}_{1-x}$ (for $x = 0.00, 0.25, 0.50, 0.75,$ and 1.00) in rock-salt ($B1$) phase have been computed and presented in Tables 1, 2, 3 and 4, respectively, with the total energy optimization calculations. The change in energy values has taken with the variation of volume values of the crystal unit cell. The graphical presentation of the energy values and unit cell volumes of the $\text{KCl}_x\text{I}_{1-x}$ and $\text{KBr}_x\text{I}_{1-x}$ (for $x = 0.00, 0.25, 0.50, 0.75,$ and 1.00) has been shown (Figs. 1, 2, 3, 4, 5 and 6). There is combination of two different slopes within these graphs. The dotted lines present the energy calculations with DFT approach, and the linear curve presents the fitted energy values with Birch-Murnaghan equation of state [25].

$$E(V) = E_0 + \frac{9V_0B_0}{16} \left\{ \left[\left(\frac{V_0}{V} \right)^{\frac{2}{3}} - 1 \right]^3 B'_0 \left[\left(\frac{V_0}{V} \right)^{\frac{2}{3}} - 1 \right]^2 \left[6 - 4 \left(\frac{V_0}{V} \right)^{\frac{2}{3}} \right] \right\}$$

The change in the structural parameters with the concentration of x has been presented (Figs. 7, 8 and 9). As the concentration of Cl and Br is increased in KI, the lattice constant decreases whereas the bulk modulus increases.

Table 1 Data obtained from the current work and observed from the previous literature of lattice parameter (a_0) for $\text{KCl}_x\text{I}_{1-x}$

Concentration	0.00	0.25	0.50	0.75	1.00
Calculated values	7.28	7.1	6.92	6.68	6.42
Vegard's law		7.065	6.85	6.635	
Norwood and Briscoe [25]	7.176	7.030	6.851	6.640	
Erdinc et al. [5]	7.07				
Pies and Weiss (1973)					6.294
Cohen and Gordon (1975)					6.2
Froyen and Cohen [7]	7.03				

Table 2 Data obtained from the current work and observed from the previous literature of bulk modulus (B_0) for KCl_xI_{1-x}

Concentration					
	0.00	0.25	0.50	0.75	1.00
Calculated values	11.45	12.89	14.2	16.2	19.7
Norwood and Briscoe [26]	10.538	11.954	12.724	16.647	21.04
Erdinc et al. [5]	12				19.7
Pies and Weiss [27]					18.6
Cohen and Gordon [28]	13.8				18.9
Froyen and Cohen [7]					19.3

Table 3 Data obtained from the current work and observed from the previous literature of lattice parameter (a_0) for KBr_xI_{1-x}

Concentration					
	0.00	0.25	0.50	0.75	1.00
Present	7.27	7.21	7.15	7.03	6.84
Vegard's law	–	7.16	7.05	6.95	–
Chen et al. [3]	7.07				6.60
Amrani et al. [4]	7.176	7.074	6.971	6.849	6.700
Pies and Weiss [27]	6.96				6.54

Table 4 Data obtained from the current work and observed from previous literature of bulk modulus (B) for KBr_xI_{1-x}

Concentration					
	0.00	0.25	0.50	0.75	1.00
Present	10	10.7	11.3	11.7	12
Zhang and Bukowinski [29]	12				15.2
Amrani et al. [4]	10.538	11.321	11.997	12.011	12.363

4 Conclusion

The purpose of present research was the determination of the structural properties of two technologically important ternary compound, that is KCl_xI_{1-x} and KBr_xI_{1-x} . LCAO method has been initiated to fulfill it. Here, the X value present in the compounds is the doping concentration which varies from 0 to 1% (0.00, 0.25, 0.50, 0.75, and 1.00). Figures have shown the results for the binary compounds and one concentration. For rest concentration, the graph will be similar. It has been concluded that, as the doping concentration of the dopant material changes, the lattice parameter changes reversely and the bulk modulus changes directly. Also, there is a good

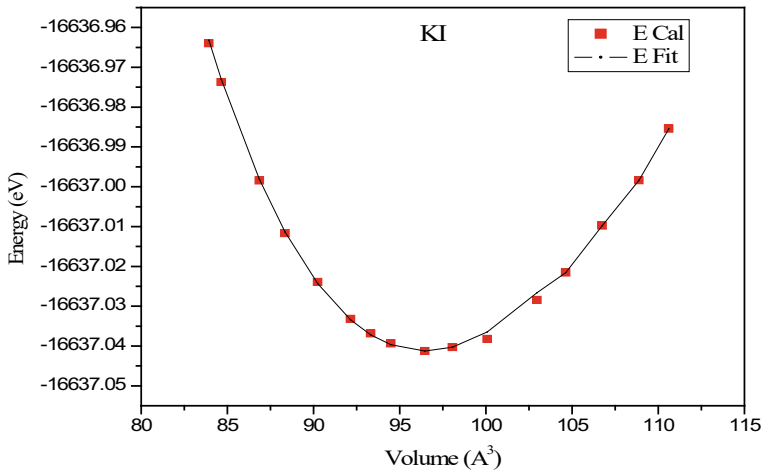


Fig. 1 Plot for energy versus volume

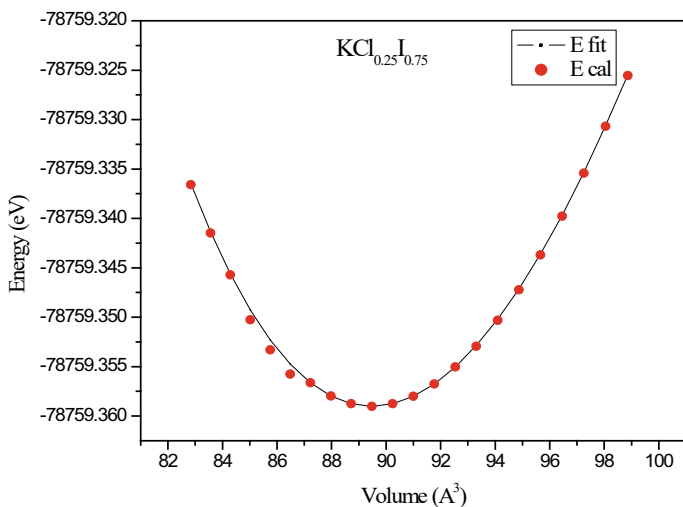


Fig. 2 Plot for energy versus volume

approximate match of the obtained values of the present work with previously calculated data. Present values of the lattice constant also have some good assessment with values determined from Vegard's law.

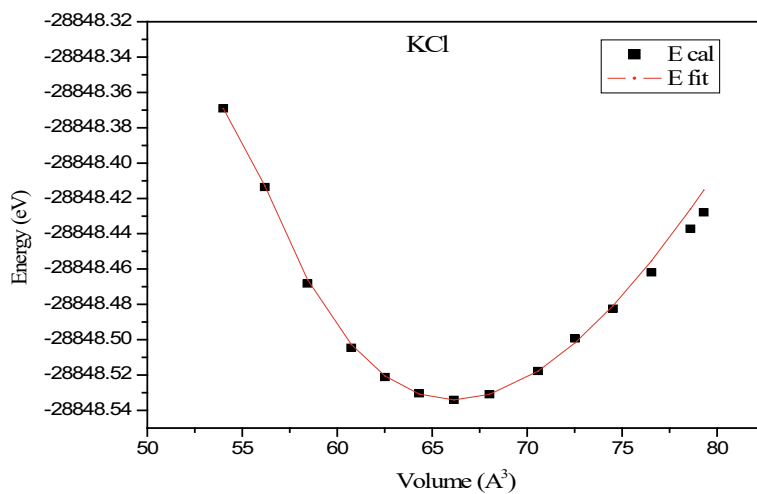


Fig. 3 Plot for energy versus volume

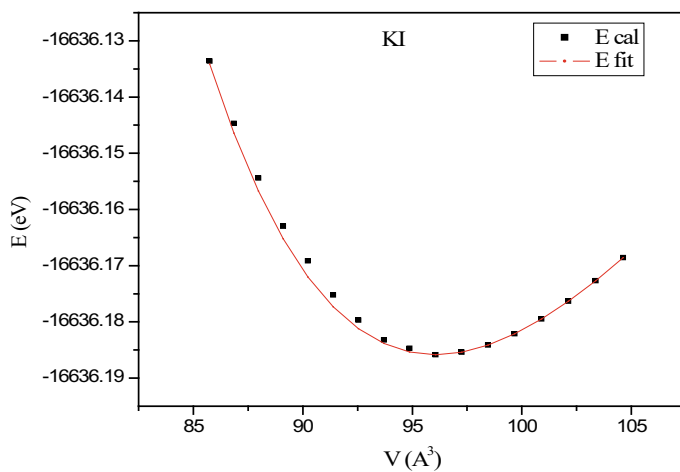


Fig. 4 Plot for energy versus volume

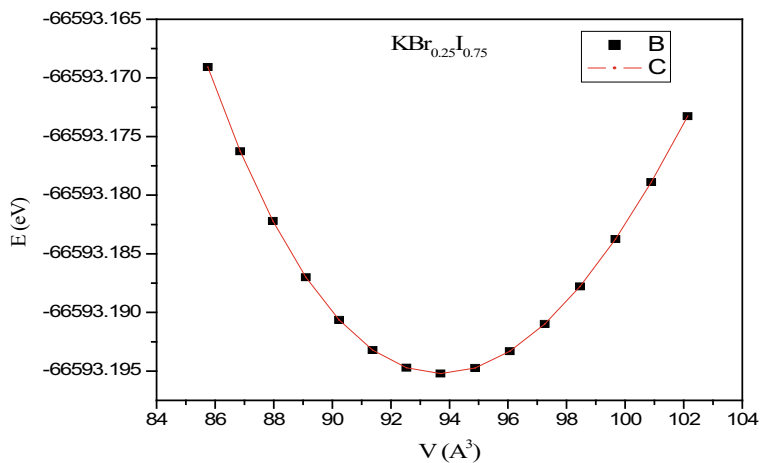


Fig. 5 Plot for energy versus volume

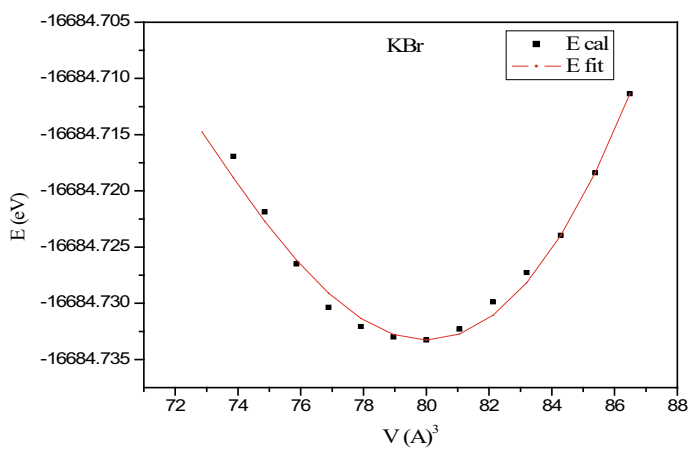


Fig. 6 Plot for energy versus volume

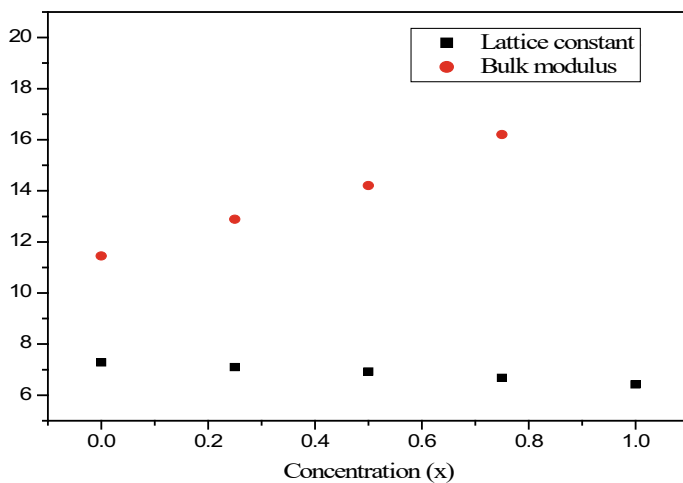


Fig. 7 Plot for variation of concentration with lattice constant and bulk modulus for KCl_xI_{1-x}

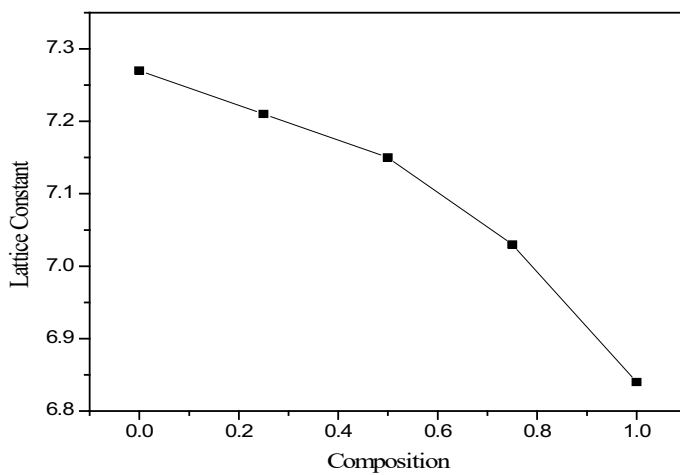


Fig. 8 Plot for variation of concentration with lattice constant for KBr_xI_{1-x}

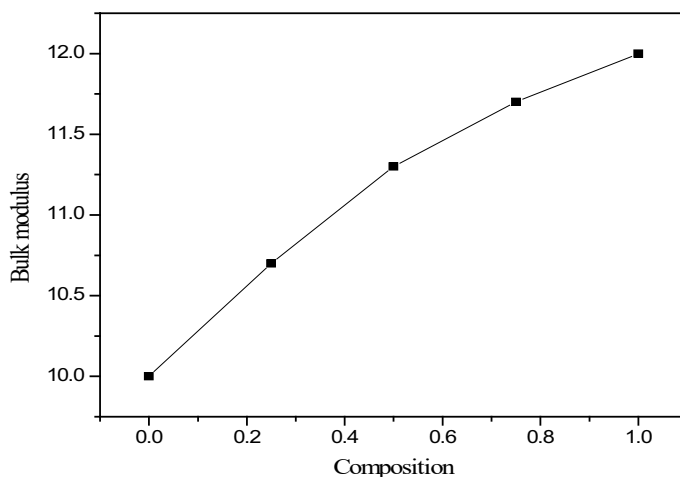


Fig. 9 Plot for variation of concentration with bulk modulus for $\text{KBr}_x\text{I}_{1-x}$

References

1. Flórez M, Recio JM, Francisco E, Blanco MA, Pendás AM (2002) First-principles study of the Rocksalt–cesium chloride relative phase stability in alkali halides. *Phys Rev B* 66(14):144112
2. Zhang S, Nan-xian C (2003) Lattice inversion for interionic pair potentials. *J Chem Phys* 118
3. Chen ZJ, Xiao HY, Zu XT (2006) First principles study of structural, electronic and optical properties of KCl crystal. *Chem Phys* 330(1–2):1–8
4. Amrani B, Kazempoor A, Khosravizadeh S, Hassan FEH, Akbarzadeh H (2008) Theoretical investigations on $\text{KCl}_x\text{Br}_{1-x}$, $\text{KCl}_x\text{I}_{1-x}$ and $\text{KBr}_x\text{I}_{1-x}$: a first-principles study. *Phys B* 403(17):2773–2779
5. Erdinc B, Secuk MN, Aycibin M, Gülebagan SE, Dogan EK, Akkus H (2015) Ab-initio calculations of physical properties of alkali chloride XCl ($\text{X} = \text{K}, \text{Rb}$ and Li) under pressure. *Comput Condens Matter* 4:6–12
6. Pies W, Weiss A, Hellwege KH, Hellwege AM, Boehm HP, Meyer HJ, Allmann R (2006) Crystal structure data of inorganic compounds. Springer
7. Froyen S, Cohen ML (1986) Structural properties of NaCl and KCl under pressure. *J Phys C Solid State Phys* 19(15):2623
8. Slagle OD, McKinstry HA (1967) Temperature dependence of the elastic constants of the alkali halides. I. NaCl, KCl, and KBr. *J Appl Phys* 38(2):437–446
9. Sirdeshmukh DB, Sirdeshmukh L, Subhadra KG (2013) Alkali halides: a handbook of physical properties, vol 49. Springer Science & Business Media
10. Sirdeshmukh DB, Sirdeshmukh L, Subhadra KG, Rao KK, Laxman SB (2001) Systematic hardness measurements on some rare earth garnet crystal. *Bull Mater Sci* 24(5):469–473
11. Dovesi R, Saunders VR, Roetti C, Orlando R, Zicovich-Wilson CM, Pascale F, Civalleri B et al (2017) CRYSTAL17
12. Majumdar AD, Munjal N, Kamboj U, Dogra K (2020) Investigation of structural and electronic properties of BaX ($\text{X} = \text{S}, \text{Se},$ and Te): a DFT study. In: *Advances in materials science and engineering*. Springer, Singapore, pp 281–289
13. Majumdar AD, Gopal R, Munjal N (2020) Structural and electronic properties of III-nitride semiconductor alloys: a first principle study. *Eur J Molecular Clin Med* 7(7):3475–3480
14. Munjal N, Majumdar AD, Kamboj U, Kumar A (2020) Structural properties of scandium chalcogenides via first principle calculations. *J Phys Conf Ser* 1531(1)

15. Munjal N (2019) A first principle study of structural and electronic properties of INN and BN. *J Gujarat Res Soc* 21(6):660–664
16. Bhambhani P (2012) First-principles study of B1 to B2 phase transition in PbS. *J Phys Conf Ser* 377(1)
17. Kumar R, Munjal N, Sharma G, Vyas V, Dhaka MS, Sharma BK (2017) Electron momentum density and phase transition in SrO. *Phase Trans* 85(12):1098–1108
18. Munjal N, Bhambhani P, Sharma G, Vyas V, Sharma BK (2014) Study of phase transition and cohesive energy in MgO. *J Phys Conf Ser* 377(1); Burke K, Lucas W (2014) ABC of ground-state DFT. University Lecture
19. Wang J, Deng M, Chen Y, Liu X, Ke W, Li D, He K (2020) Structural, elastic, electronic and optical properties of lithium halides (LiF, LiCl, LiBr, and LiI): first-principle calculations. *Mater Chem Phys* 244:122733
20. Prakash C, Singh S, Pabla BS, Uddin MS (2018) Synthesis, characterization, corrosion and bioactivity investigation of nano-HA coating deposited on biodegradable Mg–Zn–Mn alloy. *Surf Coat Technol* 346:9–18
21. Rajak DK, Pagar DD, Kumar R, Pruncu CI (2019) Recent progress of reinforcement materials: a comprehensive overview of composite materials. *J Market Res* 8(6):6354–6374
22. Jilte R, Afzal A, Panchal S (2021) A novel battery thermal management system using nano-enhanced phase change materials. *Energy* 219:119564
23. Nyayban A, Panda S, Chowdhury A, Sharma BI (2020) First principle studies of rubidium lead halides towards photovoltaic application. *Mater Today Commun* 24:101190
24. Vegard L (1921) IV. Recent results of northlight investigations and the nature of the cosmic electric rays. *Lond Edinb Dublin Philos Mag J Sci* 42(247):47–87
25. Birch F (1947) Finite elastic strain of cubic crystals. *Phys Rev* 71(11):809
26. Norwood M H, Briscoe C V (1958) Elastic constants of potassium iodide and potassium chloride. *Phys Rev* 112(1):45
27. Pies W, Weiss A (1973) a566, I. 1.3 Complex fluorides and fluorine double salts. In: *Key Elements: F, Cl, Br, I*. Springer, Berlin, Heidelberg, pp 104–115
28. Cohen AJ, Gordon RG (1975) Theory of the lattice energy, equilibrium structure, elastic constants, and pressure-induced phase transitions in alkali-halide crystals. *Phys Rev B* 12(8):3228
29. Zhang H, Bukowinski MST (1991) Modified potential-induced-breathing model of potentials between close-shell ions. *Phys Rev B* 44(6):2495

First Principle Study on Structural Properties of Boron Compounds



Agnibha Das Majumdar, P. Padmakumar, Rajni, Neha Munjal, and Uma Kamboj

Abstract Present study has been presented the different structural properties of the boron-V compounds. Boron Nitride (BN), Boron Phosphide (BP) and Boron Arsenide (BAs) have been taken for the experimentation. Lattice constant (a), bulk modulus (B_0) and pressure derivative of bulk modulus has been determined. To determine the structural properties, linear combination of atomic orbitals (LCAO) method has been used and this is a density functional theoretical approach. All the results have been compared with other theoretical data and it was observed that it has maintained a good comparison.

Keywords Density functional theory (DFT) · Boron-V compounds · Computational study · LCAO · Structural properties

1 Introduction

In this paper, the structural properties of boron-V compounds (BN, BP, BAs) in rock salt and zinc blende phases are investigated. These compounds are of great interest due to their different applications. Boron Nitrate can be used in extremely high temperatures due to its high thermal resistance, as a lubricant due to its hexagonal structure, as a wide gap semiconductor, in abrasive and cutting implements, etc. Boron phosphide is used to produce semiconductor devices such as LEDs and lasers, as protective coating for soft infrared transmitting substrate, etc. Boron arsenide is used in high-temperature devices due to its high thermal conductivity, as a component of a wide range of semiconductor devices, etc. Here a first-principles study is done using the Linear Combination of Atomic Orbitals (LCAO) method to find the structural properties of these compounds such as its bulk modulus, lattice parameter and its pressure derivatives for BN, BP and BAs. We are curious about the $B1$ and $B3$ phases of these compounds and the differences between them are investigated.

A. Das Majumdar · P. Padmakumar · Rajni · N. Munjal (✉) · U. Kamboj
Department of Physics, Lovely Faculty of Science & Technology, Phagwara, Punjab, India
e-mail: nehamunjalphy@gmail.com

CRYSTAL software is used to perform all the Density Functional Theory (DFT) calculations. The Birch-Murnaghan equations are used to verify the results obtained from DFT calculations. Ustundag et al. [1] have observed that as the atomic number increases so does the lattice constant. Yalcin [2] explains how the value of lattice parameter is overestimated by GGA and underestimated by LDA. Cui et al. [3] shows that the refracted index of BSB increases with high pressure. The structural transition from the zincblende structure to rock salt was discovered at 56 GPa. Fatmi et al. [4] explains why cubic BN does not dissolve in iron or steel due to its high crystal rigidity. Daoud et al. [5] shows that BN is one of the hardest materials even comparable to diamond. Abdulkareem and Elias [6] determines the total energy for different values of lattice constant using LDA and GGA. Mal et al. [7] obtained the ground state of BBi is zincblende phase and the lattice constant for ZB phase is obtained by arranging the total energy as a function of lattice constant. Bencherif et al. [8] the most stable state of BN compound was obtained by drawing the energy-volume curve and fitting it with the Birch-Murnaghan equation of state. Jiménez-Villacorta and Prieto [9] determines the structural transition by determining the gibbs energy for the two phases namely rock salt and zincblende. Bioud et al. [10] calculates the structural equilibrium parameters from the different values of total energy as a function of unit cell volume. Viswanathan et al. [11] showed that the lattice parameter decreases as the concentration of nitrogen increases. Wang and Ye [12] used the plane-wave pseudopotential calculations to investigate elastic properties and phase stability of binary III–V semiconductors.

2 Computational Method

In this paper, a DFT analysis of the structural properties of boron-V compounds is done using first principle LCAO method. This method have been proved efficient in many cases [13–15]. Calculations are done using CRYSTAL code by fixing the equation of KH in DFT. CRYSTAL is one of the best software that can be used to calculate accurately the structural properties of compounds as well as their magnetic, vibratory, piezoelectric, elastic and dielectric properties. The Gaussian basis set types were used as a reference for the nearby functions of these compounds. The Kohn–Sham Hamiltonian was constructed thinking of the Becke trade programme and PBE correlation scheme. To calculate structural properties the self-consistency is achieved with 10 cycles. These methods were chosen as they have given accurate results for similar compounds and the results obtained from for boron-V compounds were comparable to the available results.

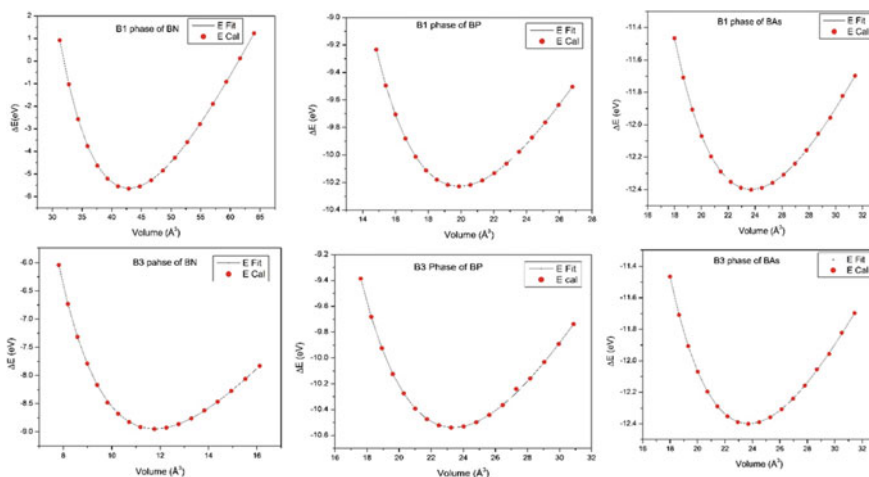


Fig. 1 Energy versus volume graphs for B1 and B3 phases of BN, BP and Bas

3 Results and Discussion

Using the Birch-Murnaghan equation, the total energy is calculated with respect to unit cell volume. The lattice constant and other properties such as the bulk modulus can also be calculated. The fitting is also done with the help of Birch-Murnaghan equations. The total energy of structures of boron-V compounds on a volume set was calculated using the LCAO method. Graphs plotting the variations between the net energy and volume in the two phases are shown in Fig. 1. Each point in the graph represents the calculated energy and the line fitting according to BM equations is given by the continuous line. Table 1 has all the calculated structural parameters.

Phase transition is obtained by using enthalpy. The phase with lower enthalpy is defined as the stable state and the transition from one structure to another occurs when the curves of enthalpy of the two-state B1 and B2 meet. Figure 2 shows the phase transition of BN at 1089.8 GPa, BP at 147.5 GPa and Bas at 133.5 GPa. All of the results obtained are comparable to available data.

4 Conclusion

Thus, in this paper, we have investigated the structural properties of boron-V compounds. Density Functional Theory was used along with the local density approximation which has followed the LCAO method. The graphs plotted between energy and volume are used to compare the results obtained from DFT methods and those obtained from BM equations. It is seen that B3 phase is the stable phase for all

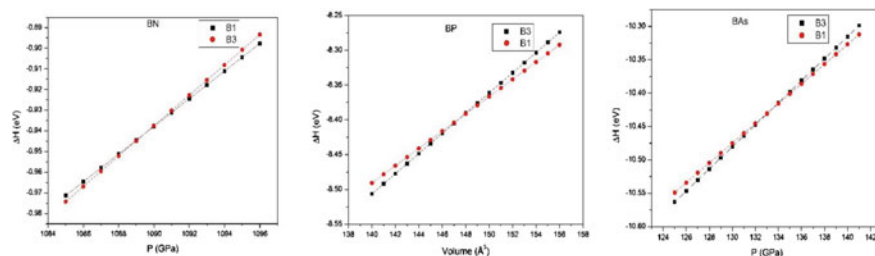
Table 1 Calculated and experimental lattice parameter (*a*), bulk modulus (*B*₀) and its pressure derivatives for BN, BP, BAs

<i>Lattice constant in Å</i>					
	Phase	Present	Experimental	Other calculations	
BN	B3	3.61	3.615 (knittle et al.)	3.627 (Ustundag et al.), 3.649 (Camp et al.), 3.623 (Sekkal et al.), 3.61 (Saib et al.), 3.623 (Zaoui et al.)	
	B1	3.50	–	3.507 (Ustundag et al.), 3.487 (Cui et al.), 3.503 (Zaoui et al.)	
BP	B3	4.53	4.543 (Xia et al.)	4.551 (Ustundag et al.), 4.551 (Mohammad et al.), 4.546 (Zaoui et al.), 4.464 (Touat et al.)	
	B1	4.30	–	4.32 (Ustundag et al.), 4.332 (Meradji et al.), 4.32 (Arbouche et al.)	
BAs	B3	4.73	–	4.812 (Ustundag et al.), 4.81 (Mohammad et al.), 4.743 (Meradji et al.), 4.817 (Ahmed et al.)	
	B1	4.56	–	4.622 (Ustundag et al.)	
<i>Bulk modulus (B₀) in GPa and its pressure derivatives (B₀['])</i>					
			Experimental	Other calculations	
BN	B ₀	B3	371.5	–	373.958 (Ustundag et al.), 392 (Cui et al.), 399 (Zaoui et al.)
		B1	407	369 (knittle et al.)	375.923 (Ustundag et al.), 366 (Camp et al.), 365 (Sekkal et al.), 370.83 (Saib et al.), 368 (Zaoui et al.)
	B ₀ [']	B3	4.02	–	4.896 (Ustundag et al.), 3.72 (Cui et al.), 2.53 (Zaoui et al.), 3.7
		B1	4.16	4(knittle et al.)	3 (Ustundag et al.), 2.91 (Camp et al.), 3.94 (Sekkal et al.), 3.64 (Saib et al.), 3.32 (Zaoui et al.)
BP	B ₀	B3	167	–	156.822 (Ustundag et al.), 161 (Meradji et al.), 163.2 (Arbouche et al.)
		B1	156.5	152 (Xia et al.)	161.34 (Ustundag et al.), 162 (Mohammad et al.), 170 (Zaoui et al.), 176 (Touat et al.)
	B ₀ [']	B3	3.88	–	4.062 (Ustundag et al.), 3.6 (Meradji et al.), 3.58 (Arbouche et al.)
		B1	4.10	4.3 (Xia et al.)	3.649 (Ustundag et al.), 3.86 (Mohammad et al.), 3.07 (Zaoui et al.), 4 (Touat et al.)
BAs	B ₀	B3	144	–	125.179 (Ustundag et al.)
		B1	141	–	130.913 (Ustundag et al.), 131 (Mohammad et al.), 133 (Meradji et al.), 131.2 (Ahmed et al.)
	B ₀ [']	B1	4.16	–	2.976 (Ustundag et al.)

(continued)

Table 1 (continued)

		B3	4.25	—	3.708 (Ustundag et al.), 3.93 (Mohammad et al.), 3.65 (Meradji et al.), 4.17 (Ahmed et al.)
--	--	----	------	---	---

**Fig. 2** Enthalpy versus pressure graphs for BN, BP and BAs

boron compounds from total energy calculations. Value of lattice constant and bulk modulus obtained from DFT calculations are in good agreement with previous data.

References

1. Ustundag M, Aslan M, Yalcin BG (2014) The first-principles study on physical properties and phase stability of Boron-V (BN, BP, BAs, BSb and BBi) compounds. *Comput Mater Sci* 81:471–477
2. Yalcin BG (2016) Structural, mechanical and thermodynamic properties of N-dope BBi compound under pressure. *Appl Phys A* 122(4):456
3. Cui S, Feng W, Hu H, Feng Z (2009) First-principles study on the boron antimony compound. *Phys Stat Sol (b)* 246(1):119–123
4. Fatmi M, Ghebouli B, Ghebouli MA, Hieba ZK (2011) First-principles study of structural, elastic, electronic, lattice dynamic and optical properties of XN (X = Ga, Al and B) compounds under pressure. *Phys Scr* 83(6):065702
5. Daoud S, Loucif K, Bioud N, Lebga N (2012) First-principles study of structural, elastic and mechanical properties of zinc-blende boron nitride (B3–BN). *Acta Phys Pol A* 122(1)
6. Abdulkareem NA, Elias BH (2013) First principle band structure calculations of zinc-Blende BN and GaN compounds. *Int J Sci Eng Res* 4:1–6
7. Mal I, Mahato RK, Tiwari V, Samajdar DP (2021) First principle studies on the structural, thermodynamic and optoelectronic properties of boron bismuth: a promising candidate for mid-infrared optoelectronic applications. *Mater Sci Semicond Process* 121:105352
8. Bencherif K, Yakoubi A, Mebtouche H (2017) Structural and electronic properties of the BN, BP and BAs in the different phases of zinc-blende, NaCl and CsCl. *Acta Phys Pol A* 131(2):209–212
9. Jiménez-Villacorta F, Prieto C (2008) Magnetic properties and interaction mechanisms of iron-based core–shell structures prepared by sputtering at low substrate temperatures. *J Phys Condens Matter* 20(8):085216
10. Bioud N, Sun XW, Daoud S, Song T, Liu ZJ (2018) Structural stability and thermodynamic properties of BSb under high pressure and temperature. *Mater Res Express* 5(8):085904

11. Viswanathan E, Sundareswari M, Jayalakshmi DS, Manjula M, Krishnaveni S (2017) Structural, electronic, mechanical, thermal and optical properties of $B(P,As)_{1-x}N_x$; ($x = 0, 0.25, 0.5, 0.75, 1$) alloys and hardness of $B(P,As)$ under compression using DFT calculations. *Indian J Phys* 91(9):999–1011
12. Wang SQ, Ye HQ (2003) First-principles study on elastic properties and phase stability of III–V compounds. *Phys Stat Sol (b)* 240(1):45–54
13. Dar SA, Sharma R, Srivastava V, Sakalle UK (2019) Investigation on the electronic structure, optical, elastic, mechanical, thermodynamic and thermoelectric properties of wide band gap semiconductor double perovskite Ba_2InTaO_6 . *RSC Adv* 9(17):9522–9532
14. Dar SA, Srivastava V, Sakalle UK (2019) Ab-initio DFT based investigation of double perovskite oxide Ba_2CdOsO_6 with cubic structure. *Comput Condens Matter* 18:e00351
15. Sharma R, Dar SA, Srivastava V (2021) Half-metallic ferromagnetism and thermoelectric properties of vanadium doped $Hf_{1-x}V_xO_2$ ($x = 0, 0.25, 0.50, 0.75$) alloys by first principles perspective. *Phys Lett A* 411:127559

On Techno-economic Aspect of Dental Crown Fabrication by DMLS and Investment Casting for Veterinary Application



Smruti Ranjan Pradhan , Rupinder Singh ,
and Sukhwant Singh Banwait 

Abstract Investment casting (IC) and direct metal laser sintering (DMLS) are widely used fabrication processes for mass production of near net shape geometrically complex parts with acceptable tolerance. But hitherto little has been reported on techno-economic analysis for fabrication of dental crowns (DC) with use of waste from DMLS as input to IC for veterinary dentistry applications. Calculating resources like raw material utilization and process selection for product development and deployment is considered as per the economic concept.

Keywords Techno-economic fabrication · Dental crown · Process waste management

1 Introduction

The manufacturing cost for developing a custom-specific product is one of the vital driving forces for market competitiveness. For meeting the techno-economic way of producing parts, re-engineering the different manufacturing processes is required. This approach follows a set of steps for selecting the current manufacturing method, identifying process gaps through analysis, involving possible opportunities by validation, designing a roadmap based on cutting-edge future processes, cost estimation, and result from the analysis [1]. DC is used for treatment and rehabilitation of fully/partial teeth or any defective teeth for meeting completeness of dental neck. It restores the anatomy, functionality, and aesthetics by compromising gum irritation and partial loss/modification of teeth occlusion due to tooth grinding [2]. Different manufacturing processes like 3D printing, IC, computer-aided design (CAD)-assisted carving, swaging, and electroforming are used to fabricate DC [3]. Crowns are fabricated to overcome dental defects due to abrasion, fractures, discoloration, wedge defects, and root canal treatment with walls [4]. The location and layout of the crown depend on aesthetics and price. Crowns are modelled according to the health of the

S. R. Pradhan · R. Singh (✉) · S. S. Banwait
National Institute of Technical Teachers Training and Research, Chandigarh, India
e-mail: rupindersingh@nitttrchd.ac.in

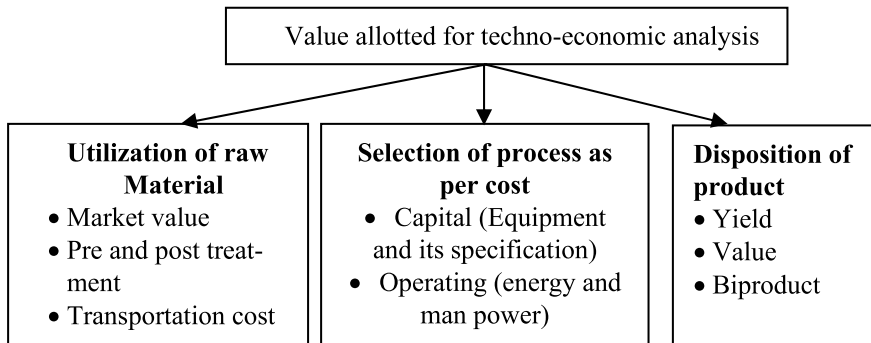


Fig. 1 Allotment of different values for techno-economic analysis

tooth and aesthetic requirements. The various cost parameters for crown making depend on the selection of material and manufacturing method involved [5]. Basically, teeth preparation for crown fitment is done by grinding the teeth with or without a threshold.

Various materials are used for making DC. Ancient Egyptians used the teeth of dead animals and bone pieces to replace material. In recent times, ivory, porcelain, and platinum have been used as artificial tooth materials. But with the implementation of modern technology, ceramic composites, low-density metallic alloys, and synthetic plastic resins are used for the fabrication of DC. The chosen material must be biocompatible as it will come in contact with oral fluids and tissues [6]. The designed crown must have a safety profile with non-allergenic and non-carcinogenic. The selected material must have to withstand high mechanical force and high moisture. Shrinkage resistance and crack resistance in the presence of oral fluid are also considered during the selection of material. The plasters (gypsum powders with water) are used as mould material, whereas adhesives are used for cementation. Some crowns can be coted to meet aesthetic needs [7, 8].

The DC should be designed as per patient-specific mouth conditions in order to mimic the bite standards. Accurate mould making of the oral cavity is very important for the successful design of DC. Different values as per their weight are considered for techno-economic analysis, as shown in Fig. 1.

2 Approach

This study proposes a design technique to aid in the techno-economic analysis of utilizing additive manufacturing to fabricate DC. The input data consists of a 3D virtual (CAD) model that has been converted to an STL file through 3D scanning, as well as the geometric dimensioning and tolerance scheme that must be followed in the final portion. These requirements are crucial for determining the desired quality

of the finished product following the manufacturing process. The research work is predicated on the analysis and simulation of different steps associated with the fabrication of DC. The techno-economic approach for the fabrication of DC is shown in Fig. 2. The first step for the fabrication of DC for a dog is the development of a dental replica in the form of mould. The mould material is gypsum powder. First, the negative dental impression (cavity) will be made by taking biting force over a colloidal solution (calcium alginate) kept on a dental tray by putting it inside the mouth of the dog. An adjustable (linear as well as angular movement supported) dental tray will be best for impression making, irrespective of breed and age of the veterinary subject. By doing this, the making of the custom-specific dental tray can be avoided, and a single adjustable dental tray will be sufficient to meet the requirements.

After finishing and final development of plaster mould, the remaining impression material as well as die stone material can be recycled and reused. In the next step, the die stone models will be scanned by a 3D scanner for the development of virtual CAD models of the crown. Here, the geometry of the virtual model can be repaired that will help to forecast minimum cost involvement in final DC fabrication through 3D printing and further post-treatment.

In fused deposition modelling (FDM)-based 3D thermoplastic (Acrylonitrile Butadiene Styrene (ABS)) printing of DC, the material consumption, printing time, and number of layers can be optimized by playing with parameters like infilled density, infilled pattern, orientation, and the virtual placing of CAD models on build platform with minimum utilization of support material (soluble polycarbonate) [9].

In the case of DMLS-based 3D metal printing, the virtual models are imported to 3DXpert software. In the 'Edit Printer' section, the probable material with the 3D printer series will be selected. The .STL files will be added to the software in the 'Add 3DP Component' section. The height of probable support structure will be chosen in the 'Position Body section' by taking overhangs, probable residual stress development, conformal cooling, and easy support removal in post-processing phases into consideration. The 3D printing simulation will be analysed in the '3DP Analysis' section for printability check with probable overhang, section-wise residual stress development during printing, etc. For creating support and print preparation, 'Support Manager' section will be selected. Different types of supports like solid, cone, wall, skirt, lattice, and solid wall are options to use in this section. Depending upon the weight, base surface, and overhangs, the type of support is selected carefully by taking support region with reference points along the part. So, the probable material consumption can be optimized by choosing appropriate support by further modelling. The advanced lattice optimization (finite element analysis (FEA)) will be provided to check whether the designed part with its lattice structure is subject to withstand the stresses and forces that determine the working life. Again, by doing lattice optimization, the design can be modified for working condition requirements. The possible modification may be the thinner or thicker lattice. By getting yield stress value and present maximum stress from FEA, if the yielding condition (yield stress > maximum stress) persists, it will recommend going for further reduction in weight.

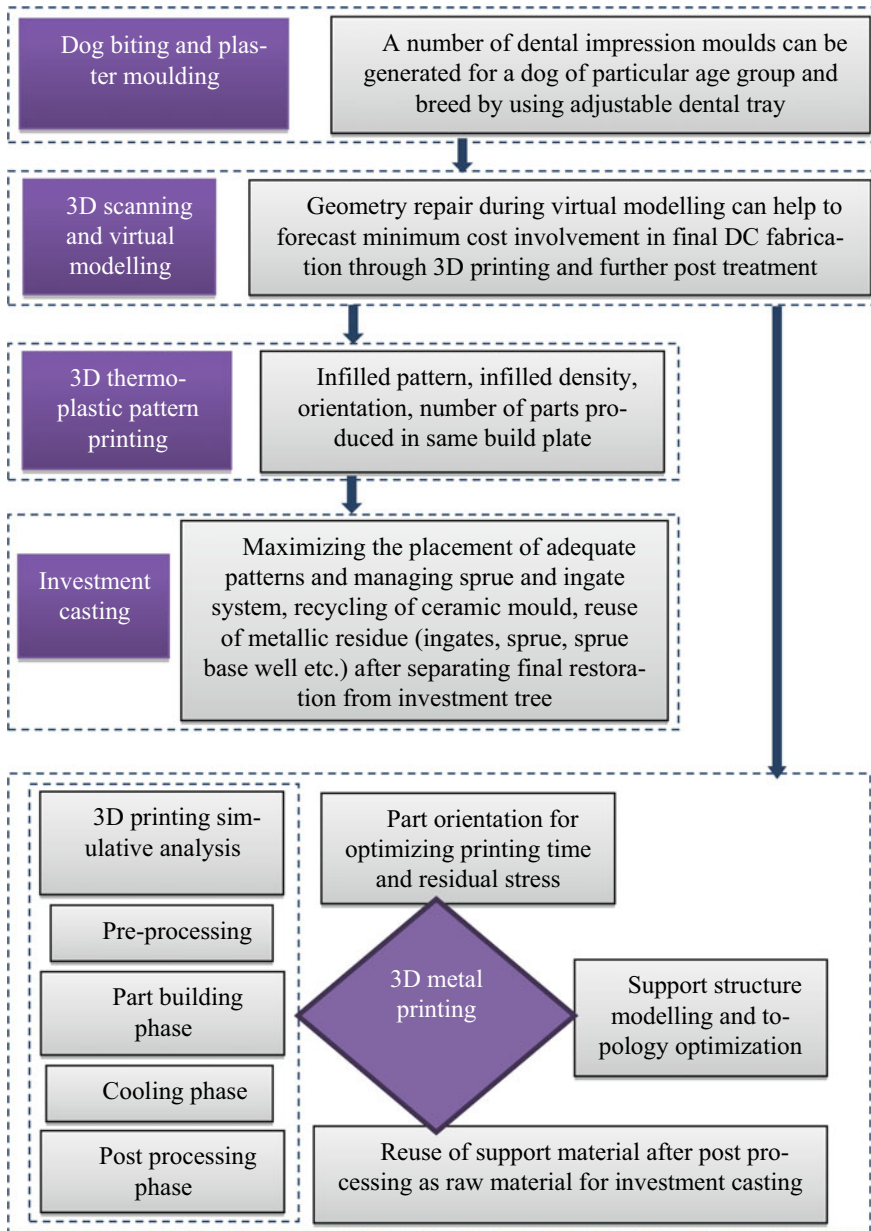


Fig. 2 Techno-economic approach for fabrication of DC

By doing this, material consumption can be minimized. The cost-effective incorporation of metal AM is about adding the chosen metal printing technology, with the efficiency of the entire production cycle affecting up to 70% of the part cost. The application experts from different AM and subtracting manufacturing fields focus on the outcomes of their tight collaboration to demonstrate workflows that reduce cost per part while maintaining high quality [10].

The thermoplastic patterns can be used as a sacrificial pattern for IC of metallic DC. The low casting yield and high energy consumption with more scrap generation can be resulted due to the use of a long sprue and riser with a bulky runner system. The energy consumed for melting the metal and heating the investment ring in the furnace must be carefully considered [11]. The waste mould shell, after breaking the investment ring in IC, can be recycled and reused. The recycling process includes mould shell roll crushing followed by grinding into finer form and then screening (component concentration) and heavy medium separation (gravity settling). It can be used as a coating in the back layer (stucco) of IC mould shell [12].

3 Case Study

A case study has been prepared on the basis of cost optimization for the fabrication of DC by one manufacturing process (IC route) by utilizing the waste of another manufacturing process (DMLS). Also, the thermoplastic (Acrylonitrile Butadiene Styrene (ABS)) pattern making followed an economic fabrication route, where the recycled ABS was utilized for IC. Here, the recycled ABS was brought from the market at a reasonable rate and filament prepared by extrusion process. The metal waste from the DMLS process includes a support structure, semi-built parts due to any unavoidable circumstances like power failure, overhaul condition of 3D metal printer, etc. IC of DC had been prepared by utilizing wax pattern as well as ABS pattern at the expense of collected waste. Further, the ABS pattern was further processed by wax coating and chemical vapour smoothing process (CVS) for surface characterization. Patterns, DMLS waste, and IC parts are shown in Fig. 3.

In this study, there are 18 samples (9 samples by 17–4 PH stainless steel and 9 samples by Ni625 alloy) that were prepared in DMLS as well as 3D thermoplastic pattern-assisted IC. Some of the thermoplastic patterns were also post-treated with wax coating and CVS. Manufacturing details are given in Table 1.

4 Cost Analysis

Here, the cost analysis was performed for fabrication of DC by DMLS and IC route. The main losses encountered in IC are melting due to volatilization or oxidation of alloying elements, higher volume to surface area ratios, type of furnace, exposer of molten metal to the atmosphere, gas contamination, etc., whereas metallic support



Fig. 3 a Pattern for IC prepared by recycled ABS, b wax pattern, c DMLS-based parts fabricated showing support structure, d collected wastes from 3D metal printing process, and e final IC parts of DC from 3D printing metal wastes

Table 1 Details of manufacturing of DC in two different routes

Part: DC	DMLS route		IC route	
	17–4 PH stainless steel	Ni625	17–4 PH stainless steel	Ni625
Material density (g/cc)	7.75	8.44	7.75	8.44
Avg. part weight (g)	1.97	2.6	2.8	3.4
No. of parts	9	9	9	9
Maximum part height (mm)	11.8	11.8	12.5	12.4
Part maximum diameter (mm)	24	24	23.66	23.74
Dimensional tolerance (mm)	± 0.15	± 0.15	± 0.7	± 0.7

structure is the only loss in DMLS [13, 14]. So, melting losses in IC can be minimized by introducing a faster melting rate with minimum disturbance, minimizing excessive liquid metal temperatures with too many liquid metal transfers, close control of melting conditions, etc. [15, 16].

The manufacturing cost for DMLS was estimated as per the resources utilized like powder, inert gas, compressed air, heat source, etc. [17]. In the pre-processing stage of 3D metal printing, the activities like build preparation, build plate loading, powder conditioning (heated in oven followed by sieving in sieve shaker), powder feeding to feed piston, and the gas filling were carried out. In the part building phase, the time was noted after analysing optimum conditions like topology, orientation, support management, etc. In the post-processing phase, the activities like powder removal,

plate removal from sintering piston, cleaning with the help of vacuum cleaner, heat treatment, final part cutting from the build plate, part finishing, and plate grinding were carried out. During part finishing, the wastes (metallic support structure) were collected. The costs involved in DMLS are fabrication file preparation in software, pre-processing phase (build plate loading, powder conditioning, feeding, laser preparation, and air supply), part building phase (inert manufacturing chamber preparation, sintering, and unloading phase), and post-processing phase (part separation from the build plate, heat treatment, finishing of fabricated parts, and plate grinding).

The manufacturing cost for IC was estimated as per the resources like pattern making, investment mould making, investment heating furnace, melting of metal, pouring of molten metal to moulds, removal of mould from crucible after solidification, fettling, and finishing, and cost of heat treatment [18]. The values of different items associated with the fabrication of DC are given in Table 2. The process cost overviews associated in DMLS and IC are shown in Tables 3 and 4, respectively.

Table 2 Values of different items associated with the fabrication of DC

S. No.	Item	Value	Unit of measure
1	Recycled ABS (pattern)	3.9	\$/kg
2	17-4 PH powder	74.75	\$/kg
3	Ni625	98.475	\$/kg
4	Argon gas	0.403	\$/l
5	Compressed air (as needed)	-	\$/unit
6	Power consumed (as needed)	-	\$/unit
7	Investment powder with curing liquid	2.21	\$/kg
8	Debubbler	0.0078	\$/ml
9	Casting ring	2.015	\$/unit
10	Polywax	3.51	\$/kg
11	Cellulose (ring liner)	0.1638	\$/mm
12	Metal (bullet form)	91	\$/kg
13	crucible	0.637	\$/kg
14	Muffle furnace	84.5	\$/piece
15	Oven	3900	\$/unit
16	Sieve shaker	390	\$/piece
17	3D metal printer	3,380,000	\$/piece
18	3D thermoplastic printer	1625	\$/piece
19	Operator for IC	10	% Of total cost
20	Operator for DMLS	10	% Of total cost

Table 3 DMLS process cost overview

S. No.	Cost associated	Cost (\$)	% Contribution
1	Fabrication file (.fab) preparation	2.09664	1.12
2	Pre-processing	12.7296	6.8
3	Part building	97.344	52
4	Post-processing	21.1536	11.3
5	Powder used	8.6112	4.6
6	Energy	3.3696	1.8
7	Gas (argon)	11.30688	6.04
8	Compressed air	1.42272	0.76
9	Machine	–	0.0
10	Labour + operator	18.72	10
11	Consumables	9.50976	5.08
12	Inspection	0.936	0.5
Total		187.2	100

Table 4 IC process cost overview

S. No.	Cost associated	Cost (\$)	% Contribution
1	3D printing pattern	0.819	1
2	Gating system making	0.61425	0.75
3	CVS and wax coating on pattern	0.4095	0.5
4	Investment preparation	9.828	12
5	Investment heating	2.457	3
6	Raw material	14.742	18
7	Melting of metal	16.9533	20.7
8	Pouring of molten metal	3.276	4
9	Solidification and mould-breaking	4.095	5
10	Post-processing	10.85175	13.25
11	Labour	8.19	10
12	Consumables	6.2244	7.6
13	Heat treatment	–	0.0
14	Energy	3.0303	3.7
15	Inspection	0.4095	0.5
Total		81.9	100

N.B.: (i) When the support structure of metal printed parts was used as raw material for IC, the total manufacturing cost was reduced by \$14.742/-; i.e. the total estimated cost for fabrication of DC in IC route was \$67.158.

(ii) The total time consumed for 3D thermoplastic pattern-assisted IC and DMLS (without considering powder recycling) is approximately six and five hours, respectively.

5 Conclusions

The present study confirms AM can create parts with complex shapes. However, the initial investments in setting DMLS must be considered. The requirement for additional machining in the post-processing phase contributes to the overall cost of DMLS. The post-processing activities included two manufacturing routes for cost analysis. The total time consumed in DMLS is 18.19% less than that of 3D thermoplastic pattern-assisted IC for the fabrication of DC. The percentage of the difference between the total manufacturing cost involved in DMLS and IC is 78.261% (by using fresh raw material) and 94.388% (by using DMLS waste as raw material), respectively. So by using the DMLS support structure as waste, the percentage of the overall cost of fabrication is minimized by 19.78%. The dimensional accuracy of fabricated DC is better controlled in DMLS than IC. In the future, a study can be conducted on the recycling of IC waste such as burnt investment and metal wastes after post-processing.

Acknowledgements Special thanks to DST-FIST (GoI) for providing research facilities (File No. SR/FST/COLLEGE/2020/997). For lab facilities, we would like to thank Precision Ceramic Artz, Dental Laboratory, Mohali, Punjab (India), GADVASU, Ludhiana, Punjab (India), GNDEC, Ludhiana, Punjab (India), National Institute of Technical Teachers Training and Research, Chandigarh (India), and Panjab University, Chandigarh (India).

References

1. Mandolini M, Campi F, Favi C, Germani M (2019) Manufacturing processes re-engineering for cost reduction: the investment casting case study. In: International design engineering technical conferences and computers and information in engineering conference, vol 59223. American Society of Mechanical Engineers, p V004T05A018
2. Bikas H, Stavropoulos P, Chryssolouris G (2016) Additive manufacturing methods and modelling approaches: a critical review. *Int J Adv Manuf Technol* 83(1–4):389–405
3. Pradhan SR, Singh R, Singh SS (2020) A frame work on crown fabrication for veterinary patients using 3D thermoplastic and metal printing. In: Reference module in materials science and materials engineering. <https://doi.org/10.1016/B978-0-12-820352-1.00063-8>
4. Enlund KB, Brunius C, Hanson J, Hagman R, Höglund OV, Gustås P, Pettersson A (2020) Dental home care in dogs—a questionnaire study among Swedish dog owners, veterinarians and veterinary nurses. *BMC Vet Res* 16(1):1–13
5. Linna M, Nordblad A, Koivu M (2003) Technical and cost efficiency of oral health care provision in Finnish health centres. *Soc Sci Med* 56(2):343–353
6. Pradhan SR, Singh R, Banwait SS, Singh S, Anand A (2021) 3D printing assisted dental crowns for veterinary patients. In: Reference module in materials science and materials engineering. <https://doi.org/10.1016/B978-0-12-820352-1.00153-X>
7. Lemmons M, Beebe D (2019) Oral anatomy and physiology. In: Wiggs’s veterinary dentistry: principles and practice, pp 1–24
8. Pradhan SR, Singh R, Banwait SS (2021) On crown fabrication in prosthetic dentistry of veterinary patients: a review. In: Advances in materials and processing technologies, pp 1–20. <https://doi.org/10.1080/2374068X.2021.1970991>

9. Singh N, Singh R, Ahuja IPS, Farina I, Fraternali F (2019) Metal matrix composite from recycled materials by using additive manufacturing assisted investment casting. *Compos Struct* 207:129–135
10. Zhang Y, Bernard A, Harik R, Karunakaran KP (2017) Build orientation optimization for multi-part production in additive manufacturing. *J Intell Manuf* 28(6):1393–1407
11. Singh G, Singh R, Singh S (2019) Partial dentures by centrifugal casting assisted by additive manufacturing. *Sadhana* 44(6):1–11
12. Peters TM, Twarog DL (1992) The feasibility of reclaiming shell material from investment casting. Hazardous Waste Research and Information Center, 004
13. Singh G, Singh R, Singh S, Bhardwaj A (2020) Comparison of thermoplastic and wax based patterns for investment casting of partial dentures: techno-economic and process capability analysis. In: Reference module in materials science and materials engineering. <https://doi.org/10.1016/B978-0-12-820352-1.00018-3>
14. Lynch P, Hasbrouck CR, Wilck J, Kay M, Manogharan G (2020) Challenges and opportunities to integrate the oldest and newest manufacturing processes: metal casting and additive manufacturing. *Rapid Prototyping J* 26(6):1145–1154
15. Lee CW, Chua CK, Cheah CM, Tan LH, Feng C (2004) Rapid investment casting: direct and indirect approaches via fused deposition modelling. *Int J Adv Manuf Technol* 23(1):93–101
16. Mun J, Ju J, Thurman J (2016) Indirect fabrication of lattice metals with thin sections using centrifugal casting. *J Visualized Exp* 111
17. Cicconi P, Mandolini M, Favi C, Campi F, Germani M (2021) Metal additive manufacturing for the rapid prototyping of shaped parts: a case study. *Comput Aided Des Appl* 18(5):1061–1079
18. Khanna OP (1993) A text book of mechanical estimating and costing, 1st edn. Dhanpat Rai & Sons, India

A Critical Study of Structural and Electronic Properties of Co_2TiN Full-Heusler Alloy



Navdeep kaur and Vipul Srivastava

Abstract The present work is intended to provide worthwhile information about the structure and half-metallicity of Co-based Heusler alloy. The first principle density functional theory was used to analyze Co_2TiN . First, the structure of an alloy was optimized through the consideration of Cu_2MnAl and Hg_2CuTi , two structure types along with different magnetic phases. The resulting stable structure Hg_2CuTi showed the metallic nature of an alloy in both spin configurations with GGA potential. However, an implication of Hubbard parameter (U) considerably affected the electronic structure and therefore bands got shifted with 100% polarization at Fermi level which increases the efficiency of spintronics. Under the effect of U, spin-up configuration showed semiconducting nature with 0.21 eV that revealed the half-metallicity in Co_2TiN full-Heusler alloy.

Keywords Heusler alloy · Electronic bands · Half-metallicity · Co_2TiN

1 Introduction

The half-metallic (HM) behavior characterized by metallic nature in one spin and semiconducting in another was initially envisaged in 1983. The first Heusler alloy that was found to be HM is NiMnSb [1] and since then hunt for these materials attained a valuable peak. Additionally, there is magnetic property of Heusler alloy in which materials with non-magnetic elements show ferromagnetic behavior, first discovered in 1903 [2]. These properties along with other remarkable properties [3–5] anticipate Heusler alloys as technologically important for spintronics devices [6], spin value detectors [7], and magneto resistive materials [8, 9]. The spintronics devices are engaged with manipulation in spin degree of freedom in the appliances based on semiconductors. This factor gave advantages like improvisation in data processing speed, less power consumption along with the non-volatility of data storage in electronic appliances [10, 11]. The possibility of 100% spin-polarized current increases

N. kaur · V. Srivastava (✉)

Department of Physics, School of Chemical Engineering and Physical Sciences, Lovely Professional University, Phagwara, Punjab 144411, India
e-mail: vipsri27@gmail.com

the efficiency of these materials in magneto electronics [12, 13]. Several Heusler alloys have been investigated based on their respective properties [14–17].

The Heusler alloys are mainly existing in four types (crystallized structure) known as Half-Heusler ($C1_b$), full-Heusler ($L2_1$), Inverse Heusler (XA), and quaternary Heusler alloys. The $C1_b$ structure contains three fcc sub-lattices with XYZ chemical formula and $L2_1$, XA structure has four fcc sub-lattices described by X_2YZ composition. However, quaternary Heuslers also consist of four fcc sub-lattices but exist with $XX'YZ$ composition [18]. In this chapter, we intend to inspect the structural and electronic properties of Co_2TiN and the half-metallic character of the material implies its importance in spintronics.

2 Methodology

The density functional theory (DFT) [19] based full-potential linearized augmented plane wave (FP-LAPW) method through wien2k code [20] has been employed to investigate the Co-based full-Heusler alloys. We utilize the generalized gradient approximation of Perdew-Burke Ernzerhof (PBE-GGA) [21] to approximate the exchange–correlation potential in appropriate modes. The product of the smallest muffin tin radius (RMT) and largest reciprocal lattice vector (K_{max}) was set to 7 which manages the convergence of the basis set. The values of RMT for Co, Sc, and N were set to 2, 2.06, and 2.1, respectively in the atomic unit (a.u.). A dense mesh of 1000 k-points integrates the Brillouin zone. The energy and charge difference between subsequent iterations were considered as 10^{-4} Ry/cell and 10^{-3} e, respectively. The minimum energy was estimated by comparing two types of structures and an evaluated stable structure was further implemented to determine the spin-dependent electronic structure. Further, the implication of GGA + U potential where U is Hubbard parameter furnishes the results and showed half-metallic behavior of the compound.

3 Results and Discussion

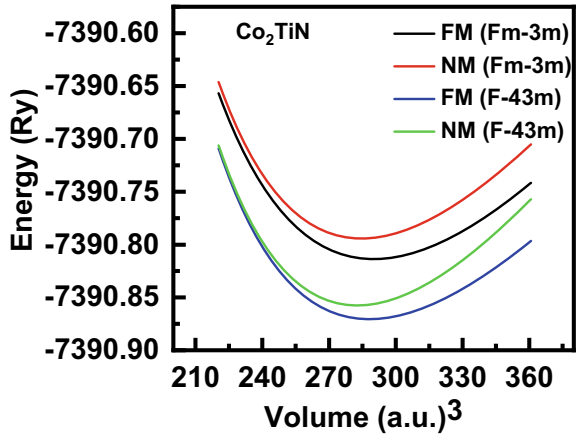
3.1 Structural Properties

The Co_2TiN full-Heusler alloy is optimized by considering Cu_2MnAl ($L2_1$) and Hg_2CuTi (XA) structure types. The former type lies under Fm-3 m (225) space group and XA structure has F-43 m (216) space group. The optimization extracted the ground state parameters of the stable structure shown in Table 1, by fitting the total energy-volume (EV) parameters to the Birch-Murnaghan equation of state [22]. The XA structure is affirmed as energetically stable structure as compared to $L2_1$ structure in Fig. 1 and Co_2TiN in XA structure has atomic positions with Co atom at

Table 1 The ground state parameters of Co₂TiN in ferromagnetic (FM) states

Alloy	Space group	<i>a</i> (Å)	<i>B</i> (GPa)	BP	<i>E</i> ₀ (Ry.)
Co ₂ TiN	Fm-3 m (FM)	5.56	173.29	3.84	-7390.813677
	F-43 m (FM)	5.54	176.56	4.53	-7390.870519

Fig. 1 Volume optimization of Co₂TiN



two different positions as (0, 0, 0) and (0.25, 0.25, 0.25), Ti located at (0.5, 0.5, 0.5) and N is at (0.75, 0.75, 0.75). Furthermore, Fig. 1 is also showing the ferromagnetic phase as a stable magnetic phase for an alloy.

3.2 Electronic Properties

The electronic structure of Co₂TiN in the irreducible zone investigates by employing GGA and GGA + U potential. In GGA potential the electronic bands for both spins cross the Fermi level (*E_f*) indicates the metallic nature of an alloy. However, in spin-up state valence bands are merely touching *E_f*. The band near *E_f* has a contribution of Co and Ti bands present between *W* and *L* and at *X*, *W* points shown in Fig. 2. Interestingly, the employment of *U* as shown in Fig. 3, shifted the bands that resulted in the semiconducting behavior in the spin-up state. The implication of *U* shifted valence electrons a bit downward implies an indirect energy gap of about 0.21 eV in the spin-up state. Thus, under the effect of GGA + U potential Co₂TiN shows half-metallicity, which signifies its applicability in spintronics.

Further, to understand the atomic contribution, the density of states (DOS) is plotted in Fig. 4 within GGA + U potential. The graph shows maximum contribution of Co atom (~ 5.11 states/eV in up spin and ~-2.3 states/eV in down spin) in total DOS. The N atom has the least contribution of about 0.49 and -1.58 states/eV in spin-up and spin-down states, respectively. However, Fig. 5 shows the orbital contribution

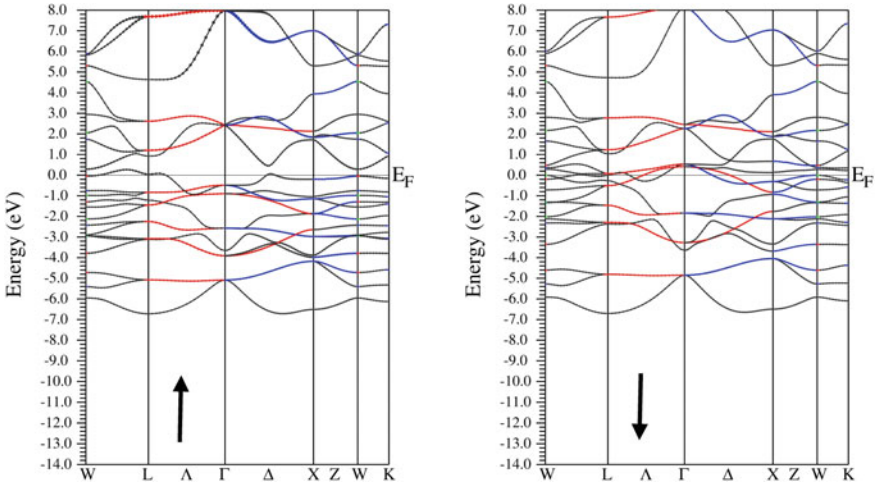


Fig. 2 Band structure for up (Left) and down (Right) spin case with GGA

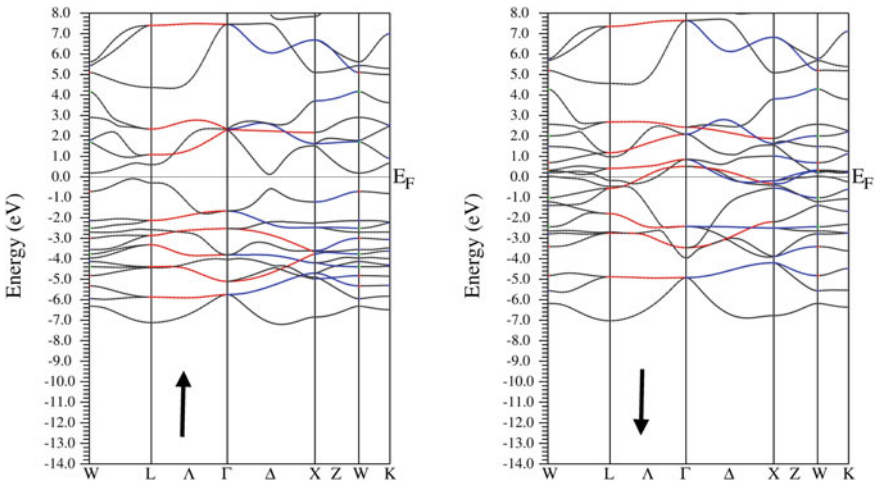


Fig. 3 Band structure for up (Left) and down (Right) down case with GGA + U

of two Co atoms (Fig. 5a, b), Ni (Fig. 5c), and N (Fig. 5d) atom. The PDOS shows a major contribution of *d* electrons and a lesser contribution of *p* electrons in the elemental DOS. The energy gap amid conduction and valence electrons in spin-up state and intersection of both types of electrons at E_f in spin-down state agrees with the half-metallic nature of Co_2TiN investigated through band structure figures.

Fig. 4 Calculated total density of states with GGA + U in both spins

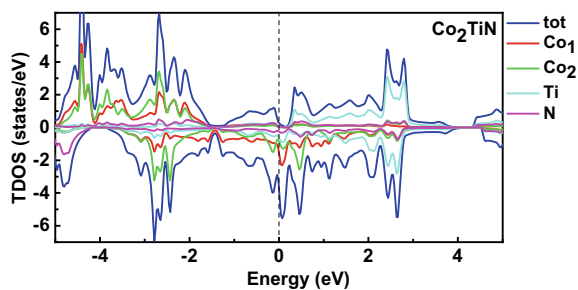
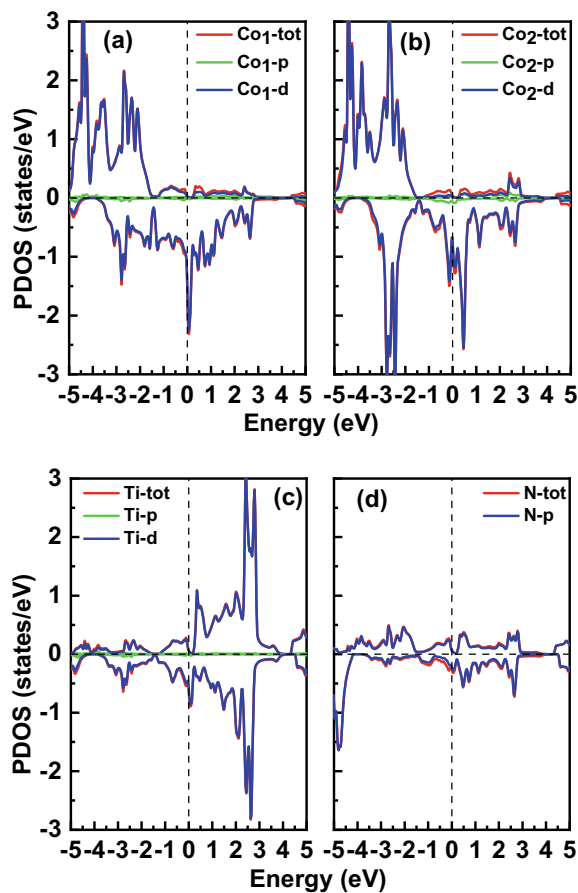


Fig. 5 Calculated partial density of states with GGA + U in both spins



4 Conclusion

We use FP-LAPW method incorporated in wien2k code to investigate the structural and electronic properties of Co_2TiN . The optimization through the energy-volume curve indicates Hg_2CuTi as an energetically more stable structure than the Cu_2MnAl structure type. The GGA potential shows the metallic nature of an alloy as a result of electronic bands at the Fermi level. However, Co_2TiN exhibits a half-metallic character within GGA + U potential with a stable ferromagnetic state. The GGA + U potential shifted the bands with ferromagnetic gap of 0.21 eV in spin-up state.

References

1. De Groot RA, Mueller FM, Van Engen PG, Buschow KHJ (1983) New class of materials: half-metallic ferromagnets. *Phys Rev Lett* 50(25):2024
2. Heusler F, Starck W, Haupt E (1903) Magnetisch-chemische studien. *Verh Dtsch Phys Ges* 5:219–232
3. Bentouaf A, Hassan FH, Reshak AH, Aïssa B (2017) First-principles study on the structural, electronic, magnetic and thermodynamic properties of full Heusler alloys Co_2VZ (Z = Al, Ga). *J Electron Mater* 46(1):130–142
4. Zenasni H, Faraoun HI, Esling C (2013) First-principle prediction of half-metallic ferrimagnetism in Mn-based full-Heusler alloys with highly ordered structure. *J Magn Magn Mater* 333:162–168
5. Wang XT, Cheng ZX, Yuan HK, Khenata R (2017) L_{21} and XA ordering competition in titanium-based full-Heusler alloys. *J Mater Chem C* 5(44):11559–11564
6. Žutić I, Fabian J, Sarma SD (2004) Spintronics: fundamentals and applications. *Rev Mod Phys* 76(2):323
7. Cahaya AB, Tretiakov OA, Bauer GE (2014) Spin Seebeck power generators. *Appl Phys Lett* 104(4):042402
8. Moodera JS, Kinder LR, Wong TM, Meservey R (1995) Large magnetoresistance at room temperature in ferromagnetic thin film tunnel junctions. *Phys Rev Lett* 74(16):3273
9. Binasch G, Grünberg P, Saurenbach F, Zinn W (1989) Enhanced magnetoresistance in layered magnetic structures with antiferromagnetic interlayer exchange. *Phys Rev B* 39(7):4828
10. Wolf SA, Awschalom DD, Buhrman RA, Daughton JM, von Molnár VS, Roukes ML, Chtchelkanova AY, Treger DM (2001) Spintronics: a spin-based electronics vision for the future. *Science* 294(5546):1488–1495
11. Prinz GA (1998) Magnetoelectronics. *Science* 282(5394):1660–1663
12. De Boeck J, Van Roy W, Das J, Motsnyi V, Liu Z, Lagae L, Boeve H, Dessein K, Borghs G (2002) Technology and materials issues in semiconductor-based magnetoelectronics. *Semicond Sci Technol* 17(4):342
13. De Boeck J, Van Roy W, Motsnyi V, Liu Z, Dessein K, Borghs G (2002) Hybrid epitaxial structures for spintronics. *Thin Solid Films* 412(1–2):3–13
14. Srivastava V, Kaur N, Khenata R, Dar SA (2020) Investigation of the electronic, magnetic, elastic, thermodynamic and thermoelectric properties of Mn_2CoCr Heusler compound: a DFT-based simulation. *J Magn Magn Mater* 513:167107
15. Srivastava V, Kaur N, Wang X, Mushtaq M, Dar SA (2021) First-principles study on structural, electronic, magnetic, elastic, mechanical and thermodynamic properties of Mn_2PtCo Heusler alloy. *Int J Energy Res* 45(7):11305–11319
16. Gupta M, Kaur D, Shan M, Diwaker (2018) Structural, electronic and magnetic properties of Heusler alloy Fe_2NiZ (Z = Mn, Co). *AIP Conf Proc* 2006(1):030028

17. Asli N, Dahmane F, Mokhtari M, Zouaneb C, Batouche M, Khachai H, Srivastava V, Naqib SH, Al-Douri Y, Bouhemadou A, Khenata R (2021) Structural, electronic, magnetic and mechanical properties of the full-Heusler compounds Ni_2Mn (Ge, Sn) and Mn_2NiGe . *Zeitschrift für Naturforschung A*
18. Graf T, Felser C, Parkin SS (2011) Simple rules for the understanding of Heusler compounds. *Prog Solid State Chem* 39(1):1–50
19. Schwarz K, Blaha P, Madsen GK (2002) Electronic structure calculations of solids using the WIEN2k package for material sciences. *Comput Phys Commun* 147(1–2):71–76
20. Blaha P, Schwarz K, Madsen GK, Kvasnicka D, Luitz J (2001) WIEN2k: an augmented plane wave + local orbitals program for calculating crystal properties 60
21. Perdew JP, Burke K, Ernzerhof M (1996) Generalized gradient approximation made simple. *Phys Rev Lett* 77(18):3865
22. Murnaghan FD (1944) The compressibility of media under extreme pressures. *Proc Natl Acad Sci USA* 30(9):244

Effect of Additive on Flowability and Compressibility of Fly Ash



Kaushal Kumar, Rishabh Arora, Jarnail Singh, Sarah Khan,
Lavesh Mishra, Prabhakar Bhandari, Saurav Dixit, and Chander Prakash

Abstract The aim of existing study is to prepare an adequate proportion of additive for better flowability of the fly ash suspension. The behavior of finer particle (fly ash) with and without addition of coarser particles added (bottom ash) has been investigated. The proportions of fly and bottom ash are 9:1, 8:2, and 7:3, respectively, (by weight). Flowability and compressibility characteristics of all the prepared combination have been determined. The addition of coarse bottom ash particles to finer fly ash particles improves the flowability as well as compressibility features. The extensive analyses also investigate the possibilities of transporting of ash through pipeline is better way.

Keywords Fly ash · Bottom ash · Flowability · Compressibility · Rheology

1 Introduction

Commonly in India, thermal power plants are the main source of electricity generation and used coal as a fuel. The use of coal as a fuel in thermal power plants, as well as its combustion, resulted in a considerable amount of ash Fly ash (FA) is made up of finer ash particles discharged with flue gases and collected through Electrostatic Precipitators (ESP), while bottom ash (BA) is made up of coarser particles collected

K. Kumar (✉) · R. Arora · J. Singh · S. Khan · P. Bhandari
School of Engineering and Technology, K.R. Mangalam University, Gurgaon 122103, India
e-mail: kaushal.kumar@krmangalam.edu.in

L. Mishra · S. Dixit
School of Management and Commerce, K.R. Mangalam University, Gurgaon 122103, India

C. Prakash
School of Mechanical Engineering, Lovely Professional University, Phagwara 144402, India

S. Dixit
Division of Research and Innovation, Uttaranchal University, Dehradun, India

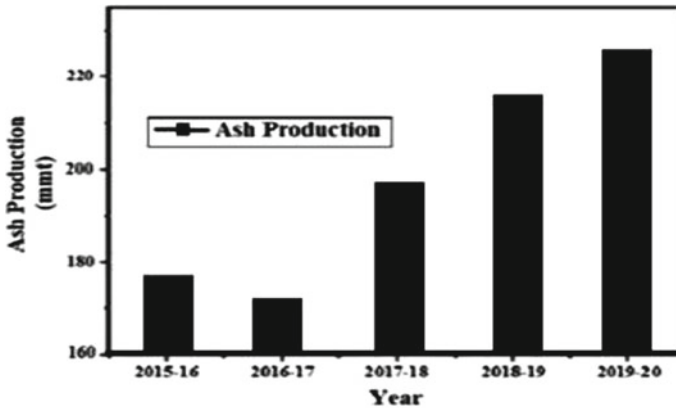


Fig. 1 Generation of ash from thermal power plants during last five calendar years

from the bottom boiler furnace. According to the 2019–20 report of Central Electricity Authority of New Delhi, India produces approx. 226.139 million metric tons of FA as shown in Fig. 1 [1]. FA is typically transported using the pneumatic mode, whereas BA is transported using the hydraulic mode via pipelines from the generating unit to the ash pond. A number of parameters affect the rheology of suspension which influences the design of transportation systems. In addition to its traditional uses, FA are now found application as a major corroboration in metal matrices for the development of composites. Low-cost FA is used to reinforce low-weight MMCs, giving them improved mechanical and tribological qualities [2].

This type of residual material contains spherical particles ranging in size from 1 to 100 μm , with oxides. Among them the hollow particles are called as cenosphere while the solid named as precipitators based on densities. The bulk density of the finer particles of FA stopped in thermal power plant chimneys maintain with in a specific limit. Authors also reported that FA has a theoretical density of about 2.17 g/cm^3 [3–5]. Precipitator particles are favored for instilling qualities such as wear resistance, stiffness, and strength in composites. Ultra-light composites, on the other hand, are made from cenosphere particles. There is a significant variance in the physical and chemical qualities of F and C type FA, which depending on the type of coal burned. In additionally, F type FA is the residual product of good quality coal like anthracite and bituminous while class C FA mainly generated by the combustion of low-rank coals. Normally, F type of FA utilized as reinforcement in the fabrication of composites using the P/M method [6–8]. Numerous studies have been conducted in order to check the rheology of the FA in the form of slurry [9–12]. But, study regarding the study of powder for conveying or use in other properties like compressibility and flowability are very limited or rare. So, through this investigation an effort has been done to study the influence of adding BA particles to the FA. The main aim of the study is to examine the effect of additive on flowability and compressibility of the FA particles.

In this study, flowability and compressibility of fine particulate FA was investigated without and with the addition of coarser particulate BA. The proportions of fly and BA are 9:1, 8:2, and 7:3, respectively, (% by weight).

2 Materials Characterization and Methods

During this study firstly the samples undergoes for the characterization and the laboratory tests has been conducted. Particle size distribution, settling and semi electron microscopy of the samples has been conducted to check the physical and morphological properties. Ash samples were collected from Rajiv Gandhi Thermal Power Station (RGTPS) located in southern part (Hisar) of Haryana, India. FA was collected from the ESP, and BA was taken under the combustion chamber. Figure 2 represented the pictorial view and SEM of BA and FA samples, respectively. In comparison to the regular shaped fine particles of FA, BA particles are thicker, asymmetrical, and have bad surface roughness. The color of bottom ash particles is quite darker as compared to fine particulate FA samples. In order to study the PSD (Particle Size Distribution), sieve analysis has been conducted. In the BA sample, approximately 62.49% of the particles are thicker than 150 μm , while only 7.39% are finer than 53 μm . The largest particle for FA is of 355 μm , with 62.79% of the particles being finer than 75 μm . as shown in Fig. 3.

3 Measurements

Prior from the physical testing the powder form of both the samples has been used for the study of the flowability and compressibility test. For this calculation the value of bulk density and tap density has been measured. The unit of both the densities was (g/cm^3). Three set of the experiments has been conducted for the each combination fly and BA. Average of three observations has been considered as the main value. The determined value of bulk and tap density further used for the calculation of Hausner's ratio and Carr's index.

4 Results and Discussion

The flowability and the compressibility of FA and BA are considered as some of the main or prime factors in order to achieving a nominal porosity [2]. The physical properties of FA and BA particles specially bulk and tap densities influences their flowability and compressibility characteristics. Flowability and compressibility characteristics of FA and BA mixtures have been determined by using Hausner's ratio and Carr's index as per Eq. (1) and (2) [13–19]:

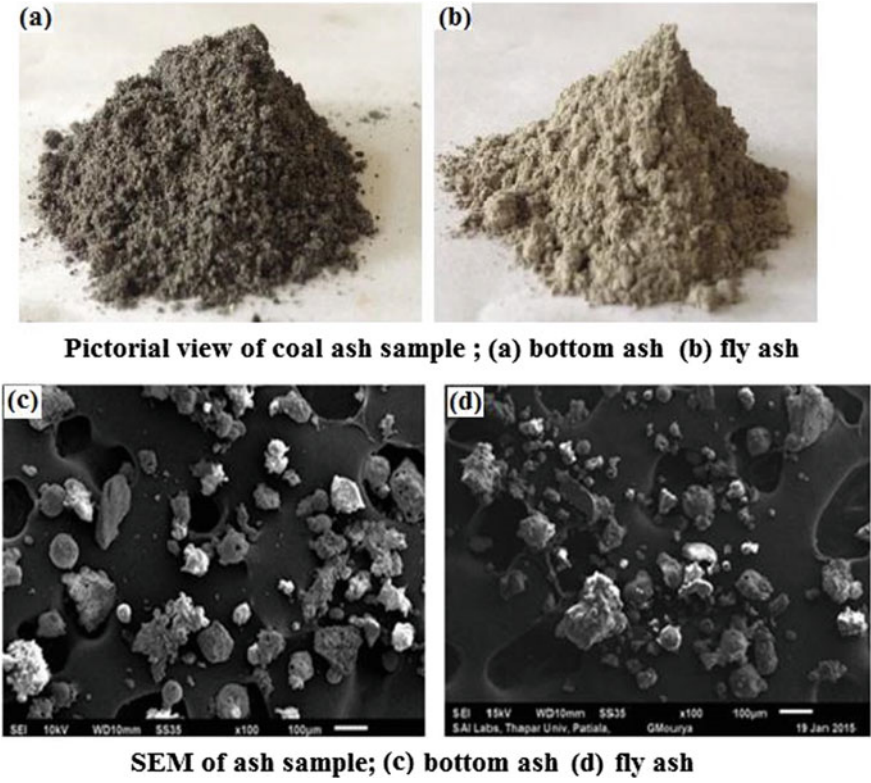


Fig. 2 Pictorial and SEM analysis of ash samples

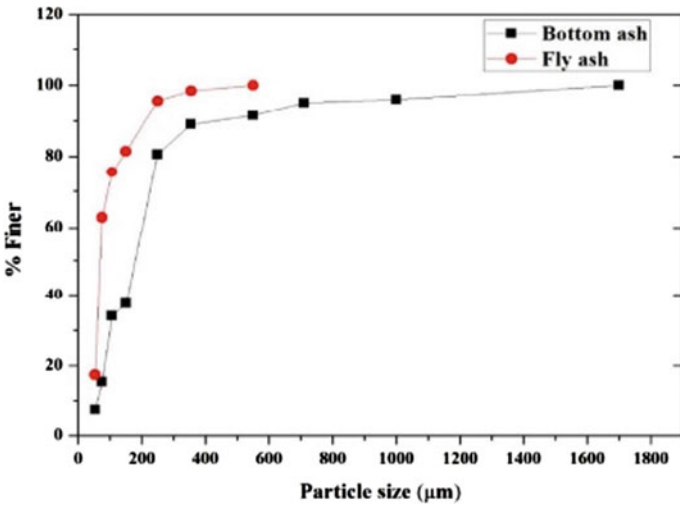


Fig. 3 Sieve analysis or PSD of the samples

Table 1 Hausner's ratio and Carr's index of the materials

Material	Composition ratio	ρ_B (g/cm ³)	ρ_T (g/cm ³)	Hausner's ratio	Carr's index
F.A.	10:0	0.95	1.03	1.08	8
F.A + B.A.	9:1	1.07	1.21	1.13	12
F.A + B.A.	8:2	1.18	1.35	1.14	13
F.A + B.A.	7:3	1.28	1.41	1.10	10

$$\text{Hausner's Ratio} = \frac{\rho_T}{\rho_B} \quad (1)$$

$$\text{Carr's Index} = 100 \times \left(1 - \frac{\rho_B}{\rho_T} \right) \quad (2)$$

where ρ_T is called as the tap density and ρ_B is called as the bulk density.

Hausner ratio is the ratio of the particle's tap density to its bulk density. Its value is set up as ≥ 1 , if it exists within the range of 1–1.1, it meant to be great flowability, and a range more than this indicates poor flowability. Similarly, Carrs index values of 0–10 are seen in particles with exceptional compressibility [13]. This is also known as the compressibility index. Table 1 shows the flowability and compressibility statistics for FA and BA mixture.

The value of bulk density is always less than the value of tap density through the experimentation, as shown in the Fig. 4. It was observed that the bulk density is just the primary stage and there is some gape between the particles which eliminates in while calculating the tap density. A similar result has been reported in the previous study also [6]. From the Figs. 4 and 5 it has been observed that up to a limit the addition of BA improves the flowability as well as compressibility of FA. It is clearly observed from the results that after the second case of additive or F.A.: B.A. (8:2). The value of Carr's Index as well as the value of Hausner's ratio is decreases, which indicate no more addition of BA in the finer particulate FA. The limit is considered as 8:2, up to which may case problem to the system or not beneficial in term of economic as well as better sustainable [14].

5 Conclusion

The behavior of FA powder without and with BA addition is studied at different additive compositions. In comparison to the irregularly shaped thicker particles of bottom ash, FA particles are finer, more uniform, and have an even surface texture. The addition of coarser BA particles to fine particulate FA increases the flowability and compressibility behavior. Initially the rates of tap density increase with the addition of BA but up to a fixed limit rather then it shows normal behavior. The mixture (FA and BA) having 8:2 ratios have been shown greatest flowability and

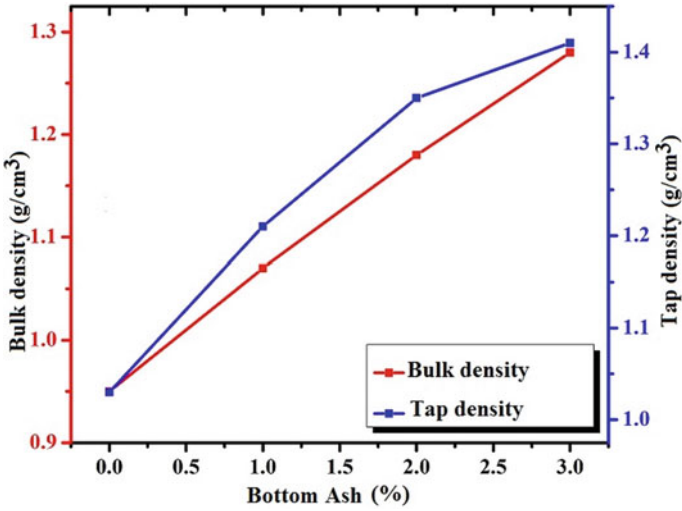


Fig. 4 Variation of densities with the addition of BA

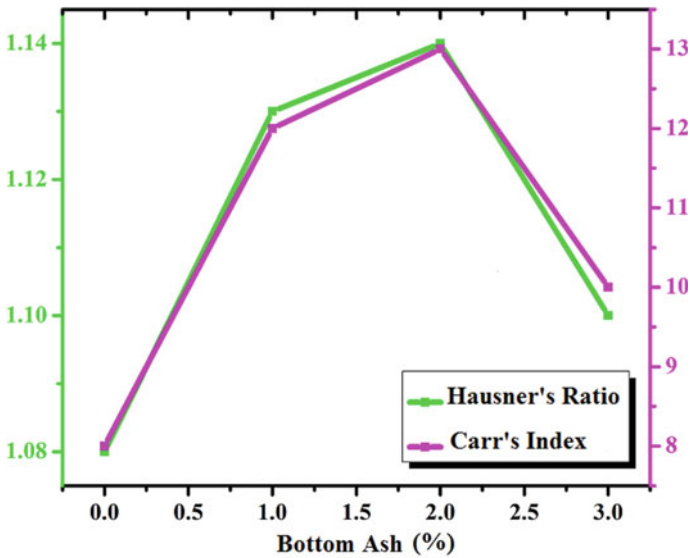


Fig. 5 Relationship between Hausner's ratio and carr's index

compressibility. It was observed from the flowability and compressibility test that addition of BA in the FA may improve the flowability but up to fixed amount beyond it may shows reverse trends.

References

1. Annual report Central Electricity authority (2019–20) New Delhi
2. Trivedi A, Sud VK (2002) Grain characteristics and engineering properties of coal ash. *Granular Matter* 4(3):93–101
3. Manimaran R, Jayakumar I, Mohammad Giyahudeen R, Narayanan L (2018) Mechanical properties of fly ash composites—a review. *Energy Sources Part A* 40(8):887–893
4. Ahmaruzzaman M (2010) A review on the utilization of fly ash. *Prog Energy Combust Sci* 36(3):327–363
5. Guo RQ, Rohatgi PK, Nath D (1996) Compacting characteristics of aluminium-fly ash powder mixtures. *J Mater Sci* 31:5513–5519
6. Kasar AK, Gupta N, Rohatgi PK, Menezes PL (2020) A brief review of fly ash as reinforcement for composites with improved mechanical and tribological properties. *JOM* 72(6):2340–2351
7. Biernacki JJ, Vazrala AK, Leimer HW (2008) Sintering of a class f fly ash. *Fuel* 87:782–792
8. Guo RQ, Rohatgi PK (1997) Preparation of aluminium-fly ash particulate composite by powder metallurgy technique. *J Mater Sci* 2(32):3971–3974
9. Kumar K, Kumar S, Kumar A (2019) Effect of additives on static settled concentration, pH and viscosity of bottom ash-water suspension. *J Mech Eng–Strojnícky Časopis* 68(3):49–58
10. Kumar K, Kumar S, Gupta M, Garg HC (2017) Effect of addition of bottom ash on the rheological properties of fly ash slurry at varying temperature. *IOP Conf Ser Mater Sci Eng* 149:012044
11. Kumar K, Kumar S, Gupta M (2016) Characterization of heavy metal trace elements in the fly ash from a thermal power plant. *Energy Sources, Part A* 38:2370–2376
12. Kumar K, Kumar S, Gupta M, Garg HC (2017) Characteristics of fly ash in relation of soil amendment. *Mater Today Proc* 4(2):527–532
13. Shishir MRI, Taip FS, Aziz NA, Talib RA (2014) Physical properties of spray-dried pink guava (*Psidium Guajava*) powder. *Agric Agric Sci Proc* 2:74–81
14. Singh A, Singh J, Sinha MK, Kumar R, Verma V (2021) Compaction and densification characteristics of iron powder/coal fly ash mixtures processed by powder metallurgy technique. *J Mater Eng Perform* 30:1207–1220
15. Verma P, Saha R, Chaira D (2018) Waste steel scrap to nanostructured powder and superior compact through powder metallurgy: powder generation, processing and characterization. *Powder Technol* 326:159–167
16. Singh A, Singh J, Sinha MK, Kumar R, Verma V (2020) Investigations on microstructural and micro hardness developments in sintered iron coal fly ash composites. *Sadhana* 45(1):1–13
17. Saker A, Cares-Pacheco MG, Marchal P, Falk V (2019) Powders flowability assessment in granular compaction: what about the consistency of hausner ratio. *Powder Technol* 354:52–63; Kumar K, Arora R, Khan S, Dixit S (2021) Characterization of fly ash for potential utilization in green concrete. *Mate Today Proc*
18. Dixit S, Stefańska A Digitisation of contemporary fabrication processes in the AEC sector. *Mater Today Proc* (2021)
19. Dixit S, Sharma K, Singh S Identifying and analysing key factors associated with risks in construction projects. In: *Emerging trends in civil engineering*

First Principle Investigations of Half-Metallicity in Co_2YZ ($Y = \text{Sc}, \text{Y};$ $Z = \text{P}, \text{As}, \text{Sb}, \text{Bi}$)



Ananya Shankar, Preetisha Goswami, Archana Tripathi, Ruby Jindal,
Rajni Gautam, Neeraj Kumari, Himani Yadav, and Sheetal Tyagi

Abstract The well-known half-metallic properties along with the electronic structure of series Co_2YZ ($Y = \text{Sc}, \text{Y}; Z = \text{P}, \text{As}, \text{Sb}, \text{Bi}$) were calculated by generalized gradient approximation of the density functional theory (DFT). The lattice parameter in the magnetic phase was optimized for both Cu_2MnAl and Hg_2CuTi structures to determine the very energetically stable structure. The magnetic properties, electronic structures and the density of states (DOS) were calculated and studied in the minority and majority spins to predict half metallicity. The hybridization of d-orbitals of neighbouring atoms in the lattice is considered to explain the half-metallic nature of these compounds.

Keywords Density Functional Theory · Heusler compounds · Half-metallicity · Ab-initio

1 Introduction

Heusler compounds have been greatly popular since they were discovered by Groot et al. [1] They are gaining preference in the spintronics field because of their stable half-metallicity, and high curie temperatures, which allow them to be operated at room temperature [2]. They have technological applications in giant magnetoresistance (GMR) [3], tunnelling magnetoresistance (TMR) and in spintronics-based-magnetic random access memory-) (MRAM) [4]. These half-metallic compounds display complete spin polarization at Fermi Level E_F , and thus have fully spin polarized currents, therefore making them efficient for spin injection, and as their lattice

A. Shankar · P. Goswami · A. Tripathi
Department of Physics, Gargi College, University of Delhi, Delhi, New Delhi 110049, India

R. Jindal (✉) · R. Gautam · N. Kumari · H. Yadav · S. Tyagi
School of Basic and Applied Sciences, K.R. Mangalam University, Gurugram, Haryana 122103,
India
e-mail: ruby.jindal@krmangalam.edu.in

structure resembles conventional semiconductors, they are useful for spintronic applications [5]. Heusler alloys are known for various types of magneto-caloric, mechanical, magnetic shape memory effect properties, thermoelectric, optical, elastic and in addition, their magnetic properties can be potentially tailored as per the need required [5–7]. There is linear correlation between the total magnetism of Heusler alloys and the valence electron no. in the compound, known as the Slater-Pauling rule. For Full Heuslers, it is given by $M_t = Z_t - 24$, where Z_t is the valence electrons number in the alloy, and 24 is double the number of occupied electrons in the minority band.

2 Computational Method

The calculations in these compounds were performed by using PWscf in DFT with the help of Quantum Espresso software package code. A plane wave pseudopotential method and the generalized gradient approximation formulated by the GGA-PBE scheme is employed [8, 9]. A kinetic energy cutoff is optimized at 50 Ry and a charge density cutoff is set to be 500 Ry in order to limit the plane wave expansion of the Kohn–Sham wave functions. The Brillouin zone is sampled by the Monkhorst–Pack Grids. A grid of $12 \times 12 \times 12$ mesh k -points was considered for calculations with a convergence criterion of less than 10^{-6} Ry.

Broyden–Fletcher–Goldfarb–Shanno (BFGS) [10] method is applied to obtain the lowest level energy and to optimize the structure. This method has an advantage of the absence of the spin-orbital coupling (SOC), which ensures a quick way to calculate the lowest energy structure. The Gaussian smearing width is taken to be 10^{-2} Ry while calculating the density of states (DOS) for each studied Heusler compound.

3 Results and Discussion

3.1 Structure of Heusler Alloys

Four interpenetrating cubic face centred cubic sublattices construct the Heusler alloys where four atomic bases are present at 4a (0, 0, 0), 4b (1/2, 1/2, 1/2), 4c (1/4, 1/4, 1/4) and 4d (3/4, 3/4, 3/4). Full Heuslers are of the form X_2YZ , where Y is transition element and Z is an sp element. Full Heuslers can adopt two structures: when the X atom occupies the 4a and 4b sites, the Y atom in 4c and the Z atom in 4d; or when the X atom occupies the 4a and 4c sites, the Y atom in 4b and the Z atom in 4d [11]. The former is known as the Cu_2MnAl or L_{21} structure, these are regular Heusler Alloys. The latter is known as the Hg_2CuTi or XA structure, these are inverse Heusler Alloys.

The studied compounds here were optimized for both structures, and an attempt is made to catch the more energetically stable structure for magnetic phase at optimized lattice parameters, and is reported in Table 1. For every studied compound, the L_{21}

Table 1 Compound under study, Optimized lattice parameter a , Energy of the more stable structure E_0 , difference in energies of the XA and L₂₁ structures ΔE , and the more stable structure

Full Heusler Compound	a (Å)	E_0 (Ry)	ΔE (Ry)	Stable Structure
Co ₂ YP	6.1	-686.9346595	0.05715383	L ₂₁
Co ₂ ScP	5.8	-701.40183478	0.07684275	L ₂₁
Co ₂ YAs	6.2	-693.33613228	0.0600629	L ₂₁
Co ₂ ScAs	6	-707.78330447	0.0719684	L ₂₁
Co ₂ YSb	6.4	-692.79239131	0.11917462	L ₂₁
Co ₂ ScSb	6.2	-707.22298105	0.11555454	L ₂₁
Co ₂ YBi	6.6	-828.01347255	0.09999769	L ₂₁
Co ₂ ScBi	6.4	-842.42651095	0.09298681	L ₂₁

structure displays more stability than the XA structure. Also, it is perceived that there is increase in lattice constant as we increase the Z atom size (P to Bi), resulting in the expansion of the crystal which is expected as well. Analogous outcomes are obtained when Sc atom is switched by Y atom.

3.2 Density of States (DOS)

For the compounds, which have been studied in this work, the DOS has been calculated and are shown in Fig. 1. Each subfigure has two parts which can be separated into upper half and lower half. The majority spin channel is represented by the upper half part, and the lower part is signified by the minority spin channel. The Fermi level (E_F) is shown as vertical line at 0 eV. In all the compounds the profiles of the majority and minority spin are entirely different, which confirms that all the studied structures in this work are of magnetic in nature.

All the compounds display semiconducting behaviour with a small band gap in the lower part of minority bands around the Fermi Level E_F , while in the upper half of majority bands, the DOS is finite around E_F displaying metallicity, thus exhibiting half-metallic nature or nearly half-metallic nature. From Fig. 1, it can be determined that Co₂YP, Co₂YAs, Co₂YSb and Co₂ScSb are half metallic and rest of them are nearly half metallic.

The general shape of the density of states is same for all the compounds near Fermi energy which can be the result of the similar valence structure of these compounds with very small differences. From the PDOS in the figure, the Co atom is found to play a prominent role near E_F as compared to the Z and Y atoms and is also responsible for the asymmetric nature between the majority and minority spin bands.

As the size of Z atom increases, the d-orbitals overlap decreases because of the loss in strength of interaction between transition elements, which in turn causes the decrease of width of the band gap. In the series Co₂YZ (Fig. 1a, c, e, g) and Co₂ScZ (Fig. 1b, d, f, h), it can be observed that as the size of the Z atom increases,

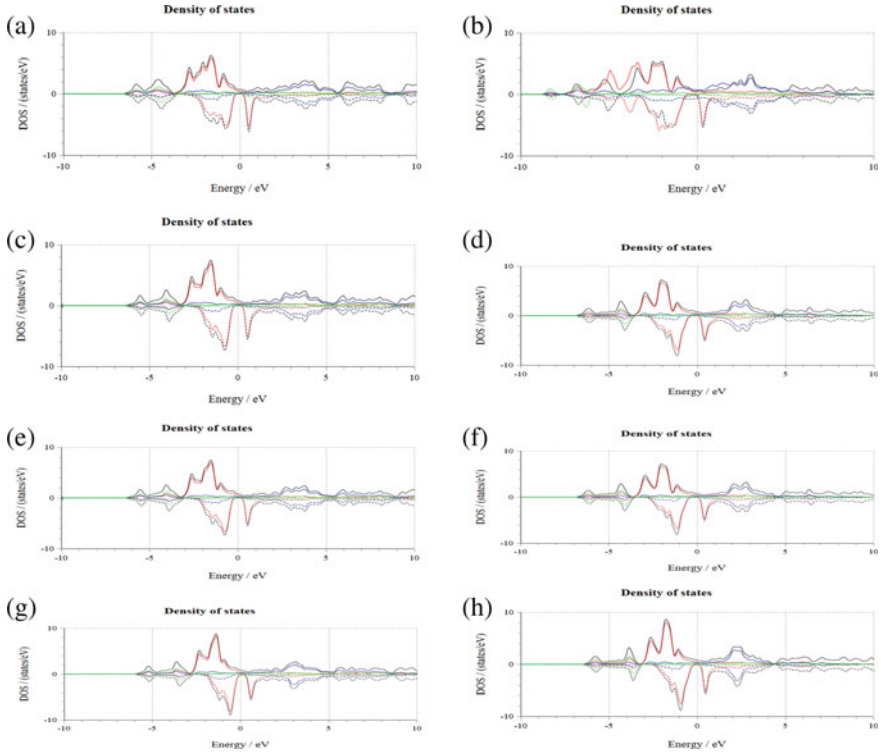


Fig. 1 Density of states for **a** Co₂YP; **b** Co₂ScP; **c** Co₂YAs; **d** Co₂ScAs; **e** Co₂YSb; **f** Co₂ScSb; **g** Co₂YBi; **h** Co₂ScBi (colour scheme: black: total DOS, red: X, blue: Y, green: Z)

the position of E_F shifts towards the valence band. Also, the second highest peaks below the E_F level in both majority and minority spin appear to merge with the rise in size of the Z atom, showing the weakening of transition elements interaction.

From Fig. 1, it can also be concluded that when we replace the Sc atom with Y atom in the Co₂ScZ compound, the shift of E_F towards valence band becomes visible.

4 Conclusion

The electronic as well as the magnetic properties of the Full Heusler alloys Co₂YZ (Y: Sc, Y; Z: P, As, Sb, Bi) have been calculated with the help of density functional theory. All the materials were optimized and had an equilibrium L2₁ structure. The density of states calculations predicted half-metallic nature for three compounds (Co₂YAs, Co₂YSb and Co₂ScSb) and rest of them are nearly half-metallic. The increase in size of the Z atom increases the lattice constant of the crystal and results in the decrease

d-orbitals overlap which eventually is accountable for the weakening of half-metallic nature in Co_2YZ series and strengthening in Co_2ScZ series in the studied alloys. This analysis reveals the prominence of the sp element (Z atom) in case of the full Heusler alloys in their electronic and magnetic properties. These nearly half-metallic alloys can be used effectively with proper doping if studied further.

References

1. De Groot RA, Mueller FM, van Engen PG, Buschow KHJ (1983) New class of materials: half-metallic ferromagnets. *Phys Rev Lett* 50:2024
2. Ram M, Saxena A, Aly AE, Shankar A (2020) Half-metallicity in new Heusler alloys Mn_2ScZ (Z = Si, Ge, Sn). *RSC Adv* 10:7661–7670
3. Chadov S, Graf T, Chadova K, Dai X, Casper F, Fecher GH, Felser C (2011) Efficient spin injector scheme based on Heusler materials. *Phys Rev Lett* 107:047202
4. Wolf SA, Awschalom DD, Buhrman RA, Daughton JM, Von Molnar S, Roukes ML, Chtchelkanova AY, Treger DM (2001) Spintronics: a spin-based electronics vision for the future. *Science* 294:1488
5. Everhart W, Newkirk J (2019) Mechanical properties of Heusler alloys. *Heliyon* 5:1–15
6. Joshi H, Rai DP, Hnamte L, Laref A, Thapa RK (2019) A theoretical analysis of elastic and optical properties of half Heusler MCoSb (M=Ti, Zr and Hf). *Heliyon* 5:1–15
7. Singh S, Gupta DC (2019) Magneto-electronic, thermoelectric, thermodynamic and optical properties of rare earth YCoTiX (X = Al, Ga, Si, Ge) alloys. *J Alloy Compd* 806:1292–1308
8. Giannozzi P, Stefano B, Bonini N, Calandra M, Car R, Cavazzoni C, Ceresoli D, Chiarotti GL, Cococcioni M, Dabo I (2009) QUANTUM ESPRESSO: a modular and open-source software project for quantum simulations of materials. *J Phys Condens Matter* 21:395502
9. Perdew JP, Burke K, Ernzerhof M (1996) generalized gradient approximation made simple *phys. Rev Lett* 77:3865–3868
10. Fischer TH, Almlof J (1992) General methods for geometry and wave function optimization. *J Phys Chem* 96:9768–9774
11. Galanakis I, Mavropoulos P, Dederichs PH (2006) Electronic structure and Slater–Pauling behaviour in half-metallic Heusler alloys calculated from first principles. *J Phys D Appl Phys* 39:765

Future of Indian Manufacturing: Lean and Green Manufacturing System (LGMS)



Arun Arora and Vijay Kumar Singh

Abstract There is a lot of demand on Indian manufacturing companies these days to keep their processes running by overcoming environmental and sociological difficulties as well as adhering to government regulations. However, neither lean manufacturing nor green manufacturing principles can offer a viable solution to these issues. As a result, now is the time to create a hybrid production system that combines lean and green manufacturing. However, implementing a lean and green manufacturing system will not be simple, as it will be hampered by a number of obstacles. The authors of this study considered all potential hurdles to the implementation of lean and green manufacturing methods, and they ranked the most essential barriers to be eliminated first for a successful lean and green manufacturing system implementation. A self-designed questionnaire was distributed to respondents, and data was collected on a 5-point Likert scale, with factor analysis used to identify the primary hurdles out of the potential 57 limitations. Resistance to change, a lack of practical expertise, and cost/benefit limits are the key roadblocks to implementing lean and green manufacturing practices.

Keywords Manufacturing firms · Lean manufacturing · Green manufacturing · Lean and green manufacturing and barriers

1 Introduction

Many researchers have looked into why companies do not use lean and green manufacturing systems in their own company, and the answer is that top-level management lacks commitment and the government does not support it enough. Consequently, high management and government support are required for the implementation of a lean and green manufacturing system [1]. Lean and environmentally friendly manufacturing processes can only be implemented with the full support of senior management and a clear grasp of the implementation process [2]. A lack of resources,

A. Arora (✉) · V. K. Singh
School of Mechanical Engineering, Lovely Professional University, Phagwara, Punjab, India
e-mail: arun13arora@gmail.com

including human capital, financial capital, and time, is another problem that small- and medium-sized firms face.

Lean and green manufacturing strategies have been found to improve quality, reduce inventory, and increase profitability in numerous industries in industrialised countries [3, 4]. Consequently, the widespread adoption of LGMS in developing nations is less prevalent than in developed countries, particularly in the manufacturing business, where LGMS is seen as a pricey new concept that requires the skills of a professional individual. When it comes to implementing a green and lean manufacturing system at work, how can manufacturers get beyond the roadblocks?

By looking at 57 potential hurdles, the study was able to identify the most relevant variables delaying the implementation of a lean and green manufacturing system, which were then verified using confirmatory factor analysis.

Among the pioneers of lean and green manufacturing were King and Lenox, Simons and Masons, who concentrated on the intersection of quality and environment, reducing processes that do not add value to the product and that increase product costs. A wide variety of industries have implemented lean and green manufacturing practices in the past. Approximately one-third of the sample size was aware of LGMS, but either declined or were unable to use it, according to Abu et al.

Only a few studies have been done to identify the most important factors that lead to the effective deployment of lean and green manufacturing systems. Since no research has been conducted on the challenges of implementing lean and green production systems, there is little information available. There are many obstacles to lean and green manufacturing adoption, which is why this author has decided to write about them.

Research Question: What are the most important hurdles in the way of implementation of lean and green manufacturing system?

2 Literature Review

A total of 24 hurdles were identified by Kumar and Vinod in their study, which included issues such as government lack of top management commitment and understanding and support for the system due to policy changes, as well as inadequate selection of change agents and improvement teams [5]. Among the many challenges faced by lean and green manufacturing systems are the following: completing daily tasks in a standardised manner (standard routine), identifying problems by analysing key indicators, communicating regularly with their employees, interacting with the support areas and higher hierarchical levels, going to the shop floor to realise the problems, prioritising the identified problems, examining any taken improvements, and ensuring that the system is sustainable; [6]. Continuous production is a given in process industries; large batch production is required to maximise capacity utilisation; lack of lean education and expertise; financial constraints; cultural barriers; and a lack of senior management support and interest in lean are all obstacles to its implementation [7].

When Abolhassani et al. looked at the barriers to LGMS implementation in Pennsylvania and West Virginia, they found that a lack of management commitment, technical ignorance, a lack of understanding of benefits, a lack of cultural fit for lean, resistance to change on the part of both management and employees, a lack of sustainability for lean, high investment costs, and previous failures of lean were all to blame [2].

There are a number of reasons why LGMS is unlikely to be implemented for workers: new difficulties and the fear of making mistakes that could result in losing one's job are some of the reasons why workers are reluctant to accept new opportunities and take on new responsibilities at work [8]. Bajjou and Chafi came up with a total of nine obstacles. A lack of government support and insufficient financial resources were among the organisational obstacles. Resistance to change, inexperienced labour, a lack of knowledge of lean construction concepts, and a lack of commitment from the top management, as well as cultural and attitudinal challenges were among the human resources-related obstacles. It can be found at [9]. According to Coetzee et al. [10], Toyota's adoption of LGMS is based on RFP and continuous improvement.

By becoming more aware of the environmental impacts of their operations, consumers have pushed the industry toward green practises such as green lean six sigma (GLSS). There have been many research on how to put it into practise, but there have been few studies on how to overcome the obstacles that stand in the way of its implementation. Kaswan et al. investigate how green and lean can be implemented in the industrial industry, as well as the challenges and solutions to those challenges. Using principal component analysis, we were able to identify and classify 18 potential roadblocks. The Decision Making Trial and Evaluation Laboratory (DEMATEL) approach is employed in this study to examine the crucial and causal relationship between the two. Managing obstacles were determined to be the most common after environmental and organisational impediments. Policymakers can use this information to better understand how to implement green and lean systems in their organisations. It is estimated that most developed countries use government agencies rather than industry to evaluate the utilisation of available capacity (CU). As an engineering manager, you must be able to identify massive capacity waste loopholes within a plant in order for industrial progress to take place. Additionally, 16 lean systems implementation obstacles were found to suggest that management-related constraints had the greatest impact on small- and medium-sized businesses' ability to successfully apply LSS. Weak supplier liaison and poor project selection are prudent factors; poor belt training selection, lack of overall employee participation, and a lack of awareness of LSS are strategic factors; and a lack of management commitment and involvement is strategic; high implementation costs, resistance to culture change, and lack of training funds are strategically important as well. The green lean six sigma (GLS) technique can help reduce environmental harm and deliver products of near-true value. The drawbacks of any one of the three techniques can be overcome by combining them. In order to reduce waste, rejection, and hazardous gas emissions, an integrated strategy is needed. Using theoretical results,

such as measurements for preparedness, barriers, and toolkits, this study incorporates elements of green, lean, and six sigma. GLS is a long-term plan to increase productivity while safeguarding the environment that can be used by practitioners and management of industrial organisations.

3 Research Methodology

A self-designed questionnaire with 57 hurdles to LGMS adoption has been developed based on a thorough literature assessment by the authors. The questionnaire is divided into three main sections. There are 22 hurdles to cultural and human attitudes, 14 barriers to knowledge, and a total of 21 impediments to resources.

3.1 Objective

Main aim of this study is to find most important factors that affect the implementation of lean and green manufacturing system.

H0: There are no factors affecting the implementation of lean and green manufacturing system.

Ha: There are few factors affecting the implementation of lean and green manufacturing system.

3.2 Data Collection

As the state's capital, Dehradun was chosen for this investigation. Dehradun-based manufacturing companies were the focus of the investigation. The researchers in this study relied on a straightforward random convenient sampling strategy to gather their data. There were 352 males and 148 ladies out of a total of 500 participants.

3.3 Methodology Adopted

Studies have used tests for data normality, reliability analysis on questionnaires, and symmetrical distribution to see if data sets are symmetrical when looking both left and right of centre points, as well as tests to determine whether or not data sets are normally distributed. The following tests were used to conduct factor analysis (Tables 1, 2 and 3).

It is possible to decrease the vast number of variables into smaller numbers of factors using the technique of confirmation factor analysis. All variables are

Table 1 Test of normality

Descriptive statistics	For study
a) Kolmogorov–Smirnov and Shapiro–Wilk test for data	To check the significant value of data

Table 2 Reliability analysis

Descriptive statistics	For study
a) Case processing summary	To check if there is any missing value in data
b) Combined reliability analysis	To check the reliability of questionnaire
c) Item-total statistics	To check if any item deleted then value of Cronbach’s alpha should be less than total reliability of Cronbach’s alpha
d) Reliability statistics of culture and human attitudinal issue	To check Cronbach’s alpha value for CHAI
e) Reliability statistics of knowledge issue	To check Cronbach’s alpha value for KI
f) Reliability statistics of resource issue	To check Cronbach’s alpha value for RI
g) Common method variance	To check the cumulative % of variance

Table 3 Factor analysis

Descriptive statistics	For study
a) KMO and Bartlett’s test	To measure the sampling adequacy
b) Total variance explained	To check cumulative % variance of rotation sum of squared loading
c) Rotated component matrix	For sub-items and factors
d) Factor naming	Naming of all factors

combined into a single common score using this method to get the most common variance possible (Fig. 1).

4 Data Analysis

All variables were found to have skewness and kurtosis values between -1.98 and $+1.98$, which is within the acceptable range for all 58 variables under consideration. The case processing summary also revealed that there were no missing variables in the data set, which included 22 barriers relating to culture and human attitude, 14 barriers concerning knowledge, 21 barriers concerning resources, and one barrier depicting item.

The Kolmogorov–Smirnov test results show that the data obtained for the study is normal, with a significance level of less than 0.05 for all variables.

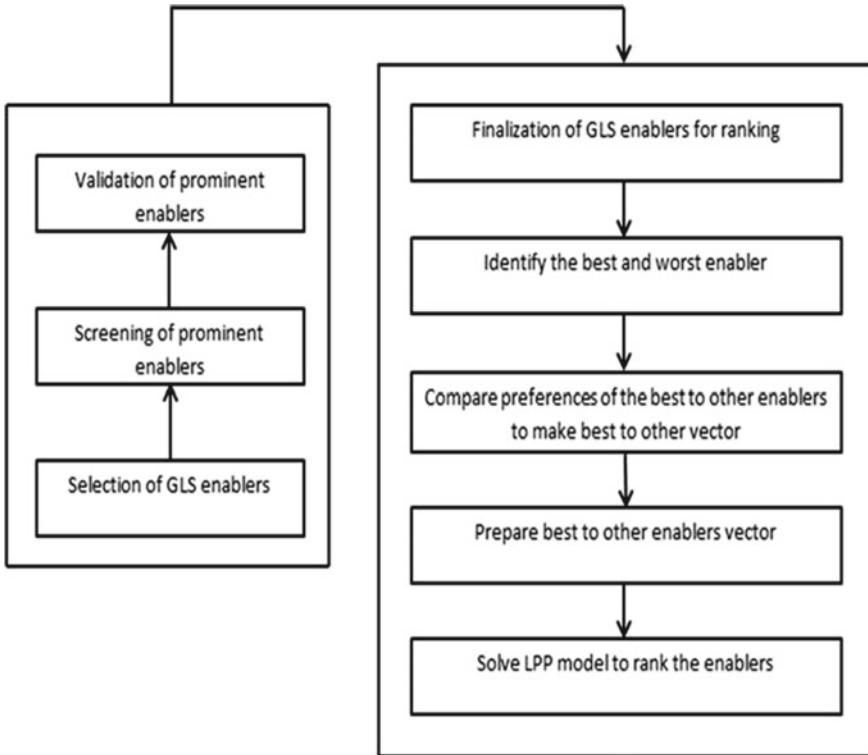


Fig. 1 Flow diagram for CFA-01

4.1 Reliability Analysis

Case processing summary shows that there are no missing variables.

The questionnaire’s combined reliability analysis is 0.960, well above the acceptable threshold of 0.50.

Assuming the same group of respondents are given a set of questionnaires with a Cronbach’s alpha value of 0.960, then there is a 96% chance that they will provide the same answer. In the table “Item-Total Statistics,” the value of “Cronbach’s alpha if item deleted” is 0.959, which is less than the Cronbach’s value of reliability analysis of the questionnaire, i.e. 0.96, hence no items in the questionnaire are to be deleted. Culture and human attitudes reliability analysis is 0.896, which is far above the acceptable value of 0.5. Knowledge issue’s reliability analysis has a rating of 0.852, which is much over the 0.50 threshold. Its reliability analysis is 0.897, well over the acceptable threshold of 0.50.

As a result, we may conclude that the questionnaire as a whole is reliable enough to achieve the study’s objectives.

There is a cumulative percentage of total variation explained of 30.325, which is less than 60% of the entire variance. The lack of a common bias in the methods used suggests that the data collected is ready for analysis.

KMO Bartlett’s test measure of 0.959 shows that the data set is eligible for factor analysis in principal component analysis (PCA).

Conclusion: The independent variable accounts for more than 50% of the dependent variable’s variation (52.167%), and hence, it falls in the allowed range of variance.

It is estimated that 12 elements and 22 sub-factors can influence the implementation of a lean and environmentally friendly manufacturing system using a rotatable component matrix. The remaining 36 variables were found to have little or no impact (Table 4).

The 12 different factors can be named as.

Table 4 Factors naming

Factor 1	Factor 2	Factor 3	Factor 4	Factor 5	Factor 6
CHAI 11 (Lack of top management commitment)	KI 4 (Complexity of design to reduce consumption of resource/energy)	RI 14 (Low customer demand)	RI 15 (Market competition)	RI 21 (Workers’ resistance)	KI 1 (Absence of sound planning systems)
CHAI 8 (Lack of mutual trust)	CHAI 10 (Lack of positive culture)	KI 9 (Lack of customer awareness about green)	RI 6 (High short-term costs)	–	–
RI 18 (Resistance to technology advancement adoption)	KI 3 (Complex to measure and monitor the environmental practice)	–	–	–	–
Factor 7	Factor 8	Factor 9	Factor 10	Factor 11	Factor 12
RI 9 (Lack of organisational resources)	KI 13 (Lack of IT implementation)	CHAI 22 (Weak legislation)	RI 10 (Lack of support and guidance from regulatory authorities)	RI 19 (Technological risk)	RI 2 (Cost implications)
CHAI 13 (Location constraints)	–	CHAI 15 (Non-adoption of cleaner technology)	CHAI 7 (Lack of human resource)	–	–
–	–	–	KI 6 (Lack of awareness about potential benefits)	–	–

Table 5 CFA - The measurement model

CMIN/DF	1.006
GFI	0.990
NFI	0.971
CFI	0.979
RMSEA	0.004
P-value	0.000

- (1) Resistance to change.
- (2) Lack of practical knowledge.
- (3) Buyer's hesitation.
- (4) Financial constraints.
- (5) HR constraints.
- (6) Operational constraints.
- (7) Supply chain constraints.
- (8) IT constraints.
- (9) Green constraints.
- (10) Cost/benefit constraints.
- (11) Business risk.
- (12) Huge cost.

Out of the 12 possible factors only three can be considered for confirmatory factor analysis as they contain more than three items [11–13].

Hence, formed three factors are confirmed using AMOS 20 (Table 5).

Because of this, we ruled out the null hypothesis and argued that there are three elements that influence implementation of the lean and green manufacturing system.

Thus, we reject the null hypothesis and assert that there are three factors that influence the deployment of the lean and green manufacturing systems.

5 Result and Discussion

It is clear that the factors and their items are valid because the loadings for the first factor, "Resistance to change," have loadings greater than or equal to 0.50 for the following reasons: Lack of top-level commitment, a trust deficit between coworkers, and a resistance to adopting new technologies. A second factor, "Lack of Practical knowledge," has loadings of 0.61 for complexity of design to reduce resource/energy consumption, 0.62 for a lack of positive culture, and 0.60 for complexity of measurement and monitoring environmental practises, which are all higher than 0.50, confirming the factors and their items.

There are three more variables that have loadings of 0.59 for lack of support from regulatory authorities, 0.55 for human resources, and a 0.56 lack of awareness about

potential advantages. These loadings are higher than 0.50, and so the factors and their items have been confirmed.

6 Limitation and Conclusion

1. However, it is possible that the study's results cannot be generalised to the entire manufacturing sector due to the fact that only a few manufacturing industries in Dehradun were included in the study.
2. Results of the study are influenced by the demographics of the participants and the size of the sample.
3. If the sample size is raised or decreased from 500 people, the findings may be affected.

If a business wants to successfully apply lean and green manufacturing techniques, we may conclude that the three primary obstacles that may stand in the way are resistance to change, a lack of practical expertise, and cost/benefit limits.

References

1. Singh C, Singh D, Khamba JS (2021) Analyzing barriers of green lean practices in manufacturing industries by DEMATEL approach. *J Manuf Technol Manag* 32:176–198
2. Abolhassani A, Layfield K, Gopalakrishnan B (2016) Lean and US manufacturing industry: popularity of practices and implementation barriers. *Int J Product Perform Manag* 65:875–897
3. Jamil N, Gholami H, Saman MZM, Streimikiene D, Sharif S, Zakwan N (2020) DMAIC-based approach to sustainable value stream mapping: towards a sustainable manufacturing system. *Econ Res Ekon Istraživanja* 33:331–360
4. Gholami H, Jamil N, Mat Saman MZ, Streimikiene D, Sharif S, Zakuan N (2021) The application of green lean six sigma. *Bus Strategy Environ* 1–19
5. Kumar DS, Vinodh S (2020) TISM for analysis of barriers affecting the adoption of lean concepts to electronics component manufacture. *Int J Lean Six Sigma* 11:1141–1173
6. Gaspar F, Leal F (2020) A methodology for applying the shop floor management method for sustaining lean manufacturing tools and philosophies: a study of an automotive company in Brazil. *Int J Lean Six Sigma* 11:1233–1252
7. Panwar A, Jain R, Rathore APS (2015) Lean implementation in Indian process industries—some empirical evidence. *J Manuf Technol Manag* 26:131–160
8. Thanki SJ, Thakkar J (2014) Status of lean manufacturing practices in Indian industries and government initiatives: a pilot study. *J Manuf Technol Manag* 25:655–675
9. Bajjou MS, Chafi A (2018) Lean construction implementation in the Moroccan construction industry: Awareness, benefits and barriers. *J Eng Des Technol*
10. Coetzee R, Dyk LV, Merwe KRVD (2018) Towards addressing respect for people during lean implementation. *Int J Lean Six Sigma* 27:79–91
11. Hair JF, Page M, Brunsveld N (2006) *Essentials of business research methods*. Routledge
12. Hair JF, Page M, Brunsveld N (Revised 2015) *Essentials of business research methods*. Routledge
13. Hair JF, Hult GTM, Ringle CM, Sarstedt M (2021) *A primer on partial least squares structural equation modeling (PLS-SEM)*. Sage publications

Experimental and Computational Wear Studies of Alumina and Zirconia Versus SS316L for Hip Prosthesis



S. Shankar, R. Nithyaprakash, and R. Naveen Kumar

Abstract Hip implants are widely used in surgeries to heal hip fracture. Even normal hip bones wear at the joint section due to aging and improper design, so hip implants must hold its original hip components design for a long period of time. The materials used for hip implants must be biocompatible and have good mechanical properties. In this present study, the selected biomaterials are SS316L stainless steel, alumina, and zirconia ceramics. The main aim of this study is to investigate the wear rates of these bio compatible materials to determine its life expectancy. This study involves experimental wear testing of SS316L and ceramic materials as ball. The test is done to predict the long-term wear analysis (10 km) under constant load for both dry and lubricated conditions (using saline solution). The test parameters considered are different sliding velocities and loads, the corresponding coefficient of friction and wear coefficient are calculated. Finite element model using ANSYS on the head and cup of hip implant are modeled to estimate the linear and volumetric wear. Contact pressure analysis is done only for a total of 5 million cycles to predict 5 years of life. The results from both tests are compared with each other to determine the best materials for the hip implants.

Keywords Implants · Biomaterials · Tribometer · Contact pressure · Wear

1 Introduction

Hip replacement involves replacing hip joint by a prosthetic implant called hip prosthesis. Hip replacement surgery is performed as a total replacement (THR) or hip resurfacing technique. Such joint replacement surgery is done to relieve arthritis pain. THR consists of replacing acetabulum and the femoral head with stem, while hip resurfacing only replaces the femoral head and acetabulum cup. In hip replacement,

S. Shankar (✉) · R. Nithyaprakash

Department of Mechatronics Engineering, Kongu Engineering College, Perundurai, Erode, India
e-mail: shankariitm@gmail.com

R. Naveen Kumar

Department of Mechanical Engineering, Kongu Engineering College, Perundurai, Erode, India

Table 1 Mechanical properties for various materials

Materials Properties	SS316L	Alumina	Zirconia
Density (kg/m ³)	8000	3950	6350
Elastic modulus (GPa)	193	300	210
Poisson's ratio	0.275	0.21	0.34

the femoral head and acetabulum are removed and replaced with artificial biomaterials. In hip resurfacing, the femoral head is not removed, but is instead trimmed and capped with a smooth metal covering. The sliding wear behavior of SS 316 L was analyzed [1]. Sliding wear experiments were carried out at various temperatures up to 55 °C at constant load (20 N) and sliding speed (0.8 m/s) using a pin-on-disc test rig. The test results showed that the wear increased considerably with the temperature. SS316L is widely used biomaterial [2].

Wear of the bearing surface increases the revision rate of the total hip replacements and one of the reasons for this the type of materials that are implanted in humans. The present study focuses on calculating the friction coefficient and wear rate of metal-on-ceramics, i.e., SS316L in contact with Al₂O₃ and zirconia considering long-term conditions (up to 10 km run) using pin-on-disc tribometer for different sliding velocities under dry and lubricated conditions. Then utilizing finite element concepts to compute the linear and volumetric wear for the hip implants subjected to normal walking cycle for the above said bearing couples.

2 Materials and Method

2.1 Biomaterials

The biocompatibility of biomaterials refer to minimal interaction with its surrounding tissues in the body when implanted. The examples of these include SS 316L, titanium, alumina, partially stabilized zirconia, and ultrahigh molecular weight polyethylene. Out of these, the wear rates of SS316L stainless steel, alumina, and zirconia are tested for tribological consequences. These materials are chosen are based on several previous works conducted experiments on alumina as biomaterial to determine its wear properties [3]. SS316L was chosen as counter face the material [4]. The mechanical properties of these materials are shown in Table 1.

2.2 Ball-On-Disc Tribometer

Initially, the weight of the ball, holder, and ball along with holder is noted and tabulated in the meantime, the disc counter face is held firmly in the disc. The holder

and specimen is placed on the end of the lever arm. A constant dead load of 20 N is applied to the ball via a pulley system. The track radius is kept at 40 mm. The experiment is done for a sliding distance of 10 km for varying velocities of 1, 1.5, 2, 2.5 m/s. Then the intender is calibrated using the computer software. During the test duration, the entire apparatus is left undisturbed, and after completion, the weight loss is calculated and tabulated. The track and the ball are cleaned using acetone. For the lubricated running conditions, the entire procedure is followed with the only difference of a constant flow of saline solution. The total set up of the tribometer is shown in Fig. 1.

The wear rate was calculated from the weight loss of the sample and expressed in terms of wear loss per unit sliding distance. In the present experiment, the parameters such as speed and time are varied for each condition while keeping the load constant. These parameters are given in Table 2.

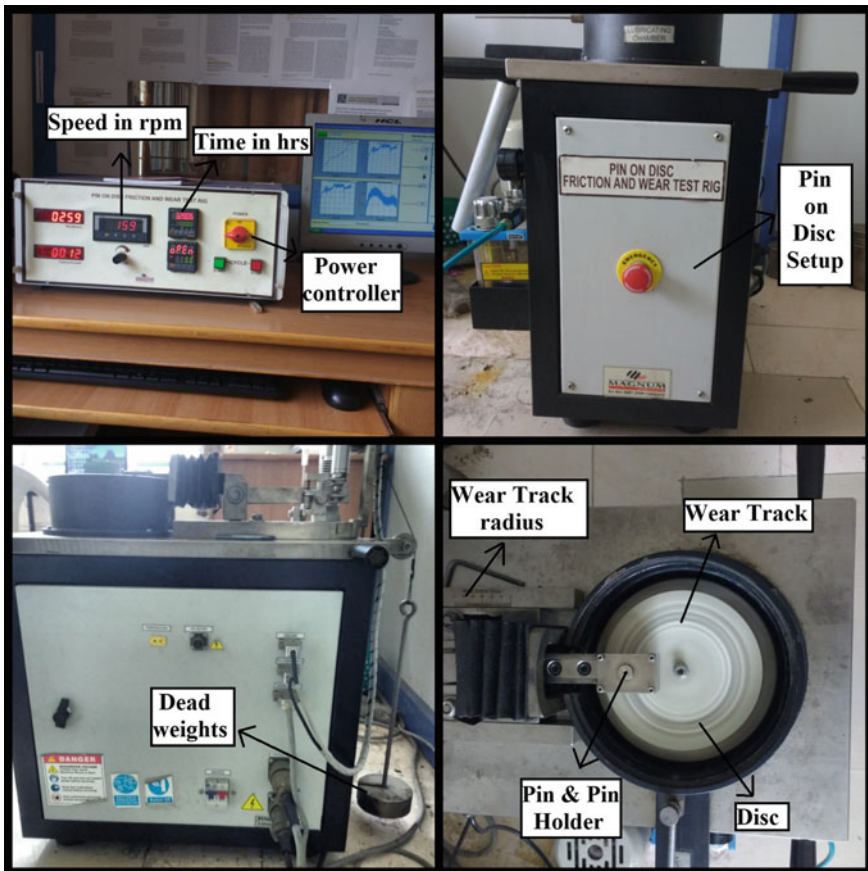


Fig. 1 Tribometer setup

Table 2 Parameters taken during sliding wear test

Ball material	Alumina and zirconia
Disc material	SS316L
Ball diameter	10 mm diameter
Sliding speed (m/s)	1, 1.5, 2, 2.5
Conditions	Dry and lubricated
Normal load (N)	20
Sliding distance (m)	10,000

2.3 Finite Element Analysis

In order to calculate the wear rates for 3D shapes of the hip implants, finite element analysis plays as vital role. The total 3D shape of the hip implant is analyzed for short term [5]. The wear test and finite analysis on the UHWMPE against metal or ceramic were reported in literature [6]. This led to the testing the SS316L against ceramics to determine its linear and volumetric wear rates. The ANSYS model of the project is shown in Fig. 2.

The ceramic materials are chosen for the acetabulum cup and the stainless is used for femur head. The experiment focuses on the contact wear analysis on the cup and head without considering the femur stem. The head and cup were meshed using SOLID 186 a 20-node higher order element which supports large deflection, hyper-elasticity, and creep behavior. The cup and head individually meshed with element edge length of 2 mm. A full model of hip implant without femur stem is formed with 16,416 elements and 64,458 nodes.

After the modeling, the boundary conditions are applied. First, the motion is arrested by locking the degree of freedom for all the areas behind the surface of the cup. This pivots the cup in place when the load is applied. A load of 2410 N is applied on the central node or key point of the head. This exact load is applied in order to simulate the gait activities. The contact analysis is done between the inner surface of cup and head. The head is chosen as the contact target where the cup is chosen as the surface. The average coefficient of friction of the dry condition is applied in

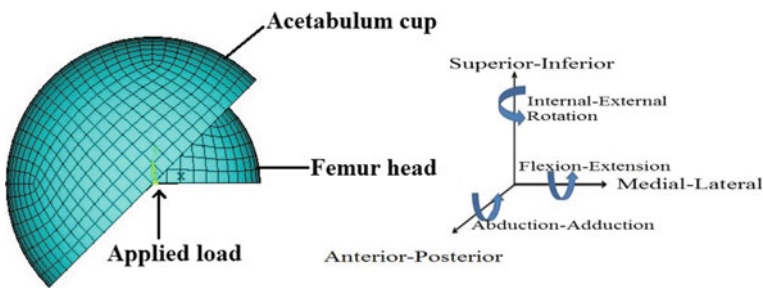


Fig. 2 FEA model

order to analyze the contact pressure. This is further used in the calculation linear and volumetric wear.

3 Results and Discussion

3.1 Friction Coefficient for Varying Velocities

The coefficient of friction developed between SS316L and ceramics for varying sliding velocity conditions is shown in Fig. 3. The experiment is conducted for a total of 10 km under constant load. In case of alumina, the friction starts to drop when the velocity increases. But as the velocity is further increased, the coefficient friction again starts to rise. For lubricated conditions, the friction starts to rise for the first increase in velocity. Then the friction starts to drop for further increase in velocity.

The friction developed between SS316L and zirconia is less compared to that of alumina. Since zirconia is less hard than alumina. It is seen in the graph that the maximum average coefficient of friction is 0.45 for dry conditions. Initial drop in coefficient of friction is comparatively high compared to further increase in velocities. Then the rate at which the friction drops is reduced by as much as 30.9% as the velocity increases. In case of lubricated condition, the COF starts at 0.39. Then the friction starts to reduce step by step for increase in sliding velocity. Finally, a 10.2% reduction in coefficient of friction is observed. Since the wear rate and is less compared to that of alumina, zirconia can last more in case hip implants.

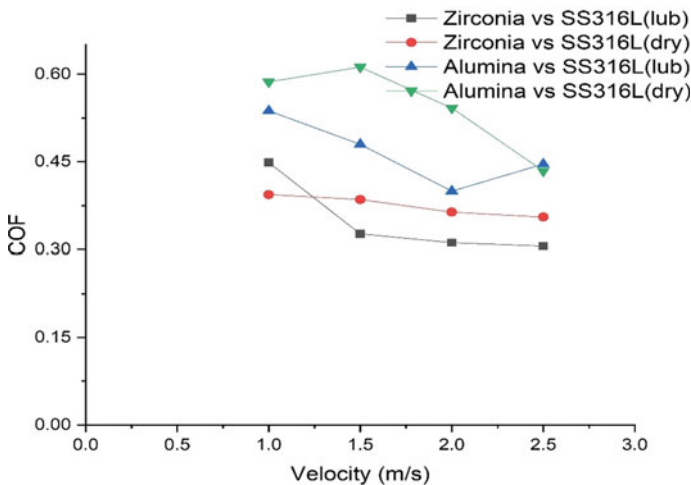


Fig. 3 Friction coefficient of alumina, zirconia in dry, and lubrication condition

3.2 Wear Coefficient for Varying Velocities

Wear is developed when there is friction between two surfaces. Also, when the materials have varying hardness. Usually, the material with lowest hardness rating starts to wear. The wear coefficient for dry sliding condition is shown in Fig. 4 which is compared with experimental results [7]. It is seen that even when it is same material while the sliding velocity is increased the wear coefficients starts to decrease. But only by 10% for every 0.5 m/s increase in sliding velocity and becomes constant upon further increasing velocity. The black line represents the experimental results of this project. The experiment is performed for a total of 10 km which is equivalent to one year for each and every test. It is in between SS316L counter face and alumina ball. In the present case, the alumina ball starts to wear. Since metal is involved the wear rates are high compared to that of ceramic-on-ceramic. It is seen from the graph that there is a drastic decrease of about 17% in wear coefficient is observed between the sliding velocities of 1 and 1.5 m/s. After that the rate at which the wear rates start to reduce becomes low. Finally, a 30.4% in reduction wear rate is observed for a sliding velocity of 2.5 m/s. The reason for the reduction in wear rate is found to be change of point contact to area contact. Since for each test a slot is formed which increases the area of contact.

Since conforming the wear rates reduces as the sliding velocities increases, further test are performed on the stainless steel counter face under different conditions. These conditions include varying velocities and constant load for both dry and lubricated conditions. Initially, for alumina the maximum wear coefficient of $3.7E-06 \text{ mm}^3/\text{Nm}$ is observed for sliding velocity of 1 m/s. Then the wear rate starts to reduce.

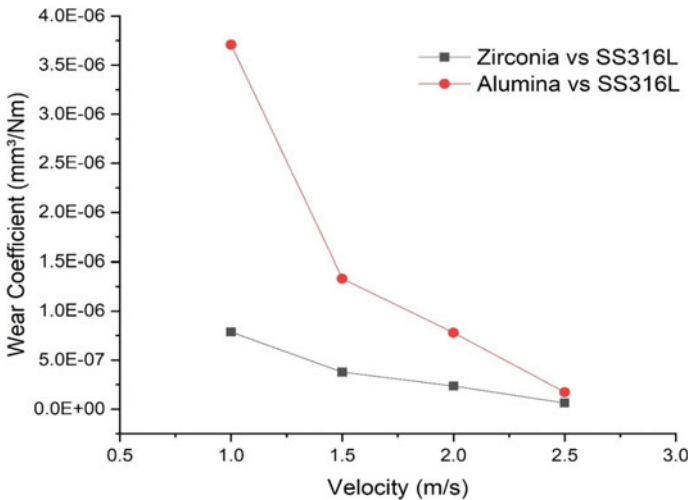


Fig. 4 Comparison of wear coefficient

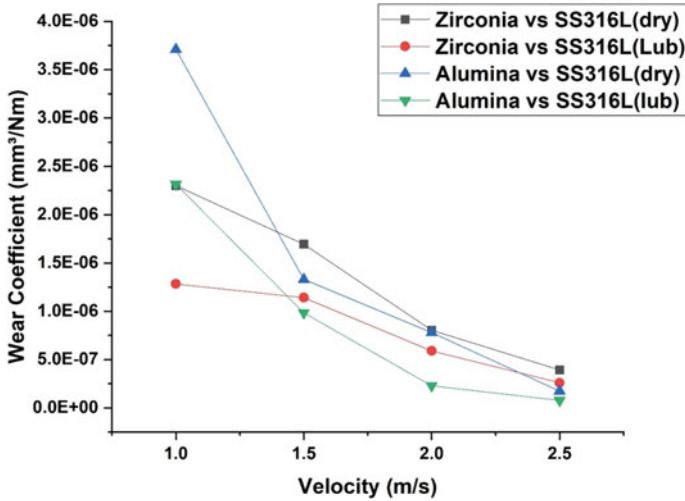


Fig. 5 Wear coefficient of alumina, zirconia in dry and lubrication condition

It is observed at $1.73E-07 \text{ mm}^3/\text{Nm}$ for a sliding velocity of 2.5 m/s. The wear rate for sliding velocity of 1 m/s for lubricated condition is $2.3E-06 \text{ mm}^3/\text{Nm}$, which is less than under dry condition. The friction reduces when lubrication is involved causing the wear to reduce. The same reduction in can be observed for lubricated condition also.

Figure 5 also shows the wear coefficients of SS316L versus zirconia. The wear rate of zirconia ball for sliding velocity of 1 m/s is maximum of $2.29E-06 \text{ mm}^3/\text{Nm}$ for dry condition and $1.28E-06 \text{ mm}^3/\text{Nm}$ for lubricated conditions.

3.3 Contact Stress Analysis

The finite element analysis is done for SS316L head and alumina and zirconia cup. The model is drawn and updated for a total of 5 million cycles, i.e., 5 years for particular gait activities. For analyzing the contact pressure developed the average friction value of the dry condition is taken into consideration. Figure 6 shows the finite element analysis of SS316L stainless steel head and alumina cup and the contact pressure developed between them. For a load of 2410 N applied on the y direction a contact pressure of 46.56 MPa is developed on the top most surface. The contact pressure developed decreases as the model is further updated. Finally, at the end of 5 million cycles or 13 updates a contact pressure of 25.76 MPa is developed.

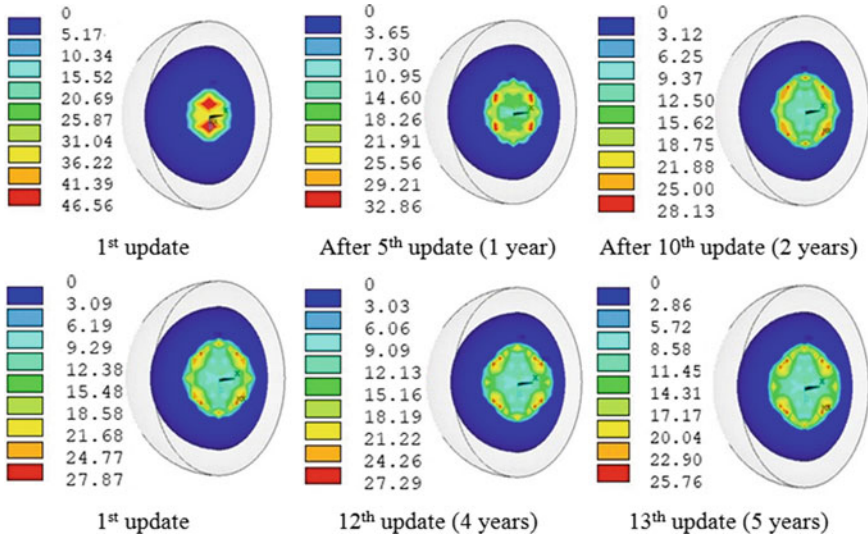


Fig. 6 Contact pressure (MPa) plot for alumina against SS316L

3.4 Cumulative Linear and Volumetric Wear Analysis

From the values of the contact pressure the linear wear values are calculated for each and every update. Also, linear wear is calculated per million cycles.

The values are tabulated and plotted. Figure 7 shows the linear wear of 13 updates of alumina and zirconia. From the figure, it is seen that linear wear increases up to 10th update (for 2 years). Then the linear wear starts to stabilize at 2032.79 μm for alumina and 1458.56 μm for zirconia.

The volumetric wear developed for alumina and zirconia against SS316L steel can be seen in Fig. 8. For alumina, it is seen that the volumetric wear steadily raises up to 10th update (2 years), and the maximum value for this is 174.66 mm^3 . Then the volumetric wear steadies out at this value. The same can be observed for zirconia also. The maximum volumetric wear observed in zirconia is found out to be 151.22 mm^3 .

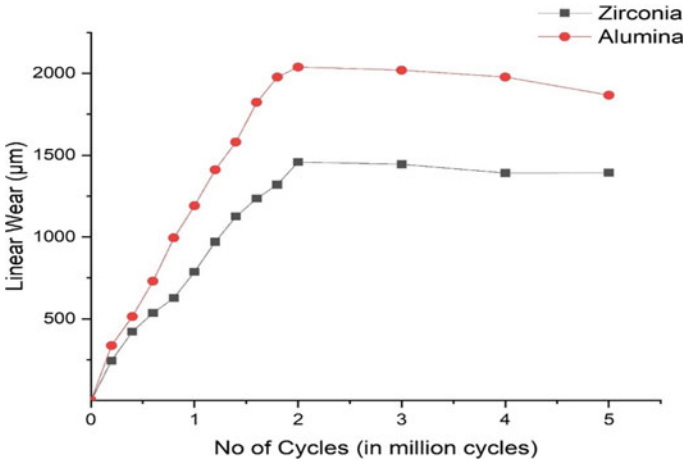


Fig. 7 Linear wear of hard on hard bearing couples

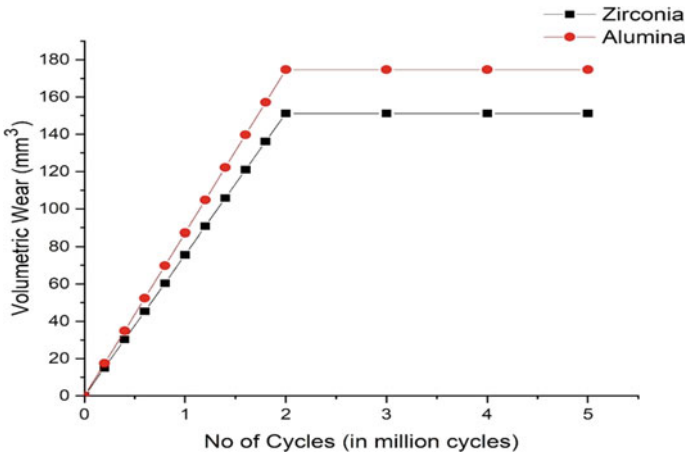


Fig. 8 Volumetric wear hard on hard bearing couples

4 Conclusion

The present study involves the wear prediction of two material combinations (SS316L-Alumina and SS316L-Zirconia) used for human hip prosthesis. It concludes about the cumulative analysis of linear and volumetric wear of the above mentioned metal on ceramic combinations. The conclusions from the present study are.

- The wear rates of the material seems to vary depending upon their mechanical properties. Both wear rate and COF decreases as the sliding velocity increases, this applies for both dry and lubricated condition.

- For SS316L-alumina combination, the average coefficient of friction developed is around 0.5430 for dry and 0.4655 for lubricated condition. For SS316L-zirconia combination, the average coefficient of friction developed is around 0.3743 for dry and 0.3442 for lubricated condition.
- Among the ceramics considered for the experiment zirconia seems to be more suitable material for the acetabulum cup.
- The same results were observed with the wear rates also. The average wear rates for dry run are as follows alumina-1.498E-06 and zirconia-1.297E-06 mm³/Nm. The average wear rates of the lubricated conditions are as follows alumina-9.015E-07 and zirconia-8.188E-07 mm³/Nm
- Linear and volumetric wear are calculated from the contact pressure values obtained from the finite element analysis of hip implant. Only dry sliding conditions are taken into consideration for analysis
- The computed linear wear and volumetric wear has highest value for SS316L-alumina combination than SS316L-zirconia combination. The model used is updated 13 times in order to simulate the conditions of 5 year gait cycle.
- The contact pressure as well as linear and volumetric wear increases at a steady rate for up to ten updates, then the value saturates.
- The linear wear values are as follows 1458.56 μm for zirconia and 2038.72 μm for alumina. The volumetric wear are as follows for alumina 174.66 and 151.25 mm³ for zirconia.

References

1. Parthasarathi N, Borah U, Albert SK (2013) Effect of temperature on sliding wear of AISI 316 L (N) stainless steel—analysis of measured wear and surface roughness of wear tracks. *Mater Des* 51:676–682
2. Hanumantharaju H, Shivananda H, Hadimani MG, Kumar KS, Jagadish S (2000) Wear study on SS316L, Ti-6Al-4V, PEEK, polyurethane and alumina used as bio-material. *Wear* 2000:0
3. Xiong F, Manory R (1999) The effect of test parameters on alumina wear under low contact stress. *Wear* 236:240–245
4. Dogan H, Findik F, Morgul O (2002) Friction and wear behaviour of implanted AISI 316L SS and comparison with a substrate. *Mater Des* 23:605–610
5. Lee MH, Seo WS, Kim H, Lee KY, Kim DJ, Lee DY (2005) Wear behaviors of UHMWPE against LTD-free zirconia/alumina composites. In: *Key engineering materials*. Trans Tech Publ, pp 1011–1014
6. Shankar S, Nithyaprakash R (2016) Predicting the wear of soft-on-hard bearing couples for human hip prosthesis using finite element concepts. *J Mech Med Biol* 16:1650020
7. Chanda A, Basu D, Dasgupta A, Chattopadhyay S, Mukhopadhyay AK (1997) A new parameter for measuring wear of materials. *J Mater Sci Lett* 16:1647–1651

An Outlook on Self-healing Materials



Nitin Kumar Gupta, Nalin Somani, Tushar Panwar, Nishant Ranaa, Faisal Ahmeda, and Abhinav Dimri

Abstract Self-healing materials are the latest categories in smart materials. They can repair the developed crack with the help of some externally provided mechanism. Many researchers around are trying to develop this biological inspired mechanism into engineering materials. This enhanced the materials properties and their life. This paper presents a brief outlook on advancement of self-healing in metals with the help of shape memory alloy and low melting point alloy, and development of self-healing in polymers and self-healing in ceramics.

Keywords Self healing metal · Ceramic · Composites

1 Introduction

Humans have progressed tremendously over last few centuries. The cause of this progress is to desire to get best from everything present in the nature or the tendency to improve and find the better version. This desire always led to the growth of the human world. Similarly, the self-healing materials are better and advanced version of commonly used materials (polymer, ceramics and metals). The self-healing material fulfills the deficiency of base materials. For example, the cracks in buildings can be healed on their own or the scratches on the car bodies can recover their original shiny appearance by itself. Indeed, this is what one experiences in case of the natural healing of wounds and cuts in living species. Thus, with the quest for the maintenance free and trouble-free long life of machines/components, the self-healing materials came into existence. The most popular types of self-healing materials are those that are designed to mimic human skin, which can heal/repair itself as needed. Hence, when these materials are cracked or damaged, a healing agent is triggered to flow into the damaged area and heal the damage; similar to a cut in human skin triggers blood flow to promote clotting.

N. K. Gupta (✉) · N. Somani · T. Panwar · N. Ranaa · F. Ahmeda · A. Dimri
Department of Mechanical Engineering, DIT University Dehradun, Dehradun 248001, India
e-mail: ghotnitin@gmail.com

Polymers are used in everyday life in products like plastics, rubber, paints etc. It is necessary to increase its age, reliability and prevent micro cracking. These all properties can be achieved by self-healing coatings [1,2]. Sadrabadi et al. used epoxy coatings (containing dual micro/Nano capsules; epoxy and amine) to heal the micro cracks [1]. Similarly, Reaz et al. used epoxy resin system (SC-15) to heal the micro crack and interfacial debonding in fibre reinforced composites [2]. The polymers like self-healing hydrogels either possess rapid and autonomous self-healing or mechanically robust properties [3] can be used for biomedical application [4].

Ceramic materials are brittle, hard, and strong in compression, chemically stable at high temperature, electrical insulators and weak in shearing and tensions. In the production of machines, working in high temperature, ceramics are used e.g., gas turbine, superconductors, household products and electrical equipment. But they are poor in tensile strength, toughness, thermal conductivity. These flaws cracks can be healed by various self-healing methods. Li et al. [5] heal a Ti_2SnC ceramic at $800\text{ }^\circ\text{C}$ temperature within 1 h by oxidation reaction. Yang et al. [6] healed Ti_2AlC by oxidation induced healing at $1200\text{ }^\circ\text{C}$. Jung et al. [7] similarly healed Si_3N_4/SiC composite ceramic from room temperature to $1400\text{ }^\circ\text{C}$ and in 10 h. Bei and Greil [8] illustrate the crack healing mechanism in MAX phase ceramics and describe how the mechanical strength and electrical conductivity of MAX phase can be restored.

Metallic materials are the advanced version of normal materials like silver, copper etc. They can be used in building industries, manufacturing of household products, machines, automobiles etc. High mechanical strength and ability to self-repair damage can be induced in these materials by adding reinforcement. Lumley [9] increase the mechanical strength of Al-Cu-Mg-Ag alloy by precipitation healing method which is also used by He et al. [10] in Fe-Cu-B-N alloys and Fe-Cu alloys. Rohatgi [11] presents the durability of Al-A380 alloy can be improved by reinforcement with NiTi SMA Wires. Similarly, Ferguson et al. [12] used wires of NiTi in Zinc alloy (ZA-8) to rebound cracked or damaged surface. Alaneme and Omosule [13] exhibits self-healing characteristics of Al Mg Si alloy reinforced with low melting point alloy (SnPb). Lucci et al. [14] also analyzed the self-healing concept in Al composite as matrix and reinforced with alumina micro-tubes (Al_2O_3) filled with $Sn_{60}Pb_{40}$ solder.

2 Self-healing Material

Self-healing materials are smart materials which are capable to sense the cracks and damage and then automatically repair that damage without any additional help. The healing can be extensive or intensive. In extensive self-healing mechanism when crack is developed the healing substance within the material is released and healing is done. Intensive mechanism is based on reversible bonding which is of dynamic nature including reversible bonding of covalent as well as non-covalent type.

2.1 Self-healing in Metallic Material

Properties of the self-healing can be achieved by few techniques which are discussed as below:

2.1.1 Self-healing with SMA Wires

Shape memory alloys (SMA) also known as Smart Material and Memory Alloys can return to its original shape even after plastic deformation when heated above critical temperature. This property of SMA enables to minimize the permanent damage of metal. Along with above property these alloys have very high fatigue and corrosion resistance and strength. These SMA can be used in metals as wires (SMA wires). Hence these SMA wires can be used in metals by reinforcing them inside metal matrix. This combination of SMA wires and metal matrix can be used in various applications where there is need of reducing chances of failure, since it possesses self-healing behaviour.

When composite cracks, due to unusual loading conditions or by some other factor, there occurs plastic deformation or strain in material. This leads to stretch of SMA wires and they cover the crack present in metal matrix. Further, on heating the material above shape transformation temperature of SMA, the SMA wires shrinks back to its original shape. This shrinkage of SMA wire leads to the origin of compressive forces in place of cracks. These compressive forces clamp the cracks and this clamping of cracks is accompanied by welding of cracks in the matrix, which is designed in such a manner that it partially liquefies at healing temperature. By this mechanism material achieves self-healing.

This approach was tested by Manuel and Olson [15] on Sn-21 wt% Bi alloy with about 95% recovery of composite Ultimate Tensile Strength (UTS) but there was loss in uniform ductility. Also, an Mg based off-eutectic alloy was also tested for healing with 160% increase in ductility but only partial crack closure was reported. Figure 1 represents the mechanism of the crack closure from the help of shape memory alloy. After applying the temperature, the shape memory alloy gets to recover its shape.

2.1.2 Self-healing with Low Melting Point Solder Reinforcement

This method is employed by encapsulating a solder material inside host matrix. The melting point of solder material is less than that of the host matrix. The original concept of self-healing employed in polymers is incorporated in this process. Solder reinforcement isn't actuated until a crack occurs in the host matrix. It then fills the crack by wetting the cracked surface employing the phenomenon of capillary action. It then solidifies thereby closing the crack. The temperature of the solder must be increased above its melting point in order to actuate the process [16].

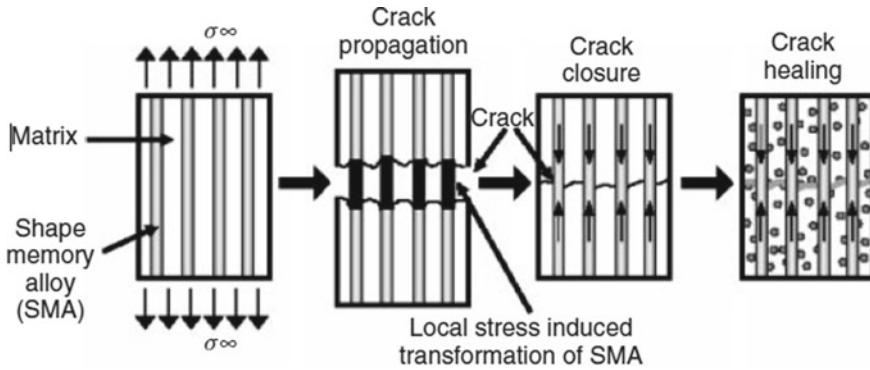


Fig. 1 Fig of MMC reinforced by SMA wires undergoing a self-healing process [15]

However, the concepts of solder reinforcements have many complications in which the designing of original microstructure is the very first difficulty. Added to this, the ceramic capsules should contain holes in order to be filled by the solder material. Moreover, even when the crack is healed some gaps are formed which possibly decrease the strength of the material. In metallic self-healing materials matrix is formed by combination of different materials which have a high melting point and even a higher ultimate tensile strength. It was Lucci et al. [17] who investigated that Al_2O_3 ceramic tubes containing $\text{Sn}_{60}\text{Pb}_{40}$ solder inside can be embedded inside the Aluminium matrix.

To achieve healing by solder reinforcement process a crack is created intentionally. Although the filling of the crack is achieved when the material is heated at a temperature which is more than its melting point, but the interface which is formed between the solder and the metal matrix is of very weak nature. A more detailed scanning done by an electron microscope showed that no part of solder was in absolute contact with metal matrix. This space between the two materials would result in insufficient bonding to stop realistic crack formal growing. Figure 2 represents the images of the self-healing through the solder materials experiments done by a group of researchers [18].

Similar experimental have been done by a group of researchers through the low melting points alloy with Al6061 as a matrix. They have reported the partial healing is successfully through low melting point alloy. Various testing has been performed to identify the physical aspect of the self-healing metals. To achieve the highest efficiency in the mechanical properties various researchers around the globe are trying to develop new class of composite materials through various technique like powder metallurgy, stir-casting, microwave heating etc. Tensile test, Charpy test and torsion test has been performed on the self-healing materials. Figure 3 represents the pictorial view of the self-healed aluminium 6061 alloy [19–27].

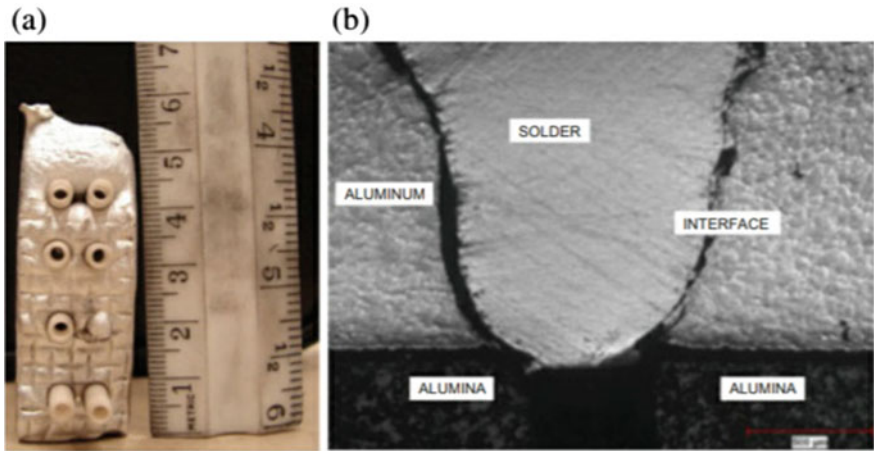


Fig. 2 a Aluminium host matrix with embedded Al_2O_3 tubes (before filling the solder). b Solder filling up of the crack by solder. A high porosity exists between the two interfaces [18]

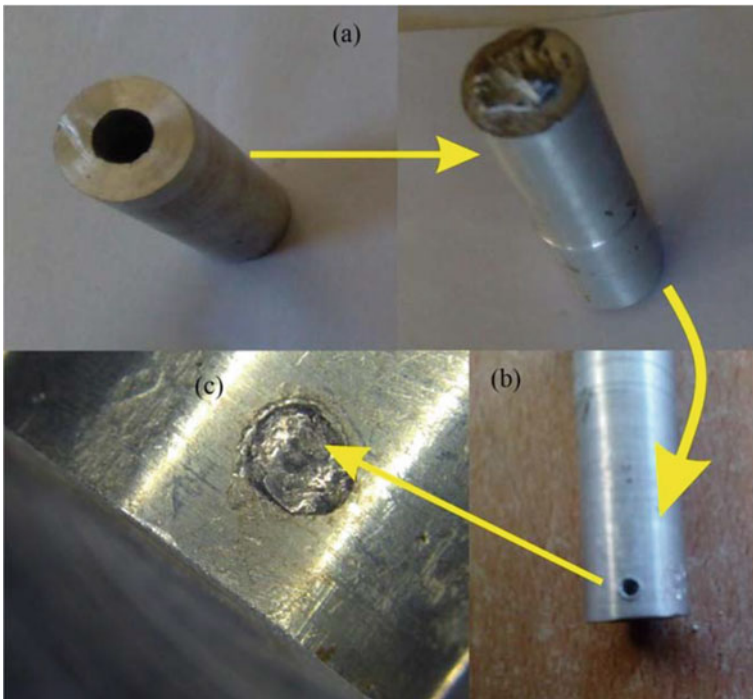


Fig. 3 Self-healing through low mantling points alloy into Al6061 [19]

2.2 Self-healing in Polymers

It is fascinating to know that in last century polymers have become a daily use material. As per recent reports and research it is found that the advancement of polymer is really quick. This growth has also been seen in its self-healing applications. As per research polymers are way ahead ceramics and metals when it comes to self-healing applications. Getting inspiration from nature (biomimetic), it follows the same biological response in three steps the very first response in the time of damage is to crank up or activate in the aftermath of when damage gets sustained. After this material is transported to the affected area and then at last the chemical repair occurs.

2.2.1 The Mechanism of Self-healing

(a) Extensive: In extensive self-healing mechanism when the crack is formed the transfer of healing agent occur after which crack is gradually healed through chemical process. (b) Intensive: It is the mechanism based on dynamic reversible bond including reversible non-covalent and covalent bond. Material conductor based self-healing material: Ag nanowires in recent years have attracted a lot of attraction, because of its high conductivity and a self-healing material property [28]. Pei et al. [29] has manufactured a conductive and self-healable polymer film by putting Ag NWs as conductor and fixing a layer of Ag NWs on the surface of a Diels–Alder (D–A) based healable network polymer. Conductive polymer based self-healing material: Yu et al. [30] has amalgamated a self-healing conductive hybrid gel by G-Zinc-tpy into Polypyrrole aero gel. This gel has high self-healing, great mechanical stability and good conductivity. In thus PPy aerogel has high conductivity and G-Zn-tpy has self-healing property.

Carbon based self-healing materials: Chen and Wu [31] worked on the development of electrically conductive graphic/branched polyethylene-ninic composite that is self-healed without any incentive at room temperature. This composite shows good self-healing properties, tackiness and resistance from applied stress. Ionic conductivity based self-healing materials: Recently researches shows ions in polymers are better in self-healing because of involvement between anions and cations. He et al. [32] developed a resilient, self-healing hydrogel compound of Au nanoparticles, poly vinyl alcohol) and poly (ionic liquids). This shows greater conductivity, better mechanical property and self-healing property due to Au-O bonds and hydrogen bond [28].

Liquid metal-elastomer composite based self-healing: In this method a soft and stretchable electronics, which is capable of self-healing is created using liquid metal embedded in elastomer. Markvicka et al. [33] made a material by dissipating the droplets of Gallium based LM alloy in silicon elastomer. When the damage is induced in material LM droplets rupture and merge to form a new electrical pathway around the damaged surface and thus ensuring continuous high electrical conductivity. Figure 4 indicates the process of the self-healing in the polymers. SEM images

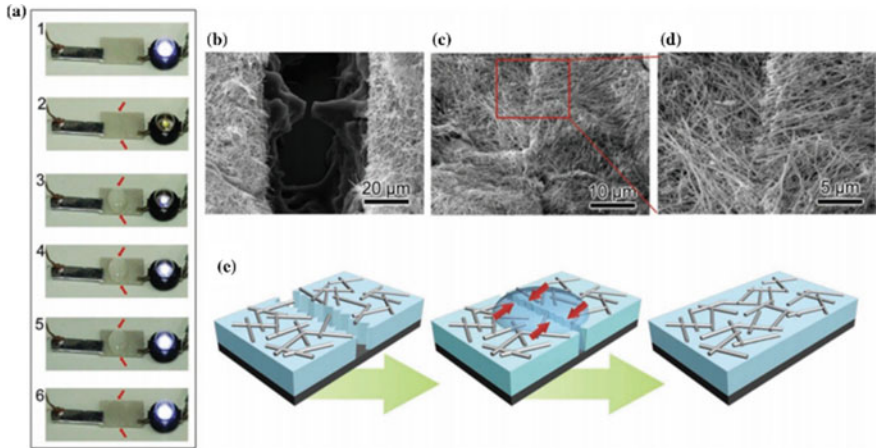


Fig. 4 It shows the different locations of self-healing material. **a** Shows different films are connected with the LED lamp. (1–6) shows the healing process in the (b, d, e) are the scanning electron microscope images of the material. **b** It is the SEM image before healing and (c, d) are the images after healing (e) It is the schematic illustration of healing process

shows that the self-healing agents helps in materials to create the bonding, heal the cracks.

2.3 Self-healing Ceramics

Ceramics were one of the first known materials and have been used for centuries. They have many properties such as high strength and durability which makes it a daily use material with vast applications. But as the advancement occurs and self-healing ceramics came in progression it changed the applications of ceramics as it is now considered in various structural applications.

Recently [34] a light weighted self-healing ceramics was unveiled for aircraft engine. Due to ceramics superior strength in high temperature, this self-healing light weighted ceramic would be a good candidate for turbine blades as the temperature of the engine is high. In fabrication of this self-healing ceramic, it was infused with 3D network of healing activator. The base material (Al_2O_3) containing 30% SiC making (Al_2O_3/SiC) that effectively self-healed, increased the strength and other properties of this material.

Self-healing in ceramics itself is major topic and has many applications. For example; recently [35] the autogenously self-healing of hydraulic concrete material, in this as the crack occurs the water permeates through crack forming hydrates and starts healing process. Figure 5 shows the self-healing rate on the materials. From last centuries humans have advanced tremendously in ceramics from the roman concrete to light weighted self-healing ceramics a lot have been covered and a lot has to be

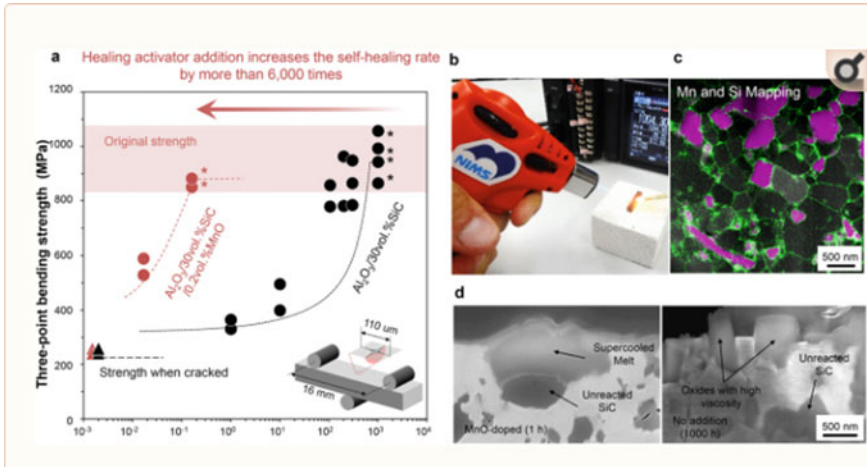


Fig. 5 It shows the self-healing and strength recovery of the material matrix. **a** Shows the increased strength in Al_2O_3 as it is infused with 30% SiC. **b** Complete self-healing by increasing temperature through gas lighter. **c** Shows the maps of Mn and Si with grain boundaries. **d** Shows surface oxidation in presence or absence of MnO [35]

discovered. And as the time progresses we will see application of self-healing in our daily life.

3 Conclusion

Developments of composite materials are an essential and important part for manufacturing industries as they have high strength, high melting point, better wear resistance capacity as well as the good corrosive resist strength. Increasing demands in the high properties of materials leads to the development in various new categories of new materials. Self-healing are the categories of materials where materials are being considered to improve the machine life. The above report is an outlook of the various new advancements in area of self-healing MMCs as well as self-healing polymers and ceramics.

Conflict of Interest Author has no conflict of interest.

References

1. Sadrabadi TE, Allahkaram SR, Towhidi N (2018) Preparation and property investigation of epoxy/amine micro/nanocapsule based self-healing coatings. *Int Polym Proc* 33(5):721–730

2. Chowdhury RA, Hosur MV, Nuruddin M, Tcherbi-Narteh A, Kumar A, Boddu V, Jeelani S (2015) Self-healing epoxy composites: preparation, characterization and healing performance 4(1):33–34
3. Liu Y, Hsu S (2018) Synthesis and biomedical applications of self-healing hydrogels. *Front Chem* 6:449
4. Taylor DL, Panhuis M (2016) Self-healing hydrogels. *Adv Mater* 28(41)
5. Li S, Bei G, Chen X, Zhang L, Zhou Y, Mačković M, Spiecke E, Greil P (2016) Crack healing induced electrical and mechanical properties recovery in a Ti₂SnC ceramic. *J Eur Ceram Soc* 36(1):25–32
6. Yang HJ, Pei YT, Rao JC, Hosson JTM (2012) Self-healing performance of Ti₂AlC ceramic. *J Mater Chem* 22(17):8304
7. Jung YS, Guo Y, Nakao W, Takashai K, Ando K, Saito S (2008) Crack-healing behaviour and resultant high-temperature fatigue strength of machined Si₃N₄/SiC composite ceramic. *Fatigue Fract Eng Mater Struct* 31(1):2–11
8. Bei G, Greil P (2016) Oxidation-induced crack healing in MAX phase containing ceramic composites. *Adv Ceram Mater* 231–260
9. Lumley R (2007) Self healing materials: an alternative approach to 20 centuries of materials science. Van der Zwaag S (ed), 219
10. He SM, van Dijk NH, Schut H, Peekstok ER, van der Zwaag S (2010) Thermally activated precipitation at deformation-induced defects in Fe-Cu and Fe-Cu-B-N alloys studied by positron annihilation spectroscopy. *Phys Rev B* 81(9)
11. Rohatgi PK (2014) Al-shape memory alloy self-healing metal matrix composite. *Mater Sci Eng A* 619:73–76
12. Ferguson JB, Schultz BF, Rohatgi PK (2015) Zinc alloy ZA-8/shape memory alloy self-healing metal matrix composite. *Mater Sci Eng A* 620:85–88
13. Alaneme K, Omosule O (2015) Experimental studies of self healing behaviour of under-aged Al-Mg-Si alloys and 60Sn-40Pb alloy reinforced aluminium metal-metal composites. *J Miner Mater Charact Eng* 3:1–8
14. Lucci JM, Amano RS, Rohatgi P, Schultz B (2008) Self-healing in an aluminum alloy reinforces with microtubes. In: ASME 2008 3rd energy nanotechnology international conference
15. Manuel M, Olson GB (2009) Biologically inspired self-healing metals. In: Proceedings of 2nd international conference on self-healing materials
16. Grabowsky B, Tasan CC (2016) Self-healing metals. Springer International publishing, Switzerland
17. Lucci JM, Rohatgi PK, Schultz B (2008) Metals experiment and computational analysis of self-healing in an aluminium alloy. In: Proceedings of ASME international mechanical engineering congress and expositions, Boston U.S.A
18. Nosonovsky M, Rohatgi PK (2012) Biomimetics in materials science: self healing, self lubricating and self cleaning materials. Springer, New York
19. Gupta N, Thakre GD (2019) The mechanical and tribological characteristics of self-healing Al6061 alloy. *Mater Res Express* 6:0865d5
20. Gupta NK, Thakre GD, Kumar M (2019) self-healing al 6061 alloy reinforced with low melting point alloys
21. Gupta N, Kumar M, Thakre GD (2020) Mechanical characterization of 60pb40sn reinforced al6061 self-healing composite. In: Advances in materials science and engineering (Lecture notes in mechanical engineering). Springer, Singapore
22. Somani N, Sharma N, Sharma A, Gautam YK, Khatri P, Solomon JAA (2018) Fabrication of Cu-SiC composite using powder metallurgy technique. *Mater Today Proc* 5:28136–28141
23. Somani N, Gautam YK, Sharma SK, Kumar M (2018) Stastical analysis of dry sliding wear and friction behavior of Cu/SiC sintered composite. In: AIP conference proceedings, p 020018
24. Somani N, Tyagi YK, Kumar P, Srivastava V, Bhowmick H (2019) Enhanced tribological properties of SiC reinforced copper metal matrix composites. *Mater Res Expr* 6:016549
25. Somani N, Kumar K, Gupta N (2020) Review on microwave cladding: a new approach. In: Advances in materials processing, pp 77–90

26. Singh S, Prakash C, Davim JP *Functional materials and advanced manufacturing*. CRP Press. ISBN 9780367275075
27. Prakash C, Singh S, Davim JP (eds) (2020) *Functional and smart materials* (1st ed). CRC Press. <https://doi.org/10.1201/9780429298035>
28. Zhang Q, Liu L, Pan C, Li D (2017) Review of recent achievements in self-healing conductive materials and their applications
29. Gong C, Liang J, Hu W, Niu X, Ma S, Hahn HT, Pei Q (2012) A healable, semitransparent silver nanowire-polymer composite conductor
30. Shi Y, Wang M, Ma C, Wang Y, Li X, Yu G (2015) A conductive self-healing hybrid gel enabled by metal–ligand supramolecule and nanostructured conductive polymer
31. Wu T, Chen B (2016) A mechanically and electrically self-healing graphite composite dough for stencil-printable stretchable conductors
32. He X, Zhang C, Wang M, Zhang Y, Liu L, Yang W (2017) An electrically and mechanically autonomic self-healing hybrid hydrogel with tough and thermoplastic properties
33. Markvicka EJ, Bartlett MD, Huang X, Majidi C (2018) An autonomously electrically self-healing liquid metal–elastomer composite for robust soft-matter robotics and electronics. *Nat Mater* 17(7):618–624
34. Osada T, Kamoda K, Mitome M, Abe T, Nakao W, Ohmura T (2014) A novel design approach for self–crack-healing structural ceramics with 3D networks of healing activator
35. Hager MD, Greil P, Leyens C, Zwaag S, Schubert U *Self healing material*

On Some Convective Mechanisms of Nanofluids



Monika Arora and Avinash Rana

Abstract Nanofluids have been attaining a great amount of recognition in the modern industrial world due to their distinctive thermophysical properties. To enhance these properties, the stability of these fluids is of major concern along with the behavior of nanofluids which depends upon different parameters such as nanoparticle size, nanoparticle type, nanoparticle aspect ratio, etc. In this context, an attempt is made to summarize the study of the convective mechanisms of nanofluids. Finally, the article describes the important slip mechanisms in magnetic nanofluids which provide useful information to study different convective mechanisms in these smart fluids.

Keywords Nanoparticles · Nanofluids · Convection

1 Introduction

From the times, the poor thermal characteristics of the regular fluids came to notice, the industries had felt the strong need to develop the variants of regular fluids with much better heat transfer characteristics and higher thermal conductivity than their regular counterparts. At room temperature, the thermal conductivity of metals in solid form is very high when compared to regular fluids. Thus, it is natural to disperse small metal particles of the order of 10^{-6} – 10^{-3} m in a fluid to increase its thermal conductivity. Many experimental and theoretical studies were performed in this regard and it is observed that such suspensions suffer from several drawbacks like erosion of components, clogging, a considerable drop in pressure, etc. [1, 2]. These problems can be dealt with by replacing small metal particles of the order of 10^{-6} – 10^{-3} m with

M. Arora (✉)

Department of Mathematics, Lovely Professional University, Phagwara 144411, India
e-mail: monika.25297@lpu.co.in

A. Rana

Department of Marketing, Lovely Professional University, Phagwara 144411, India
e-mail: avinash.21033@lpu.co.in

“nanosized” particles of order (1–100) nm and the resulting suspension is known as nanofluids.

Choi [3] was the first who originated the term nanofluid. Nanofluids have higher cooling rates, minimized friction coefficients, because of these two and several other features they are very useful in a wide range of industrial applications. Some of these specific applications of the nanofluids are cooling of engines, solar water heating, drilling, heating, and cooling of buildings and refrigeration (domestic refrigerator, chillers). These fluids are also used in transformer oil, diesel-electric generators, nuclear systems, military devices, various electronic types of equipment, etc. [4].

2 Synthesis of Nanofluids

Synthesis of nanofluids is done by 1-step process and 2-step process. In the 1-step process, nanoparticles are simultaneously formed and dispersed in the fluid by some chemical method [5, 6]. In the 2-step process, nanoparticles are finely crushed and then this nanopowder is distributed in the fluid [7, 8]. Because of the abundance of nanopowder, the 2-step process is more economical compared to the 1-step method stated by Li et al. [9]. But the degree of agglomeration in nanofluids becomes very high when it is prepared by a 2-step process due to the involvement of drying, storage, and transportation process. This leads to the low rate of thermal conductivity of nanofluids. Therefore, to deal with this problem surfactants are usually added to the fluids which also help in refining the dispersion process. On the other hand, in the 1-step process, the problem of agglomeration is taken care of to a large extent. Although, it is not a viable source for producing nanofluids on a large scale. Ghadimi et al. [10] reported that the 2-step process is in favor of oxide nanoparticles while it is less significant for metal nanoparticles.

3 Magnetic Nanofluids

A distinctive class of nanofluids is obtained when magnetic nanoparticles are dispersed in the base fluid, termed as “magnetic nanofluids”. Magnetic nanofluids display both magnetic and fluid properties. In industrial applications sometimes it is important and useful to suitably control the flow field, by some external agency, set up by the fluid containing “nanosized” particles. The flow fields set up with the magnetic nanofluids can be suitably controlled by using an external magnetic field. Metals such as iron, nickel, cobalt, magnetite, etc. are used in the construction of magnetic nanoparticles. To lower the surface tension arising between liquid–solid interface the particles are usually laminated with surfactant for better stability [11]. Temperature-dependent magnetic nanofluids are considered the most viable source for augmenting heat transfer in miniature heat transport devices [12].

4 Thermal Conductivity of Nanofluids

The thermal conductivity of nanofluids has attracted the attention of many researchers. We provide here a brief overview of the literature on the same. Choi et al. [7] reported that nanotubes have the highest thermal conductivity enhancement among all the nanostructured materials suspended in regular fluids. Dondapati et al. [13], simulated the micro heat exchange properties of, Al_2O_3 , SiO_2 , SiC , CuO , and TiO_2 nanoparticles in Liquid Nitrogen (LN_2 , at 3% volume concentration), and confirmed an enhancement in heat transfer rate in micro heat exchangers due to increased volume concentration of nanoparticles. The authors concluded that the dispersion of the nanoparticles in LN_2 is beneficial to be used in micro heat exchangers. Das et al. [14] observed a 4-times increase in the thermal conductivity after varying the temperature from 21^0 to 51^0 C. Further, they observed that the CuO -water system is more influenced by temperature than the Al_2O_3 -water system but particle concentration's effect is more on the Al_2O_3 -water system. Yu et al. [15] observed strong dependence on the size of suspended particles for augmenting thermal conductivity. Hwang et al. [16] considered four types of nanofluids in their investigation and measured the thermal conductivity through the transient hot-wire method. The authors' analyzed nanofluids' thermal conductivity is greatly affected by the thermal conductivity of nanoparticles and base fluids' thermal conductivity. Xuan and Li [17] had taken Cu -water nanofluids for experimental investigation and argued that the dispersed nanoparticles are responsible for anomalous heat transfer enhancement.

In an experimental study with graphite nanofluid, Yang et al. [18] reported an increase in the Nusselt number with the dispersion of nanoparticles in laminar flow but the experimentally observed increase was comparatively less than that predicted by correlation techniques. Emphasis was laid on developing an appropriate heat transfer correlation for nanofluid systems. The transport characteristics of magnetic nanofluids were examined experimentally by Li et al. [19]. The authors found that thermal conductivity remains unchanged when the magnetic field makes an angle of 90^0 with a temperature gradient. However, when the magnetic field is aligned with the temperature gradient, particles developed chains and network structures for energy transport inside the magnetic fluid in the temperature gradient's direction leading to the enhancement in thermal conductivity. Sandhu et al. [20] tested the utilization of nanofluids in heat pipes using VoF (Volume of Fluid) model and confirmed that nanofluids enhance the thermal characteristics of heat pipes which results in the enhancement of heat dissipation. Jilte et al. [21] proposed a liquid-cooled novel heat sink geometry made from four channels to test the cooling performance of the heat sink using different volume fractions of nanoparticles. A higher rate of heat rejection was reported from nanofluid cooled heat sink compared with water. Chatterjee et al. [22], investigated heat transfer characteristics for the flow of Al_2O_3 -water nanofluid in two microchannels (with a trapezoidal configuration having a hydraulic diameter of 301 and 212 μm with steady, laminar flow of Al_2O_3 -water nanofluid at 1%

volume concentration) and concluded that use of nanofluid enhances the heat transfer characteristics for both the channels with less expense of pressure-drop.

5 Thermo-Magnetic Convection

Some studies related to convection in the presence of a magnetic field are presented in this section. Schwab et al. [23] conducted an experimental study to observe the onset of convection. They plotted the Nusselt number as a function of the Rayleigh number where the discontinuity in the slope of the graph corresponds to the critical Rayleigh number. They further noted that the magnetic body force augments the gravitational body force in the liquid and thus convection sets in at relatively low-temperature gradients. Ganguly et al. [24] conducted a parametric study to associate the heat transfer with properties of magnetic fluid, variation in temperatures, magnetic field strength, etc.

Temperature gradient and magnetic field, both were found to be responsible for thermo-magnetic convection. It was also stated that this mechanism is very significant in nano-scale applications where buoyancy-driven convection is less effective as the decreased length scale enhances the thermo-magnetic convection under the constant dipole strength of the source magnet. Banerjee et al. [25] carried out a steady-state simulation study of the thermo-magnetic convection in a square cavity with localized heat sources. The computation of the Kelvin body force was carried out by employing Langevin's magnetization law which helps in the placement of external field sources and also in assessing the dimensions of the enclosures for heat transfer augmentation. They reported that the magnetization of the ferrofluid approaches a point of saturation as the field strength increases. One can study more about thermo-magnetic convection in magnetic nanofluids in [26–28] and references therein.

6 Convection in Rotating Magnetic Nanofluids

The phenomenon of rotation in the thermal convective instability is technically very important due to its applications in various rotating machinery like nuclear reactors, petroleum industry, biomechanics, and spacecraft fuels where ferromagnetic particles are used. The key parameter in this phenomenon is the non-dimensional Taylor number T_A which arises due to the Coriolis force.

One of the pioneers in the field was Jeffreys, who in 1928 analyzed theoretically the effect of rotation on convection and concluded that the effect of rotation is to maintain the stability of the system [29]. Chandrasekhar [30] covered thoroughly the systematic theoretical study of convection in the fluid layer heated from below with rotation along the vertical axis for various types of boundary conditions. He reported that rotation tends to suppress the onset of convection and the degree of this suppression depends upon the Taylor and the Prandtl numbers. Chand [31]

investigated analytically and numerically the thermal instability in a horizontal layer of nanofluid in the presence of rotation. Stabilizing effect of rotation was found. The author also derived sufficient conditions for the non-existence of over stability: $P_r > 1$ and $R_n > 0$, where P_r is the Prandtl number and R_n is the concentration Rayleigh number. Nonlinear stability analysis for rotating magnetized ferrofluid heated from below was performed by Sunil and Mahajan [32]. They demonstrated the tight coupling between the buoyancy and the magnetic forces in the presence of rotation. Some other aspects of thermal convection in the presence of rotation are discussed in [33–37] and references therein.

7 Double-Diffusive Convection in Magnetic Nanofluids

Double-diffusive convection is a special type of convection that is driven by two density gradients with different molecular diffusivities. When a nanofluid is heated and salted from below it becomes a sort of triple diffusion involving the diffusion of three agencies namely: heat, nanoparticles, and the solute.

Malashetty and Gaikwad [38] investigated the double-diffusive convection in the presence of horizontal thermal and solute gradients with the effects of cross-diffusion, viz., Soret and Dufour coefficients. Using normal mode analysis, the conditions for the onset of stationary and oscillatory instabilities were formulated. The authors reported the dependence of the maximum growth rate of instability, the slope of the wavefront, and the wave number on Soret and Dufour parameters. The effects of thermodiffusion of nanoparticles and solute in binary nanofluids on the convective instabilities of a binary nanofluid were investigated by Kim et al. [39]. They observed that the Soret effect of the solute is destabilizing while the volume fraction of nanoparticles has a stabilizing effect on the binary nanofluids. An analytical study of the problem of double-diffusive convection in a nanofluid layer using one term Galerkin method was conducted by Nield and Kuznetsov [40]. Both non-oscillatory and oscillatory cases were studied and stability boundaries were approximated by simple analytical expressions. The same problem was studied in [41] in a layer of a saturated porous medium. For more studies on double-diffusive convection, the reader is referred to [42–46] and references therein.

8 Bioconvection

By a microorganism, we mean an organism that is too small to be seen by a naked human eye. Examples of microorganisms include bacteria, green algae, planktons, etc. They constitute the major portion of the world's biomass. Microorganisms are usually made up of a single cell and are found in different types of aqueous environments. Bioconvection is the process of spontaneous pattern formation in the suspensions of swimming microorganisms [47]. The trajectory of a microorganism along

which it swims in a fluid is not entirely random. Mechanisms like changes in swimming style, speed, etc. can make microorganisms assemble in certain regions of the fluid or depart from certain parts of the environment with particular properties. The reader can study in detail about the bioconvection in [48–55] and references therein.

9 Important Slip Mechanisms in Magnetic Nanofluids

Brownian motion, thermophoresis, and magnetophoresis are the three important slip mechanisms in modeling convective transport in magnetic nanofluids. Here we are providing a brief description of these slip mechanisms (to know more about the same, the reader can see [56]).

9.1 *Brownian Motion*

Brownian motion is the random motion of the nanoparticles suspended in the base fluid. It was discovered by botanist Robert Brown in 1827. Einstein was the first to provide a physical explanation of Brownian motion. In a streamline flow, Brownian diffusion becomes an important slip mechanism [56]. In conventional heat transfer fluids, where particle size is big, the Brownian motion of the particles is not taken into consideration. But in nanofluids, where the particle is nano-meter sized, nanoparticles' Brownian motion is one of the significant mechanisms [56].

9.2 *Thermophoresis*

Nanoparticles' diffusion due to temperature gradient is called thermophoresis. The direction of the movement of particles is opposite to that of the temperature gradient. When nanoparticles move from the hot region of the liquid to the cold region due to thermophoresis a thin layer forms at the interface of particle and solvent [57]. The thermophoresis effect is significant in various engineering and scientific applications.

9.3 *Magnetophoresis*

The movement of nanoparticles under the effect of the non-uniform magnetic field is called magnetophoresis [58]. Magnetophoresis causes nanoparticles to be concentrated in those regions of the fluid where the magnetic field intensity is high. Magnetophoresis can be positive or negative, depending on whether the nanoparticles are

more or less magnetizable than the surrounding medium. In recent years, magnetophoresis has attracted attention due to its usefulness in microscale applications in fields like microbiology, nanotechnology, and biotechnology where magnetic particles are used.

10 Conclusion

In this paper, we have covered the study of various important convective mechanisms in magnetic nanofluids. This study provides a useful insight to the researcher in the field of convection in magnetic nanofluids in different aspects. Though much research has been done in the field of convective heat transfer enhancement in nanofluids but still there is a dire need to study the behavior of these fluids to form a stable suspension containing magnetic nanoparticles.

References

1. Ahuja AS (1975) Augmentation of heat transport in laminar flow of polystyrene suspensions. I. experiments and results. *J Appl Phys* 46(8):3408–3416
2. Liu KV, Choi US, Kasza KE (1988) Measurements of pressure drop and heat transfer in turbulent pipe flows of particulate slurries. No. ANL-88-15, Argonne National Lab, IL USA
3. Choi SUS (1995) Enhancing thermal conductivity of fluids with nanoparticles. ASME-Publications-Fed 231:99–106
4. Saidur R, Leong KY, Mohammad HA (2011) A review on applications and challenges of nanofluids. *Renew Sustain Energy Rev* 15(3):1646–1668
5. Eastman JA, Choi SUS, Li S, Yu W, Thompson LJ (2001) Anomalous increased effective thermal conductivities of ethylene glycol-based nanofluids containing copper nanoparticles. *Appl Phys Lett* 78(6):718–720
6. Zhu HT, Lin YS, Yin YS (2004) A novel one-step chemical method for preparation of copper nanofluids. *J Colloid Interface Sci* 277(1):100–103
7. Choi SUS, Zhang ZG, Yu W, Lockwood FE, Grulke EA (2001) Anomalous thermal conductivity enhancement in nanotube suspensions. *Appl Phys Lett* 79(14):2252–2254
8. Paul G, Philip J, Raj B, Das PK, Manna I (2011) Synthesis, characterization, and thermal property measurement of nano-Al₁₉S₂Zn₀₅ dispersed nanofluid prepared by a two-step process. *Int J Heat Mass Transf* 54(15):3783–3788
9. Li Y, Zhou J, Tung S, Schneider E, Xi S (2009) A review on development of nanofluid preparation and characterization. *Powder Technol* 196(2):89–101
10. Ghadimi A, Saidur R, Metselaar HSC (2011) A review of nanofluid stability properties and characterization in stationary conditions. *Int J Heat Mass Transf* 54:4051–4068
11. Rosensweig RE (1997) *Ferrohydrodynamics*. Courier Dover Publications
12. Lian W, Xuan Y, Li Q (2009) Characterization of miniature automatic energy transport devices based on the thermomagnetic effect. *Energy Convers Manage* 50(1):35–42
13. Dondapati RS, Saini V, Verma KN, Usurumarti PR (2017) Computational prediction of pressure drop and heat transfer with cryogen based nanofluids to be used in micro-heat exchangers. *Int J Mech Sci* 130:133–142
14. Das SK, Putra N, Thiesen P, Roetzel W (2003) Temperature dependence of thermal conductivity enhancement for nanofluids. *J Heat Transfer* 125(4):567–574

15. Yu W, Xie H, Chen L, Li Y (2009) Investigation of thermal conductivity and viscosity of ethylene glycol based ZnO nanofluid. *Thermochim Acta* 491:92–96
16. Hwang YJ, Ahn YC, Shin HS, Lee CG, Kim GT, Park HS, Lee JK (2006) Investigation on characteristics of thermal conductivity enhancement of nanofluids. *Curr Appl Phys* 6(6):1068–1071
17. Xuan Y, Li Q (2003) Investigation on convective heat transfer and flow features of nanofluids. *J Heat Transfer* 125(1):151–155
18. Yang Y, Zhang ZG, Grulke EA, Anderson WB, Wu G (2005) Heat transfer properties of nanoparticle-in-fluid dispersions (nanofluids) in laminar flow. *Int J Heat Mass Transf* 48(6):1107–1116
19. Li Q, Xuan Y, Wang J (2005) Experimental investigations on transport properties of magnetic fluids. *Exp Thermal Fluid Sci* 30(2):109–116
20. Sandhu RS, Agarwal R, Dondapati RS (2020) Computational investigation on the thermal characteristics of heat pipe using nanofluids. In: *Advances in intelligent manufacturing*. Springer, Singapore, pp 169–180
21. Jilte R, Ahmadi MH, Kumar R, Kalamkar V, Mosavi A (2020) Cooling performance of a novel circulatory flow concentric multi-channel heat sink with nanofluids. *Nanomaterials* 10(4):647
22. Chatterjee C, Agarwal R, Dondapati RS, Saini V (2019) Investigation on thermohydraulic characteristics of Al₂O₃ based nanofluids in microchannels. *JP J Heat Mass Transfer* 17:183–188
23. Schwab L, Hildebrandt U, Stierstadt K (1983) Magnetic benard convection. *J Magn Magn Mater* 39:113–114
24. Ganguly R, Sen S, Puri IK (2004) Thermomagnetic convection in a square enclosure using a line dipole. *Phys Fluids* 16(7):2228–2236
25. Banerjee S, Mukhopadhyay A, Sen S, Ganguly R (2011) The effects of magnetization saturation on thermomagnetic convection in a locally heated square enclosure. *Numer Heat Transfer Part A* 59:693–718
26. Nkurikiyimfura I, Wang Y, Pan Z (2013) Heat transfer enhancement by magnetic nanofluids: a review. *Renew Sustain Energy Rev* 21:548–561
27. Blums E, Mezulis A, Kronkalns G (2008) Magnetoconvective heat transfer from a cylinder under the influence of a nonuniform magnetic field. *J Phys Condens Matter* 20(20):204128(1–5)
28. Yamaguchi H, Zhang XR, Niu XD, Yoshikawa K (2010) Thermomagnetic natural convection of thermo-sensitive magnetic fluids in cubic cavity with heat generating object inside. *J Magn Magn Mater* 322(6):698–704
29. Jeffreys H (1928) Some cases of instability in fluid motion. *Proc Roy Soc London. Series A, Containing Pap Math Phys Charact* 118(779):195–208
30. Chandrasekhar S (1981) *Hydrodynamic and Hydromagnetic Stability*. Dover, New York
31. Chand R (2013) Thermal instability of rotating nanofluid. *Int J Appl Math Mech* 9(3):70–90
32. Sunil, Mahajan A (2008) A nonlinear stability analysis for rotating magnetized ferrofluid heated from below. *Appl Math Comput* 204:299–310
33. Eltayeb IA, Rahman MM (2013) Model III: Benard convection in the presence of horizontal magnetic field and rotation. *Phys Earth Planet Inter* 221:38–59
34. Mahajan A, Arora M (2013) Convection in rotating magnetic nanofluids. *Appl Math Comput* 219(11):6284–6296
35. Stevens RJ, Clercx HJ, Lohse D (2013) Heat transport and flow structure in rotating Rayleigh-Benard convection. *Eur J Mech B/Fluids* 40:41–49
36. Yadav D, Agrawal GS, Bhargava R (2011) Thermal instability of rotating nanofluid layer. *Int J Eng Sci* 49(11):1171–1184
37. Varshney H, Baig MF (2008) Rotating Rayleigh-Benard convection under the influence of transverse magnetic field. *Int J Heat Mass Transf* 51:4095–4108
38. Malashetty MS, Gaikwad SN (2002) Effect of cross diffusion on double diffusive convection in the presence of horizontal gradients. *Int J Eng Sci* 40:773–787
39. Kim J, Choi CK, Kang YT, Kim MG (2006) Effects of thermodiffusion and nanoparticles on convective instabilities in binary nanofluids. *Nanoscale Microscale Thermophys Eng* 10(1):29–39

40. Nield DA, Kuznetsov AV (2011) The onset of double-diffusive convection in a nanofluid layer. *Int J Heat Fluid Flow* 32(4):771–776
41. Kuznetsov AV, Nield DA (2010) The onset of double-diffusive nanofluid convection in a layer of a saturated porous medium. *Transp Porous Media* 85(3):941–951
42. Ryskin A, Pleiner H (2004) Influence of a magnetic field on the Soret-effect-dominated thermal convection in ferrofluids. *Phys Rev E* 69:046301
43. Sunil, Sharma A, Sharma RC (2006) Effect of dust particles on ferrofluid heated and soluted from below. *Int J Therm Sci* 45(4):347–358
44. Harfash AJ (2013) Magnetic effect on instability and nonlinear stability of double-diffusive convection in a reacting fluid. *Continuum Mech Thermodyn* 25:89–106
45. Mahajan A, Sharma MK (2019) Double-diffusive convection in a magnetic nanofluid layer with cross diffusion effects. *J Eng Math* 115:67–87
46. Aly AM, Mohamed EM, Alsedais N (2021) Double-diffusive convection from a rotating rectangle in a finned cavity filled by a nanofluid and affected by a magnetic field. *Int Commun Heat Mass Transfer* 126
47. Pedley TJ, Kessler JO (1992) Hydrodynamic phenomena in suspensions of swimming microorganisms. *Annu Rev Fluid Mech* 24:313–358
48. Wager H (1910) The effect of gravity upon the movements and aggregation of *Euglena viridis*, Ehrb. and other micro-organisms. *Proc Roy Soc London. Series B, Containing Pap Biol Charact* 83(562):94–96
49. Platt JR (1961) Bioconvection Patterns in cultures of free-swimming organisms. *Science* 133(3466):1766–1767
50. Plesset MS, Winet H (1974) Bioconvection patterns in swimming microorganism cultures as an example of Rayleigh-Taylor instability. *Nature* 248:441–443
51. Kuznetsov AV, Avramenko AA (2004) Effect of small particles on the stability of bioconvection in a suspension of gyrotactic microorganisms in a layer of finite depth. *Int Commun Heat Mass Transfer* 31(1):1–10
52. Kuznetsov AV, Geng P (2005) The interaction of bioconvection caused by gyrotactic microorganisms and settling of small solid particles. *Int J Numer Meth Heat Fluid Flow* 15(4):328–347
53. Sharma YD, Kumar V (2011) Overstability analysis of thermo-bioconvection saturating a porous medium in a suspension of gyrotactic microorganisms. *Transp Porous Media* 90:673–685
54. Shaw S, Sibanda P, Sutradhar A, Murthy PVS (2014) Magneto-hydrodynamics and Soret effects on bioconvection in a porous medium saturated with a nanofluid containing gyrotactic microorganisms. *J Heat Trans* 136:052601(1–10)
55. Kaur K, Danesh M, Arora M (2021) Effect of microorganisms on the stability analysis in magnetic nanofluids. *J Phys Conf Ser* 1849:012008
56. Buongiorno J (2006) Convective transport in nanofluids. *J Heat Transfer* 128(3):240–250
57. Piazza R (2008) Thermophoresis: moving particles with thermal gradients. *Soft Matter* 4(9):1740–1744
58. Suwa M, Watarai H (2011) Magnetoanalysis of micro/nanoparticles: a review. *Anal Chim Acta* 690(2):137–147

Study of Erosion Behavior of Al₂O₃ Coatings Deposited by Plasma Spray on SS-304



Gaurav Prashar and Hitesh Vasudev

Abstract The current work, investigates mechanical and microstructure features of Al₂O₃ ceramic coating deposited on AISI-304 substrate by employing the plasma spraying (PSing) technique. Scanning electron microscope (SEM) analysis, energy dispersive X-ray analyzer (EDAX), and X-ray diffractometer (XRD) were used to examine the microstructure and phase composition properties of the Al₂O₃ ceramic coating. The microstructure and microhardness, of the as-sprayed coating, were determined.

Keywords Al₂O₃ · Thermal spraying · Erosion · Coating · AISI-304

1 Introduction

The selection of a material for the strenuous conditions requires specific solutions; a material with a blend of multiple features like good mechanical properties, better erosion, and corrosion resistant features is regarded to be useful and efficient for manufacturing sector. Since most of the industrial applications generally deal with surfaces of the structural components which can degrade due to various mechanisms, by applying a suitable surface treatment (in the form of wear-resistant coatings) boost the beneficial set of properties to the level called for, because in aggressive environments, surface of the component has to play a decisive role [1]. Among the various surface modification procedures, currently accessible and recognized around the globe by big industry giants is thermal spraying (TS), popularly known to provide various merits regarding the optimization of distinct properties like resistance to degradation by corrosion and erosion along with thermal insulation. Different materials (i.e., metals, composites, ceramics, and alloys) can be deposited in the form of coatings having aforementioned properties. However, the ceramics may be recommended as captivating candidate for various manufacturing applications because of their remarkable high-temperature features (i.e., resistance to erosion,

G. Prashar · H. Vasudev (✉)

School of Mechanical Engineering, Lovely Professional University, Phagwara, Punjab 144411, India

e-mail: hiteshvasudev@yahoo.in

Table 1 Reported chemical composition for AISI-304 substrate (wt %)

(Wt %)							
Carbon	Manganese	Silicon	Chromium	Nickel	Phosphorous	Sulfur	Iron
0.16	1.21	0.42	16.31	8.43	0.032	0.02	Balance

chemical stability, and higher hardness). In the field of coatings requiring erosive wear properties in specific, oxides like Al_2O_3 , Cr_2O_3 , TiO_2 , etc. can be recommended and may be deposited by different TS processes relying on the final properties required [2, 3]. But the final deposited microstructure of the TS process solely relies on the TS technique selected for the coating deposition.

The Al_2O_3 was selected as coating material on account of its (a) better chemical stability at peak temperatures, (b) better hardness, and (c) less price [4, 5]. The PSing process was selected for the coating formulation. The PSing is preferred because of its advantage of spraying high melting point materials like superalloys and ceramics. Moreover, it provides economical and quality coatings.

2 Experimental Set-Up Details

2.1 Base Material

In this experimental study, AISI-304 was taken as the base material. The material was purchased from *Ludhiana (Punjab)* in the form of flat strip with having rectangular cross-section with 5 mm thickness. The chemical composition of selected substrate material was verified according to ASTM E 1086-08 test method and same is communicated in Table 1.

The specimens with each dimension measuring $15 \times 10 \times 5 \text{ mm}^3$ were cut using EDM operation from the AISI-304 flat strip and thereafter subsequently grit blasted for strong adhesion between AISI-304 substrate surface and deposited coating [6]. The average value reported for surface roughness (Ra) of base substrate was set around $6 \pm 1.02 \text{ }\mu\text{m}$. This value was maintained for better metallurgical bonding.

2.2 Coating Feedstock Powder

Commercially available Al_2O_3 powder was selected as the coating feedstock material in PSing process for the deposition of coating. The morphology and EDAX of Al_2O_3 powder are shown in Fig. 1a, b. The size of the particles ranges between 45 and 50 μm . Al_2O_3 powder is irregular and angular in shape and the EDS compositional study clearly specifies significant occupancy of the Alumina and Oxygen elements in the selected coating feedstock powder corresponding to point 1 in Fig. 1a.

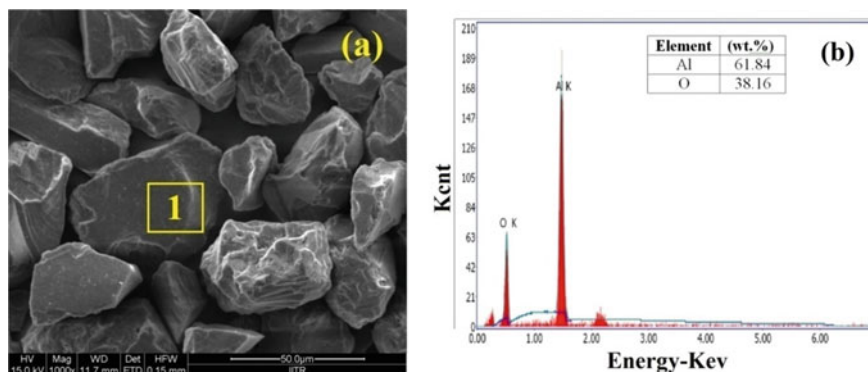


Fig. 1 a SEM photograph, and b EDS spectra of selected Al₂O₃ coating powder

2.3 Deposition of Coating

At Anod Plasma Ltd. in Kanpur, the PS coating was deposited using commercialized available plasma equipment (40 kW Miller, USA) (India). The selected Al₂O₃ material was introduced into the high-temperature plasma jet. Inert gas (Ar) was utilized as a protective gas to reduce oxide levels in deposited coating and to help propel Al₂O₃ powder. The PSing process deposition parameters once selected (Table 2) were kept constant during deposition of coating. The thickness of Al₂O₃ coating rest in the range of 140 ± 10 μm.

3 Characterization

The XRD profiles evaluated for the selected Al₂O₃ powder and deposited coating were investigated (*Make by: Bruker, and Model No: D8-Advance*) at XRD set-up facility available with Lovely Professional University, Phagwara with Cu-Kα radiation source operated at power 40 kV and current 40 mA. The final scanning angle

Table 2 Spraying parameters selected for spraying Al₂O₃ feedstock powder

Description	
Spraying technique	Commercial plasma system
Current	700A
Voltage	30–40 V
Powder flow rate (rev/min)	3.3
Spraying distance (mm)	95–111
Plasma arc gas (psi)	61
Carrier gas (psi)	43

selected was in range of 10° – 80° , with step time $1^{\circ}/\text{min}$. Furthermore, the final deposited samples were cut along the depth of the coating by a slow-speed cutter with having diamond blade (*Model No: MS-10, and Make by: Ducom Instru. Pvt. Limited, Bangalore, India*). The mirror polishing of the PS specimens for SEM/EDAX purposes was done on a cloth wheel polishing m/c with help of $1\ \mu\text{m}$ diamond paste. Further, porosity of the PS specimens was found out by studying BSE images (*Make by: Dewinter Material Plus, and Model No: 4.3*) at IKGPTU Kapurthla. The microhardness measurements of the PS specimens were carried out with Digital Micro Vickers hardness tester (*Model No : QS-IAT-8, Make by : Qualitech systems, Ludhiana*). The hardness indents were taken along polished cut section of the PS coating (load of 200 g) with dwell period of 10 s. Finally, the average value of 10 readings: both in case of porosity and microhardness measurements were recorded for Al_2O_3 coating.

4 Results and Discussion

Al_2O_3 ceramic coating was successfully deposited by plasma technique on AISI-304 substrate as explained in the previous section. In this section characterization of uncoated and coated samples was explained with suitable illustrations.

4.1 Microstructural and Mechanical Features of PS Coating

The XRD patterns of Al_2O_3 ceramic powder are shown in Fig. 2a. indicating a significant presence of α - Al_2O_3 phase in the selected ceramic powder (JCPDS refer: number. 00-001-1243). The XRD patterns of PS Al_2O_3 coating on AISI-304 consist of α - Al_2O_3 and γ - Al_2O_3 phases (Fig. 2b). Both α and γ -phase content present in the as-sprayed coating relies on melting condition of incoming impacting powder particles which in turn was a function of flame heat enthalpy and the particle residence duration in the heated plasma jet. The α - Al_2O_3 phase is attributed to the un-melted Al_2O_3 particles or fully molten Al_2O_3 particles cooling down at a lesser rate, whereas metastable γ - Al_2O_3 nucleates due to lower nucleation energy, and higher quenching rates of the Al_2O_3 molten splats which prevent transformation to the α - Al_2O_3 phase [7, 8]. The electrical insulation and better wear resistance properties [9], may be described by this hexagonal close-packed structure of α - Al_2O_3 in contrast with the γ - Al_2O_3 cubic structure. Hence α - Al_2O_3 is the preferred phase.

The surface-scale morphology of PS Al_2O_3 coating on the AISI-304 substrate is presented in Fig. 3. The microstructure of the PS coating comprise of Al_2O_3 splats (in melted state), un-melted state along with existence of pores (with varying sizes) which are trademark structural features for PS coatings.

Surface-scale morphological characteristics and EDAX patterns from a point on deposited coating were shown in Fig. 4. The EDAX spectrum exhibits the well-built

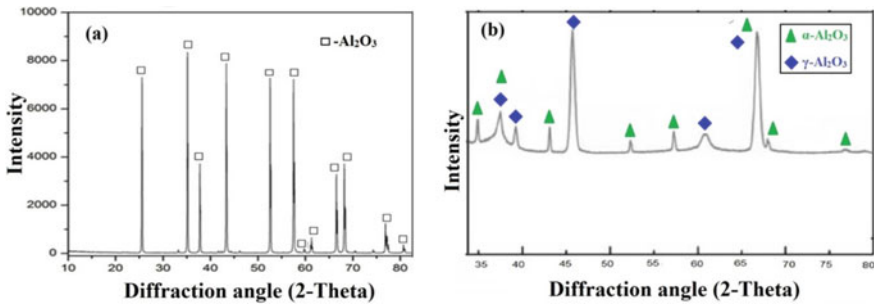
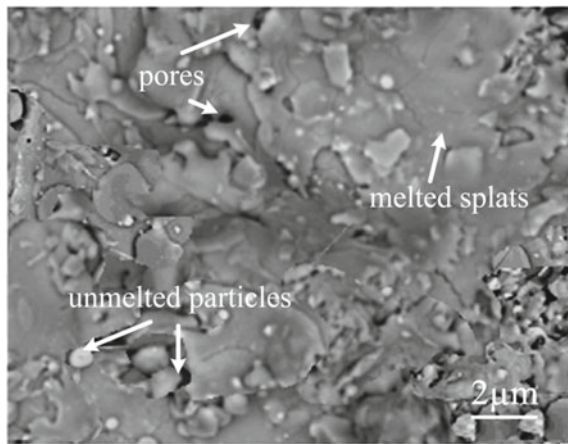


Fig. 2 XRD image patterns: **a** of ceramic Al₂O₃ feedstock powder, and **b** on AISI-304 steel substrate

Fig. 3 SEM micrograph of PS Al₂O₃ coating



presence of Alumina and Oxygen elements, which indicates that the Al₂O₃ ceramic particles have preserved its uniqueness because of its high melting point.

The cross-sectional photograph of the PS coating is presented in Fig. 5. Coating cross-sectioned micrographs confirm a good mechanical interlocking among Al₂O₃ coating and AISI-316. A particular splat formulation can be observed in the PS coating micrograph. Further, interface of AISI-304 and PS coating are without any defect and free from foreign particles. The coating exhibited a dense, smooth and stable microstructure. The evaluated thickness of Al₂O₃ coating rest in the range of $140 \pm 10 \mu\text{m}$.

Hardness is the utmost variable that decides the act of deposited coating. In current work average digital microhardness value of the PS Al₂O₃ coating is recorded as $880 \pm 50 \text{HV}0.2$. The ceramic Al₂O₃ coatings deposited in past by using PSing technique and hybrid low-velocity oxy-fuel process showed the value of $870 \pm 60 \text{HV}0.2$ and $795 \pm 20 \text{HV}$, respectively. Yin et al. in their findings reported an average value of $870 \pm 60 \text{HV}0.2$ for PS Al₂O₃ coatings [9]. Islak et al. measured an average value

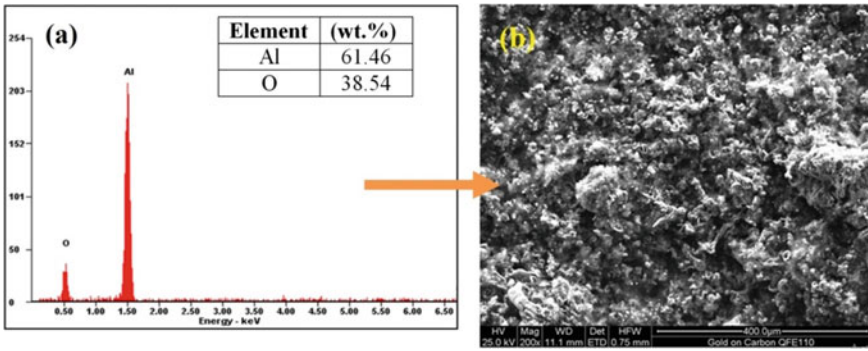


Fig. 4 PS Al₂O₃: **a** surface-scale morphological characteristic and **b** EDAX pattern from a point on Al₂O₃ as-coated AISI-304steel

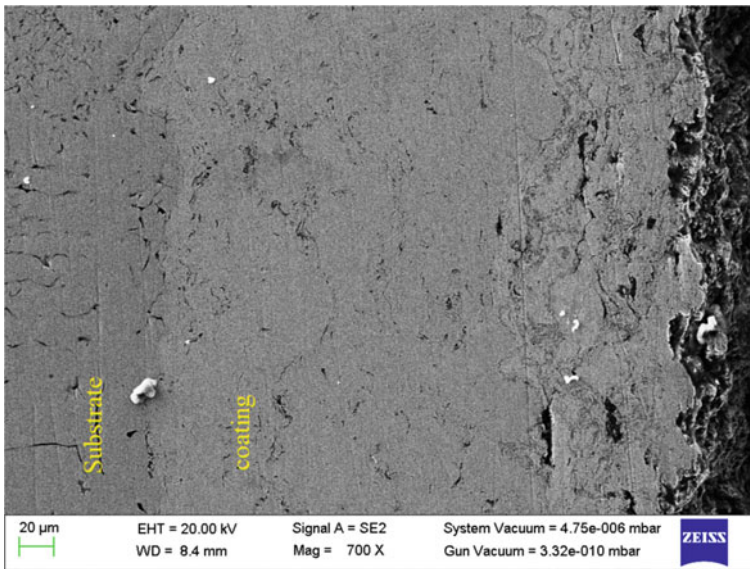


Fig. 5 Cross-sectional image of the PS Al₂O₃ coating on AISI-304 substrate

of about 905 HV0.2 for PS Al₂O₃ coating [10]. The average value of PS Al₂O₃ was reported to be 850 HV0.2 [11]. The higher value of hardness in PS coating is due to hard ceramic Al₂O₃ content present in the final deposited microstructure. Porosity of PS Al₂O₃ coating rest in range of 1–2% in present work.

5 Conclusion

This investigation of microstructural and mechanical properties of PS Al₂O₃ coating has resulted in the below-mention specified conclusions:

- The PSing technique was successful in depositing Al₂O₃ ceramic coating on the AISI-304.
- A detailed and in-depth microstructural & mechanical study was conducted to understand the Al₂O₃ ceramic coating structure–property correlation.
- A deposited coating has hardness value: of 880 ± 50HV0.2.
- Porosity of PS Al₂O₃ coating rest in range of 1–2%.

References

1. Singh S, Prakash C, Singh H (2020) Deposition of HA-TiO₂ by plasma spray on β-phase Ti-35Nb-7Ta-5Zr alloy for hip stem: characterization, mechanical properties, corrosion, and in-vitro bioactivity. *Surf Coat Technol* 25(398):126072
2. Singh H, Prakash C, Singh S (2020) Plasma spray deposition of HA-TiO₂ on β-phase Ti-35Nb-7Ta-5Zr alloy for hip stem: characterization of bio-mechanical properties, wettability, and wear resistance. *J Bionic Eng* 17(5):1029–1044
3. Singh H, Kumar R, Prakash C, Singh S (2021) HA-based coating by plasma spray techniques on titanium alloy for orthopedic applications. *Mater Today: Proc* 50(5):612–628
4. Grewal HS, Singh H, Agrawal A (2013) Microstructural and mechanical characterization of thermal sprayed nickel-alumina composite coatings. *Surf Coat Technol* 216:78–92
5. He L, Tan Y, Wang X, Xu T, Hong X (2014) Microstructure and wear properties of Al₂O₃–CeO₂/Ni-base alloy composite coatings on aluminum alloys by plasma spray. *Appl Surf Sci* 314:760–767
6. Pramanik A, Basak AK, Prakash C (2019) Understanding the wire electrical discharge machining of Ti6Al4V alloy, *Heliyon*, 5(4):e01473.
7. Tailor S, Vasishthal N, Modi A, Modi SC High-performance Al₂O₃ coating by hybrid-LVOF (low-velocity oxyfuel) process. *J Therm Spray Tech*. <https://doi.org/10.1007/s11666-020-01033-6>
8. Toma FL, Berger LM, Stahr CC, Naumann T, Langner S (2012) Thermally sprayed Al₂O₃ coatings having a high content of corundum without any property reducing additives and method for the production thereof. U S Patent 8318261:B2
9. Yin Z, Tao S, Zhou X, Ding C (2008) Microstructure and mechanical properties of Al₂O₃–Al composite coatings deposited by PSing. *Appl Surf Sci* 254:1636–1643
10. Islak S, Emin N, Özorak C, Hraam HRH (2019) Microstructure, hardness and biocompatibility properties of ceramic based coatings produced by plasma spray method. *Res Eng Struct Mat* 5(2):127–136
11. Prashar G, Vasudev H (2021) High temperature erosion behavior of plasma sprayed Al₂O₃ coating on AISI-304 stainless steel. *World J Eng*. <https://doi.org/10.1108/WJE-10-2020-0476>

Erosion Behaviour of Al₂O₃ Coatings Deposited by Plasma Spray on AISI-316 Substrate



Gaurav Prashar and Hitesh Vasudev

Abstract The current experimental study focuses on the deposition of Al₂O₃ ceramic coating on AISI-316 samples by the plasma spray (PS) technique. Erosive wear test was performed at 30° and 90° angle of impact in a hot air-jet erosion tester (HAET) at a temperature 400 °C. The microstructure and erosive wear performance of the PS coated and AISI-316 uncoated samples were determined. The deposition of Al₂O₃ ceramic coating onto AISI-316 steel substrate has shown to be a promising means for protecting surface of the steel substrate from erosive wear. The PS coated AISI-316 samples show better erosive wear resistance at an angle of 30° in contrast with 90° angle. The wear mechanism for erosion as observed from SEM micrographs of eroded samples indicates micro-cutting, ploughing and pull out of Al₂O₃ ceramic particles. In nut shell, PS coated samples were successful in combating erosion in comparison with AISI-316 sample.

Keywords Plasma spray · Al₂O₃ · Erosion · Coating · AISI-316

1 Introduction

Austenitic steel (AISI-316) is a commonly used material in power plant industry today due to its lower cost and capability to combat the combined effects of erosion-corrosion in aggressive conditions [1, 2]. However, lower hardness of AISI-316 can reduce its wear resistance and can cut down the life of the structural components operating at higher temperatures [3, 4]. Therefore, in order to enhance the hardness of these austenitic steels, its surface is exposed to different methods of treatments, namely high-velocity oxy-fuel (HVOF), PS, thermo-chemical treatments, PVD and CVD and also laser treatments [5–9]. PS technique is regarded to be productive approach for the deposition of the ceramics like Al₂O₃ for improving the life of components in industrial and medical field [10–13]. The current experimental study is an attempt to boost the high temperature erosion performance of AISI-316 substrate

G. Prashar · H. Vasudev (✉)

School of Mechanical Engineering, Lovely Professional University, Phagwara, Punjab 144411, India

e-mail: hiteshvasudev@yahoo.in

Table 1 Reported chemical composition for AISI-316 substrate (wt %)

(Wt %)							
C	Mn	Si	Cr	Ni	P	S	Fe
0.16	1.21	0.42	16.31	8.43	0.032	0.02	Remaining

by coating it with hard Al_2O_3 ceramic particles. The Al_2O_3 was selected as coating material on account of its (a) better chemical stability at peak temperatures, (b) better hardness and (c) less price [14, 15]. The PS process was selected for the coating formulation. The PS is preferred because of its advantage of spraying high melting point materials like superalloys and ceramics. Moreover, it provides economical and quality coatings. Hence, the main idea behind the current experimental study is to find out the erosive wear behaviour of Al_2O_3 coatings at elevated temperatures. The PS coated and uncoated AISI-316 samples were tested with HAET at a temperature 400°C for 3 h. SEM analysis, EDAX and XRD methods were used to examine the microstructure and wear mechanism of tested samples. The findings of current experimental study may be helpful to resist the erosive wear of the AISI-316 metal.

2 Experimental Set-Up Details

2.1 Base Metal

In this experimental study, AISI-316 was taken as the base metal. The metal for experimental study was purchased from *Jalandhar (Punjab)* in the form of flat solid strip having rectangular cross-section with 5 mm thickness. The chemical composition of selected metal was verified according to ASTM E 1086-08 test method, and same is communicated in Table 1.

The specimens with each dimension measuring $15 \times 10 \times 5 \text{ mm}^3$ were cut using EDM operation from the AISI-316 flat solid strip and thereafter grit blasted for strong adhesion between AISI-316 metal surface and deposited coating [16]. The average value reported for surface roughness (Ra) of base metal was set around $6 \pm 1.02 \mu\text{m}$. This value was maintained for better metallurgical bonding.

2.2 Deposition of Coating

At Anod Plasma Ltd. in Kanpur, the PS coating was deposited using commercialized available plasma equipment (40 KW Miller, USA) (India). The selected Al_2O_3 material was introduced into the high temperature plasma jet. Inert gas (Ar) was utilized as a protective gas to reduce oxide levels in deposited coating and to help propel Al_2O_3 powder. The PSing process deposition parameters once selected (Table

Table 2 Spraying parameters selected for spraying Al₂O₃ feedstock powder

Description	
Spraying technique	Commercial plasma system
Current	700 A
Voltage	30–40 V
Flow rate for powder (rev/min)	3.3
Spraying distance between gun and surface (mm)	95–111
Plasma arc gas (psi)	61
Carrier gas (psi)	43

2) were kept constant during deposition of coating. The thickness of Al₂O₃ coating rests in the range $140 \pm 10 \mu\text{m}$.

2.3 Erosion Testing

High temperature erosion testing (HET) of PS Al₂O₃ coated and AISI-316 uncoated samples were conducted according to the ASTM G76-02 standard using HAET (*TR-471-M10; Make by; Ducom Inst., Bangalore, India*) to examine the erosive wear resistance. The HAET rig comprises of (a) air compressor, (b) particle feeder and (c) air particle mixing and accelerating chamber. Compressed air was properly mixed with sharp and angular erodent particles, and then, mixture is accelerated further by passing it via heat resistant tungsten carbide nozzle having standard diameter of 4 mm. These erodent particles strike on the samples placed in sample holder (30° and 90°) with an impact. The impacting velocity of erodent particles can be adjusted by altering the air pressure. The average erodent particle size was 45 μm and was heated before experiment at temperature 900 °C for duration 60 min to remove moisture from erodent (alumina) if any. The HET was performed in simulated environment at 900 °C (air temperature) and 400 °C (sample temperature) in an HAET, and the time fixed for one sample is 180 min. The weight of all samples before and after studies was measured using electronic balance *m/c* and then pen down. For comparison purpose, both PS Al₂O₃ coated and AISI-316 uncoated specimens undergo the same steps. The conditions for HET are shown in Table 3.

3 Results and Discussion

Al₂O₃ ceramic coating was successfully deposited by plasma technique on AISI-316 substrate as explained in the previous section. In this section, characterization of uncoated and coated samples was explained with suitable illustrations.

Table 3 HET parameters

Erosion conditions	
Erodent material	Alumina (irregular shape)
Average erodent particle size (μm)	45
Particle velocity (m/s)	35
Erodent feed rate (g/min)	2
Impact angle (degree)	30 and 90
Air temperature (degree)	900
Specimen temperature (degree)	400
Nozzle diameter (mm)	4
Test time (min)	180

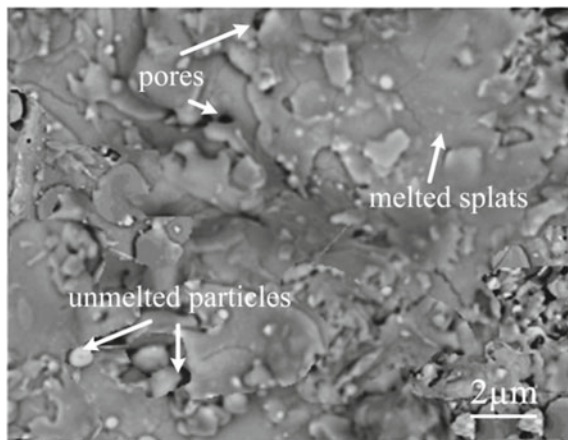
3.1 Microstructural Features of PS Coating

The surface scale morphology of PS Al_2O_3 coating on the AISI-316 substrate is presented in Fig. 1. The microstructure of the PS coating comprises Al_2O_3 splats (in melted state), un-melted state along with existence of pores (with varying sizes) which are trademark structural features for PS coatings.

Surface-scale morphological characteristic and EDAX pattern from a point on deposited coating were shown in Fig. 2. The EDAX spectrum exhibits the well-built presence of alumina and oxygen elements, which indicates that the Al_2O_3 ceramic particles have preserved its uniqueness because of its high melting point.

The cross-sectional photograph of the PS coating is presented in Fig. 3. Coating cross-sectioned micrographs confirm a good mechanical interlocking among Al_2O_3 coating and AISI-316. A particular splat formulation can be observed in the PS coating micrograph. Further, interface of AISI-316 and PS coating is without any defect and free from foreign particles. The coating exhibited a dense, smooth and

Fig. 1 SEM micrograph of PS Al_2O_3 coating



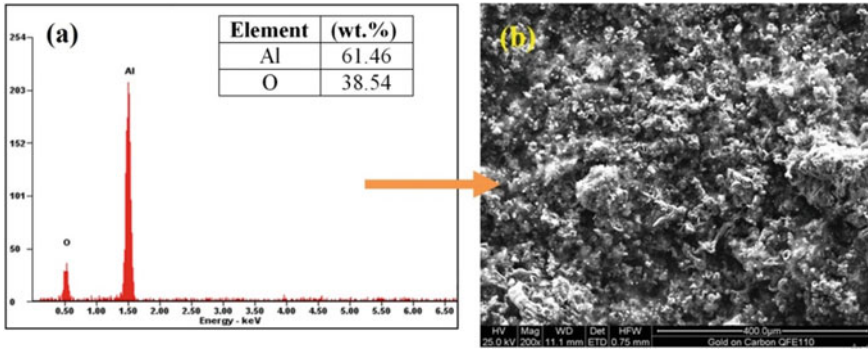


Fig. 2 PS Al₂O₃: **a** Surface-scale morphological characteristic and **b** EDAX pattern from a point on Al₂O₃ as-coated AISI-316 steel

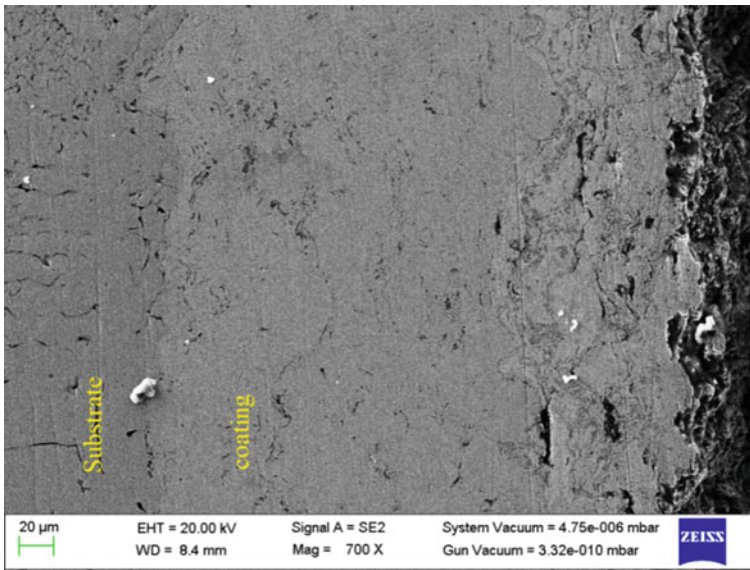


Fig. 3 Cross-section of the PS Al₂O₃ coating on AISI-316 substrate

stable microstructure. The evaluated thickness of Al₂O₃ coating rests in the range 140 ± 10 µm.

3.2 Effect of Striking Angles on Erosion

For all the specimens, the erosive wear initiates from the centre initially and then excels to the specimen edges. At normal striking angle, material erodes, setting up

a circular shaped depression, whereas when striking angle was oblique, depression changes its shape from circular to elliptical. The macrographs of worn out specimens have 3 zones: a central region from where bulk of the erosion occurs, a 2nd region having faint in colour where somewhat little erosion can be noticed and a 3rd outside area where a minor erosion is observed. Erosive wear rate for the uncoated AISI-316 specimen is higher at 30° impingement angle in comparison with 90° impingement angle, whereas for coated Al_2O_3 specimen, maximum erosion takes place at 90° striking angle. The coated specimen at 30° striking angle exhibits 2.3 times improvement in erosion resistance than uncoated, while for 90° improvement is 1.24 times the uncoated specimen. Therefore, deposition of Al_2O_3 ceramic coatings (PS) onto the AISI-316 is concluded to be a promising method for protecting surface of the steel substrate from erosive wear.

3.3 Erosion Mechanism of Specimens

The mechanisms of the material removal (MR) during HET from the uncoated and PS coated specimens are discussed in this section. For the uncoated specimen, higher erosion rate comes off at oblique striking angle, whereas for coated specimens, peak erosion comes off at normal striking angle. The differences in the specimen erosion rates can be related with MR mechanisms for these two striking angles. The viable erosion mechanism of the tested specimens is examined by SEM images. The AISI-316 specimen surface subjected to the solid particle erosion firstly undergoes the plastic deformation forming grooves and craters at normal striking angle. Due to the cutting action by the hard erodent particles at 30° striking angle, lips developed at the periphery of grooves which are further fractured and removed finally from these grooves as the erosion progresses further (Fig. 4). Bellman and Levy [17] during their experimental studies also observed similar outcomes as the erosive wear of the steel specimens was higher for oblique impact angle. Prashar and Vasudev also have similar findings [18].

The erosive wear mechanisms responsible for PS Al_2O_3 coatings include pull out of Al_2O_3 splats, micro-cutting and ploughing. The ploughing mechanism relates with the plastic smearing and material cutting. Brittle materials such as Al_2O_3 are not simply plastically deformed. Therefore, the erosion rate is minimal at 30° striking angle. In Fig. 5a, existence of craters specifies that the erosion mechanism comprises Al_2O_3 splat removal at 30° striking angle. At 30° striking angle, the large forces (tangential) act onto the Al_2O_3 splats because of incoming hard erodent particles. This is the reason behind the removal of the Al_2O_3 splats [19–21]. At 90° striking angle, the high kinetic energy of striking particles results in repeated impact. Brittle nature of Al_2O_3 allows the cracks to initiate and propagate forming crack networks. Hence, the MR rate is more in brittle materials. In Fig. 5b, the micrograph of PS coated Al_2O_3 eroded surfaces exhibits craters, and Al_2O_3 pull out as the prime erosion mechanism.

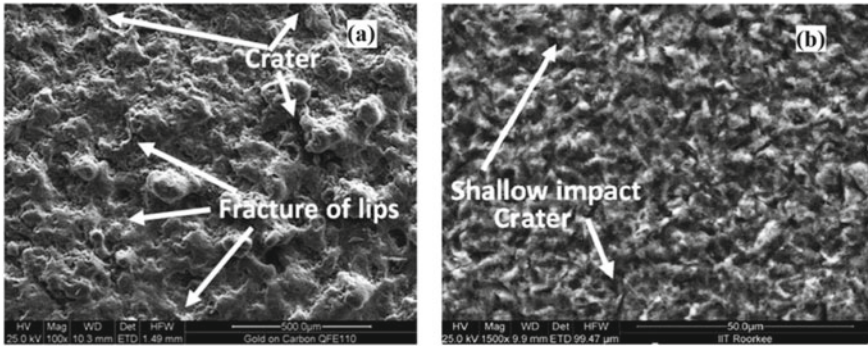


Fig. 4 SEM micrographs of uncoated AISI-316 at a 30° striking angle and b at 90° striking angle

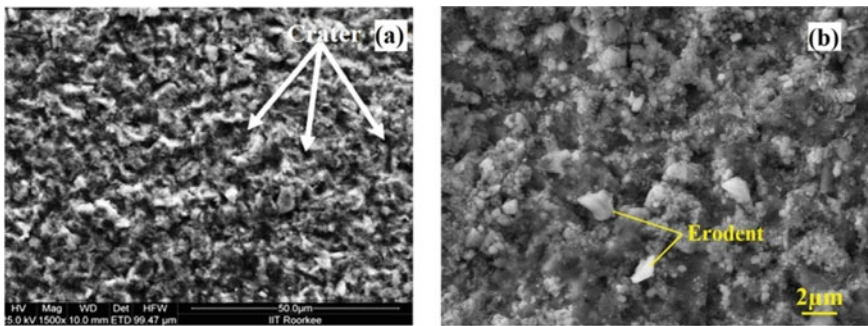


Fig. 5 SEM micrographs of the PS Al₂O₃ eroded coating at a 30° striking angle and b 90° striking angle

4 Conclusion

This investigation on elevated temperature erosive wear testing of PS Al₂O₃ coating has resulted in the below-mention specified conclusions:

- The PS technique was successful in depositing Al₂O₃ ceramic coating on the AISI-316.
- Deposition of Al₂O₃ ceramic coating on the AISI-316 steel substrate has shown to be a promising means for protecting surface of the steel substrate from erosive wear.
- Al₂O₃ ceramic coating in present investigation showed brittle erosion behaviour with the maximum erosion occurs at 90° striking angle.

References

1. Ali S, Abdul Rani AM, Altaf K, Hussain P, Prakash C, Hastuty S, Rao TV, Aliyu AA, Subramaniam K (2019) Investigation of alloy composition and sintering parameters on the corrosion resistance and microhardness of 316L Stainless Steel alloy. In: international scientific-technical conference manufacturing, Springer, Cham, pp 532–541
2. Martinez-Villafañe A, Almeyra MF, Gaona C, Gonzalez JC, Porcayo J (1998) High-temperature degradation and protection of ferritic and austenitic steels in steam generation. *J Mater Eng Perform* 7(1):108–113
3. Gil L, Brižhl S, Jimenez L et al. (2006) É corrosion performance of the plasma nitrided 316L stainless steel. *É Surf Coat Technol* 201:4424–4429
4. Meinert K, Wolf G (1998) Corrosion studies of stainless steel 316L, modified by ion beam techniques, under simulated physiological conditions. *Surf Coat Technol* 98:1148–1156
5. Fossati A, Borgioli F, Galvanetto E, Bacci T (2006) Glow-discharge nitriding of AISI 316L austenitic stainless steel: influence of treatment time. *Surf Coat Technol* 200:3511–3517
6. Yetim AF, Alsarhan A, Celik A (2010) Investigation of tribological and electrochemical properties of dual layer after low temperature plasma carbo-nitriding. *Surf Eng* 26:178–184
7. Abubakar T, Rahmon M, Dowling DP et al (2010) Adhesion performance of TiN coating with amorphous NiTi alloy interlayer onto 316L stainless biosteel deposited by sputtering process. *Surf Eng* 26:499–505
8. Yýldýz F, Yetim F, Alsarhan A, Efeođlu Ý (2010) Multipass scratch test behavior of TiAlN thin film deposited on 316L stainless steel and Ti6Al4V alloy with dc biased and pulsed magnetron sputtering. *Surf Eng* 26:578–583
9. Shankar AR, Kamachi UM (2009) Laser surface modification of plasma sprayed yttria stabilised zirconia coatings on type 316L stainless steel. *Surf Eng* 25:241–248
10. Singh S, Prakash C, Singh H (2020) Deposition of HA-TiO₂ by plasma spray on β -phase Ti-35Nb-7Ta-5Zr alloy for hip stem: characterization, mechanical properties, corrosion, and in-vitro bioactivity. *Surf Coat Technol* 25(398):126072
11. Singh H, Prakash C, Singh S (2020) Plasma spray deposition of HA-TiO₂ on β -phase Ti-35Nb-7Ta-5Zr alloy for hip stem: characterization of bio-mechanical properties, wettability, and wear resistance. *J Bionic Eng* 17(5):1029–1044
12. Singh H, Kumar R, Prakash C, Singh S, (2021) HA-based coating by plasma spray techniques on titanium alloy for orthopedic applications. *Mater Today: Proc* 50(5):612–628
13. Li CJ, Yang GJ, Ohmori A (2006) Relationship between particle erosion and lamellar microstructure for plasma-sprayed alumina coatings. *Wear* 260:1166–1172
14. Sarikaya O (2005) Effect of the substrate temperature on properties of plasma sprayed Al₂O₃ coatings. *Mater Des* 26:53–57
15. Nakamichi M, Takabatake T, Kawamura H (1998) Material design of ceramic coating by plasma spray method. *Fusion Eng Des* 41:143–147
16. Grewal HS, Singh H, Agrawal A (2013) Microstructural and mechanical characterization of thermal sprayed nickel-alumina composite coatings. *Surf Coat Technol* 216:78–92
17. Bellman R Jr, Levy A (1981) *Wear* 70:1
18. Prashar G, Vasudev H (2021) High temperature erosion behavior of plasma sprayed Al₂O₃ coating on AISI-304 stainless steel. *World J Eng.* <https://doi.org/10.1108/WJE-10-2020-0476>
19. Tabakoff W, Vittal BVR (1983) High temperature erosion study of INCO 600 metal. *Wear* 86:89–99
20. Grewal HS, Agrawal A, Singh H, Shollock BA (2014) Slurry erosion performance of Ni–Al₂O₃ based thermal-sprayed coatings: effect of angle of impingement. *J Therm Spray Technol* 23(3):389–401
21. Ramesh MR, Prakash S, Nath SK, Sapra PK, Venkataraman B (2010) Solid particle erosion of HVOF sprayed WC–Co/NiCrFeSiB coatings. *Wear* 269:197–205

A Detailed Investigation of Structural and Optical Properties of CTAB-Assisted Cr₂O₃ Nanoparticles



Jarnail Singh , Mayank Dotiyal, Pankaj Bhardwaj, Prabhakar Bhandari, Kaushal Kumar, Saurav Dixit, and Vikram Verma

Abstract Surfactant-assisted co-precipitation has been employed to synthesize chromium oxide (Cr₂O₃) nanoparticles. CTAB (cationic surfactant) was used in synthesis of nanoparticles of chromium oxide (Cr₂O₃). The concentrations of surfactants were tailored from 2 to 10 wt%. X-ray diffraction (XRD), field emission scanning electron microscopy (FESEM), fourier-transform infrared spectroscopy (FTIR), and Raman spectroscopy techniques were performed to demonstrate the structural properties. The crystallite size of the CTAB-assisted Cr₂O₃ nanoparticles was found to be decreasing as the surfactant concentration increased up to a critical concentration value, determined using the Scherrer's formula. The induced lattice strain in the nanoparticles was attributed to the shifting of the XRD peaks. The structural structure of the produced nanoparticles was confirmed as rhombohedral by the FT-IR and Raman spectra, as well as the XRD patterns. UV–Vis spectroscopy was used to evaluate the optical properties. The optical band gap energy of as-prepared nanoparticles at different CTAB-contents was determined using the Kubelka–Munk (K-M) technique, and revealed that the optical band gap energy of CTAB-assisted Cr₂O₃ nanoparticles was increasing as crystallite size decreases.

Keywords Surfactant · Rietveld refinement · Particle size · Band gap

J. Singh (✉) · M. Dotiyal · P. Bhandari · K. Kumar · V. Verma
Department of Mechanical Engineering, K.R. Mangalam University, Gurgaon 122103, India
e-mail: jarail.singh@krmangalam.edu.in

P. Bhardwaj
Department of Material Science and Engineering, National Institute of Technology,
Hamirpur 177005, India

S. Dixit
School of Management and Commerce, K.R. Mangalam University, Gurgaon 122103, India

Division of Research & Innovation, Uttaranchal University, Dehradun, India

1 Introduction

Recent research in the realm of nanoparticles has focused on tailoring their unique properties to meet specific requirements. The size (diameter) and shape of the metal/transition metal oxide nanoparticles have a big impact on these properties. The size of nanoparticles as a function of optical band gap energy is an essential characteristic (optical band gap is inversely proportional to the crystallite size). As a result, reducing the size of nanoparticles is a top objective for expanding the optical band gap. Because of their unique properties, the transition metal oxides (TMOs) have drawn significant attention. The majority of these unique features are deeply affected by imperfections in the material, such as vacancy defects, dislocation presence, stacking faults, and grain boundaries. Surfactants have been extensively researched for their ability to control the size and morphology of nanoparticles that have been synthesized. The surface tension reduces by surfactant owing to regulating the existing surface energy of the nanoparticles. Because of the lower surface tension, more particles can escape the aggregation process, resulting in a smaller mean particle size. With wide band gap energy of 3.1 eV, chromium oxide (Cr_2O_3) is one of the most important *p*-type semiconductor TMOs. It is a great option for photocatalytic and photovoltaic devices, as well as optical storage systems, due to its large band gap [1–6]. Below the Neel temperature, T_N of ~ 308 K, bulk chromium oxide exhibits antiferromagnetic behavior. By reducing the nanoparticles size, the magnetic characteristics can be improved (due to reduced coordination of the surface atoms). Because of its elevated melting point of ~ 2300 °C and exceptional oxidation resistance at extremely high temperatures, chromium oxide is often used as a refractory material. Wear resistance materials, electrochromic materials, catalysts, advanced coloring agents, hydrogen sorption materials, pigment, digital recording systems, coating materials for thermal protection, black matrix films, solar energy applications, and liquid crystal displays [7–10]. Singh et al. [1] used the co-precipitation approach to successfully synthesize Cr_2O_3 nanoparticles at various pH values. The pH values were varied from 6 to 10 with a step size of 1, and the crystallite size was reported with tailored pH value. The crystallite size was shown to have a direct relationship with the pH value, having lower crystallite size achieved at pH 6. Zhao et al. [2] used the surfactant-modified precipitation approach to successfully prepare Cr_2O_3 nanoparticles with an average size of 17 nm. To obtain the smallest nanoparticles size, several surfactants such as CTAB, PEG, SDBS, and PVP were employed at pH values ranging from 4.8 to 7.9. The average crystallite sizes for nanopowders samples treated with PVP, PEG, SDBS, and CTAB were 21, 21, 30, and 30 nm, respectively, demonstrating that crystallite size is a function of the type of surfactant used in the synthesis process. The optimum conditions for obtaining the smallest particle size were identified to be $\text{PEG}/\text{Cr}_2\text{O}_3 = 5$ wt% and $\text{pH} = 5.2$.

The surfactant-assisted co-precipitation approach resulted in a considerable reduction in nanoparticles size, as reported in the literature [2, 3, 11–17]. Sol-gel method [8], mechanical ball milling technique [19], detonation method [20, 21], chemical spray pyrolysis [17], hydrothermal reduction [6], microemulsions technique

[10], solid thermal breakdown [13], and sonochemical reaction [18] have all been used to synthesize Cr_2O_3 nanoparticles. The majority of these procedures necessitate costly equipment and complicated environmental conditions. In comparison to other approaches, the co-precipitation method has the following advantages such as easy control over particle size and morphology, simple preparation and quick; high yield and purity, and relatively inexpensive. Therefore, in this investigation, Cr_2O_3 nanoparticles were prepared using the co-precipitation technique and demonstrated its detailed structural and optical properties.

2 Experimental Details

Utilizing the co-precipitation approach, surfactant-assisted chromium oxide nanoparticles were successfully prepared using chromium (ii) nitrate nonahydrate [$\text{Cr}(\text{NO}_3)_3 \cdot 9\text{H}_2\text{O}$] as the chromium precursor and CTAB and SDS as cationic and anionic surfactants, respectively. With 150 ml of deionized water, a 0.1 M solution of chromium nitrate was first prepared. The surfactant (CTAB) was added to this solution at the desired concentration. The entire solution was aggressively agitated until the surfactant was completely dissolved and the mixture was homogenous. Drop by drop, ammonium hydroxide (NH_4OH) was added to the solution until the pH reached 6. This method was repeated with surfactant weight percentages ranging from 2 to 10%. To allow the precipitation process to take place, the solution was left overnight. The formed precipitate was found to be greenish in color. A centrifuge machine was used to filter the precipitate. The washed precipitate was dried in the heating mantle at 80–85 °C. To obtain the powdered sample, the precipitates were crushed and then calcined in the tube furnace for 4 h at 600 °C.

3 Results and Discussion

3.1 XRD Analysis

The structural information on the crystal structure, crystallite size, lattice parameters, and lattice strain in the unit cell was obtained using the X-ray diffraction technique. The wavelength (λ) of the X-ray employed in the XRD diffractometer was 1.5406 Å (Cu-K radiation) at 30 kV and 10 mA. With a step size of 0.2°, the scan range (1°/min) was taken within the range from 20° to 80°. The X-ray diffraction pattern for pure Cr_2O_3 nanoparticles is shown in Fig. 1. According to the miller indices, each recorded peak is identified and assigned a plane. The planes (012), (104), (110), and (116) have the most extreme peaks at two values: 24.50°, 33.56°, 36.15°, and 54.8°, respectively. The detected peaks corresponded to the previously reported values [1, 2]. The XRD peaks corresponding to various CTAB concentrations are shown in

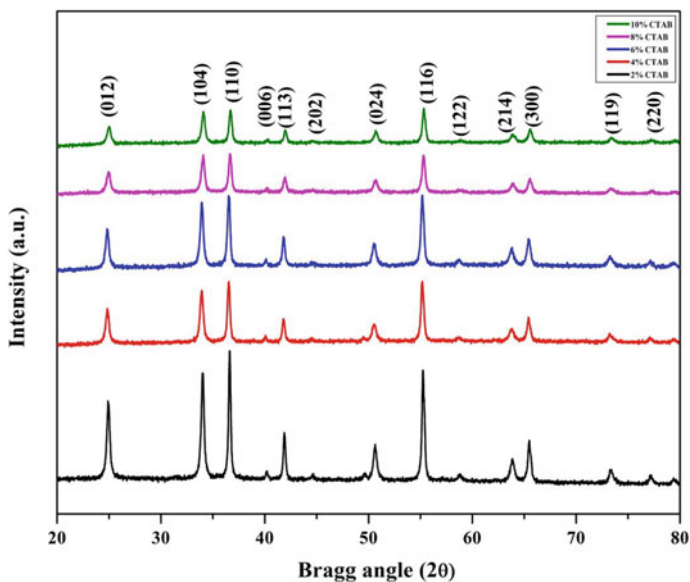


Fig. 1 X-ray diffraction patterns for the CTAB assisted Cr₂O₃ nanoparticles

Fig. 1. Because there is no extra peak in the samples prepared with CTAB surfactant, it may be inferred that the surfactant does not introduce any impurity into the samples. With increasing CTAB concentration, the intensity of the peaks diminishes. In the most intense XRD peaks, there is a notable shift towards a higher Bragg angle. With increasing CTAB concentration (up to a concentration of 8% w/w), the FWHM value of the peaks increases.

The cell volumes, bond lengths together with other structural data are provided in Table 1. Up to a threshold concentration, the edge lengths or lattice parameters, and hence the cell volume, decrease with increasing surfactant concentration. A contraction in the unit cell occurs as a result of the volume reduction, causing a compressive strain in the lattice. The displacement of the XRD peaks is due to this lattice strain. Furthermore, the intensities of diffraction peak for both surfactants drop systematically as the surfactant concentration increases. The reduction in intensity is also attributed to lattice change or rearrangement, because the crystallinity of the samples is retained. The Scherrer's equation was used to calculate the mean crystallite size (D):

$$D = \frac{K\lambda}{\beta \cos \theta} \quad (1)$$

where K is the Scherrer's constant (0.94 for spherical nanoparticles), marks the incident X-ray wavelength (0.15406 nm for Cu-K radiation), and represents the Bragg angle. The average crystallite size for various surfactant concentrations is

Table 1 Structural parameters for CTAB assisted Cr₂O₃ nanoparticles

Surfactant concentration (% w/w)	Crystallite size (nm)	Lattice parameters		Cell volume (Å ³)	Bond lengths (Å)	Lattice strain ($\times 10^{-3}$)
		<i>a</i> (Å)	<i>c</i> (Å)			
2	31.84	4.9648	13.609	290.51	1.963, 2.026	1.01
4	27.15	4.9619	13.602	290.01	1.958, 2.029	1.04
6	25.51	4.9621	13.601	290.03	1.954, 2.036	1.06
8	22.95	4.9497	13.573	287.98	1.953, 2.025	1.43
10	23.94	4.9645	13.610	290.50	1.956, 2.034	1.07

shown in Table 1. At 8% w/w CTAB concentration, the minimum values obtained are 22.48 nm. After reaching a specific concentration, the crystallite size increases.

3.2 FTIR Analysis

The Cr₂O₃ nanoparticles' FTIR spectrum is shown in Fig. 2. The IR spectra were measured between 4000 and 400 cm⁻¹. The vibration modes of the Cr-O bond were assigned four distinct bands at 620, 565, 443, and 410 cm⁻¹. The stretching modes of the Cr-O bond were ascribed to the peaks at 620 and 565 cm⁻¹, confirming the existence of crystalline pristine Cr₂O₃ nanoparticles [11].

The other two peaks, 443 and 410 cm⁻¹, correspond to the Cr-O bond's bending vibration modes. The deformed rhombohedral structure of Cr₂O₃ accounts for the two different values of stretching and bending modes for the Cr-O bond. The E_u modes are responsible for the peaks at 620, 565, and 443 cm⁻¹, whereas the infrared active A_{2u} vibration mode is responsible for the peak at 410 cm⁻¹.

3.3 Raman Spectroscopy Analysis

Our investigation found four vibrational modes at 320, 360, 561, and 621 cm⁻¹, as depicted in Fig. 3. The most intense peak, at 561 cm⁻¹, is attributed to the A_{1g} vibrational mode, which corresponds to the Cr-O stretching vibration. The E_g mode is assigned to the other minor peaks at 320, 360, and 621 cm⁻¹. The introduction of lattice strain and change in bond length causes a considerable shift in the Raman shift value of the most intense peak, as confirmed by XRD analysis.

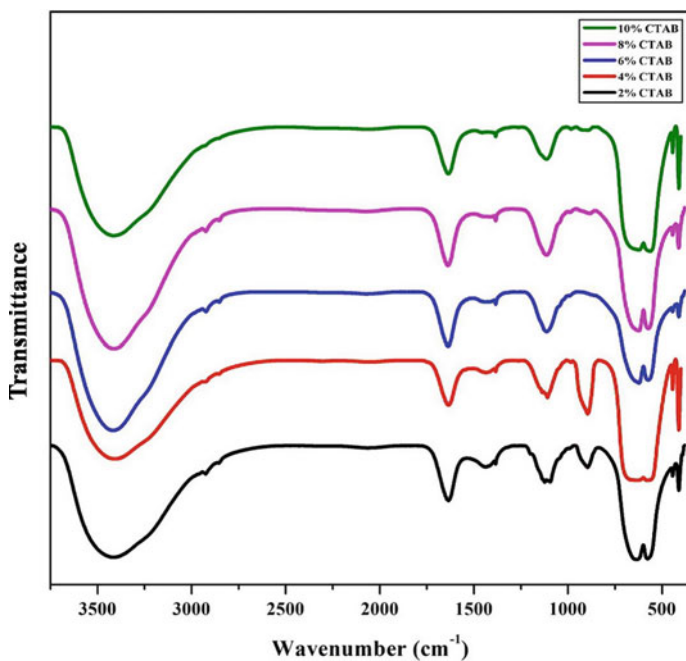


Fig. 2 CTAB-assisted Cr_2O_3 samples FTIR spectra at various concentrations

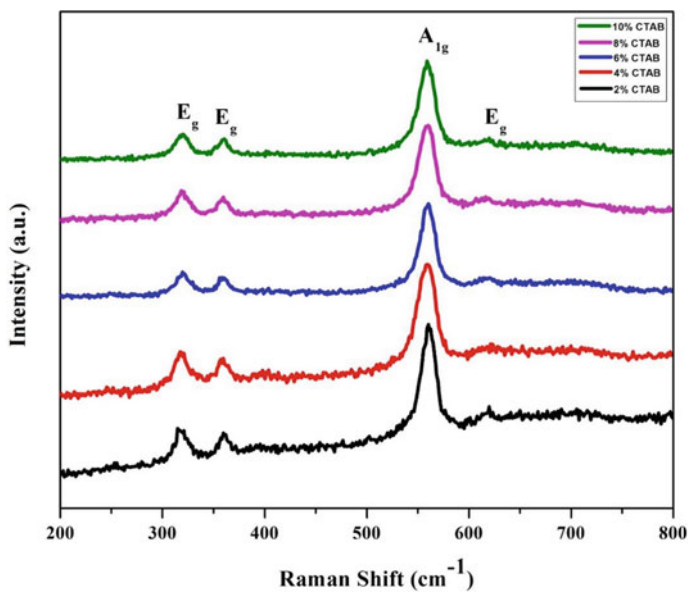
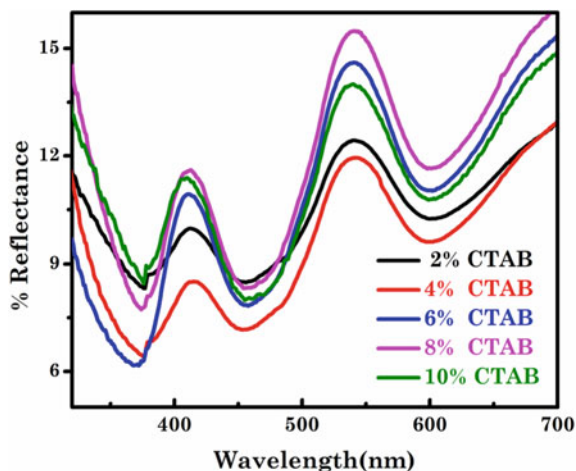


Fig. 3 Raman spectra of CTAB assisted Cr_2O_3 nanoparticles at different contents

Fig. 4 Spectra of UV–Vis reflectance for CTAB-assisted Cr_2O_3 nanoparticles at various concentrations



3.4 UV–Vis Spectroscopy Analysis

The diffused reflectance spectra (DRS) of the produced Cr_2O_3 nanoparticles at various CTAB concentrations are shown in Fig. 4. Three peaks can be seen in the reflectance spectra: 365, 457, and 610 nm. The peak at 365 nm can be used to calculate the band gap energy. The 3d orbital in Cr_2O_3 is separated into two sub-bands due to octahedral splitting, namely, double degenerate (e_g) and triple degenerate (t_{2g}). The ${}^4A_{2g} \rightarrow {}^4T_{1g}$ electronic transition of the Cr^{3+} ions is represented by a peak at 457 nm, and another peak at 610 nm shows the ${}^4A_{2g} \rightarrow {}^4T_{2g}$ d^3 electronic transition of the Cr^{3+} ions [1].

The KM plots for the CTAB aided samples with their corresponding band gap are shown in Fig. 5. With CTAB concentration increasing from 2 to 8%, the band gap energy increases from 2.72 to 3.00 eV. The fluctuation of the band gap energy with crystallite size is readily visible. The maximal band gap energy produced in the experiment was somewhat less than that of bulk Cr_2O_3 ($E_g = 3.1$ eV), despite the fact that the band gap energy increased with the decrease in crystallite size.

4 Conclusion

Using the co-precipitation approach, single phase Cr_2O_3 nanoparticles were successfully synthesized. XRD patterns were used to calculate lattice parameters, and it was revealed that the application of surfactants caused the lattice to decrease. A high degree of lattice strain results from this contraction in the unit cell, as seen by a substantial shift in the XRD peaks. The Scherrer's equation was used to determine the crystalline sizes, and the lowest sizes were achieved at a concentration of

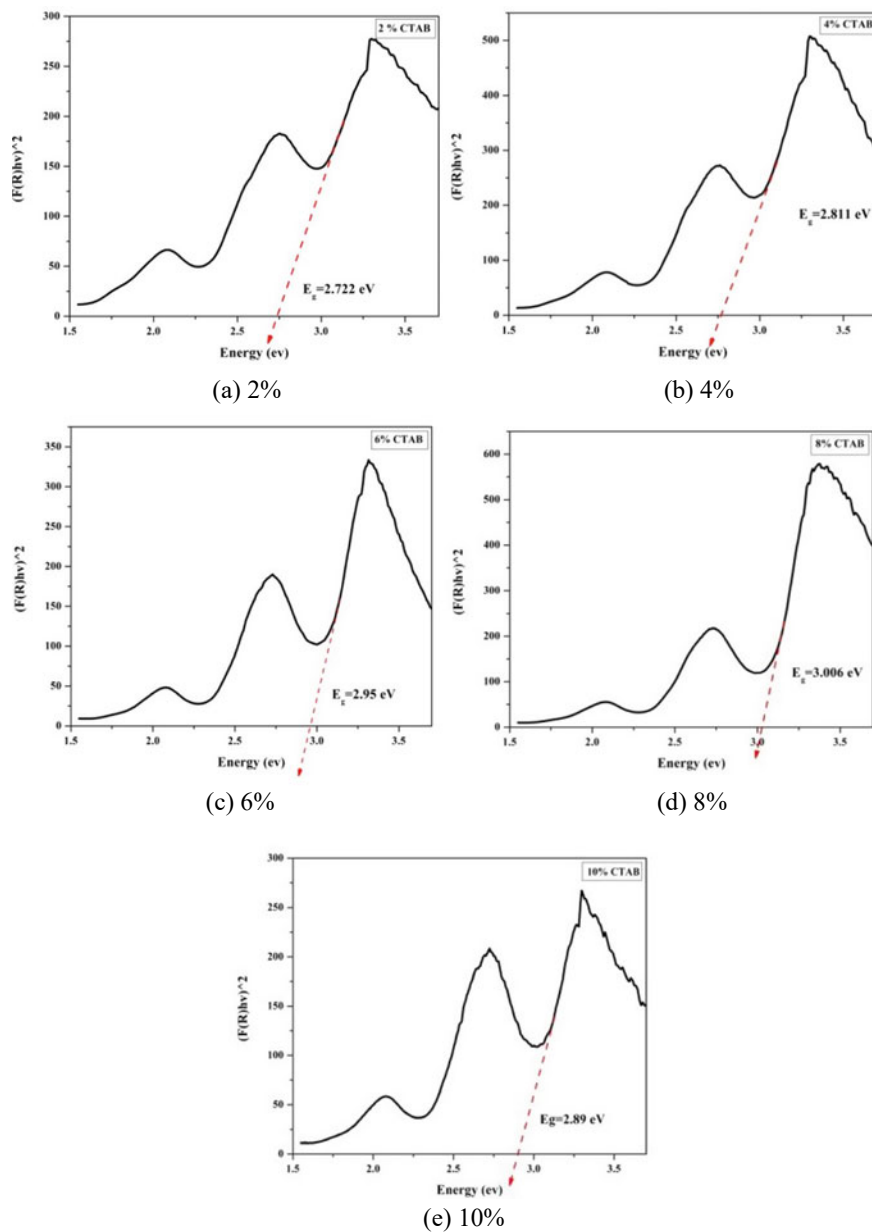


Fig. 5 KM plot of a 2, b 4, c 6, d 8, and e 10% CTAB treated Cr_2O_3 nanoparticles

8% CTAB. The CTAB surfactant was more successful at reducing the size of the nanoparticles. The spectra acquired using infrared spectroscopy clearly indicated the chromium oxide nanoparticles' distinctive peaks, along with some surfactant residue. The XRD data was supplemented by Raman spectra, which indicated the shift in lattice strain and bond lengths. The band gap energy of synthesized nanoparticles was calculated using the Kubelka–Munk method, and it was determined that the band gap rises as the crystallite size is reduced.

References

1. Singh J, Verma V, Kumar R, Sharma S, Kumar R (2019) Effect of structural and thermal disorder on the optical band gap energy of Cr_2O_3 nanoparticles. *Mater Res Express* 6:085039
2. Zhao W, Zhang H, Liu J, Deng X, Bi Y, Zhang S (2017) Preparation of Cr_2O_3 nanoparticles via surfactants-modified precipitation method and their catalytic effect on nitridation of silicon powders. *J Ceram Soc Jpn* 125(8):623–627
3. Varghese D, Tom C, Chandar NK (2017) Effect of CTAB on structural and optical properties of CuO nanoparticles prepared by coprecipitation route. In: IOP conference series: materials science and engineering, vol 263, No. 2, p 022002
4. Roy M, Ghosh S, Naskar MK. Solvothermal synthesis of Cr_2O_3 nanocubes via template-free route. *Mater Chem Phys* 159:101–106
5. Anandan K, Rajendran V (2014) Studies on structural, morphological, magnetic and optical properties of chromium sesquioxide (Cr_2O_3) nanoparticles: synthesized via facile solvothermal process by different solvents. *Mater Sci Semicond Process* 19(1):136–144
6. Abdullah MM, Rajab FM, Al-Abbas SM (2014) Structural and optical characterization of Cr_2O_3 nanostructures: evaluation of its dielectric properties. *AIP Adv* 4(2):027121
7. Aghaie-Khafri M, Kakaei Lafdani MH (2012) A novel method to synthesize Cr_2O_3 nanopowders using EDTA as a chelating agent. *Powder Technol* 222:152–159
8. Cao H, Qiu X, Liang Y, Zhao M, Zhu Q (2006) Sol-gel synthesis and photoluminescence of p-type semiconductor Cr_2O_3 nanowires. *Appl Phys Lett* 88(24):241112
9. Sangwan P, Kumar H (2017) Synthesis, characterization and antibacterial activities of chromium oxide nanoparticles against *Klebsiella pneumoniae*. *Asian J Pharm Clin Res* 10(2):206–209
10. Ritu D (2015) Synthesis and characterization of chromium oxide nanoparticles. *IOSR-JAC* 8(3): 05–11, Version I
11. Sone BT, Manikandan E, Gurib-Fakim A, Maaza M (2016) Single-phase $\alpha\text{-Cr}_2\text{O}_3$ nanoparticles “green synthesis using *Callistemon viminalis*” red flower extract. *Green Chem Lett Rev* 9(2):85–90
12. Babukutty B, Parakkal F, Bhalero GM, Aravind PB, Nair SS (2015) Structural, morphological and optical properties of chromium oxide nanoparticles. In: AIP conference proceedings vol 1665, No. 1. AIP Publishing LLC, p 050148
13. Li L, Yan ZF, Lu GQ, Zhu ZH (2006) Synthesis and structure characterization of chromium oxide prepared by solid thermal decomposition reaction. *J Phys Chem B* 110(1):178–183
14. Zhang YL, Yang Y, Zhao JH, Tan RQ, Cui P, Song WJ (2009) Preparation of ZnO nanoparticles by a surfactant-assisted complex sol–gel method using zinc nitrate. *J Sol-Gel Sci Technol* 51(2):198–203
15. Shahi AK, Pandey BK, Swarnkar RK, Gopal R (2011) Surfactant assisted surface studies of zinc sulfide nanoparticles. *Appl Surf Sci* 257(23):9846–9851
16. Studenyak I, Kranjčec M, Kurik M (2014) Urbach rule in solid state physics. *Int J Opt Appl* 4(3):76–83
17. Singh J, Verma V, Kumar R, Kumar R (2019) Influence of Mg^{2+} -substitution on the optical band gap energy of $\text{Cr}_{2-x}\text{Mg}_x\text{O}_3$ nanoparticles. *Results Phys* 13:102106

18. Noguchi S, Mizuhashi M (1981) Optical properties of Cr: co oxide films obtained by chemical spray deposition: substrate temperature effects. *Thin Solid Films* 77(1–3):99–106
19. Arul Dhas N, Kolytyn Y, Gedanken A (1997) Sonochemical preparation and characterization of ultrafine chromium oxide and manganese oxide powders. *Chem Mater* 9(12)
20. Mishra SR, Dubenko I, Griffis J, Ali N, Marasinghe K (2009) Exchange bias effect in ball milled Co-Cr₂O₃ FM-AFM nanocomposites. *J Alloy Compd* 485(1–2):667–671
21. Comet M, Pichot V, Siegert B, Fousson E, Mory J, Moitrier F, Spitzer D (2011) Preparation of Cr₂O₃ nanoparticles for superthermites by the detonation of an explosive nanocomposite material. *J Nanopart Res* 13(5):1961–1969

Effect of Glazing Materials and Shading Position on the Energy Consumption Pattern and Indoor Visual Comfort of Office Building



Ramkishore Singh, Ian J. Lazarus, and Dharam Buddhi

Abstract There has been an increase in the use of glazed façades in new buildings, allowing access to daylight, solar gain, and external view. Hence, a significant attention needs to be devoted on the design of these facades with focus on their impact in terms of energy efficiency in buildings and indoor visual comfort. Discomfort glare, high heating, and cooling demands are major issues in the buildings with highly glazed facades and this needs to be addressed with appropriate solar shadings. In this study, a comparative performance of venetian blinds assumed to be positioned externally, internally and in between the panes and adjusted at different slat angles has been investigated. Simulations have been performed for an office room with south glazing in hot-dry and cold-cloudy climates. Results clearly reveal that regardless of the climatic condition and glazing types, the blind solar shade positioned externally performs best in terms of energy efficiency as well as indoor visual comfort. With low e-coated glazing (G-III), externally positioned blind fixed at 45° and 90° can be the most energy efficient options in hot-dry and cold climates, respectively. However, the options to achieve the most desirable indoor visual comfort may differ from the options that have been identified from the best energy efficiency point of view.

Keywords Energy performance · Visual comfort · Glazed façade · Shading control strategies

R. Singh (✉)

School of Chemical Engineering and Physical Sciences, Lovely Professional University, Phagwara 144411, India

e-mail: singh.ramkishore@gmail.com; ramkishore.26500@lpu.co.in

I. J. Lazarus

Department of Physics, Durban University of Technology, Durban 4000, South Africa

KZN Industrial Energy Efficient Training and Resource Centre (IEETR), Durban University of Technology, Durban 4000, South Africa

D. Buddhi

Uttaranchal University, Prem Nagar, Arcadia Grant, ChandanwariDehradun, Uttarakhand 248007, India

1 Introduction

In an urbanized city, about a third of total electrical consumption is allocated for indoor lighting and air conditioning system in residential and commercial buildings. Various options and strategies are being explored and adopted for improving indoor thermal comfort, reducing energy consumption and enhancing indoor visual performance of different buildings [1, 2]. In addition, the solar power and alternative low energy materials are being explored to be used to reduce dependency on the fossil fuels [3–6]. Glazing unit is an indispensable part of a building, which provides passive solar energy gain and air ventilation. However, in general, thermal performance of glazing units is poor among the building components, and hence they play a significant role in energy consumption of buildings. Larger glazed façades in modern office buildings, used to provide higher access to natural light and view to outdoor, often lead to a higher energy demand in HVAC and discomfort glare, due to the high solar gain and excessive natural light. However, effect of glazing units on energy loss from building envelope becomes much more drastic when the glazing area is large. The heat loss through the glazing envelope is accounted for 30% of energy consumption of the building envelope [7, 8]. Good thermal performance and controlled natural light access strategies of glazed components are beneficial to buildings to increase energy performance and indoor visual comfort. Therefore, there is a need for these glazed façades to be given immediate attention for providing suitable solutions for the associated issues. Solar shading devices, once properly designed, are considered an integral part of the glazed façades in order to improve the performance of the building. Venetian blinds are common type of a shading device. They can reflect and transmit light efficiently into buildings by adjusting the slat angle and at the same time allow adequate outdoor viewing. They can also block direct solar radiation while allowing mostly reflecting diffuse solar radiation into the space [9]. Recently, the performance of venetian blinds with fixed or dynamic control of slat angle has been investigated by placing the shading device at external, in between and at an internal side of the panes [10–12]. Inappropriate arrangement and functioning of the blinds not only increase the energy demands for lighting, heating and cooling but also lead to indoor visual discomfort [10]. Also, the control strategies of the blind shading can vary with the purpose of the device [13]. In most cases, the blind performance was assessed by placing either externally, internally, or in-between the panes separately [14–19]. Hence, it could be worth to investigate the comparative performance of the solar shadings, to get most effective and efficient solution out of the three potential positions with a static and dynamic adjustment of slat angle.

In this study, energy efficiency and visual comfort in an office room have been assessed with static and dynamic horizontal blinds assumed to be positioned at internal, external, and in-between the glass panes of the glazing system. The study aims to provide a more accurate and effective blind solar shading strategy for the energy efficient operation of the office building with better indoor visual comfort. Simulations have been performed in an integrated manner (thermal and daylighting)

for an office room with south facing window using three different glazing types in hot-dry and cold-cloudy climates.

2 Methodology

2.1 Simulation Tool

In this study, a whole building simulation software, EnergyPlus promoted by the Building and Technology Program of the Energy Efficiency and Renewable Energy Office [20], has been used. The software has received a wider acceptance in the building energy analysis community because of its capabilities to calculate the energy demand including the effect of heating, cooling, lighting, and a variety of renewable energy based components (e.g. solar PV, solar water heating system, etc.) in an integrated manner [21]. The tool is also capable for modeling the buildings solar irradiance, illuminance under different sky conditions, advanced fenestration systems, blind controls, indoor illuminance maps, and artificial lighting controls [16]. The tool use, the ray tracing method ‘Radiance’ and the thermal algorithm to study the effect of the solar shading on the illuminance level at different points as well as the thermal loads in the office [22].

2.2 Simulation Model

Simulations have been performed for a standard air-conditioned office room ($4 \times 4 \times 3$ m), which is assumed to be 60% glazed window only on the south wall. An extra frame of width 0.0572 m, which accounts 5.41% of the total wall area, has also been taken into account during the simulations. The conductance and absorptance of the frame used are $5.68 \text{ W/m}^2 \text{ K}$ and 0.6, respectively. The room is assumed to be located at an intermediate floor in a multi-storey office building and only glazed facades are exposed to outdoor environment. All the other opaque surfaces including ceilings and the floors are assumed to be attached to adjacent offices at the same indoor temperature. Therefore, there will not be any heat transfer through the internal adjacent surfaces. The heat transmittance coefficients (U -values) of the opaque portion, in the external wall are set as recommended by the energy conservation building code (ECBC) [23]. The interior surface reflectance of the floor, ceiling, and walls are set at 50%, 70%, and 60%, respectively. The exterior surface absorptance of the external façade has been taken as 0.6. Other characteristics of the office room are given in Table 1.

A HVAC system that delivers the theoretical loads necessary to keep the temperature within the heating and cooling set point temperatures are used in the simulation. During office hours (9 am – 5 pm), the room temperature is maintained at $22 \text{ }^\circ\text{C}$

Table 1 Description of office room and internal gain

Parameter	Description
Climate	Hot-dry (Jodhpur lat. 26° 17' N, long. 73°1'E) Cold and cloudy (Shillong lat. 25° 34' N, long. 91°52' E)
Dimension of room	4 × 4 × 3 m
Window size	3.6 × 2.0 m (7.2 m ²)
Shading strategies	Static slat angle at 30, 45, 60, 75 and 90° Dynamic slat: for high glare, and high outdoor temperature
Internal gain Equipment	5.4 W/m ²
Lighting (daylight continuous dimming)	11.8 W/m ² [23]
Personnel occupancy	0.11 p/m ² (office hours: 9:00 am – 5:00 pm) with sensible heat gain from each occupant is 76 W
Daylight illuminance sensor points	2 (x = 2, y = 1 m; x = 2, y = 3 m)

in winter and 24 °C in summer. Heating and cooling temperature set points during non-office hours are also assumed to be at 18 °C and 30 °C, respectively. An hourly time-series meteorological data used in this study is taken from [24].

For office spaces, the minimum desirable work plane illuminance is set 500 lx. Two daylight photo sensors are assumed to be positioned at a work plane height of 0.8 m above the floor. If the illuminance levels drop below this, artificial lighting switched on. The lighting system is continuously dimmable to compensate for the daylight illuminance to reach the desirable value (i.e. 500 lx) on the work plane [25]. Each of the sensor points controls lighting in half of the room space. For glare based control a maximum allowable glare index is set to 22, which is defined borderline between comfort and discomfort. The values lower than 22 indicate comfort [12].

2.3 Shading and Glazing Types and Arrangement

The shading systems studied are all a horizontal type venetian blind. A number of blind arrangements, with three different double glazed windows have been simulated in order to clarify how various blind shading arrangements affect the indoor visual comfort and the energy consumption. Two panes of glass in double glazed window are assumed to be separated by an air gap of 12.7 mm for internally and externally placed shadings and 52 mm for in-between blind shading. The main characteristics of glazing units are given in Table 2.

The objective of this study was a continuous comparison of blind shading alternatives to obtain a reasonable picture of the venetian blind type shading performance, i.e. its ability to reduce the overall energy consumption and to improve indoor visual

Table 2 Thermal and optical properties of glazing materials and panes arrangement

Glazing	Layer arrangement	SHCC	T_{vis}	U -value of glazing (W/m ² K)
G-I	Clear(6) + Air(12.7) + Clear(6 mm)	0.818	0.832	2.677
	Clear(6) + Air(52) + Clear(6 mm)	0.818	0.832	2.744
G-II	Parsol green (6) + air(12.7) + Parsol green(6 mm)	0.415	0.536	2.677
	Parsol green(6) + air(52) + Parsol green(6 mm)	0.414	0.536	2.677
G-III	Low e-coated(6) + air(12.7 mm) + Low e-coated	0.370	0.851	1.628
	Low e-coated(6) + air(52 mm) + Low e-coated	0.370	0.851	1.778

comfort and thus its applicability in different positions. The horizontal venetian blind positioned at three different locations, i.e. at external, internal, and in-between the glass panes, have been simulated in static and dynamic conditions. The venetian blind, with slat thickness, width, and distance equal to 0.22 mm, 50 mm, and 42.5 mm, respectively, has been used in this study. The slats are assumed to be made from aluminum with a thermal conductivity of 159 W/(m K), reflectance of 0.54 and surface emissivity of 0.9. The fixed shading has been modeled as being fixed at a pre-fixed slat angle and not retractable, and thus active all the time. The dynamic shading has been modeled for two cases, i.e. (A) if the outdoor temperature is higher than 26 °C, (B) if the glare exceeds the set value of 22. In both cases, variable slat angle options have been included. For cold climate, only (B) case is valid and the first case need not to be assessed as the outdoor temperature always remains below 26 °C.

2.4 Evaluation Criteria

Based on the simulation results, each shading alternative and its effect in relation to energy performance and indoor visual comfort have been evaluated. The evaluations have been performed on the basis of the total source energy demand of the office room, energy demands for heating, cooling, fans and lighting, daylight autonomy (DA) and useful daylight illuminance (UDI). Moreover, the energy performance of the office room with the glazed system has also been compared with the energy performance of the base case (similar room but without glazed component). The UDI values have been estimated and compared using the three bins suggested by Nabil and Mardaljevic [25]. The maintained illuminance level for a work space should be higher than 500 lx. The DA represents the illuminance occurrence higher than 500 lx over the simulation period.

3 Results and Discussion

3.1 Energy Performance

The simulation results for source energy consumption in the office with south glazing in two selected climatic conditions are shown in Fig. 1. The data are arranged according to static and dynamic adjustment of the blind slat angle for external (a), in-between (b), and internal (c) of the panes of three different glazings. All alternatives of the blind shadings have been simulated for an entire year and results correspond to annual source energy demand per square meter (kW h/m^2 year). The source energy demand was also compared to the base case energy demand. The base case in this study is a similar office room with one completely opaque façade, in which all illuminance requirements are met by electric lighting only. The source energy demands in the base case for hot-dry and cold-cloudy climates have been estimated to be 245 kW h/m^2 year and 155 kW h/m^2 year, respectively. As seen in Fig. 1a, the energy demand with different alternatives varies between a maximum 564.25 kW h/m^2 year and a minimum of 215.17 kW h/m^2 year for hot-dry climate of Jodhpur. The highest energy efficiency was realized in the office room with the glazing G-III and an external blind adjusted at 45° static slat angle. On the other hand, the office room with the glazing G-I and an internal blind slat angle adjustment based on the outdoor temperature was found to be highly energy inefficient. This is expected as the solar gain is highly undesirable inside the office in hot-dry climate and only externally based solar shading can block the access of solar radiation into the building efficiently. Only six cases, all with glazing G-III and with an external blind position, show lower energy demand than base case. In the dynamic slat adjustment condition, only the high outdoor temperature based control showed a positive effect, however, energy saving that can be achieved by this control is insignificant (only 1%). The energy saving potential with the static adjustments of slat angle varies between 12.2 and 1.8%. The maximum energy saving has been estimated with a slat angle at 45° , while blind adjusted at 90° shows least saving potential (below 2%).

Figure 1b shows the energy performance results for a cold-cloudy climate in Shillong. It can be seen from the figure that the energy demand with simulated alternatives varies between 251 k Wh/m^2 year and 103 k Wh/m^2 year. Out of 54 alternatives, 18 cases show a negative effect while 36 perform better than the base case scenario. Again the negative impact is most pronounced for internally positioned blind with glazing G-I. Thus, this study highlights that a blind solar shading should not be installed internally of the panes without thoroughly investigating the glazing types. In most cases, glare base dynamic shading found to be the worst performer, except for blind solar shade positioned external of the panes. Also, the glare based dynamic shading device performed best only with highly transparent glazing G-I in the cold and cloudy climate. However, maximum energy saving (approx. 33%) can be achieved with externally based static blind adjusted as 90° slat angle. The reason could be a higher access of solar radiation and daylight (both are desirable in cold climate) that help in lowering the heating and artificial lighting demands. In

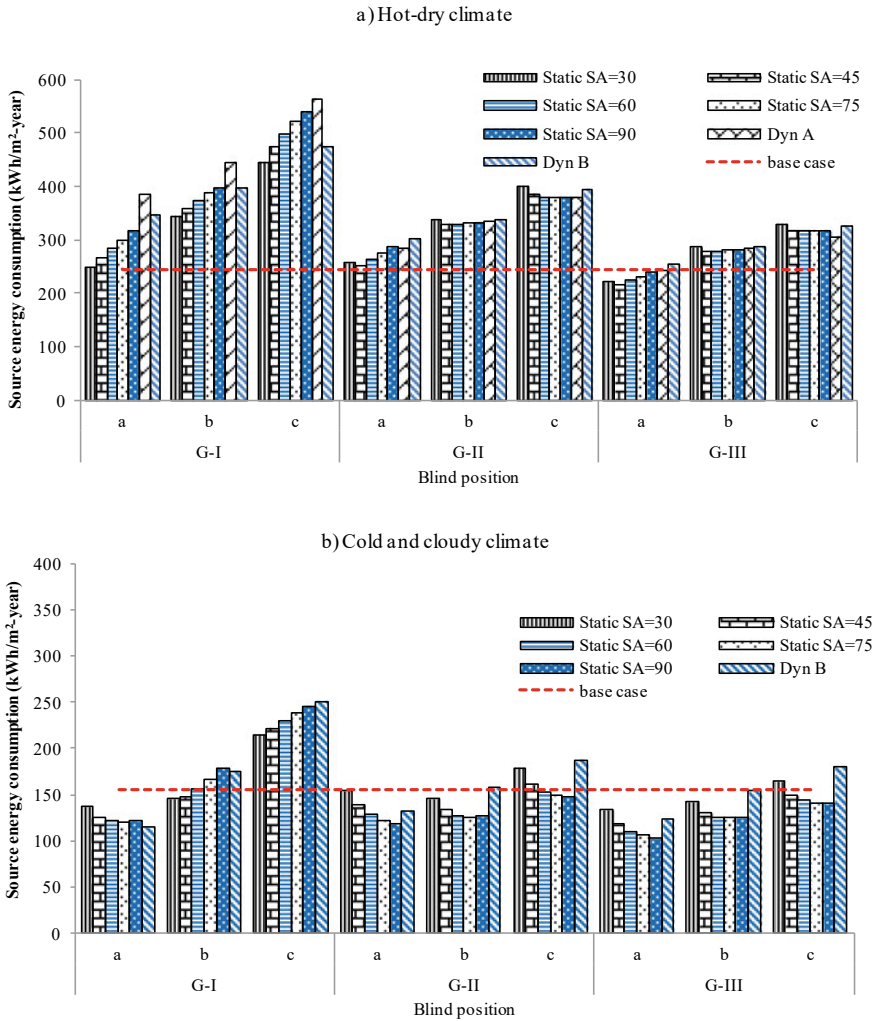


Fig. 1 Variation of source energy consumption with glazing type and shade position: **a** hot-dry climate, **b** cold climate

general, the energy savings decrease by changing the slat angle from 30° to a higher value. The reason of lower energy savings could be a higher amount of the solar radiation allowed by the blind adjusted at larger slat angle than the blind adjusted at a smaller slat angle. Moreover, the energy demand was estimated higher for shading device positioned in-between the panes and followed by blinds installed internally. The reason could be less effectiveness, to control the solar radiation of the blind positioned in-between and internally compared to the blind place outside the panes. The higher solar access to the office space could potentially lead to overheating and

eventually higher cooling demand. The effect occurs higher for case b and highest for case c.

3.2 Daylighting Performance

Figure 2 shows the DA and the UDI values for each of the simulated cases. Comparatively, the DA has been estimated to be higher for the hot-dry climate of Jodhpur than the cold-cloudy climate of Shillong. This could be due to brighter sky conditions in Jodhpur than in Shillong. The position of the blind solar shading does not greatly affect the DA, as shown in Fig. 2. However, a significant effect of glazing type and control strategies for slat angle is clearly visible from the values. The values increase linearly with slat angle and estimated to be highest for 90° slat angle. A small value of the DA for low slat angle is due to the fact that a small slat angle can block the access of majority of the illuminance. Dynamic control provides lower DA values than static slat adjusted at 60, 75, and 90°. Figure 3 shows the variation in the UDI values with position, control type and glazing types. It can be observed that the UDI values decrease with the slat angle and positioning of the shading device from outside to inside in hot-dry climate. In the cold-cloudy climate, variation in the UDI values is not significant with position of the shading device as well as the slat angle, except with glazing G-I. The dynamic shading device produce comparatively better UDI values.

The UDI values in the second bin (500–1000 lx) is free from discomfort glare and can eliminate the use of electrical lighting and hence the second bin is most desirable. Figure 3a shows that in hot-dry climate, the UDI value in the second bin has been estimated above 40% with the blind's slat angle at 30 and 45° with the glazing G-I, and with any slat angle except 30° with the glazings G-II and G-III. In the cold-cloudy climate, with the glazing G-I the blinds adjusted at a fixed slat angles 45 and 60° or controlled dynamically can produce the UDI, in the second bin, above 40% (see Fig. 3b). While to achieve this UDI value with the glazing G-II, the blinds need to be adjusted at a slat angle 75 or 90°. With the glazing G-III, the blind's slat angle can be adjusted at either 60, 75, or 90° to achieve the second bin's UDI above 40%. The UDI in the second bin decreases in all other cases either because of low natural light (most of the illuminance is blocked by the blinds) or of excessive daylight in the room.

4 Conclusions

Simulations have been performed for a number alternatives of venetian blind shading, positioned externally, internally and in-between the panes, for an office room with south façade in hot-dry and cold-cloudy climates. Energy performance has been compared with the base case in terms of source energy demand in each simulated

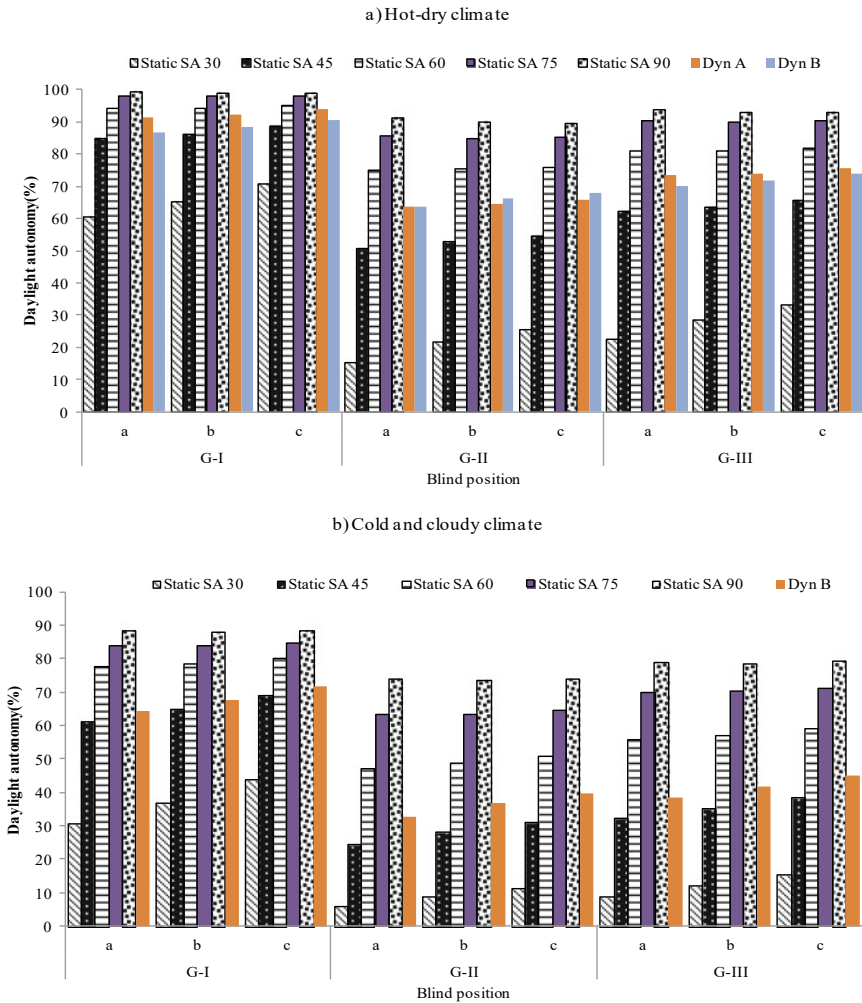


Fig. 2 Variation of daylight autonomy with glazing type and shade position: **a** hot-dry climate, **b** cold and cloudy climate

case. Visual performance has also been discussed using daylight autonomy and useful daylight illuminance matrices. Results show that the blind solar shade performs best if placed externally, however, energy savings vary with slat angle and glazing types. Comparatively, higher energy efficiency, in the office building, can be achieved with the shading device in the cold-cloudy climate.

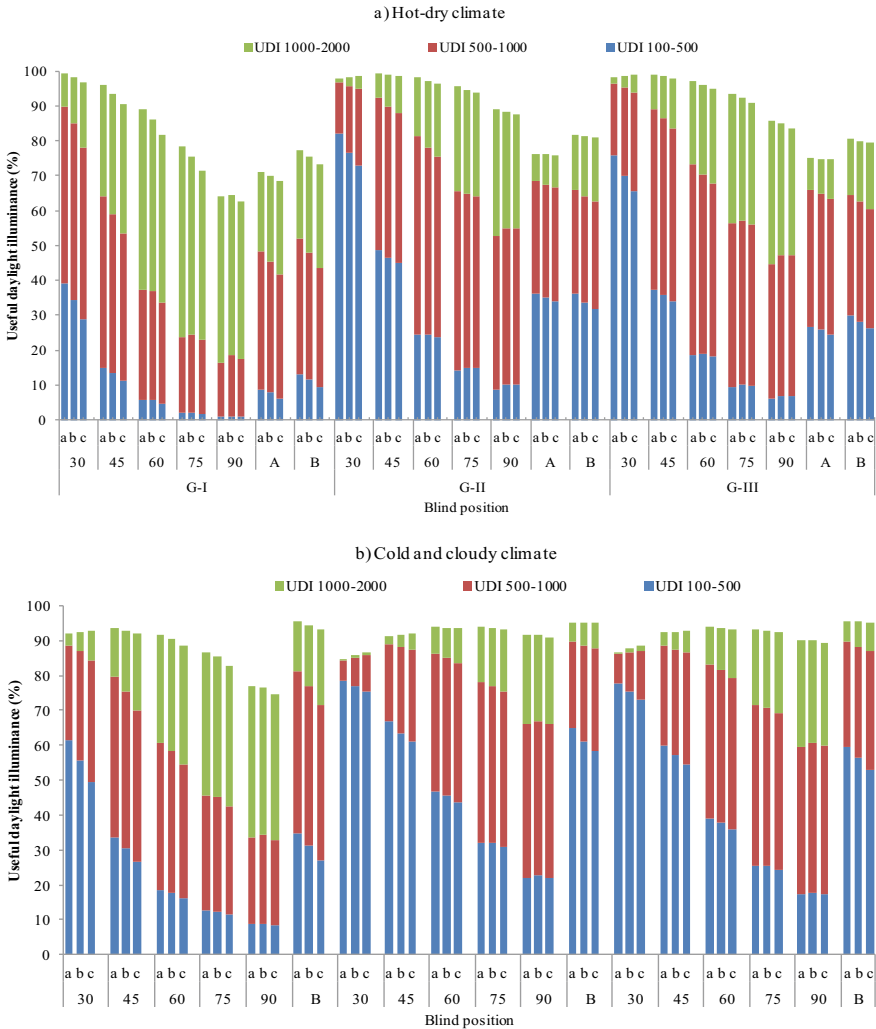


Fig. 3 Variation of Useful daylight autonomy with glazing type and shade position: **a** hot-dry climate, **b** cold and cloudy climate

References

1. Singh R, Kishore VVN (2018) Introduction to energy-efficient building development and sustainability. In: Sustainability through energy-efficient buildings. CRC Press, pp 1–31
2. Singh R, Lazarus IJ (2015) Energy and daylighting performances of highly glazed buildings. In: Building simulation conference, international building performance simulation association. Hyderabad, pp 2363–2370
3. Khan MA, Mishra S, Harish VS (2017) Grid connected energy efficient building with roof top SPV. In: 2017 Recent developments in control, automation & power engineering (RDCAPE),

- pp 120–124. <https://doi.org/10.1109/RDCAPE.2017.8358252>
4. Mehta BS, Kumar A (2016) Optimization of member size and materials for multistoried RCC buildings using ETABS. *Indian J Sci Technol* 9:1–6. <https://doi.org/10.17485/ijst/2016/v9i44/105254>
 5. Kumar A, Sharma S, Goyal N, Singh A, Cheng X, Singh P (2021) Secure and energy-efficient smart building architecture with emerging technology IoT. *Comput Commun* 176:207–217. <https://doi.org/10.1016/j.comcom.2021.06.003>
 6. Khan MA, Mishra S, Bharath KVS (2018) Simulation of lumped parameter building model for observing dynamics of energy efficient buildings. In: 2018 International conference on intelligent circuits and systems (ICICS), pp 372–377. <https://doi.org/10.1109/ICICS.2018.00082>
 7. Cuce E, Riffat SB (2015) A state-of-the-art review on innovative glazing technologies. *Renew Sustain Energy Rev* 41:695–714. <https://doi.org/10.1016/j.rser.2014.08.084>
 8. Hee WJ, Alghoul MA, Bakhtyar B, Elayeb O, Shameri MA, Alrubaihi MS et al (2015) The role of window glazing on daylighting and energy saving in buildings. *Renew Sustain Energy Rev* 42:323–343. <https://doi.org/10.1016/j.rser.2014.09.020>
 9. da Silva PC, Leal V, Andersen M (2012) Influence of shading control patterns on the energy assessment of office spaces. *Energy Build* 50:35–48. <https://doi.org/10.1016/j.enbuild.2012.03.019>
 10. Chan Y-C, Tzempelikos A (2013) Efficient venetian blind control strategies considering daylight utilization and glare protection. *Sol Energy* 98:241–254. <https://doi.org/10.1016/j.solener.2013.10.005>
 11. Nielsen MV, Svendsen S, Jensen LB (2011) Quantifying the potential of automated dynamic solar shading in office buildings through integrated simulations of energy and daylight. *Sol Energy* 85:757–768. <https://doi.org/10.1016/j.solener.2011.01.010>
 12. Grynning B (2014) Steinar, time, Berit, Matusiak, solar shading control strategies in cold climates-heating, cooling demand and daylight availability in office spaces. *Sol Energy* 107:182–194
 13. Yun G, Yoon KC, Kim KS (2014) The influence of shading control strategies on the visual comfort and energy demand of office buildings, Elsevier B.V. <https://doi.org/10.1016/j.enbuild.2014.07.040>
 14. Simmler H, Binder B (2008) Experimental and numerical determination of the total solar energy transmittance of glazing with venetian blind shading. *Build Environ* 43:197–204. <https://doi.org/10.1016/j.buildenv.2006.10.011>
 15. Saelens D, Parys W, Roofthoof J, Tablada de la Torre A (2013) Assessment of for modeling louver shading devices in building energy simulation programs. *Energy Build* 60:286–297. <https://doi.org/10.1016/j.enbuild.2012.10.056>
 16. Thanachareonkit A, Scartezzini J-L (2010) Modelling complex fenestration systems using physical and virtual models. *Sol Energy* 84:563–586. <https://doi.org/10.1016/j.solener.2009.09.009>
 17. Dalal R, Naylor D, Roeleveld D (2009) A CFD study of convection in a double glazed window with an enclosed pleated blind. *Energy Build* 41:1256–1262. <https://doi.org/10.1016/j.enbuild.2009.07.024>
 18. Meerbeek B, te Kulve M, Gritti T, Aarts M, van Loenen E, Aarts E (2014) Building automation and perceived control: a field study on motorized exterior blinds in Dutch offices. *Build Environ* 79:66–77. <https://doi.org/10.1016/j.buildenv.2014.04.023>
 19. Lee ES, DiBartolomeo DL, Selkowitz SE (1998) Thermal and daylighting performance of an automated venetian blind and lighting system in a full-scale private office. *Energy Build* 29:47–63. [https://doi.org/10.1016/S0378-7788\(98\)00035-8](https://doi.org/10.1016/S0378-7788(98)00035-8)
 20. EnergyPlus (2015) www.eere.energy.gov/buildings/energyplus
 21. Bojić M, Djordjević S, Malesević J, Miletić M, Cvetković D (2012) A simulation appraisal of a switch of district to electric heating due to increased heat efficiency in an office building. *Energy Build* 50:324–330. <https://doi.org/10.1016/j.enbuild.2012.04.004>

22. David M, Donn M, Garde F, Lenoir A (2011) Assessment of the thermal and visual efficiency of solar shades. *Build Environ* 46:1489–1496. <https://doi.org/10.1016/j.buildenv.2011.01.022>
23. ECBC (2009) Energy conservation building code: user guide, bureau of energy efficiency. New Delhi, India
24. Bellia L, De Falco F, Minichiello F (2013) Effects of solar shading devices on energy requirements of standalone office buildings for Italian climates. *Appl Therm Eng* 54:190–201. <https://doi.org/10.1016/j.applthermaleng.2013.01.039>
25. Nabil A, Mardaljevic J (2006) Useful daylight illuminances: a replacement for daylight factors. *Energy Build* 38(7):905–913. <https://doi.org/10.1016/j.enbuild.2006.03.013>

Sn-Based Perovskites for Photovoltaic Applications



Amit Kumar Sharma and Deepak Kumar

Abstract Organic–inorganic metal halide perovskites are the promising aspirants for the photovoltaic applications due to their high-power conversion efficiency (PCE). Despite owing high PCE, these perovskite solar cells (PSC) are limited at commercial scale due to presence of toxic elements such as lead (Pb). At present, tin (Sn) based PSC has emerged as a potential candidate to substitute Pb-based PSCs exhibiting PCE above 12%. In this article, the progress of perovskite materials for photovoltaic applications is discussed. A special emphasis is on Pb-free and environment-friendly Sn-based PSC is discussed. Further few studies on Sn-based perovskite solar cells with strategies for improvements of performance are also discussed.

Keywords Perovskite materials · Photovoltaic application · Lead and tin-based perovskites · Solar cell

1 Introduction

The photoelectric phenomenon was first noticed in eighteenth century by French scientist A.E. Becquerel while studying the illuminating effect of light on electrodes dipped into electrolytes for photochemical reactions. He invented a device that can measure the photo intensity by measuring the photoelectric current produced by the device. In 1883 an American scientist Charles Fritts made working photoelectric cell and in the same year, a German scientist Paul Nipkow used the same cell creating “Nipkow’s disk” for taking pictures of the dark and the bright areas on the object and converting them into electrical pulses. Further Modern photoelectric cell was invented and used in cathode ray tubes by German physicists Hans Geitel and Julius Elster. During mid of nineteenth century, many scientists investigated the phenomena

A. K. Sharma (✉)

Department of Physics, Maharana Pratap Govt. College Amb, Una, H.P 177203, India
e-mail: ksharma_amitt@yahoo.com

D. Kumar

Department of Physics, Lovely Professional University, Phagwara, Punjab 144411, India

of “generation of electric current during day time than at night”, i.e., solar light conversion to electric current using solar cells.

The photovoltaic cell popularly known as solar cell is an electrical device that converts light energy directly into electric energy by photovoltaic effect. The property of the cell like current, voltage, and resistance changes when light falls on it. The basic principle of the operation of a solar cell are.

- (a) absorption of light
- (b) separation of electrons and holes
- (c) collection of the separated electrons and holes to external circuit.

1.1 Absorption of Light

When a photon (whose energy is equal to or greater than band gap energy of absorbing material) is absorbed, the electron is excited from valence band to the conduction band where it is free to move within the semiconductor. The network of covalent bonds that the electron was previously a part of now has one new empty site, known as a hole. It can be said that photons absorbed in the semiconductor generate electron–hole pairs.

1.2 Extraction of Electrons and Holes

Drift of photogenerated carriers takes place due to the built-in potential developed across the pn-junction. The drift causes separation of charge carriers. The built-in potential depends on the carrier density or doping.

1.3 Transport of Electrons/Holes to External Circuit

Metal–semiconductor contacts (electrodes) are made to the both sides of the solar cell and the electrodes are connected to an external load. The separated electrons and holes are collected through the wire until they reach the semiconductor–metal contact before they recombine. The voltage measured is equal to the difference in the quasi-Fermi levels at the two terminals.

2 Materials and PV Phenomena

There is a wide range of materials that can serve as a good absorbers of solar energy. Semiconductors (in wafer form or thin films) can absorb light falling on it. For

example, the materials like Si, GaAs, InP, CIGS, CdTe, CZTS, etc. are the semiconductor materials used in solar cells. “When a suitable light (having energy greater than band gap) incident on absorbing material, the electrons are excited from the lower energy states (ground state) to the higher energy state (excited state)”. In the absence of the junction, the motion of the free electron is random. But in the presence of the junction, the induced electric field setup that result in the separation of excited (photogenerated) charge carriers. Subsequently, the charge carriers (electron and holes) are collected at the respective electrodes.

In the solar cell fabrication, one prime condition is to construct cell with large area for illuminating light because power is proportional to the illuminated area. Cost and manufacturing technologies stimulated the advancements in the PV industry more effectively. Pure silicon-based PV industry has reached a power conversion efficiency more than 25%, which enables the silicon wafer technology (1st Generation) ideal for commercialization. However, the improved generations of PV technology, due to simple deposition methods to produce low-cost semiconductors for highly efficient solar cells, have potential to surpass silicon-based technology. PV technology is categorized into three generations, in which basic generation often called as 1st generation is based upon wafer (Si) based and advance generation called as 2nd and 3rd generations which are based upon thin film technology. Silicon wafer-based technology either single or multi-crystalline covering most of the solar cell market due to high efficiencies. Whereas thin film technology-based solar cells absorb light more efficiently than silicon solar cells. Out of thin film technology, a very promising class of materials were evolved in a very small span of time (3rd generation PV materials), and these materials have potential to overcome current power conversion efficiencies limit and performance in comparison to silicon-based solar cells. The materials belonging to 3rd generation PV technology are dye-sensitized solar cells (DSSC), organic solar cells (OSC), quantum dot solar cells (QSC), and perovskite solar cells (PSC). An overview of the classification of PV technology (generation-wise) is shown in Fig. 1.

PV technology belongs 3rd generation have shown steeper growth than the other technology. These technologies have shown a remarkable increase in the power conversion efficiency in a very small span of time. Even out of 3rd generation emerging materials, perovskite material-based solar cells can be ranked on the top.

2.1 Perovskite Material

Perovskite is a mineral of calcium titanate (CaTiO_3) which is found on the earth naturally. It was first found by German mineralogist Gustav Rose in 1839 and named “Perovskite” for honoring the Russian mineralogist Lev Perovski (1792–1856). In general, the materials resembling to the crystal structure of CaTiO_3 are referred to as perovskite materials. These materials have the tetragonal or the cubic crystal structure having general formula ABX_3 , where A and B are metal cations and X is a metal anion. Cation B is octahedrally coordinated to anions X forming the basic building

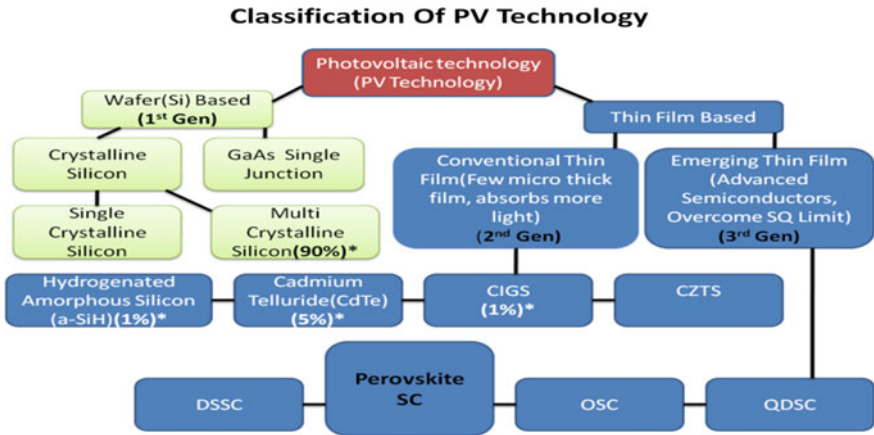


Fig. 1 Generations of PV technology

crystal of perovskite. For neutralizing the structural charge, the formed octahedral BX_6 is connected to cation A in a 3-dimensional structure configuration. Moreover, perovskite materials are so popular among researchers these days [1–2].

2.2 Perovskite-Based Solar Cell

Different and multiple metals, anions, and cations-based complex perovskites nowadays becoming the center of attraction for research for the photovoltaic applications. Synthesis and composition techniques are very important for the state-of-the-art performance. The basic layered structure with two main architectures is shown in Fig. 2.

The above figures show two basic structures for perovskite-based solar cells, Planar regular and planar inverted. In a regular architecture, the layer after glass

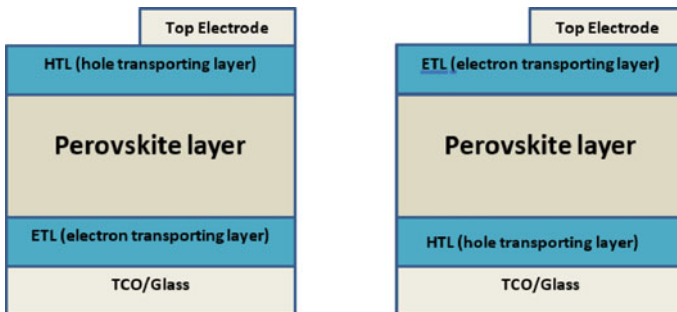


Fig. 2 a Planar regular (n-i-p) layered structure b Planar inverted (p-i-n) layered structure

substrate is electron selective, and on the top after electrode is hole selective. On the other hand, in the planar inverted architecture the layer after glass substrate is hole selective and on the top after electrode is electron selective.

2.3 Progress of Perovskite in Solar Cell as Absorber Layer

The perovskite material has attracted the attention of the many material scientists due to their natural abundance. The material properties have also oriented the research in the field of superconductivity, magneto resistivity, ionic conductivity, and many more. The perovskite materials also have the light absorbing property like all other photovoltaic materials.

Miyasaka and coworkers [3] studied for the first time in 2009 the ability of the perovskite materials for photoconductive studies. The team suggested the dye-sensitized TiO₂ film as photoanode for solar cells for vacuum-free deposition process. They investigated the organic–inorganic lead halides (CH₃NH₃PbI₃ and CH₃NH₃PbBr₃) for the first time to use as photo absorbers in photo-electrochemical cells. These materials demonstrated sensitization of TiO₂ for photoconductive properties in the visible region. They obtained the PV device characteristics for CH₃NH₃PbBr₃ and CH₃NH₃PbI₃ as listed below (incident area 0.24 cm² under 100 mW/cm² AM 1.5 simulated under sunlight irradiation).

Perovskite material	J_{sc} (mA/cm ²)	V_{oc} (V)	FF	PCE (%)
CH ₃ NH ₃ PbBr ₃	5.57	0.96	0.59	3.13
CH ₃ NH ₃ PbI ₃	11.0	0.61	0.57	3.81

Later, Nam-Gyu Park and team [4] fabricated a QDSSC (quantum dot sensitized solar cell) using CH₃NH₃PbI₃ perovskite layer as quantum dots on TiO₂ and reported highest power conversion efficiency of 6.54% (under 100 mW/cm² AM 1.5 simulated under sunlight irradiation). In comparison to the Tsutomu Miyasaka et al. prediction of the PCE of 3.8% and the poor stability of the cell, Nam-Gyu Park et al. improved the cell by modifying the method of preparation/depositing and electrolyte formulation. The team also predicted that the thin layer of perovskite layer CH₃NH₃PbI₃ was powerful for harvesting light in comparison to mostly used N719 ruthenium sensitizer. Michael Gratzel et al. demonstrated the highly efficient solid-state perovskite solar cells with the power conversion efficiency exceeding 9%. They first time deposited the methyl ammonium lead iodide (CH₃NH₃PbI₃) nanoparticles on TiO₂ (few microns mesoscopic thin film) having pores pervaded with spiro-MeOTAD as a hole transport layer (HTL) illuminated with standard sunlight, generated photocurrent of 17 mA/cm², open circuit voltage of 0.888 V, fill factor of 62% with power conversion efficiency of 9.7%. They also reported in their findings that with the use of solid HTL, the stability of these cells improved in comparison of the perovskite DSSC. They also studied that with the increase of the thickness of

the TiO₂ layer, open circuit voltage and fill factor of the solid-state cell degenerated [5]. Again, Gratzel and team reported for the first time a hole transport layer free solid-state perovskite solar cell, methyl ammonium lead iodide (CH₃NH₃PbI₃)/TiO₂ heterojunction perovskite solar cell with device parameters, $J_{sc} = 16.1 \text{ mA/cm}^2$, $V_{oc} = 0.631$, $FF = 57\%$ and $PCE = 5.5\%$ under standard illumination AM 1.5 with power 1000 W/cm^2 and successively reported the PCE of 7.3% when illuminated under low sun exposure of 100 W/cm^2 . For the very first time team studied the perovskite layer as light harvesting as well as hole transporting layer in the cell making a CH₃NH₃PbI₃/TiO₂ heterojunction perovskite solar cell. Their work on extra hole transport layer may lead a path for making highly efficient solar cells [6]. Stranks and coworkers [7] demonstrated the first ever lead-free organic–inorganic tin halide as light-harvesting layer in a perovskite solar cell with the power conversion efficiency of more than 6%, open circuit voltage of above 0.88 V with such a material having band gap of 1.23 eV. As the performance of the lead-based perovskite is very effective in the field but toxicity of lead is of great concern and thus, most common substitute of lead as tin belonging to the same group in the periodic table was adopted for non-toxic perovskite material. The semiconducting properties of tin-based perovskite solar cells were investigated using mesoporous heterojunction CH₃NH₃SnI₃/TiO₂ which yielded more than 6% power conversion efficiency. The low efficiency is attributed to the low carrier mobility of CH₃NH₃SnI₃ ($1.6 \text{ cm}^2/\text{V/s}$) and low diffusion length of 30 nm (which is few microns in CH₃NH₃PbI₃). In order to avoid the recombination of the charge carriers due to self-doping, the background concentration of holes should be reduced, and hence the stability could be further improved. Stoumpos et al. [8], Hao F [9], and Zhao and Zhu [10] investigated the lead–tin hybrid flexible perovskites. They reported large carrier mobility and tunable band gap of materials promising for photovoltaics. The electrical and optical properties were strongly depended on the deposition methods. The compound was investigated with high electron and hole mobility of $2000 \text{ cm}^2/\text{V/s}$ and $300 \text{ cm}^2/\text{V/s}$, respectively for CH₃NH₃SnI₃. Hao and team [9] demonstrated for the first time lead-free perovskite harvesting layer. CH₃NH₃SnI₃ with a band gap of 1.3 eV with organic HTL spiro-OMeTAD was studied with initial power conversion efficiency of 5.73% under sunlight. They showed the 950 nm absorption onset compared to the CH₃NH₃PbI₃ having band gap of 1.55 eV. The study reported a notable initiation in terms of eco-friendly, low-cost, and high-performance solid perovskite solar cells. Gratzel and coworkers [11] reviewed the promises and challenges of the perovskite solar cells in terms of efficiency and stability. As the photocurrent limit is near the theoretical values, they reviewed the possibilities of increase of open circuit voltage by tailoring the material for charge carrier lifetime and selective contacts. The stability of perovskite-based solar cells was the major concern and required to overcome for minimum degradation and for long-term use of both indoor and outdoor operating mechanisms. The testing protocols for the stability of these perovskite material-based solar cells were to be redesigned to account degradation of PSCs with the passage of time. Wang R [12], Lyu M [13], Kanatzidis [14] along with their coworkers reviewed on the lead-free perovskite solar cells and a comparison made between different lead-free perovskite solar cells like tin (Sn) based, Germanium (Ge)

based, double perovskite, etc. and proposed high potential of Sn-based perovskites in spite of the fact that these solar cells have comparatively stability issues. They suggested if the stability issues for tin-based perovskites addressed properly then these perovskite solar cells (Sn-based) could be a game changer in the market. If the Sn^{4+} oxidation state issue was resolved and the charge recombination rate was reduced in comparison of MAPbI_3 to maintain open circuit voltage of 0.8–1.0 V then these materials could be competitive contenders. It was suggested that in addition to the PV efficiency, the selection of the material should also be focused on stability, long life (around 1000 h.) at high temperatures, and humid environment. The review of Huang, Mari and Soro, and Wang and teams [15, 16] highlighted the rapid progress of the perovskites in the photovoltaics for challenging the existing traditional solar cell. In a very short span of ten years perovskite became the choice for the manufacturer of the solar cells with the PCE of more than 24%. The hindrance like stability and resistance to humidity, in the path of the perovskites, to be the first choice for solar cells commercialization.

Zang and coworkers [17] demonstrated the progress and perspective of tin-based PSCs due to their suitable semiconducting properties, i.e., high carrier mobility and tunable band gap. Due to some hindrances such as fast crystallization of tin-based PSCs, high defect density, high p-type carrier concentration and instability of tin restrict the commercialization of tin-based PSCs. But these all problems can be overcome by adding suitable additives. The certified efficiency of tin-based PSCs crossed over 12%. Wang et al. [18] enlightened the work on lead-free 2D perovskite-based solar cells and further development. They investigated the various options to the lead-free perovskite solar cell which were more conducive and environmentally friendly for commercial production. Cao and team [19] reviewed the lead-free organic–inorganic halide perovskite solar cells (PSCs) with highest power conversion efficiency over 13% using tin (Sn) to replace lead (Pb). They proposed the suitable reducing agents to proscribe the oxidation of Sn^{2+} , solvent modulation technique for thin film architecture, and optoelectronic properties dealing with chemical substitutions.

3 Conclusion

Organic–inorganic Sn-based perovskites are the most promising Pb-free materials for the solar cells as eco-friendly options. In the last one decade, these materials achieved a remarkable efficiency (PCE of 13%). Major challenges in the synthesis of Sn-based perovskite materials are fast crystallization, high p-type carrier concentration, and high defect density. With the addition of suitable additives and advanced synthesis techniques, the stability and performance of tin-based perovskites may be enhanced for further low-cost and high-performance commercial use.

References

1. Sharma R, Dey A, Dar SA, Srivastava V (2021) A DFT investigation of CsMgX₃ (X= Cl, Br) halide perovskites: electronic, thermoelectric and optical properties. *Comput Theor Chem* 1204:113415
2. Dar SA, Ali MA, Srivastava V (2020) Investigation on bismuth-based oxide perovskites MBiO₃ (M = Rb, Cs, Tl) for structural, electronic, mechanical and thermal properties. *Euro Phys J B* 93:1–11
3. Kojima A, Teshima K, Shirai Y, Miyasaka T (2009) Organometal halide perovskites as visible-light sensitizers for photovoltaic cells. *J Am Chem Soc* 131(17):6050–6051
4. Im JH, Lee CR, Lee JW, Park SW, Park NG (2011) 6.5% efficient perovskite quantum-dot-sensitized solar cell. *Nanoscale* 3(10):4088–93
5. Kim HS, Lee CR, Im JH, Lee KB, Moehl T, Marchioro A, Moon SJ, Humphry-Baker R, Yum JH, Moser JE, Grätzel M (2012) Lead iodide perovskite sensitized all-solid-state submicron thin film mesoscopic solar cell with efficiency exceeding 9%. *Sci Rep* 2(1):1–7
6. Etgar L, Gao P, Xue Z, Peng Q, Chandiran AK, Liu B, Nazeeruddin MK, Grätzel M (2012) Mesoscopic CH₃NH₃PbI₃/TiO₂ heterojunction solar cells. *J Am Chem Soc* 134(42):17396–17399
7. Noel NK, Stranks SD, Abate A, Wehrenfennig C, Guarnera S, Haghhighrad AA, Sadhanala A, Eperon GE, Pathak SK, Johnston MB, Petrozza A (2014) Lead-free organic–inorganic tin halide perovskites for photovoltaic applications. *Energy Environ Sci* 7(9):3061–3068
8. Stoumpos CC, Malliakas CD, Kanatzidis MG (2013) Semiconducting tin and lead iodide perovskites with organic cations: phase transitions, high mobilities, and near-infrared photoluminescent properties. *Inorg Chem* 52(15):9019–9038
9. Hao F, Stoumpos CC, Cao DH, Chang RP, Kanatzidis MG (2014) Lead-free solid-state organic–inorganic halide perovskite solar cells. *Nat Photonics* 8(6):489–494
10. Zhao Y, Zhu K (2016) Organic–inorganic hybrid lead halide perovskites for optoelectronic and electronic applications. *Chem Soc Rev* 45(3):655–689
11. Correa-Baena JP, Saliba M, Buonassisi T, Grätzel M, Abate A, Tress W, Hagfeldt A (2017) Promises and challenges of perovskite solar cells. *Science* 358(6364):739–744
12. Wang R, Mujahid M, Duan Y, Wang ZK, Xue J, Yang Y (2019) A review of perovskites solar cell stability. *Adv Func Mater* 29(47):1808843
13. Lyu M, Yun JH, Chen P, Hao M, Wang L (2017) Addressing toxicity of lead: progress and applications of low-toxic metal halide perovskites and their derivatives. *Adv Energy Mater* 7(15):1602512
14. Ke W, Kanatzidis MG (2019) Prospects for low-toxicity lead-free perovskite solar cells. *Nat Commun* 10(1):1–4
15. Mari B, Soro D (2020) Advances in perovskite solar cells. *Int Res J Eng Technol* 07(04):475–478
16. Huang YT, Kavanagh SR, Scanlon DO, Walsh A, Hoye RL (2021) Perovskite-inspired materials for photovoltaics and beyond—from design to devices. *Nanotechnology* 32(13):132004
17. Jiang X, Zang Z, Zhou Y, Li H, Wei Q, Ning Z (2021) Tin halide perovskite solar cells: an emerging thin-film photovoltaic technology. *Acc Mater Res* 2(4):210–219
18. Wang M, Wang W, Ma B, Shen W, Liu L, Cao K, Chen S, Huang W (2021) Lead-free perovskite materials for solar cells. *Nano Micro Letters* 13(1):1–36
19. Cao J, Yan F (2021) Recent progress in tin-based perovskite solar cells. *Energy Environ Sci* 14(3):1286–1325
20. Kumari P, Srivastava V, Khenata R, Dar SA, Naqib SH (2021) A first-principles prediction of thermophysical and thermoelectric performances of SrCeO₃ perovskite. *Int J Energy Res*

Phase Transformation Analysis of Fe-Substituted Cr₂O₃ Nanoparticles Using Rietveld Refinement



Jarnail Singh , Pankaj Bhardwaj, Ravi Kumar, Saurav Dixit, Kaushal Kumar, and Vikram Verma 

Abstract In this present report, effect on iron (Fe) substitution on the structural properties of chromium oxide (Cr₂O₃) nanoparticles has been investigated in detail. Simple and cost-effective co-precipitation technique was used to synthesize Fe-substituted Cr₂O₃ nanoparticles at various Fe-concentrations. Structural properties of as-prepared nanoparticles were examined using X-ray diffraction (XRD) technique and Fourier transform infrared (FTIR) spectroscopy. XRD results demonstrated that crystal structure remains single phase up to $x = 0.20$ of Fe-content. Single-phase Cr₂O₃ nanoparticles crystallize in rhombohedral crystal structure with space group. Beyond $x = 0.20$ of Fe-content into Cr₂O₃ nanoparticles, formation of secondary phase in the form of iron oxide (Fe₂O₃) has been initiated. Both Cr₂O₃ and Fe₂O₃ materials crystallize in same corundum structure with same space group. Hence, we have performed Rietveld refinement for detailed structural study of multi-phase compound. In a multi-component system, phase fraction has also been determined using Rietveld refinement method. FTIR spectra also complement the XRD results and demonstrated the Cr–O and Fe–O vibration band in octahedral environment.

Keywords Multi-phase · Rietveld refinement · Phase fraction

1 Introduction

Transition metal oxides (TMOs) have received great attention as they exhibit distinctive optical, electrical and magnetic properties [1]. These properties can be further modified by using appropriate counteraction, which can acquire optoelectronic and

J. Singh (✉) · S. Dixit · K. Kumar
Department of Mechanical Engineering, K.R. Mangalam University, Gurgaon 122103, India
e-mail: jarail.singh@krmangalam.edu.in

P. Bhardwaj · R. Kumar · V. Verma
Department of Material Science and Engineering, National Institute of Technology Hamirpur,
Hamirpur 177005, India

S. Dixit
Division of Research & Innovation, Uttaranchal University, Dehradun, India

magneto-optical applications [2–4]. In transition metal oxides, chromium oxide (Cr_2O_3) material has been widely explored by various researchers for a various applications in the field of optoelectronics, refractory materials, inks, paints, corrosion-resistant materials and catalysts (ref). The chromium oxide exists in various crystalline forms such as CrO_2 , CrO_3 , CrO_4 , Cr_2O_3 , Cr_2O_5 and Cr_5O_{12} . But Cr_2O_3 is the most stable magnetic-dielectric material among abovementioned crystalline form [5]. It is refractory material due to its high melting point (2435 °C) and high temperature oxidation resistance. In addition, it also comprises various applications in different fields such as electrochromic, hydrogen storage, solar energy application, catalysts, advanced colorants, dye and pigments, wear resistance materials, digital recording system and thermal protection coating [6]. Chromium oxide (Cr_2O_3) is *p*-type wide gap semiconducting material and antiferromagnetic in nature with a Neel temperature of $T_N = 307$ K [7]. However, depending on the deposition parameters, it can also demonstrate *n*-type semiconducting behavior. This type of *p*-type transparent semiconducting material can be a potential candidate for applications like optical storage system and UV-light emitter [8]. But, from electrical point of view, Cr_2O_3 material lies on the insulating side. Therefore, various studies have been performed to improve the electrical properties of valuable Cr_2O_3 material. It is well-known fact that the properties of nanomaterials can be modified by introducing an appropriate cationic and/or anionic dopant. Therefore, various dopants such as Mg, Al, In, Ni, Li, Ca and Zn have been tried to enhance its electrical properties [1]. The substitution of Al, In, Li and Ca leads to insulating behavior, while Mg, Ni and Zn cations enhanced the electrical conductivity of Cr_2O_3 material in thin-film form. Apart from that, other transition metal ions (i.e., Fe, Co and Mn) can also be tried as dopants into wide band gap materials and improved their electrical and magnetic properties as well, which is advantageous for optoelectronic and optomagnetic applications. Earlier, Ni-dopant has already been used as a dopant in the case of Cr_2O_3 material (and other wide band gap semiconductors) and obtained results are exciting, making non-magnetic material like Cr_2O_3 a promising candidate for spintronic devices-based applications [7]. Following the above discussion, we have investigated a systematic study to substitute Fe into Cr_2O_3 nanoparticles at various concentrations and demonstrated its structural properties. The aim of present study is to illustrate that at which concentration of Fe-substitution, multi-phase formation is initiating, because multi-phase formation is not desirable from the point of view of device performance. The Fe-substitution into Cr_2O_3 nanoparticles may be of great interest, as it not only enhances the electrical properties, but it may induce magnetic properties into antiferromagnetic Cr_2O_3 material, superior for optoelectronic and magneto-optical applications [9, 10]. Considering the synthesis methods for the preparation of Fe-substituted Cr_2O_3 nanoparticles, various chemical and physical methods have already been such as hydrothermal synthesis, thermal decomposition, laser-induced deposition, sonochemical synthesis, microwave-plasma assisted growth, mechanochemical reaction, sol–gel synthesis, hydrazine reduction and combustion synthesis [11]. Most of abovementioned techniques require high temperature and special lab set-up, costly and environmentally sensitive in nature. But, co-precipitation technique has appeared

as a simple, swift, cost-effective and economical technique with large-scale production ability. Besides, this method provides defined control over the stoichiometry and homogeneity. In this present report, we have prepared Fe-substituted Cr₂O₃ nanoparticles at various Fe-contents using co-precipitation technique. Structural investigation was performed using X-ray diffraction (XRD) and Fourier transformation infrared (FTIR) spectroscopy of as-synthesized nanoparticles. XRD data was further analyzed by Rietveld refinement using FullProf software for detailed structural study.

2 Experimental Details

Co-precipitation technique was used to synthesize the pristine chromium oxide (Cr₂O₃) and iron (Fe)-substituted Cr₂O₃ at different Fe-contents. Analytical grade powder of chromium nitrate nonahydrate (Cr(NO₃)₃·9H₂O) and iron nitrate nonahydrate (Fe(NO₃)₃·9H₂O) was used as the chromium and iron-metal precursor, purchased from Sigma Aldrich having purity of 99.998%. The 0.5 M solution of Cr(NO₃)₃·9H₂O was prepared with double distilled water, and subsequently, 0.05 M solution of Fe(NO₃)₃·9H₂O was prepared in double distilled water separately under constant magnetic stirring for 30 min. After that, both the solutions were mixed into each other as per stoichiometric amount and again stirred for uniform mixing. Initially, prepared solutions were acidic in nature due to the presence of nitrate ions. After that, 0.1 M solution of ammonium hydroxide (NH₄OH) was added dropwise to form the precipitates. The precipitate formation was initiated at pH value of 6. Thereafter, precipitates formed in the mother liquid were allowed to settle down overnight and centrifuged several times with double distilled water to eradicate the soluble ammonium ion impurities. Then, precipitates were placed on a heating mantle at 90 °C to gently evaporate the solvent. Later, as-received powder was crushed into fine powder with the help of agate pestle mortar and, finally, annealed under ambient atmosphere in muffle furnace at 900 °C for 5 h.

3 Results and Discussion

3.1 XRD Analysis

Figure 1 shows the XRD pattern of as-prepared Fe-substituted Cr₂O₃ nanoparticles at various Fe-concentrations. At first look, it seems like that the crystal structure of Cr₂O₃ nanoparticles remains unchanged with Fe-substitution up to $x = 0.50$ of Fe-content, because iron oxide in the form of Fe₂O₃ also crystallizes in corundum structure (rhombohedral phase) with same space group of R-3c, which is similar to Cr₂O₃ material [12]. Hence, it is difficult to distinguish between the Cr₂O₃ and Fe₂O₃ phase because of their similar crystal structure and space group. Due to this, we have

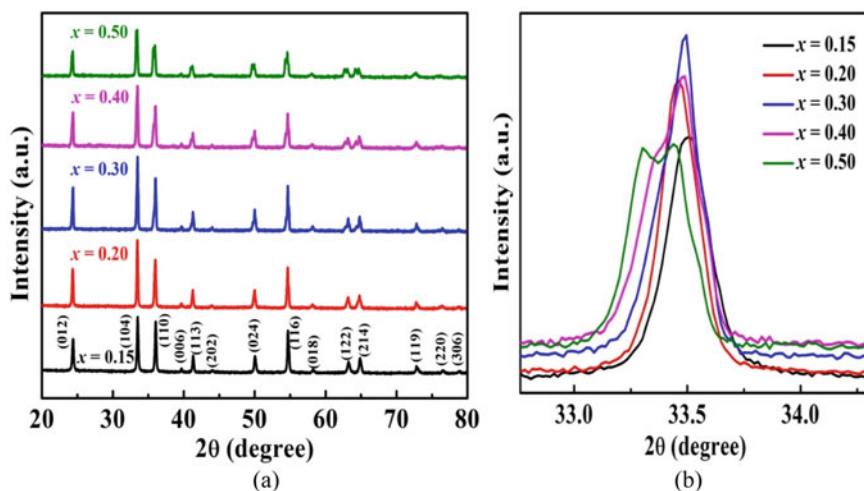


Fig. 1 **a** XRD patterns of Fe-substituted Cr_2O_3 nanoparticles. **b** Magnified view of highly intense to demonstrate the doublet peak due to secondary Fe_2O_3 phase formation

magnified the highly intense peak of every XRD pattern at Bragg's angle from 32.5° to 34.5° , as shown in Fig. 2. From this enlarged view, it is clearly depicted that doublet peaks have been illustrated in XRD pattern of Fe-substituted Cr_2O_3 nanoparticles at $x = 0.30$ of Fe-content. Below this Fe-concentration, structure remains unchanged with Fe-substitution. As it is difficult to differentiate between the both phases, therefore, we have Rietveld refined all the XRD patterns of as-synthesized nanoparticles to determine its structural parameters in detail.

3.2 Rietveld Refinement Analysis

Rietveld refinement of XRD pattern of Fe-substituted Cr_2O_3 nanoparticles at various Fe-concentrations was performed using FullProf software [13]. Refinement of diffraction data was carried out in two different steps. Firstly, it was performed by considering only single Cr_2O_3 phase. Thereafter, both Cr_2O_3 and Fe_2O_3 phases were considered for Rietveld refinement in order to evaluate where multi-phase formation has been initiated. The initial parameters required for Rietveld refinement such co-ordinates of each atom, structural parameters and space group were taken from crystallography open database (COD), matching reference pattern with Cr_2O_3 material. The chromium oxide crystallizes in rhombohedral crystal structure having R-3c space group which has been taken as starting model for refinement of as-prepared nanoparticles. Fourier series having six coefficients polynomial function was used for refining the background of all samples. And pseudo-voigt function was modeled

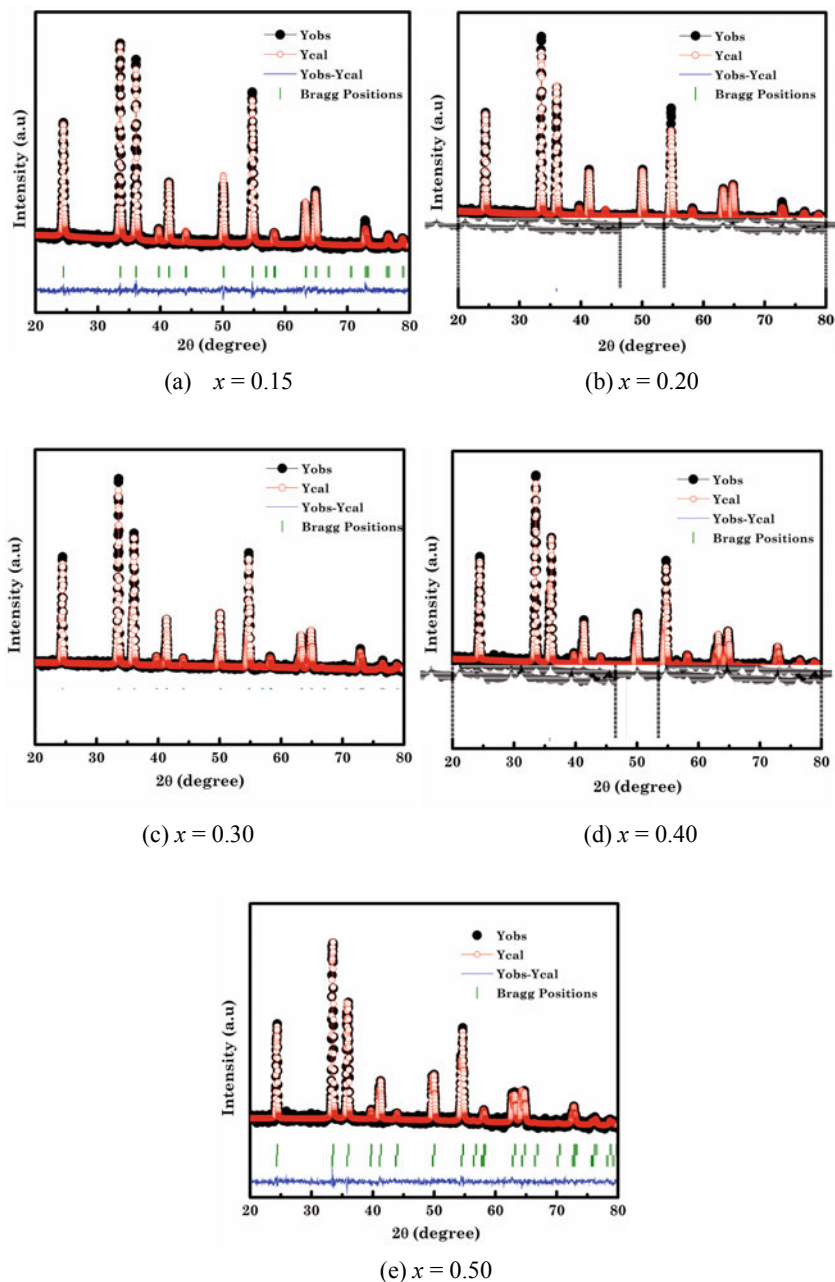


Fig. 2 Refined XRD patterns of Fe-substituted Cr_2O_3 nanoparticles at different Fe-content

for diffraction peak shape refinements. Pseudo-voigt function is a linear combination of Gaussian and Lorentz functions, which can be used for determining the size and strain contribution to broadening of diffraction peaks. At the start, refinement of background coefficients was performed and number of successive refinements was carried out for zero shift error correction of peak positions. Consequently, the structural and micro-structural parameters, i.e., unit cell parameters, position parameters, occupancy, scale factor and structure factor, were refined. Figure 2 shows the Rietveld refinement and experimental diffraction profile of Fe-substituted Cr_2O_3 nanoparticles prepared at value of pH 6. The characteristic peaks demonstrated in the refined XRD pattern are highly intense and indicate the fine degree of crystallinity.

Up to $x = 0.20$ of Fe-content, the refined XRD patterns reveal that prepared nanoparticles crystallize in single rhombohedral phase of Cr_2O_3 , which is well consistent with JCPDS card no. 85-0869. Apart from that, marginal difference between the calculated and experimentally observed pattern indicates the superior quality of fitting. Furthermore, low χ^2 values of every refined XRD pattern also demonstrated the goodness of fit of observed diffraction profile of as-prepared nanoparticles. Beyond $x = 0.20$ of Fe-content, Fe cations are no longer substituted at the Cr^{3+} cationic sites. Substitution of Fe into Cr_2O_3 nanoparticles beyond $x = 0.20$ results in formation of another phase in the form Fe_2O_3 along with Cr_2O_3 material. With the further increase of Fe-content, Fe_2O_3 phase started dominating and while Cr_2O_3 phase was diminishing. The structural parameters such as lattice parameters, cell volumes and bond lengths were also determined from the Rietveld refinement and summarized in Table 1. Lattice parameters and cell volumes of Cr_2O_3 nanoparticles are found to be increasing with Fe-content due to ionic radii mismatch. As ionic radii of Fe^{3+} ions (0.78 \AA) are higher than host Cr^{3+} cations (0.75 \AA), hence, lattice parameters are expected to expand. Increment in asymmetric bond length of Cr and O ions also confirmed the successful incorporation of Fe into the Cr_2O_3 matrix. As discussed above, incorporation of Fe-content into Cr_2O_3 nanoparticles above $x = 0.20$ leads to multi-phase compound formation, which results in irregular distortion in lattice structure of Cr_2O_3 nanoparticles.

Table 1 Variation of lattice parameters and cell volumes of Fe-substituted Cr_2O_3 nanoparticles with varying Fe-content

Sample name	Cr_2O_3 phase			Fe_2O_3 phase		
	a (\AA)	c (\AA)	Vol. (\AA^3)	a (\AA)	c (\AA)	Vol. (\AA^3)
$x = 0.15$	4.975	13.601	291.502	–	–	–
$x = 0.20$	4.982	13.606	292.466	–	–	–
$x = 0.30$	4.976	13.598	291.526	5.005	13.632	295.691
$x = 0.40$	4.979	13.601	291.956	5.012	13.642	296.818
$x = 0.50$	4.986	13.618	292.961	5.018	13.653	297.747

3.3 Phase Fraction Analysis

We have also determined the amount of each phase present in the multi-phase component system using Rietveld refinement method. If crystal system has comprised of a mixture of N number of crystalline phases, then phase fraction of each component can be calculated by using a following relation [13].

$$W_p = \frac{S_i Z_i M_i V_i}{\sum_{j=1}^n S_j Z_j M_j V_j} \quad (1)$$

where W_p is the relative phase fraction of phase i , Z_i is number of formula units per unit cell, S_i is the Rietveld scale factor, V_i is the unit cell volume for phase i , and M_i is the mass of the formula unit. All the terms mentioned above can be evaluated by Rietveld refinement method using FullProf software. Figure 3 illustrated the variation of quantitative phase fraction of both Cr₂O₃ and Fe₂O₃ phases at different Fe-content. Up to $x = 0.20$ of Fe-content, structure remains single rhombohedral phase. As the concentration of Fe-substitution increases beyond $x = 0.20$, Fe₂O₃ phase rises linearly, whereas Cr₂O₃ phase started diminishing.

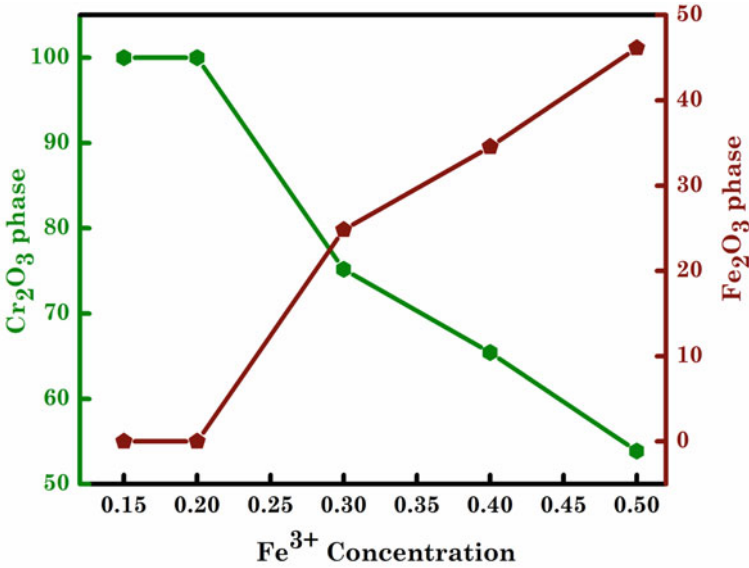


Fig. 3 Illustration of phase fraction of both components as a function of Fe-concentration

3.4 Williamson-Hall Method

Williamson-Hall method is employed to determine the effect of broadening due to Fe ion substitution into Cr_2O_3 nanoparticles by considering both crystallite size (D) and microstrain (ε) together using the following equation [14]:

$$\beta_{hkl} \cos \theta = \frac{0.9\lambda}{D} + 4\varepsilon \sin \theta \quad (2)$$

$$\beta_{hkl}^2 = \beta_{\text{measured}}^2 - \beta_{\text{instrumental}}^2 \quad (3)$$

where λ is the wavelength of X-rays (1.54 Å), k is the shape factor (0.9), β_{measured} is FWHM in radians of prominent intense peak centered at diffracting angle θ , and $\beta_{\text{instrumental}}$ is FWHM in radians of standard instrumental XRD sample. A linear fitting is drawn between $\beta \cos\theta$ versus $4 \sin\theta$, and its slope and intercept give the value of microstrain and crystallite size, respectively, enlisted in Fig. 4. The crystallite size and microstrain within the lattice system follow the same trend with Fe-substitution into Cr_2O_3 nanoparticles. The crystallite increases with Fe-substitution into Cr_2O_3 nanoparticles (up to $x = 0.20$ of Fe-content) indicating improved crystallinity in as-prepared nanopowders. The increase in crystallite size and decrease in microstrain suggest that atoms shifting from non-equilibrium to equilibrium position result in strain relaxation. After that, there is a formation of multi-phase compound which comprises Fe_2O_3 and Cr_2O_3 phase. Due to which, strain has been induced into the crystal lattice and increases with Fe-substitution.

3.5 Dislocation Density

The crystallite size is inversely proportional to dislocation lines which indicate structural disorder in a system, known as dislocation density. The dislocation density can be calculated by using the following relation.

$$\delta = \frac{1}{D^2} \quad (4)$$

D is the crystallite size obtained from W–H plot, depicted in Table 2. The decrease in dislocation density is related to the expansion of crystallite size and reduced microstrain in as-synthesized nanoparticles. When strain is increased due to the formation of multi-phase, dislocation density also increases [15, 16].

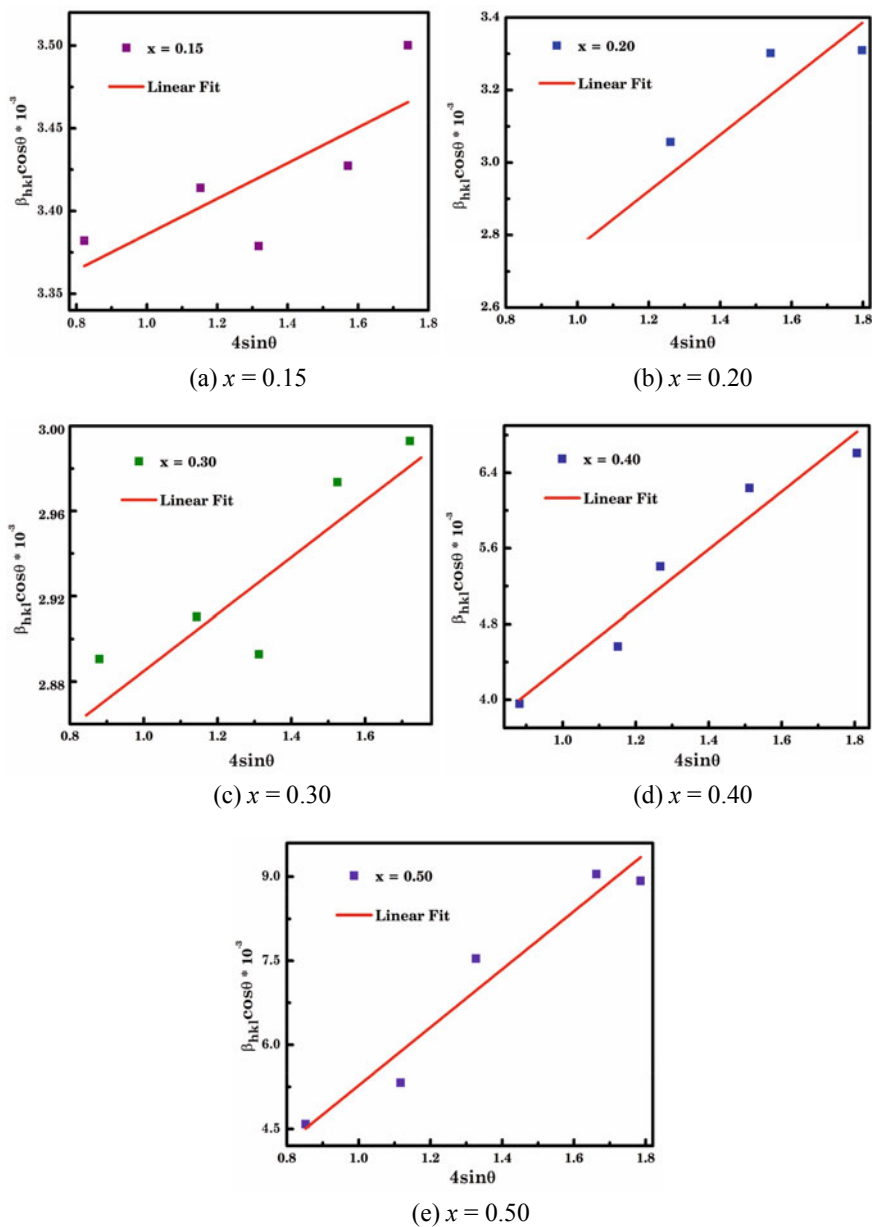


Fig. 4 A linear fitting between $\beta \cos \theta$ versus $4 \sin \theta$, and its slope

Table 2 Bond lengths, strain, average crystallite size and dislocation density of Fe-substituted Cr₂O₃ nanoparticles at various Fe-content

Sample name	Bond length (Å)	Strain (ϵ)	Crystallite size D (nm)	Dislocation density (δ)
$x = 0.15$	2.052, 1.943	3.39×10^{-3}	34.95	8.186×10^{-4}
$x = 0.20$	2.056, 1.948	3.07×10^{-3}	37.54	7.095×10^{-4}
$x = 0.30$	2.0644, 1.9415	2.96×10^{-3}	39.51	6.407×10^{-4}
$x = 0.40$	2.066, 1.940	4.35×10^{-3}	26.99	1.373×10^{-3}
$x = 0.50$	2.068, 1.953	5.52×10^{-3}	22.06	2.054×10^{-3}

3.6 FTIR Analysis

FTIR spectra of Fe-substituted Cr₂O₃ nanoparticles at various Fe-contents are illustrated in Fig. 5. The four distinct absorption modes at 418, 445, 556 and 640 cm⁻¹ have been demonstrated in every spectra. Every observed mode is well consistent with previously reported spectra of Cr₂O₃ nanoparticles [1]. The relatively weak absorption band observed at 418 and 445 cm⁻¹ corresponds to Cr–O vibrations in bending mode. The absorption band observed at 556 cm⁻¹ corresponds to Cr–O stretching mode vibration of Cr–O₆ octahedra, while the broad absorption band centered around 640 cm⁻¹ identifies the chromium oxide as Cr₂O₃ rhombohedral phase, which is well in agreement with our XRD results. Considering the group theory, band observed at 445, 556 and 640 cm⁻¹ indexed to the E_u modes, whereas band illustrated at 418 cm⁻¹ ascribed to A_{2u} vibration modes. As both Cr₂O₃ and Fe₂O₃ belong to same space group R-3c, it is difficult to distinguish the vibration modes of both nanomaterials. The FTIR absorption bands of Fe₂O₃ nanoparticles are expected to be observed at 554 and 614 cm⁻¹ [17, 18]. The peak depicted at 614 cm⁻¹ corresponds to the longitudinal absorption mode having A_u symmetry, while the band centered at 572 cm⁻¹ is assigned to the transverse absorption mode with E_u symmetry. Due to this, absorption band peaks of both nanomaterials overlap, which results in broadening of absorption band, as depicted in Fig. 5. It is clearly evident that, when the crystal structure is transforming from chromium oxide (Cr₂O₃) to iron oxide (Fe₂O₃), narrowing of absorption band has been observed, which is well consistent with phase fraction calculation determined from Rietveld refinement. With the increase of Fe-content into Cr₂O₃ nanoparticles, Fe₂O₃ crystal structure starts dominating, while on the other, Cr₂O₃ phase starts diminishing. It is responsible for the narrowing of absorption band with Fe-concentration. Apart from that, the presence of Cr–O and Fe–O vibration mode in FTIR spectra revealed the successful elimination of impurities during the annealing process under ambient atmosphere.

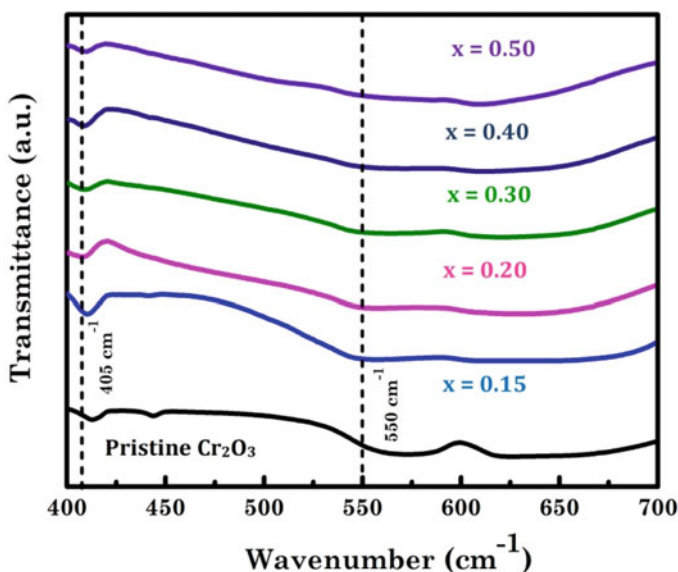


Fig. 5 FTIR spectra of Fe-substituted Cr₂O₃ nanoparticles at different contents of Fe

4 Conclusion

Single-phase Fe-substituted Cr₂O₃ nanoparticles (up to $x = 0.20$ of Fe-content) have been successfully synthesized using co-precipitation technique. After $x = 0.20$ of Fe-substitution into Cr₂O₃ nanoparticles, Fe ions are no longer substituted at the host cationic sites, but start forming the secondary phase (i.e., Fe₂O₃) by reacting with environmental oxygen. With further increase in Fe-content, Fe₂O₃ phase starts dominating, whereas Cr₂O₃ phase begins diminishing. Even at $x = 0.50$ of Fe-content, weak traces of Cr₂O₃ are present, as determined from phase fraction analysis. It indicates that phase transformation from Fe₂O₃ to Cr₂O₃ is still not completed at $x = 0.50$ of Fe-content. Further work can be extended based on this study that optical, electrical and magnetic properties can be recorded for single-phase Fe-substituted Cr₂O₃ nanoparticles. Therefore, this study can lead to development of potential material which can acquire applications in the field of optoelectronic and magneto-optical devices.

References

1. Singh J, Kumar R, Verma V, Kumar R (2020) Role of Ni²⁺ substituent on the structural, optical and magnetic properties of chromium oxide (Cr_{2-x}Ni_xO₃) nanoparticles. *Ceram Int* 46:24071–24082. <https://doi.org/10.1016/j.ceramint.2020.06.185>
2. Bhuvana S, Ramalingam HB, Vadivel K, Kumar ER, Ayesh AI (2016) Effect of Zn and Ni

- substitution on structural, morphological and magnetic properties of tin oxide nanoparticles. *J Magn Magn Mater* 419:429–434. <https://doi.org/10.1016/j.jmmm.2016.07.004>
3. Kaushik A, Dalela B, Kumar S, Alvi PA, Dalela S (2013) Role of Co doping on structural, optical and magnetic properties of TiO_2 . *J Alloy Compd* 552:274–278. <https://doi.org/10.1016/j.jallcom.2012.10.076>
 4. Srinet G, Kumar R, Sajal V (2013) Structural, optical, vibrational, and magnetic properties of sol-gel derived Ni doped ZnO nanoparticles. *J Appl Phys* 114. <https://doi.org/10.1063/1.4813868>
 5. Abdullah MM, Rajab FM, Al-Abbas SM (2014) Structural and optical characterization of Cr_2O_3 nanostructures: evaluation of its dielectric properties. *AIP Adv* 4:027121. <https://doi.org/10.1063/1.4867012>
 6. Cao H, Qiu X, Liang Y, Zhao M, Zhu Q (2006) Sol-gel synthesis and photoluminescence of p-type semiconductor Cr_2O_3 nanowires. *Appl Phys Lett* 88:241112. <https://doi.org/10.1063/1.2213204>
 7. Bhardwaj P, Singh J, Kumar R, Kumar R, Verma V (2021) Structural, optical and magnetic characterization of Ni^{2+} ions doped chromium oxide (Cr_2O_3) nanoparticles. *Solid State Sci* 115:1–13. <https://doi.org/10.1016/j.solidstatesciences.2021.106581>
 8. Tobia D, Winkler E, Zysler RD, Granada M, Troiani HE (2008) Size dependence of the magnetic properties of antiferromagnetic Cr_2O_3 nanoparticles, physical review B-condensed matter and materials. *Physics* 78:1–7. <https://doi.org/10.1103/PhysRevB.78.104412>
 9. Carey JJ, Legesse M, Nolan M (2016) Low valence cation doping of bulk Cr_2O_3 : charge compensation and oxygen vacancy formation. *J Phys Chem C* 120:19160–19174. <https://doi.org/10.1021/acs.jpcc.6b05575>
 10. Singh J, Kumar R, Verma V, Kumar R (2021) Structural and optoelectronic properties of epitaxial Ni-substituted Cr_2O_3 thin films for p-type TCO applications. *Mater Sci Semicond Process* 123:105483. <https://doi.org/10.1016/j.mssp.2020.105483>
 11. Singh J, Verma V, Kumar R, Sharma S, Kumar R (2019) Effect of structural and thermal disorder on the optical band gap energy of Cr_2O_3 nanoparticles. *Mater Res Expr* 6:85039. <https://doi.org/10.1088/2053-1591/ab195c>
 12. Roy M, Ghosh S, Naskar MK (2015) Solvothermal synthesis of Cr_2O_3 nanocubes via template-free route. *Mater Chem Phys* 159:101–106. <https://doi.org/10.1016/j.matchemphys.2015.03.058>
 13. Rodriguez-Carvajal J (1997) Program for Rietveld Refinement. Full Prof, LLB JRC, Version 3.7
 14. Mote V, Purushotham Y, Dole B (2012) Williamson-Hall analysis in estimation of lattice strain in nanometer-sized ZnO particles. *J Theor Appl Phys* 6:2–9. <https://doi.org/10.1186/2251-7235-6-6>
 15. Rana AK, Kumar Y, Rajput P, Jha SN, Bhattacharyya D, Shirage PM (2017) Search for origin of room temperature ferromagnetism properties in Ni-doped ZnO nanostructure. *ACS Appl Mater Interfaces* 9:7691–7700. <https://doi.org/10.1021/acsami.6b12616>
 16. Muthukumaran S, Gopalakrishnan R (2012) Structural, FTIR and photoluminescence studies of Cu doped ZnO nanoparticles by co-precipitation method. *Opt Mater* 34:1946–1953. <https://doi.org/10.1016/j.optmat.2012.06.004>
 17. Kulal PM, Dubal DP, Lokhande CD, Fulari VJ (2011) Chemical synthesis of Fe_2O_3 thin films for supercapacitor application. *J Alloy Compd* 509:2567–2571. <https://doi.org/10.1016/j.jallcom.2010.11.091>
 18. Ramesh R, Ashok K, Bhalero GM, Ponnusamy S, Muthamizhchelvan C (2010) Synthesis and properties of α - Fe_2O_3 nanorods. *Cryst Res Technol* 45:965–968. <https://doi.org/10.1002/crat.201000140>

A Review Study on Advancement and Development of First Generation to Next Generation Optical Fibers



Puja Acharya, Vivek Singh Tanwar, and Bhavesh Vyas

Abstract The Optical Fiber is an important structure that upcoming technologies like 5G will employ for a successful connection with customers. Optical fiber has the speed and ability required for daily uses, without any data or distance limitations thus it is a perfect and global future testimonial solution that can solve the industry's demands for the ages to come and eliminate the current technology for data transfer with its high speed and reception. Optical fiber is robust and communicates waves through unpretentious external factors such as temperature or electromagnetic fields, and signal distortion is very less compared to previous technologies. Telecom service providers, for 5G sector will need to employ a dependable infrastructure, has strong bandwidth, meets speed requirement and safe which only optical fiber will provide. Optical Fiber will have huge applications in every sector where the internet is used which is now everywhere.

Keywords Types of fiber generation · 2G · 3G · 4G · 5G · Optical fiber

1 Introduction

Optical Fiber as a signal channel is an optimal option for terrestrial connections with communication expanses of millions of miles and billions of kilometers and data transmission flow over several Gb/s. Its evolution has brought significant innovations and the creation of the low loss Optical Fiber during the 1970s [1, 2]. Additionally, in short- stretch, high-density transmission in data centers, the essential data rates, distances (couple of kms), and those form factors of the transmission link make optical fiber the only considerable transport medium for the case of the in-house pre-5G wireless networks certain circumstances are still same, as the amount of transmitted information (tens to hundreds of Mb/s) and typical distances (in case of a typical enterprise building its hundreds of meters) and have several advantages over wireless links and coaxial copper link. In this manner, the role of optical fiber

P. Acharya (✉) · V. S. Tanwar · B. Vyas
K.R. Mangalam University, Gurgaon, Haryana 122103, India
e-mail: puja.acharya@krmangalam.edu.in

acting as a carrier channel in indoor wireless networks has changed over the past 20 years. Simultaneously, the network architecture has been advancing from a basic distribution system to a complex RAN, capable of coinciding assistance of numerous technologies (Wi-Fi, short-range guidelines, and numerous ages of cell principles—GSM, WCDMA, LTE, 5G new radio), multiple operators and multiple frequency bands.

2 Expansion of Fiber Optical and 5G

To establish the connection between optical fiber expansion on a fixed network and 5G, it is important to understand the requirements set by 5G for mobile radio network connectivity and the driving force that leads to the expected cell concentration. To date, the key features of the mobile network are outlined below starting with:

- i. Mobile networks are made up of interlocking cells as a sense of less disruptive resources. The size of the cells is influenced by the transmission capacity and the frequency-dependent distribution conditions, i.e. greater the frequency range, the greater the attenuation, and thus may decrease the cell size.
- ii. Depending on the power of transmission, it divides between macro cells and small cells. The first is usually provided by transmitting locations on the roof or towers and represents the most prominent form of the telephone network. Small cell stations were often found inside buildings (household appliances) or “city furniture” (e.g., streetlights, bus stops, etc.) or on higher ground in buildings.
- iii. The data rate available to a single user depends on mobile technology, frequency bandwidth used, user distance from the transmitting antenna, and the number of synchronized users in a shared mobile cell (“mobile phone cell”), and the reduction of mobile cell interference.

Therefore, the following options to increase the data rate of mobile phone users:

- i. Utilization of the latest mobile technology for higher efficiency
- ii. Transmission of multiple frequencies to the transmission area (e.g., 4G or LTE Advanced with multiple of 20 MHz)
- iii. Reduction in the number of users per mobile cell.[3].

With the advent of 5G deployment, the need for 5G is becoming more and more clear. According to the current proposal of the International Telecommunications Union (ITU), 5G technology is intended to be defined by the following structures:

- i. Higher data rates up to 20/10 Gbps (downstream/upstream) under optimal conditions.
- ii. 100/50 Mbps (downstream/upstream) for user access at any time in downtown.
- iii. 1 ms short delay times for services with excessive delay requirements or 4 ms for mobile broadband applications.
- iv. Traffic congestion of 10 Mbps/m² of rough areas within buildings.

In summary, it can be said that 5G allows a significant increase in the data rate that must be discharged per transmitter location and requires the commissioning of numerous new mobile radio stations. And these requirements can only be achieved by high-density optical fibers because of their high bandwidth and low latency connections [4].

3 5G—Focused on Optical Networks

The optical communications network comprises metro, core, and optical access networks, as depicted in Fig. 1.

The modern optical system is designed to manage maximum variety of facilities such as mobile applications, suburban services, and company communications. 5G spectrum incorporates network connectivity to new uses such as wide bandwidth, minimal latency, precise synchronization, and capability of using network slicing to maximize 5G targeted use in any application possible. For maximum 5G usage, the optical system should be modified and upgraded, directing to optical networking or networks. [5, 6].

A new trend of open communication is the extensive construction of data centers, which has successfully supported both basic and municipal networks through cloud computing systems and centralized resource sharing. With cellular networks, shifting from 4 to 5G era, cloud-radio access network is very prominent as it provides necessary functions like centralized baseband processing, cross-cell interference cancellation, disruption of central office resources, and facilitation of remote radio units [7].

Therefore, it provides the key to the 5G- tailored optical networks as wide sharing of cloud-based centers. Also in recent years, internet providers have not only based

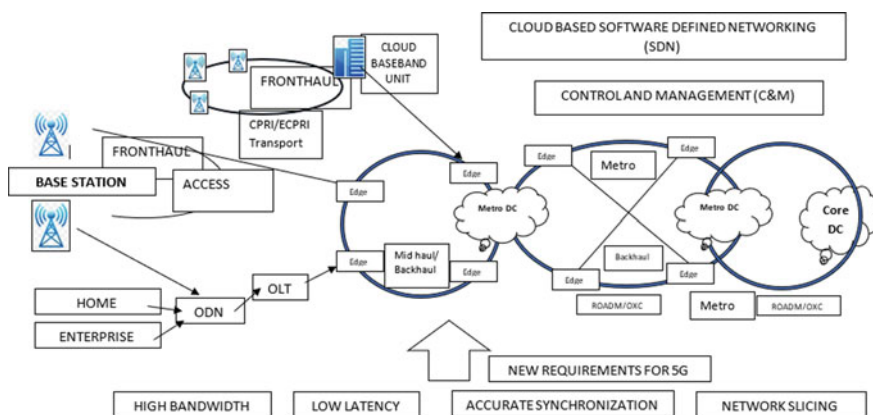


Fig. 1 The complete radio access and fixed access optical system applications involving optical distribution Network

their infrastructure on data centers but also network service providers have reframed the culture of optical networks direct to data center networks as shown in Fig. 2. Because database connection interface (DCI) requires high transfer volume which is almost full-mesh networking and also needs reconfiguration of bandwidth to its full potential. The pathway of wireless technology has moved onwards from second-generation to fifth-generation with a significant organizational change as shown in Fig. 3.

Some of the main features of these generations are listed here: In the second-generation base transceiver station and base station controller are divided. This optical technology now primarily works on SONET and SDH. With the third generation, base transceiver station and base station controller advanced to Node B and radio network controller, respectively, which continued to be split.

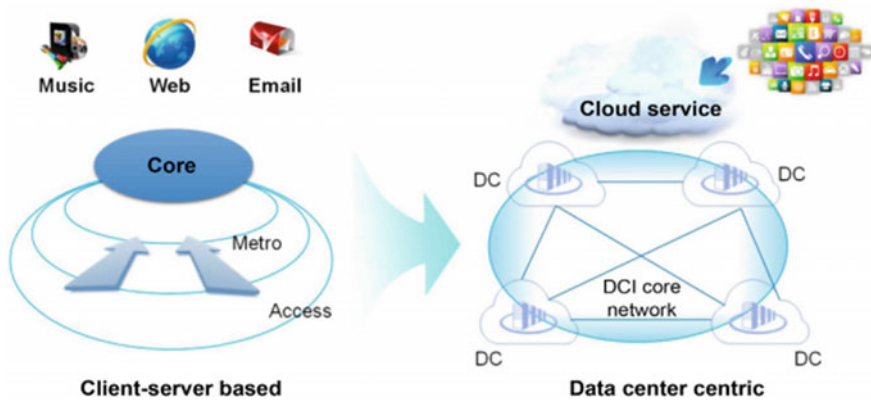


Fig. 2 The complete radio access and fixed access optical system applications involving Optical Distribution Network

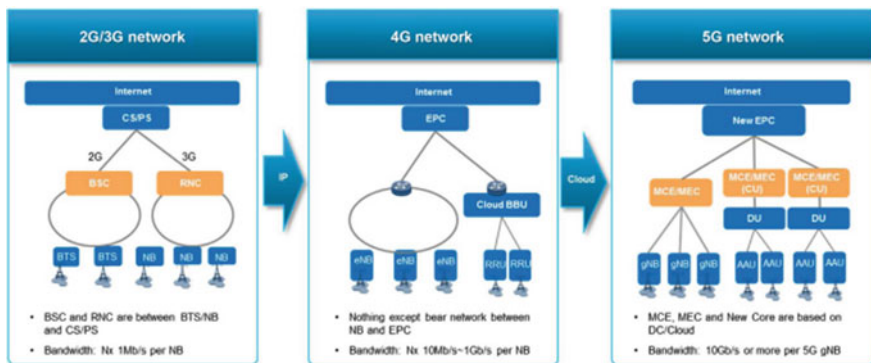


Fig. 3 Growth of wireless technology structures from 2G/3G, 4G-5G

The sustaining optical networks are now largely grounded on multiservice transport platforms. With 4G, BSC completely vanished, because of the emergence of C-RAN (Cloud-radio access networks/Centralized-radio access networks). C-RAN is computer-based access to radio access networks (RANs) that supports 2nd, 3rd, and 4th generations and other wireless communication benchmarks in the future. C-RAN aids centralized processing, synergic radio, and uncomplicated remote radio units (RRU). C-RAN reduces the total cost of proprietorship/ownership (TCO) and increases performance improvements for mobile networks. The optical support networks are principally internet protocol-based radio access networks (IP-RAN). With the escalation, advancement, and construction of 5G networks have been established upon cloud architecture, adding a supplement of mobile cloud engine and mobile edge computing that possesses widely distributed data centers. Mobile cloud engines and mobile edge computing are the prominent and promising, radio access technology (RATs) supported. Connections between multiple RATs can be obtained by source superior integration and user experience. In addition, network construction and flexibility with both distributed and single controls can also be built, allowed to open demand posting of novel network services. A visible supporting network is deemed to be a new 5G- adapted optical network. Both the 5G wireless networks and OTN (Optical Transport Networking) can distribute significant shared media like distributed data centers and cloud computing applications.

4 Optical Fiber in Generation of Interior Mobile Network

The unacceptable intrusion of radio waves from cell-phone towers within buildings and houses, especially for higher frequency spectrums, and the resulting cutback in cell phone handling availability have encouraged the introduction of the domestic distributed antenna system (DAS) whose major aim was originally to distribute the same replica of the RF signals across the houses.

The typical assembly of distributed antenna system (DAS) as in Fig. 4.

Remote units (RUs) consist of several antennas responsible for receiving and transmitting RF signals. Transportation delivers front haul (FH) functionality. It unites remote units with several intermediate communication hubs that are joined to the operator device through either optical/copper cable or could be a wireless connection. The transport medium units (TMU) units work to aggregate and distribute the signal. The 1st generation of Distributed Antenna systems dispersed RF signal over an analog area dependent upon coaxial cables or radio over-Optical Fiber (RoF) linking to unite a base to multiple remote units [8]. The RoF resolution was chosen for transmitting distances of more than 29–100 m due to low loss, form factor, and weight gain matching with the coaxial cables. Operating several base stations on a neutral host, all radio signals through multiple base stations operators are combined into single and wide modulated RF up to 5 GHz optical carrier at the common lengths of cellular wavelength of 80 nm using 1.3 or 1.56 μm multimode [9] or single-mode optical fiber. The benefit of this method allows the use of wide bandwidth RF signals

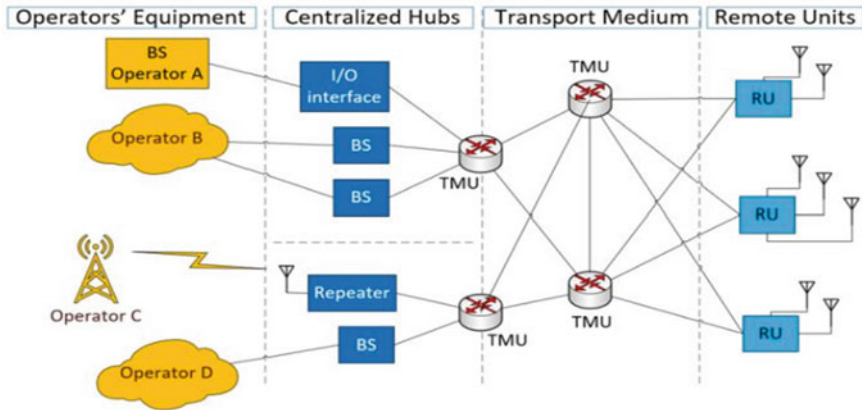


Fig. 4 The structures of the Distributed Antenna Systems (DAS) consist of three large components: multiple remote units (Rus), transit area as well as central hubs provided to Base station (BS) operation to networks

over hundreds of miles with low deprivation to boost many frequency bands for mobile or other communication protocols as Wi-Fi.

The second generation of Distributed Antenna System can be recognized as a medium of digital transmission and reception but analog distortion extends to the outer base station. In that case, several choices have been available to transmit signal through by employing optical fiber, coaxial cable, power cable, or through wireless link. Such transmission medium can be used to attain the digital RF signal to achieve the required amount of FH capacity. The RF spectrum samples at twice the maximum frequency to get high data rate transfer quickly and faster. On the other hand, the samples are filtered and improved into different bands with next multiplexing in the digital generation domain that decreases the required FH capacity at the expense of complexity in hardware. In addition, the delay requirements between a base station and user tool, are determined by synced processes flexibility and minimizing the potential advantages of band sampling. At last, the use of the Community Public Radio Interface (CPRI) [10] ultimately created a carrier channel that is based on optical fiber and has been a popular resolution in DAS 2nd generation.

In the 3rd generation, in-house wireless networks have thrown a digital port between a base station, distribution system, and radio unit operational flexibility called as split [11]. Transferring high performance to a remote unit with high-performance separation leads to a reduction in the rate of transport data. Rendering to the term, low-level separation leaves minimum functionality in remote units and necessitates only a digitized baseband port like CPRI between the remote unit and base station (or more generally, one-unit, centralized unit). In contrast, the high-layer split option the first layer converts the remote unit into a small cell base station version. The 5G new radio standard presents fresh bands in the millimeter-wave spectrum. In addition to amplified wave b/w (20 MHz on LTE matched to 401 MHz

on new radio), mm-wave communication means more local channels powered by antenna array beamforming. As per a recent study by 3GPP, the essential amount of FH volume may change of hundreds of Gb/s, maintaining on the variant, taking an instance where option 1.1 downlink FH split only requires data rates of 4 Gb/s, option 8 splits (CPRI based) requires more than 150 Gb/s. Split options of 6, 7–2 and 7–1 for high input cell (401 MHz bandwidth, QAM 256, antenna ports) providing FH power rated at 18 Gb/s, 117 Gb/s and 454 Gb/s, respectively [12]. The retention of these bit levels paves to the tremendous amounts of interchange that can only be achieved with optical fiber technology.

5 Development of Optical Fiber Technology

5.1 Dispersion Optimization for Optical Fibers G.655 and G.656

In the 1990s it was seen that widespread adoption of long-distance communication, the development of amplification in optical domain using Dense Wavelength Division Multiplexing (DWDM). For handling the demand, the need for creating an advanced optical system, many single-mode fiber with scattered chromatic scattering characters were established, called as Non-Zero Dispersion Shifted Optical Fiber (NZDSF's) which are modified by G.655 Optical Fibers [13, 14]. After 2002, further refinement of the NZDSF's distribution structures continued to work on S, C, and L bands and this has been approved by the ITU-T with special recommendations of G.656 [15]. Further, these NZDSF references G.655 and G.656 were amended to improve their chromatic distribution details of the implementation of an enhanced system as described further. ITU-T recommendations such as G.655 has begun the construction in the year 1996. It defines one mode of optical fiber with a total chromatic distribution should be greater than the non-zero value in total distance from 1500 to 1570 nm. The non-zero distribution rate decreases the development of the indirect outcomes which in particularly significantly destructive to DWDM systems, and further matched to dispersion-shifted fibers or G.653 having a zero-dispersion. These NZDSFs produce minor distribution rates matched to standard G.652 optical fiber mode called a "standard" single-mode fiber (SSMF), which continues to handle the effects of non-linear crossing between medium but makes way for larger dispersion requirements.

The two types of G.655 marked in tables a–c (G.655.A–G.655.C), define chromatic distribution in terms of wavelength self-finding minimum and maximum range, for a specified value of 1531–1564 nm (C-band) as stated in Fig. 5a. As these chromatic scattering of optical fibers changes with wavelength with different ranges of WDM transmission requires a true definition of such behavior. In 2006, the 3rd version has been allowed to announce some new classes of G.655.D and G.655.E which is the chromatic scattering limit with coupling lines versus wavelength of

the range 1459–1624 nm. With G.655.D (low optical fibers dispersion) chromatic scattering of wavelength above 1531 nm has adequate magnitude to subdue non-linear deformities, which makes DWDM applications based on these wavelengths see Fig. 5b the next page.

Although the distribution may change the signal to wavelengths below 1531 nm, the presence of some low wavelengths is envisioned delivering data to sustenance coarse wavelength division multiplexing (CWDM) applications with non-linear disabilities as in G.655.E (medium distribution optical fibers) the chromatic distribution is a bit more than G.655.D having very little channel space. The G.655.E optical fibers have shown very good and non-zero chromatic distribution ranges of wavelengths greater than 1461 nm, throwing a new potential S, C, and L-band windows for potential (DWDM) Dense Wavelength Division Multiplexing transmission as in Fig. 5(c).

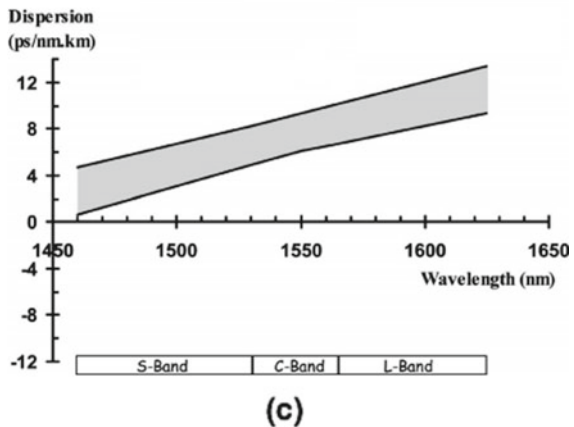
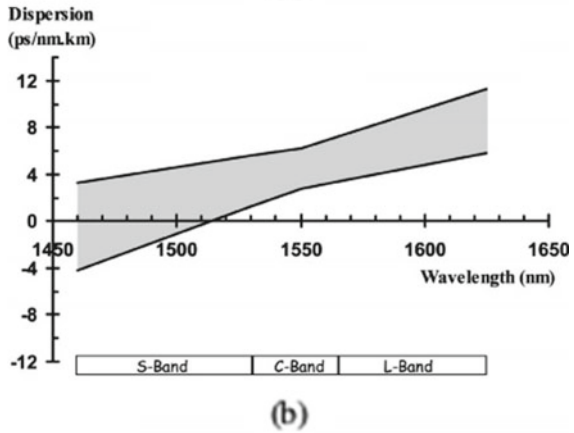
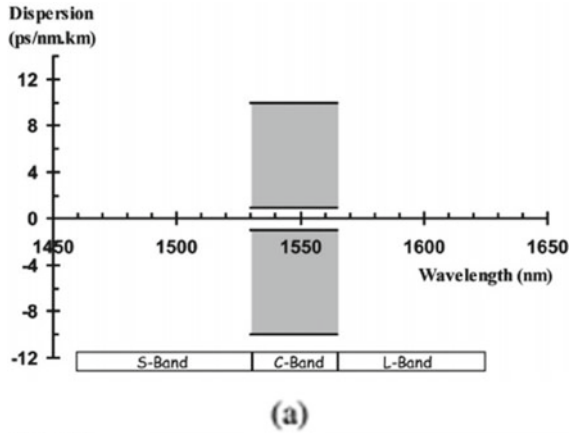
In the year 2004, ITU-T came up with a novel reference G.656, including NZDSF allowed broadband optical transmission in S, C, and L-band (1461 nm–1624 nm), having greater chromatic scattering with higher values during the wavelength ranges of 1460–1625 nm. This evolution had arisen indirect effects which meant to be potentially more destructive to DWDM systems, and reduced transmission as compared to the specific NZDSF of G.655. Initially, in the first system, chromatic propagation was also expressed in maximum and minimum, independent ranges of wavelength as in Fig. 6a. In the year 2006, the recommendation of G.656 was revised to express the chromatic propagation equilibrium requirements such as the pairing of binding curves relative to wavelengths of 1461–1624 nm Fig. 6b.

5.2 *Advanced Developments for FTTH Applications*

Soon with a decline of the internet effervesce era, the attention on optical fiber input has been shifted from long-haul communication to access networks and especially to (FTTx) applications. It started from Asia (Japan, Korea), followed by North America and now increasingly in Europe, the area used should have toughness property of optical fiber, to assist comfortable and cheap installation. Therefore, yielding the sensitivity character became the first investigative point for the optical fiber producers.

For some FTTH applications, especially residential houses, it's advisable to model the most effective multimode optical fiber format consumed made business networks affordable. Combined with operating switches in the basement, such densely populated buildings or houses can be mounted at high speed with a rapid internal network. In 2007, ITU-T employing FTTH released new G.651.1 reference for affordable one Gigabits/second for ethernet applications with connector wire from 600 m which were earlier mostly established on the 851 nm transceivers. This advancement eliminates the previous G.651 fibers.

Fig. 5 a G.655 NZDSF, b low dispersion G.655.D NZDSF dispersion boundary, c medium dispersion G.655.E NZDS. F dispersion boundary



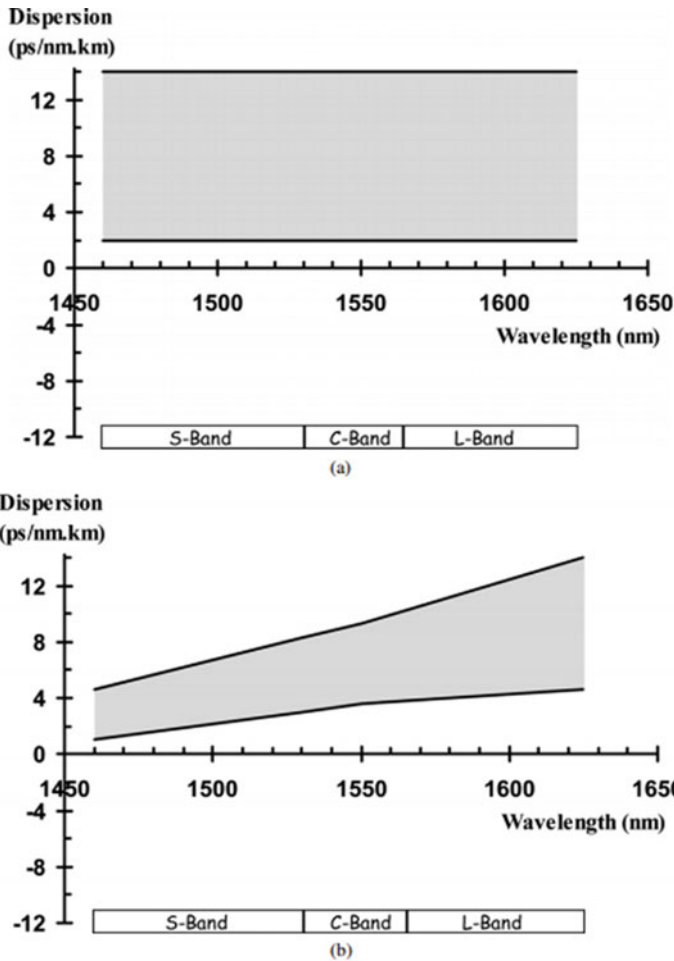


Fig. 6 a G.656 NZDSF dispersion boundary, b G.656 NZDSF dispersion boundary

5.3 Ultra-High-Speed Multimode Optical Fiber

With the evolution of generation of telecommunication in its full swing, the requirement for high speed is astounding. Ever since the encapsulation of IEEE first Gigabit Ethernet standard in year 1998, it has paved the way to high-speed fibers of 10 Gb/s leading to level of 10–11 Gigabit Ethernet in the year 2002. This provides solutions for long expanses but short distance low-cost connection which is less than 10 Gb/s is vital in many areas, such as Local Area Network, data centers, and telecom offices, which led to multi-dimensional applications, particularly in the development of datacom’s speed, a new multimode fast optical fiber has been advanced, commonly denoted as OM3 optical fiber.

This optical fiber which operates at 851 nm in amalgamation with VCSEL source can tie 301 m at 10 Gb/s. More information on multimode threads is further discussed in the article. Currently, IEEE is operative on the succeeding high-speed program 40 Gb/s and 100 Gb/s.

6 Review of Band Intensive Optical Fiber Technology

Macro bend loss of single-mode optical fiber has been significantly reduced over years ago in classical telecommunication. This is in line with ITU-T references and IEC standards for at present high demand requirement which is one hundred times more giving a 0.1 dB loss at 1626 nm possessing radius of 30 mm [17].

The recent FTTH telecommunications systems which have recently created some stimulating needs, the source of latest G.657 (A&B) ITU-T references stated earlier. For such difficult situation, low capacity in storage areas is essential (with radius up to 15 mm), and additional resistance results from improper delivery of optical fiber, sharp bends in the angles, or also, from attaching the cable to the wall.

Many designing strategies of refractive index to manufacture optical fibers compatible with G.657A have been suggested and/or the recommendations of G.657B.

For the traditional step-index single-mode optical fiber, a popular result for reducing bending sensitivity comprises lowering the Mode Field Diameter (MFD) above the cut-off wavelength ratio by intensifying wavelength length or reducing the size of the mode field [18–20]. Still, bending loss rate stays very high when inserting emerging bends with radius in a row of 1 to 10 mm. Additionally, due to less space, the MAC values are taken less if the optical fiber has to match with ITU-T G.657 “class A” standards.

Undeniably, Mode Field Diameter may vary in the precise range as shown in Table 1. Therefore, the step-index database has been created which is found to be compatible with G.657A (small core) or G.657B, but there have been no keys for obtaining threads corresponding to G.657A & B. New era optical fibers have been suggested to find a remedy for this difficulty. They all show the location of the depressed index inside the cladding layer of fiber near the core part that permits to enhance the boundary of light in the core section or any Optical fiber situation. So, there can be possibility of separate three categories of depressed-assisted profiles: solid-trench-assisted type, with a variety of choices ([21] and [22]), random-void-assisted type [17], and hole-assisted type [23] step-index structures type.

Although solid-trench-assisted were developed designs and showcase manufacturing coherence, random-void-assisted, substituting the trench in the cladding by a ring of voids around the core part of the Optical Fiber, it shows the favorable outcomes but raises concerns about splicing technique, connectorization technique, operation homogeneity, and physical strength conditions. Similar conditions apply to the last phase, therefore called hole-assisted designs, called the initial phases

Table 1 Key features of G.675A and G.675B optical fibers

Parameters	G.675A		G.675B		
MFD 1310 nm					
Nominal range	8.3–9.5 μm		6.3–9.5 μm		
Tolerance	$\pm 0.4 \mu\text{m}$		$\pm 0.4 \mu\text{m}$		
Macro bending loss					
Radius (mm)	15	10	15	10	7.5
Number of turns	10	1	10	1	1
Max. at 1550 nm (dB)	0.25	0.75	0.03	0.1	0.5
Max. at 1625 nm (dB)	1.0	1.5	0.1	0.2	1.0
Main transmission attributes (PMD/Chrom. Dispersion)	As per G.652D		TBD		

Table 2 Fiber name, specified wavelength, applications

Fiber name	Other names	Mode	Specified wavelength (nm)	Applications
G.651	micron graded-index fiber	Multimode	850	LAN, MAN, access network
G.652	Zero-Dispersion/non-dispersion-shifted fiber, or standard SMF	Single mode	1310, <1550 (highly dispersive)	LAN, MAN, access network, and CWDM transmission
G.653	Dispersion-Shifted optical fiber	Single mode	1310, >1550 (ZERO dispersion)	Long-haul signal-mode transmission system using erbium-doped fiber amplifiers (EDFA)
G.654	Cut-off shifted optical fiber	Single mode	1550	Submarine systems and backhaul systems
G.655	The non-zero dispersion-shifted optical fiber (NZDSF)	Single mode	1550–1625	Long-Haul systems employing Dense WDM (DWDM) transmission
G.656	Non-Zero dispersion for wideband optical Transport fiber	Single mode	1460–1625	Long-haul systems that use CWDM and DWDM transmission over the specified wavelength range
G.657	Bending loss insensitive optical fiber for access networks	Single mode	1260–1625	Fiber-to-the-home networks. (FTTH)

of advancement, and similar foremost production features such as costs, splicing, connectorization, and physical strength have been studied thoroughly.

6.1 Trench-Aided Optical Fiber Projects

As stated in previous sections, the trench-aided solutions [24, 25] (Fig. 8) contain a standard step-index core with a cladding that comprises a compressed layer (known as a “trench”). In Fig. 9: the effect of the trench on the extension of the optical field is quite absent from the core part, but it contributes to the overall structure as it approaches the core part. Altering the essential -mode tail only limits the Optical Fiber internal mode and confines the bending loss without changing the central mode, which is its MFD and its chromatic distribution. Therefore, the previous trade among bend loss and The MAC value is enhanced because of this trench solution.

Fig. 8 Graphics of trench-assisted profile cross-portions

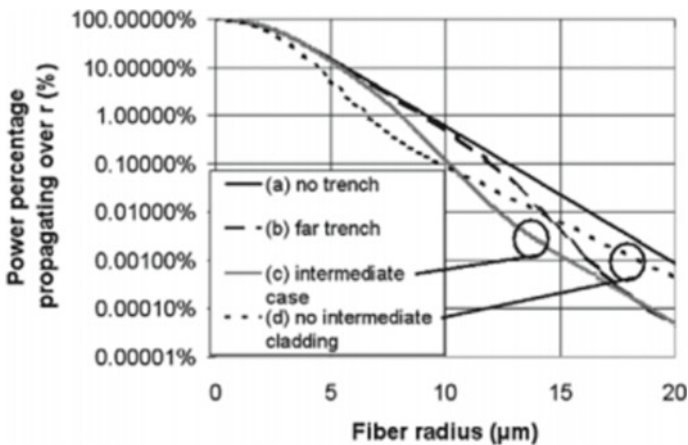
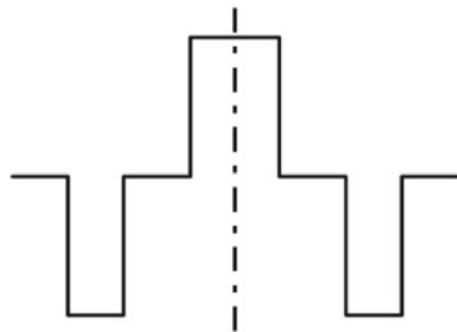


Fig. 9 Calculations of the optical field for various trench-assisted refractive index outlines

Optical Fibers that fully comply with the recommendations of G.657A and B are indicated by the type of structure, show a less bending loss, and G.652 criterion features [26]. The trench part promotes micro bending sensitivity, which is supplemented enhanced when using reduced primary coating modulus. On the other part, this has reduced sensitivity to micro bending losses that showcased new ways for a novel, reduced, and stronger Optical Fibers for applications in homes and businesses [27].

They also, provide better performances at lower temperatures, e.g. up to $-61\text{ }^{\circ}\text{C}$ as stated in [16]. It's been proved that trench-aided Optical Fibers provide advanced security in excessive power purposes fluctuating from 1360 to 1625 nm in the application of tight bending of Optical Fiber [28].

The hazard of degradation occurs when power loss at the bend is attracted by the coating and the temperature surpasses $\sim 84\text{ }^{\circ}\text{C}$. Now using an established power of 2.5 W and bending 4 mm radius, a standard trench-aided optical fiber shows a temperature of $30\text{ }^{\circ}\text{C}$ compared to a standard G652 step-index optical fiber extends to a temperature of about $150\text{ }^{\circ}\text{C}$. The trench-assisted optical fiber is appreciated to endure 1 W at 1625 nm at the bend as low as 3 mm and the orientation point of the G652 step-index is regulated to a 10 mm radius.

The above observations showed trench notably develops an efficiency of optical fiber bending. These enhancements can be achieved by ensuring full backward usage with the later generation of step-index optical fiber. Joining splicing among these two kinds of optical fiber provides the same functioning as the combination of the previous joint between the normal step-index optical fibers [29].

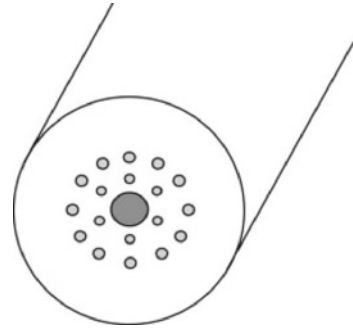
6.2 Hole-Aided Optical Fiber Projects

Hole-aided optical fibers (HAF) have a center core part, its refractive index alteration being very near to regular single-mode optical fiber (SMF), is enclosed by a minor number of air hole rings as stated in Fig. 10. In this design, the holes play as a trench/drain with an inferior refractive index that permits limiting fundamental modes resulting in lesser bending loss.

This kind of optical fiber was developed in the year, 2001 [30]. The authors have suggested surrounding the standard SMF-core with a 6-hole ring, which will further aid the orientation process. By doing so, the alignment will still transpire even if the holes are closed, which is non-existent in the case of silica photonic crystal optical fibers, and which is possible when fusion splicing technique. The low-bending-loss potential of this assembly has also been observed, and the lowest losses ever found with an air holes structure (0.8 dB/km at $1.55\text{ }\mu\text{m}$) have been registered. Optical Fiber has been developed by using pure silica core and F-doped cladding comprising holes.

This part also introduces an improved version of HAF in [31] to bending function, while preserving decent order with SMF. These designs are denser, with two rings

Fig. 10 Cross-section of HA-SMF part. The center dark-gray part shows the core part, GeO₂ doped. The light-gray disks show the air holes, implanted in silica



with six holes and 12 holes correspondingly (same width) around the typical GeO₂-doped core part. Optical fiber having a final diameter of 80 μm to avoid breakouts effectively in the upper bending area. The loss of 1.55 dB reduced to 0.53 dB/km and was additionally enhanced at 0.39 dB/km at [32].

Since then, Nakajima has printed on HAF with diverse design parameters and optical properties. The easy single-ring structure with bend-resistant was seen on [33] while structures with 2-hole rings are explained in and [34], with extensive modeling production in [34]. The [34] assembly has two rings of holes containing diverse diameters on the two foremost rings; however, this fabrication process is more complicated. The 2-hole rings are needed to confirm the low-bending-loss of the basic model and the maximum bending loss of the first high order approach is also caused. [31].

The altered and uncomplicated structure has been suggested in that comprises GeO₂ core doped enclosed by two rings of only three holes. The diameter of the hole differs for each ring. Low losses of 0.27 dB/km at 1.55 μm and very short splice losses of 0.05 dB have been stated. Table 3 shows important features which have been reported earlier. It's well-defined stated from this table that the lowest loss rates have been registered, but optical fibers show the lowest MAC values.

7 Latest Multimodal Optical Fibers

Multimode optical fibers (MMF) are being employed in the domain of datacom (short distances for business networking). These fibers having large core diameter (50 μm or 62.5 μm) that provides greater tolerance to the link between the optical fibers and the sources. The source of optical fiber integration leads to less expensive transfer matching to single-mode optical fiber transmitters (with reduced assembly costs), the requirement for datacom uses with point-to-point construction where (higher cost) of resource is limited to some users only.

Most datacom-based MMF systems have been mounted in the past with a target below 1 Gb/s, using inexpensive and stress-free Light Emitting Diodes (LEDs) have

Table 3 Summary of propagation characteristics for prototype optical fibers published in the literature

Year (λ_0)	Loss 1.55 μm	λ_c	Disp. 1.55 μm	MFD/MAC 1.55 μm	Bend loss $R = 10/7.5/5$ mm 1.55 μm	Splice to SMF
	dB/km	nm	ps/nm/km	μm	dB/m	dB
[2]-2003	0.53	1490		6.9/4.63	- /0.04/0.06	0.13
[3]-2004	0.39	1280	35.7	6.2/4.84	0.003/ ~ 0.007/0.01	0.2
[4]-2003				-	0.001/ - / -	<0.5
[5]-2004 (1300 nm)	0.34	<1310		11.3/ >8.63	- / <0.1 dB/m(1310 nm)/ -	0.2
[6]-2005	2.3	1100	21.8	9.3/8.45	0.032/ - /0.35	0.08
[7]-2004	0.273	1240	26.1	8.67/6.99	0.13/0.45/1.97	0.05

been employed for foundations possessing certain limitations like restricted bandwidth (<1 Gb/s) but large spectral bandwidth which when mixed with chromatic dispersion brings a significant limit of optical fiber transmission volume (bandwidth system). The development of inexpensive, faster 860 nm Vertical Cavity Surface Emitting Lasers (VCSELs), resulting in a small spectral width is an important aspect for gaining high speed. With the introduction of laser-optimized graded-index multimode optical fibers, IEEE equals 1 Gb/s ethernet over 550 m (1000 BASE-SX) in the year, 1998 10 Gb/s ethernet above 300 m was achieved (10GBASE-SX) and in the year 2002, datacom have been used in business networks, especially wireless communications. These distances include many connections to networks stated. The single-mode compared to multimode optical fibers shows several modes, moving through an optical fiber core containing altered velocities that cause differential mode (DMD) delays. These results show a volume limit which is known as intermodal bandwidth that depends upon the conditions for the presentation of multimode optical fiber. Some of the provisions control the quantity of energy transmitted in several modes.

In the year 2002, the construction of the 10 GBASE-SX, the latest 50 μm core diameter multimode optical fibers was launched and designed for laser launch. These optical fibers present significantly enhanced bandwidth and are categorized by DMD. These are designed for a realistic and real-time index formation which leads to differences in modal delays of less than 0.3 ps/m. OM3 is quite a famous dictionary for Optical Fibers.

8 Conclusion

It may be predicted that 5G may replace visible cables. However, given the experience gained by the huge investment needed for the economic implications of the transition

from 2 to 3G and more recently from 3 to 4G, and the fact that the shorter 5G bandwidth has put limits to the continuous investment in optical fibers.

Optical fiber will support and improve high cell density and access points per km. The adoption of 5G with optical networks will empower many upcoming technologies to a new level such as IoT, games, Smart cities, learning devices, visible light communication, and more. Henceforth, 5G comes with a lot of potential and possibilities with its reinforced optical fiber.

References

1. Kao KC, Hockham GA (1966) Dielectric-fibre surface waveguides for optical frequencies. *Proc IEE* 113(7):1151–1158
2. Maurer RD (1973) Glass Optical Fibers for optical communications. *Proc IEEE* 61(4):452–462
3. Optical Fiber expansion and 5G—correlations and synergies “digital networks and mobility” platform, pp.4 (2017)
4. Vissers M (2018) Introduction to mobile-optimized multi-service metro OTN (M-OTN). In: Invited talk in ECOC workshop WS15—technology trends for optical networks towards 2020 and beyond. Rome, Italy
5. Liu X et al. (2019) Enabling technologies for 5G-oriented optical networks. In: Optical fiber communication conference (OFC), Invited paper Tu2B.4
6. China Mobile Research Institute (2013) C-RAN: the road towards green RAN. Whitepaper v. 2.6, Sep 2013
7. Sauer M, Kobayakov A, George J (2007) Radio over optical fiber for pico cellular network architectures. *IEEE J Lightwave Technol* 25(11):3301–3320
8. Sauer M, Kobayakov A, Fields L, Annunziata F, Hurley J, George J (2006) Experimental investigation of multimode optical fiber bandwidth requirements for 5.2 GHz WLAN signal transmission. In: 2006 optical fiber communications conference (OFC), paper JThB27
9. De la Oliva A, Hernandez JA, Larrabeiti D, Azcorra A (2016) An overview of the CPRI specification and its application to C-RAN-based LTE scenarios. *IEEE Commun Mag* 54(2):152–159
10. 3GPP TR 38.801, Study on new radio access technology: radio access architecture and interfaces, V14.0.0 (2017-03). 3GPP TR 38.816, Study on CU-DU lower layer split for NR, V15.0.0 (2017-12)
11. Nouchi P, de Montmorillon L-A, Sillard P, Bertaina A, Guenot P (2003) Optical optical fiber design for wavelength-multiplexed transmission. *C R Phys* 4:29–39
12. ITU-T Recommendation G655 (2006)
13. ITU-T Recommendation G656 (2007)
14. ITU-T Recommendation G657 (2006)
15. ITU-T Recommendation G652 (2005)
16. Sakabe I, Ishikawa H, Tanji H, Terasawa Y, Ueda T, Ito M (2004) Enhanced bending loss insensitive optical fiber and new cables for CWDM access networks. In: Proceedings of the 53rd international wire and cable symposium, pp 112
17. Ieda K, Nakajima K, Matsui T, Tsujikawa K, Shibata T, Ikeda S, Tomita S, Sankawa I, Haibara T (2005) Transmission characteristics of a hole-assisted optical fiber cord for flexible optical wiring. In: Proceedings of the 54th international wire and cable symposium, p 63
18. Matthijsse P, de Montmorillon LA, Krabshuis GJ, Gooijer F (2005) Bend-optimized G652 compatible single mode optical fibers. In: Proceedings of the 54th international wire and cable symposium, p 327
19. Kuyt G et al. (2007) The impact of new bend-insensitive single-mode optical fibers on FTTH connectivity and cable designs. In: Proceeding of 56th IWCS conference, pp 363–371, Nov 2007

20. Li M-J (2008) Ultra-low bending loss single-mode optical fiber for FTTH. In: Proceeding of OFC/NFOEC conference, PDP10, Mar 2008
21. Fini J et al. (2008) Solid low-bend-loss transmission optical fibers using resonant suppression of higher-order modes. In: ECOC'08, paper Mo.4.B. 4
22. Himeno K, Matsuo S, Guan N, Wada A (2005) Low-bending-loss single-mode optical fibers for optical fiber-to-the-home. *IEEE J Lightwave Tech* 23:3494
23. de Montmorillon LA, Matthijsse P, Gooijer F, Achten F, Molin D, Montaigne N, Maury J (2006) Bend-optimized G. 652D compatible trench assisted single mode optical fibers. In: Proceedings of the 55th international wire and cable symposium p 342
24. Kuyt et al. (2007) The impact of new bend-insensitive single-mode optical fibers on FTTH connectivity and cable designs. In: Proceeding of 56th IWCS conference, pp 363–371, Nov 2007
25. Kuyt G, Mathijsse P, Gasca L, de Montmorillon L.-A, Berkers A, Doorn M, Nothofer K, Weiss A (2007) Bend-insensitive single mode optical fibers used in new cable designs. In: Proceedings of optical cabling and infrastructure (OC & I) conference Kista, Sweden
26. Bigot-Astruc M, de Montmorillon L-A, Sillard P (2008) High-power resistance of bend-optimized single-mode optical fibers. In: Proceedings of optical optical fiber communication conference JWA2
27. Provost L, Overton B, Gasca L, Kuyt G (2008) Cabling and installation aspects of full-silica bend-insensitive single-mode fibres. In: Proceedings of optical cabling and infrastructure (OC & I) conference, Krems, Austria
28. Hasegawa T et al. (2001) Novel hole-assisted lightguide optical fiber exhibiting large anomalous dispersion and low loss below 1 dB/km. In: Proceedings of optical optical fiber communication (OFC2001), post-deadline paper PD5, Anaheim, CA, USA
29. Hasegawa T et al. (2003) Bend-insensitive single-mode holey optical fiber with SMF-compatibility for optical wiring applications. In: Proceedings of European conference on optical communications (ECOC2003), paper We2.7.3, Rimini, Italy
30. Nishioka D et al. (2004) Development of holey optical fiber supporting extra-small diameter bending. *SEI Tech Rev* 58:42–47
31. Nakajima K et al (2003) Hole-assisted optical fiber design for small bending and splice loss. *IEEE Photonics Technol Lett* 15(12):1737–1739
32. Tsuchida Y et al (2005) Design and characterization of single-mode holey optical fibers with low bending losses. *Opt Express* 13(12):4470–4479
33. Guan N et al. (2004) Hole-assisted single-mode optical fibers for low bending loss. In: Proceedings of european conference on optical communications (ECOC2004), paper Mo3.3.5, Stockholm, Sweden
34. Miyake K et al. (2004) Bend resistant photonic crystal optical fiber compatible with conventional single mode optical fiber. In: Proceedings of European conference on optical communications (ECOC2004), paper Mo3.3.4, Stockholm, Sweden

Review on the Mechanical Properties and Performance of Permeable Concrete



Priyanka Singh, Tejasvi Bishnoi, Saurav Dixit, Kaushal Kumar, Nikolai Ivanovich Vatin, and Jarnail Singh

Abstract Permeable Concrete (PC) is well known for its ability to allow water to pass through it quickly due to its high void ratio. It acts as a feasible solution in controlling runoff water during rain and hence prevents the clogging of water on the surface of road pavement. Normal concrete which is impermeable does not have such interconnected voids due to which water tends to go straight away to the drainage system. Thus in heavy rainfall, the drainage system fails. PC solves this problem significantly by allowing most of the water pass through it which also helps in groundwater recharge. But due to its high porosity, the mechanical properties of concrete including its compressive strength and fatigue life are reported to be lesser than that of the normal concrete. Clogging is also a problem in PC. So, it is necessary to enhance the compressive strength of concrete which eventually will boost its performance. Therefore, to provide consolidated and precise guidelines, numerous experimental studies were investigated in this study to obtain solutions to avoid confusion. It was found that there are several ways to increase the performance of concrete as; using polymer, maintaining proper w/c ratio, adding 1% Superplasticizer (SP), using single-sized uniform aggregates, and using 0.8% silica fume. Also, clogging can be prevented by providing vertical channels while making PC blocks.

Keywords Compressive strength · Clogging · Ground water recharge · Mechanical properties · Permeable concrete · Runoff water

P. Singh · T. Bishnoi
Department of Civil Engineering, Amity University Noida, Noida, India

S. Dixit (✉) · N. Ivanovich Vatin
Peter the Great St. Petersburg Polytechnic University, Saint Petersburg 195251, Russia
e-mail: sauravarambol@gmail.com; diksit_s@spbstu.ru

N. Ivanovich Vatin
e-mail: vatin@mail.ru

S. Dixit
Division of Research & Innovation Uttarakhand University, Dehradun 248007, India

K. Kumar · J. Singh
School of Engineering and Technology, K.R. Mangalam University, Gurgaon, India

1 Introduction

Permeable concrete; as the name indicates to have a unique property to allow surface water to flow through it and this become possible due to the absence and/or limited presence of fine aggregates in the concrete. The use of single-size coarse aggregate in the concrete mix provides greater void ratio. Hence, higher porosity is achieved in range of 15% to 35%. These voids allow the water to pass through the concrete.

Due to this ability, permeable concrete has always been considered as the best material for constructing pavements that can support the water drainage system of urban areas by handling the stormwater at the time when the water runoff is increased rapidly during heavy rainfalls. The problem of waterlogging has been widely observed in major cities around the world. This waterlogging results in hindering the traffic control as well as the safety [1]. In addition, a lot of water gets wasted which could have been harvested by allowing it to pass through the surface of pavement and resituate it to the groundwater table. Under drainage pipe system can also be provided below the sub-base coarse layer. This water can either be allowed to infiltrate into the soil gradually or can be transported to a targeted water reservoir through this underground pipe water channel. Permeable concrete is considered to be environment friendly as the surface not only permits water to pass through it and reach groundwater table but also reportedly [1–4] possesses air permeability. This property enables it to exchange heat with air along with moisture, which balances surrounding temperature. However, the mechanical properties of permeable concrete are found to be on lower side [5–7] as compared to the conventional concrete. Various experimental studies [6–9] suggested measures to improve its compressive strength and other properties in order to compensate for its performance and make it sustainable hence, feasible material. Preparing a satisfactory permeable concrete requires disciplined water-to-cement w/c ratio, use of certain admixtures into the design mixture and unified selection of coarse aggregate. These factors are further investigated in this study.

2 Materials

Permeable concrete just like normal concrete consists of three main components, i.e. cement, water, and aggregates but unlike normal concrete, it omits the use of fine aggregates so that interconnected voids can be created and required porosity can be achieved. The cement paste is supposed to cover each coarse aggregate completely and form a rigid block of concrete. Due to this, use of same size angular coarse aggregate is suggested in some studies. However, it is obvious that increase in porosity within the concrete eventually can result in showing less strength. Studies suggested [3] this assumption to be true. This concrete is designed to be used in paving driveways, roads or any pathway which clearly indicates that it is only meant to be used in

flatwork applications. So, its responsibility to maintain a significant level of compressive strength increases along with certain other factors as providing satisfactory surface friction and flexural strength. The behavior of this concrete under varied and adverse conditions is also a matter of concern as the fatigue life will be compared directly with normal concrete. While making a pavement these all factors can't be neglected.

Cement: the use of ordinary portland cement (OPC) is recommended for this concrete which in Indian scenario is of grade 43 as per IS 8112. There are several reasons behind suggesting this cement over PPC for constructing a permeable pavement.

1. It has higher water permeability which makes it more favorable
2. Higher strength at initial stage
3. Less final setting time
4. Fineness is less, i.e., 225m²/kg
5. Resistance to sulfates, alkalis, chlorides, and other chemicals.

Aggregates: selection of aggregate is the key factor in making a permeable concrete. We can use any kind of locally available coarse aggregate but it should be well graded and clean. The size of aggregate however depends on the required permeability as larger size coarse aggregate will provide high porosity due to larger voids and smaller size aggregate will give relatively less porosity. It should also be noted that high porosity will give less compressive strength and chances of raveling are more in the pavement. Studies showed [7] that precise aggregate gradation is quite important [8] found dolomite to be the best coarse aggregate among other igneous rock aggregates. As mentioned earlier, pc does not have any fine aggregate but it can be used specifically in low quantity. In some studies, [6] fine sand was added and tested. It was found that adding 5% fine sand of total aggregate weight improved surface friction, stiffness, and tensile strength while compromising significant level of porosity. Use of both angular and round edge coarse aggregate is found to be good for use as the main aim is to achieve required range of void ratio with cement paste covering each aggregate properly.

Water: If the aggregate is damp then comparatively less water is required for concrete mix than if it is fully dry. Finding the correct amount of water to add is the trickiest part in making Permeable Concrete. If we add too much water to the mix then the concrete could lose its impermeability and if added too little, some aggregates could come out loose from the surface of concrete once it has set. The in-situ way to check correct consistency after the mixing of concrete is by squeezing a handful of the concrete mix paste into a ball shape, the ball should hold together and the cement paste should have a shine to it as it indicates the correct amount of water into it, i.e., the paste will shine but is thick enough to stick to itself as shown in Fig. 1.

Investigating a wide range [2–10] of experimental studies it is concluded that the optimum water-to-cement ratio of 0.32–0.35 should be considered. Once required



Fig. 1 Observation of water

w/c ratio is obtained, we can make a larger batch to pour a path, a solid base for a flagstone patio or even an entire driveway.

Superplasticizer: Superplasticizers are water content reducing agents which in many studies [5–10] have been tested under various experimental conditions. Many studies indicated a significant increase in the overall strength of concrete by using superplasticizers in limited dosage. In general, using 1 percent superplasticizer by weight of cement is optimum for permeable concrete design mix. In [5] developed high-performance permeable concrete by using superplasticizer along with thickening agents and uniform-sized aggregates. There is a wide range of superplasticizers in market, and anyone of them can be considered accordingly.

3 Raveling

Sometimes aggregate can come out loose from permeable concrete, this is known as raveling. Raveling doesn't affect the depth of the pavement but only the surface (topmost layer). Evaporation is the main reason for raveling. It is usually most prevalent among the edges and joints of the pavement. If raveling occurs, it begins to show up in few weeks of placement. It can be common with permeable concrete but its extreme raveling can be avoided by stopping evaporation which is the main reason of raveling. Permeable Concrete has always allowed water to pass through it, these voids give the material a large surface area this means the topmost layer of freshly placed pavement has a lot of contact with the air due to which the rate of evaporation increases. Permeable Concrete significantly has different properties and has its own unique timings of placement. In normal concrete excess of water known as “bleed water” slowly rises to the top surface after placement, replacing water on the surface



Fig. 2 Raveling in pavement

that is lost due to evaporation. Permeable Concrete on the other hand doesn't have any excess water to give hence there is no bleeding of water in Permeable Concrete. The amount of water in the mix is narrow as Permeable Concrete basically consists of a thin layer of cement paste coating over each piece of aggregate. Since the cement paste is so thin, the water that evaporates does not get replaced. If the cement coating gets dry after some time due to lack of moisture, the bond between the aggregate and cement paste will be compromised shortly after placing. Hence the bond can fail and rock comes loose Fig. 2.

In this way, too much evaporation can lead to raveling. The rate of evaporation is affected by the surface area, wind, humidity, and temp so it can be disastrous for Permeable Concrete installation. It doesn't take much to exceed the critical point as it is just 5% of the mix water that is evaporated from the surface of Permeable Concrete. It will become noticeably stiffer and may tear down. At this point the Permeable Concrete surface becomes unworkable it becomes harder to blend and do final finish. Permeable Concrete made with small aggregate not only has a larger surface area but it also has thinner coating of cement coating around Fig. 3.

Having the Permeable Concrete in full shade rather than full sun can easily lengthen the working time by a factor of 5 or more. There are some admixtures also to prevent this evaporation so it is very important to keep Permeable Concrete hydrated. Misting fans can be used to humidify the concrete placement but it should be noted that the droplets should be very tiny as big size of water droplets can cause the cement paste to wash off from the surface of aggregate, resulting in raveling. If this happens then the wash-offed spot should be covered with fresh material and refinished it but if the concrete has already begun to set Fig. 4.

It is preferred to make joints using wedges that compact the Permeable Concrete from edges not cut it like other partition forms. The use of wooden floats is prescribed to initially level the concrete which later can be followed by aluminum or magnesium floats for final finish. This should be noted that steel floats are not recommended because it seals up the pores of the concrete surface. In general, the sooner the



Fig. 3 Sun exposure



Fig. 4 Cement coating

compaction is applied the less force needed later to compact and finish. In large applications, spin screeds are often used followed by heavy cross rollers. Equipment like TRAILrider™ Slipform Paver can place and compact the Permeable Concrete for faster installation. Curing process is very important as the water content should be locked in to get it hydrated and cured over the period of days. Plastic cover should be used to cover the pavement which is recommended to be removed after 10 days.

4 Findings Obtained from Previous Studies

Prediction of permeability: The permeability of concrete in a study [12] is predicted by following Katz–Thompson relationship and to model the pore size distribution, Weibull probability distribution function is used. Pore Connectivity Factor is found

to be responsible in maximizing the water transport behavior. Water-to-cement ratio of 0.33 was considered and varied sizes of aggregate were used. It was found that the experimental and predicted permeability were matched. Precise blending and aggregate gradations enhanced the pore phase connectivity and increased the permeability of pervious concretes.

Polymer and admixture modified concrete: Silica fume and superplasticizer were used to enhance pervious concrete strength along with polymer (styrene butadiene rubber) for improving workability, permeability, and strength. In this study [13–18], void ratio is 15–25% and w/c ratio was kept at 0.33–0.30. They used supplementary cementitious (fly ash) material-modified pervious concrete and polymer-modified pervious concrete. It was found that concrete that was polymer modified, has shown higher flexural strength and the flexural to compressive strength was also higher than that of standard concrete. Supplementary permeable concrete and polymer-modified concrete both have shown enhanced fatigue property than conventional permeable concrete but polymer-modified concrete have more fracture toughness than other and have extended resistance to cracking and its propagation.

Optimum mix design: The optimum mix design of permeable concrete was investigated experimentally in a study [19] to achieve maximum compressive strength with good permeability. In this study, igneous rocks were used as coarse aggregate out of which dolomite was found to be the best coarse aggregate among them to make permeable concrete. According to this study, optimum w/c ratio is 0.32 and 0.8% Superplasticizer was used which improved workmanship and the compressive strength extensively. Tests were conducted on uniaxial compressive strength and flexural strength permeability testing ring.

Role of compaction and aggregate: Modification of compaction technique was studied in which the design procedure was investigated by meso and macro scale mechanical testing, computed tomography, microscopy along with X-Ray diffraction. This study [20–24] suggests that coarse aggregate play most important role in creating skeleton structure. Compaction turned out to be important factor in packing particles closely, hence given strength. Meso-scale testing revealed that silica fume enhanced ITZ properties. Quartzite aggregate with calcite thin layers produced the highest value of bonding.

Effective porosity: Relationship between compressive strength and porosity for permeable concrete is determined by a study [10] in 2011 using a mathematical model and then experimental results and derivations were carried out. Griffith's theory was used to develop a new model to determine the credibility of existing equation. The model presented in this paper provides significant predictions of the compressive strength of the porous concrete. The w/c ratio was kept between 0.30–0.38 and cylindrical samples of 100 mm were made. Investigation in this paper revealed that the total porosity predicted had a significant relationship with the measured effective porosity. They obtained low correlation coefficient by deriving exponential function using experimental data. They proposed a new model using Griffith's fracture theory which gave regression statistic R^2 of up to 0.99 showing stronger relationship between the compressive strength and the porosity of permeable concrete which was sampled and tested.

Relationship between porosity and density: The effect of different sized coarse aggregate, w/c ratio, cement content also the relationships between compressive strength, porosity, tensile strength, and permeability of different specimens were investigated in 2013. 24 PCPC (Portland Cement Pervious Concrete) mixes were prepared in this study [12–15]. In order to establish relationships among porosity and density, compressive strength and permeability, permeability and tensile strength, and compressive strength and porosity, the researchers used linear regression relationships. Mechanical properties of all mixtures were measured as per standard of ASTM. The w/c ratio was kept at 0.30, 0.35, and 0.40. Pervious concrete containing one or/and two sizes of aggregate were investigated in absence of any fine aggregate. It was found that hydrological properties of the concrete, i.e., permeability and porosity depend on aggregate size and water permeability will decrease if the density of permeable concrete increases.

Image analysis method: The pore structure including pore area fractions, mean free spacing, pore sizes, 3D pore distribution density, and specific surface area are analyzed [9] using image analysis methods. Researchers determined the compressive stress–strain response of pervious concretes, its relationship with several of the pore structure features and a created a model to predict the stress–strain response. Monte-Carlo simulation is used to estimate the compressive strength sensitivity which is predicted in the statistical model. It was found that pore sizes, their spacing, and distributions affected the compressive response. OPC and limestone aggregates were used in making specimens. The water-cement ratio (w/c) was 0.33 for each mix. Test methods included determination of compressive response and determination of pore structure features. This study suggests that increased compressive strength is obtained by using increasing aggregate sizes for the pervious concrete. Regarding pore structures, increasing pore volume fraction nearly by 10% results in a reducing 50% of the compressive strength.

High-performance permeable concrete: To increase the strength of conventional permeable concrete, high-performance porous concrete (HPPC) was developed in 2012 [6] which established higher strength as compared to the normal or conventional permeable concrete. Uniform-sized coarse aggregate at lower w/c ratio was used and the range of void ratio is from 18 to 25%. HPPC showed enhanced workability than conventional permeable concrete at same void ratio. Vibration for compaction is not required in HPPC and it showed good cohesiveness along with negligible segregation. HPPC contained Superplasticizer and thickening agent.

Addition of fine sand: Compaction energy at different levels provided significant results. In 2015, addition of 5% fine sand (by the total weight of aggregates) into pervious concrete mixtures showed [7] that sand enhanced friction due to the rough cement paste texture while compromising the porosity. In addition, it also improved tensile strength, stiffness, friction of concrete. In this study, w/c ratio was kept between 0.27–0.35 for different samples. Fine sand was used at 5% and 10% and this result was obtained by testing bulk densities of mix, void content of mix, drainability of sample, Stiffness of sample, tensile strength of sample, particle-loss resistance, and surface friction.

Impact of vertical porosity: In order to understand the impact of vertical porosity distribution on the overall permeability of permeable concrete, a study was carried out [11] which tells that it is determined by generating a porosity–permeability relationship of uniformly permeable specimens and then analyzing it with surface compacted permeable concrete specimens. It was found that effective permeability gets affected mostly by minimum permeability. This was concluded by examining the relationship b/w the effective permeability and distribution of permeability of the specimens. The w/c ratio was kept at 0.30 and a/c ratio was kept between 0.25–0.28 for all samples.

Falling-head permeameter was used for all experiments.

Results showed that effective permeability calculated had considerably more relationship with the definite permeability of such specimens and it is suggested to use this method rather than predicting the permeability of samples by using just the average of all porosities.

5 Future Scope

There was a time when Permeable Concrete use to get neglected due to its questionable strength but now we have many experimental studies that have shown this assumption to be false. There are various techniques to improve the compressive strength and other mechanical properties of the Permeable Concrete. The future scope of Permeable Concrete is quite potential in areas with heavy rainfall and also it has proven its efficiency in the traffic management by providing effective drainage to the rainwater. As an emerging construction technology, Permeable Concrete have vivid scope of advancements too. Exploring this technology will definitely help the future construction practices.

6 Conclusion

Permeable Concrete has proved its feasibility and performed well under various test conditions. In this study, a wide range of such experimental investigations were analyzed, and on the basis of which it is found that using 1% Superplasticizer and 5% silica fume along with small aggregate significantly enhanced the compressive strength of permeable concrete. However, excessive amount of silica fume does not improve strength. Also, water/cement ratio, aggregate/cement ratio, and size of aggregate have shown significant impact on the permeability as well as strength of permeable concrete. The optimum water-to-cement ratio in order to achieve maximum strength and permeability was found in range of 0.30–0.35. Use of uniform size aggregate has improved the overall strength of permeable concrete even more. When aggregate to cement ratio is kept low, permeable concrete showed great strength,

but the permeability coefficient is insignificant. It is found that the abrasion resistance, as well as corrosion resistance of modified permeable concrete, is better than that of regular permeable concrete. Polymer-modified Permeable Concrete (PPC) indicated corrosion resistance of sulfate than corrosion resistance on chloride and has higher flexural-compressive strength than standard permeable concrete having same porosity. Compaction has also been an important factor and adding 5% of fine sand improved surface friction which is beneficial for pavements. It was also observed that fatigue life of permeable concrete considerably depends on the level of stress and flexural stiffness when compared to frequency of repetition of load cycle. Vertical porosity distribution study suggests that minimum permeability had the largest impact over the effective permeability. Hence, Permeable Concrete is undoubtedly a sustainable type of concrete having satisfactory performance under various test conditions. Mechanical properties of standard permeable concrete are good but it can be improved further by introducing some modifications. This makes Permeable Concrete a great option to choose while making pavement in areas that are prone to high rain exposure too.

References

1. Kia A, Wong HS, Cheeseman CR (2017) Development of clogging resistant permeable concrete
2. Kia A, Wong HS, Cheeseman CR (2017) Control of clogging in conventional permeable concrete and development of a new high strength clogging resistant permeable concrete pavement
3. Lian C, Zhuge Y (2010) Optimum mix design of enhanced permeable concrete—an experimental investigation
4. Agar-Ozbek AS, Weerheijm J, Schlangen E, Van Breugel K (2013) Investigating porous concrete with improved strength: testing at different scales
5. Aamer Rafique Bhutta M, Tsuruta K, Mirza J (2012) Evaluation of high-performance porous concrete properties
6. Bonicelli A, Giustozzi F, Crispino M (2015) Experimental study on the effects of fine sand addition on differentially compacted pervious concrete
7. Chindaprasir P, Hatanaka S, Chareerat T, Mishima N, Yuasa c Y (2008) Cement paste characteristics and porous concrete properties
8. Neithalath N, Sumanasooriya MS, Deo O (2010) Characterizing pore volume, sizes, and connectivity in pervious concretes for permeability prediction
9. Chen Y, Wang K, Wang X, Zhou W (2013) Strength, fracture and fatigue of pervious concrete
10. Deo O, Neithalath N (2010) Compressive behavior of pervious concretes and a quantification of the influence of random pore structure features
11. Ibrahim A, Mahmoud E, Yamin M, Patibandla VC (2014) Experimental study on Portland cement pervious concrete mechanical and hydrological properties
12. Lian C, Zhuge Y, Beecham S (2011) The relationship between porosity and strength for porous concrete
13. Martin WD, Kaye NB, Putman BJ (2014) Impact of vertical porosity distribution on the permeability of pervious concrete
14. Zhou J, Zheng M, Wang Q, Yang J, Lin T (2016) Flexural fatigue behavior of polymer-modified pervious concrete with single sized aggregates
15. Lucke T, Beecham S (2013) An investigation into the differences in infiltration capacity between porous and permeable concrete pavers installed on sloping sub-catchments

16. Brown RA, Borst M (2014) Evaluation of surface infiltration testing procedures in permeable pavement systems
17. Borgwardt S (2015) Long-term in-situ infiltration performance of permeable concrete block pavement
18. Kia A, Wong HS, Cheeseman CR (2018) Defining clogging potential for permeable concrete
19. Dai S, Wu X, Zhou H, Li W, Jiang X, Liang B (2019) Experimental study on mechanical properties of permeable concrete
20. Xie N, Akin M, Shi X (2019) Permeable concrete pavements: a review of environmental benefits and durability
21. Putman BJ, Neptune AI (2011) Comparison of test specimen preparation techniques for pervious concrete pavements
22. Dixit S, Stefańska A, Musiuk A (2021) Architectural form finding in arboreal supporting structure optimisation. *Ain Shams Eng J* 12(2):2321–2329
23. Dixit S (2021) Impact of management practices on construction productivity in Indian building construction projects: an empirical study. *Organ Technol Manage Constr* 13(1):2383–2390
24. Dixit S (2020) Study of factors affecting the performance of construction projects in AEC industry. *Organ Technol Manage Constr: Int J* 12(1):2275–2282

Effect of Machining Parameters on Surface Roughness and Material Removal Rate in Dry Turning of AISI 1080 Mild Steel Using HSS Tools



Job M. Wambua, Celestine K. Kinyua, Royston K. Mwikathi,
Ayub O. Owino, Martin M. Kirimi, Fredrick M. Mwema, and T. C. Jen

Abstract This study involves the dry turning of mild steel AISI 1080 in the universal lathe machine using high-speed steel (HSS) right-hand cutting tools. The experiments were designed using the Taguchi method and three process parameters, viz., cutting speed, depth of cut, and clearance angle, each with four levels. To obtain the tool angles, the HSS tool blanks were ground to obtain several clearance angles. The design yielded an L9 orthogonal array, which led to nine experimental trials. After the experiments, the samples were investigated for average surface roughness and the material removal rate. The average surface roughness was measured using the T200 handheld surface roughness tester, while the material removal rate was computed from the mass of chips and turning time. The responses were evaluated using the Taguchi analysis and the analysis of variance (ANOVA). From the Taguchi analysis, the signal-to-noise ratios were obtained. From the ratios, the minimum average surface roughness was obtained as $0.906 \mu\text{m}$, as well as the maximum material removal rate of 0.1888 kg/min . These values represented the optimal responses. For the minimum average surface roughness, the optimal parameters were clearance angle of 22.65° , 755 rpm cutting speed and 0.7 mm depth of cut. Consequently, for the maximum material removal rate, the optimal parameters were a clearance angle of 22.65° , a cutting speed of 755 rpm and a depth of cut of 0.5 mm. From the ANOVA, the clearance angle was identified as the most significant factor contributing to surface roughness. Moreover, the depth of cut was identified as the largest contributor to the material removal rate.

J. M. Wambua · C. K. Kinyua · R. K. Mwikathi · A. O. Owino · M. M. Kirimi · F. M. Mwema (✉)
Department of Mechanical Engineering, Dedan Kimathi University of Technology, Private Bag,
Nyeri 10143, Kenya
e-mail: fredrick.mwema@dkut.ac.ke

F. M. Mwema · T. C. Jen
Department of Mechanical Engineering Science, University of Johannesburg, Auckland
Park 524-2006, South Africa

1 Introduction

Turning involves material removal as the tool moves linearly while the work piece rotates. Dry turning process does not utilize cutting fluid, primarily to reduce cost of machining, safety of the operator, and environmental protection [1]. It is environmentally desirable, and it will be well-thought-out as a requirement for manufacturing firms in the near future. This type of machining ensures high quality of products (since the cutting fluid may cause reactions to the surfaces), higher efficiency, increased tool durability, and reliability of the cutting process [2].

Dry turning can be used to achieve suitable surface quality through the selection of the correct cutting parameters, which include high cutting speed and reduced feed rate. This machining method, however, can lead to increased cutting temperatures, which affect the cutting tool life through an increase in the wear factor [3]. Molenda reports that during the turning process, two major factors tend to affect the surface quality of machined components, and which are the feeding rate, and the depth of cutting. The author further explains that in order to obtain the best surface quality, moderate levels of the depth of cut, feeding rate and cutting speed should be adopted, while the worst quality result from very high cutting speeds coupled with low feed rates [4]. From this study, it is quite evident that the turning machining process is regulated by the various machining parameters, the major ones being the rate of feed, the depth of cut, and the cutting speed.

These factors tend to influence the quality and integrity of the machined surface. The knowledge on quality and surface integrity is important in selecting suitable set of machine tool factors for a strategic manufacturing [5]. This paper aims at investigating the impacts of the speed of cut, tool clearance angle, and the cutting depth on the rate of material removal and surface quality in dry turning of AISI 1080 mild steel.

2 Literature Review

Understanding the material removal process of a material is an integral step in the selection of the material for applications as well as for the design process. This allows for in-depth information on the behavior of the surface integrity, tool life, and the accuracy of dimensions in the final machined component. Research on machinability of various materials has shown that various machining parameters like cutting speed, tool angles, geometry, and presence or absence of coolant have an influence on the output parameters such as the quality of surface, the tool wear, power consumption, the rate of material removal, and microstructure of the material. Saglam et al. [6] conducted a study on the evaluation of the impacts of rake angles, the cutting speeds, and the geometry of tools on the shape and wear of the tool tip in a turning machining process. From the study, it was concluded that the rake angle was the largest contributor toward the production of machining forces with a rake angle of

12° being the optimal. They further observed that higher cutting speed increased the cutting temperatures but reduced the cutting forces.

The effects of the machining parameters, as documented in various studies, therefore necessitate the evaluation of the best/optimal machining parameters to feed into the machine tools in order to produce the desired products' quality at the required rate. In their research, Thomas and Beauchamp investigated dry turning and the impacts of the factors on the properties and functionality of the machining tool [7]. The study found out that the depth of cut and the feed rates were the highest determinants of machining forces. In terms of the surface quality, the analysis of variance depicted that the cutting speed has the main effect. Moreover, an increase in the depth of cut increased the tool vibrations, and which was undesirable. To add on that, a study involving the dry machining of Inconel 718 using cemented carbide coated with PVD depicted that machining at low speeds of cut led to an increase in the built up edges (BUEs) which increased the rate of tool wear [8]. Furthermore, Bordin et al. observed that two major factors, that is, the cutting speed and the feed rate influenced the integrity of the surface of alloy Co-Cr-Mo during the dry turning process. As the feed rate increased so did the compressive stresses on the machined samples.

In similar studies, the effects of the nose radius, machining time, and the feeding rate in the dry turning process of coated tungsten carbide inserts were evaluated [9]. Using statistical analysis models, the authors found out that the feeding rate had greater contribution toward the surface roughness in comparison to cutting time and nose radius. Similar investigations have been carried out on other machining operations like milling and drilling. For end milling, high speeds of cut and low feed rates were observed to create better surface finishes in a study conducted by Azmi et al. [10]. In further studies, the end milling process of CFRP aluminum composite laminates depicted the feed rate contributed most to the output parameters. This was probably due to the variation in chip formation mechanisms at different feed rates [11]. During drilling of Inconel 718, similar impacts of the cutting speed as well as the feed rate were observed [12]. It is therefore evident from previous literature that the cutting parameters have a major influence on the quality of machining as well as the quality of the final product.

From literature, it can be concluded that the turning process is majorly affected by various machining parameters which include the cutting speed, the rate of feed and the depths of cutting. In this regard, this study evaluates several turning parameters, that is, the cutting speed, the depth of cut and the clearance angles, and their interaction with the responses, that is, the rate of material removal and the surface roughness, during the machining of mild steel using a high-speed steel right hand cutting tool on a universal lathe machine.

3 Methodology

3.1 Tools

The following tools and machines were adopted in the study.

- Universal lathe machine
- Surface grinder
- HSS right hand cutting tools
- Electronic weighing machine
- TR200 handheld surface roughness tester
- Stopwatch
- Profile projector.

3.2 Material

This study used AISI 1080 mild-steel as the material under machining. This material finds a wide application in areas like forming tools and molding dies. The material also exhibits a higher balance of strength, toughness, and ductility. The chemical and mechanical properties of the material are shown in Tables 1 and 2, respectively. The workpiece was a round bar of 150 mm length and 50 mm diameter.

Table 1 Chemical composition of AISI 1080 mild steel [13]

Element	Content (%)
Carbon, C	0.14–0.20
Iron, Fe	98.81–99.26
Manganese, Mn	0.60–0.90
Phosphorous, P	≤ 0.040
Sulfur, S	≤ 0.050

Table 2 Mechanical properties of AISI 1080 mild steel [13]

Mechanical property	Metric value
Brinell hardness	126
Rockwell hardness	71
Ultimate Tensile strength	440 Mpa
Modulus of elasticity	205Gpa

Table 3 Process parameters

S. No.	Process parameters		
	Cutting speed (rpm)	Depth of cut (mm)	Clearance angle (degrees)
1	300	0.3	22.65
2	460	0.5	29.44
3	755	0.7	31.02

Table 4 Experimental array

Factor	Level		
	1	2	3
Clearance angle (degrees), α	31.02	22.65	29.44
Cutting speed (rpm), v	300	450	755
Depth of cut (mm), d_c	0.3	0.5	0.7

3.3 Selection of Parameters

The turning process was carried out in the Universal lathe machine. The parameters under investigation were cutting speed, depth of cut, and end clearance angle for the cutting tools. The feed rate was kept constant at 0.122 mm/rev. These machining parameters were varied in three levels as shown in Table 3.

The input factors and levels were put into an experimental design using the Taguchi approach. The *L9* orthogonal array for the experiment was developed using the levels given in Table 4.

3.4 Experimental Procedure

The HSS tool blanks were ground into the respective end clearance angles. The workpiece was then clamped into a three-jaw self-centering chuck on the universal lathe machine. Using the parameters dictated in Table 3 and the experiments designed in the Taguchi *L9* orthogonal array in Table 5, the samples were turned in the lathe machine. For each combination run, the material removal rate was determined in kg/min using Eq. 1. The average surface roughness was determined using the TR200 handheld surface roughness tester.

$$MRR = (m/t) \tag{1}$$

where m = mass in kgs

t = time in minutes

Table 5 *L9* Orthogonal array

Run	Factors		
	Clearance angle (degrees)	Cutting speed (rpm)	Depth of cut (mm)
1	31.02	300	0.3
2	31.02	450	0.5
3	31.02	755	0.7
4	22.65	300	0.5
5	22.65	450	0.7
6	22.65	755	0.3
7	29.44	300	0.7
8	29.44	450	0.3
9	29.44	755	0.5

4 Results and Discussion

4.1 Taguchi Design and Analysis

Using the outputs of the *L9* orthogonal array from the Taguchi design, nine machining experiments were run on mild steel using a constant feed rate of 0.122 mm/rev in the universal lathe machine. After the machining, the workpieces were measured for the average surface roughness (μm) and the material removal rate (kg/min). The outputs (responses) are presented in Table 6.

The outputs obtained were analyzed using the Taguchi technique. In the analysis of the average surface roughness, the '*smaller is better*' model was adopted, since

Table 6 Machining outputs

Run	Factors			Responses	
	Clearance angle (degrees)	Cutting speed (rpm)	Depth of cut (mm)	Average surface roughness (μm)	Material removal rate (kg/min)
1	31.02	300	0.3	4.036	0.0549
2	31.02	450	0.5	6.302	0.0561
3	31.02	755	0.7	2.354	0.1092
4	22.65	300	0.5	3.542	0.1460
5	22.65	450	0.7	1.556	0.1643
6	22.65	755	0.3	0.906	0.0410
7	29.44	300	0.7	1.959	0.0636
8	29.44	450	0.3	2.007	0.0190
9	29.44	755	0.5	1.748	0.1885

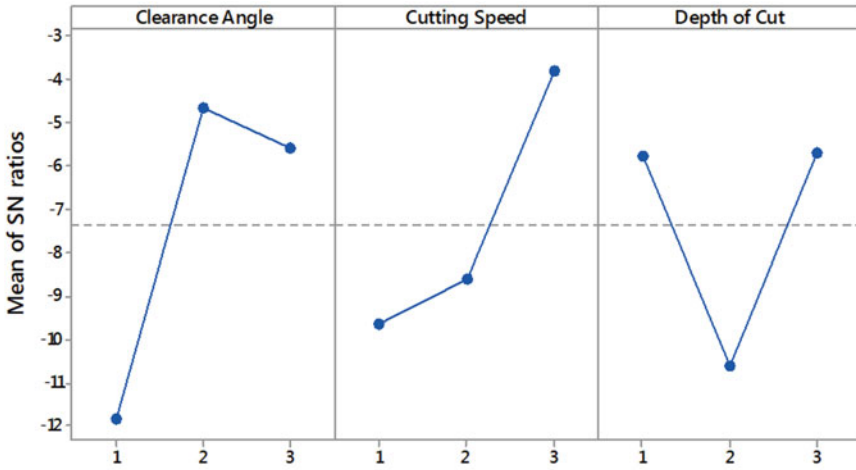
Table 7 S/N ratios of average surface roughness and material removal rate

Run	Factors			Responses		S/N Ratios	
	Clearance angle (degrees)	Cutting speed (rpm)	Depth of cut (mm)	Average surface roughness (μm)	Material removal rate (kg/min)	S/N ratio for average surface roughness	S/N ratio for material removal rate
1	31.02	300	0.3	4.036	0.0549	-12.1190	-25.2086
2	31.02	450	0.5	6.302	0.0561	-15.9896	-25.0207
3	31.02	755	0.7	2.354	0.1092	-7.4361	-19.2355
4	22.65	300	0.5	3.542	0.1460	-10.9850	-16.7129
5	22.65	450	0.7	1.556	0.1643	-3.8402	-15.6872
6	22.65	755	0.3	0.906	0.0410	0.8574	-27.7443
7	29.44	300	0.7	1.959	0.0636	-5.8407	-23.9309
8	29.44	450	0.3	2.007	0.0190	-6.0509	-34.4249
9	29.44	755	0.5	1.748	0.1885	-12.1190	-14.4938

in every product, the goal is normally to reduce the surface roughness to as low as possible. On the other hand, in the analysis of the material removal rate, the goal was to increase productivity to the maximum, and hence the highest material removal rate. In this regard, the *'larger is better'* model was adopted. The analysis conducted yielded the signal-to-noise (S/N) ratios, which are useful elements in arriving at the optimal machining factors for the mild steel. These S/N ratios are presented in Table 7.

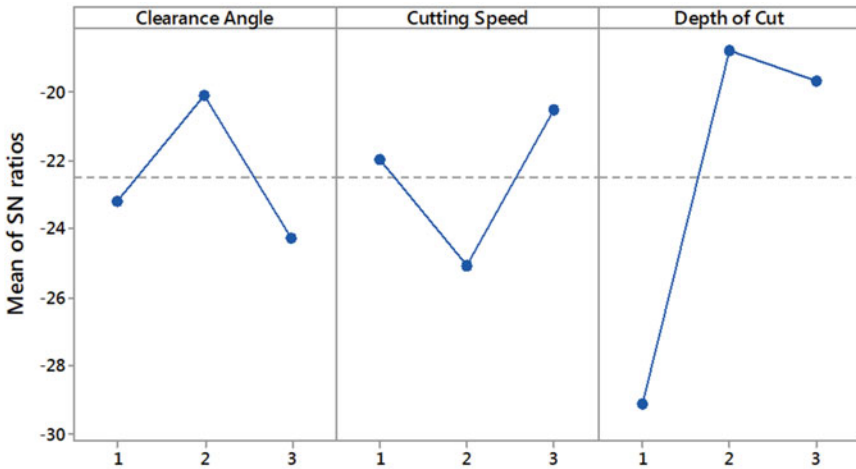
The Taguchi analysis has it that in the minimization of the average surface roughness and maximization of the material removal rate, the signal-to-noise ratios should be the largest/maximum. The signal-to-noise ratios for the minimum average surface roughness was obtained as **0.8574** for an average surface roughness of **0.906 μm** as shown in Table 7. For the maximum material removal rate, the signal-to-noise ratio was obtained as **-14.4938** which corresponded to a material removal rate of **0.1885 kg/min**.

In the determination of the optimum parameters for the turning of AISI 1080 mild steel, that is, for the minimization of the average surface roughness and the maximization of the material removal rate, the S/N ratios are presented in Table 8, and for each output, the highest S/N ratios are bolded. Considering the average surface roughness, the highest values of the signal to noise ratios for the three factors were obtained as -4.656, -3.810, and -5.706 corresponding to 22.65° clearance angle, 755 rpm cutting speed, and 0.7 mm depth of cut, respectively. For the material removal rate, the highest S/N ratios were obtained as -20.05, -20.49, and -18.74, and which corresponded to 22.65° clearance angle, a cutting speed of 755 rpm and a depth of cut 0.5 mm, respectively. The values of the S/N ratios for the two responses are also shown in the mean effect plots, Figs. 1 and 2 (Table 8).



Signal-to-noise: Smaller is better

Fig. 1 Main effect plots for S/N ratios of the average surface roughness



Signal-to-noise: Larger is better

Fig. 2 Main effect plots for S/N ratios of the material removal rate

4.2 Analysis of Variance (ANOVA)

The analysis of variance was conducted using a significance level of 5% (confidence level of 95%) to come up with the significance of clearance angle, cutting speed, and depth of cut to the average surface roughness and the material removal rate.

Table 8 Responses for the S/N ratios of average surface roughness and material removal rate

Level	Average surface roughness (μm)			Material removal rate (kg/min)		
	Clearance angle	Cutting speed	Depth of cut	Clearance angle	Cutting speed	Depth of cut
1	-11.848	-9.648	-5.771	-23.15	-21.95	-29.13
2	-4.656	-8.627	-10.608	-20.05	-25.04	-18.74
3	-5.581	-3.810	-5.706	-24.28	-20.49	-19.62
Delta	7.192	5.838	4.903	4.24	4.55	10.38
Rank	1	2	3	3	2	1

The factor sums of squares, mean of sums, percentage contributions, *F*-values and *p*-values were obtained for each of the response and presented in Table 9.

Considering the average surface roughness, the *p*-values for the clearance angle, the speed of cutting and cutting depth were found to be 0.030, 0.047, and 0.057 respectively. Comparing with the level of significance of 0.05, the *p*-values for the clearance angle and the cutting speed were less. This meant that the contribution of these two factors to surface roughness was significant. This was also confirmed by the percentage contributions. The clearance angle seemed to exhibit the highest contribution to the average surface roughness, with a contribution 45.82%, followed by the cutting speed with a contribution of 29.09%. The S/N ratio analysis depicted that the lowest clearance angle was desired, as well as the highest cutting speed. This could be related to the increase in the cutting capacity of the machining tool, as well

Table 9 ANOVA for average surface roughness and material removal rate

Source	DF	Adj SS	Adj MS	% Contribution	<i>F</i> -Value	<i>P</i> -Value
<i>Average surface roughness</i>						
Clearance angle	2	91.866	45.933	45.82	32.19	0.030
Cutting speed	2	58.334	29.167	29.09	20.44	0.047
Depth of cut	2	47.444	23.722	23.66	16.63	0.057
Residual Error	2	2.853	1.427	1.43		
Total	8	200.497				
<i>Material removal rate</i>						
Clearance angle	2	28.86	14.43	8.49	0.36	0.734
Cutting speed	2	32.43	16.22	9.54	0.41	0.711
Depth of cut	2	198.99	99.49	58.51	2.49	0.286
Residual error	2	79.83	39.91	23.46		
Total	8	340.10				

as the boost in hardness and hence a reduced surface roughness [14]. However, the *p-value* for the depth of cut (0.057) was above the significance level of 0.05, which meant that it was insignificant. It also exhibited the least percentage contribution of 23.66% among the factors.

Conducting an ANOVA for the material removal rate with the same level of significance of 0.05, the *p-values* obtained were 0.734, 0.711 and 0.286 for the clearance angle, cutting speed and depth of cut, respectively. All these *p-values* were above the level of significance, which meant that the factors had an insignificant impact on the rate of material removal. Evaluating the percentage contributions, the depth of cut seemed to contribute the highest with 58.51%, followed by the cutting speed and clearance angle with contributions of 9.54% and 8.49%, respectively. An increase the depth of cut increases the volume of material swept/removed per pass in the turning exercise. Further, increasing the cutting speed also leads to an increase in the material removal rate. This has also been confirmed in other studies [15, 16].

5 Conclusions

From the Taguchi analysis, the following observations can be deduced.

- The minimum average surface roughness of 0.906 μm is obtained when turning at 22.65° clearance angle, 755 rpm cutting speed, and a depth of cut of 0.3 mm.
- The highest material removal rate of 0.1885 kg/min is obtained when turning at 29.44° clearance angle, 755 rpm cutting speed, and depth of cut of 0.5 mm.

From the analysis of variance, the following conclusions can be obtained.

- For the minimum average surface roughness, the optimum mild steel turning parameters on a universal lathe machine should be 22.65° clearance angle, 755 rpm cutting speed, and 0.7 mm depth of cut.
- For the maximum material removal rate, the optimum mild steel turning parameters on a universal lathe machine should be 22.65° clearance angle, 755 rpm cutting speed, and a depth of cut of 0.5 mm.
- The clearance angle turns out to be the most significant factor contributing to surface roughness. The cutting speed comes second and finally the cutting depth.
- The depth of cut contributes the most to the rate of material removal, followed by the cutting speed and lastly the clearance angle.

6 Future Study

It is recommended that a similar study on the dry turning of mild steel be conducted with the investigation of the impacts of the rate of tool wear as well as other machining parameters, such as the cutting zone temperature.

References

1. Sivarajan S, Padmanabhan R (2014) Green machining and forming by the use of surface coated tools. *Procedia Eng.* 97:15–21. <https://doi.org/10.1016/j.proeng.2014.12.219>
2. Gupta N, Singla N, Sabo T, Bathinda I, Kanwal I, Singh J (2014) Analysis of machining properties in dry, near dry & wet machining on EN9 steel. Available. www.ijert.org
3. N. I. Galanis, D. E. Manolakos, and N. M. Vaxevanidis, "Comparison between Dry and Wet Machining of Stainless Steel," in *Proceedings of the 3rd International Conference on Manufacturing Engineering*, 2008, pp. 91–98, doi: 10.1.1.522.9317.
4. Molenda J (2020) The experimental investigation of surface roughness after dry turning of steel S235. *J KONES* 26(4):179–184. <https://doi.org/10.2478/kones-2019-0106>
5. Vaxevanidis NM, Galanis NI, Petropoulos GP, Karalis N, Vasilakakos P, Sideris J (2020) Surface roughness analysis in high speed-dry turning of a tool steel. In *Proceedings of the asme 2020 10th biennial conference on engineering systems design and analysis*, pp 1–7, <https://doi.org/10.1115/ESDA2010-24811>
6. Saglam H, Yaldiz S, Unsacar F (2007) The effect of tool geometry and cutting speed on main cutting force and tool tip temperature. *Mater Des* 28(1):101–111. <https://doi.org/10.1016/j.matdes.2005.05.015>
7. Thomas M, Beauchamp Y (2003) Statistical investigation of modal parameters of cutting tools in dry turning. *Int J Mach Tools Manuf.* [https://doi.org/10.1016/S0890-6955\(03\)00131-7](https://doi.org/10.1016/S0890-6955(03)00131-7)
8. Hao Z, Gao D, Fan Y, Han R (2011) New observations on tool wear mechanism in dry machining Inconel718. *Int J Mach Tools Manuf.* <https://doi.org/10.1016/j.ijmachtools.2011.08.018>
9. Qehaja N, Jakupi K, Bunjaku A, Bruçi M, Osmani H (2015) Effect of machining parameters and machining time on surface roughness in dry turning process. <https://doi.org/10.1016/j.proeng.2015.01.351>
10. Azmi AI, Lin RJT, Bhattacharyya D (2013) Machinability study of glass sss-reinforced polymer composites during end milling. *Int J Adv Manuf Technol.* <https://doi.org/10.1007/s00170-012-4006-6>
11. Nurhaniza M, Ariffin MKAM, Mustapha F, Baharudin BHTHT (2016) Analyzing the effect of machining parameters setting to the surface roughness during end milling of CFRP-aluminium composite laminates. *Int J Manuf Eng.* <https://doi.org/10.1155/2016/4680380>
12. Akhavan Farid A, Sharif S, Namazi H (2009) Effect of machining parameters and cutting edge geometry on surface integrity when drilling and hole making in inconel 718. *SAE Int J Mater Manuf.* <https://doi.org/10.4271/2009-01-1412>
13. Shridhar AS, Tukkar A, Vernekar A, Badderu V, y Patil A, Kotturshettar BB (2019) Modeling and analysis of ATV roll cage. In: Li C, Chandrasekhar U, Onwubolu G (eds) *Advances in engineering design and simulation: select proceedings of NIRC 2018*. Springer Nature, p 345
14. Moneim A (1981) Effect of the clearance angle on the wear of high speed steel tools. *Elsevier Sequoia* 72:1–11. [https://doi.org/10.1016/0043-1648\(81\)90279-9](https://doi.org/10.1016/0043-1648(81)90279-9)
15. Kumar S, Gupta D (2016) To determine the effect of machining parameters on material removal rate of aluminium 6063 using turning on lathe machine. *Int J Multidiscip Curr Res* 4, pp 688–691 Accessed Nov 01 2020. [Online]. Available. <http://ijmcr.com>
16. Shinge AR, Dabade UA (2018) The effect of process parameters on material removal rate and dimensional variation of channel width in micro-milling of aluminium alloy 6063 T6. *Proc Manuf* 20:168–173. <https://doi.org/10.1016/j.promfg.2018.02.024>

Garnet: Structural and Optical Properties



Anu Bala and Suman Rani

Abstract Garnets are seems like good material for solid-state light because of their excellent chemical and physical stability and favorable luminescence properties. These materials emit multicolors (red, blue, and green). They have been recommended optical properties as they have large emission range and have excellent thermal conductivity, high mechanical strength, high-temperature resistance, and radiation resistance. Research had been done for the improvement of luminescence properties with doping at sites A and B in $[A]_3[B]_2[C]_3[O]_{12}$ (Garnet). Garnets included rare-earth series have great luminescence properties and were also very defendable for the amazing down-conversion properties.

Keywords Garnet · Rare earth · Optical · Luminescence

1 Introduction

Garnets have general formula $[A]_3[B]_2[C]_3[O]_{12}$, where A site is occupied by dodecahedral coordination and B site by octahedral coordination and C site by tetrahedron coordinate. Garnet has cubic lattice structure where space A can be occupied by alkali metal, alkali earth metal, and rare-earth metals. They belong to body-centered cubic Ia3d space group. Garnets are seems like good material for solid-state light because of their excellent chemical and physical stability and favorable luminescence properties. These materials emit multicolors (red, blue, and green). Most common garnets like Terbium aluminum garnet (TAG), Yttrium aluminum garnets (YAG), gadolinium gallium garnet (GGG), Europium Gallium Garnet (EGG), etc. have been

A. Bala · S. Rani (✉)

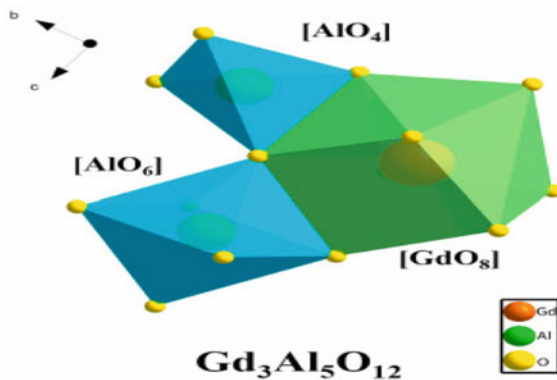
Department of Physics, School of Chemical Engineering and Physical Sciences, Lovely Professional University, Phagwara, Punjab 144411, India

e-mail: Suman.rani@lpu.co.in

recommended optical properties as they have large emission range and has excellent thermal conductivity, high mechanical strength, high-temperature resistance, and radiation resistance. They were well-known garnets to explore their magnetic, optical, electronic, and structural properties. Whenever garnets were doped with transition metals and lanthanides, luminescence properties get enhanced which were beneficial in optoelectronic devices like white light lamps, solid-state laser material, and display devices. Till the date huge research had been done for the improvement of luminescence properties with doping at sites A and B in $[A]_3[B]_2[C]_3[O]_{12}$ Garnet. Garnets included rare-earth series have great luminescence properties and were also very defendable for the amazing down-conversion properties. Most common garnets like yttrium aluminum garnets were studied very far which gave great feasibility to explore other garnets such as gadolinium aluminum garnets (GAG), gadolinium gallium garnets (GGG), etc. [1–6].

In garnets formula placement of Gd^{3+} at sites A and B leads to the formation of stable garnet. At room, temperature GAG has cubic space grouped I a3-d. Doped GAG can transfer charge easily as gadolinium has less electro negativity. By the previous researches concluded that GAG can attain stability around 1573 K, and above this temperature, it may be decomposed into $GdAlO_3$ and Al_2O_3 as shown in Fig. 1. Accordingly, GAG synthesized by Gd^{3+} as a critical element has instability. This is the reason behind the delayed study of GAG. Nowadays, mostly in garnet formula of GAG about 10–15% of doping with some suitable transition metals, lanthanide elements, and with rare-earth ions of less radius (like Lu^{3+} , Y^{3+} , etc.) to stabilize the GAG crystal structure and to decrease the average ion radius of Ln^{3+} . By the addition of dopant, it gives rise to a more effective and efficient red phosphor. The crystal structure of GAG is shown in Fig. 1 [7, 8].

Fig. 1 Crystal structure of GAG



2 Materials and Method

Numbers of method were available to synthesize GAG such as solid-state method, sol-gel method, chemical precipitation method, and combustion method. Research may choose any method according to flexibility of requirement. Among all these methods sol-gel method is highly preferable as it gives homogeneous, less-agglomerated, and précised material. Sol-gel method uses to fabricate the metal oxides and conversion of monomers to the colloidal solution. This method is very useful in formation of powder as well as fibers. The materials that obtain from sol-gel method have good purity, composition, and similar chemical and physical properties as experimental ones. Method includes reaction of hydrolysis of the precursor in the acidic or basic mediums and poly-condensation of the hydrolyzed products. Sol-gel method involves following steps:

- Hydrolysis and poly-condensation
- Chelation and sol-formation
- Gelation
- Drying
- Densification
- Crystallization

Sol-gel method beneficial for the preparation of garnets as

- It is simple, economical, most efficient, and low-cost method,
- Prepare material with uniform composition and highly purity,
- Useful to produce thin coating to ensure adhesion between substrate and top layer as well as can produce thick layer coating to prevent the material from corrosion and
- It has capacity to sinter material at relatively lower temperatures also.

Sol-gel method considered as useful method to synthesize inorganic compounds at low and medium range of temperatures, this method takes up as exclusive to synthesis rear-earth luminescence synthesis due to unbeatable advantages [9, 10].

3 Characterization Analysis of Gadolinium Aluminum Garnet

The properties of the GAG were examined with the combined study of characterization techniques such as: X-Ray diffractometry (XRD), field emission scanning

Electron Microscopy (FE-SEM), transmission electron microscopy (TEM), Photoluminescence (PL) Spectroscopy and Fluorescence decay analysis. Luminescent properties of the GAG were correlated with the processing temperature, particle size of the powder, and mainly with doping contents.

3.1 Gadolinium Aluminum Garnet Doped with Eu³⁺

FT-IR analyzed for GAG:Eu around 400–4000 cm^{-1} and number of peaks for the metal–oxygen bond observed in range 400–700 cm^{-1} and at 1037, 1312, 1399, 1619 and 2154 cm^{-1} aluminum hydroxyl peaks was observed. XRD revealed the crystal phase formation of Eu³⁺ + doped GAG at temperature of 1100 °C and this XRD was indexed with JCPDS that gave confirmation of body-centered cubic structure. In range of 350–700 nm emission spectra were observed which resulted in sharp and intensive peaks around 378–437 nm. The intensity of these peaks reduced with the doping of Eu [11] (Fig. 2).

3.2 Gadolinium Aluminum Garnet Doped with Tb³⁺

XRD studies observed that with the small concentration of Tb in GAG the pure phase of crystal was observed around 1300 °C. This spectrum was indexed with the JCPDS file (1-73-1371) which gave assurance of the formation of stable crystal phase or structure. FE-SEM morphologies of material heat at 1500 °C for few common compositions and observed that particles were roughly agglomerated and composed of very fine primary particles of size about ~40 nm. PLE spectra for GAG:Tb was observed at the emission of 544 nm and found strong bands around 277, weak bands at 227 nm, and 323 nm [12] (Fig. 3).

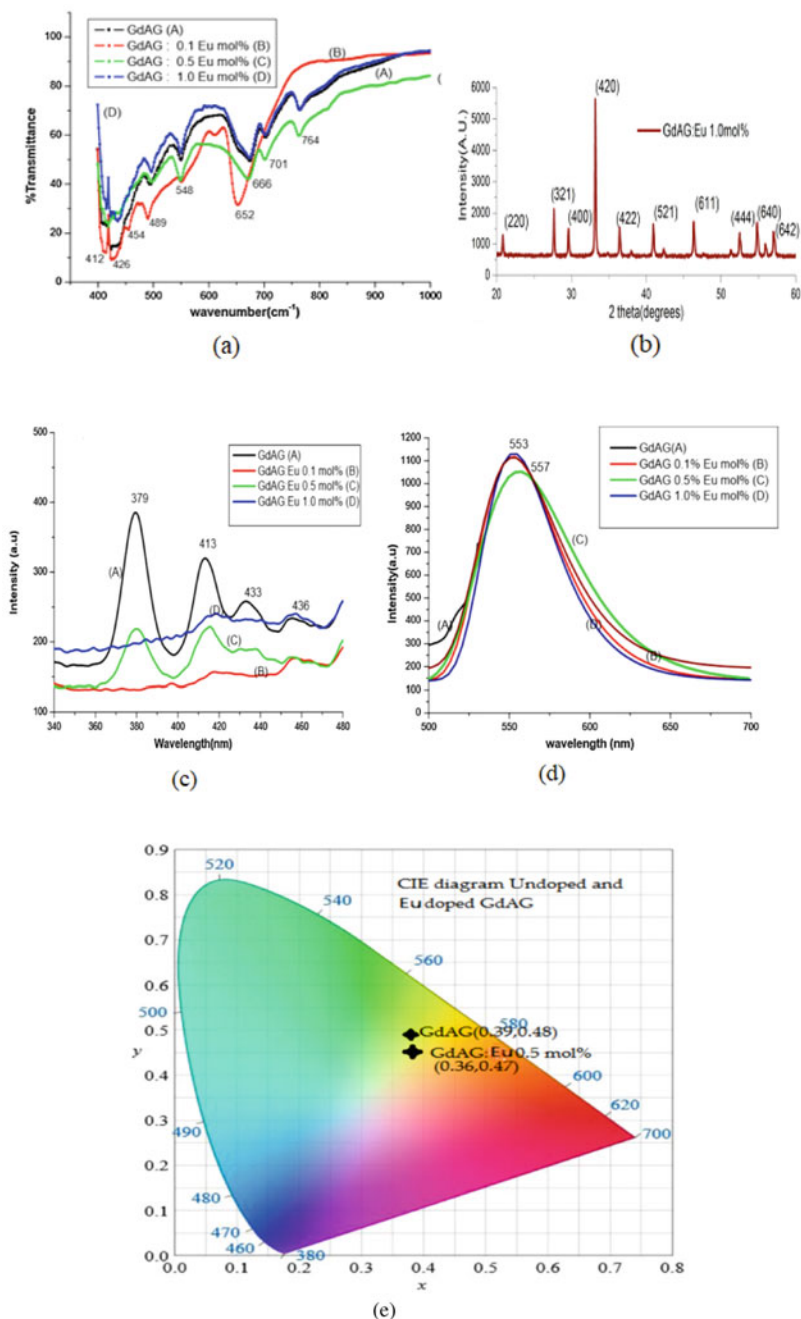


Fig. 2 (a) FT-IR spectra of pure GdAG and Eu^{+3} doped GdAG (b) XRD of GdAG and Eu^{+3} doped GdAG (c) emission spectra in the range of 340-480 nm for pure GdAG and Eu^{+3} doped GdAG (d) emission spectra in the range of 500-700 nm for pure GdAG and Eu^{+3} doped GdAG (e) CIE diagram of pure GdAG and Eu^{+3} doped GdAG with doping concentration of 0.5 mol%

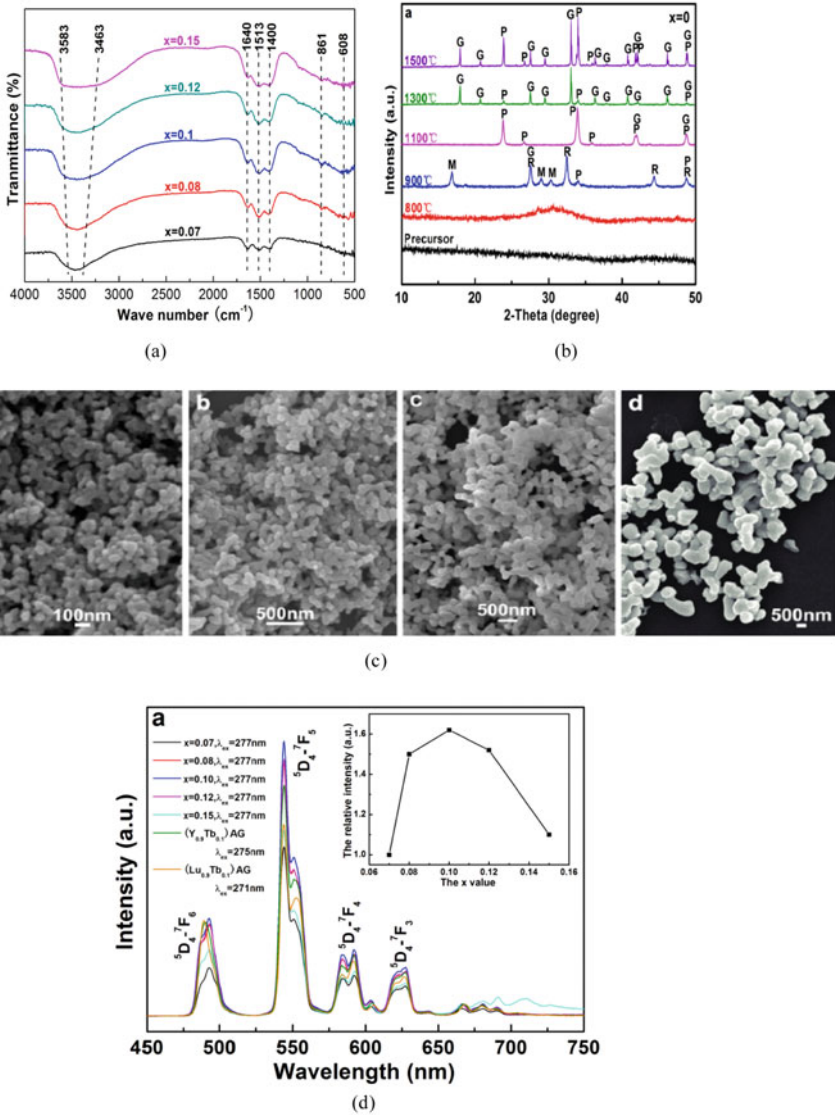


Fig. 3 **a** FT-IR spectroscopy of GdAG doped Ce, **b** X-ray diffraction patterns of GAG:Ce nanoparticles, **c** FE-SEM morphologies of the Gd AG powders calcined at **a** 1000, **b** 1150, **c** 1300 and **d** 1500 and **e** PL emission and excitation spectra of GAG nanoparticles doped with different concentrations of Cerium [13].

4 Conclusion

GAG garnets were studied from their application and found applicable for photo luminescent and scintillation. The material must have high density that can assure high stopping power of x-ray by this it becomes new type of scintillation material. It also found applications in magnetically guided deep PDT as well as efficiency to work in high-energy and high-power solid-state lasers. Along with this, they have wide range of applications in optoelectronic devices.

References

1. Wang X, Wang Y (2015) Synthesis, structure, and photoluminescence properties of Ce³⁺-doped Ca₂YZr₂Al₃O₁₂: a novel garnet phosphor for white LEDs. *J Phys Chem C* 119(28):16208–16214
2. Cheng HJ, Zhou SJ, Peng JX, Kundu A, Li HX, Jin L, Feng XL (2021) Tripartite entanglement in a Laguerre-Gaussian rotational-cavity system with an yttrium iron garnet sphere. *JOSA B* 38(2):285–293
3. Manhas SS, Rehan P, Kaur A, Acharya AD, Sarwan B (2019) Evaluation of optical properties of polypyrrole: polystyrene nanocomposites. In: AIP conference proceedings. vol 2100, no 1. AIP Publishing LLC, p 020037
4. Samra KS, Singh R, Singh L (2018) Copper (50 MeV) and Oxygen (84 MeV) ion irradiation probed thermal, structural and optical behavior of polyethylene terephthalate. *J Macromol Sci, Part B* 57(10):691–698
5. Thakur S, Thakur S, Sharma J, Kumar S (2018) Comparative study of Ni and Cu doped ZnO nanoparticles: Structural and optical properties. In: AIP conference proceedings. vol 1953, no 1. AIP Publishing LLC, p 030218
6. Wang J, Han T, Lang T, Tu M, Peng L (2015) Synthesis and photoluminescence properties of cerium-doped terbium–yttrium aluminum garnet phosphor for white light-emitting diodes applications. *Opt Eng* 54(11):117106
7. Liu G, Wang B, Li J, Cao B, Lu Y, Liu Z (2021) Research progress of gadolinium aluminum garnet based optical materials. *Phys B* 603:412775
8. Li J, Li JG, Zhang Z, Wu X, Liu S, Li X, Sun X, Sakka Y (2012) Effective lattice stabilization of gadolinium aluminate garnet (GdAG) via Lu³⁺ doping and development of highly efficient (Gd, Lu) AG: Eu³⁺ red phosphors. In: Science and technology of advanced materials
9. Yilmaz E, Soylak M (2020) Functionalized nanomaterials for sample preparation methods. In: Handbook of nanomaterials in analytical chemistry, pp 375–413
10. Carter CB, Norton MG (2013). Sols, gels, and organic chemistry. In: Ceramic materials, pp 411–422
11. Kaur J, Rani S, Lal B (2020) Luminescence properties of Eu³⁺ doped gadolinium aluminum garnet phosphors. *Optik* 212:164745
12. Teng X, Li J, Duan G, Liu Z (2016) Development of Tb³⁺ activated gadolinium aluminate garnet (Gd₃Al₅O₁₂) as highly efficient green-emitting phosphors. *J Lumin* 179:165–170
13. Jain A, Koyani R, Muñoz C, Sengar P, Contreras OE, Juárez P, Hirata GA (2018) Magnetic-luminescent cerium-doped gadolinium aluminum garnet nanoparticles for simultaneous imaging and photodynamic therapy of cancer cells. *J Colloid Interface Sci* 526:220–229

Molecular Interaction Study of PEGs in Butyl p-hydroxybenzoate and Methanol Mixtures at 303.15 K and 308.15 K Temperatures Using Acoustic Method



Ashima Prince Kumar and K. C. Juglan

Abstract Acoustic parameters such as acoustic impedance, intermolecular free length, and adiabatic compressibility of polyethylene glycols of molecular weight 200 and 600 in methanol and butyl p-hydroxybenzoate solution were investigated using ultrasonic velocity and density measurements at temperatures $T = 303.15$ K and 308.15 K and experimental pressure $p = 0.1$ MPa. The experimental effects of viscosity were analyzed using Jone–Dole’s equation. The parameters like relaxation time and ultrasonic attenuation have also been computed by using viscosity data. The acoustic parameters adiabatic compressibility and intermolecular free length obey the same pattern as these measured parameters; however, the parameter acoustic impedance follows the opposite trend. In the current scheme under investigation, there are strong interactions between the solute and solvent molecules.

Keywords Acoustic impedance · Intermolecular free length · Methanol · Density · Ultrasonic velocity

1 Introduction

The characteristics of chemical liquid mixture are after influenced by the intermolecular forces. These characteristics include both the physical and chemical characteristics. Rao et al. [1], Deepali et al. [2], Galka et al. [3], Kannappan and Santhi [4], Bolotnikov et al. [5], and Valles et al. [6] found that the study of density and velocity helps in understandings chemical operations, equipment construction, solvent theory, heat transfer, fluid movement, and molecular mechanics. The study of molecular interactions is binary liquid mixture which has been systematically carried out from both theoretical and experimental standpoint. Ali et al. [7] and Marcus [8] suggested

A. P. Kumar (✉)

Department of Physics & Astronomical Sciences, Central University of Jammu, Samba, Jammu and Kashmir, India

e-mail: ashimathakur97@gmail.com

K. C. Juglan

Department of Physics, Lovely Professional University, Phagwara, Punjab 144401, India

e-mail: kc.juglan@lpu.co.in

that most of the manufacturing process is dependent on multi-component liquid mixture because a diverse range of solution is provided by them with right formulation and properties. Tabhane and Patki [9] studied that ultrasonic studies of liquid are relied heavily for the understanding of the nature and strength of molecular interaction. The variation in ultrasonic velocity and related parameter show the intermolecular interactions and structural changes of liquid mixes with weakly interacting and strongly interacting components. Kannappam and Rajendra [10] and Prahraj et al. [11] concluded that the ultrasonic parameter is used to study molecular interactions on a large scale in pure liquids and binary liquid mixtures. Ultrasonic parameter are also used to study ionic interactions in single and mixed salt bio-liquid solutions. The thorough understanding of the physiochemical properties of interacting components in polymer solutions is aided by acoustic studies by Entkatramanan et al. [12]. At a temperature of 303.15 K and 308.15 K, ultrasonic velocity, density, and viscosity measurements of liquids both pure and mixed were carried out to establish various acoustic parameter such as adiabatic compressibility, intermolecular free length, acoustic impedance, ultrasonic attenuation, relaxation time, relative association, and Gibb's free energy. This research aims to look into the molecular relationships in: (1) polyethylene glycols (200 and 600) + (2) butyl paraben (0.01 and 0.05 mol/kg) + (3) methanol (medium) polyethylene glycol (PEG) is a petroleum-derived polyether compound that has a lot of uses in industrial engineering and pharmacy. PEG's structure is defined as $H-(O-CH_2-CH_2)_n-OH$. PEG hydrophilic molecule is used in the passivate microscope glass slides or single molecule Florence experiments to present non-specific protein sticking. PEGs of different molecular weight are used in a wide range of scientific and technological applications. Han et al. [13] and Lorenzo et al. [14] suggested that the parabens are used as preservatives in cosmetics, personal care devices, food meat, and pharmaceuticals. It is so because of the strong antiviral and physiochemical characteristics of parabens. Wang et al. [15] studies show the paraben's poor ergogenic function, which causes endocrine system disruption and adverse effect on human-wildlife. Mizuno et al. [16] found that the methyl parabens which are weak estrogenic agents show stronger efficiency than the other parabens. Colborn et al. [17] shows that the parabens have a negative impact on immunity, development, and reproduction. Kaur et al. [18–21], Chakraborty et al. [22–24], and Thakur et al. [25, 26] have studied the volumetric and acoustic properties of glycols in various organic solvents at different temperatures. Ahmad et al. [27] have done the investigation on thermodynamic and thermoelectric properties of wide band gap semiconductor. Chawla et al [28] have studied the molecular dynamics simulation of carbon nanotube pull-out from polyethylene matrix. Kumara et al [29] have done the physiochemical characterization and release rate studies of solid dispersions of Ketoconazole with Pluronic F127 and PVP K-30. Kumar et al. [30] have studied the interactions of oxidative stress in chronic respiratory diseases: an emerging need for novel drug delivery systems. It is intended to analyze the speed and density of sound findings for PEGs with molecular weight 200 and 600 in butyl paraben methanol solutions at atmospheric pressure and temperature pressure and temperature $T = (303.15 \text{ K and } 308.15 \text{ K})$.

2 Materials and Method

2.1 Chemicals

Loba Chemie Pvt. Ltd., India, provided the chemicals used in the recent work, including polyethylene glycol-200, polyethylene glycol-600, methanol, and butyl paraben. The whole collection of chemicals with a purity of ≥ 0.99 mass fraction is used without filtration as acquired. The chemical (butyl paraben) was vacuum dehydrated and kept in desiccators over P2O5 before use to reduce moisture suction.

2.2 Methodology

The density and ultrasonic speed were determined using an Anton Paar DSA 5000 M density and sound velocity meter, while viscosity was determined using an Oswald viscometer. To investigate the effect of temperature, both viscosity measurements were taken in a water thermostat with an accuracy of ± 0.001 K. Some acoustical characteristics to consider are acoustic impedance, intermolecular free length, adiabatic compressibility, relaxation time, ultrasonic attenuation, Gibb's free energy, and relative association. The formula below is used to calculate the above-mentioned parameters.

2.2.1 Acoustic Impedance

Acoustic impedance is the resistance to the propagation of ultrasonic waves in a medium, and it can be measured as the product of the medium's density (ρ) and the same medium's ultrasonic frequency (U).

$$z = \rho \times U \quad (1)$$

2.2.2 Adiabatic Compressibility

When no heat flows in or out, adiabatic compressibility refers to a fractional decrease in volume per unit rise in strain. This difference is linked to the thermodynamic compressibility in a medium relationship. The ultrasonic velocity (U) and density (ρ) of the medium can also be used to quantify adiabatic compressibility using the equation.

$$\beta = 1/U^2 \times \rho \quad (2)$$

2.2.3 Intermolecular Free Length

Jacobson proposed an analytical relationship for measuring liquid intermolecular free length in 1952. L_f is given by the following sources, according to studies.

$$L_f = K_T \times \beta^{1/2} \quad (3)$$

3 Results and Discussion

The density and sound velocity of ternary mixtures of polyethylene glycols, given as polyethylene glycol-200 and polyethylene glycol-600, in methanol and in (0.01 and 0.05) mol.kg⁻¹ methanol-BuPB solutions at various concentrations and temperatures $T = 303.15$ K and 308.15 K are calculated. The data for density and sound velocity of PEG-200 and PEG-600 in methanol-BuPB is taken from our previous work.

The previous analysis yielded the acoustical velocity and density of BuPB with PEG in methanol medium at 303.15 K and 308.15 K temperatures. Various acoustical parameters such as acoustic impedance, adiabatic compressibility, and intermolecular free length are calculated from the measured parameters.

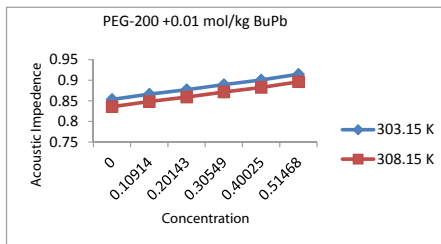
The reflection and propagation of sound waves are affected by the aforementioned major factor in liquid molecules as well as in the medium. The value of acoustic impedance gradually increases with concentration, meaning that the liquid mixtures under investigation have a strong interaction. The magnitude of impedance increases with concentration from PEG-200 to PEG-600, meaning that the molecules in PEG-600 are more intensely interacted than those in PEG-200 (Fig. 1).

With increasing solute concentration and BuPB concentration, the value of adiabatic compressibility decreases. It indicates that the components of the investigated ternary liquid mixes are firmly bonded together. In comparison with PEG-200, it shows that the molecules of PEG-600 are closely bound to each other. As a result, adiabatic compressibility behaves in the opposite direction of ultrasonic speed, proving the formula (Fig. 2).

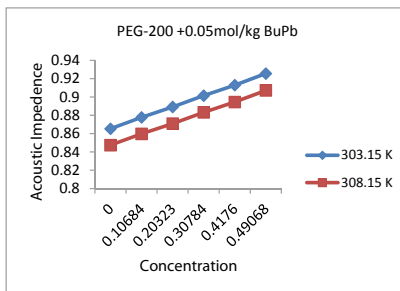
4 Conclusion

The ultrasonic analysis of ternary fluid mixtures of polyethylene glycols in methanol-Butyl paraben predicts the existence of molecular interactions between the molecules of the mixture. Since the intermolecular free length of the mode tested decreases with increasing concentration, the ultrasonic speed increases. Acoustic impedance increases as concentration increases and adiabatic compressibility decreases with increase in concentration. The absence of complex formation in the structure is suggested by the fact that all acoustical parameters differ linearly with concentration.

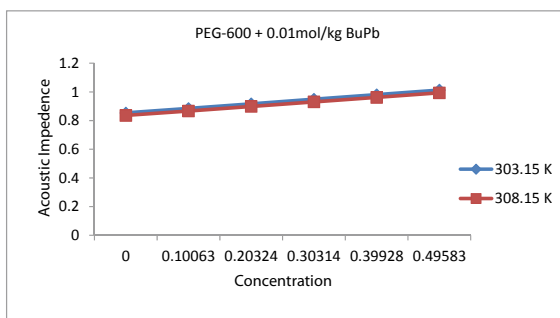
Fig. 1 Representation of acoustic impedance for a ternary mixture of polyethylene glycols in methanol-BuPB at 303.15 K and 308.15 K with different concentrations



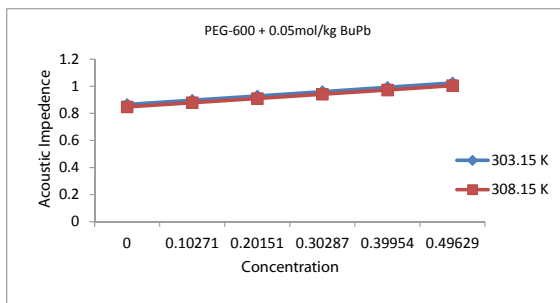
(a)



(b)



(c)



(d)

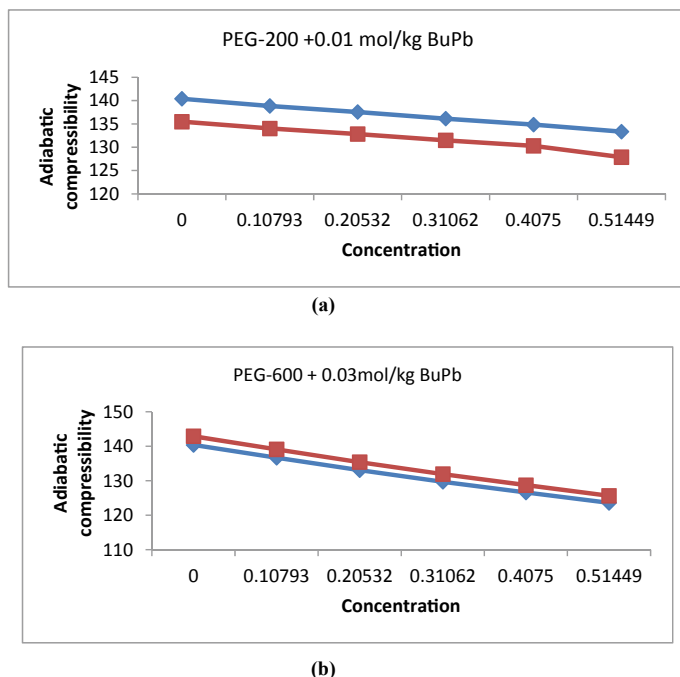


Fig. 2 Representation of adiabatic compressibility for a ternary mixture of polyethylene glycols in methanol-BuPB at 303.15 K and 308.15 K with different concentrations

References

1. Rao JP, Jyothi KKNG, Srinivas G (2017) Ultrasonic studies in binary liquid mixtures of richloroethylene with three alcohols at 303.15 k. *Rasayan J Chem* 10:488–498
2. Deepali P, Gulwade M.L, Narwade and Wadodkar K.N (2012) Ultrasonic behaviour in study of molecular interactions of substituted zole in N, N-diemethyl formide at different temperatures and concentration. *Indian J Chem.*43A:2102–2104
3. Galka J, Suaki L and Tomczy K.P (1997) Temperature dependent acoustical study of thermophysical properties of binary mixtures of diethyl carbonates + 2-methoxyethanol. *J Chem Thermodyn* 9:673
4. Kannappan V, Santhi J (2005) ultrasonic study of induced dipole-dipole interactions in binary liquid mixtures. *Indian J Pure Appl Phys* 43:750–754
5. Bolotnikov MF, Neruchev YA, Melikhov YF, Verveiko VN, Verveiko MV (2005) Temperature dependence of the speed of sound, densities, and isentropic compressibility of hexane+hexadecane in the range of (293.15–373.15) K. *J Chem Eng. Data* 50:1095–1098
6. Valles C, Perez JE, Mainar A.M, Santafe J and Dominguez M (2006) Density and speed of sound measurements of 1-and 2-butanol. *J Chem Eng Data* 51
7. Ali A, Hyde S, Nain AK (2000) Thermo acoustic parameters of tetrabutylammonium borate and perchlorate in non-aqueous solvents. *Indian J Phys* 74B:63–67
8. Marcus Y (1977) *Introduction to Liquid State Chemistry*. Interscience 162
9. Tabhane VA, Patki BA (1985) *Indian J Pure Appl Phys* 2
10. Kannappam AN, Rajendra V (1992) *J Mol Liq* 541:27–31
11. Praharaj MK, Satapathy A, Mishra P, Mishra S (2013) *J Chem bio Phys* 3:2825–2838

12. Entkatramanan KV, himankra OPC, Dudhe CM, Tabhane VA (2012) *Der Chem Sin* 39:44–947
13. Han F, He YZ, Yu CZ (2008) Online pretreatment and determination of parabens in cosmetic products by combination of flow injection analysis, solid phase extraction and micellar electrokinetic chromatography. *Talanta* 74:1371–1377
14. Lorenzo MA, Arribas AS, Moreno M, Bermejo E, Chicharro M, Zapardiel A (2013) Potentiometric determination of salbutamol using carbon paste electrode assisted with multi-walled carbon nanotubes. *Microchemical* 110:510–516
15. Wang J, Zhang D (2010) Chu Q and Ye J : Enhancement of catalytic activity and oxidative ability for graphitic carbon nitride. *Chin J Chem* 28:313–319
16. Mizuno H, Hirai H, Kawai S, Nishida T (2009) Detoxification of aflatoxin, B₁ by manganese peroxides from the white-rotfungus *phanerochaete sordila*. *Biodegradation* 20:533–539
17. Colborn T, vomSaal FS, Soto AM (1993) Development effects of endocrine-disrupting chemicals in wildlife and humans. *Environ Health Perspect* 101:373–384
18. Kaur K, Juglan KC, Kumar H (2017) Acoustic and thermodynamic study of D-Panthenol in aqueous solutions of glycol at different temperatures. *J Chem Thermodyn* 62:3769–3782
19. Kaur K, Behal I, Juglan K.C, Kumar H (2018) Volumetric and ultrasonic studies on interactions of ethylene glycol, diethylene glycol and triethylene glycol in aqueous solutions of glycerol at temperatures (T=293.15K-308.15K). *J Chem Thermodyn* 125:93–106
20. Kaur K, Juglan KC, Kumar H (2018) Temperature dependent physicochemical studies of polyethylene glycols (PEG-400 and PEG-4000) in aqueous sorbitol solutions. *J Mol Liq* 268:700–706
21. Kaur K, Juglan KC (2015) Studies of molecular interaction between binary mixture of chloroform and methanol by using ultrasonic technique. *Der Pharm Chem* 7:160–167
22. Chakraborty N, Kumar H, Kaur K, Juglan K.C (2018) Acoustic and thermodynamic of D-Panthenol in aqueous solutions of glycol at different temperatures. *J Chem Thermodyn* 126:137–146
23. Chakraborty N, Kaur K, Juglan KC, Kumar H (2020) Volumetric and ultrasonic studies on interaction of glycols in aqueous solution of Xylitol at different temperatures. *J Chem Eng Data* 65:1435–1446
24. Chakraborty N, Juglan KC, Kumar H (2021) Volumetric and ultrasonic study of polyethylene glycols in aqueous solutions of niacin at different temperatures. *J Chem Thermodyn* 154:106326
25. Thakur A, Juglan KC, Kumar H, Kaur K (2019) Investigation on molecular interaction of glycols in methanol solution of methylparaben (methyl-p-hydroxybenzoate) at different temperatures through thermo-acoustic analysis. *J Mol Liq* 288:111014
26. Thakur A, Juglan KC, Kumar H, Kaur K (2020) Apparent molar properties of glycols in methanol solutions of propyl-4-hydroxybenzoate (propylparaben) at (T=293.15 to 308.15) K: an acoustic and volumetric approach. *Phys Chem Liq* 58:803–819
27. Ahmad S, Sharma R, Srivastava V, Sakalle U (2019) Investigation on the electronic structure, optical, elastic, mechanical, thermodynamic and thermoelectric properties of wide band gap semiconductor double perovskite Ba₂InTaO₆. *RSC Adv* 9
28. Chawla R, Sharma S (2017) Molecular dynamics simulation of carbon nanotube pull-out from polyethylene matrix. *Compos Sci Technol* 144:169–177
29. Kumara P, Mohanb C, Uma Shankara MKS, Gulatia M (2020) Prediction of the price of Ethereum blockchain cryptocurrency in an industrial finance system. *Comput Electr Eng* 81
30. Kumar V, Kumar V, Upadhyay N, Sharma S (2015) Interactions of atrazine with transition metal ions in aqueous media: experimental and computational approach. *3 Biotech* 5:791–798

Application of Efficient Naturally Occurring Clay Mineral for Fuchsin Basic Dye Removal



Chandra Mohan, Neeraj Kumari, Ruby Jindal, and Rajni Gautam 

Abstract Due to toxic nature of dyes, they are known as objectionable type of pollutant. When dye molecules are present in water bodies, they can cause adverse effect on human being as well as marine species. In present study, adsorption study of triphenylmethane dye, Fuchsin Basic, was done using Montmorillonite (Mt), a naturally occurring clay mineral by varying pH, contact time and initial concentration. The result revealed that 101 mg/g dye was adsorbed at pH 9 within 20 min of contact time. The structural changes of Mt before and after adsorption of dye were studied by XRD and FT-IR techniques.

Keywords Pollutant · Triphenylmethane · Fuchsin Basic · Kinetic · Isotherm

1 Introduction

More than 1,00,000 dyes are commercially available in the markets, and more than 8×10^5 tons of dyes are generated annually. It was estimated that approximately 20% of dye production is discarded directly into the water resources [1]. The dyes like basic, acidic, reactive, direct, disperse and azo dyes are generally used by various industries like textile, paper and printing industries. Out of these dyes, basic dyes (also called cationic dyes) are considered more toxic as they interact with the negatively charged cell membrane. They enter into cell after interacting and concentrate in cytoplasm. The dyes are toxic in nature due to their recalcitrant nature and complex structure due to which they make water bodies inhibitory for aquatic as well as human lives [2]. Most of the dyes are bright colored due to which they can be noticed even when present in very small concentration. Presence of these colored complexes in aquatic resources has a direct impact on photosynthesis phenomenon and disturbs aquatic life, food chain and ecosystem [3].

The techniques used for water treatment are categorized into three categories: chemical, biological and physical methods. Chemical methods include oxidation,

C. Mohan · N. Kumari (✉) · R. Jindal · R. Gautam
School of Basic and Applied Science, K.R. Mangalam University, Gurugram 122103, India
e-mail: yadav.neeraj.1987@gmail.com

coagulation, flocculation, precipitation and irradiation. Although these methods remove the dye effluents completely, there are some disadvantages also: (1) excessive use of chemicals generates secondary pollution problems, (2) these are costly and commercially unattractive and (3) high electrical energy demand. Biological methods include adsorption by microbial biomass, fungal decolorization and bioremediation. Although biological techniques have been proved most economical due to its flexible design and operation, these methods are unsatisfied for removing of color with current conventional biological treatment processes. Membrane filtration and adsorption processes are included mainly in physical treatment. Among these two techniques, adsorption is more superior to remove color compounds because of its simple design, flexible nature and ease operation [4, 5].

There are various types of non-conventional, low-cost adsorbents used for colored effluent removal from water bodies such as clay, coir pith and fly ash. Elimination of dyes using clay minerals like Montmorillonite (Mt) is going to be interested day by day due to low cost, its high sorption potential, wide abundance and high specific surface area [6–8]. Montmorillonite consists of one octahedral sheet sandwiched between two tetrahedral sheets and belongs to 2:1 smectite group of clay. Mt is negatively charged clay mineral which is due to isomorphous substitution of Al^{3+} in place of Si^{4+} in tetrahedral sheet and Mg^{2+} in place of Al^{3+} in octahedral sheet. Negative charge of Mt is balanced through exchangeable inorganic cations (Na^+ , Ca^{2+}) present in Mt interlayer space [9] (Fig. 1).

Fuchsin Basic, a cationic triphenylmethane dye (Fig. 2), is used as colorant in textile industry for dyeing cotton, fibers, papers, etc., and as a staining agent. When someone comes in contact with FB dye by physically, inhalation or ingestion, eye

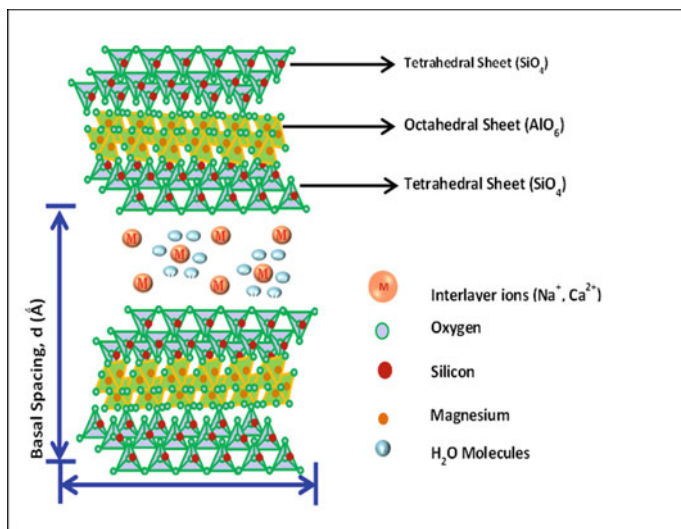
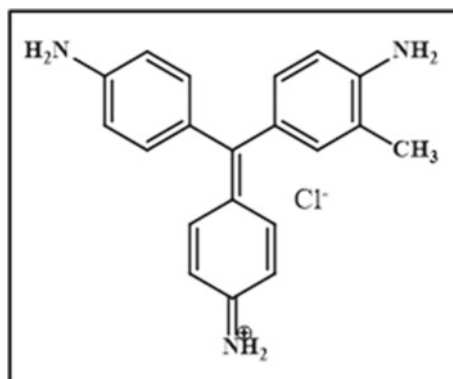


Fig. 1 Structure of Montmorillonite clay

Fig. 2 Structure of Fuchsin Basic dye



and skin irritation, nausea, diarrhea and irritation to respiratory tract can be caused. The exposure of FB dye may also affect nervous system with dizziness, headache and muscle contraction. Thus, keeping all these points in mind, it is essential to develop an effective method for removal of FB dye [10].

The major goal of the present paper is to use the batch extraction method to explore the efficacy of Mt for adsorption of Fuchsin Basic (FB) dye. The influence of pH, contact time and initial dye concentration was also studied in batch method.

2 Materials and Method

2.1 Materials Used

The procurement of Montmorillonite clay mineral was from Sigma Aldrich Chemical Pvt. Ltd., USA. The cationic dye, Fuchsin Basic (C. I. No. = 42,510, M. F. = $C_{20}H_{19}N_3 \cdot HCl$, M. Wt. = 337.85, λ_{max} = 548 nm), was purchased from Fischer Chemie Pvt. Ltd.

2.2 Preparation of Stock Solution of FB Dye

A specified amount of FB dye was dissolved in double distilled water to make the stock solution. The standard solutions of known concentration were prepared on further dilution of stock solution. UV-visible spectrum of FB dye is in Fig. 3 at its original pH (pH 6).

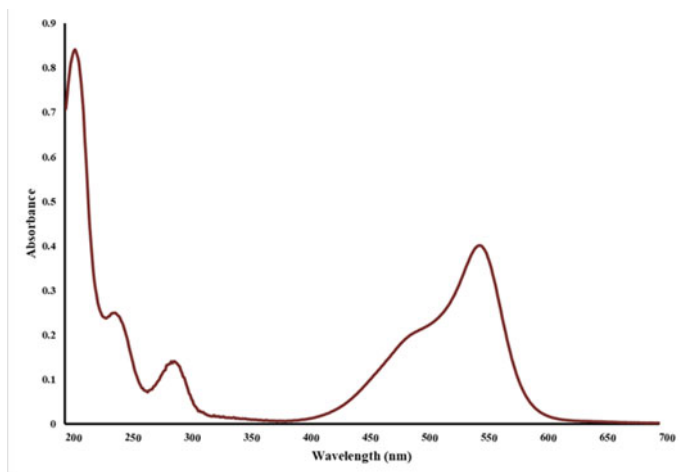


Fig. 3 UV-visible spectra of basic fuchsin dye

2.3 Characterization

X-ray diffraction analysis was performed by Phillip X' Pert—PRO MRD system operating at 2θ value between 2 and 40° . To determine the presence of functional groups in Mt before and after dye adsorption, FT-IR spectrophotometer (PerkinElmer) was used by recording the spectra over wavenumber range $4000\text{--}400\text{ cm}^{-1}$.

2.4 Batch Extraction Studies

The effect of various parameters like pH, contact time and initial concentration was studied using batch extraction studies at room temperature by adding fixed quantity of Mt in 25 ml dye solution by shaking on a mechanical shaker up to a pre-determined time. Further, solution was centrifuged using centrifuge machine (REMI, R-24) to separate the dye solution as supernatant and residue (adsorbent). The uptake of dye onto Mt was calculated at a specific wavelength ($\lambda_{\text{max}} = 548\text{ nm}$) using absorbance, which was used to quantify the concentration of supernatant (C_e). The following formula is used to determine dye adsorbed amount:

$$q_e = \frac{C_i - C_e \times V}{m}$$

where q_e (mg/g) is the dye adsorbed amount,

C_i (mg/L) is the initial concentration of dye solution,

C_e (mg/L) is the dye concentration in solution at equilibrium,

V (L) is the volume, and

m (g) is the adsorbent amount.

3 Result and Discussion

3.1 Influence of Various Parameters on Adsorption Capacity of Mt for FB Dye

3.1.1 Influence of pH on Adsorption of Dye

The capacity of Mt to adsorb dye is influenced by its surface charge which is affected by pH of dye solution. In adsorption process, the pH effect was studied in pH range of 1–10 by keeping amount of concentration and adsorbent dose constant in pre-determined time (Fig. 4).

As the pH increases, the adsorption efficacy of Mt for uptake of FB dye increases. No significant effect of pH of FB dye solution was observed on the adsorption capability of Mt from pH 2 to 10. At pH 9, the maximum uptake of dye was 12.46 mg/g. At low pH, Mt surface is positively charged having H⁺ ions and competes with cationic dye causing decrease in uptake of dye. On increasing pH of dye solution, Mt surface becomes more negative which enhances the positively charged dye due to electrostatic interaction. So, pH 9 was optimum pH for further batch studies.

Fig. 4 pH effect on adsorption capacity of Mt for FB dye

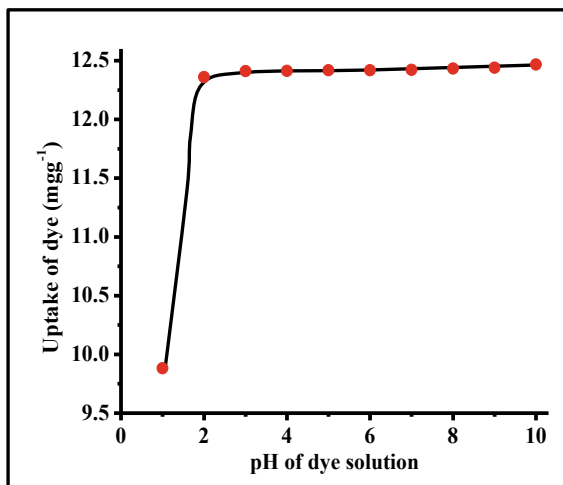
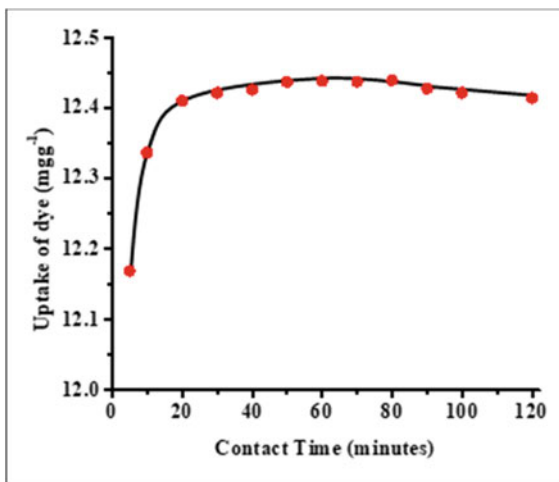


Fig. 5 Contact time effect on adsorption capacity of Mt for FB dye



3.1.2 Effect of Contact Time

Adsorption of FB dye was performed in time range of 5–120 min with fixed concentration of dye solution.

Figure 5 shows that in the initial stage of contact time (5–20 min), the uptake of dye was very fast due to abundant availability of functional sites on Mt surface. The maximum uptake of dye was 12.44 mg/g which was obtained in 80 min. This time is known as equilibrium time, and this stage is known as equilibrium stage. After attaining equilibrium time, the uptake of dye slightly decreases which could be due to the repulsive interaction between dye molecules on adsorbent surface and in bulk phases hinder the empty active sites to be occupied.

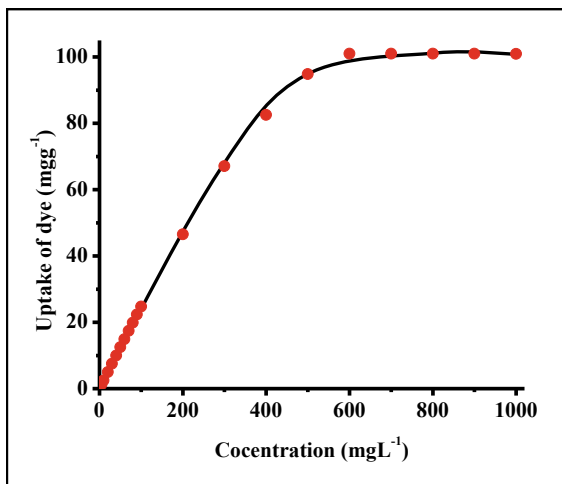
3.1.3 Effect of Initial Dye Concentration

In batch investigation, the adsorption rate of dye is influenced by the transport of molecules of dye into interior sites of adsorbent.

On increasing initial concentration of FB dye solution from 5 mg/L to 600 mg/L, uptake of dye increased from 1.23 mg/g to 101 mg/g, and after that, it decreased slightly (Fig. 6).

This can be explained in terms of active site availability on the adsorbent surface. When dye solution concentration becomes low, ratio of active sites to dye molecules is high. So, dye molecules interact with adsorbent to occupy active sites on adsorbent surface. As the dye solution concentration increases, saturation of active sites is found on Mt surface.

Fig. 6 Initial concentration effect on adsorption capacity of Mt for FB dye



3.2 Characterization of Mt Before and After Dye Adsorption

3.2.1 FT-IR Study

FT-IR spectrum study of naturally occurring Mt and dye-loaded Mt was done from 4000–400 cm^{-1} wavenumber range (Fig. 3). The vibration bands above 3000 cm^{-1} give information about H-O-H stretching of adsorbed water and OH^- stretching of silica present in clay. The vibration band at 1638 cm^{-1} is due to OH^- bending mode of water, band at 1110 cm^{-1} corresponds to Si-O stretching, band at 1038 cm^{-1} denotes to Si-O-Si stretching (siloxane), and the vibration bands at 530 cm^{-1} and 464 cm^{-1} are due to Al-O-Si and Si-O-Si bending vibrations [11].

After adsorption of FB dye, there are two extra vibration bands at 1593 cm^{-1} and 1370 cm^{-1} which are due to C = C stretching vibration of aromatic ring and C-N stretching vibration present in triphenylmethane dye confirms the interaction of FB dye with Mt (Fig. 7).

3.2.2 XRD Analysis

XRD pattern of Mt and dye-loaded Mt is shown in Fig. 8. XRD pattern of Mt revealed a strong diffraction peak of Mt in 001 plane at $2\theta = 6.2^\circ$ representing 14.25 Å basal spacing [9]. But after adsorption of FB dye, there is shifting of diffraction peak toward left, $2\theta = 6.04^\circ$ resulting in increase of basal spacing 14.63 Å. The data suggested the intercalation of FB dye in interlayer of Mt by replacing the interlayer ions and forming a monolayer of dye molecules in Mt interlayer.

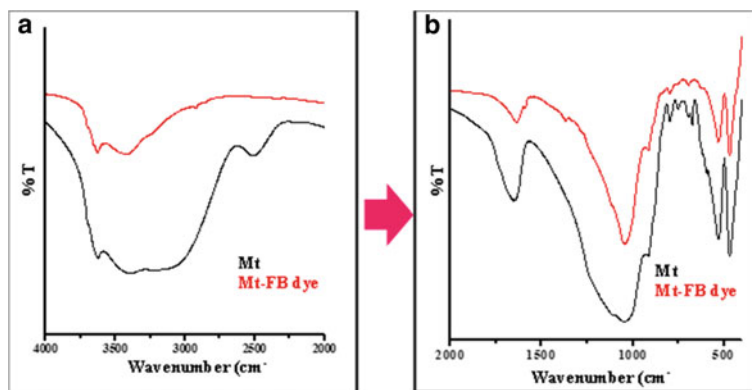


Fig. 7 FT-IR spectra of Mt and dye-loaded Mt

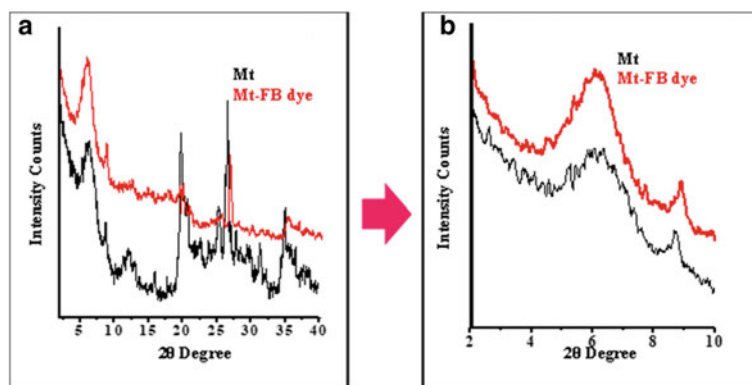


Fig. 8 XRD pattern of Mt and dye adsorbed clay

4 Mechanism of Adsorption of FB Dye onto Mt

Fuchsin Basic is a cationic dye which belongs to triphenylmethane class. FB dye adsorption on Mt surface is through electrostatic interaction, and dye is also found in between interlayer of Mt which is only possible through ion exchange method. The interaction occurs between amine group of FB dye (positively charged) and negative surface of Mt as discussed in earlier section (influence of pH on adsorption efficiency of Mt) (Fig. 9).

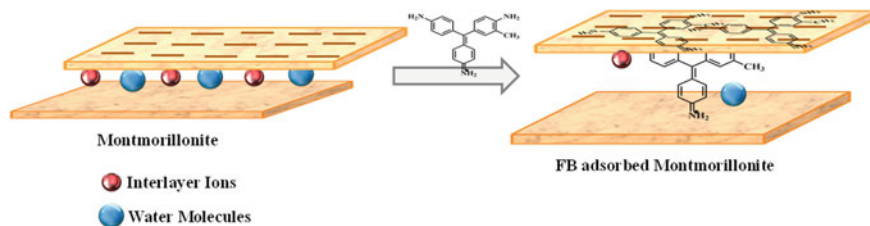


Fig. 9 Diagrammatic representation of adsorption of FB dye onto Mt

5 Conclusion

In present work, the adsorption efficiency of Mt was investigated using batch extraction method as a function of pH, contact time and initial concentration of dye. It was found that maximum uptake of FB dye was 101 mg/g at pH 9 within 80 min. The interaction of FB dyes with Mt onto its surface and also in the interlayer was confirmed by XRD and FT-IR techniques. Based on adsorption study, it can be concluded that Mt can act as efficient adsorbent for Fuchsin Basic dye removal from wastewater.

Acknowledgements The authors wish to express their thanks to K.R. Mangalam University for supporting the research.

References

1. Patil S, Patil J, Patel N (2005) Comparative study of kinetics of removal of fuchsin basic from aqueous solutions using biosorbents. *J Environ Sci Toxicol Food Technol* 9(4):8–20
2. Azarkohan A, Shemirani F, Alvand M (2013) Fast Analysis of water samples for trace amount of crystal violet dye based on solid phase extraction using nanoporous sba-3 prior to determination by fiber optic-linear array detection spectrophotometry. *J Chem* 2013:1–8
3. Fil BA, Ozmetin C, Korkmaz M (2012) Cationic dye (Methylene Blue) removal from aqueous solution by montmorillonite. *Bull Korean Chem Soc* 33:3184–3190
4. Gonawala KH, Mehta MJ (2014) Removal of color from different dye wastewater by using ferric oxide as an adsorbent. *Int J Eng Res Appl* 4(5):102–109
5. Katheresan V, Kansedo J, Lau SY (2018) Efficiency of various recent wastewater dye removal methods: a review. *J Environ Chem Eng* 6(4):4676–4697
6. Sarma GK, Sen GS, Bhattacharyya KG (2019) Removal of hazardous basic dyes from aqueous solution by adsorption onto kaolinite and acid-treated kaolinite: kinetics, isotherm and mechanistic study. *SN Appl Sci* 1:211
7. Bożęcka AM, Orlof-Naturalna MM, Kopec M (2021) Methods of dyes removal from aqueous environment. *J Ecol Eng* 22(9):111–118. <https://doi.org/10.12911/22998993/141368>
8. Sun H, Peng T, Liu B, Xian H (2015) Effects of montmorillonite on phase transition and size of TiO₂ nanoparticles in TiO₂/Montmorillonite nanocomposites. *Appl Clay Sci* 114:440–446
9. Kumari N, Mohan C (2021) Basics of clay minerals and their characteristic properties. *Clay Clay Miner.* <https://doi.org/10.5772/intechopen.97672>

10. El Haddad M (2016) Removal of basic fuchsin dye from water using mussel shell biomass waste as an adsorbent: equilibrium, kinetics, and thermodynamics. *J Taibah Univ Sci* 10(5):664–674
11. Kumari N, Datta M (2016) An integrated approach for the removal of indigo carmine dye from its aqueous solution and the synthesis of nano pigment. *Int J Environ Ecol Family Urban Stud* 6(5):7–16

Prevention of Reversal Blood Flow Phenomenon into Intravenous Line with the Aid of Smart Device



Rajasekar Rathanasamy, Yogeswaran Baskar, Vinith Ravichandran, Rohit Kannan, and Santhosh Sivaraj

Abstract Glucose drips which are also known as dextrose, are widely used in medical sector as an energy supplement. When the glucose drip bottle is emptied and if not detached from the body, blood will start to flow in a reverse direction through the tube and fills the glucose bottle making the condition of the patient worse. The conventional method needs to change the glucose drip bottle once it is emptied with the new one as per requirement. This demands a skilled person for monitoring the patient and dextrose level. This present work aims to analyze the smart device to control the reverse flow of blood from the intravenous line. The device uses the specially designed unidirectional valve, automatic flow limiting valve and storage cylinder to meet the above problems. Static analysis of cylinder and unidirectional valve has been analyzed. Flow analysis of glucose through the unidirectional valve, arresting of blood during the reverse flow has been analyzed through mathematical calculation and simulation.

Keywords Intravenous Line · Reverse flow of blood · Simulation · ANSYS

1 Introduction

The need of glucose drip or dextrose is intensively high in each and every hospital. But monitoring of glucose drip demands a skilled person for individual patients. When the glucose bottle is completely drained and if the glucose drip is not detached from the patient's body then due to pressure difference, blood will start to flow in reverse direction and fills the empty glucose bottle. This cause even death to the victims [1]. In current scenario, a device to deliver the required amount of glucose to the particular patient is not developed naturally. Still conventional method, i.e. changing of glucose bottle in a sequence manner to inject the required amount of glucose, is followed.

R. Rathanasamy (✉) · Y. Baskar · V. Ravichandran · R. Kannan · S. Sivaraj
Department of Mechanical Engineering, Kongu Engineering College, Perundurai,
TamilNadu 638060, India
e-mail: rajasekar.cr@gmail.com

After a comprehensive study of the existing literature, a number of hindrances were identified in automation of glucose drips. Some of the challenges faced during the infusion of dextrose into the veins of human body [2]. Most of the researchers have investigated and developed the device to indicate the level of glucose in the glucose bottle [3, 4]. Literature review reveals that the researchers have carried out most of the work on developing an indicating device and no consideration has been given to automate the glucose drip [5, 6]. However, rarely available literatures help us to study the effect of reverse flow of blood from the intravenous line. No common storage of glucose has been implemented in health centres [7]. Hundreds of people died and ten thousand people were harmed due to reverse flow of blood till 2019.

Various types of analysis should be done for the individual components. The components should be analyzed to whether it can withstand the real-time conditions in hospitals. Flow of glucose and reverse flow of blood in unidirectional valve should be studied [8]. The main objective is to design the smart device to control the reverse flow of blood from the intravenous line and to analyze it. Initially, the components were designed and assembled according to our requirement using Solidworks 2018. After the design, to analyze the device under the working conditions were been carried out using ANSYS2020 R2.

2 Construction and Working of Smart Device for Unidirectional Blood Flow

The reversal flow of blood can be controlled through the designed unidirectional valve. This valve can be fabricated using 3D printing technique. Several parameters were taken into account for the fabrication of smart devices for the prevention of blood flow in the reverse direction. Some of the deciding factors for the device fabrication are economic and technical feasibility. Some of the major parts associated with the assembled device were glucose storage tank, supply pipe, designed unidirectional valve and syringe.

The glucose cylinder was used to store the dextrose solution. The solution comprises of vitamins and vital nutrients as a energy supplement for the human body. In general, the storage cylinder was produced using the HDPE (high-density polyethylene) due to its transparent nature and higher pressure handling ability. They are stronger and stiffer than the polyethylene. HDPE finds its applications in real-time as milk jugs and gallon-sized water bottles. HDPE hold the special character of lesser hazardous toxic which involves them in the medical sector. The main supply tube was designed in such a way that the stored fluid can be transferred to various beds through distribution holes in the main tube. The flow for each subdivided pipe can be regulated using the regulator affixed with it. The transfer pipeline was usually preferred as HDPE for its high chemical resistant and corrosive resistant properties with high strength.

Automatic flow control valve was mostly preferred for the coma patients and bedridden aged persons. It permits the preset quantity of dextrose fluid into the supply line. Beyond the set limit, the fluid flow was indicated through beep alert sound [9]. When the specified amount of glucose is passed, the valve closes automatically and an alert sound beeps out [10]. In addition to the automatic flow control valve, there is a unidirectional valve which was designed through modelling software. The major purpose of the unidirectional valve was to restrict the reverse flow of blood from human body to the glucose bottle through capillary action and pressure head difference [11]. This condition persists for longer period of time, then the blood from the patient comes out without stopping. This further leads to death of the patient. In order to prevent such adverse conditions, the unidirectional valve was used in the passage of dextrose fluid (as in Fig. 1) [12]. The unidirectional valve consists of piston, outer covering, bush and tension spring [13]. Whenever the spring is compressed by fluid flow, the interconnected piston moves upward and makes a pathway for the fluid flow.

On contrary, retraction of spring tends to close the fluid flow path through piston movement. The spring was made of spring steel; meanwhile, the other parts of valve were fabricated by means of ABS through 3D printing technique [14]. The assembled view of the designed and fabricated unidirectional valve was depicted in Fig. 1. The final part of the dextrose transmission was syringe needle, which was penetrated into the nerve of the patient facilitating glucose transfer. The 3D model of device to control the reverse flow of blood from intravenous line is as shown in the following Fig. 2. This 3D model has been drawn using SOLIDWORKS version 2018 software package.

Fig. 1 Designed unidirectional valve

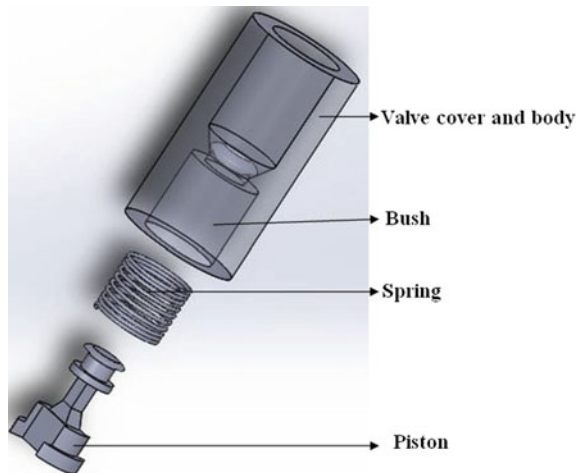
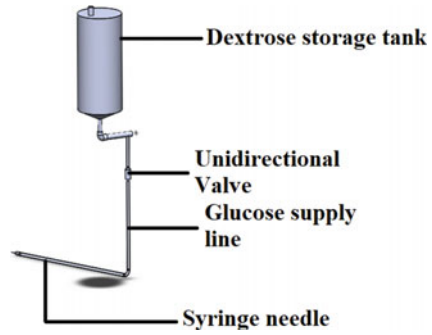


Fig. 2 Assembly of smart device coupled with restriction of blood flow (reverse direction)



3 Results and Discussion

3.1 Design Calculation for Storage Tank

Some of the mathematical calculations for the design, analysis and fabrication of smart devices coupled with restriction of blood flow in reverse direction. Through mathematical calculation, the average capacity of storage tank approximated flow rate, pressure exerted in the dextrose storage tank and stress developed within the thin cylinder were been calculated.

The obtained results were taken into account for the design, analysis and fabrication of the smart device for inhibiting the blood flow. Some of the fundamental specifications of the transparent dextrose storage tank were mentioned in Table 1. Equations 1, 2 and 3 represent the formulae for calculating the pressure inside the cylinder (p) and stress developed in the cylinder (σ).

$$\text{Volume of cylinder} = \pi r^2 h \tag{1}$$

$$\text{Pressure } (P) = \rho gH \tag{2}$$

$$\text{Stress developed in cylinder} = p \times d/4t \tag{3}$$

Table 1 Specifications of storage tank

Height (h)	300 mm
Radius (r)	75 mm
Thickness (t)	3 mm
Minimum height at which cylinder placed (H)	1830 mm
Density of glucose (ρ)	1560 kg/m ³

3.2 Design Calculation for Unidirectional Valve Spring and Supply Tube

The calculated volume, pressure inside the cylinder (p) and stress developed in the cylinder (σ) were found to be $52,987.5 \text{ mm}^3$, $28,005.58 \text{ N/m}^2$ and $353,570.44 \text{ N/m}^2$. Also, the spring inside the unidirectional valve is subjected to design and analysis phase. Some of the specifications for the spring with the view of attaining the better functionality. The total number of turns (n), thickness (t), inner diameter of spring (d), spring constant (K) and tensile spring were found to be 11, 0.50 mm, 9 mm and 25 N/mm, respectively. The force acting on spring, pressure imposed by dextrose fluid, were been evaluated using Eqs. 4, 5, 6 and 7, respectively.

$$\text{Hookes Law } F = K X \quad (4)$$

where,

F —force;

X —deflection of spring.

$$\text{Pressure acting on spring by the dextrose fluid } (P) = \rho g H \quad (5)$$

$$\text{Cross - sectional Area of spring } (A) = \pi r^2 \quad (6)$$

$$\text{Force acting over spring } (F) = P/A \quad (7)$$

From the relation (4),

$$59,459.8 = 25 \times 10^3 \times X$$

$$\text{Deflection } X = 2.3 \text{ mm}$$

From the mathematical calculation, the pressure (P), cross-sectional area(A), force (F) and deflection of spring (X) in unidirectional valve were calculated as 4667.598 N/m^2 , 0.0785 m^2 , $59,459.8 \text{ N}$ and 2.3 mm . Further, the diameter (d) and acceptable velocity (V) of the dextrose supply tube were 5 mm and 0.7 m/s , respectively.

$$\text{Maximum flow rate, } Q = A \times V \quad (8)$$

$$Q = 3.2986 \times 10^{-3} \text{ m}^3/\text{min}$$

3.3 Analysis of Smart Device

The stress and pressure exerted in the HDPE storage tank under static and dynamic conditions were evaluated using simulation software (ANSYS 2020R2). The analysis was performed in ANSYS workbench under static structural category and fluid flow (fluent). The analysis can be categorized into two parts static analysis and flow analysis.

3.4 Static Analysis of Storage Cylinder

Designed glucose storage cylinder is analyzed under static structural category. The geometry of the cylinder is designed using modelling software and meshed using ANSYS. Figure 3 shows the meshing the cylinder component. The main purpose of meshing was to converge the solution at faster rate.

Von-mises stress was the indication of the equivalent stress for the specimen before distortion energy attaining its yield point. The maximum von-Mises stress developed in the glucose storage tank is 58477 Pa. Von-Mises stress analysis of the glucose storage tank is shown in Fig. 4.

The maximum principal stress developed in the storage cylinder is 60741 Pa. The maximum principal stress analysis of the glucose storage tank showed that failure might occur at the apex of the storage tank. Total deformation of storage cylinder

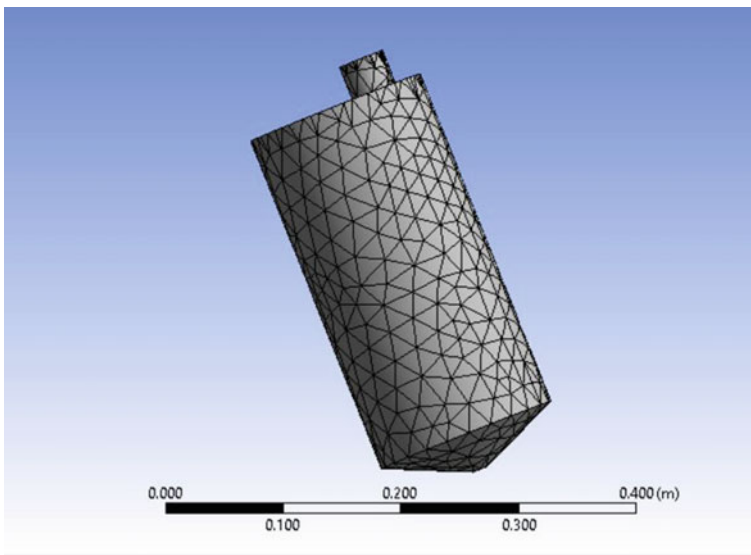


Fig. 3 Meshing of storage cylinder

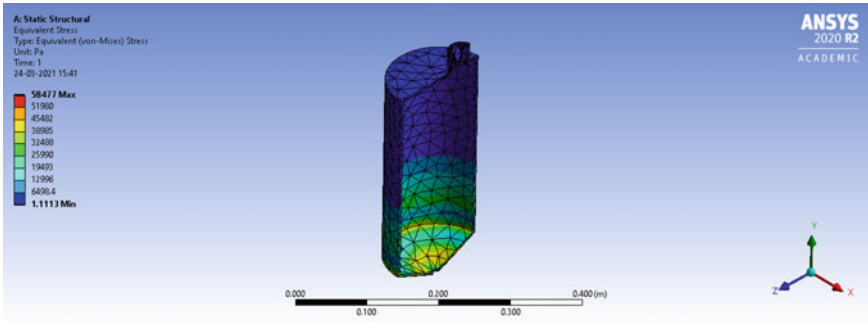


Fig. 4 Von-Mises stress analysis of storage cylinder

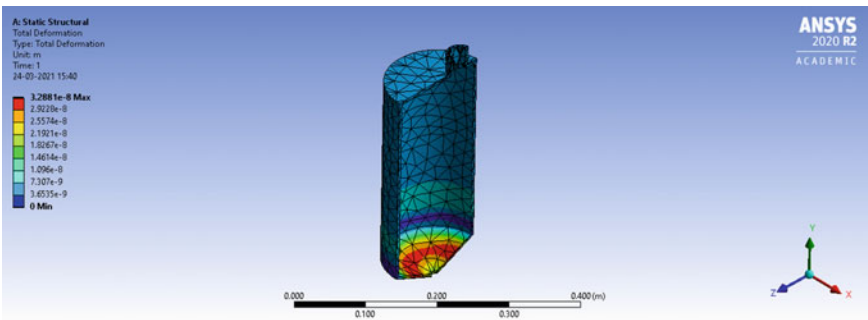


Fig. 5 Total deformation of storage cylinder

is 3.2881×10^{-8} m. The equivalent elastic strain analysis of the glucose storage cylinder is shown in Fig. 5. The maximum calculated deformation for the HDPE material was within the range of its elasticity. Hence, plastic deformation will not occur in most of the cases.

3.5 Unidirectional Valve Analysis

The maximum von-Mises stress developed in the unidirectional valve is 2.4136×10^{-9} MPa. The von-Mises stress analysis of the glucose storage tank is shown in Fig. 6. If the designed valve was able to withstand the specified stress, then the rate of failure occurrence will be very less.

The maximum principal stress developed in the storage cylinder is 2.4457×10^{-9} MPa. Total deformation of storage cylinder is 5.1658×10^{-14} mm. The equivalent elastic strain analysis of the glucose storage cylinder is shown in Fig. 7.

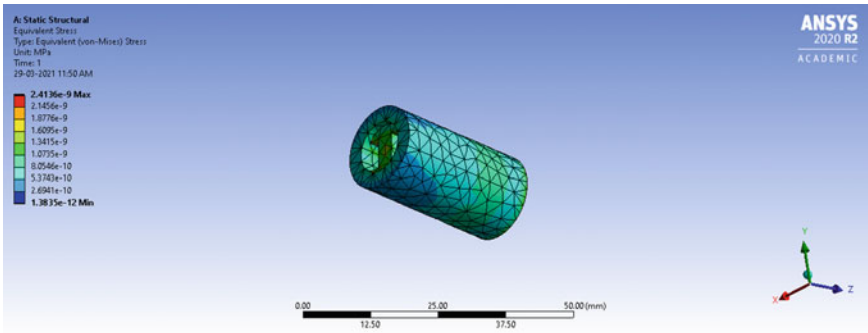


Fig. 6 Von-Mises stress analysis of unidirectional valve

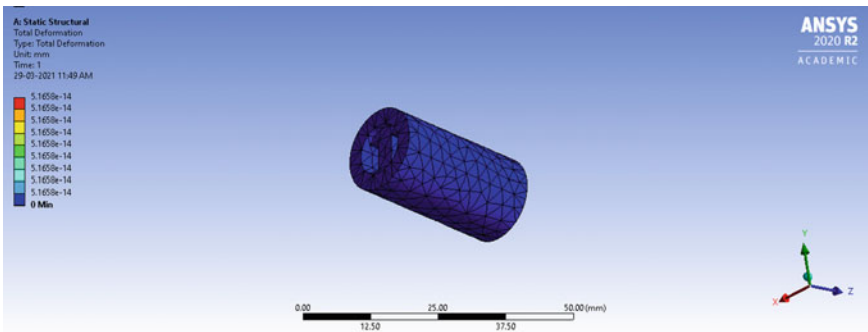


Fig. 7 Total deformation of unidirectional valve

3.6 Fluid Flow Analysis of Unidirectional Valve

However, the design was safe under static conditions, there may be failure due to the fluid flow at nominal velocity. Analysis of glucose flow and blood flow through the unidirectional valve ANSYS fluid flow (fluent) is used. First the volume extraction of flow of glucose through unidirectional valve is executed. Figure 8 depicts the volume extraction of glucose flow.

To visualize the flow of glucose through the unidirectional valve, streamline flow of glucose is generated. Figure 9 represents the streamline flow of glucose through the unidirectional valve.

To analyze the inlet and outlet velocity of glucose through unidirectional valve velocity contour of glucose is generated. To analyze pressure during the glucose flow, pressure contour of glucose flow through unidirectional valve is generated. The maximum pressure generated during the flow is 7.808 Pa. From the pressure contour output, the maximum pressure exerted at the interconnection between the storage tank and the unidirectional valve inlet. Hence, the outer surface needs to be thickened for the unidirectional valve, especially at the interconnection with the

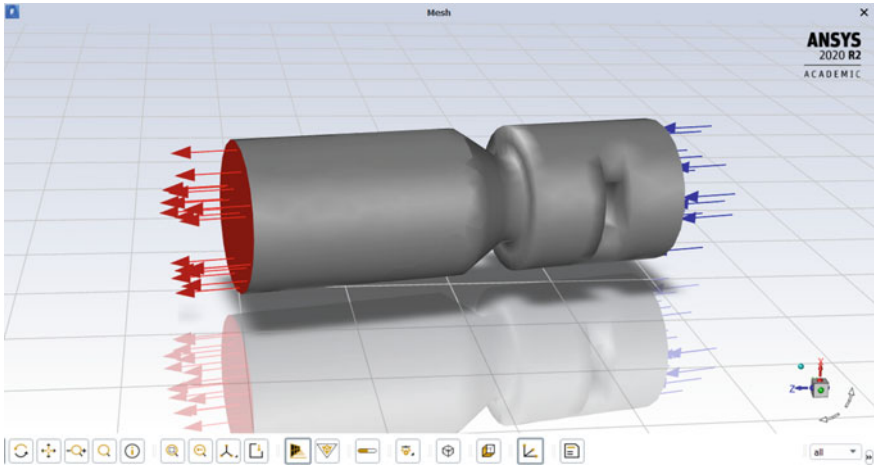


Fig. 8 Volume extraction of glucose flow

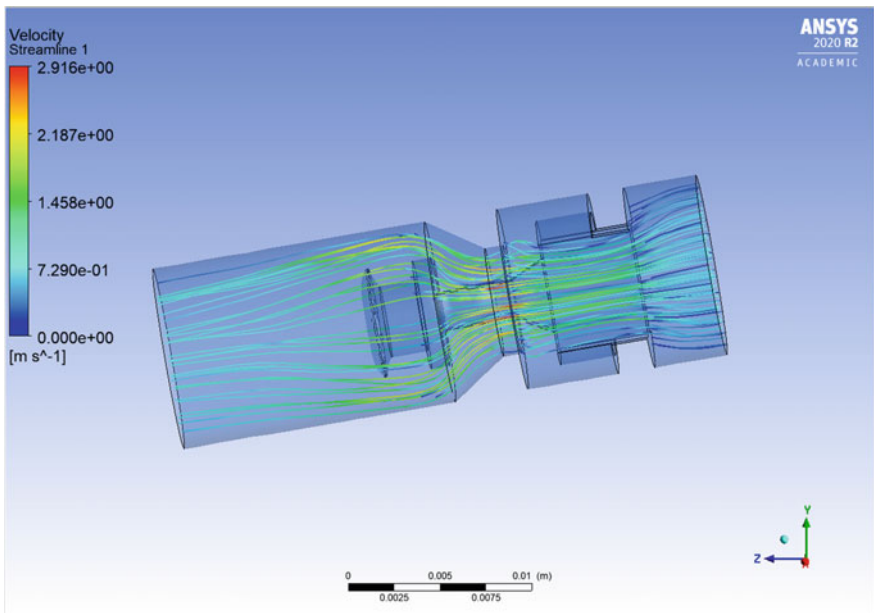


Fig. 9 Streamline flow of glucose

storage tank. The net results obtained from the analysis is given in the below. Table. 2 represents the results for cylinder and unidirectional valve.

Table 2 Consolidated results of cylinder and unidirectional valve analysis

<i>Cylinder</i>	
Max. principal stress	0.60741 MPa
Von-Mises stress	0.58477 MPa
Equivalent elastic strain	2.98×10^{-7}
Total deformation	3.28×10^{-8} m
<i>Unidirectional valve</i>	
Max. principal stress	$24,457 \times 10^{-2}$ Pa
Von-Mises stress	$24,136 \times 10^{-2}$ Pa
Total deformation	5.1658×10^{-11} m

4 Conclusion

The main purpose of the project is to design and analyze the smart device to control the reverse flow of blood from the intravenous line. The device automates the glucose drip in hospitals. In the present practice, for every individual patient, a skilled person is required to monitor the level of glucose and to detach the glucose drip, if it is drained. If the drained glucose bottle is not detached from the patient body, the blood starts to flow in the reverse direction. Also to inject the required amount of glucose, the drained glucose bottle should be changed and been replaced with filled glucose bottle. The smart device sorts out all the above-mentioned issues. The unidirectional valve arrests the reverse flow of blood. The automatic flow control valve allows the required amount of glucose which eliminates the frequent change of glucose bottles. The glucose storage tank act as the reservoir of glucose and so glucose can be supplied to many number of patients based on the requirement. From the derived results, we can conclude that the device can withstand the pressure due to glucose storage and glucose flow and it also accurately arrests the blood during the reverse flow with the automatic cut-off mechanism along with alert sound.

References

1. Dremine V, Kozlov I, Volkov M, Margaryants N, Potemkin A, Zhrebtsov E, Dunaev A, Gurov I (2019) Dynamic evaluation of blood flow microcirculation by combined use of the laser Doppler flowmetry and high-speed videocapillaroscopy methods. *J Biophotonics* 12(6):e201800317
2. De Mul F, Van Spijker J, Van der Plas D, Greve J, Aarnoudse J, Smits T (1984) Mini laser-Doppler (blood) flow monitor with diode laser source and detection integrated in the probe. *Appl Opt* 23(17):2970–2973
3. Rajasekar R, Nayak G, Malas A, Das C (2012) Development of compatibilized SBR and EPR nanocomposites containing dual filler system. *Mater Des* 35:878–885
4. Ayyar M, Mani MP, Jaganathan SK, Rathanasamy R (2018) Preparation, characterization and blood compatibility assessment of a novel electrospun nanocomposite comprising polyurethane and ayurvedic-indhulekha oil for tissue engineering applications. *Biomed Eng/Biomed Tech* 63(3):245–253

5. Jaganathan SK, Mani MP, Ayyar M, Rathanasamy R (2019) Biomimetic electrospun polyurethane matrix composites with tailor made properties for bone tissue engineering scaffolds. *Polymer Testing* 78:105955
6. Nayak GC, Sahoo S, Rajasekar R, Das CK (2012) Novel approach for the selective dispersion of MWCNTs in the Nylon/SAN blend system. *Compos A Appl Sci Manuf* 43(8):1242–1251
7. Gileva K, Gazimagomedova A (2021) Reconstruction of supraorbital region with a pedicled skin flap from periauricular region under reverse blood flow. *Khirurgiia* 8:107–111
8. Nokovitch L, Peyrachon B, Chaux-Bodard A-G, Poupart M, Roux P-E, Devauchelle B, Deneuve S (2021) Reverse blood flow in cervicofacial veins after venous ligations: potential implications in microsurgery. *J Plast Reconstr Aesthet Surg* 74(9):2042–2049
9. Duraikannu J, Jawahar U (2021) Reverse blood flow cause of fatal bleeding in severe atonic post-partum hemorrhage. *Univ J Surg Surg Spec* 7(3)
10. Tennent DJ, Hylden CM, Johnson AE, Burns TC, Wilken JM, Owens JG (2017) Blood flow restriction training after knee arthroscopy: a randomized controlled pilot study. *Clin J Sport Med* 27(3):245–252
11. Chang S-M, Gu Y-D, Li J-F (2003) Comparison of venous drainage in reverse-flow island flaps: an experimental study of the rabbit saphenous fasciocutaneous flap. *Ann Plast Surg* 51(2):177–181
12. Shen X, Schnell S, Barker AJ, Suwa K, Tashakkor L, Jarvis K, Carr JC, Collins JD, Prabhakaran S, Markl M (2018) Voxel-by-voxel 4D flow MRI-based assessment of regional reverse flow in the aorta. *J Mag Reson Imaging* 47(5):1276–1286
13. Wilkins E, Atanasov P (1996) Glucose monitoring: state of the art and future possibilities. *Med Eng Phys* 18(4):273–288
14. Rankouhi B, Javadpour S, Delfanian F, Letcher T (2016) Failure analysis and mechanical characterization of 3D printed ABS with respect to layer thickness and orientation. *J Fail Anal Prev* 16(3):467–481

Thermodynamic and Acoustic Investigation of D-Panthenol in Homologous Series of Polyethylene Glycol at Different Temperatures



Prachi Patnaik, Nabaparna Chakraborty, Parminder Kaur, K. C. Juglan, and Harsh Kumar

Abstract The densities and ultrasonic speed for liquid mixtures comprising homologous series of polyethylene glycol (PEG 200 and PEG 400) in aqueous D-panthenol at (0.0, 0.03, 0.06, and 0.09) mol kg⁻¹ concentration are measured at the variation of temperatures from (293.15 to 308.15) K with Anton Paar DSA 5000 M. Various thermodynamic and acoustic parameters like intermolecular free length, acoustic impedance, adiabatic compressibility, Wada's constant, Rao's constant, and Van der Waal's constant were calculated using experimental data which helped to understand the intermolecular reactions inside the ternary mixture of D-panthenol and PEG 200 and PEG 400.

Keywords D-panthenol · PEG

1 Introduction

The thermodynamic volumetric and acoustic analysis play a crucial role for comparing the macroscopic properties and molecular structure of multicomponent liquid mixtures [1, 2]. The alteration in the molecular interaction arises during the creation of liquid mixtures and difference in component structure packaging becomes superficial. When a hydrogen bond network is developed in any solvents, then properties of the mixture get changed in a specific way [3–5]. The interpretation of combined effect between various compounds mixed in different composition can be contemplated by determining factors like density, velocity, acoustic impedance, intermolecular free length, etc. We can determine the synergy of ternary mixture from these traits on macroscopic scale. The examination of subsequent mixtures concerning molar properties plays a necessary role for understanding the codependency and equation of the given mixture [6–11].

P. Patnaik · N. Chakraborty · P. Kaur · K. C. Juglan (✉)
Department of Physics, Lovely Professional University, Phagwara, Punjab 144401, India
e-mail: kc.juglan@lpu.co.in

H. Kumar
Department of Chemistry, Dr. B R Ambedkar NIT, Jalandhar, Punjab 144 011, India

Chakraborty et al. [12–14] have given the acoustic and volumetric investigation of the ternary mixture of polyethylene glycols with molecular weight 200 and 400 in the aqueous solution of vitamin B₅ (D-panthenol) as the function of temperatures and molality of solute. The apparent molar volume, partial molar volume, and partial molar volume of transfer for PEG 200 and PEG 400 in the aqueous solution of D-panthenol are calculated from density data, as are the apparent molar isentropic compression, partial molar isentropic compression, and partial molar isentropic compression of transfer. The pair and triplet coefficients as functions of temperature are calculated using the partial molar volume of transfer and partial molar isentropic compression of transfer, and the partial molar expansibilities with their first-order derivative are obtained.

Polyethylene glycols are very appropriate for chemical conjugation in biomolecules because they are soluble in different aqueous solutions and organic solvents because of the existing hydrogen–oxygen bond. They are widely used in clinical settings, as a dispersant in toothpaste, plasticizers, industrial sectors, pharmaceuticals, textiles, cosmetics, petrochemicals, and food industries, among other things. As these compounds are widely used and the possibility of these entities being used together is huge, the chemical investigation of their mixture can be very helpful [15–17].

The wide use of polyethylene glycol has led to the wide range of study that has been done on it. Živković, Nikola et al. [18] investigated the densities, viscosities, and refractive indices of binary mixtures with 2-butanol and polyethylene glycols of various molecular weights, tetra ethylene glycol dimethyl ether, or N-methyl-2-pyrrolidone at temperatures ranging from 288.15 to 323.15 K and at atmospheric pressure.

In this paper, using the data from the investigation mentioned above, various acoustic and thermodynamic parameters such as intermolecular free length, acoustic impedance, adiabatic compressibility, Wada's constant, Rao's constant, and Van der Waal's constant are obtained regarding the interaction in the liquid system of D-panthenol (Vitamin B₅) and PEG 200 and PEG 400.

2 Calculations

The next expressions are used for the computation of given parameters [10, 13].

Acoustic impedance (Z)

The acoustic impedance is the product of the velocity of ultrasound in a medium and its density and can be computed by the equation is

$$Z = U\rho$$

where ρ is the density of the solution and U is the ultrasonic velocity of the solution.

Adiabatic compressibility (β)

$$\beta = \frac{1}{U^2 \rho}$$

The variation of acoustic impedance (Z) and adiabatic compressibility (β) is given in Table 1.

Intermolecular free length (L_f)

$$L_f = K_t \sqrt{\beta}$$

K_t is Jacob's constant.

Rao's constant (R)

$$R = \frac{U^{\frac{1}{3}} M}{\rho}$$

M is the molecular mass of D-panthenol.

Wada's constant (W)

$$w = \frac{m_{\text{eff}}}{\rho} \beta^{\frac{1}{3}}$$

where m_{eff} is a molecular weight of the solution.

Vander Waal's constant (b)

$$b = V_m \left[1 - (RT - MU^2) \left\{ \left(1 + \left(\frac{MU^2}{3RT} \right) \right) - 1 \right\} \right]$$

Table 1 gives the variation of values of acoustic impedance and adiabatic compressibility of PEG 200 and PEG 400 in aqueous solution of D-panthenol in a range of temperatures.

The variation of acoustic impedance and adiabatic compressibility is linear, which shows that there is no complex bond formation in ternary mixture. Also, the fashion of their variation is opposite as it should be according to the formulas.

The graphs in Figs. 1, 2, 3, and 4 show the proof of linear and opposite variation of both the entities.

Table 1 Values of acoustic impedance, Z , and adiabatic compressibility, β , of PEG 200 and PEG 400 in aqueous solution of *D*-panthenol at different temperatures

Molality (mol/kg)	$\beta \times 10^{-7} \text{ (Nm}^{-2}\text{)}$							
	293.15 K	298.15 K	303.15 K	308.15 K	298.15 K	303.15 K	308.15 K	293.15 K
<i>PEG 200+0.0 mol kg⁻¹ D-panthenol</i>								
0	1465.505	1491.437	1510.086	1521.213	4.653	4.482	4.359	4.280
0.10009	1480.274	1506.555	1524.777	1533.951	4.574	4.406	4.288	4.222
0.20044	1493.902	1520.346	1537.735	1548.031	4.503	4.339	4.228	4.157
0.30136	1508.36	1534.777	1552.165	1561.66	4.429	4.269	4.162	4.096
0.40026	1521.774	1546.764	1564.216	1574.738	4.363	4.214	4.108	4.039
0.49999	1534.838	1561.135	1579.039	1588.023	4.299	4.147	4.041	3.982
<i>PEG 200+0.03 mol kg⁻¹ D-panthenol</i>								
0.00000	1470.631487	1497.020773	1515.141677	1525.46788	4.626	4.455	4.336	4.261
0.09934	1485.479742	1511.376556	1529.274424	1538.210839	4.547	4.383	4.268	4.203
0.20021	1499.082621	1525.588578	1542.584979	1552.324198	4.477	4.314	4.207	4.139
0.30010	1513.279911	1539.425888	1556.64285	1566.063958	4.405	4.248	4.143	4.078
0.39977	1527.001459	1552.161619	1568.966548	1578.958888	4.338	4.189	4.088	4.022
0.50000	1539.718679	1566.467538	1583.46182	1592.265431	4.277	4.123	4.024	3.965
<i>PEG 200+0.06 mol kg⁻¹ D-panthenol</i>								
0.00000	1476.422	1502.364	1519.872	1532.572	4.595	4.428	4.314	4.242
0.10210	1491.786	1516.627	1534.006	1545.901	4.514	4.358	4.247	4.180
0.20006	1505.133	1530.648	1547.109	1559.134	4.446	4.290	4.187	4.121
0.30009	1519.076	1544.68	1560.791	1572.742	4.377	4.224	4.125	4.060
0.39991	1532.789	1557.585	1573.151	1585.742	4.309	4.164	4.070	4.004

(continued)

Table 1 (continued)

Molality (mol/kg)	Z ($\text{kgm}^{-2} \text{s}^{-1}$)						β 10^{-7} (Nm^{-2})					
	293.15 K	298.15 K	303.15 K	308.15 K	308.15 K	298.15 K	303.15 K	308.15 K	308.15 K	303.15 K	298.15 K	293.15 K
0.50058	1545.322	1571.509	1587.653	1596.516	1596.516	4.250	4.101	4.006	4.006	4.101	3.947	3.947
<i>PEG 200+0.09 mol kg⁻¹ D-panthenol</i>												
0	1481.019	1507.018	1524.104	1533.373	1533.373	4.571	4.406	4.294	4.294	4.406	4.226	4.226
0.10001	1496.023	1520.798	1537.557	1546.577	1546.577	4.493	4.338	4.231	4.231	4.338	4.166	4.166
0.1995	1509.537	1535.052	1550.875	1559.791	1559.791	4.425	4.270	4.170	4.170	4.270	4.107	4.107
0.30007	1523.558	1548.848	1564.65	1573.679	1573.679	4.355	4.205	4.108	4.108	4.205	4.045	4.045
0.40046	1537.404	1561.898	1577.424	1586.886	1586.886	4.287	4.145	4.051	4.051	4.145	3.988	3.988
0.50008	1549.496	1575.53	1591.665	1600.174	1600.174	4.230	4.083	3.988	3.988	4.083	3.932	3.932
<i>PEG 400+0.0 mol kg⁻¹ D-panthenol</i>												
0.00000	1465.505	1491.437	1510.086	1521.213	1521.213	4.653	4.482	4.359	4.359	4.482	4.280	4.280
0.10015	1496.153	1523.057	1540.297	1553.394	1553.394	4.493	4.326	4.217	4.217	4.326	4.131	4.131
0.20004	1525.142	1552.221	1569.71	1583.078	1583.078	4.350	4.190	4.084	4.084	4.190	4.001	4.001
0.29995	1553.921	1580.177	1597.688	1611.345	1611.345	4.213	4.065	3.964	3.964	4.065	3.883	3.883
0.40100	1583.052	1608.676	1626.588	1639.317	1639.317	4.081	3.942	3.844	3.844	3.942	3.771	3.771
0.50006	1612.809	1635.611	1652.302	1665.31	1665.31	3.950	3.831	3.743	3.743	3.831	3.671	3.671
<i>PEG 400+0.03 mol kg⁻¹ D-panthenol</i>												
0	1470.631	1497.021	1515.142	1525.468	1525.468	4.626	4.455	4.336	4.336	4.455	4.261	4.261
0.10141	1501.113	1528.947	1546.271	1558.604	1558.604	4.468	4.298	4.190	4.190	4.298	4.108	4.108
0.20037	1529.953	1557.477	1575.672	1588.187	1588.187	4.326	4.166	4.058	4.058	4.166	3.980	3.980

(continued)

Table 1 (continued)

Molality (mol/kg)	Z (kgm ⁻² s ⁻¹)						β 10 ⁻⁷ (Nm ⁻²)					
	293.15 K	298.15 K	303.15 K	308.15 K	298.15 K	303.15 K	298.15 K	303.15 K	308.15 K	293.15 K	308.15 K	293.15 K
0.29982	1557.754	1584.889	1603.342	1616.453	4.195	4.044	3.940	3.862				
0.40009	1586.98	1613.405	1632.146	1644.129	4.062	3.922	3.822	3.752				
0.49996	1616.3	1640.088	1657.831	1670.04	3.934	3.813	3.721	3.654				
<i>PEG 400+0.06 mol kg⁻¹ D-pantphenol</i>												
0	1476.422	1502.364	1519.872	1529.767	4.595	4.428	4.314	4.242				
0.0992	1506.368	1533.451	1550.032	1562.53	4.441	4.277	4.173	4.091				
0.19	1532.78	1559.906	1577.641	1589.767	4.312	4.155	4.050	3.973				
0.30007	1563.559	1590.227	1608.796	1620.853	4.168	4.021	3.917	3.845				
0.4015	1593.433	1618.634	1637.203	1649.274	4.033	3.900	3.801	3.732				
0.50006	1622.368	1644.868	1662.138	1674.177	3.908	3.794	3.705	3.638				
<i>PEG 400+0.09 mol kg⁻¹ D-pantphenol</i>												
0	1481.019	1507.018	1524.104	1533.373	4.571	4.406	4.294	4.226				
0.10091	1512.281	1538.333	1554.621	1566.738	4.411	4.254	4.152	4.073				
0.20034	1540.818	1567.292	1584.691	1596.302	4.273	4.121	4.019	3.945				
0.30007	1568.656	1594.742	1613.048	1624.305	4.144	4.001	3.899	3.831				
0.39977	1598.135	1622.334	1640.824	1652.296	4.012	3.884	3.786	3.720				
0.50015	1627.308	1648.73	1666.095	1677.085	3.886	3.777	3.688	3.627				

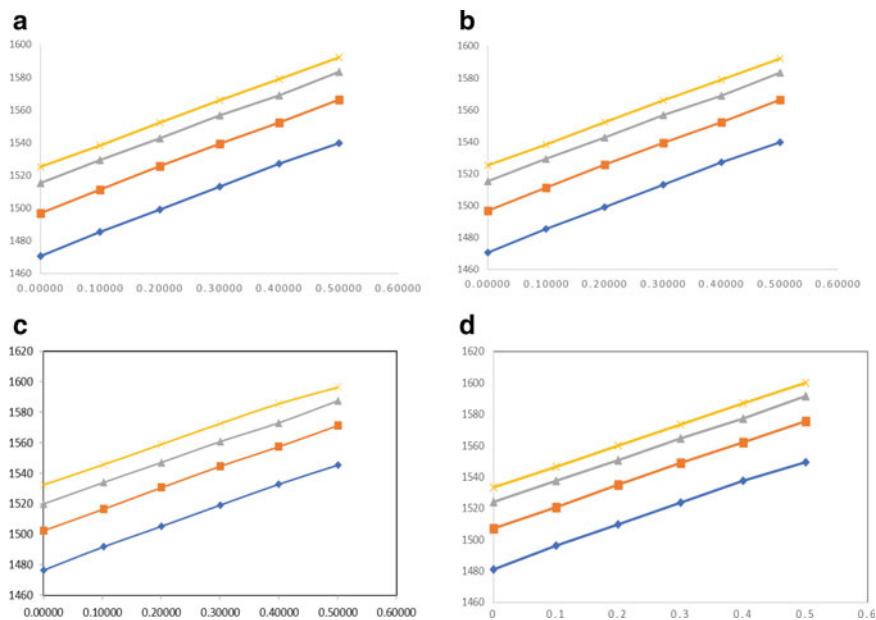


Fig. 1 Variation of Acoustic Impedance of PEG 200 at different concentrations of D-Panthenol (a=0.0 mol kg⁻¹, b=0.03 mol kg⁻¹, c=0.06 mol kg⁻¹ and d=0.09 mol kg⁻¹) different temperatures

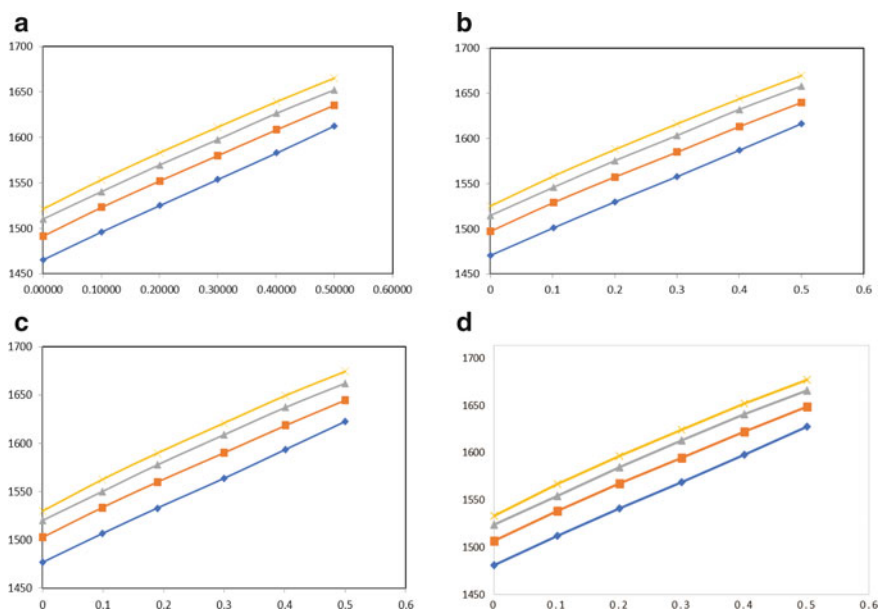


Fig. 2 Variation of Acoustic Impedance of PEG 400 at different concentrations of D-Panthenol (a=0.0 mol kg⁻¹, b=0.03 mol kg⁻¹, c=0.06 mol kg⁻¹ and d=0.09 mol kg⁻¹) different temperatures

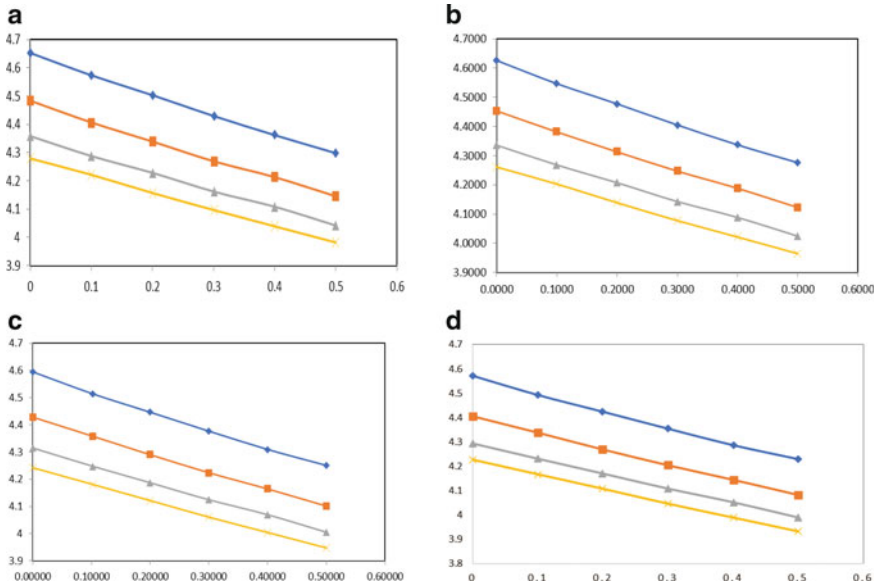


Fig. 3 Variation of Adiabatic compressibility of PEG 200 at different concentrations of D-Panthenol (a=0.0 mol kg⁻¹, b=0.03 mol kg⁻¹, c=0.06 mol kg⁻¹ and d=0.09 mol kg⁻¹) different temperatures

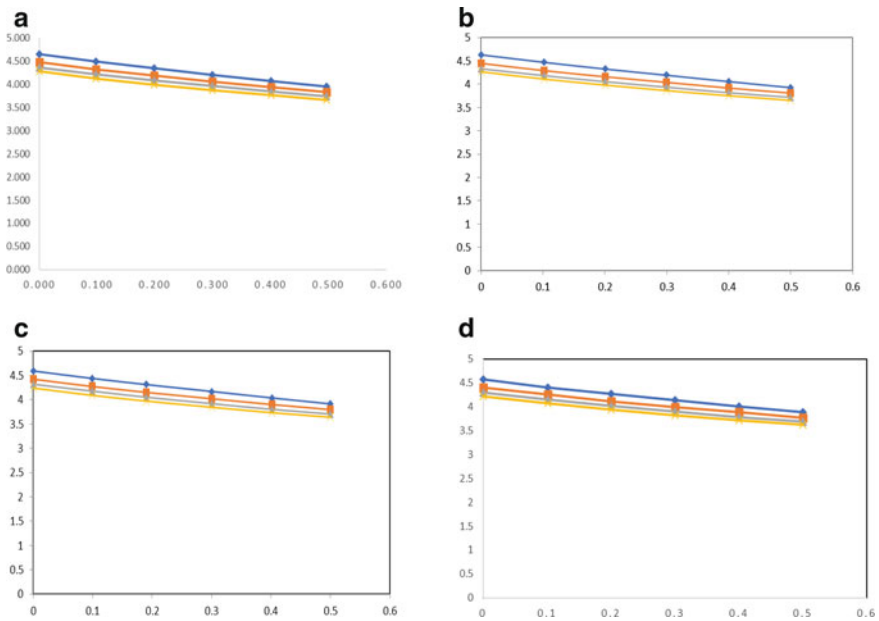
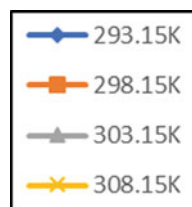


Fig. 4 Variation of Adiabatic compressibility of PEG 400 at different concentrations of D-Panthenol (a=0.0 mol kg⁻¹, b=0.03 mol kg⁻¹, c=0.06 mol kg⁻¹ and d=0.09 mol kg⁻¹) different temperatures

Fig. 5 Representation of Temperatures over different D-Panthenol concentrations and polyethylene glycol molalities



Figures 1 and 2 show the variation of acoustic impedance (Z) of PEG 200 and PEG 400 at different concentrations of D-panthenol ($a = 0.0 \text{ mol kg}^{-1}$, $b = 0.03 \text{ mol kg}^{-1}$, $c = 0.06 \text{ mol kg}^{-1}$, and $d = 0.09 \text{ mol kg}^{-1}$) different temperatures (Fig. 5 shows the representations of temperatures). The x -axis shows the values of molality, and y -axis shows the value of acoustic impedance (Figs. 1 and 2) and adiabatic compressibility (Figs. 3 and 4), respectively.

The absence of specific interaction like complex formation in the binary mixture is the reason of the linear variation in acoustic impedance as shown in Figs. 1 and 2. The adiabatic compressibility decreases with increasing concentration which is due to the strong molecular interaction among the solute and solvent molecules shown in Figs. 3 and 4 [6, 11].

The variation of intermolecular free length of PEG 200 and PEG 400 in aqueous solution of D-panthenol is given in Table 2 and Figs. 6 and 7.

Figures 6 and 7 show the variation of intermolecular free length of PEG 200 and PEG 400 at different concentrations of D-panthenol ($a = 0.0 \text{ mol kg}^{-1}$, $b = 0.03 \text{ mol kg}^{-1}$, $c = 0.06 \text{ mol kg}^{-1}$, and $d = 0.09 \text{ mol kg}^{-1}$) different temperatures. The x -axis shows the values of molality, and y -axis shows the value of intermolecular free length.

Tables 3 and 4 show the variation of Rao's constant, Wada's constant, and Van der Waal's constant of aqueous solution of D-panthenol with PEG 200 and PEG 400 at different temperatures.

Figures 8 and 9 show the variation of Rao's constant of PEG 200 and PEG 400 at different concentrations of D-panthenol ($a = 0.0 \text{ mol kg}^{-1}$, $b = 0.03 \text{ mol kg}^{-1}$, $c = 0.06 \text{ mol kg}^{-1}$, and $d = 0.09 \text{ mol kg}^{-1}$) different temperatures. The x -axis shows the values of molality, and y -axis shows the value of Rao's constant (Figs. 8 and 9) and Wada constant (Figs. 10 and 11), respectively.

The ultrasonic velocity of the mixture is directly proportional to the acoustic impedance. According to the mathematical relationships, acoustic impedance and adiabatic compressibility should have opposing behavior, but adiabatic compressibility and intermolecular free length should have the same behavior. This is evident in the findings of the experiments. The intermolecular free length rises with increasing temperature but decreases with increasing D-panthenol concentration. Because the ultrasonic velocity rises as concentration increases, the intermolecular free length must decrease as concentration increases and vice versa [19].

The Wada constant varies with molality at different temperatures, indicating that solute solvent molecules are becoming closer to one other and the area between them

Table 2 Values of intermolecular free length, L_f , of glycols in aqueous solution of niacin at different temperatures

Molality (mol/kg)	Intermolecular free length (L_f)			
	293.15 K	298.15 K	303.15 K	308.15 K
<i>0.0 mol kg⁻¹ D-panthenol+PEG 200</i>				
0	4.3949	4.3534	4.3323	4.3314
0.10009	4.3575	4.3161	4.2970	4.3019
0.20044	4.3238	4.2830	4.2668	4.2689
0.30136	4.2882	4.2485	4.2330	4.2375
0.40026	4.2558	4.2210	4.2058	4.2078
0.49999	4.2247	4.1873	4.1714	4.1778
<i>0.03 mol kg⁻¹ D-panthenol+PEG 200</i>				
0.00000	4.3822	4.3399	4.3207	4.3219
0.09934	4.3447	4.3049	4.2870	4.2924
0.20021	4.3113	4.2708	4.2561	4.2595
0.30010	4.2766	4.2381	4.2233	4.2279
0.39977	4.2435	4.2087	4.1955	4.1989
0.50000	4.2136	4.1754	4.1622	4.1690
<i>0.06 mol kg⁻¹ D-panthenol+PEG 200</i>				
0.00000	4.3676	4.3272	4.3097	4.3122
0.10210	4.3290	4.2928	4.2763	4.2809
0.20006	4.2964	4.2591	4.2458	4.2504
0.30009	4.2625	4.2260	4.2142	4.2189
0.39991	4.2296	4.1962	4.1863	4.1895
0.50058	4.2003	4.1639	4.1530	4.1596
<i>0.09 mol kg⁻¹ D-panthenol+PEG 200</i>				
0	4.3563	4.3160	4.2999	4.3041
0.10001	4.3187	4.2829	4.2683	4.2735
0.1995	4.2858	4.2488	4.2374	4.2431
0.30007	4.2518	4.2164	4.2055	4.2112
0.40046	4.2187	4.1863	4.1766	4.1813
0.50008	4.1906	4.1548	4.1440	4.1515
<i>0.0 mol kg⁻¹ D-panthenol+PEG 400</i>				
0.00000	4.3949	4.3534	4.3323	4.3314
0.10015	4.3189	4.2768	4.2610	4.2553
0.20004	4.2494	4.2089	4.1935	4.1879
0.29995	4.1823	4.1457	4.1313	4.1257
0.40100	4.1160	4.0827	4.0683	4.0657

(continued)

Table 2 (continued)

Molality (mol/kg)	Intermolecular free length (L_f)			
	293.15 K	298.15 K	303.15 K	308.15 K
0.50006	4.0495	4.0248	4.0143	4.0115
<i>0.03 mol kg⁻¹ D-panthenol+PEG 400</i>				
0	4.3822	4.3399	4.3207	4.3219
0.10141	4.3068	4.2628	4.2473	4.2437
0.20037	4.2377	4.1967	4.1801	4.1768
0.29982	4.1732	4.1352	4.1189	4.1149
0.40009	4.1065	4.0722	4.0564	4.0559
0.49996	4.0412	4.0151	4.0028	4.0023
<i>0.06 mol kg⁻¹ D-panthenol+PEG 400</i>				
0	4.3676	4.3272	4.3097	4.3122
0.0992	4.2940	4.2525	4.2389	4.2349
0.19	4.2310	4.1912	4.1756	4.1733
0.30007	4.1598	4.1233	4.1068	4.1054
0.4015	4.0920	4.0610	4.0456	4.0448
0.50006	4.0280	4.0052	3.9939	3.9937
<i>0.09 mol kg⁻¹ D-panthenol+PEG 400</i>				
0	4.3563	4.3160	4.2999	4.3041
0.10091	4.2793	4.2410	4.2284	4.2255
0.20034	4.2118	4.1742	4.1597	4.1589
0.30007	4.1477	4.1129	4.0971	4.0978
0.39977	4.0810	4.0525	4.0373	4.0381
0.50015	4.0167	3.9965	3.9850	3.9874

is shrinking as temperature rises. This contributes to the high solute–solvent interaction observed in liquid solution. Rao’s constant or molar sound velocity increases as concentration and temperature rise. The rising trends of molar sound velocity and Wada’s constant or molar compressibility with concentration indicate the availability of a higher number of components in a given location, resulting in a compact packing of the medium and therefore enhancing the interactions [20–28].

It is possible to see a decline in Van der Waal’s constant as concentration increases. This means that the molecules in the mixture have a weak connection [29–31].

3 Conclusion

The ultrasonic technique or UT is an effective tool for investigating the acoustical properties of mixtures. These factors can be used to recognize the nature of molecular

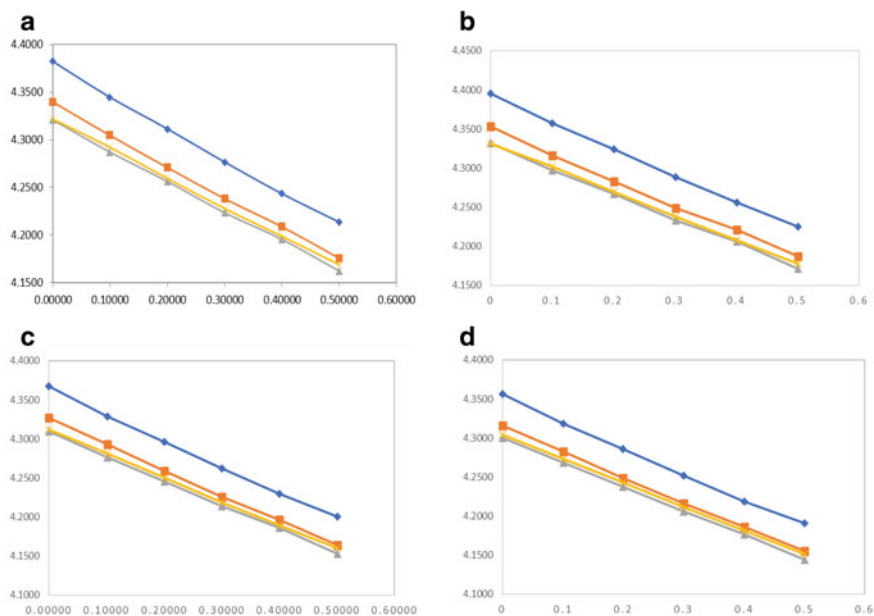


Fig. 6 Variation of Intermolecular free length of PEG 200 at different concentrations of D-Panthenol (a=0.0 mol kg⁻¹, b=0.03 mol kg⁻¹, c=0.06 mol kg⁻¹ and d=0.09 mol kg⁻¹) different temperatures

interaction between solute and solvent, which is crucial for the materials' application areas. Basic parameters such as acoustic impedance, adiabatic compressibility, intermolecular free length, Wada constant, Rao's constant, and Van der Waal's constant are calculated using ultrasonic velocity and density values. Acoustic impedance and adiabatic compressibility should have opposed tendency, while adiabatic compressibility and intermolecular free length should have the same behavioral patterns, according to the mathematical equations. The experimental results illustrate this. The intermolecular free length increases as the temperature increases but decreases with D-panthenol concentration. Because the ultrasonic velocity increases with concentration, the intermolecular free length must decrease with concentration and vice versa. The Wada constant fluctuates with molality at different temperatures, suggesting that as temperature increases, solute solvent molecules become closer to one another and the space between them shrinks. This helps to explain the significant solute–solvent interaction found in liquid solution. Rao's constant, or molar sound velocity, increases with increasing concentration and temperature. The rising trends in molar sound velocity and Wada's constant or molar compressibility with concentration imply the readiness of a greater number of components in each place, resulting in a more compact packing of the medium and so improving interactions. As concentration grows, Van der Waal's constant may decrease. This signifies that the molecules in the mixture are only loosely connected [32, 33].

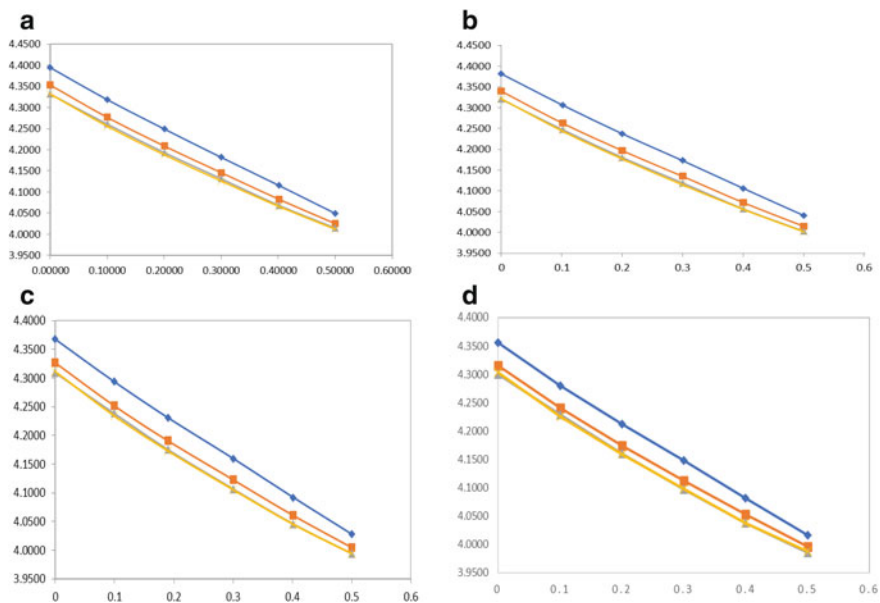


Fig. 7 Variation of Intermolecular free length of PEG 400 at different concentrations of D-Panthenol (a=0.0 mol kg⁻¹, b=0.03 mol kg⁻¹, c=0.06 mol kg⁻¹ and d=0.09 mol kg⁻¹) different temperatures

Table 3 Values of Wada's constant (W) and Rao's constant of glycols in aqueous solution of D -panthenol at different temperatures

Molality (mol/kg)	Values of Wada's constant (W) and Rao's constant of glycols in aqueous solution of D -panthenol at different temperatures									
	293.15 K	298.15 K	303.15 K	308.15 K	298.15 K	303.15 K	308.15 K	308.15 K	293.15 K	293.15 K
<i>PEG 200+0.0 mol kg⁻¹ D-panthenol</i>										
0	160.681	161.898	163.036	164.072	2273.986	2294.083	2312.910	2330.071		
0.10009	160.600	161.816	162.931	163.898	2272.649	2292.728	2311.175	2327.184		
0.20044	160.503	161.714	162.793	163.787	2271.047	2291.054	2308.899	2325.352		
0.30136	160.447	161.647	162.719	163.680	2270.125	2289.934	2307.663	2323.569		
0.40026	160.390	161.534	162.599	163.583	2269.176	2288.080	2305.675	2321.976		
0.49999	160.332	161.510	162.579	163.508	2268.224	2287.668	2305.348	2320.729		
<i>PEG 200+0.03 mol kg⁻¹ D-panthenol</i>										
0.00000	160.623	161.835	162.946	163.986	2273.024	2293.047	2311.426	2328.636		
0.09934	160.553	161.742	162.835	163.819	2271.864	2291.504	2309.583	2325.870		
0.20021	160.456	161.652	162.709	163.707	2270.266	2290.030	2307.507	2324.015		
0.30010	160.398	161.577	162.630	163.607	2269.317	2288.783	2306.199	2322.372		
0.39977	160.348	161.488	162.520	163.505	2268.477	2287.319	2304.368	2320.680		
0.50000	160.279	161.459	162.488	163.428	2267.342	2286.830	2303.840	2319.406		
<i>PEG 200+0.06 mol kg⁻¹ D-panthenol</i>										
0.00000	160.583	161.772	162.876	163.904	2272.369	2292.005	2310.269	2327.284		
0.10210	160.520	161.666	162.757	163.755	2271.331	2290.25	2308.293	2324.815		
0.20006	160.437	161.596	162.651	163.640	2269.946	2289.092	2306.535	2322.913		
0.30009	160.379	161.535	162.571	163.550	2269.002	2288.081	2305.213	2321.428		
0.39991	160.334	161.461	162.474	163.463	2268.259	2286.868	2303.607	2319.973		
0.50058	160.270	161.432	162.454	163.402	2267.196	2286.387	2303.283	2318.976		

(continued)

Table 3 (continued)

Molality (mol/kg)	293.15 K	298.15 K	303.15 K	308.15 K	298.15 K	303.15 K	308.15 K	293.15 K
	<i>PEG 200+0.09 mol kg⁻¹ D-panthenol</i>							
0	160.537	161.730	162.825	163.833	2271.61	2291.31	2309.414	2326.111
0.10001	160.481	161.627	162.701	163.693	2270.68	2289.61	2307.364	2323.784
0.1995	160.401	161.561	162.600	163.581	2269.36	2288.52	2305.705	2321.929
0.30007	160.353	161.500	162.530	163.505	2268.57	2287.5	2304.543	2320.683
0.40046	160.320	161.437	162.452	163.430	2268.024	2286.472	2303.252	2319.436
0.50008	160.256	161.413	162.439	163.379	2266.972	2286.078	2303.031	2318.594
<i>PEG 400+0.0 mol kg⁻¹ D-panthenol</i>								
0.00000	321.362	323.795	326.072	328.144	4547.971	4588.165	4625.82	4660.142
0.10015	320.878	323.354	325.526	327.703	4539.978	4580.87	4616.79	4652.829
0.20004	320.450	322.918	325.091	327.262	4532.901	4573.669	4609.587	4645.517
0.29995	320.140	322.546	324.700	326.874	4527.791	4567.511	4603.116	4639.104
0.40100	319.945	322.309	324.472	326.571	4524.574	4563.606	4599.347	4634.08
0.50006	319.935	322.120	324.198	326.297	4524.412	4560.482	4594.821	4629.548
<i>PEG 400+0.03 mol kg⁻¹ D-panthenol</i>								
0	321.246	323.670	325.892	327.971	4546.049	4586.093	4622.852	4657.271
0.10141	320.803	323.269	325.399	327.555	4538.731	4579.465	4614.692	4650.372
0.20037	320.456	322.865	325.007	327.134	4533.002	4572.785	4608.209	4643.406
0.29982	320.160	322.508	324.639	326.762	4528.127	4566.885	4602.111	4637.254
0.40009	320.046	322.320	324.431	326.458	4526.248	4563.778	4598.670	4632.210
0.49996	320.047	322.142	324.167	326.173	4526.264	4560.842	4594.304	4627.501

(continued)

Table 3 (continued)

Molality (mol/kg)	293.15 K	298.15 K	303.15 K	308.15 K	298.15 K	303.15 K	308.15 K	293.15 K
	<i>PEG 400+0.06 mol kg⁻¹ D-panthenol</i>							
0.00000	321.167	323.544	325.753	327.808	327.808	4544.738	4584.011	4620.538
0.09920	320.755	323.169	325.288	327.464	327.464	4537.951	4577.82	4612.843
0.19000	320.440	322.826	324.987	327.108	327.108	4532.748	4572.144	4607.872
0.30007	320.123	322.451	324.628	326.709	326.709	4527.517	4565.953	4601.931
0.40150	320.035	322.257	324.404	326.455	326.455	4526.061	4562.743	4598.235
0.50006	320.034	322.090	324.135	326.159	326.159	4526.048	4559.992	4593.787
<i>PEG 400+0.09 mol kg⁻¹ D-panthenol</i>								
0	321.075	323.460	325.649	327.666	327.666	4543.219	4582.626	4618.828
0.10091	320.744	323.107	325.218	327.371	327.371	4537.756	4576.786	4611.686
0.20034	320.417	322.784	324.930	327.019	327.019	4532.364	4571.449	4606.923
0.30007	320.166	322.491	324.664	326.697	326.697	4528.224	4566.617	4602.532
0.39977	320.119	322.323	324.482	326.494	326.494	4527.444	4563.835	4599.515
0.50015	320.152	322.184	324.247	326.200	326.200	4527.996	4561.543	4595.634

Table 4 Values of Van der Waal's constant (b) of glycols in aqueous solution of niacin at different temperatures

Molality (mol kg ⁻¹)	Van der Waal's constant (b) (m ³ /mol)			
	293.15 K	298.15 K	303.15 K	308.15 K
<i>0.0 mol kg⁻¹ D-panthenol+PEG 200</i>				
0	395.7379	396.6466	397.8616	399.3362
0.10009	394.6066	395.5061	396.7084	398.1612
0.20044	393.5256	394.4198	395.6050	397.0482
0.30136	392.4914	393.3760	394.5544	395.9797
0.40026	391.5296	392.3980	393.5624	394.9787
0.49999	390.5985	391.4690	392.6245	394.0184
<i>0.03 mol kg⁻¹ D-panthenol+PEG 200</i>				
0.00000	395.2787	396.1543	397.3486	398.8819
0.09934	394.1698	395.0423	396.2208	397.7256
0.20021	393.0949	393.9595	395.1249	396.6109
0.30010	392.0777	392.9400	394.0916	395.5569
0.39977	391.1148	391.9698	393.1063	394.5575
0.50000	390.1847	391.0386	392.1659	393.5953
<i>0.06 mol kg⁻¹ D-panthenol+PEG 200</i>				
0.00000	394.8182	395.6784	396.9001	398.4367
0.10210	393.6973	394.5489	395.7588	397.2767
0.20006	392.6712	393.5232	394.7202	396.2141
0.30009	391.6749	392.5260	393.7116	395.1858
0.39991	390.7292	391.5813	392.7557	394.2121
0.50058	389.8235	390.6782	391.8441	393.2869
<i>0.09 mol kg⁻¹ D-panthenol+PEG 200</i>				
0	394.4228	395.2930	396.5231	398.0592
0.10001	393.3424	394.2039	395.4180	396.9366
0.1995	392.3184	393.1766	394.3815	395.8837
0.30007	391.3395	392.1960	393.3905	394.8773
0.40046	390.4150	391.2687	392.4527	393.9213
0.50008	389.5405	390.3972	391.5729	393.0207
<i>0.0 mol kg⁻¹ D-panthenol+PEG 400</i>				
0.00000	791.4759	793.2933	795.7232	798.6724
0.10015	786.4891	788.3401	790.7620	793.7063
0.20004	781.9335	783.8073	786.2318	789.1499
0.29995	777.7487	779.6418	782.0543	784.9646
0.40100	773.8502	775.7798	778.1912	781.0673

(continued)

Table 4 (continued)

Molality (mol kg ⁻¹)	Van der Waal's constant (<i>b</i>) (m ³ /mol)			
	293.15 K	298.15 K	303.15 K	308.15 K
0.50006	770.3516	772.2718	774.6698	777.5274
<i>0.03 mol kg⁻¹ D-panthenol+PEG 400</i>				
0	790.5574	792.3085	794.6972	797.7638
0.10141	785.6983	787.4235	789.7527	792.7493
0.20037	781.3519	783.0533	785.3352	788.2660
0.29982	777.3292	779.0006	781.2581	784.1286
0.40009	773.6019	775.2512	777.4633	780.2765
0.49996	770.1860	771.8069	773.9783	776.7355
<i>0.06 mol kg⁻¹ D-panthenol+PEG 400</i>				
0	789.6365	791.3567	793.8002	796.8735
0.0992	784.9339	786.6515	789.0512	792.0749
0.19	780.9705	782.6759	785.0549	788.0211
0.30007	776.5519	778.2480	780.5940	783.5013
0.4015	772.8192	774.5125	776.8264	779.6813
0.50006	769.4604	771.1554	773.4270	776.2404
<i>0.09 mol kg⁻¹ D-panthenol+PEG 400</i>				
0	788.8457	790.5861	793.0462	796.1185
0.10091	784.1662	785.9141	788.3391	791.3632
0.20034	779.9345	781.6934	784.0877	787.0518
0.30007	776.0324	777.7998	780.1725	783.0730
0.39977	772.4461	774.2242	776.5740	779.4167
0.50015	769.1436	770.9152	773.2158	776.0004

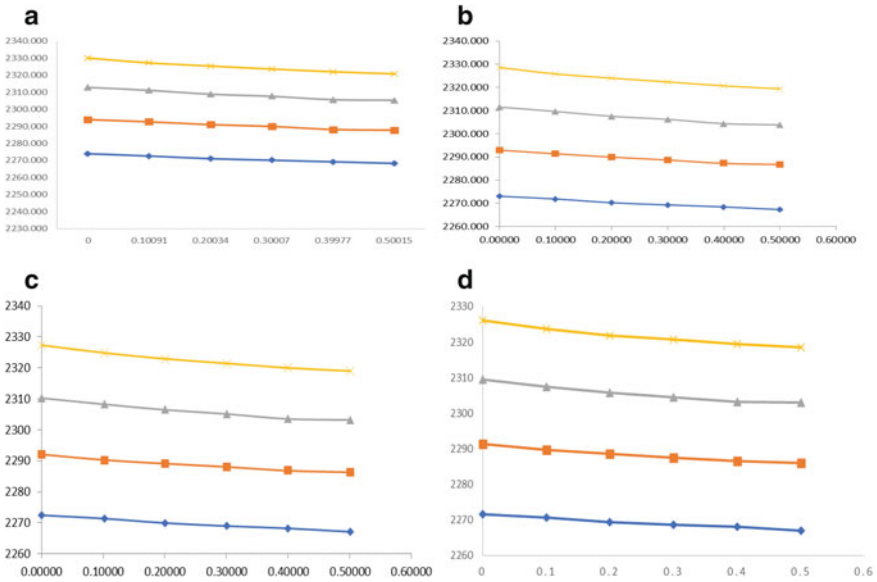


Fig. 8 Variation of Rao's constant of PEG 200 at different concentrations of D-Panthenol (a=0.0 mol kg⁻¹, b=0.03 mol kg⁻¹, c=0.06 mol kg⁻¹ and d=0.09 mol kg⁻¹) different temperatures

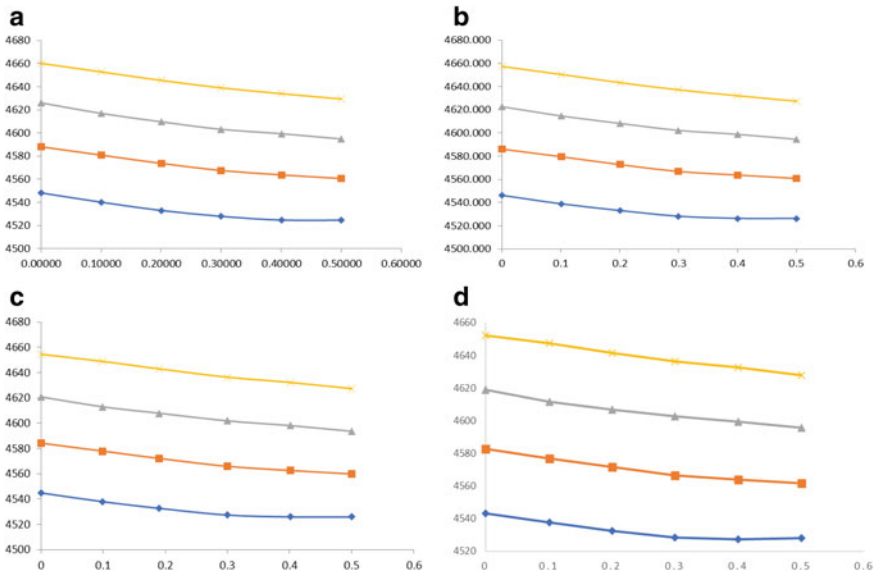


Fig. 9 Variation of Rao's constant of PEG 400 at different concentrations of D-Panthenol (a=0.0 mol kg⁻¹, b=0.03 mol kg⁻¹, c=0.06 mol kg⁻¹ and d=0.09 mol kg⁻¹) different temperatures

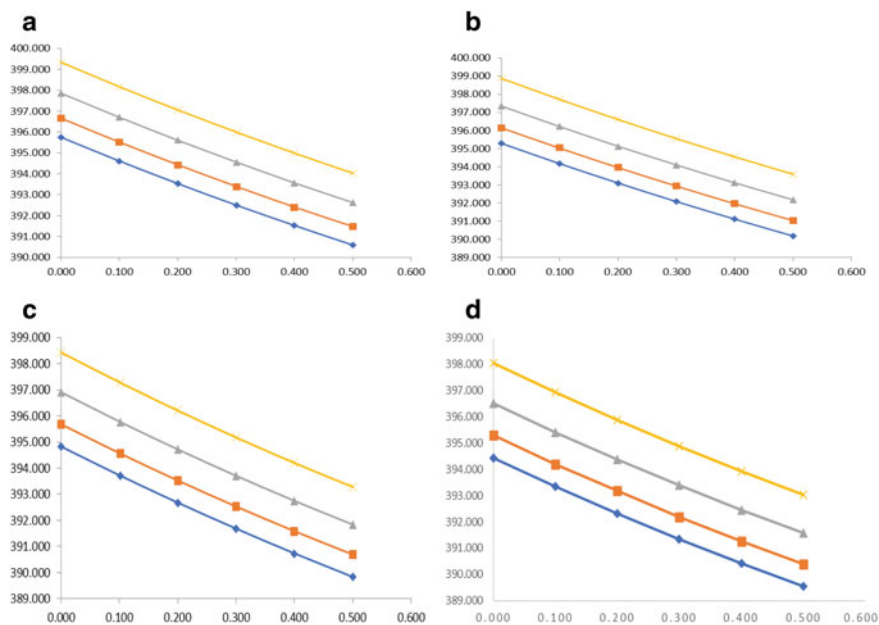


Fig. 10 Variation of Wada's constant of PEG 200 at different concentrations of D-Panthenol (a=0.0 mol kg⁻¹, b=0.03 mol kg⁻¹, c=0.06 mol kg⁻¹ and d=0.09 mol kg⁻¹) different temperatures

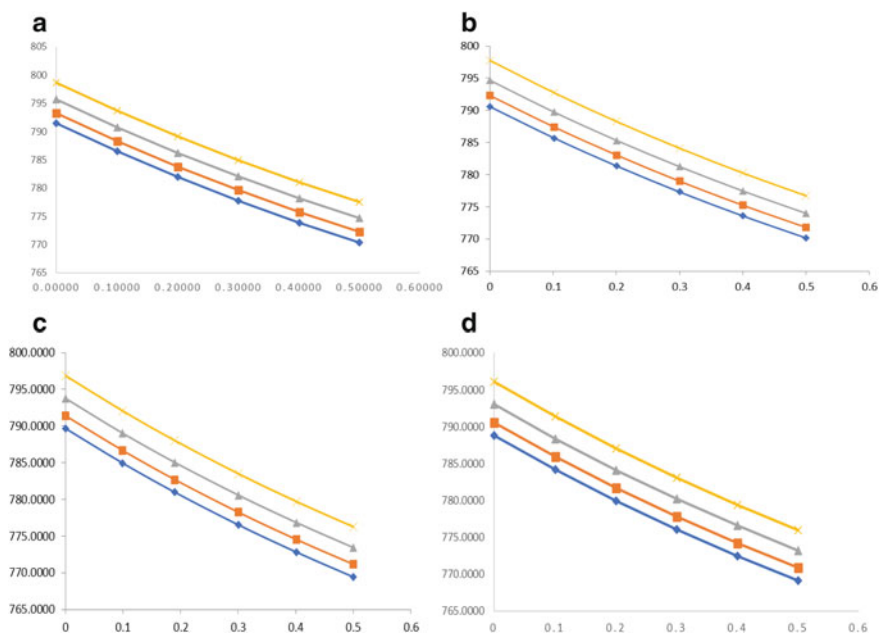


Fig. 11 Variation of Wada's constant of PEG 400 at different concentrations of D-Panthenol (a=0.0 mol kg⁻¹, b=0.03 mol kg⁻¹, c=0.06 mol kg⁻¹ and d=0.09 mol kg⁻¹) different temperatures

References

1. Chakraborty N, Juglan KC, Kumar H (2021) Volumetric and ultrasonic study of polyethylene glycols in aqueous solutions of niacin at different temperatures. *J Chem Thermodyn* 154:106326
2. Kaur K, Juglan KC, Kumar H (2017) Investigation on temperature-dependent volumetric and acoustical properties of homologous series of glycols in aqueous sorbitol solutions. *J Chem Eng Data* 62(11):3769–3782
3. Egorov GI, Makarov DM, Kolker AM (2013) Liquid phase PVT_x properties of binary mixtures of (water+ ethylene glycol) in the range from 278.15 to 323.15 K and from 0.1 to 100 MPa. I. Experimental results, partial and excess thermodynamics properties. *Fluid Phase Equilib* 344:125–138
4. Chawla D, Chakraborty N, Juglan KC, Kumar H (2021) Temperature-dependent physicochemical studies of some glycols in aqueous d-mannitol solution. *Chem Papers* 75(4):1497–1506
5. Kaur P, Chakraborty N, Juglan KC, Kumar H (2020) Volumetric and ultrasonic studies of molecular interactions of glycols in aqueous glutaraldehyde solutions at different temperatures. *J Mol Liq* 315:113763
6. Kaur K, Juglan KC, Kumar H (2017) Thermo-acoustical molecular interaction study in binary mixtures of glycerol and ethylene glycol. *Conf Proceedings* 1860:020026
7. Ayranci E, Sahin M (2008) Interactions of polyethylene glycols with water studied by measurements of density and sound velocity. *J Chem Thermodyn* 40(8):1200–1207
8. Kaur P, Chakraborty N, Singh S, Juglan KC, Kumar H (2020) Study of intermolecular interaction of binary mixture of adrenaline and KOH. *J Physics Conf Series* 1531:012015
9. Sannaningannavar FM, Navati BS, Ayachit NH (2013) Studies on thermos-acoustic parameters of poly (ethylene glycol)-400 at different temperatures. *J Therm Anal Calorim* 112(3):1573–1578
10. Kaur K, Juglan KC (2015) Studies of molecular interaction in the binary mixture of chloroform and methanol by using ultrasonic technique. *Der Pharma Chemica* 7(2):160–167
11. Thakur A, Kaur H, Juglan KC, Kumar H (2020) Molecular interactions in ternary system of ethane-1, 2-diol with methanol and methyl 4-hydroxybenzoate at 298 K: An acoustic approach. *J Phys Conf Ser* 1531:012017
12. Chakraborty N, Juglan KC, Kumar H (2021) Thermodynamics of various interactions in homologous series of polyethylene glycols in aqueous medium of d-panthenol at T=(288.15, 298.15, 308.15 and 318.15) K: a volumetric and acoustic approach. *Braz J Chem Eng* 1–16
13. Sathish M, Venkataramanan K, Padmanaban R, Ruth H, Vadivel K, Ramalingam G (2021) Acoustic, thermal and optical properties of organic based disodium tartrate salt. *Int J Sci Res Arch* 2(1):012–027
14. Chakraborty N, Kumar H, Kaur K, Juglan KC (2018) Acoustic and thermodynamic study of D-Panthenol in aqueous solutions of glycol at different temperatures. *J Chem Thermodyn* 126:137–146
15. Kaur K, Juglan KC, Kumar H (2018) Temperature dependent physicochemical studies of polyethylene glycols (PEG-400 and PEG-4000) in aqueous sorbitol solutions. *J Mol Liq* 268:700–706
16. Kaur K, Juglan KC, Kumar H (2018) Acoustical and volumetric investigation of polyethylene glycol 400 and polyethylene glycol 4000 in aqueous solutions of glycerol at different temperatures. *J Chem Thermodyn* 127:8–16
17. Juglan KC, Kumar H (2020) Volumetric and ultrasonic investigation of polyethylene glycols (PEG-200 and PEG-600) in aqueous solutions of sodium methylparaben at various temperatures. *J Chem Thermodyn* 140:105916
18. Živković NV, Serbanovic SS, Kijevčanin ML, Živkovic EM (2013) Volumetric and viscometric behavior of binary systems 2-butanol+ PEG 200,+ PEG 400,+ tetraethylene glycol dimethyl ether, and+ N-methyl-2-pyrrolidone. *J Chem Eng Data* 58(12):3332–3341
19. Gajghate V, Kanwar A (2021) Effect of temperature and concentration on the physical properties of cholesteryl Pelargonate near transition temperatures. *J Sci Research* 13(2):483–493

20. Singh JP, Sharma R (2013) Variation of Wada constant, Raos constant and acoustic impedance of aqueous cholesteryl oleyl carbonate with temperature. *RN* 10:1026
21. Panda S (2020) Molecular interaction of polymer dextran in sodium hydroxide through evaluation of thermo acoustic parameters. *Ind J Pharma Edu Res* 54(3):630–636
22. Thakur A, Juglan KC, Kumar H, Kaur K (2019) Investigation on molecular interaction of glycols in methanol solutions of methylparaben (methyl 4-hydroxybenzoate) at different temperatures through thermo-acoustical analysis. *J Mol Liq* 288:111014
23. Kaur K, Behal I, Juglan KC, Kumar H (2018) Volumetric and ultrasonic studies on interactions of ethylene glycol, diethylene glycol and triethylene glycol in aqueous solutions of glycerol at temperatures $T=(293.15\text{ K} - 308.15)\text{ K}$. *J Chem Thermodyn* 125:93–106
24. Ravi S, Amoros J, Arockia JK (2008) Effective method of characterizing specific liquid fluorocarbon interactions using ultrasound. *J Phys Chem B* 112(20):6420–6425
25. Kaur P, Chakraborty N, Juglan KC, Kumar H, Singla M (2021) Temperature dependent physico-chemical studies propylene and hexylene glycols in methanol solutions of chlorhexidine. *J Mol Liq* 339:116810
26. Mohabansi NP, Satone AK, Hirani SN (2021) Partial and apparent molar volume of azithromycin in its solutions in ethanol, 1-propanol, and 1-butanol at 300.15, 305.15, 310.15 K and ambient pressure. *Russ J Phys Chem A* 95(1):S1–S7
27. Thakur A, Juglan KC, Kumar H, Kaur K (2020) Apparent molar properties of glycols in methanol solutions of propyl 4-hydroxybenzoate (propylparaben) at $T=(293.15\text{ to }308.15)\text{ K}$: an acoustic and volumetric approach. *Phys Chem Liq* 58(6):803–819
28. Ravichandran S, Pushpanathan K, Sagadevan S, Marlinda AR, Mohammad F, Al-Lohedan HA, Johan MR (2021) Influence of graphene concentration towards the thermo-acoustic and vibrational properties of graphene: polyvinyl alcohol composites. *J Mat Sci Mat Elec* 32(8):10359–10367
29. Buddiga LR, Gara T, Gajula GR, Kumar KC (2020) Ultrasonic Studies on the thermodynamic and excess thermodynamic properties of bromobenzene substituted with ethyl methyl ketone at 308.15 K. *J Pure App Ultras* 42(2):26–35
30. Juglan KC, Kumar H (2020) Ultrasonic and volumetric behaviour of glycols with sodium ethylparaben in aqueous medium from $T = 293.15\text{ to }308.15\text{ K}$ at atmospheric pressure. *Res Chem* 2:100049
31. NP M, Satone AK (2020) Thermo acoustical studies of molecular interaction of N-[[2S)-1-ethylpyrrolidin-2-yl] methyl]-2-methoxy-5-sulfamoylbenzamide at different temperature. *measurement* 9:10
32. Chakraborty N, Juglan KC, Kumar H (2021) Volumetric and ultrasonic studies of molecular interactions of glycols in aqueous Niacin (vitamin B3) at different temperatures. *J Mol Liq* 332:115869
33. Praharaj MK, Mishra S (2020) Ultrasonic and ionic study of aqueous KCL through walden plot

A Feasibility Investigation of Photo Voltaic Cell-Assisted Linke Hofmann Busch Coach Used in Indian Railways: A Case Study in Context to Present Scenario



Abhishek Barua, Dilip Kumar Bagal, Siddharth Jeet, Swastik Pradhan, Asini Kumar Baliarsingh, and Deepak Kumar Bagal

Abstract Indian Railway which is world's 4th largest railway network by size operates more than 13,500 passenger trains daily which comprises of fleets of either ICF coaches or LHB coaches. Old aging ICF coaches are equipped with self-generation system of electricity to operate electrical equipment fitted inside them on its own. The Linke Hofmann Busch (LHB) coaches are more reliable in every aspect when compared to ICF coaches except in the case of self-electricity generation by individual coaches. Hence, LHB coaches have to rely on Head on Generation (HOG) or End on Generation (EOG) system for electricity supply inside the coaches. About 90% of LHB coaches' trains have to dependent upon diesel generator driven EOG system. This investigation stats solar photovoltaic (PV) modules use in a LHB coach and how previous researchers have investigated the proficiency of this type of electricity generation technique earlier.

Keywords ICF coach · Indian railway · LHB coach · Solar cell

A. Barua · S. Jeet

Department of Mechanical Engineering, Centre for Advanced Post Graduate Studies, BPUT, Rourkela, Odisha, India

D. K. Bagal

Department of Mechanical Engineering, Government College of Engineering, Kalahandi, Bhawanipatna, Odisha, India

S. Pradhan (✉)

School of Mechanical Engineering, Lovely Professional University, Phagwara, Punjab, India
e-mail: swastik.22644@lpu.co.in

A. K. Baliarsingh

Department of Electrical Engineering, Government College of Engineering, Kalahandi, Bhawanipatna, Odisha, India

D. K. Bagal

Department of Electrical Engineering, Veer Surendra Sai University of Technology, Burla, Odisha, India

Nomenclature

Dimension (length and breadth)	(Mm)
Module Power Tolerance	(W_p)
Indian Rupees (INR)	(Rs)

1 Introduction

Old aging ICF coaches of Indian Railway generates the electricity of its own while in motion for running electrical equipment present inside it [1]. They have been fitted with two number of 25 kW alternators for AC coach and one 4.5 kW for non-AC coach, which is driven by a pulley-belt arrangement with the coach axle [2, 3]. Using this arrangement, electricity is produced while the coach is in motion, which is rectified to 110 V and stored in batteries present under the coach which will be employed for running the electrical equipment. This arrangement limits the train speed to 110 kmph only. In spite of the fact that this innovation is green and does not requires and other sustainable sources to run, ICF coach production have been halted because of their ageing technology and demand of a more reliable and faster traveling railway passenger coach [4, 5].

The recent Linke Hofmann Busch (LHB) coaches have come out as a permanent substitute of ICF coaches which because of their reliability in almost every aspect with the exception of in the instance of self-electricity generation by an individual coach. As LHB coaches are designed to achieve a high speed more than 160 kmph, they are not equipped with self-electric generation mechanism. Hence, they are fully dependent upon Head on Generation (HOG) or End on Generation (EOG) system of train for electricity supply inside the coaches. About 90% of LHB trains are dependent on EOG system with diesel generators to cater electricity for the whole train. Rest LHBfied trains uses HOG system where electric locomotive draws electricity from 25 kV OHE wires, which is rectified and converted into direct current and supplied to the whole train for its uses [1–13]. EOG system comprises of diesel fueled generators which not just creates noise but also discharges exhaust gases mixed with black smoke which is very harmful. Comparatively, more consumption of diesel has been reported for powering diesel generators in full AC LHB trains comparatively than mixed type or non-AC LHB trains.

2 Literature Review and Objectives

First trail of LHB coach fitted with solar photovoltaic cell was conducted by Vasisht et al. [1, 2] in India. Agarwal and Pimple [3] proposed solar photovoltaic cell based brushless DC motor system for fan by employing maximum power point tracking

algorithm system by simulating it in Matlab Simulink thus reporting 7.78 kWh of energy saving every day from an individual coach. A novel approach has been made by Mate et al. [4] by designing and installing solar distillation system onsite of Ajni loco shed, Nagpur, Maharashtra, India for the production of distilled water. George and Chowdhury [5] proposed the roof-top solar power amplification for ancillary supply of passenger train running in South Africa. Rohollahi et al. [6] conducted a case study for prediction of energy generation using photovoltaic cells attached on passenger coaches roof of Kerman-Tehran rail line in Iran beneath different environments showing the significance of departure time and train speed in determination of quantity of electrical energy spawned by photovoltaic panels. Thelkar et al. [7] presented enactment of interfacing the solar charge control with regulator and rectifier unit by simulating it using Simulink Matlab and testing a model hardware of solar charge controller. Alam et al. [8] proposed a design and analyzed photovoltaic and fuel cell based 110 V DC microgrid by employing hydrogen energy storage which can meet railways carriage load demand. A real-world enactment of energy ingathering, observing, and analysis arrangement for solar energy using photovoltaic cell in LHB coaches has been reported by Darshana et al. [9]. Bagal et al. [13] also suggested the use photovoltaic cell for powering electrical units of a fully air conditioned LHB coach train and reported the energy tapping and cost cutting technique.

Based on previous researches, this investigation emphasis on the use of solar photovoltaic cell on LHB coach and comparative study with HOG technique. Use of photovoltaic cells by Indian railway in present time has also been stated in this investigation.

3 Electrical Supply Used in LHB Coaches

Indian Railways has adapted Head on Generation (HOG) and End on Generation (EOG) for catering electrical power supply to the LHB coach train. EOG system powers electrical load or hotel load present in LHB coach train consisting of air conditioning units, fans, lights, etc., via generator cars attached at both ends of a train rake. Generator car comprises of two Diesel Alternator sets for generation of three-phase 750 V 50 Hz power supply and transferring it to the whole rake by the help of two parallel feeder cables (Feeder-A and Feeder-B) which runs through the whole train. This electricity is tapped by the help of 60 kVA transformers fitted inside LHB coach and transformed to 415 V AC and 110 V DC running electrical equipment working at respective voltage (Fig. 3). Layout of generator car with EOG supply is shown in Figs. 1 and 2 shows the LHB Luggage Brake and Generator Car, where the EOG system is installed in Indian Railways [10].

For HOG, electricity is cater from electric locomotive to train for powering electrical load or hotel load present in LHB coach train. Electric locomotive taps electricity from the 25 kV overhead electrical wire by its pantograph to traction transformer with hotel load winding of 945 kVA installed in it. This winding delivers 750 V single-phase supply to hotel load converter for giving an output power of

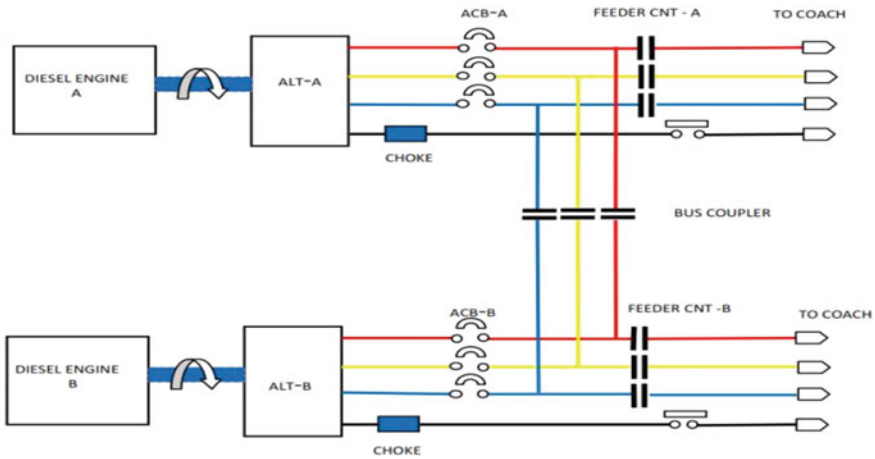


Fig. 1 Layout of generator car with EOG supply [10]



Fig. 2 LHB luggage brake and generator car

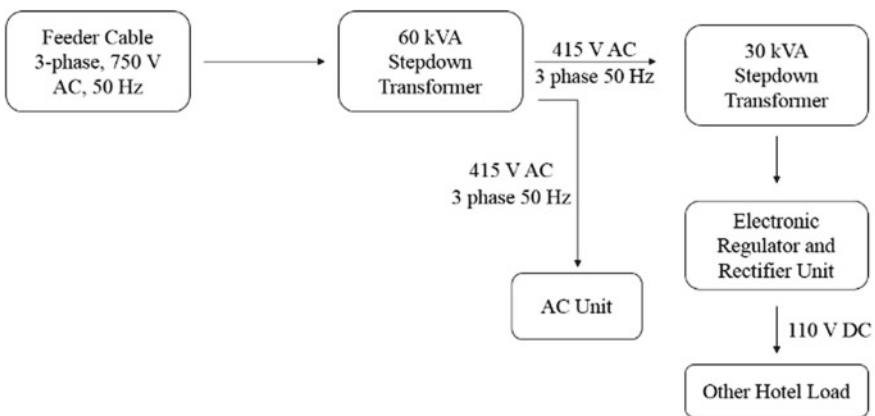


Fig. 3 LHB coach electricity supply layout [1]

750 V 3-phase 50 Hz to cater the electrical equipment of entire rake [10]. Layout of HOG supply is shown in Figs. 4 and 5, while Fig. 6 shows the connection of electric locomotive with power car.

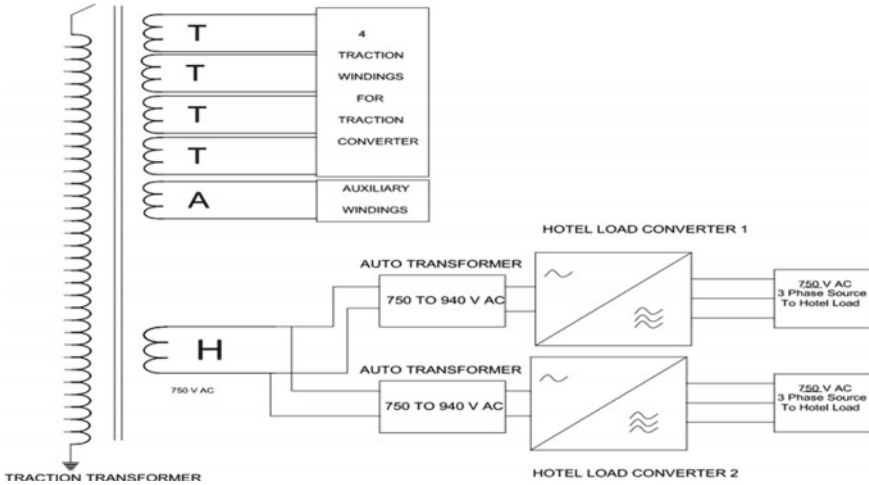


Fig. 4 Layout of HOG process [3]

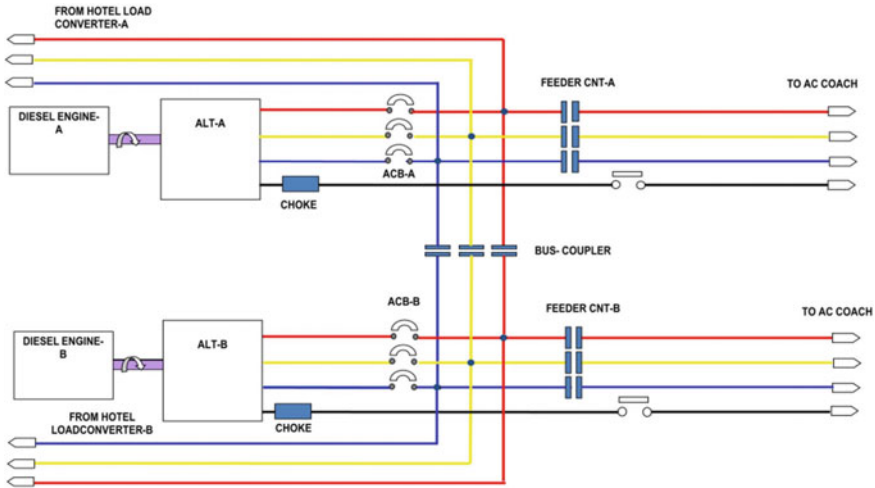


Fig. 5 Layout of generator car with HOG supply [3]

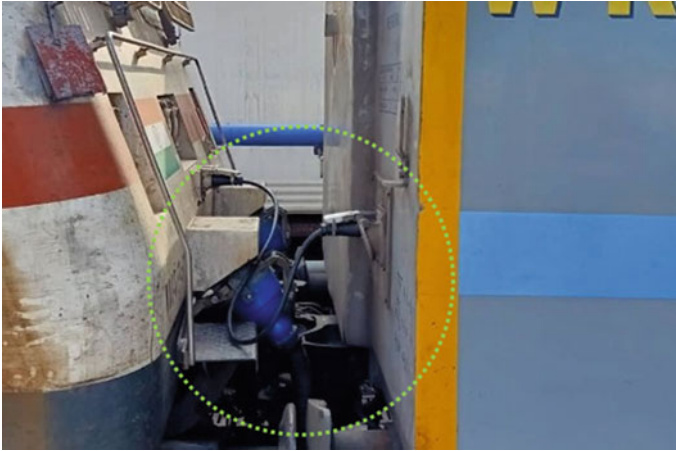


Fig. 6 HOG enabled electric locomotive (WAP 7) connected to power car using multi-unit connector

4 Photovoltaic Cell for Powering Electrical Units of LHB Coaches

India Railway attaches two generator cars at both the ends of LHBfied train. These cars consists of 3000 L capacity diesel tank which are fully filled before the commencing of journey. Only one generator car is used since the electricity generated by single alternator is enough to cater the electrical load of entire train, and the other is kept as a backup which can be used in accordance to the requirement [1–13]. But, during summer or if the train is fully air conditioned the consumption of diesel increases as in case of AC Duronto Express, Garib Rath Express, Vande Bharat Express, Rajdhani Express, Shatabdi Express, Tejas Express, and Humsafar Express (Fig. 7). Table 1 shows types of passenger LHB coaches used by Indian Railway. Table 2 shows all the types of electrical loads present inside LHB coaches.

The actual availability of area for mounting photovoltaic cell over the roof top is less as clearances has to be left for easy admittance for many purposes and RMPU unit (Roof mounted AC package unit) in respective non-AC and AC LHB coach.

Figures 8 and 9 depicts allocation of PV cells on four equal areas with alleys between them. The solar cell electricity generation will time and direction of travel dependent which will fluctuate accordingly. A sleeper class LHB coach fitted with two flexible solar panels is shown in Fig. 10. Figure 11 illustrates the electrical power supply system of an LHB coach (both AC and non-AC) assisted by photovoltaic cell.



Fig. 7 Different types of LHB coaches (for passenger) used by Indian Railways

Table 1 Types of passenger LHB coaches with class used by Indian Railways

Coach type	Class code	Sleeping/ Sitting capacity
AC 1st class	1A	24
AC two tier	2A	54
AC first cum two tier	1A/2A	30
AC three tier	3A	72
Sleeper class	SL	80
Executive chair car	EC	56
AC chair car	CC	78
Double-Decker AC chair car	CC	120
Second sitting	2S	108
Second class	UR/GEN	100
AC hot buffet car (Pantry car)	PC	–

Table 2 Types of electrical loads present inside LHB coach [1]

Hotel load equipment	Rating	Units	AC coach	Non AC coach	Pantry car
AC units	11,500 W	2	✓		
Deep freezer	500 W	1			✓
Emergency lamps	50	6	✓	✓	✓
Fan	60	30		✓	✓
Hot cases	500 W	3			✓
Lavatory lamp	20	4	✓	✓	✓
Night lamp	15 W	5	✓	✓	✓
Other loads	100	1	✓	✓	
Power socket for laptops and mobile phones	100 W	18	✓	✓	
Refrigerator	500 W	1			✓
Tube light (variant 1)	25 W	5	✓	✓	✓
Tube light (variant 2)	40 W	10	✓	✓	✓
Vacuum flush	50	4	✓	✓	✓
15 L water boiler	2000 W	1			✓
11 L soup warmer	500 W	1			✓

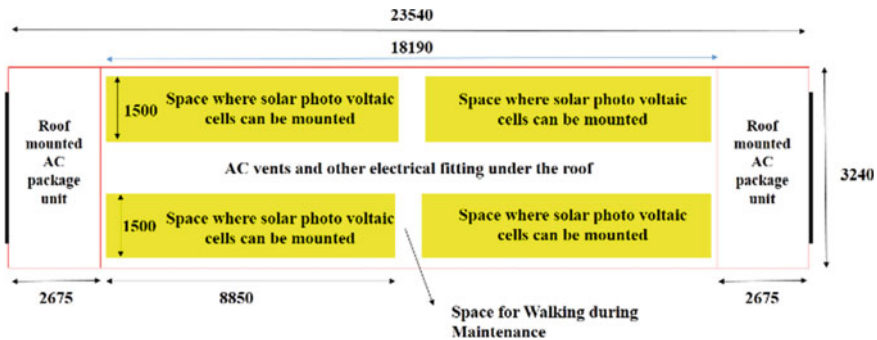


Fig. 8 Proposed design for fitting PV cell on AC LHB coach [1, 2] (dimensions are in mm)

5 Current Scenario of Solar Cell Assisted Power Supply in LHB Coaches in Indian Railway

The Research Design and Standards Organization (RDSO) reported that annually Rs. 80 lacs will be the cost for running hotel load of a 19 AC LHB coach train using HOG technique which is Rs. 100 lacs less than running the same train with EOG system. Hence, installation of PV cell on the LHB coaches can help in saving a lot of money since it is a one-time investment.

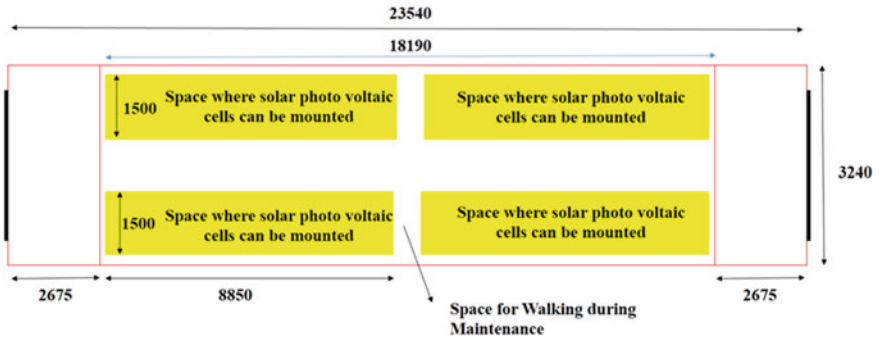


Fig. 9 Proposed design for fitting PV cell on non-AC LHB coach [1, 2] (dimensions are in mm)



Fig. 10 A sleeper class LHB coach fitted with two flexible solar panels

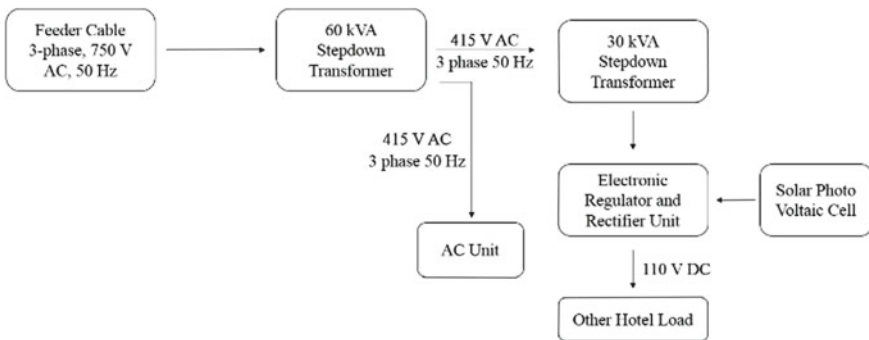


Fig. 11 Power supply diagram of an LHB coach with solar photovoltaic cell [1]

A research team from Indian Institute of Science (IISc), Bangalore has reported about the electricity savings of 7200 units annually per coach. They also stated if solar panels are mounted on all the coaches used by Indian Railway, they can yield 450 million units of electricity thus saving 10.8 crore liters of diesel. In addition to that carbon dioxide emission will be reduced by around 3 lakh tonnes. Return of investment can be gained within 2 year 6 month after proper operation and maintenance. Annually, more than 90,000 L units of diesel will also be saved on a train.

The team from IISc, Bangalore travelled in LHB coach rakes of Chennai-Coimbatore Shatabdi Express from 24 to 26th June 2015, Chennai Mysore Shatabdi Express from 27 to 29th June 2015 and Chennai-Bangalore Double Decker Express on 1st July 2015. They chose those days when sunshine was meagre for conducting the investigation to comprehend enactment in the worst-case consequence. They measured the achievability and capability of generation of electricity by a moving train mounted with solar panels where they considered the influence of aspects such as curves in railway track, sunshine, number of scheduled and unscheduled halts, and train speed. Since all the three express trains were have only sitting class (AC and non-AC), a distinct sleeper class LHB coach was mounted with two number of flexible 180 W solar PV panels at the Integral Coach Factory, Chennai, Tamil Nadu, India and attached to Chennai-Coimbatore Shatabdi Express during the testing day.

Three years after the studies conducted by IISc, Bangalore, Railway officials noted that putting into practice of this venture on broader scale could offer an incentive to local solar panel manufacturing industry under 'Make in India' initiative. Finally, Northern Railways Division of Indian Railways launched its first solar-power assisted diesel electrical multiple unit (DEMU) passenger train on July 14, 2018, originating from Delhi Sarai Rohilla railway station, New Delhi to Farukhnagar railway station, Haryana as shown in Fig. 12. Total six coaches were fitted with 16 nos. of solar panel where each panel can produce 300 Wp around Rs. 54 lacs. The solar panels have the capacity of about 17 units power generation in single day for powering electrical equipment fitted in the coach.

Similarly, Southern Railway Division of Indian Railways fitted six non-AC coaches of Coimbatore-Mayiladuthurai Jan Shatabdi Express train (Fig. 13) with PV panels in December 2018, with the cost of Rs. 15.2 lakh where the panels provided 4.8 kW to each coach.

6 Conclusions

Various conclusions can be drawn after investigating the feasibility and scope of using solar PV cell on LHB coach. Photovoltaic cell which will be used in LHB coach will be advantageous for Indian Railways as a lot of money can be saved which was earlier spent on buying diesel fuel. This venture can help in recovery of the investment done in solar PV cell can be mended in 3 years. The Research Design and Standards Organization (RDSO) reported that annually Rs. 80 lacs will be the cost for running hotel load of a 19 AC LHB coach train using HOG technique which



Fig. 12 India's 1st solar-power assisted DEMU train



Fig. 13 PV cell mounted on the roof of Coimbatore-Mayiladuthurai Jan Shatabdi Express train

is Rs. 100 lacs less than running the same train with EOG system. Hence, installation of PV cell on the LHB coaches can help in saving a lot of money since it is a one-time investment.

It can be noteworthy that the trains which are completing their major part of their journey in the daylight will be more beneficial by the use of this technology. Though those trains which are covering major part of their journey at night can also take advantage of the PV cell as during the daylight will be stranded in a station for its cleaning and maintenance before its next trip where it can charge its batteries whole day in the daylight. As Indian Railway has large fleet of train running in different parts of the country, the PV cell will not be ideal to those places where sunshine is very less throughout the year e.g., Jammu and Kashmir valley; Himachal Pradesh where snow fall occurs; Northeast Frontier Railway division where rainfall occurs. Though more research can be done for tapping the maximum amount of sunlight via PV cell so that it can be used by the LHB coaches of the Indian Railway.

Acknowledgements The authors acknowledge Senior Divisional Mechanical Engineer, Diesel Locomotive Shed, Bondamunda, Rourkela, Odisha and Dy. Chief Mechanical Engineer, Carriage Repair Workshop, Mancheswar, Bhubaneswar, Odisha for their valuable suggestions for completion of this case study.

References

1. Vasisht MS, Vishal C, Srinivasan J, Ramasesha SK (2014) Solar photovoltaic assistance for LHB rail coaches. *Curr Sci* 107:255–259
2. Vasisht MS, Vishal C, Srinivasan J, Ramasesha SK (2017) Rail coaches with rooftop solar photovoltaic systems: a feasibility study. *Energy* 118:684–691
3. Agarwal NH, Pimple BB (2015) Solar photovoltaic array based brushless DC motor for fans in Indian Railways using maximum power point tracking algorithm. In: 39th National systems conference (NSC), Noida, pp 1–6. <https://doi.org/10.1109/NATSYS.2015.7489122>
4. Mate A, Katekar BVP, Bhatkulkar CHS (2017) Performance investigation of solar still for batteries of railway engine, Indian Railways, at Ajni Loco Shed, Nagpur. In: International conference on advances in thermal systems, materials and design engineering (ATSMDE 2017). <https://ssrn.com/abstract=3101269>
5. George N, Chowdhury SD (2018) Roof-top solar power augmentation to auxiliary supply of passenger train. In: 2018 IEEE PES/IAS PowerAfrica, Cape Town, pp 793–798. <https://doi.org/10.1109/PowerAfrica.2018.8521156>
6. Rohollahi E, Abdolzadeh M, Mehrabian MA (2014) Prediction of the power generated by photovoltaic cells fixed on the roof of a moving passenger coach: a case study. In: *Proc Inst Mech Eng Part F: J Rail and Rapid Transit* 229:830–837
7. Thelkar R, Veerasamy B, Mekonnen T, Ahmmed M, Alem A, Jote A (2016) Interfacing of regulator and rectifier unit with solar charge controller for optimal utilization of solar power on railway coaches. In: 2016 IEEE international conference on renewable energy research and applications (ICRERA), Birmingham, pp 730–735. <https://doi.org/10.1109/ICRERA.2016.7884430>
8. Alam M, Kumar K, Dutta V (2019) Design and analysis of fuel cell and photovoltaic based 110 V DC micro grid using hydrogen energy storage. *Energy Storage* 1(3):e60. <https://doi.org/10.1002/est.2.60>

9. Darshana MK, Karnataki K, Shankar G, Sheela KR (2015) A practical implementation of energy harvesting, monitoring and analysis system for solar photo voltaic terrestrial vehicles in Indian scenarios: a case of pilot implementation in the Indian Railways. In: 2015 IEEE international WIE conference on electrical and computer engineering (WIECON-ECE), Dhaka, pp 542–545. <https://doi.org/10.1109/WIECON-ECE.2015.7443989>
10. Kesari OP, Deo SK, Head on Generation (HOG)-a step towards energy efficiency. Research Designs and Standards Organization (RDSO). <https://rdso.indianrailways.gov.in/works/uploads/File/Paper%20on%20HOG.pdf>
11. Maintenance manual for AC LHB coaches, research designs and standards organization (RDSO) (2013), <https://rdso.indianrailways.gov.in/works/uploads/File/Maintenance%20Manual%20for%20AC%20LHB%20Coaches.pdf>
12. Maintenance manual for LHB Coaches, research designs and standards organization (RDSO) (2013), [https://rdso.indianrailways.gov.in/works/uploads/File/Maintenance%20Manual%20for%20LHB%20Coaches\(8\).pdf](https://rdso.indianrailways.gov.in/works/uploads/File/Maintenance%20Manual%20for%20LHB%20Coaches(8).pdf)
13. Bagal DK, Barua A, Jeet S, Giri A, Pattanaik AK, Panda SN (2021) Scope of using photo voltaic cell to power electrical units of air conditioned Linke Hofmann Busch (LHB) coaches used in Indian Railways. In: Advances in air conditioning and refrigeration. Lecture notes in mechanical engineering. Springer, Singapore. https://doi.org/10.1007/978-981-15-6360-7_37

Drilling Simulation of AA7075 T351 Graded Aluminium Alloy Using Deform-3D



Dilip Kumar Bagal, Siddharth Jeet, Abhishek Barua, Swastik Pradhan, Arati Rath, and Surya Narayan Panda

Abstract The article develops a three-dimensional drilling model using DEFORM-3D software based on the Usui Tool Wear model, the Johnson and Cook model and the Lagrangian approach. Thermal, structural and chip morphology analyses were performed in this section. The effect of output responses is examined through the lens of their simulation results. The workpiece is made of AA7570 T351 Aluminium alloy with machining type and the drill bit is made of tungsten carbide (WC) with a diameter of 10 mm. Due to its high strength and resistance to corrosion, this alloy is widely used in the aerospace and biomedical equipment manufacturing industries. Thermal analysis reveals that the tool's maximum temperature is 254.8 °C, while the highest temperature is 273.1 °C in the case of AA7075 T351 graded alloy workpiece.

Keywords Aluminium alloy · Drilling · Deform 3D

D. K. Bagal

Department of Mechanical Engineering, Government College of Engineering, Kalahandi, Bhawanipatna, Odisha, India

S. Jeet · A. Barua

Department of Mechanical Engineering, Centre for Advanced Post Graduate Studies, BPUT, Rourkela, Odisha, India

S. Pradhan (✉)

School of Mechanical Engineering, Lovely Professional University, Phagwara, Punjab, India
e-mail: swastik.22644@lpu.co.in

A. Rath

School of Computer Engineering, Kalinga Institute of Industrial Technology, Bhubaneswar, Odisha, India

S. N. Panda

Department of Production Engineering, Birsa Institute of Technology, Sindri, Dhanbad, Jharkhand, India

1 Introduction

In recent years, finite element analysis has become the primary technique for modelling metal cutting operations. Simulation of machining test using finite element analysis is especially essential owing to time and expense consuming in the real cutting test., therefore it is chosen over experimental work. Moreover, the findings acquired from the finite element analysis remain near to the results obtained from the experimental study. Finite element approach has proven to be an efficient methodology for studying chip formation processes and in forecasting process variables such as temperatures, pressures and stresses, etc. [1]. The aim of this study was to evaluate the effect of drilled suction holes on a 7075 graded Aluminium alloy. The effects of the suction holes were investigated using FE modelling by evaluating the produced stresses surrounding the holes' locations as well as the stress distribution. More than 30 years ago, the finite element method (FEM) was applied to machining. From basic two-dimensional orthogonal cutting simulation analysis in the beginning to three-dimensional orthogonal and oblique cutting simulation today and from simple parameter setup to multiple parameter setting, etc. In recent years, several software programmes for simulating cutting processes have been developed, including ANSYS, DEFORM and ABAQUS. DEFORM-3D is a finite element simulation software that is based on a process simulation system. It produces functions for modelling, shape, heat conductivity and forming equipment, among others. DEFORM-3D provides numerous benefits, including high robustness, simplicity of use and a powerful simulation engine [2].

Pawar et al. presented a study of the diamond tool drilling process as applied to Ti-6Al-4V titanium alloy and Al6061 Aluminium alloy materials using Deform-3D software. While titanium alloys are extensively used in biomedical applications, Aluminium alloys are mostly used in the automotive and aerospace sectors. The drilling process was modelled and simulated using finite element analysis and DEFORM 3D software to determine the stress and temperature that occurred throughout the operation. The titanium alloy has a maximum effective stress and temperature of 1500 Mpa and 618 °C, respectively, according to the simulated findings [3].

The FDS forming process was successfully simulated using an improved remeshing technique for a DP590/Al6061-T6 lap structure by Liu et. al. [4]. Remeshing effectively solves the meshing problem of significant mesh deformation during conventional finite element simulation. The petal and bushing sizes are more than 95% accurate, with a peak temperature inaccuracy of 2 °C.

Aluminium alloy AA7075 is mainly used to manufacture critical components for aerospace, construction and automotive applications. Despite the AA7075 alloy's excellent machinability, hole quality may vary depending on the tool shape and drilling settings used. Yaşar studied the impact of various feed rates and cutting speeds on surface roughness (Ra) and thrust (Fz). Thrust force calculations were carried out numerically using the Third Wave Advant Edge finite element simulation programme. The optimal settings for thrust force generation and surface roughness are as follows:

0.05 mm/rev feed rate, diamond-coated WC drills, 40 m/min cutting speed and 140° drill tip angle. The improvement was made by using the grey relation analysis (GRA) method. The optimal parameter was 0.236 and the recovery percentage was 39.86% [5].

Kaneriya and Sharma conducted experiments in order to decrease the temperature generated in the drill tool during dry drilling of AISI 304 austenitic stainless steel (AISI 304). On a vertical machining centre (VMC 1050) machine with a maximum spindle speed of 8000 revolutions per minute and an electric drive motor of 15.8 kW, the tests were carried out. Drilling parameters are being studied in order to reduce the temperature of the drill tool bit. Response surface methodology (RSM) was used to optimise drilling parameters such as feed rate and spindle speed in order to minimise temperature while simultaneously increasing material removal rate (MRR). The K20 Solid Carbide drill tool has a longer tool life when compared to HSS and Cobalt coated HSS drill tools in this study. For dry drilling of austenitic stainless steel AISI 304, a temperature of 190 °C was discovered to be the optimum [6].

Attanasio et al. investigated a finite element analysis (FEA) model for simulating tool wear when drilling nickel-based alloys, namely Inconel 718. Tool wear is produced by a variety of processes (adhesion, abrasion, erosion, diffusion, corrosion and fracture, to name a few) that vary according to the cutting parameters used (cutting speed, velocity, feed rate, etc.). An appropriate subroutine that takes tool geometry updates into account has been designed and implemented in the SFTC DEFORM-3D finite element analysis software. As a result, they will be able to mimic a variety of cutting circumstances in order to investigate their impact on human body tissue [7].

Bagci and Ozelik monitored drill temperatures using thermocouples inserted into the coolant of carbide drills covered with TiN/TiAlN. Drilling is a highly nonlinear operation and the cutting temperature at the tool-chip interface is critical because it has a direct effect on workpiece integrity, tool wear, hole diameter and cylindricity. In successively dry drilling, a high degree of concordance between measured and analysed temperature results was observed. The experimental findings were compared to the FEM results based on the Lagrange code [8].

Mediouni et al. created a three-dimensional (3D) elastic–plastic acetabular bone model and used a variety of simulated drilling techniques using finite element modelling (FEM). The FEM findings demonstrate unequivocally that both the depth of drilling and the drill speed have a substantial impact on the temperature generated during drilling operations. Reduced feeding speed results in a decrease in the temperature of the bone. This research is the first step in assisting any surgeon who drills bone to determine the optimal pressure to apply and the drill speed to use [9].

Gao et al. investigated the drilling mechanism of general-purpose twist drills using FEM analysis through Deform-3D software to determine how they work. The axial force and torque rise in direct proportion to the increase in diameter, speed and feed rate. It had been anticipated that the drill temperature field and the wear of the drill tip would occur. The wear is particularly severe in the area just in front of the primary cutting edge and the chisel edge [10].

Giasin et al. conducted experiments to determine the effect of machining settings on the quality of holes and cutting forces while drilling Al2024-T3 aerospace alloy.

Drilling at 100 and 300 mm/min feed rates with spindle speeds of 1000, 3000 and 6000 rpm are suggested for creating holes with less surface roughness, departure from the nominal hole size, circularity error and burrs. The study's findings indicate that cutting parameters significantly affect cutting forces and examined hole quality metrics [11].

Glaa et al. studied the effects of regeneration chatter and cutting process dampening during a drilling operation using a numerical approach. The method identifies numerically the three-dimensional evolution of the cutting force components and cutting torque generated by the drilling process of a titanium alloy. The effectiveness of the model and algorithm is verified by good agreement between simulation results with those of cutting tests under different cutting conditions. More study is being done on predicting cutting forces during titanium drilling to enhance the material's machinability and tool wear. Researchers have worked hard to better understand drilling and develop theoretical cutting force models to anticipate and replicate the event. Experiments on a vertical machine for the titanium alloy Ti6Al4V confirm the model's efficiency. The measurement errors between maximum values of thrust cutting force and drilling torque are less than 10% for thrust cutting force and 7% for drilling torque [12].

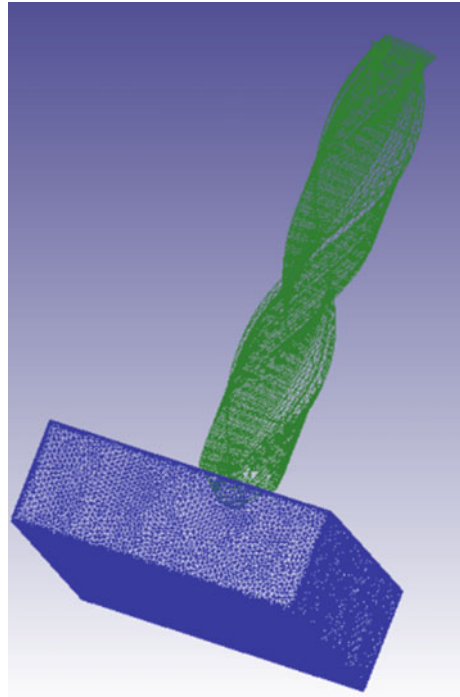
2 Materials and Methods

In the pre-processor stage of DEFORM 3D software, the workpiece of Aluminium alloy of graded 7075 T351 was considered for the analysis which has plastic properties and has dimension of diameter as 20 mm and thickness as 5 mm. The cutting speed and feed rate were chosen as 1000 mm/s and 0.25 mm/rev correspondingly. The coolant of surrounding was chosen as air and convection coefficient of air is assumed as 0.02 N/s/mm/°C. The work item is considered as plastic and tool, i.e. drill bit as rigid body during drilling operation. The shear friction factor coefficient of 0.6 is chosen for the tool-workpiece contact during simulation. The heat transmission coefficient was estimated as 45 N/s/mm. A tetrahedral shape element with size ratio of 1:4 is chosen for tool while similar shape element of size ratio of 1:7 is considered for workpiece [13]. The total number of components for workpiece and tool with their appropriate size ratio was set as 5 lakhs and 3 lakhs correspondingly which is displayed in Fig. 1.

For the simulation run, number of steps was set to 10,000 and steps to store on hard drive as 25 steps with full drill depth. For tool wear modelling, The Usui Tool Wear model was studied where the wear rate is the function of pressure, velocity and temperature and the generalised equation of it is provided below:

$$\frac{dw}{dt} = A\sigma_u V_s e^{-\left(\frac{B}{T}\right)} \quad (1)$$

Fig. 1 Mesh for both considered workpiece and drill bit



where A and B are constant terms and the values of A and B for this analysis were taken as 1e-5 and 1000, respectively [1].

DEFORM 3D utilises Lagrangian meshing because it has the capacity of remeshing at each and every step when deformation happens in drilling simulation. Lagrangian meshing offers the benefit of resuming the simulation from the place where the model stopped if the model pauses at any circumstance [14]. The geometry of drill bit is illustrated in Fig. 2 and matching values of parameters to construct the drill bit in DEFORM 3D software are calculated in Table 1.

The generalised Johnson and Cook model is considered for the flow stress in the simulation and its mathematical model is provided as follows:

$$\bar{\sigma} = (A + B\bar{\epsilon}^n) \left(1 + C \ln \left(\frac{\dot{\bar{\epsilon}}}{\dot{\bar{\epsilon}}_0} \right) \right) \left(\frac{\dot{\bar{\epsilon}}}{\dot{\bar{\epsilon}}_0} \right)^\alpha (D - E(T^*)^m) \tag{2}$$

where $T^* = \frac{(T - T_{room})}{(T_{melt} - T_{room})}$ and $D = D_0 e^{|k(T - T_b)^\beta|}$

The parameters of generalised Johnson and Cook (J-C) model are listed in Table 2 for the modelling of drilling operation for the material of Aluminium alloy of graded 7075 T351.

Fig. 2 Parameters of drill bit for simulation in deform 3D

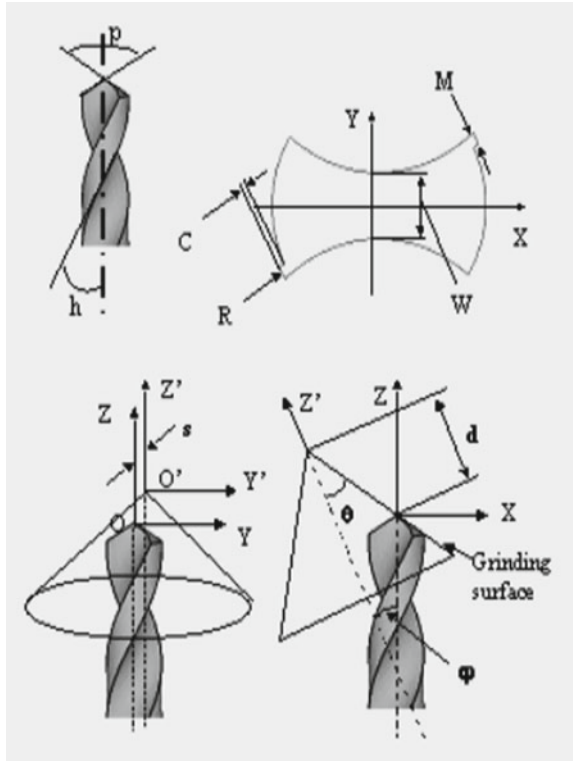


Table 1 Dimension of drill bit used for simulation

<i>Drill geometry parameters</i>		
R	Drill radius	5 mm
W	Web thickness	1.8 mm
h	Helix angle	30°
p	Point angle	118°
M	Margin	0.4 mm
C	Clearance	0.2 mm
<i>Grinding cone parameters</i>		
d	Shift	5.5 mm
s	Shift	1 mm
θ	Cone angle	30°

3 Results and Discussions

Figures 3 and 4 illustrate the flow stress data with graph at constant strain rate and temperature, respectively for the assumed Aluminium alloy as a workpiece.

Table 2 Parameters of Johnson and Cook model used in the simulation of drilling process

Parameter	Value
<i>A</i>	527
<i>B</i>	575
<i>C</i>	0.017
<i>D</i> ₀	1
<i>E</i>	1
<i>n</i>	0.72
<i>m</i>	1.61
α	0
β	0
$\dot{\epsilon}_0$	1
<i>T</i> _{room}	20
<i>T</i> _{melt}	635
<i>T</i> _b	20
<i>k</i>	0

The temperature of the room was assumed to be 20 °C throughout the entire simulation in the DEFORM 3D software. Figure 3 shows a temperature range of 20–630 °C with a constant strain rate of 1 and Fig. 4 shows a temperature range of 0 to 4 °C with a constant strain rate of 4. Figure 3 shows a temperature range of 20–630 °C with a constant strain rate of 1 and Fig. 4 shows a temperature range of 0 to 4 °C with a constant strain rate of 4.

Before the drill bit disintegrates into the Aluminium alloy workpiece, the initial velocity vectors of the drill bit are depicted in Fig. 5. Transparent workpieces are used in this illustration to allow for better visualisation of the working drill bit and workpiece set up.

At step number 7838, where chips are flown outwards from the centre of the workpiece, as depicted in Fig. 6, the temperature distribution in the workpiece is shown. Figure 7 depicts the temperature distribution of the drill bit at the step number 7852, which is similar to the previous figure. Figure 7 shows that the drill bit’s maximum temperature was reached at the end portions of the tool’s web thickness, which is consistent with previous findings.

Figure 8 depicts the total displacement of the drill bit in millimetres (mm) during the post-processing stage, with a maximum value of 18 mm and an average value of 1.10 mm. Figure 9 depicts the total velocity of a drill bit made of WC material, with the maximum total velocity of a drill bit reaching a value of 5008.2 mm/s at the extreme end of the range of values. Figure 10 depicts the thermal plot of a drill bit after simulation, with the maximum temperature of the tool reaching 254.8 °C at the time of the simulation.

Figures 11 and 12 depict the total displacement and velocity of the workpiece when the circumferences of the surrounding boundary circumferences were assumed to be

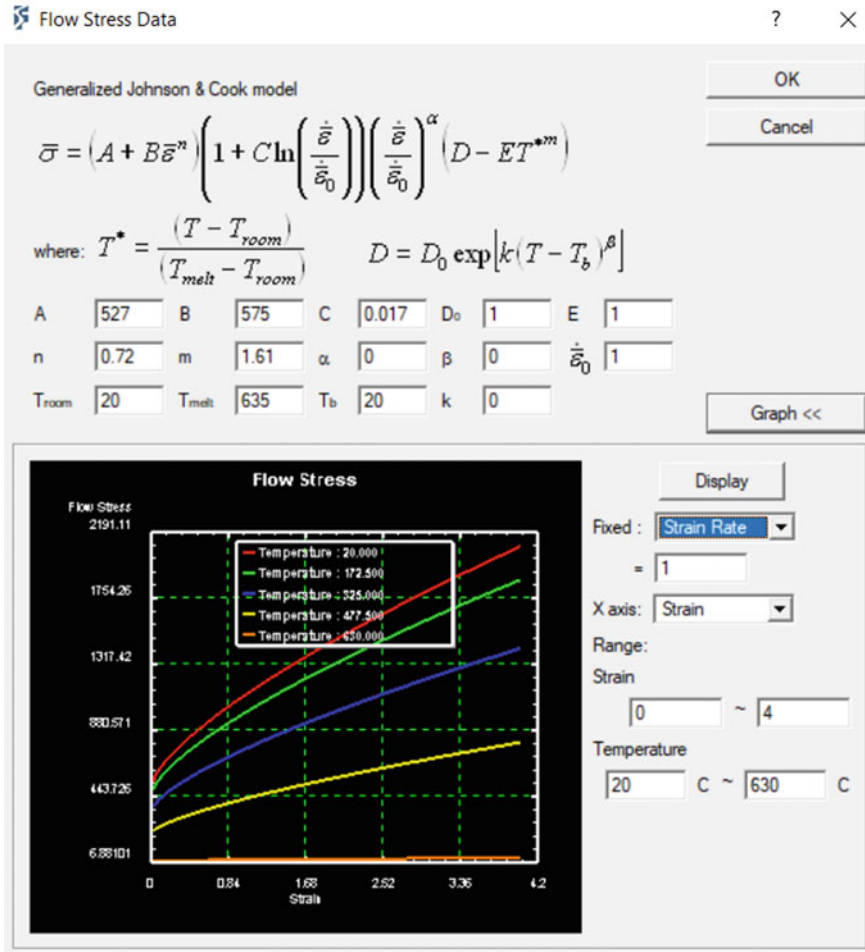


Fig. 3 J–C model flow stress data with graph at constant strain rate for AA7075 T351 material

constant throughout the simulation. Figure 11 shows that the total displacement of the workpiece was 19.1 mm as a result of the pressure applied by the drill bit during operation, with the average value of total displacement being only 1.3 mm over the course of the simulation. Additionally, the total velocity plot of the workpiece is depicted in Fig. 12; in this plot, the peak value of the workpiece velocity increased to 4907.6 mm/s and the average value of 267.6 mm/s was obtained throughout the entire simulation of drilling operation. As shown in Fig. 13, the effective strain of the workpiece is 11.2 mm/mm at its highest point, with an average of 2.1 mm/mm at its lowest point.

Using the measurement option in the DEFORM 3D software, the width of chips of Aluminium alloy graded 7075 T351 was measured. The results are shown in Fig. 14,

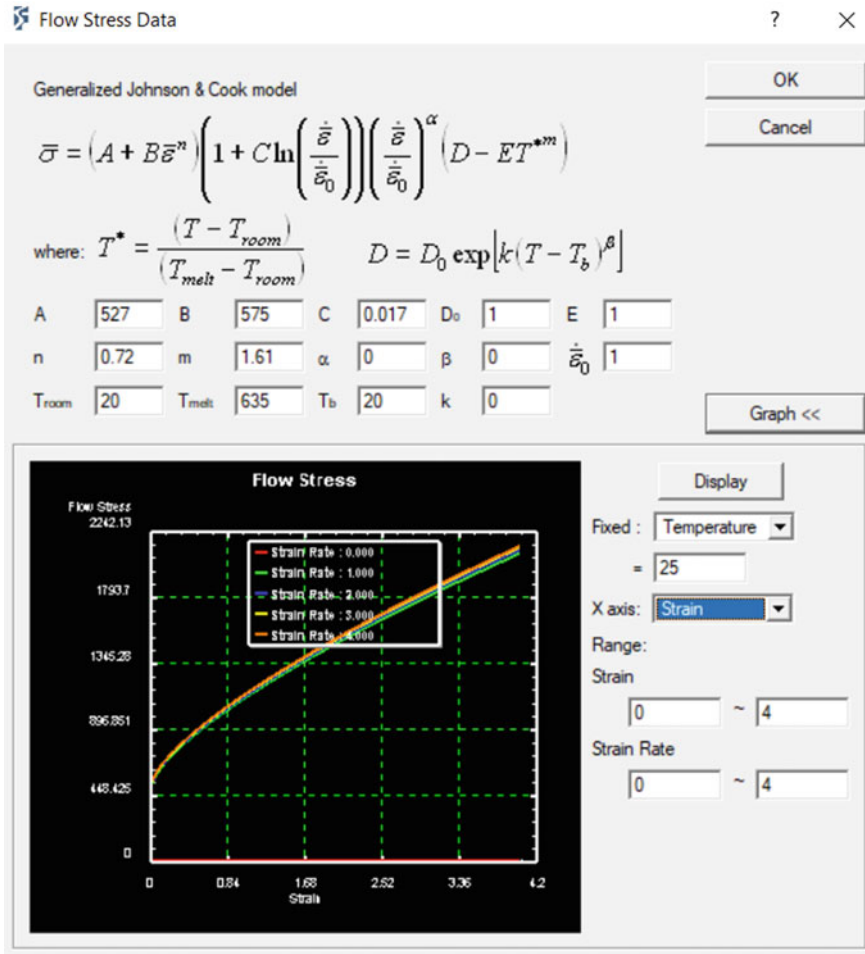


Fig. 4 J-C model flow stress data with graph at constant temperature for AA7075 T351 material

where the lowest and maximum chip width values were determined as 0.76359 mm and 1.59188 mm, respectively. Additionally, the thickness of the workpiece chip was measured and determined to be 0.412254 mm, which is very close to the width value of 0.835617 mm, as seen in the plotted values in Fig. 15.

Furtherly, the thermal analysis is done on the AA7075 T351 alloy workpiece where the maximum value of temperature is at 273.1 Degree Celsius and have average value is 63.9 °C which is shown in Fig. 15. Figures 16 and 17 illustrates the temperature distribution of workpiece throughout the simulation where it can be seen that the temperature is highest at the chip-tool interface and the value of temperature decreases along the chips of workpiece.

Fig. 5 Initial velocity vectors of drill bit before dispersion

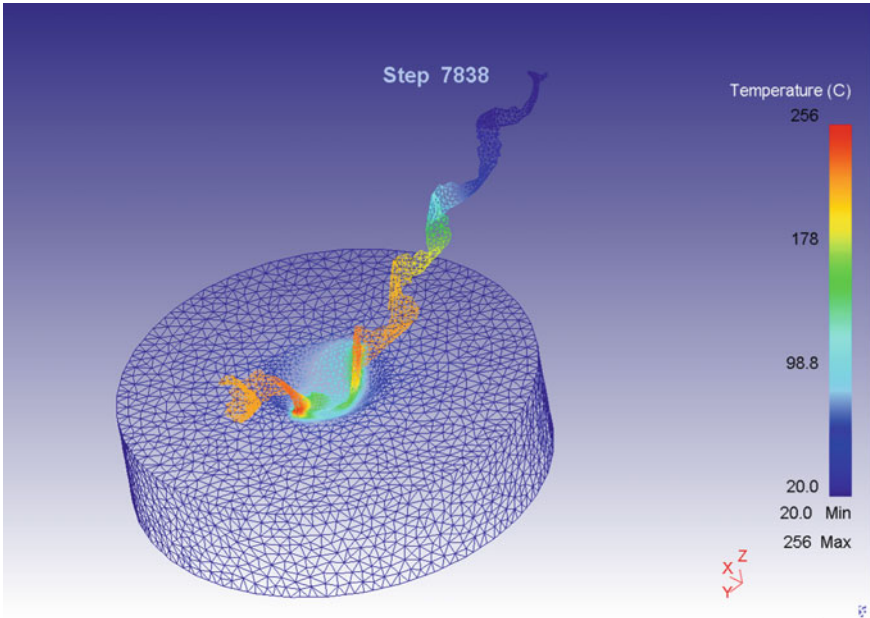
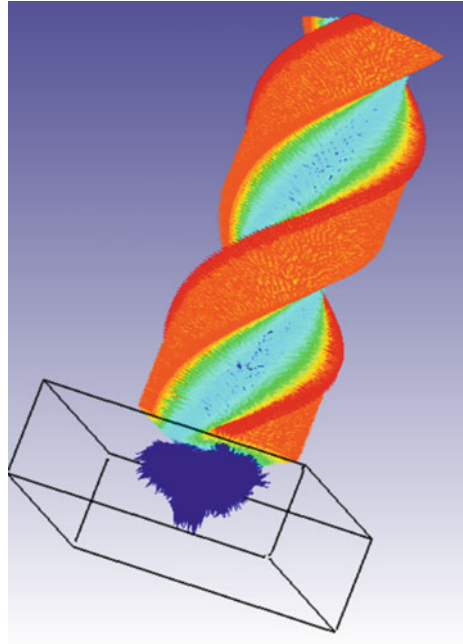


Fig. 6 Temperature distribution in the workpiece

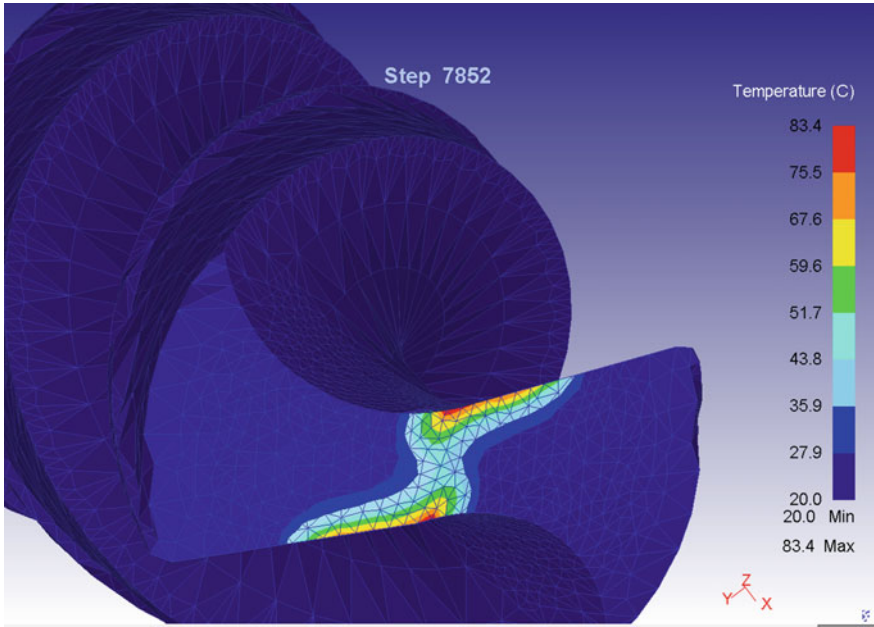


Fig. 7 Temperature distribution in the drill bit

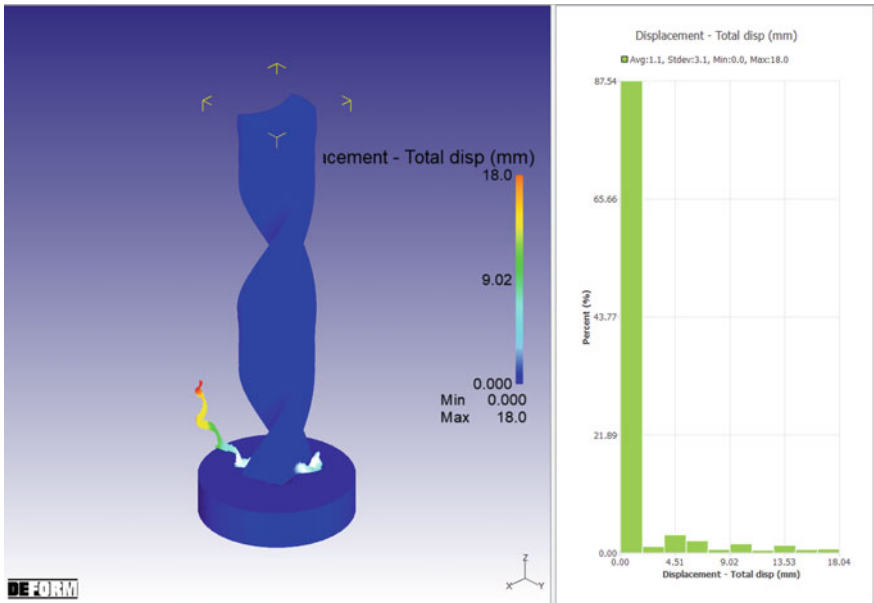


Fig. 8 The total displacement of the drill bit after simulation

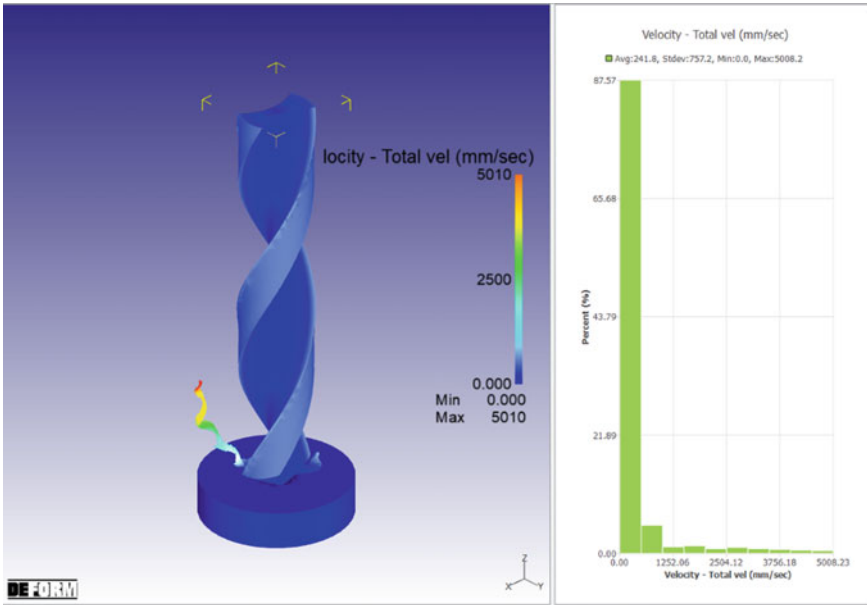


Fig. 9 The total velocity of the drill bit after simulation

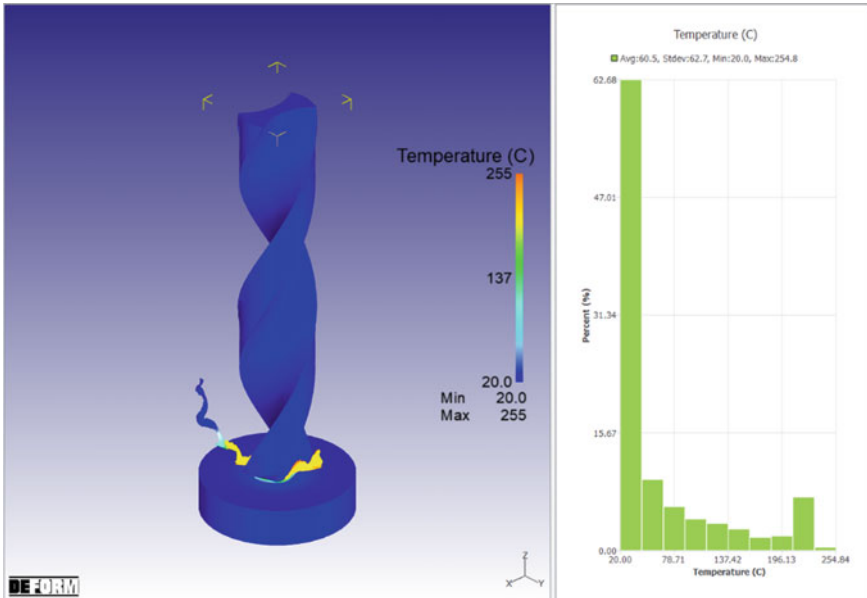


Fig. 10 The temperature distribution of the drill bit after simulation

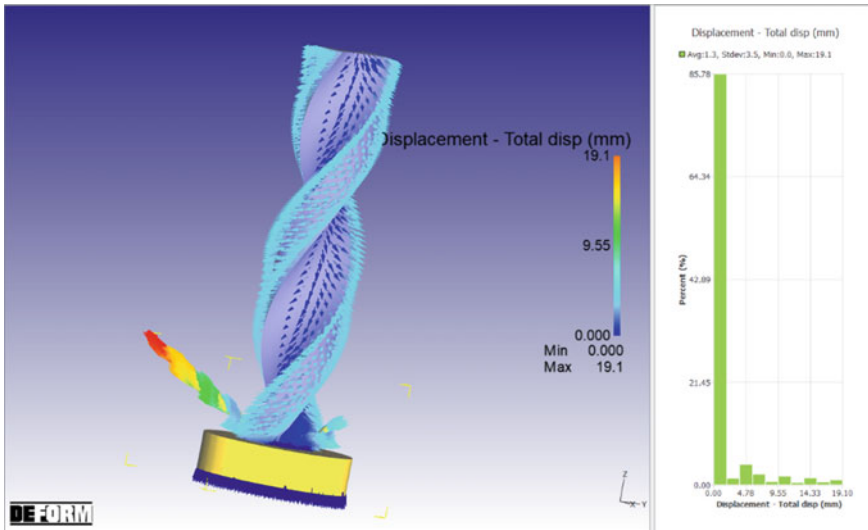


Fig. 11 The total displacement of the workpiece after simulation

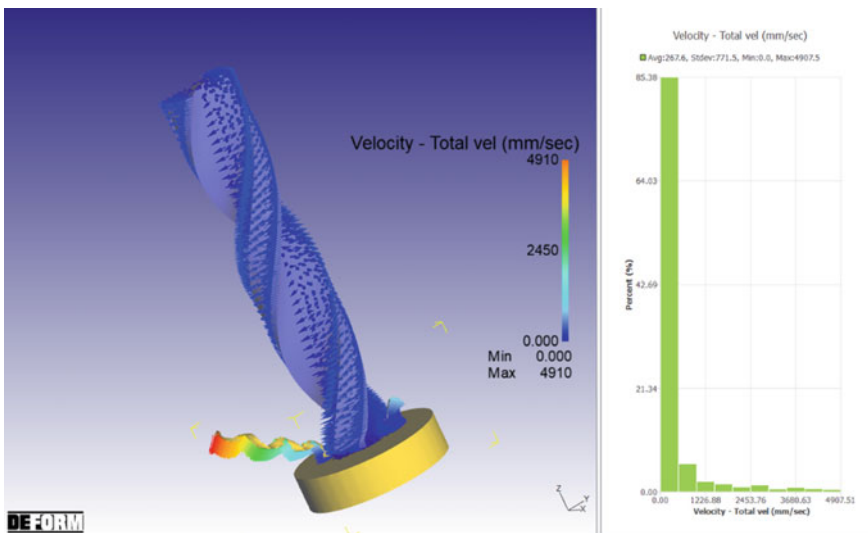


Fig. 12 The total velocity of the workpiece after simulation

The effective, mean, max principal and min principal stress of workpiece is shown in Figs. 18, 19, 20 and 21 where on the right side the corresponding average, standard deviation, minimum and maximum value is given. Again, the tension in X, Y and Z axis directions is shown in Figs. 22, 23 and 24. Lastly, the stress on XY, YZ and ZX planes is shown in Figs. 25, 26 and 27.

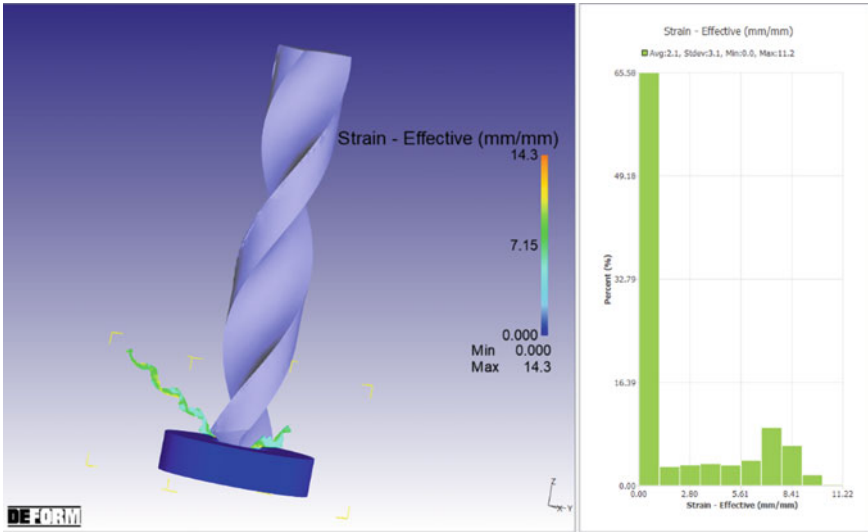


Fig. 13 The effective strain of the workpiece after simulation

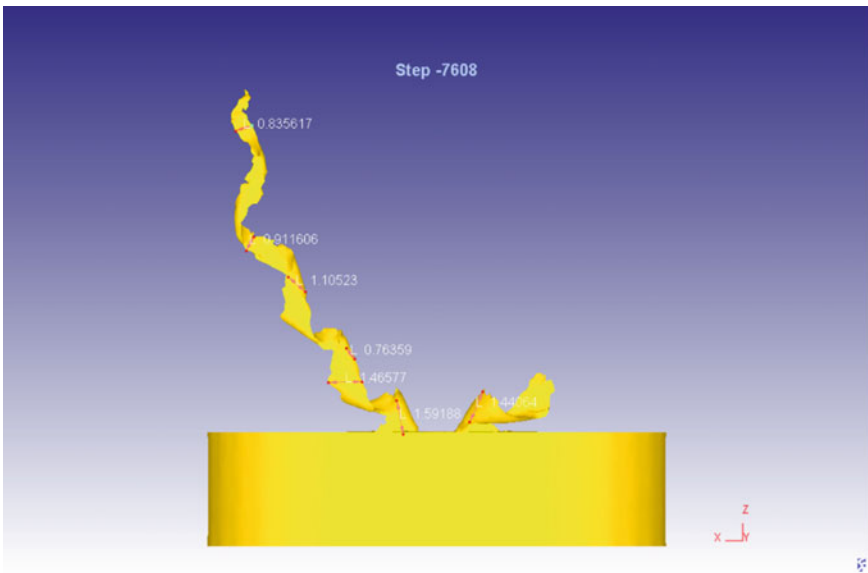


Fig. 14 The width of chips of the workpiece

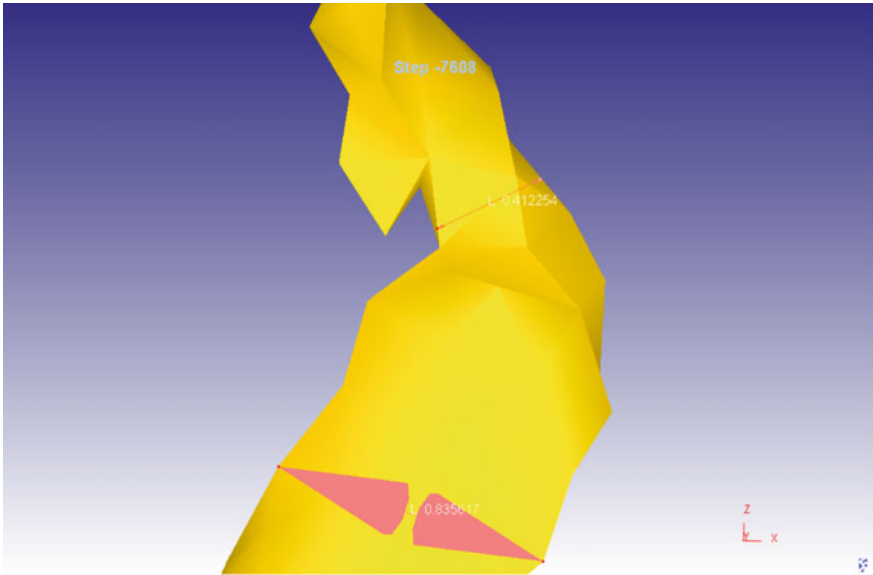


Fig. 15 The thickness of chips of the workpiece

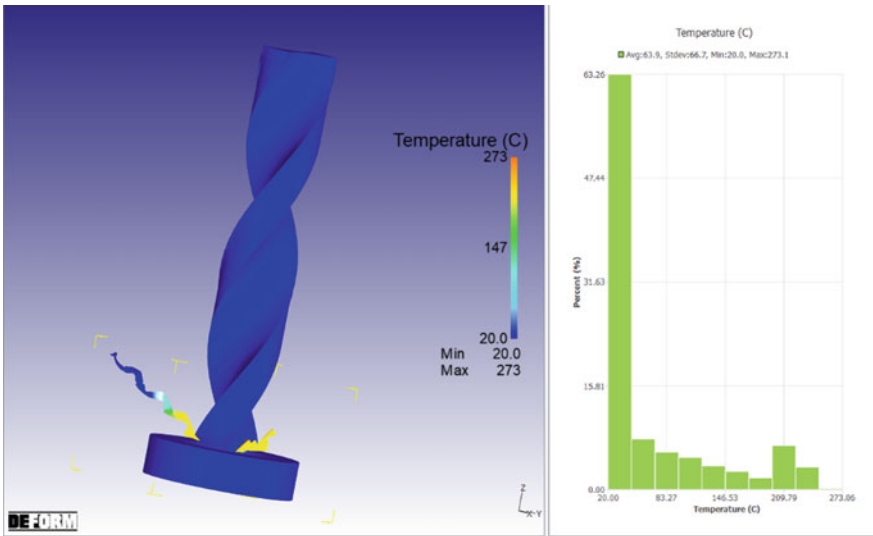


Fig. 16 Temperature distribution of workpiece after simulation

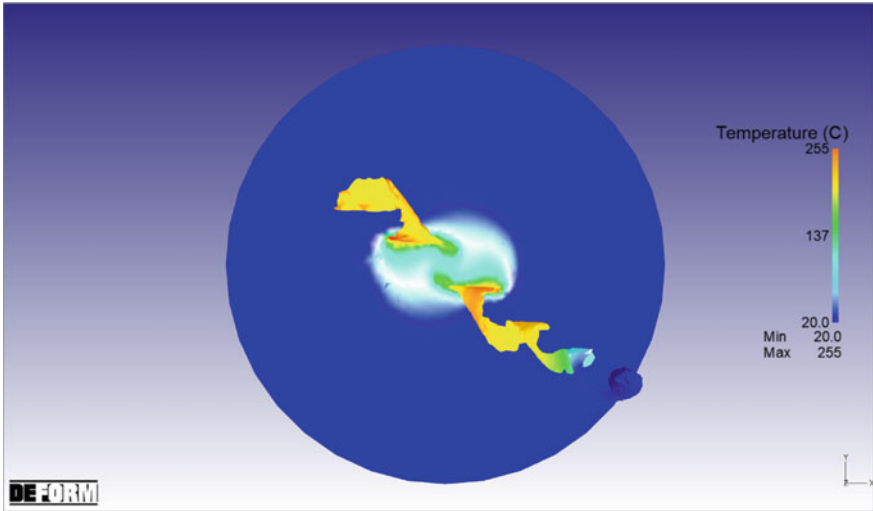


Fig. 17 Temperature distribution of workpiece during simulation

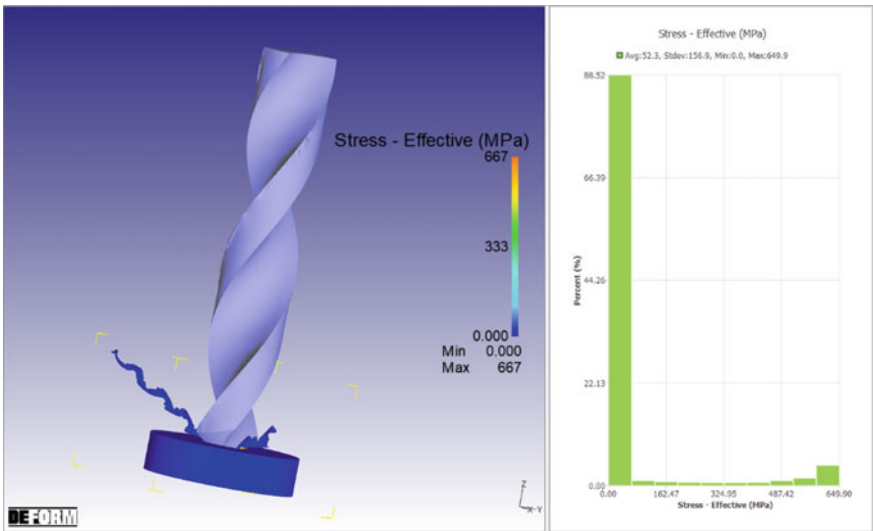


Fig. 18 Effective stress of workpiece after simulation

4 Conclusion

The present study witnessed the three-dimensional modelling of drilling by employing DEFORM-3D platform. There are different approaches, i.e. Usui Tool Wear model, the Johnson and Cook model and the Lagrangian approach are used for

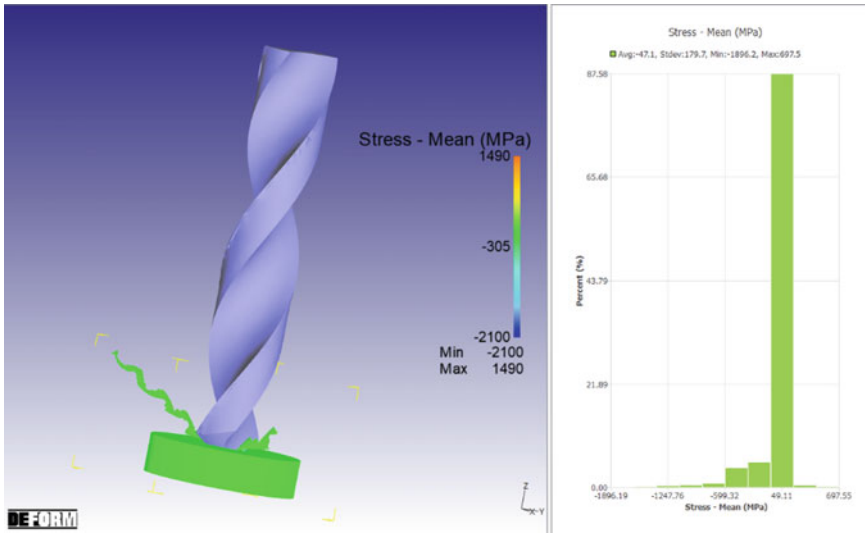


Fig. 19 Mean stress of workpiece after simulation

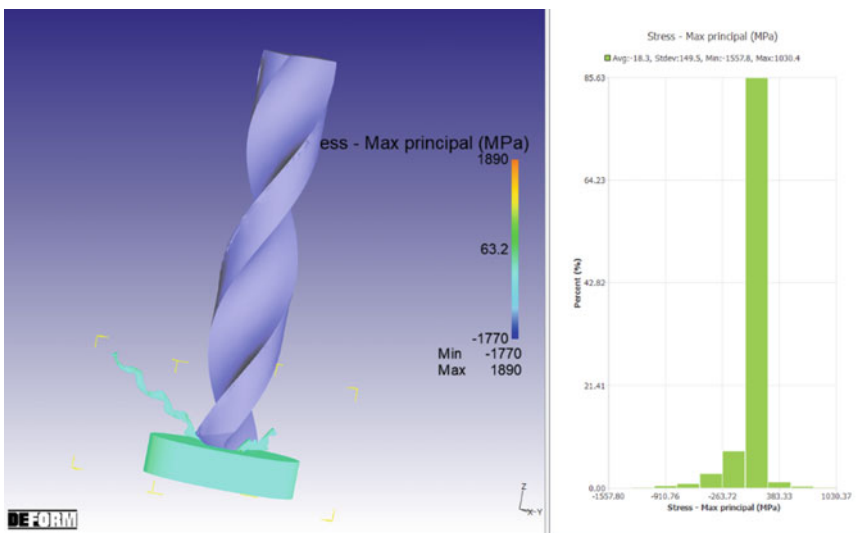


Fig. 20 Maximum principal stress of workpiece after simulation

predicting the thermal, structural and chip morphology of AA7570 T351 Aluminium Alloy plate drilled using tungsten carbide drill bit. Important conclusions were drawn based on the DEFORM-3D outputs.

The temperature distribution of the drill bit at the step number 7852 was maximum at the end portions of the tool’s web thickness which was about 254.8 °C. Maximum

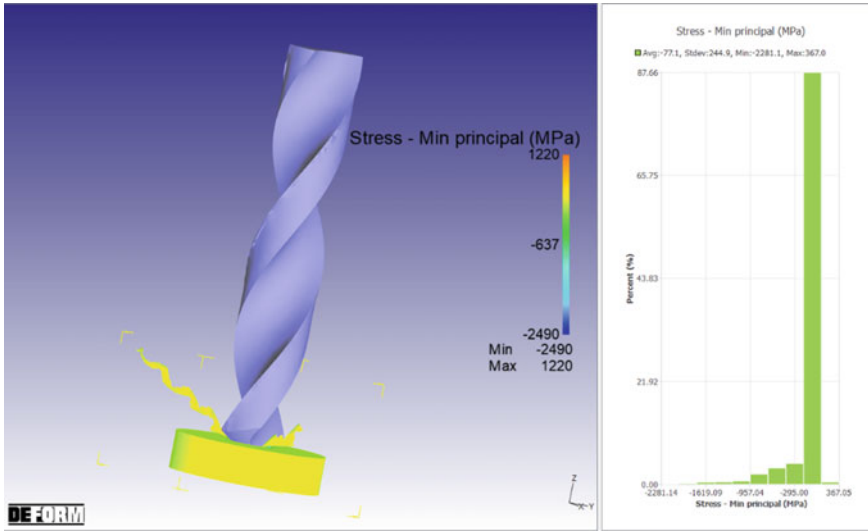


Fig. 21 Minimum principal stress of workpiece after simulation

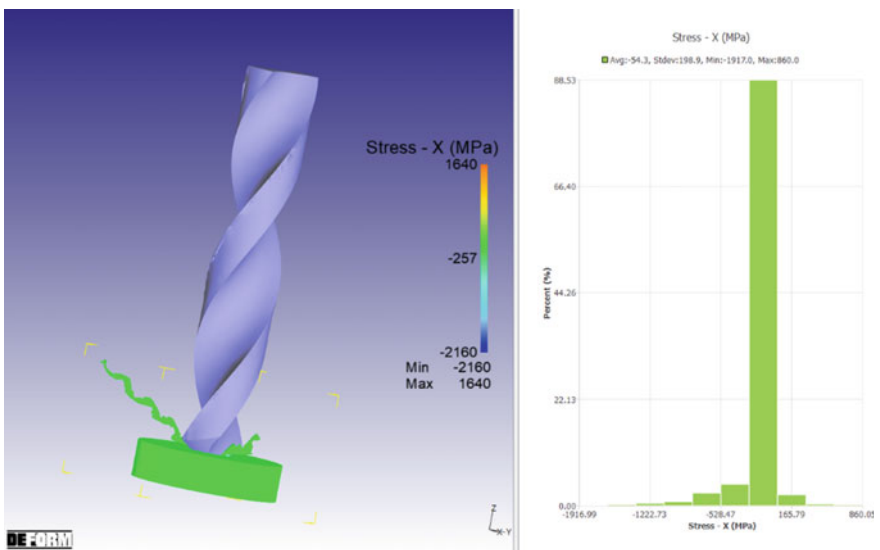


Fig. 22 X-axis stress of workpiece after simulation

velocity of drill bit made of WC material was reached to 5008.2 mm/s at the extreme end of the range of values.

Total displacement of the workpiece was 19.1 mm as a result of the pressure applied by the drill bit during operation, with the average value of total displacement

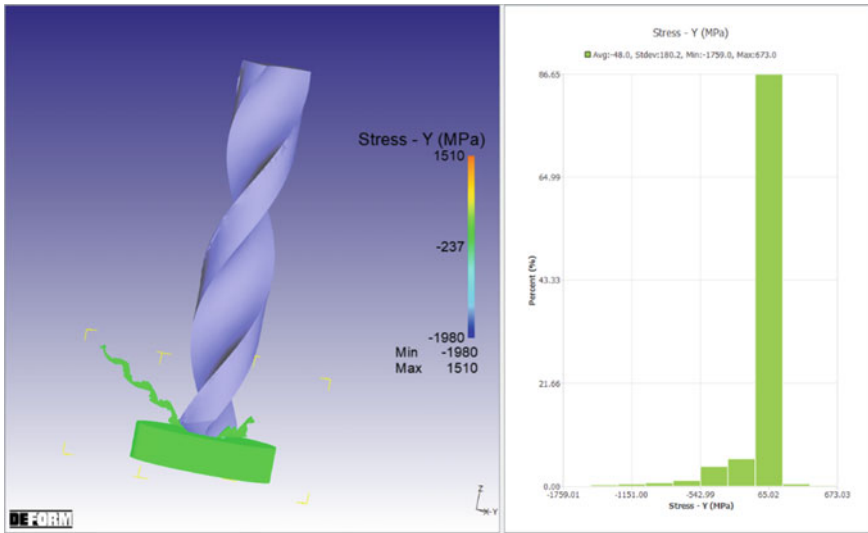


Fig. 23 Y-axis stress of workpiece after simulation

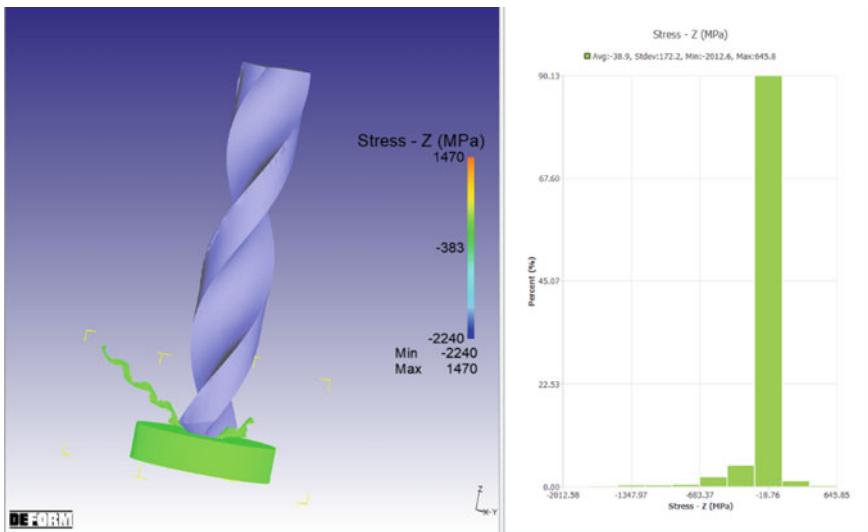


Fig. 24 Z axis stress of workpiece after simulation

being only 1.3 mm over the course of the simulation. The peak value of the workpiece velocity increased to 4907.6 mm/s and the average value of 267.6 mm/s was obtained throughout the entire simulation of drilling operation. The effective strain of the workpiece is 11.2 mm/mm at its highest point, with an average of 2.1 mm/mm at its lowest point.

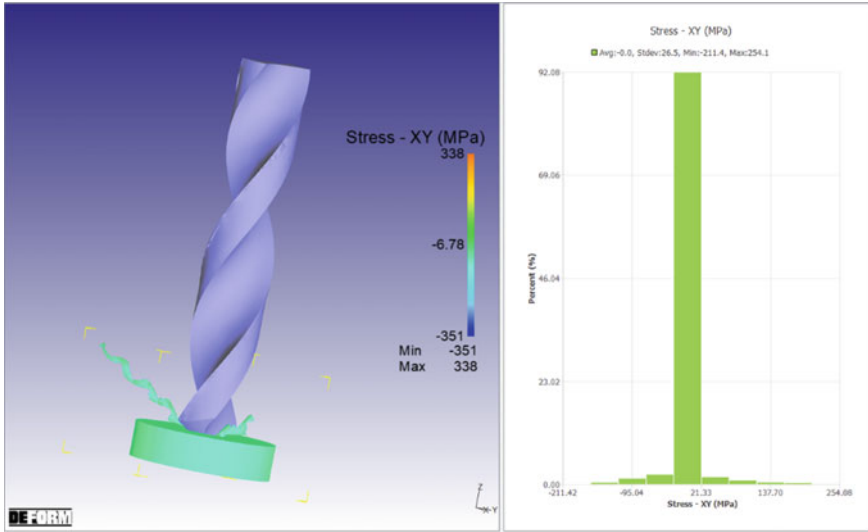


Fig. 25 XY-plane stress of workpiece after simulation

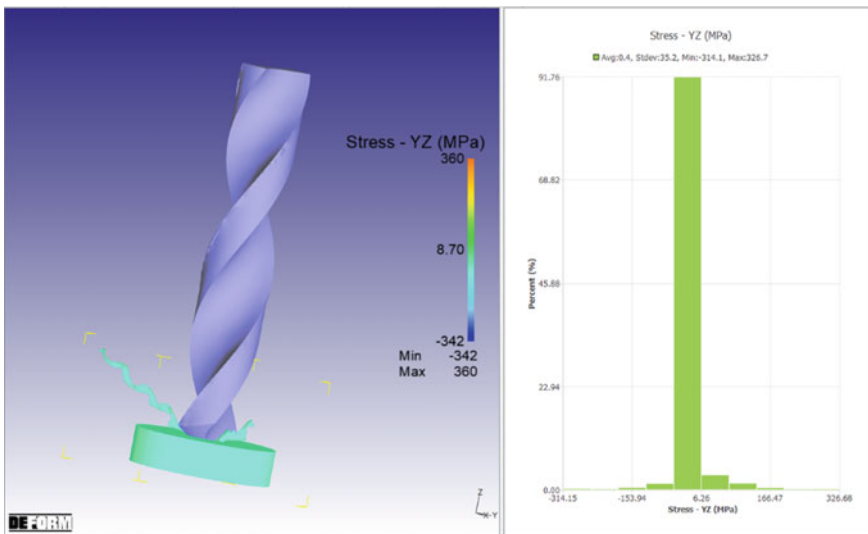


Fig. 26 YZ-plane stress of workpiece after simulation

Using the measurement option in the DEFORM 3D software, the width of chips of Aluminium alloy graded 7075 T351 was measured. The lowest and maximum chip width values were determined as 0.76359 mm and 1.59188 mm, respectively. Additionally, the thickness of the workpiece chip was measured and determined to be 0.412254 mm, which is very close to the width value of 0.835617 mm.

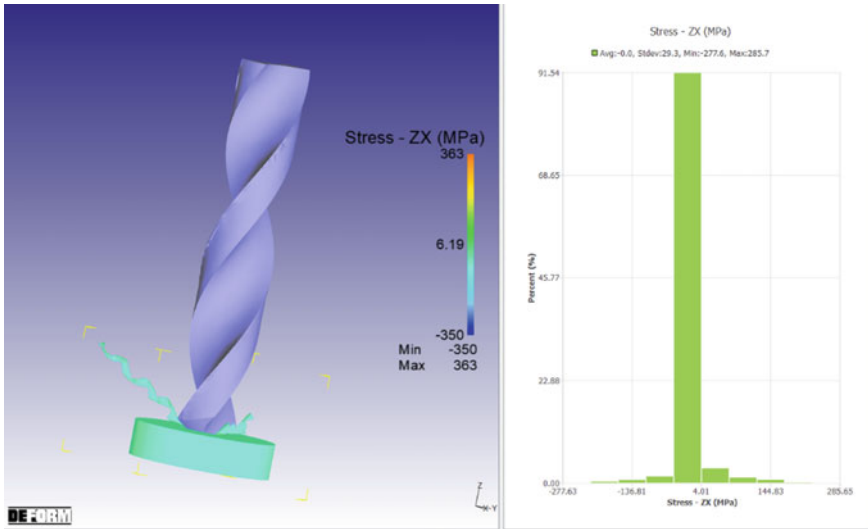


Fig. 27 ZX-plane stress of workpiece after simulation

Furtherly, the thermal analysis is done on the AA7075 T351 alloy workpiece where the maximum value of temperature is at 273.1 °C and has average value is 63.9 °C. It was found that temperature was highest at the chip-tool interface and the value of temperature decreased along the chips of workpiece.

References

1. Tamizharasan T, Kumar S (2012) Optimization of cutting insert geometry using DEFORM-3D: numerical simulation and experimental validation. *Int J Simul Model* 11(2):65–76
2. Chen Z, Qin LF, Yang LJ (2006) Cutting force simulation of titanium based on DEFORM-3D. In: 3rd international conference on material, mechanical and manufacturing Engineering, pp 1846–1849
3. Pawar P, Ballav R, Kumar A (2017) Modeling and simulation of drilling process in Ti-6Al-4V, Al6061 using deform-3D software. *Int J ChemTech Res* 10(3):137–142
4. Liu W, Zhu X, Zhou Q, He H, Liu J, Xu C, Li L (2020) Modeling and simulation of the flow drill screw process of a DP590/Al6061-T6 multi-material joint used for vehicle body. *Int J Adv Manuf Technol* 110(5):1189–1201
5. Yaşar N (2019) Thrust force modelling and surface roughness optimization in drilling of AA-7075: FEM and GRA. *J Mech Sci Technol* 33(10):4771–4781
6. Kaneriya NG, Sharma GK (2014) Experimental evaluation and optimization of dry drilling parameters of AISI304 austenitic stainless steel using different twist drills. In: 26th AIMTDR. IIT Guwahati India
7. Attanasio A, Faini F, Outeiro JC (2017) FEM simulation of tool wear in drilling. *Procedia Cirp* 58:440–444
8. Bağcı E, Özcelik B (2006) Finite element and experimental investigation of temperature changes on a twist drill in sequential dry drilling. *Int J Adv Manuf Technol* 28(7–8):680–687

9. Mediouni M, Schlatterer DR, Khoury A, Von Bergen T, Shetty SH, Arora M, Dhond A, Vaughan N, Volosnikov A (2017) Optimal parameters to avoid thermal necrosis during bone drilling: a finite element analysis. *J Orthop Res* 35(11):2386–2391
10. Gao XJ, Li H, Liu Q, Zou P, Liu F (2011) Simulation of stainless steel drilling mechanism based on Deform-3D. In: *Advanced materials research*, vol. 160. Trans Tech Publications Ltd, pp 1685–1690
11. Giasin K, Hodzic A, Phadnis V, Ayvar-Soberanis S (2016) Assessment of cutting forces and hole quality in drilling Al2024 aluminium alloy: experimental and finite element study. *Int J Adv Manuf Technol* 87(5):2041–2061
12. Glaa N, Mehdi K, Zitoune R (2018) Numerical modeling and experimental analysis of thrust cutting force and torque in drilling process of titanium alloy Ti6Al4V. *Int J Adv Manuf Technol* 96
13. Chatterjee S, Mahapatra SS, Abhishek K (2016) Simulation and optimization of machining parameters in drilling of titanium alloys. *Simul Model Pract Theory* 62:31–48
14. Deform T (2006) 3D version 6.1 (sp1) user's manual. Scientific Forming Technologies Corporation, Columbus OH

Numerical Modeling of Explosive Welded Ti/Al7075-T6 Bimetal Composite Plate Using Smoothed Particle Hydrodynamics



Abhishek Barua, Swastik Pradhan, Siddharth Jeet, Dilip Kumar Bagal, Kanchan Kumari, Saujanya Kumar Sahu, and Arati Rath

Abstract In several mechanically linked sectors, including power plants and the aerospace industry, explosive welding (EXW) has been utilised successfully. Furthermore, it has been effectively used in the production of biocompatible materials in medical and associated areas, among other things. This technique is beneficial for joining various types of metals and alloys that are difficult to join using other methods of welding, such as stick welding. The majority of earlier experimental research on titanium and aluminium layered composites concentrated on the microstructural and mechanical properties of the materials. However, the exact mechanism through which titanium and aluminium are formed during explosive welding is still a mystery. Only a few simulations have been piloted to study the explosive welding process of titanium and aluminium layers. Even so, there is potential for investigating the EXW of titanium in conjunction with an aerospace-grade aluminium alloy. This article describes the development of a more physically accurate 2D numerical model for

A. Barua · S. Jeet

Department of Mechanical Engineering, Centre for Advanced Post Graduate Studies, BPUT, Rourkela, Odisha, India

S. Pradhan (✉)

School of Mechanical Engineering, Lovely Professional University, Phagwara, Punjab, India
e-mail: swastik.22644@lpu.co.in

D. K. Bagal

Department of Mechanical Engineering, Government College of Engineering, Kalahandi, Bhawanipatna, Odisha, India

K. Kumari

Department of Mechanical Engineering, Parala Maharaja Engineering College, Berhampur, Odisha, India

S. K. Sahu

Department of Civil Engineering, Government College of Engineering, Kalahandi, Bhawanipatna, Odisha, India

A. Rath

School of Computer Engineering, Kalinga Institute of Industrial Technology, Bhubaneswar, Odisha, India

simulating the whole process of explosive welding titanium and the aluminium alloy Al7075-T6. The smoothed particle hydrodynamics (SPH) approach was utilised in this simulation, which is included in the ANSYS Autodyn software package. The numerical model is capable of modelling the standard physics of explosive welding, including explosive expansion, flyer plate bending, metal plate collisions, jetting and plate contact throughout the operation. Physical properties that change throughout the explosive welding process are discussed in detail. The aluminium plate served as the foundation for the majority of the jet's components. As predicted by the model, the jet travelled at a speed of 1100 m/s. Furthermore, the pressure at the explosion site was insufficient for causing the two plates to bind together successfully. Due to the fact that the detonation energy is steady and much larger than the yield strength of both plates, the pressure may reach 1.6 GPa, an order of magnitude bigger than each material's yield strength. This led to the formation of a distinct small area of plastic strain at the impact zone. There were no indications of shear tensions between the two plates, despite the fact that they were in different directions. During the experiment, the interface morphology altered from being straight to being wavelike as the detonation wave propagated across it.

Keywords Al7075-T6 · ANSYS autodyn · Explosive welding · Numerical simulation · Smoothed particle hydrodynamics · Titanium

1 Introduction

Welding is a helpful method for connecting two materials that are either similar or dissimilar in composition. The employment of different welding methods, such as arc welding, plasma cutting, friction welding, laser cutting and explosive welding (EXW), among others, has become more popular in numerous sectors. In contrast to traditional welding methods, it is a solid-state welding technique wherein a flyer plate is driven through an explosion and quickly connected to another piece of material (Fig. 1). Throughout the welding process, a high-velocity jet is used to clean the surfaces of the substrates. In several mechanically linked sectors, including power plants and the aerospace industry, explosive welding has been utilised for years. It has also been successfully used to create biocompatible materials in the medical sector [1–3], which is a promising development. This technique is beneficial for joining various types of metals and alloys that are difficult to join using other methods of welding, such as stick welding. Al7075-T6 is an aluminium alloy that is suitable for use in aeronautical applications. It has a high degree of malleability and

is corrosion resistant. Although it has a poor mechanical strength, it is highly reactive with air when exposed to high temperatures. In terms of strength to mass ratio, titanium and its alloys are the strongest naturally occurring materials on the planet. A fantastic industrial application may be created as a result of their combination. When it comes to connecting these two metal alloys together, explosive welding is one of the better options since the two work pieces have a significant variation in their melting temperatures and mechanical strengths [4].

Explosive welding is one of the most successful methods for producing laminated metal composites. It fabricates layered metal composites with variable thermal conductivity, superior mechanical characteristics, enhanced erosion resistance and clear economic profits. Explosive welding methods may be used to create over 260 different types of materials that are both comparable and distinct.

Mahmood et. al. [1] investigated the explosive welded joints of Ti6Al4V plate with copper plate with pure titanium interlayer both experimentally and numerically and reported wavy interaction in both the plates. Campanella et. al. [2] investigated explosive welded joints of AA5083, A516 steel and AA1050 plates by employing a two-step Lagrangian–Eulerian numerical model in the ABAQUS platform and reported wavy interaction along with voids in welded joints. Yang et al. [3] claimed that SPH simulations might quantitatively predict the microstructure development during high-speed impact welding of copper foil and iron. Sun et. al. [4] reported different types of plate surface interaction while conducting SPH 2D/3D based explosive welding both experimentally and numerically. Elango et. al. [5] investigated explosive welded joints of aluminium and steel plates by employing varying masses of the explosive

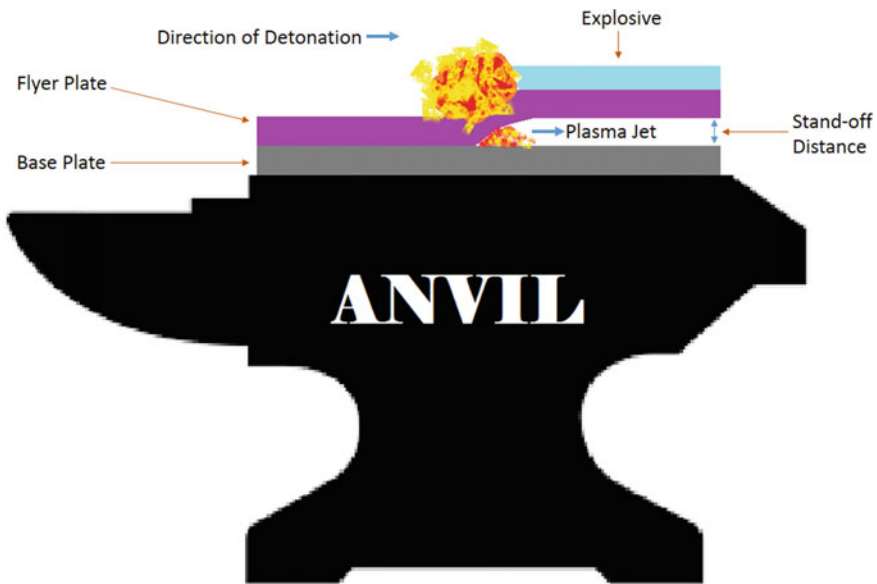


Fig. 1 Explosive welding terminology

and flyer plate and reported different results based on microstructures. Wang et. al. [6] investigated explosive welded joints of Mg/Al plates by the addition of aluminium buffer plates and reported wavy interaction of plates during both experimental and simulation analysis. Yang et. al. [7] investigated explosive welded Ag coating on Fe substrate and reported an enhancement in surface characteristics. Wu et. al. [8] investigated explosive welded titanium and aluminium composites with and without buffer plates and reported a reduction in welding energy while using the interlayer plates. He et al. [9] examined the microstructural inhomogeneity non the bonding zone of explosively welded AISI 410S/A283GrD plates using both experiment and modelling methods and concluded that both results were significant, as was the wavy interaction between the two plates. Kumar et al. [10] used computational and experimental methods to study the microstructural properties and interface behaviour of explosive welded Al6061 V-grooved SS304 and discovered that the impact and shear strengths of V-grooved plate clads were higher than those of plain clads. Tian et. al. [11] investigated the explosive welded plates of Al5083H116 and SS 304 on the Autodyn platform and reported significant results related to jet propagation and plate interaction. Mahmood et al. [12] examined the microstructure and mechanical properties of explosively welded Ti6Al4V and Al1060 plates before and after thermal processing. They also simulated the experiment using SPH in Autodyn. Li et al. [13] used explosive welding to produce a Ti/Al bimetal composite from titanium and aluminium. Investigators replicated the experimental results using Autodyn and found that the plate interface transformed from straight to wavelike throughout the transmission of the detonation wave in both the real and simulation output.

Bimetal composites made of titanium and aluminium are used in industry. In spite of this, there are an abundance of reports on Titanium and Aluminium EXW stating some gaps. Prior research has concentrated on the microstructure and mechanical characteristics of titanium and aluminium alloys layered in a variety of combinations. However, the forming procedure for titanium and aluminium explosive welding is still a mystery. Only a few people have used computer modelling to better understand the explosive welding process for titanium and aluminium alloys. However, there is still room to investigate titanium's EXW in combination with an aerospace-grade aluminium alloy.

Research on numerical modelling of a titanium and Al7075-T6 bimetal composite produced by explosive welding has led to the development of a numerical model that is more accurate. Some physical factors like impact velocity, strain, pressure and stress are addressed along with the typical explosive welding events. Additionally, the shape of the welded joint's interfacial region was investigated. We may use numerical simulations to better understand the underlying physics of explosive welding by studying the results.

2 Material and Experimental Model

The solids model used Lagrangian elements and liquids using Eulerian and SPH (smooth particle hydrodynamics) elements, which enables you to capture any kind of event using the most appropriate technology from Autodyn’s technological spectrum. One model may include several solvers and the interactions between the different domains can be represented in order to provide efficient and accurate results. It was decided to utilise the ANSYS Autodyn R17.2 platforms for this investigation.

2.1 Geometric Model of Explosive Welding

For the purposes of this research, titanium and the Al7075-T6 aluminium alloy were utilised to conduct explosive welding on titanium. Figure 2 illustrates the created geometric model for the explosive welding simulation. This component modeller was used to cast off ANFO (ammonium nitrate-fuel oil mixture) from an anvil made of iron (ARMCO®), a base plate made of aluminium 7075-T6, a flyer plate made of titanium and an anvil made of iron. Table 1 is a list of the geometry sizes available. Installation of the detonator is done at the surface edge of the explosive layer. Some equidistant gauge points have been defined as 15 mm in x-direction (difference between two points), 16 mm in y-direction and 40 mm in z-direction on the Al7075-T6 plate. A stand-off distance of 5 mm was kept between titanium and Al7075-T6 plates.

2.2 Equation of State (EOS) and Constitutive Model

Jones-Wilkins-Lee Model (JWL)

The ANFO takes the use of the JWL equation of state to explain expansion of the explosive product down to 1 kbar of pressure for high-energy explosives.

$$P = A \left(1 - \frac{\omega}{R_1 V} \right) e^{-R_1 V} + B \left(1 - \frac{\omega}{R_2 V} \right) e^{-R_2 V} + \frac{\omega E_0}{V} \tag{1}$$

The initial specific internal energy is E_0 and the explosive constants R_1 , R_2 , A , B and ω are given in Table 2 as pressure, volume and relative volume, respectively.

Mie-Gruneisen EOS

As the equation of state, the plates and anvil were subjected to a Mie-Gruneisen EOS. An impact event’s shock Hugoniot developed the Mie-Gruneisen EOS, which was extensively used for materials with significant deformation. A particle’s velocity and shock velocity are related in a number of ways, as described in this EOS:

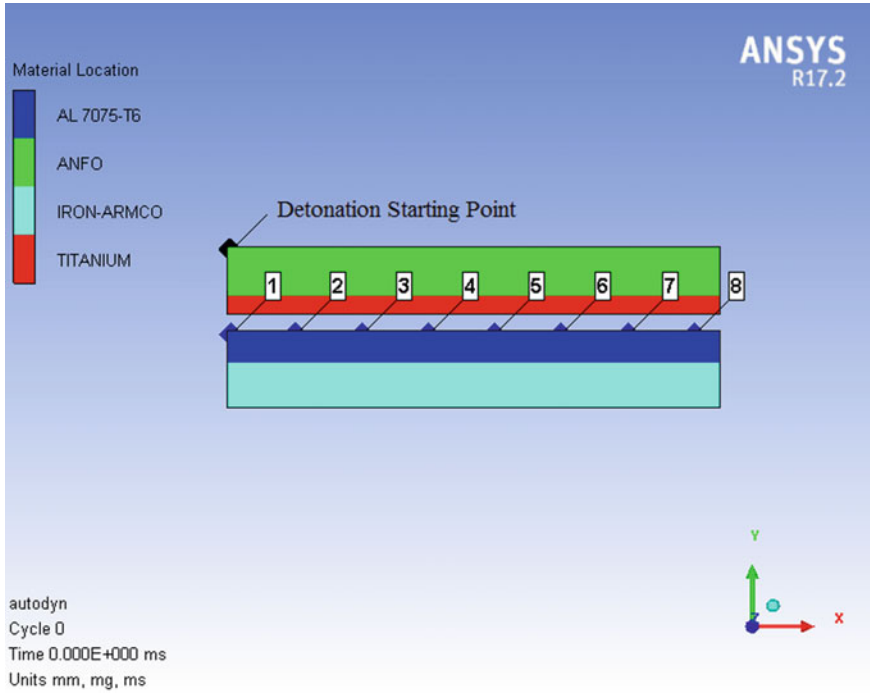


Fig. 2 Geometric part modelling of the simulation

Table 1 Dimensions of geometrical part for modelling

Position	Material	Dimension (l × b × h)
Explosive	ANFO	110 mm × 80 mm × 10 mm
Flyer plate	Titanium	110 mm × 80 mm × 5 mm
Base plate	Al7075-T6	110 mm × 80 mm × 6 mm
Anvil	Iron	110 mm × 80 mm × 10 mm

Table 2 EOS parameters of ANFO

A, GJ	V	B, GJ	R ₁	R ₂	ω	E ₀ , GJ/m ³	Density, kg/m ³	Detonation Velocity, m/s	Pressure, GPa
49.46	0.74	1.89	3.9	1.11	0.33	2.48	931	4.16	5.15

$$\rho = \rho_H + \Gamma_\rho(e - e_H), \tag{2}$$

where,

$$\Gamma_\rho = \Gamma_0 \rho_0 = \text{Constant}, \tag{3}$$

and

$$\rho_H = \frac{\rho_0 c_0 \mu (1 + \mu)}{[1 - (g - 1)\mu]^2}, \tag{4}$$

$$e_H = \frac{1}{2} \frac{\rho_H}{\rho_0} \left(\frac{\mu}{1 + \mu} \right), \tag{5}$$

$$\mu = \left(\frac{\rho}{\rho_0} \right) - 1, \tag{6}$$

This is defined as follows: where Γ_0 is the Gruneisen coefficient and ρ is the initial density, c_0 is the bulk speed of sound, ρ_0 is the current density. Throughout the simulations, the default Autodyn shock EOS material constants were utilised.

Steinberg–Guinan Strength Model

The Steinberg–Guinan Strength Model was utilised to investigate the behaviour of titanium and Al7075-T6. As per their theory, shear modulus improves with pressure and temperature; therefore, they intended to include the Bauschinger effect into their calculations. As a consequence, the shear modulus and yield strength have been described in terms of effective plastic strain, pressure and internal energy (in terms of temperature). High strain rates have the following constitutive laws for shear modulus G and yield stress Y :

$$G = G_0 \left\{ 1 + \left(\frac{G_p}{G_0} \right) \frac{p}{\eta^{1/3}} + \left(\frac{G_T}{G_0} \right) (T - 300) \right\} \tag{7}$$

$$Y = Y_0 \left\{ 1 + \left(\frac{Y_p}{Y_0} \right) \frac{p}{\eta^{1/3}} + \left(\frac{Y_T}{Y_0} \right) (T - 300) \right\} (1 + \beta \varepsilon)^n \tag{8}$$

where ε denotes effective plastic strain, T signifies temperature (degrees K), η is compression, i.e. v_0/v and the primed parameters with the subscripts p and T are derivatives of that variable with respect to pressure and temperature at the reference state ($T = 300$ K, $p = 0$, $\varepsilon = 0$). Additionally, the subscript zero refers to the values of G and Y in the reference state.

Johnson–Cook Model

Metal mechanical behaviour should be represented by the constitutive model. Due to the Johnson–Cook model’s ability to explain massive deformation behaviour of materials at high strain rates, i.e. Equation (9), it was used to analyse the mechanical behaviour among the base plate, flyer plate and anvil:

$$\sigma = (A + B \varepsilon_{\text{eff}}^n) (1 + C \ln \dot{\varepsilon}) (1 - T^{*m}) \tag{9}$$

Table 3 Parameters of materials

Material	ρ , kg/m ³	C	m	n	T_{melt} , °K	R_{τ} , GPa	Y_0 , GPa
Titanium	4510	–	–	0.1	2260	43.4	0.085
Al7075-T6	2804			0.1	1220	26.7	0.042
Iron	7890	0.06	0.55	0.32	1811	80	0.175

$$T^{*m} = \frac{T - T_{\text{room}}}{T_{\text{melt}} - T_{\text{room}}} \quad (10)$$

where σ denotes the flow stress, ε_{eff} refers the effective plastic strain, $\dot{\varepsilon} = \frac{\varepsilon_{\text{eff}}}{\varepsilon_0}$ signifies the normalised effective plastic strain rate, R_{τ} represents shear stress of materials, Y_0 denotes yield stress of materials, T_{room} denotes room temperature, T_{melt} symbolises the melting point of materials, $C =$ strain rate constant, n denotes hardening exponent, A denotes yield strength of the material, m denotes softening exponent and B denotes the strain hardening coefficient. As stated in Table 3, the material constants were retrieved from the Autodyn material library.

Smooth Particle Hydrodynamics (SPH) Method

Gridless numeric ANSYS Autodyn used Smooth Particle Hydrodynamics (SPH) to simulate Lagrangian hydrodynamics. The SPH technique uses kernel approximation of field variables to simplify conservation equations. The discrete particle finds field information while the adjacent particles solve integrals. The following describes the field parameter for non-zero kernel estimation:

$$f(r) = \sum \frac{m_p}{\rho_p} f_j W(|r - r_j|, h|X|, h) \quad (11)$$

Here, m_p , ρ_p are particle mass and density, $f(r)$ is a field variables and h is the distance between particles. For the present simulation of explosive welding, the flyer and base plate collide at a certain velocity and angle. Figure 3 shows the schematic model for SPH simulation with 0.5 mm particles.

3 Results from Simulation

3.1 Kinematic Characteristics and Jet Formation

Due to the explosive gas spreading rapidly all around during the explosion, the flyer plate was twisted and collided obliquely with the base plate soon after the explosion began. To establish the model's validity, the whole kinematic process of real explosive welding was recreated.

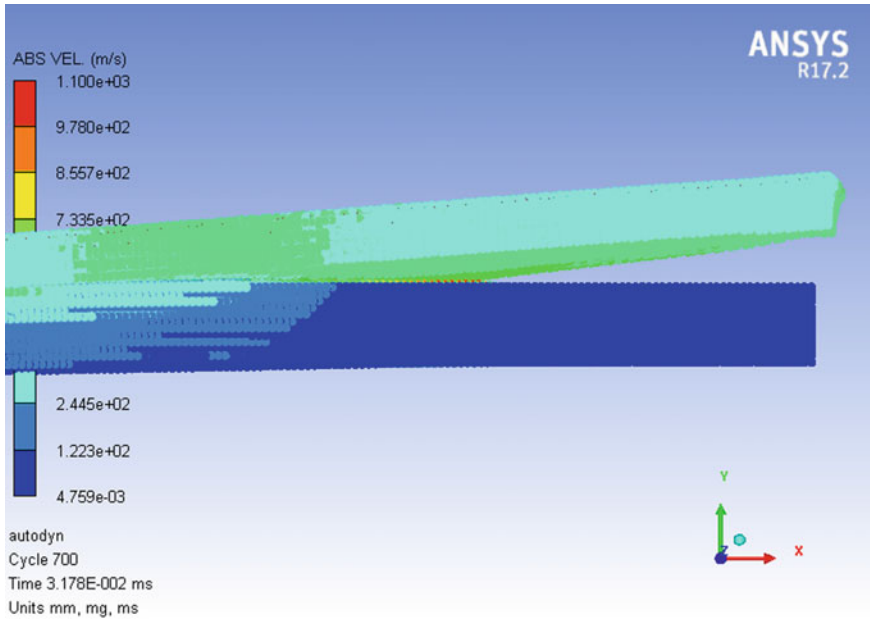


Fig. 3 Velocity distribution contour

According to Fig. 3, the bulk of the jet in the impact area originated from the aluminium plate, which is indicative of the fact that aluminium has a lower density than titanium and therefore generates more jets. A jet is a common event in explosive welding that is difficult to identify in the experiment due to the experiment’s design. As is widely known, clean bonding surfaces are important for creating a strong connection and producing a strong bond in explosive welding. To just get the atoms of the two materials into interatomic distances, the jet must first remove the oxide layer and any impurities from the two adhesion surfaces. As a consequence, it was discovered that metallurgical bonding between two materials needed the employment of a jet. Due to the inclusion of the physical variables discussed before, the current numerical results are intrinsically more realistic than those produced using a simpler technique such as high-velocity impact welding [14].

3.2 Distribution of Velocity

The velocity curve in Fig. 3 is shown at a certain moment during the simulation process (the explosive and anvil are hidden here, the same below). It can be seen that the collision zone has a higher velocity than the other areas of the figure. The jet velocity reaches a maximum of 1100 m/s at this location. Both the x- and y-direction velocities may be used to understand the collision and bonding processes and as

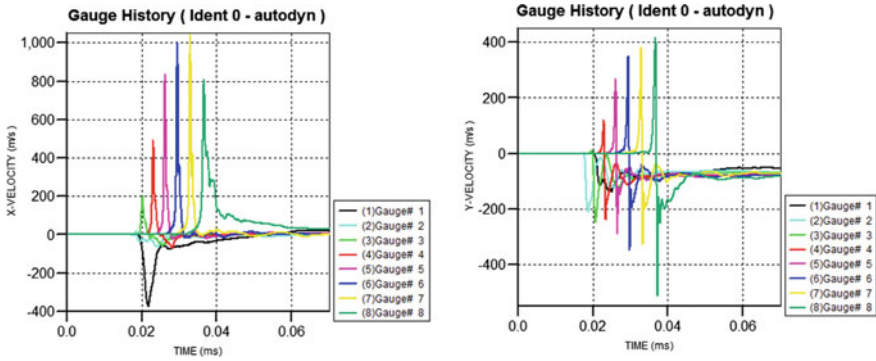


Fig. 4 Velocity-time curves of the special points

indices for further investigation of the bonding state. As can be seen in Fig. 4, the velocity at each gauge gradually increases throughout the current simulation before dropping after the collision is complete.

As shown in Fig. 4, after the collision occurs, the velocity of gauge point 4 absorbs the flyer plate’s kinetic energy immediately rises, as if the gauge point were experiencing a pulse. Figure 4 shows the time interval between impacts is very short at special points. The y-direction velocity of gauge points 4–8 shows a similar fluctuating pattern and ultimately falls to zero after impact, showing that the points have established a link. The down curves show that a flyer plate in motion at the time of the collision should decelerate as energy is lost and transferred to the other sample. Instantaneously after a collision, the flyer plate’s absorbed kinetic energy increases dramatically, as if the flyer plate were experiencing a pulse. The time interval between impacts is very short. Gauge point y-direction velocity follows the same pattern as gauge point x-direction velocity and eventually decreases to zero after impact, showing that the two points have established a connection. The x-direction figure in Fig. 4 may be used to analyse the jet’s propagation. At gauge point 7, the jet speed was about 1100 m/s.

3.3 Pressure Distribution

The contour of the pressure distribution at a given moment in time is shown in Fig. 5. The pressure values at the collision site are higher in contrast to the pressure values at other locations, as can be seen in the diagram. There is an uneven distribution of pressure at the site of impact. By using materials with the identical material characteristics on both the flyer and base plates, it is possible to create a symmetric,

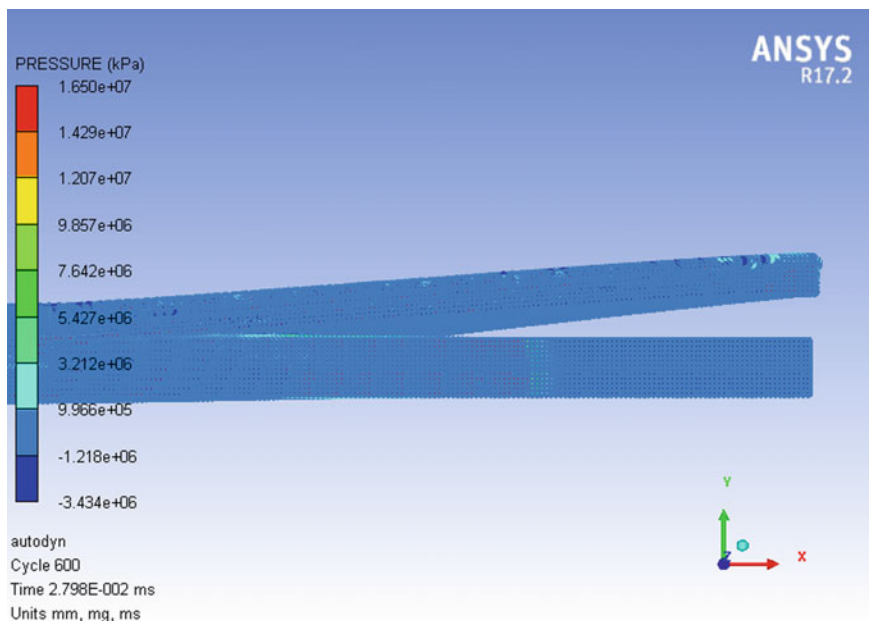


Fig. 5 Pressure distribution contour

confined high-pressure zone. High pressure surrounding the collision point encourages the interfacial material to develop jetting collision points are more prominent as compared to other points on the collision point are more prominent.

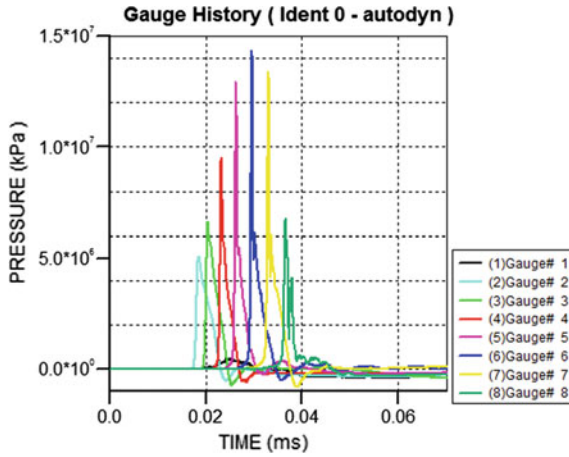


Fig. 6 The pressure–time curves of special points

The high pressure around the collision site promotes the development of jetting in the interfacial material during the high-speed impact phase. Jetting is possible as long as the pressure applied to the impact surface exceeds the material's dynamic strength. In the collision zone, the maximum pressure that may be produced is close to 1.65 GPa. As illustrated in Table 3, since the applied pressure at the interface is much more than the material's dynamic strength, all materials on the collision surface are pushed into a transient fluid-like state, which causes the creation of the jetting in this situation. Illustration of the pressure–time curves of specific locations in Fig. 7. As shown in Fig. 6, the lowest pressure was achieved at the explosion sites (Points 2 and ignoring zero pressure) throughout the propagation of the detonation wave, which may be ascribed to the unstable energy present during the initial detonation stage.

3.4 Strain and Stress Dissemination

Figures 7 and 8 show the contour of effective strain and the distribution of effective plastic strain after 700 cycles of simulation, respectively. As shown in Figs. 7 and 8, there is a tiny area of plastic strain at the collision site. This agrees with the preceding section on pressure analysis, which stated that the pressure is higher at the collision contact. High-pressure results in considerable plastic deformation, which leads to severe plastic strain. The high quantity of plastic deformation that happens at the contact is one of the bonding stages of explosive welding. Numerous experimental studies of explosive welding have shown the presence of grain refinement and high-density dislocations near the interface, indicating that substantial plastic deformation occurs near the interface during the welding process. Thus far, the numerical results produced have supported the experimental findings. Based on test findings, certain melt zones and intermetallic compounds may also be found at the interface. However, due to restrictions in the AUTODYN programme, this is not feasible to accomplish in the present simulation.

A good bonding index may be used to identify the appearance of excellent bonding by measuring the shear stress. Figure 9 depicts a distribution of shear stress after 600 cycles of shear force application. As can be observed, the shear stress directions on the two plates are diametrically opposed, with the flyer plate having a negative

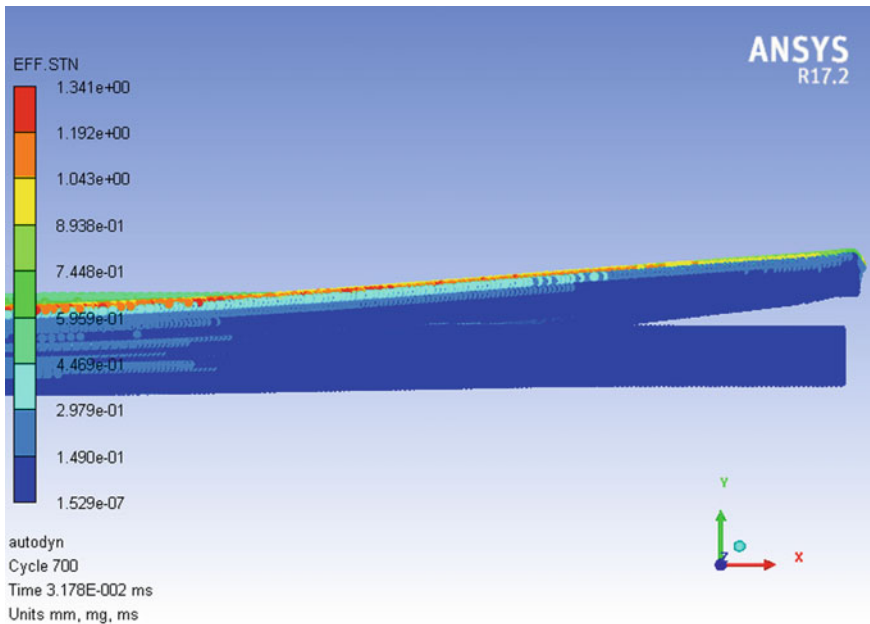


Fig. 7 Effective strain at 700 cycles

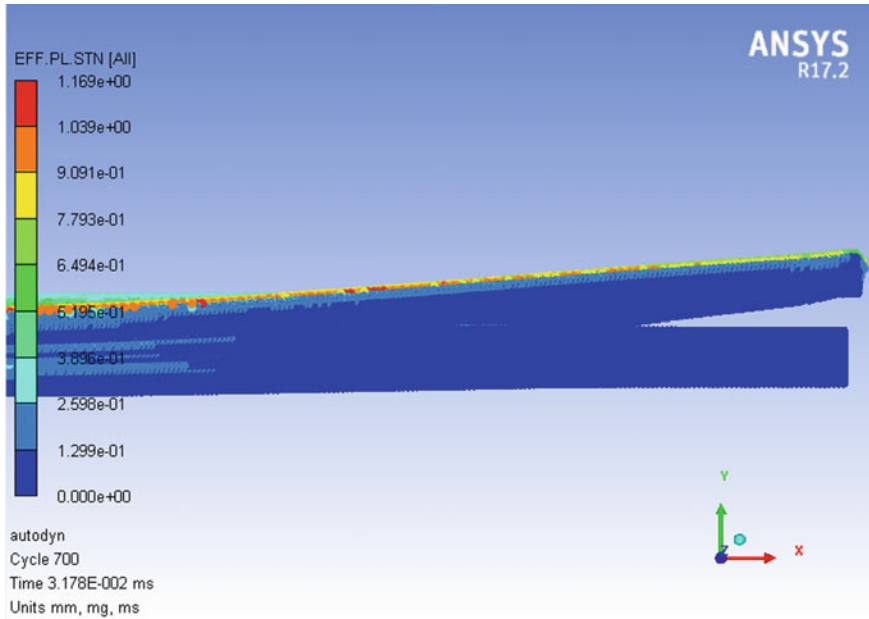


Fig. 8 Effective plastic strain at 700 cycles

shear stress and the base plate having a positive shear stress and the shear stress distributions on the two plates are not uniform in either plate direction. Additionally, the base plate's absolute shear stress is higher than the flyer plate's, which may result in greater material loss in the base plate than in the flyer plate, confirming that jetting is mainly produced by the base plate. Figure 10 depicts the Von-Mises stress contour, which demonstrates a similar kind of outcome.

3.5 Plate Interface Morphology

The interaction of the titanium and Al7075-T6 is shown in Fig. 11. Additionally, no macroscopic fractures can be observed, with the exception of a few tiny zones around the explosion site, as well as a distorted flyer plate after the conclusion of detonation. In order to truly comprehend the interfacial morphology of the composite plate, three cross-sections of the specimen were obtained along the detonation path of the explosion. Because of the explosive welding boundary effect seen in Fig. 12, there was no bonding detected. As previously stated, the pressure at the detonating site was insufficient for bonding to take place. The cross-sections with straight and wavy interactions were shown in Figs. 13 and 14, respectively. As can be observed, the welding quality was satisfactory and neither the simulation nor the testing revealed any cracks or pores, which is promising. In general, the existence of jetting at the

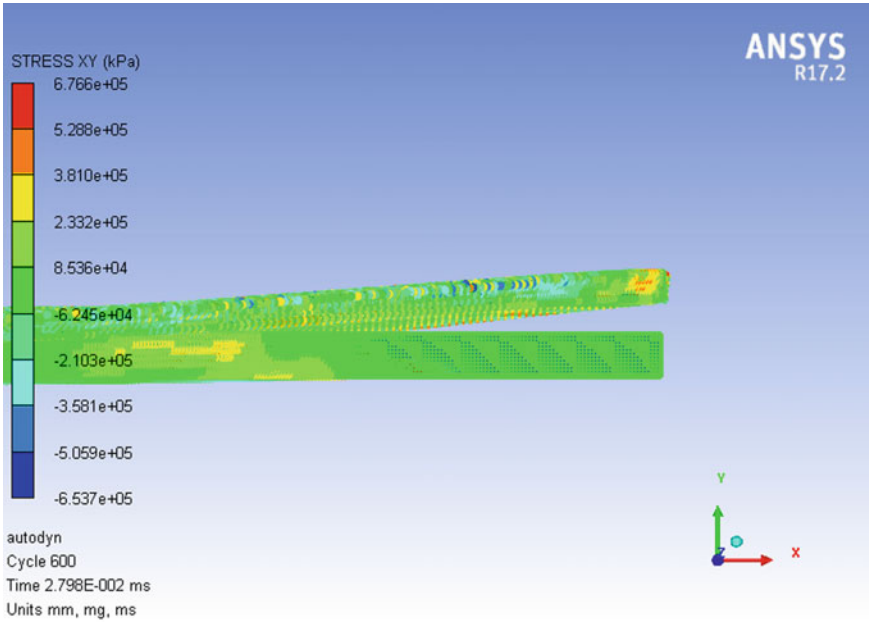


Fig. 9 Shear stress in xy -direction at 600 cycle

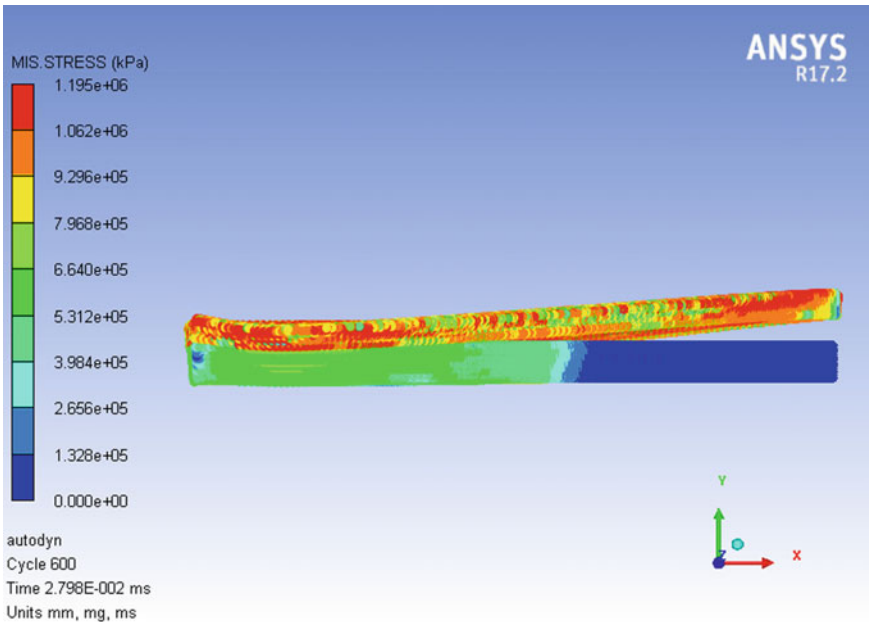


Fig. 10 Von-mises stress at 600 cycle

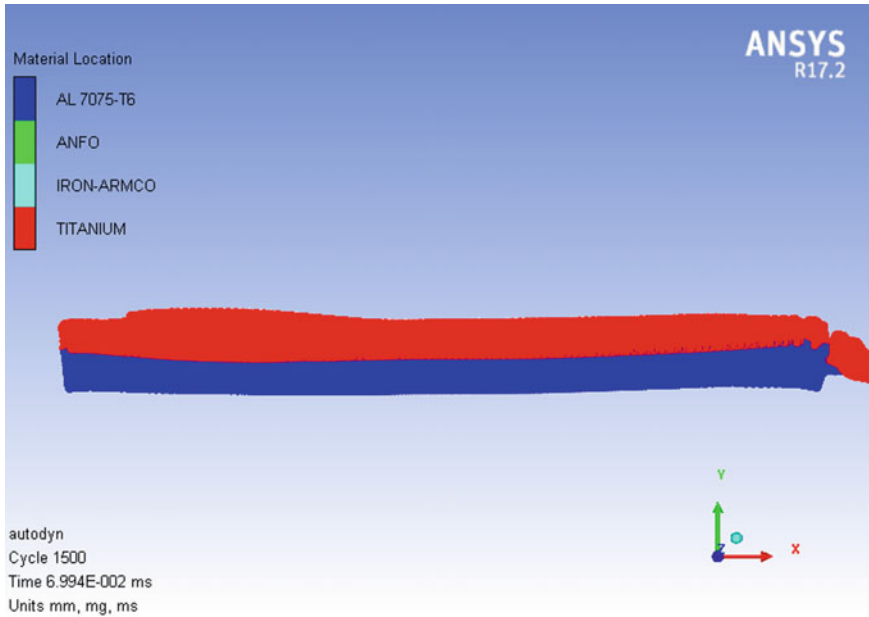


Fig. 11 The final welded plate interface

point of collision is regarded as a necessary criterion for the formation of a wavy interface. The jet was not apparent at the start of the explosion, but as the impact point advanced, periodic wave trends were formed by the jetting and the explosion proceeded.

4 Conclusions

Simulation analysis was piloted for explosive welding of titanium and Al7075-T6 aluminium alloy on ANSYS Autodyn software package. Some of the important conclusions based on simulation results were drawn below:

1. In the impact area, it was possible to see the jet phenomena, which emanated mostly from the aluminium alloy plate.
2. The flyer plate accelerates progressively after the explosion and collides with the base plate as a result of this. The jet velocity is the fastest, reaching speeds of up to 1100 m/s in the intersection zone.
3. As a result, the pressure at the explosion location is inadequate to bind two plates, resulting in the boundary effect observed during explosive welding.

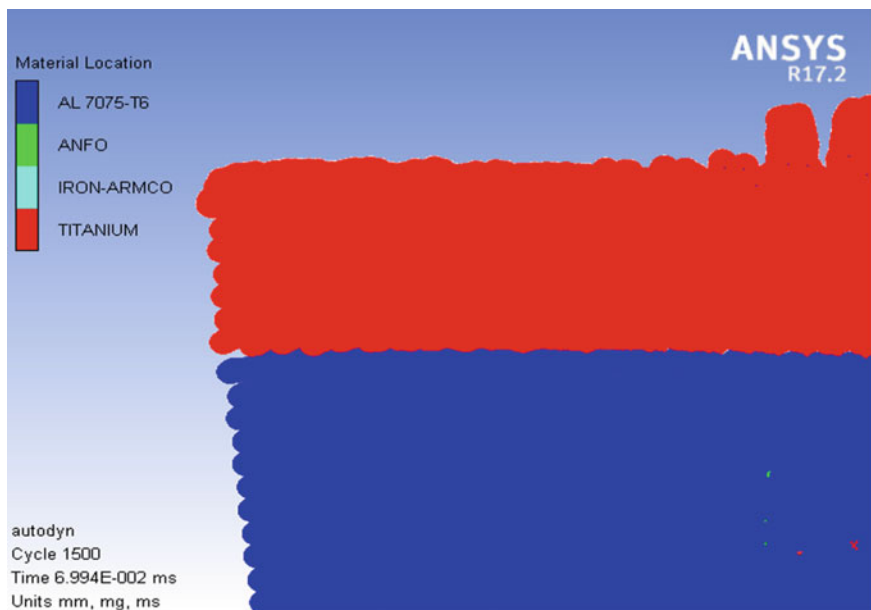


Fig. 12 No bond at the starting

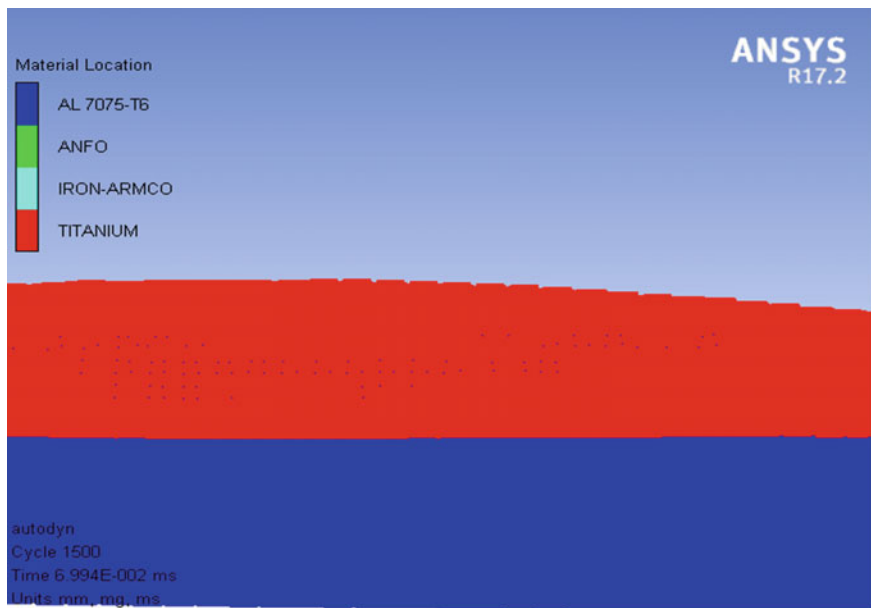


Fig. 13 Straight interaction

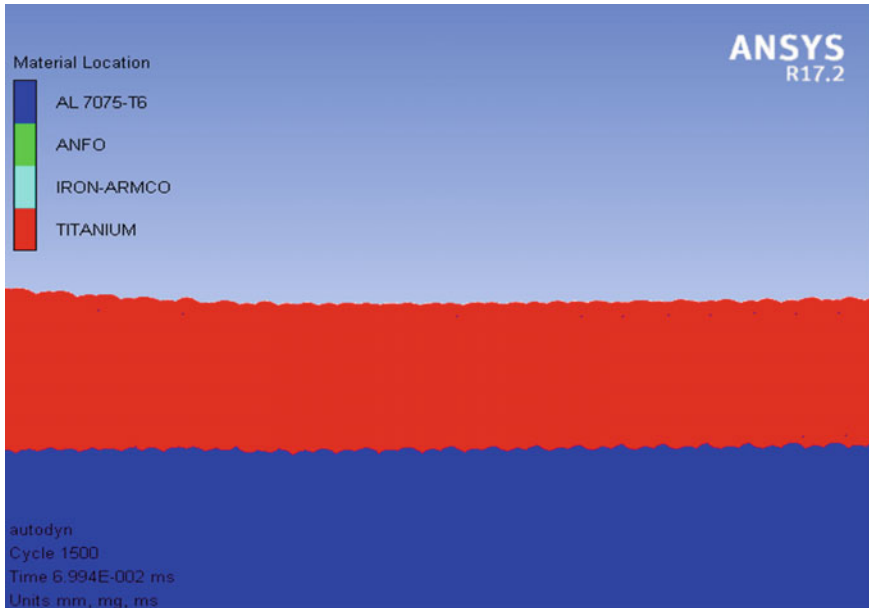


Fig. 14 Wavy interaction

4. A clear, small area of plastic strain is seen at the impact zone. Also, the shear stress between the two plates is inversely proportional to the shear stress between them.
5. The wavy contact between the plates reveals a stronger connection between the plates than the flat interaction.

References

1. Mahmood Y, Chen PW, Bataev IA, Gao X (2020) Experimental and numerical investigations of interface properties of Ti6Al4V/CP-Ti/Copper composite plate prepared by explosive welding. *Defence Technol*
2. Campanella D, Buffa G, Fratini L (2021) A two steps Lagrangian-Eulerian numerical model for the simulation of explosive welding of three dissimilar materials joints. *CIRP J Manuf Sci Technol* 35:541–549
3. Yang M, Xu J, Ma H, Lei M, Ni X, Shen Z, Zhang B, Tian J (2021) Microstructure development during explosive welding of metal foil: morphologies, mechanical behaviors and mechanisms. *Compos Part B: Eng* 212:108685
4. Sun Z, Shi C, Xu F, Feng K, Zhou C, Wu X (2020) Detonation process analysis and interface morphology distribution of double vertical explosive welding by SPH 2D/3D numerical simulation and experiment. *Mater Des* 191:108630

5. Elango E, Saravanan S, Raghukandan K (2020) Experimental and numerical studies on aluminum-stainless steel explosive cladding. *J Cent South Univ* 27(6):1742–1753
6. Wang Q, Li X, Shi B, Wu Y (2020) Experimental and numerical studies on preparation of thin AZ31B/AA5052 composite plates using improved explosive welding technique. *Metals* 10(8):1023
7. Yang M, Xu J, Chen D, Ma H, Shen Z, Zhang B, Tian J (2021) Understanding interface evolution during explosive welding of silver foil and Q235 substrate through experimental observation coupled with simulation. *Appl Surf Sci* 566:150703
8. Wu X, Shi C, Fang Z, Lin S, Sun Z (2021) Comparative study on welding energy and Interface characteristics of titanium-aluminum explosive composites with and without interlayer. *Mater Des* 197:109279
9. He Y, Zhang S, Ding Q, Wang G, Liu F, Ma Y (2021) Comprehensive investigation of microstructural inhomogeneity in the bonding zone of explosive-welded AISI 410S/A283GrD composite. *Compos Interfaces* 1–21
10. Kumar CWD, Saravanan S, Raghukandan K (2020) Numerical and experimental investigation on aluminum 6061-V-grooved stainless steel 304 explosive cladding. *Defence Technol*
11. Tian X, Wang Z, Teng X, Shi D, Sun Y (2020) Numerical simulation of explosive welding of marine aluminum steel transition joint based on AUTODYN. In: *IOP conference series: Materials science and engineering*, vol. 811(1), IOP Publishing, pp 012013
12. Mahmood Y, Dai K, Chen P, Zhou Q, Bhatti AA, Arab A (2019) Experimental and numerical study on microstructure and mechanical properties of Ti-6Al-4V/Al-1060 explosive welding. *Metals* 9(11):1189
13. Li Y, Liu C, Yu H, Zhao F, Wu Z (2017) Numerical simulation of Ti/Al bimetal composite fabricated by explosive welding. *Metals* 7(10):407
14. Barua A, Jeet S, Kumari K, Bagal DK, Pradhan S (2022) Numerical simulation of explosive welded titanium and Al7075-T6 bimetal composite plate using ANSYS autodyn. *Weld Int* 1–14. <https://doi.org/10.1080/09507116.2022.2099322>

Parametric Investigation of Injection Moulding for LDPE using Capuchin Search Algorithm and Honey Badger Algorithm



Siddharth Jeet, Abhishek Barua, Dilip Kumar Bagal, Swastik Pradhan, Surya Narayan Panda, and Siba Sankar Mahapatra

Abstract In our rapidly expanding world, there is a rising demand for low-cost, long-lasting, and less dangerous medicinal products. Medical items ranging from intravenous fluid containers to medical syringes are created to satisfy their demands using a range of thermoplastics and Plastic Injection Moulding (PIM). However, even advanced profile mouldings can suffer from dimensional inaccuracies. The current study advances our understanding of thermoplastics, specifically Low-Density Polyethylene (LDPE) material moulding for medical syringe plungers using injection moulding equipment. Eight injection moulding input factors were investigated in order to decrease the depth sink marks and weight created during the injection moulding of thermoplastic LDPE material. The 27 trials were piloted in accord with Taguchi's Design of Experiment, and the variables were optimised using the newly developed Honey Badger and Capuchin Search Algorithms, as well as analysis of variance, for determining the most dominating parameter. The cooling time and melt temperature of the plastic injection moulded part are the most significant factors influencing the sink-mark depth and weight of the part, respectively, according to the Analysis of Variance (ANOVA) test.

S. Jeet · A. Barua

Department of Mechanical Engineering, Centre for Advanced Post Graduate Studies, BPUT, Rourkela, Odisha, India

D. K. Bagal

Department of Mechanical Engineering, Government College of Engineering, Kalahandi, Bhawanipatna, Odisha, India

S. Pradhan (✉)

School of Mechanical Engineering, Lovely Professional University, Phagwara, Punjab, India
e-mail: swastik.22644@lpu.co.in

S. N. Panda

Department of Production Engineering, Birsra Institute of Technology, Sindri, Dhanbad, Jharkhand, India

S. S. Mahapatra

Department of Mechanical Engineering, National Institute of Technology, Rourkela, Odisha, India

Keywords Low-density polyethylene (LDPE) · Plastic injection moulding · Medical syringe · Taguchi method · Honey badger algorithm · Capuchin search algorithm

1 Introduction

In today's fast-paced world, medical materials that are low in cost, durable, and less harmful are becoming increasingly popular. Medical items ranging from intravenous fluid containers to medical syringes are created to satisfy their demands utilising a range of thermoplastics using Plastic Injection Moulding (PIM), which involves injecting molten plastic material into a mould to generate the profile represented in Fig. 1. They are expected to be less costly than other methods, such as 3D printing. The injection moulding method is widely used in the manufacture of medical goods, and a wide range of thermoplastic polymers, including ABS, Nylon, Polyethylene, Polypropylene, PVC, and others, are frequently used in this process [1–10].

According to the findings of most studies, cooling time has the greatest impact on dimensional accuracy followed by other parameters. Additional research into further injection moulding aspects and their optimisation utilising multi-objective optimisation criteria is lacking, however. An eight-criteria approach was used for plastic injection moulding of medical syringe plungers made of commercial-grade thermoplastic Low-Density Polyethylene (LDPE) to reduce sink marks' depth and weight while also increasing injection pressure and back pressure. This was done in accordance with Taguchi's Design: 27 trials were piloted, and variables were optimised using the newly created Honey Badger Algorithm and Capuchin Search Algorithm and analysis of variance in order to find the most dominant one.

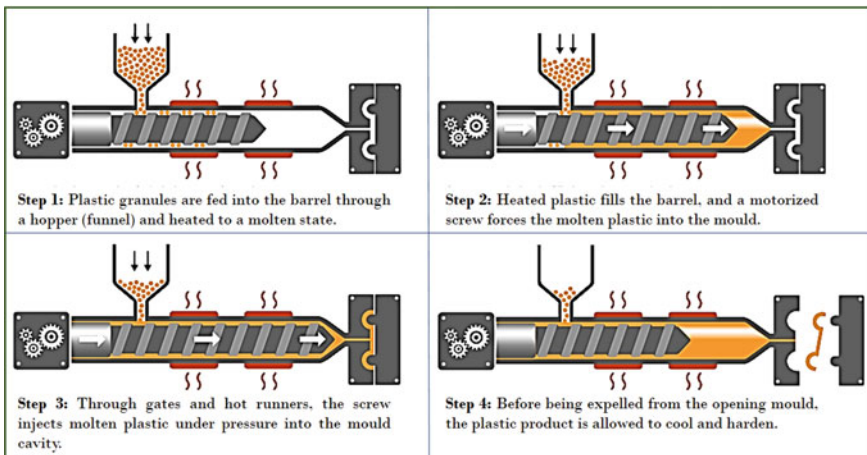


Fig. 1 Plastic injection moulding process

2 Experimental Procedure

In this investigation, commercial-grade LDPE plastic was used for injection moulding. In the experiment, a medical injection plunger was employed. We used a Maruti Engineers Fully Automatic Horizontal Moulding Machine (Yudo brand: Model No. CW662) produced by Maruti Engineers to formulate the experiments under various situations. Warming raw material, machine, and component data input into computer-aided engineering (CAE) software is used in the testing.

After a 2.5-hour heat treatment at 90 °C, the LDPE (Table 1) was dried to eliminate any leftover moisture before usage. On had finished configuring the operation and poured the melt into the machine. The mould chiller is set to 185 °C for 45 seconds before being switched off. According to the cycle time, the component was made in 75 seconds. To assess whether or not the injected component was faulty, it was inspected for shrinkage in the front view, short fill in the rib area, and flash in the locking rib. The current research, in particular, tries to minimise the appearance of weld lines on the component under evaluation. The moulding parameters and their levels are shown in Table 2 of this document.

A stable process state was established by experimenting with each process condition for 45 min during the trials. Figure 2 depicts a top sheath moulded specimen.

Table 1 Physical properties of low-density polyethylene (LDPE)

Commercial name	(SASOL™ LM2065)
Density (g/cm ³)	0.918
Moulding shrinkage %	1.9
MFI	6.5 g/10 min
Tensile strength (MPa)	10.5
Hardness (HRB)	275
Tensile Impact Strength (MPa)	286
Flexural Modulus (MPa)	252
Vicat softening point	0.961

Table 2 Experiment factors and their levels

Code	Factor	Unit	L (1)	L (2)	L (3)
A	Injection pressure	MPa	35	42	46
B	Mould temperature	°C	50	60	70
C	Back pressure	MPa	7	10	12
D	Holding pressure	MPa	15	20	25
E	Melt temperature	°C	215	225	240
F	Ambient temperature	°C	20	25	30
G	Cooling time	Sec	15	20	25
H	Holding time	Sec	5	7	9

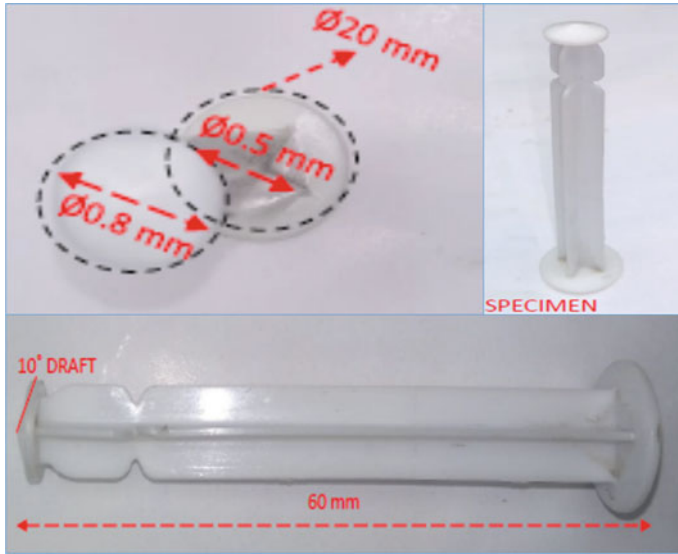


Fig. 2 Moulded specimen of medical syringe plunger

Upon achieving the required injection pressure, all injections have been monitored as they transitioned from the injection phase to holding phase to ensure that the required injection pressure has been acquired. After 24 h of assembly, the parts are weighed and measured. A Nikon Epiphot 300/200 optical microscope was used to measure the sink-mark depth.

3 Honey Badger Algorithm (HBA)

It has been created by researchers from Egypt and Pakistan and is based on the hunting behaviour of honey badgers in nature [11]. As stated before, HBA is split into two stages, which are the ‘digging phase’ and the ‘honey phase’, described in detail as follows:

Step 1: Initialisation phase. Initialise the number of honey badgers (population size N) and their corresponding locations based on Eq. (1):

$$x_i = lb_i + r_i \times (ub_i - lb_i), r_i \text{ is a random number between 0 and 1} \quad (1)$$

where x_i is i th honey badger position referring to a candidate solution in a population of N , while lb_i and ub_i are, respectively lower and upper bounds of the search domain.

Step 2: Determining the degree of intensity (I). Intensity is proportional to the prey’s concentration strength and the distance between it and the honey badger. It is the prey’s scent strength; if the smell is strong, the motion will be rapid, and vice

versa, as described by Eq. (2).

$$\begin{aligned}
 I_i &= r_2 \times \frac{S}{4\pi d_i^2}, r_i \text{ is a random number between 0 and 1} \\
 S &= (x_i - x_{i+1})^2 \\
 d_i &= x_{\text{prey}} - x_i
 \end{aligned}
 \tag{2}$$

where S denotes the intensity of the source or the concentration of prey. di indicates the distance between the prey and the ith badger in Eq. (2).

Step 3: Recalculate the density factor. The density factor (α) is used to regulate time-varying randomness in order to guarantee a seamless transition from exploration to exploitation. Utilise Eq. (3) to update a lowering factor α that lowers with iterations in order to reduce randomness:

$$\alpha = C \times \exp\left(\frac{-t}{t_{\text{max}}}\right), t_{\text{max}} = \text{maximum number of iterations}
 \tag{3}$$

where C is a constant ≥ 1 (default = 2).

Step 4: Getting away from the local optimum. This step, along with the two next ones, is used to exit local optima areas. In this context, the suggested method makes use of a flag F to change the direction of search, thus providing agents with a greater opportunity to thoroughly scan the search field.

Step 5: Updating the locations of the agents. As previously stated, the process of updating the HBA position (xnew) is split into two phases: the ‘digging phase’ and the ‘honey phase’. The following provides a more detailed explanation:

Step 5 (i): The digging phase. During the digging phase, a honey badger executes an activity similar to that of a cardioid [2], as shown in Fig. 3. Equation (4) may be used to mimic the cardioid motion:

$$\begin{aligned}
 x_{\text{new}} &= x_{\text{prey}} + F \times \beta \times I \times x_{\text{prey}} + F \times r_3 \times \alpha \times d_i \\
 &\times |\cos(2\pi r_4) \times [1 - \cos(2\pi r_5)]|
 \end{aligned}
 \tag{4}$$

where xprey is location of the prey which is the best position discovered so far—global best position in other words. $\beta \geq 1$ (default = 6) is ability of the honey badger to obtain food. di is distance between prey and the ith honey badger, see Eq. (2). r3, r4, and r5 are three distinct random integers between 0 and 1. F acts as the flag that changes search direction, it is calculated using Eq. (5):

$$F = \begin{cases} 1 & \text{if } r_6 \leq 0.5 \\ -1 & \text{else,} \end{cases} r_6 \text{ is a random number between 0 and 1}
 \tag{5}$$

In the digging phase, a honey badger significantly depends on scent intensity I of prey xprey, distance between the badger and prey di, and time-varying search

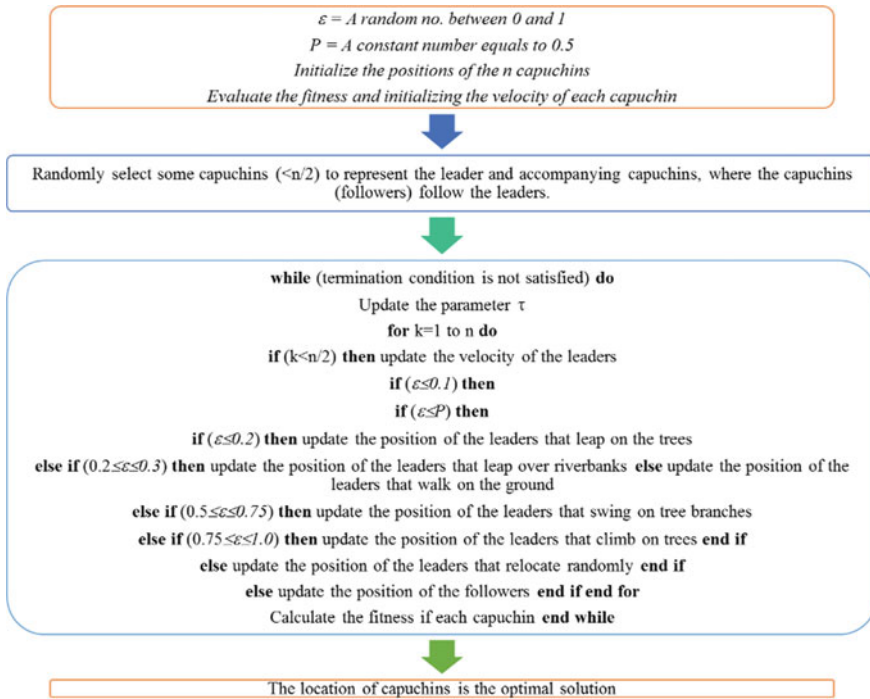


Fig. 3 CSA flowchart

influence factor α . Moreover, while digging activity, a badger may get any disruption F which enables it to locate even better prey position.

Step 5 (ii): Honey phase. The situation where a honey badger follows honeyguide bird to approach beehive may be represented as Eq. (6):

$$x_{\text{new}} = x_{\text{prey}} + F \times \alpha \times r_7 \times d_i, r_6 \text{ is a random number between 0 and 1} \quad (6)$$

where x_{new} denotes the honey badger’s new position and x_{prey} denotes the prey location, and F and α are calculated using Eqs (5) and (3), respectively. According to Eq. (6), a honey badger searches near to the prey site x_{prey} discovered thus far, based on distance information d_i . At this step, the search is affected by time-varying search behaviour (α). Additionally, a honey badger may detect disruption F .

4 Capuchin Search Algorithm (CSA)

It is based on the food hunting behaviour of South American Capuchin monkeys. During foraging, the capuchin leader and followers employ three strategies [12]:

Group members follow the male alpha (global leader), who leads and controls the group and is in charge of finding food sources.

Figure 3 depicts the CSA process flow.

5 Result and Discussions

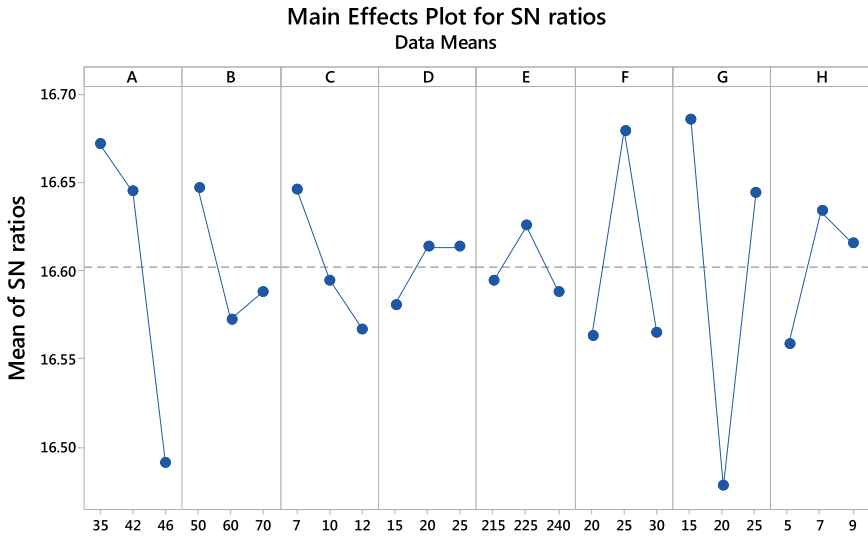
The exploratory findings in the Taguchi L27 array [13–18] are given in Table 3, along with the sink-mark depth and weight as outcomes. Among the 27 trials, it should be noted that trial no. 16 has the smallest sink-mark depth and trial no. 4 has the smallest weight.

The principal impact plot (Fig. 4) shows that A3B2C3D1E3F1G2H1 has the least factor setting when utilising Taguchi's approach for sink-mark depth. Similarly, as stated in the problem description, A3B3C1D3E3F2G1H3 exhibits the least factor setting utilising Taguchi's weight approach, as seen in Fig. 5. As a consequence, these are the best control parameters for reducing the depth and weight of sink marks on injection-molded LDPE components. The R-squared value obtained was greater than 98 percent, suggesting the relevance of the experiment in an area where error is quite tiny.

The most significant control factor for the moulded part, cooling time, accounts for 37.72% of the variance in sink-mark depth, while melt temperature for the moulded part accounts for 43.88% of the variance in weight reduction of the injection moulded LDPE component, according to the ANOVA table (Table 4).

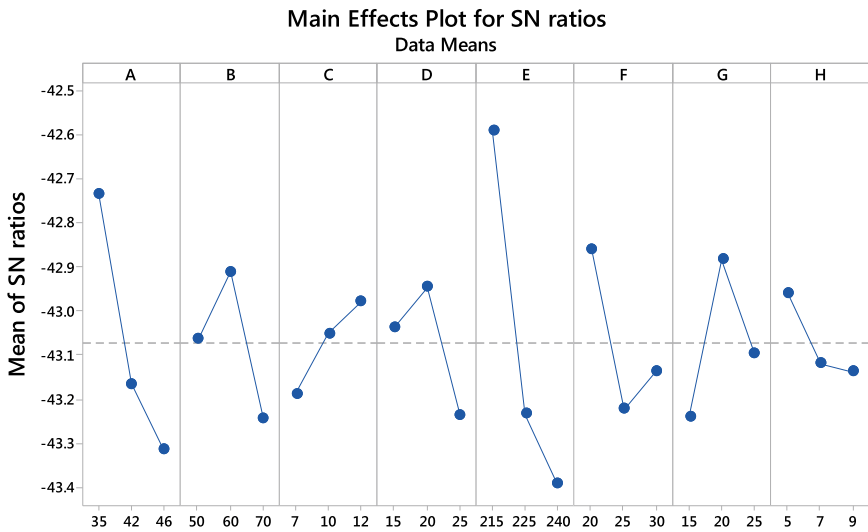
Table 3 L27 experimental run with outputs

Run No	A	B	C	D	E	F	G	H	Sink-marks depth (μm)	Weight (g)
1	35	50	7	15	215	20	15	5	0.1459	128.3
2	35	50	7	15	225	25	20	7	0.1456	141.0
3	35	50	7	15	240	30	25	9	0.1454	145.7
4	35	60	10	20	215	20	15	7	0.1461	125.0
5	35	60	10	20	225	25	20	9	0.1472	135.1
6	35	60	10	20	240	30	25	5	0.1482	137.0
7	35	70	12	25	215	20	15	9	0.1463	133.7
8	35	70	12	25	225	25	20	5	0.1487	141.0
9	35	70	12	25	240	30	25	7	0.1471	148.3
10	42	50	10	25	215	25	25	5	0.1454	139.4
11	42	50	10	25	225	30	15	7	0.1448	153.7
12	42	50	10	25	240	20	20	9	0.1490	145.9
13	42	60	12	15	215	25	25	7	0.1464	135.1
14	42	60	12	15	225	30	15	9	0.1471	146.9
15	42	60	12	15	240	20	20	5	0.1526	136.1
16	42	70	7	20	215	25	25	9	0.1442	142.5
17	42	70	7	20	225	30	15	5	0.1462	151.4
18	42	70	7	20	240	20	20	7	0.1491	146.1
19	46	50	12	20	215	30	20	5	0.1526	131.1
20	46	50	12	20	225	20	25	7	0.1489	143.1
21	46	50	12	20	240	25	15	9	0.1469	154.9
22	46	60	7	25	215	30	20	7	0.1512	139.4
23	46	60	7	25	225	20	25	9	0.1488	148.9
24	46	60	7	25	240	25	15	5	0.1481	157.7
25	46	70	10	15	215	30	20	9	0.1544	139.5
26	46	70	10	15	225	20	25	5	0.1504	146.1
27	46	70	10	15	240	25	15	7	0.1470	160.4



Signal-to-noise: Smaller is better

Fig. 4 Main effect plot for sink-mark depth



Signal-to-noise: Smaller is better

Fig. 5 Main effect plot for weight

Table 4 ANOVA for sink-mark depth and weight

Source	DF	Sink-mark depth						Weight					
		Adj SS	Adj MS	% Influence	F	P	Adj SS	Adj MS	% Influence	F	P		
A	2	0.1706	0.0853	29.58	81.12	0.000	1.6317	0.8158	22.13	5263.23	0.000		
B	2	0.0275	0.0137	4.77	13.09	0.002	0.4967	0.2483	6.74	1602.30	0.000		
C	2	0.0288	0.0144	4.99	13.69	0.001	0.2013	0.1006	2.73	649.41	0.000		
D	2	0.0064	0.0032	1.12	3.07	0.091	0.3986	0.1993	5.41	1285.87	0.000		
E	2	0.0072	0.0036	1.25	3.43	0.073	3.2354	1.6177	43.88	10,436.24	0.000		
F	2	0.0800	0.0400	13.87	38.04	0.000	0.6540	0.3270	8.87	2109.54	0.000		
G	2	0.2176	0.1088	37.72	103.46	0.000	0.5805	0.2902	7.87	1872.51	0.000		
H	2	0.0280	0.0140	4.86	13.34	0.002	0.1728	0.0864	2.34	557.58	0.000		
Residual Error	10	0.0105	0.0010	1.82			0.0015	0.0001	0.02				
Total	26	0.5770					7.3728						

Total relative significance was used to build the regression equation. This regression equation will be used as the fitness function in the Honey Badger and Capuchin Search Algorithms that were created using Matlab R2018a.:

Minimise:

$$\begin{aligned}
 \text{Sink Mark Depth} = & -0.8767 - 0.002919x_1 + 0.01302x_2 - 0.01274x_3 \\
 & + 0.02572x_4 + 0.005375x_5 - 0.01360x_6 + 0.001132x_7 \\
 & + 0.01164x_8 + 0.000054x_1x_1 - 0.000008x_2x_2 \\
 & - 0.000013x_3x_3 + 0.000011x_4x_4 + 0.000002x_5x_5 \\
 & + 0.000079x_6x_6 - 0.000136x_7x_7 - 0.000565x_8x_8 \\
 & - 0.000164x_1x_8 - 0.000063x_2x_5 + 0.000064x_2x_6 \\
 & + 0.000021x_2x_7 + 0.000019x_2x_8 - 0.000039x_3x_5 \\
 & + 0.000599x_3x_6 + 0.000327x_3x_7 + 0.000090x_3x_8 \\
 & - 0.000116x_4x_5
 \end{aligned} \tag{7}$$

$$\begin{aligned}
 \text{Weight} = & -1676 + 3.206x_1 - 4.522x_2 - 0.8296x_3 \\
 & - 4.567x_4 + 15.96x_5 + 8.000x_6 - 8.111x_7 + 5.167x_8 \\
 & - 0.02886x_1x_1 + 0.03889x_2x_2 + 0.007407x_3x_3 \\
 & + 0.1222x_4x_4 - 0.03393x_5x_5 - 0.1511x_6x_6 \\
 & + 0.1956x_7x_7 - 0.3194x_8x_8
 \end{aligned} \tag{8}$$

Subject to:

$$\begin{aligned}
 & 35 \leq x_1 \leq 46; 50 \leq x_2 \leq 70; 7 \leq x_3 \leq 12; 15 \leq x_4 \leq 25; 215 \leq x_5 \leq 240; 20 \\
 & \leq x_6 \leq 30; 15 \leq x_7 \leq 25; \\
 & 5 \leq x_8 \leq 9.
 \end{aligned}$$

According to the issue statement, the width and depth of weld lines and sink marks on injection moulded LDPE components must be reduced. To get optimum moulding parameters, certain fixed parameters were specified in the honey badger method with a total population size of 30 and a maximum iteration limit of 100. Figures 6 and 7 illustrates the fitness convergence curve when the HBA is used. Similarly, certain fixed parameters have been specified in the Capuchin Search method, with a total population size of 100 and a maximum iteration limit of 500. Figures 8 and 9 illustrates the fitness convergence curve when the CSA is used. Table 5 summarises the optimal factor setting together with projected fitness values.

To assess the significance of the predictive value, unconfirmed predictions made by the optimization algorithm were examined [19–25]. The following information might be useful in determining the ideal factor setting for sink-mark depth and weight reduction during LDPE injection moulding: Because sink marks depth and weight have been reduced by utilising the HBA and CSA factor settings rather of the Taguchi technique factor settings, the HBA and CSA findings are more accurate than the Taguchi method values for injection moulded LDPE components (Table 5).

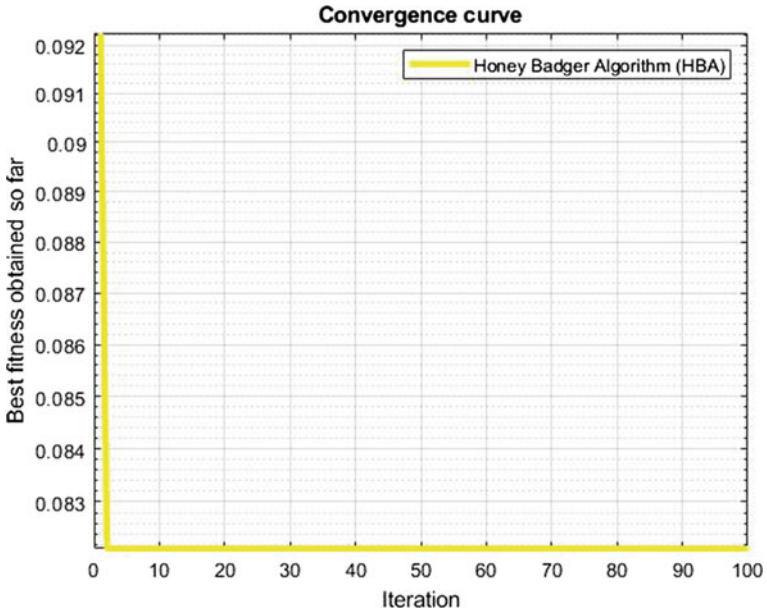


Fig. 6 Convergence plot for sink-mark width (HBA)

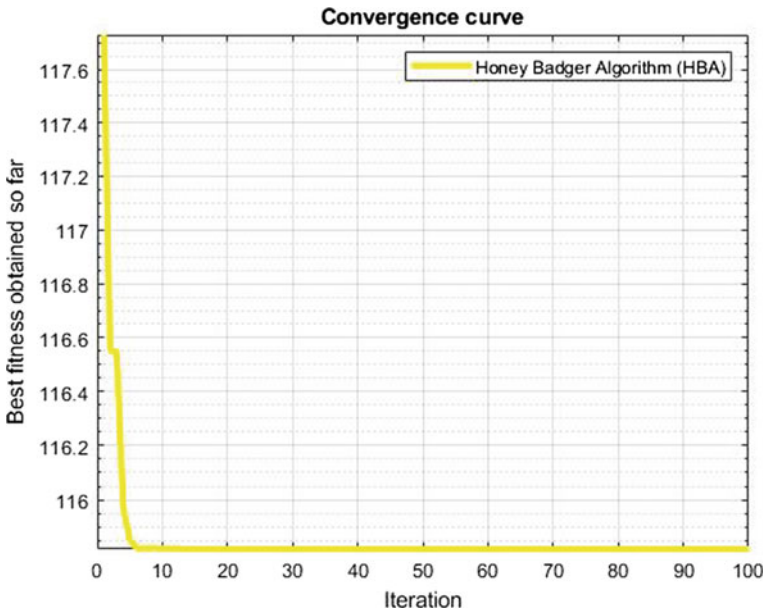


Fig. 7 Convergence plot for weight (HBA)

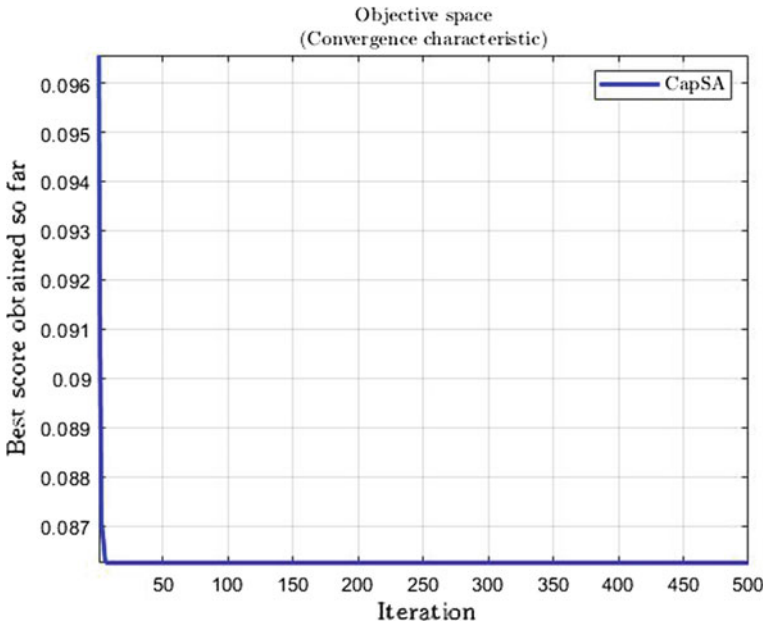


Fig. 8 Convergence plot for sink-mark width (CSA)

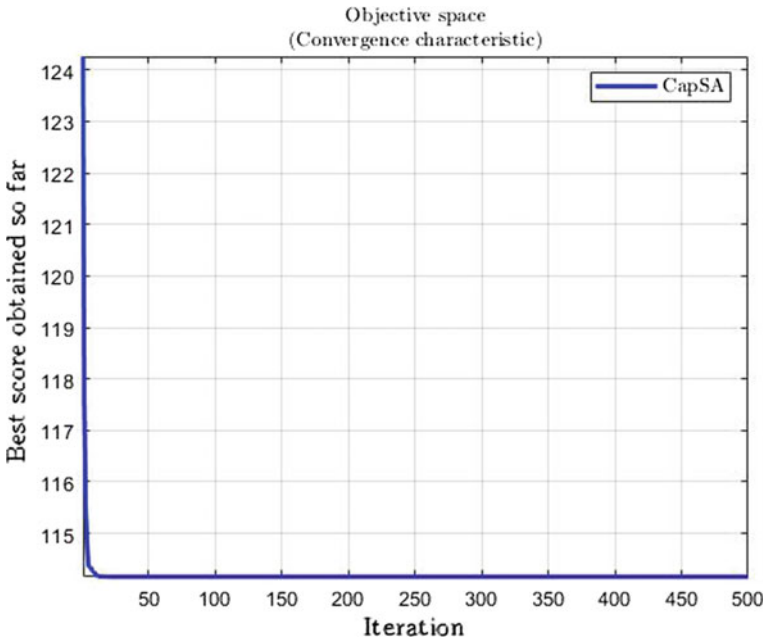


Fig. 9 Convergence plot for weight (CSA)

Table 5 Control parameters using different approaches

Algorithms	Parameters	Factor setting for optimal sink marks depth	Factor setting for optimal weight
Taguchi method	Injection pressure	46 MPa	46 MPa
	Mould temperature	60 °C	70 °C
	Back pressure	12 MPa	7 MPa
	Holding pressure	15 MPa	25 MPa
	Melt temperature	240 °C	240 °C
	Ambient temperature	20 °C	25 °C
	Cooling time	20 s	15 s
	Holding time	5 s	9 s
	Predicted value of Sink marks depth	0.1551 μm	–
	Experimental value of Sink marks depth	0.1540 μm	–
	Predicted value of weight	–	165.85 g
	Experimental value of weight	–	158.58 g
	Honey badger algorithm	Injection pressure	46 MPa
Mould temperature		70 °C	60 °C
Back pressure		12 MPa	12 MPa
Holding pressure		25 MPa	15 MPa
Melt temperature		240 °C	215 °C
Ambient temperature		20 °C	20 °C
Cooling time		15 s	20 s
Holding time		9 s	5 s
Predicted value of Sink marks depth		0.0821 μm	–
Experimental value of Sink marks depth		0.0811 μm	–
Predicted value of weight		–	115.81 g
Experimental value of weight		–	115.50 g
Capuchin search algorithm		Injection pressure	46 MPa
	Mould temperature	70 °C	60 °C
	Back pressure	12 MPa	12 MPa
	Holding pressure	25 MPa	15 MPa
	Melt temperature	240 °C	215 °C
	Ambient temperature	20 °C	20 °C

(continued)

Table 5 (continued)

Algorithms	Parameters	Factor setting for optimal sink marks depth	Factor setting for optimal weight
	Cooling time	15 s	20 s
	Holding time	9 s	5 s
	Predicted value of Sink marks depth	0.0821 μm	–
	Experimental value of sink marks depth	0.0811 μm	–
	Predicted value of weight	–	114.81 g
	Experimental value of weight	–	115.50 g

Cooling time was shown to be a substantial determinant in sink-mark depth, while melt temperature was found to be a significant factor in weight in early study. The findings of this investigation were consistent with earlier research.

6 Conclusion

In this experiment, plastic injection moulding parameters were investigated on the moulding of an LDPE medical syringe plunger. Eight plastic injection moulding factors were investigated in order to reduce sink-mark depth and weight during LDPE injection moulding. To improve the control settings, metaheuristic optimisation approaches such as the Taguchi method were utilised in combination with the Honey Badger and Capuchin Search Algorithms.

The most significant control factor for the moulded part, according to the ANOVA results, is cooling time, which accounts for 37.72% of the variance in sink-mark depth, and the most significant control factor for the injection moulded LDPE component is melt temperature, which accounts for 43.88% of the variance in weight reduction for the component. The expected and experimental values provided by the Honey Badger and Capuchin search algorithms are substantially equal to those found by confirmatory testing because their output is more exact than that of the Taguchi technique.

References

1. Lal SK, Vasudevan H (2013) Optimization of injection moulding process parameters in the moulding of low density polyethylene (LDPE). *Int J Eng Res Dev* 7(5):35–39
2. Jaya H, Zulkepli NN, Omar MF, Abd Rahim SZ, Halim KAA (2020) Optimization of injection moulding processing parameters for LDPE/RH composites tensile strength through full factorial experiment. In: IOP conference series: Materials science and engineering, vol. 957(1). IOP Publishing, p 012039
3. Roslan N, Abd Rahim SZ, Abdellah AEH, Abdullah MMAB, Bloch K, Pietrusiewicz P, Ghazali MF (2021) Optimisation of shrinkage and strength on thick plate part using recycled LDPE materials. *Materials* 14(7):1795
4. Bakshi P, Pappu A, Bharti DK, Patidar R (2021) Accelerated weathering performance of injection moulded PP and LDPE composites reinforced with calcium rich waste resources. *Polym Degrad Stab* 192:109694
5. Khan A, Patidar R, Pappu A (2021) Marble waste characterization and reinforcement in low density polyethylene composites via injection moulding: towards improved mechanical strength and thermal conductivity. *Constr Build Mater* 269:121229
6. Adeodu AO, Kanakana-Katumba MG, Maladzhi RW, Daniyan IA (2021) Optimization of injection process parameters of plastic reinforced composites using response surface methodology and central composite design. In: Proceedings of the American society for composites—Thirty-sixth technical conference on composite materials
7. Jaya H, Noriman NZ, Rahim SZA, Omar MF, Hamzah R, Dahham OS, Umar MU (2020) Impact strength of LDPE/RH composites for industrial injection moulded parts. In: AIP conference proceedings, vol. 2213(1). AIP Publishing LLC, pp 020256
8. Jaya H, Noriman NZ, Rahim SZA, Omar MF, Hamzah R, Dahham OS, Umar MU (2020) Flexural properties of rice husk (*Oryza sativa*) reinforced low density polyethylene composites for industrial injection moulded parts. In: AIP conference proceedings, vol 2213(1). AIP Publishing LLC, p 020254
9. Jaya H, Zulkepli NN, Omar MF, Abd Rahman SZ, Halim KAA (2019) Injection moulding recommended parameters simulation analysis of rice husk composite. In: IOP conference series: materials science and engineering, vol. 701(1). IOP Publishing, p 012048
10. Ravikiran B, Pradhan DK, Jeet S, Bagal DK, Barua A, Nayak S (2022) Parametric optimization of plastic injection moulding for FMCG polymer moulding (PMMA) using hybrid Taguchi-WASPAS-Ant Lion optimization algorithm. *Materials Today: Proceedings* 56(5):2411–2420.
11. Hashim FA, Houssein EH, Hussain K, Mabrouk MS, Al-Atabany W (2022) Honey badger algorithm: new metaheuristic algorithm for solving optimization problems. *Math Comput Simul* 192:84–110
12. Braik M, Sheta A, Al-Hiary H (2021) A novel meta-heuristic search algorithm for solving optimization problems: capuchin search algorithm. *Neural Comput Appl* 33(7):2515–2547
13. Sahoo AK, Jeet S, Bagal DK, Barua A, Pattanaik AK, Behera N (2022) Parametric optimization of CNC-drilling of Inconel 718 with cryogenically treated drill-bit using taguchi-whale optimization algorithm. *Mater Today: Proc* 50(5):1591–1598. <https://doi.org/10.1016/j.matpr.2021.09.121>
14. Sahoo UK, Jeet S, Bagal DK, Sahu MK, Kumari K, Barua A (2022) Optimization of industrial coatings tribological parameters by studying its application on mechanical components using taguchi coupled WASPAS method. *Mater Today: Proc* 50(5):1405–1412. <https://doi.org/10.1016/j.matpr.2021.08.326>
15. Challan M, Jeet S, Bagal DK, Mishra L, Pattanaik AK, Barua A (2022) Fabrication and mechanical characterization of red mud based Al2025-T6 MMC using lichtenberg optimization algorithm and whale optimization algorithm. *Mater Today: Proc* 50(5):1346–1353. <https://doi.org/10.1016/j.matpr.2021.08.274>
16. Behera NC, Jeet S, Nayak CK, Bagal DK, Panda SN, Barua A (2022) Parametric appraisal of strength & hardness of resin compacted sand castings using hybrid taguchi-WASPAS-material

- generation algorithm. *Mater Today: Proc* 50(5):1226–1233. <https://doi.org/10.1016/j.matpr.2021.08.104>
17. Malik S, Jeet S, Bagal DK, Nayak RP, Barua A, Mahapatra SS (2022) Parametric appraisal of collapsibility and core shrinkage of phenol binded unbaked casting moulds using taguchi-sunflower optimization algorithm. *Mater Today: Proc* 50(5):1138–1144. <https://doi.org/10.1016/j.matpr.2021.08.031>
 18. Jena S, Jeet S, Bagal DK, Baliarsingh AK, Nayak DR, Barua A (2022) Efficiency analysis of mechanical reducer equipment of material handling industry using sunflower optimization algorithm and material generation algorithm. *Mater Today: Proc* 50(5):1113–1122. <https://doi.org/10.1016/j.matpr.2021.08.005>
 19. Mohanty A, Nag KS, Bagal DK, Barua A, Jeet S, Mahapatra S, Cherkia H (2022) Parametric optimization of parameters affecting dimension precision of FDM printed part using hybrid taguchi-MARCOS-nature inspired heuristic optimization technique. *Mater Today: Proc* 50(5):893–903. <https://doi.org/10.1016/j.matpr.2021.06.216>
 20. Bagal DK, Naik B, Parida B, Barua A, Jeet S, Singh SK, Pattanaik AK (2020) Comparative mechanical characterization of M30 concrete grade by fractional replacement of portland pozzolana cement with industrial waste using CoCoSo and CODAS methods. *IOP Conf Ser: Mater Sci Eng* 970(1):012015
 21. Bagal DK, Parida B, Barua A, Naik B, Jeet S, Singh SK, Pattanaik AK (2020) Mechanical characterization of hybrid polymer SiC nano composite using hybrid RSM-MOORA-whale optimization algorithm. *IOP Conf Ser: Mater sci Eng* 970(1):012017
 22. Pradhan DK, Sahu B, Bagal DK, Barua A, Jeet A, Pradhan S (2022) Application of progressive hybrid RSM-WASPAS-grey wolf method for parametric optimization of dissimilar metal welded joints in FSSW process. *Mater Today: Proc* 50(5):766–772. <https://doi.org/10.1016/j.matpr.2021.05.471>
 23. Mangaraj SR, Bagal DK, Parhi N, Panda SN, Barua A, Jeet S, (2022) Experimental study of a portable plasma arc cutting system using hybrid RSM-nature inspired optimization technique. *Mater Today: Proc* 50(5):867– 878. <https://doi.org/10.1016/j.matpr.2021.06.138>
 24. Bagal DK, Barua A, Jeet S, Satapathy P, Patnaik D (2019) MCDM optimization of parameters for wire-EDM machined stainless steel using hybrid RSM-TOPSIS genetic algorithm and simulated annealing. *Inter J Eng Adv Technol* 9(1):366–371
 25. Barua A, Jeet S, Bagal DK, Satapathy P, Agrawal PK (2019) Evaluation of mechanical behavior of hybrid natural fiber reinforced nano sic particles composite using hybrid taguchi-Cocoso method. *Inter J Innovative Technol Exploring Eng* 8(10):3341–3345

Bibliometric Analysis of Friction Stir Spot Welded Joints using SCOPUS Database



Dilip Kumar Bagal, Siddharth Jeet, Abhishek Barua, Swastik Pradhan, Surya Narayan Panda, and Saujanya Kumar Sahu

Abstract Friction stir spot welding (FSSW) is an eco-friendly high efficient welding technique in the field of solid-state welding. Using this technique dissimilar metal lap joints can be done such as aluminum alloy with the copper alloy. Moreover, bibliometric research is an essential method of statistical analysis of publications in a certain research field. This commonly used technique categorizes the information using different variables such as active journals, countries, and authors. In this paper, a systematic review of the research carried out in the area of FSSW process is presented by use of bibliometric research indicators thus recognizing the most influential research in this field. The SCOPUS repository is used to retrieve the research published regarding the FSSW since 1960. The paper is divided into several analysis sections that focus on the most influential years, journals, authors, affiliations, countries, document type, subject area, and keywords that have contributed to the field of FSSW. The aim of this study is to be informative regarding FSSW and use the bibliometric indicators to highlight the vital research conducted in the field of FSSW.

Keywords Bibliometric analysis · Dissimilar metal · FSSW

D. K. Bagal

Department of Mechanical Engineering, Government College of Engineering, Kalahandi, Bhawanipatna, Odisha, India

S. Jeet · A. Barua

Department of Mechanical Engineering, Centre for Advanced Post Graduate Studies, BPUT, Rourkela, Odisha, India

S. Pradhan (✉)

School of Mechanical Engineering, Lovely Professional University, Phagwara, Punjab, India
e-mail: swastik.22644@lpu.co.in

S. N. Panda

Department of Production Engineering, Birsa Institute of Technology, Sindri, Dhanbad, Jharkhand, India

S. K. Sahu

Department of Civil Engineering, Government College of Engineering, Kalahandi, Bhawanipatna, Odisha, India

1 Introduction

The introduction of new information technology such as the internet of things, artificial intelligence, big data, cloud computing, and smart manufacturing is changing welding processes. Intelligent welding systems (IWS) are gaining interest from academic and industrial audiences using these technologies [1]. As the aircraft and the automobile sector required materials that are providing good performance to their weight characteristics. Hence lightweight materials are considered for this purpose. The lightweight metal like aluminum and copper are used for the same as it has excellent thermal and electrical conductivity as well as high ductility and lightweight [1–5]. Mostly resistance spot welding, laser spot welding are considered to weld this type of material.

Friction stir spot welding (FSSW) is a very useful version of traditional friction stir welding (FSW), which shows tremendous potential to replace processes such as resistance spot welding and riveting with single-point joining. There were several articles about FSSW and some manufacturing applications. The process characteristics and variations, macro and microstructural characteristics, and mechanical properties of the resulting joints and computational simulations of the FSSW process have been outlined on the basis of open literature. Furthermore, several FSSW implementations in the aerospace, aircraft, and automotive sectors have also been reviewed. Finally, the existing concerns and problems that occurred in the FSSW were seen [6].

The method of FSSW is a variant of the process of friction stir welding (FSW), lacking the tool's lateral motion during the welding process. It has been used in the Japanese automobile industry to make aluminum doors, engine hoods, and deck-lids. It has the advantages of cost savings in service and investment, weight loss, high repeatability and durability, low maintenance, improved working atmosphere, and recyclability relative to other types of aluminum spot joining such as resistance spot welding (RSW) and riveting. This paper offers a detailed technology literature analysis, covering processes for joining, process regulation, creation of process parameters, fracture behaviors, metallurgy, temperature, geometry of instruments, and material flow. There is also talk of process variations, joining of aluminum to concrete, steel to steel, magnesium, weld bonding (with adhesive), process modeling, and manufacturing applications [7].

FSSW is a variant of FSW in this the non-consumable rotating tool is used to join the two dissimilar overlapping plates. In other words, Friction stir spot welding (FSSW), a variant of Friction Stir Welding (FSW) practice where series of solid state friction stir spot welds are made to join the dissimilar overlapping plates, by a non-consumable rotating tool. An individual spot weld is shaped by pressing the non-consumable tool which has a shoulder and pin using FSSW. The sheet is plunged with the tool pin until the shoulder is put on a high forging pressure thus bonding the constituents through metallurgical process without melting [3, 8–11].

This investigation has been carried out in two phases. In first phase, bibliometric analysis has been carried out to find out the advancement in FSSW done by numerous researchers across the globe and indexed in SCOPUS database. In the last phase,

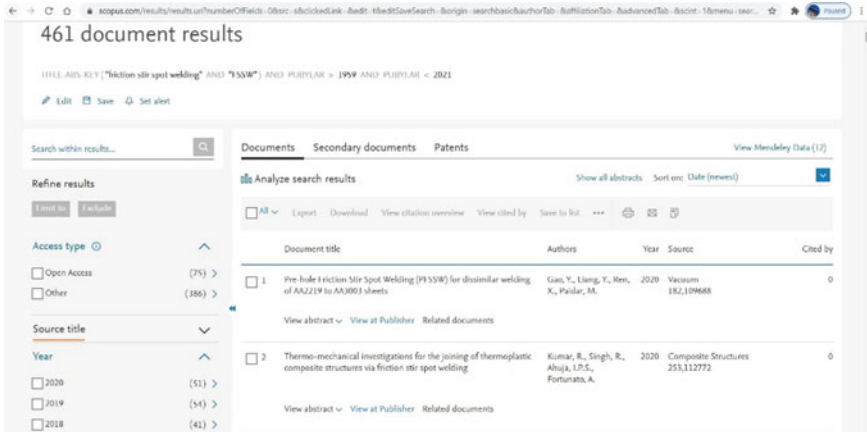


Fig. 2 Obtained documents results in SCOPUS repository

3 Bibliometric Analysis

Bibliometric is basically divided in two Greek words, i.e., “biblio” means “books” and “metric” means “measurement” [5]. In other words, to calculate their effect on scientific areas, “bibliometric” is a tool that requires statistical study of published papers and citations therein. Therefore, bibliographic data predictive analysis is typically based on citation analysis of research outputs and publications [6].

In general, the study field that seeks to examine current developments in literature in a given area and offers recommendations and reasons for possible research work is bibliometric or scientometric review. Basically, it includes a general outline of the study field and an overall framework. Broadus (1987) have provided us with an appropriate description of bibliometric analysis in the past. Heck and Bremser further expanded the work by evaluating writers and organizations in the field of accounting [7, 12].

Earlier, the use of bibliometric techniques in the field of library and information science was very frequent. It is trending in every domain nowadays. It is used to include scholarly literature for quantitative research. Citation analysis, focused on the creation of citation graphs and networks, is a widely used bibliographic tool. Many branches of study use bibliometric methods to investigate the influence of their area [13]. There are some advantages of bibliometric analysis which are enlisted below:

1. Growth of literature review.
2. Growth of domain knowledge.
3. Straight forward analysis by considering Counts, Frequencies, and Descriptive data.
4. Growth of further directions for future research.
5. Analysis of quantitative as well as qualitative in nature [14].

In multiple tasks including this type of strategy assists in different activities such as:

1. Show the significance of your own area of study and its effects.
2. Define a region of strength and vulnerability in science.
3. Recognition of the best scientists in the subject field.
4. To recognize historical, current, and future developments in writing.
5. To research the performance of organizations and funders.

With some advantages, bibliometric research also comprises of some limitations:

1. Within different disciplines, citation patterns may vary.
2. While ranking the top ten of any category of selection variant all selected attributes are placed in alphabetical order. So, some attributes with same ranking may be deselected in bottom rows.
3. Only good sources are counted, leaving a vast number of documents missing.
4. The article may be quoted in a negative rather than a positive fashion, but the quote would also be counted.
5. Informal publications and correspondence are not included. Scientific growth may thus not be adequately forecast [12].

Specifically, 302 (65.51%) number of documents from Article Type, 10 (2.17%) documents from Book Chapter, 139 (30.15%) documents from conference paper, 1 (0.22%) documents from letter, and 9 (1.95%) documents from review type category documents are found from the SCOPUS repository which is shown in Fig. 3. Similarly, Fig. 4 shows the distribution of documents per each year ranging from 2005 to 2020 onwards. In Fig. 4, both color and size of the column show the sum of documents for each year. It is observed that the citation counts per year have increased exponentially with respect to the number of publications. From the bibliometric analysis, the results show that research in the FSSW field and its citations have considerably increased over the past five years especially [15].

Total of 45 countries from all over world contributed the research documents based on FSSW and the country wise analysis of documents is mapped in Fig. 5. In Fig. 5, United States and China Country have contributed highest number of documents, i.e., 88 (15.466%) and 85 (14.938%), respectively. In Table 1, the total number of documents by country/territory is tabulated with each percentage contribution on FSSW research field.

The total 461 number of documents based on FSSW research field have been further classified according to the subject area and is plotted in Fig. 6. In Fig. 6 of documents by subject area, engineering and material science have shown highest number of documents, because the FSSW research has contributed more to the field of engineering applications and the science of materials as compared to other subject areas.

Out of 461 documents from SCOPUS database, only 137 sources or journals were found where the documents based on FSSW research documents have been published. The top 10 sources with documents per year are tabulated in Table 2 and

DOCUMENTS BY TYPE

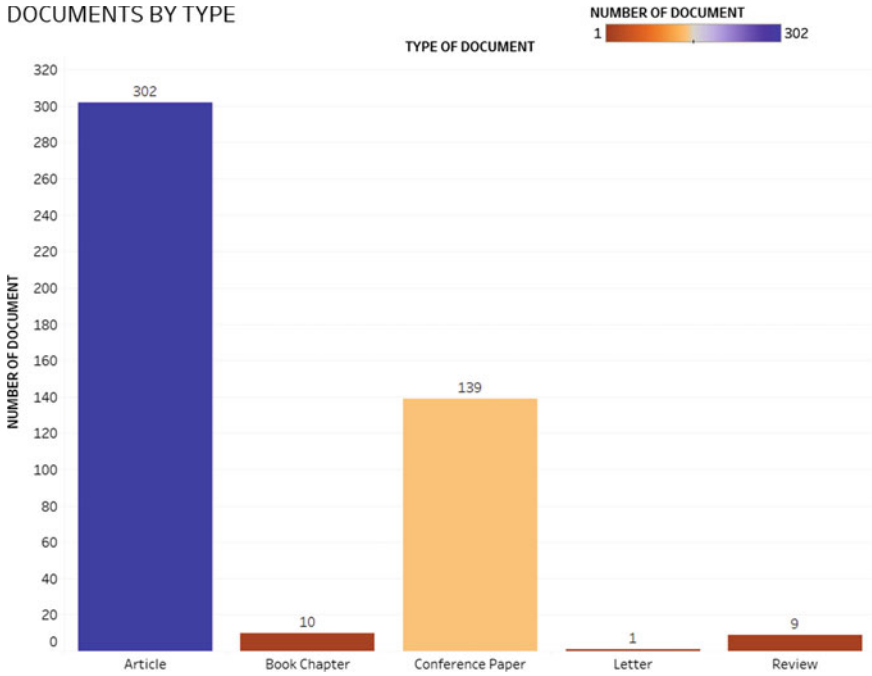


Fig. 3 Documents by type

DOCUMENTS BY YEAR

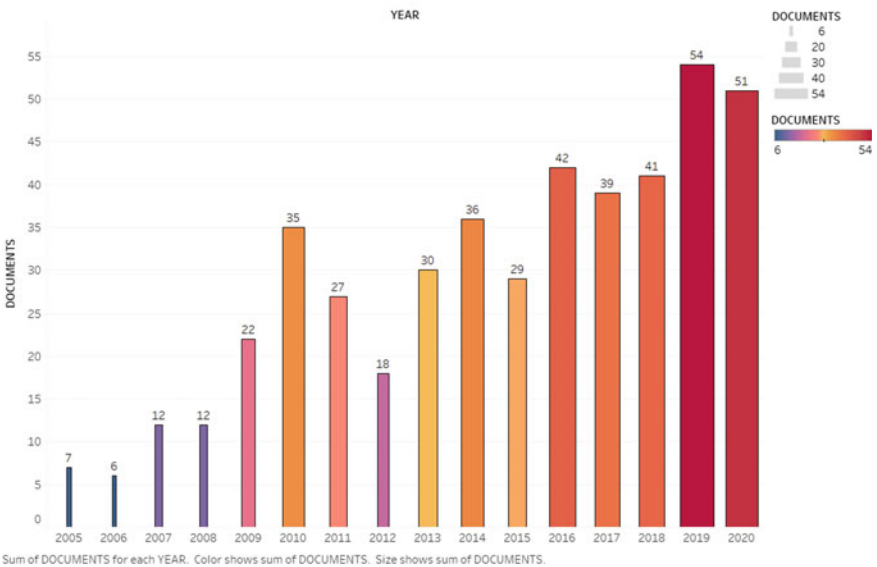


Fig. 4 Documents by year

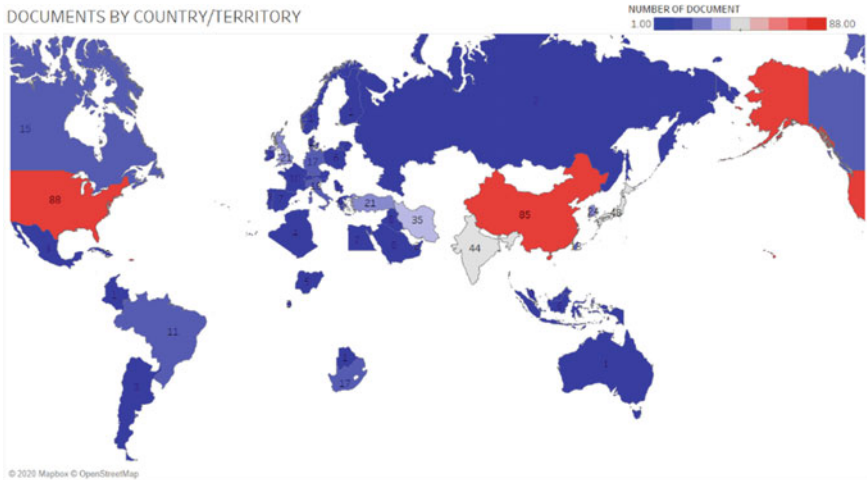


Fig. 5 Documents by country/territory

all the sources with documents per year is plotted in Tree graph format in Fig. 7. International Journal of Advanced Manufacturing Technology (Springer) and Science and Technology of Welding and Joining (Taylor and Francis) sources have shown highest 18 number of documents published per year in the research field of FSSW only.

There is 160 number of affiliated institutes are found in total 461 number of documents with FSSW research where the faculties and research scholars have an interest of research area in FSSW field and also published their works in various publications. The University of Johannesburg, Northwestern Polytechnical University, and the University of Manchester contributed highest number of documents with 17, 15, and 13, respectively. The plot of number of documents with affiliation is displayed in Fig. 8. In Fig. 8, the color and size of the column are marked as per the number of documents.

Based on the number of articles, the most active authors for SCOPUS are extracted and sorted out. According to the number of documents, the authors with the same number of publications count, then the ranking is given. Authors named “Akinlabi” and “Mubiayi” have published highest number of papers on FSSW research field with 17 and 12 number of documents, respectively. Table 3 showed the top 10 authors who have contributed highest number of documents in terms of publication in SCOPUS repository or database with their published document numbers. Figure 9 shows the top researchers with their contributing number of documents in area of FSSW investigations.

Total 103 number of sponsored funders from all over the world have contributed their funds by investing in FSSW research field to various researchers. In Table 4, it is mentioned only top ten funding sponsor agencies for the total 461 number of documents and in Fig. 10, few funding agencies with contributing significant number of documents are plotted. It can be observed from this analysis that “National Natural

Table 1 Countries/Territories publishing work on FSSW in SCOPUS

S. No	Country/Territory	No. of documents	Contribution (%)	S. No	Country/Territory	No. of documents	Contribution (%)
1	United States	88	15.466	26	Argentina	3	0.527
2	China	85	14.938	27	Cuba	3	0.527
3	Japan	48	8.436	28	Mexico	3	0.527
4	India	44	7.733	29	Portugal	3	0.527
5	Iran	35	6.151	30	Egypt	2	0.351
6	South Korea	24	4.218	31	Lithuania	2	0.351
7	Turkey	21	3.691	32	Russian Federation	2	0.351
8	United Kingdom	21	3.691	33	Slovenia	2	0.351
9	Italy	18	3.163	34	United Arab Emirates	2	0.351
10	Germany	17	2.988	35	Australia	1	0.176
11	South Africa	17	2.988	36	Botswana	1	0.176
12	Canada	15	2.636	37	Colombia	1	0.176
13	Taiwan	13	2.285	38	Denmark	1	0.176
14	Brazil	11	1.933	39	Finland	1	0.176
15	France	10	1.757	40	Ireland	1	0.176
16	Malaysia	9	1.582	41	Norway	1	0.176
17	Austria	8	1.406	42	Serbia	1	0.176
18	Iraq	8	1.406	43	Singapore	1	0.176

(continued)

Table 1 (continued)

S. No	Country/Territory	No. of documents	Contribution (%)	S. No	Country/Territory	No. of documents	Contribution (%)
19	Saudi Arabia	8	1.406	44	Switzerland	1	0.176
20	Spain	7	1.230	45	Undefined	3	0.527
21	Greece	6	1.054				
22	Indonesia	6	1.054				
23	Poland	6	1.054				
24	Nigeria	5	0.879				
25	Algeria	4	0.703				

DOCUMENTS BY SUBJECT AREA

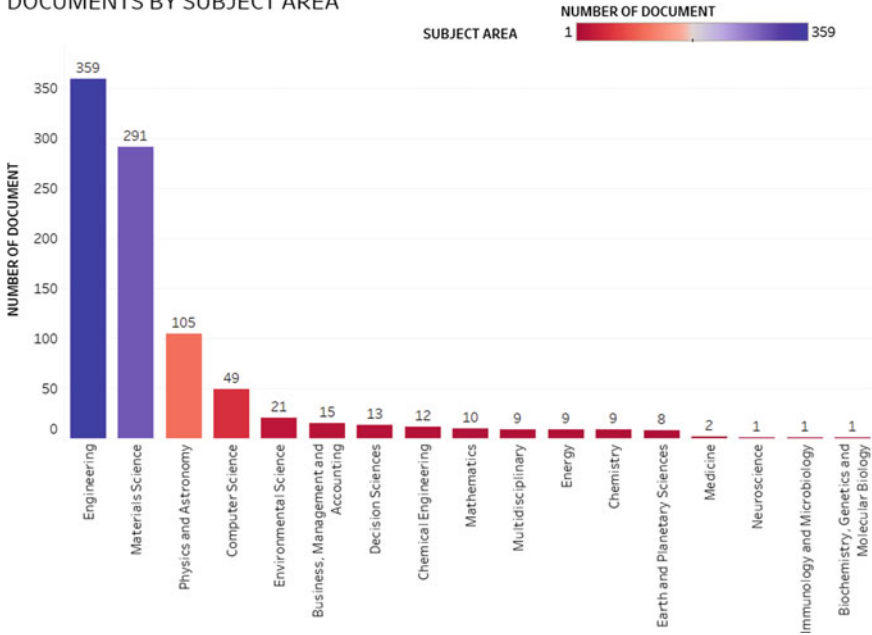


Fig. 6 Documents by subject area

Table 2 Top 10 journals publishing works on FSSW in SCOPUS

S. No	Source title	No. of documents per year
1	International journal of advanced manufacturing technology	18
2	Science and technology of welding and joining	18
3	Journal of materials processing technology	16
4	SAE technical papers	16
5	TMS annual meeting	16
6	Materials and design	15
7	Journal of manufacturing processes	13
8	Materials today proceedings	11
9	Journal of materials engineering and performance	9
10	Welding in the world	9

Science Foundation of China” contributed the highest number of documents in research of FSSW, i.e., 34. Besides this sponsor agency, there are two funders named “Engineering and Physical Sciences Research Council” and “National Science Foundation” also have contributed significant number of documents, i.e., 11 for both agencies in the field of FSSW-related research area.

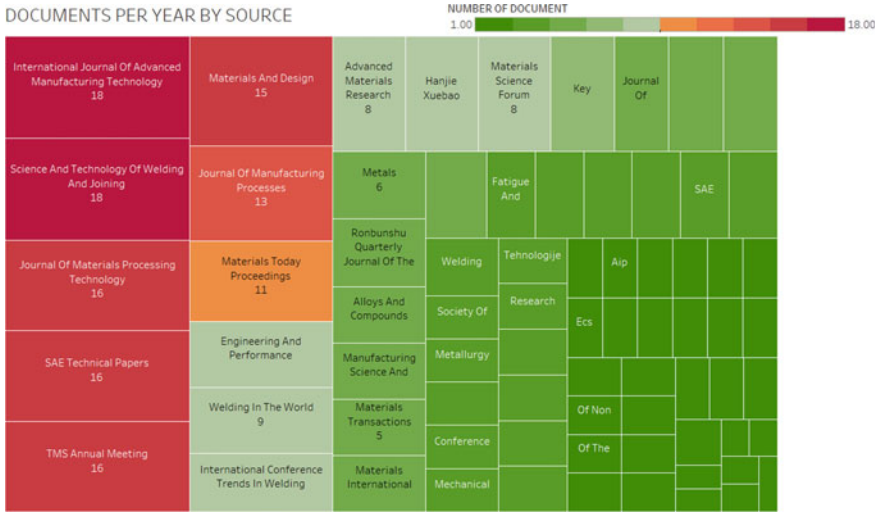


Fig. 7 Documents per year by source

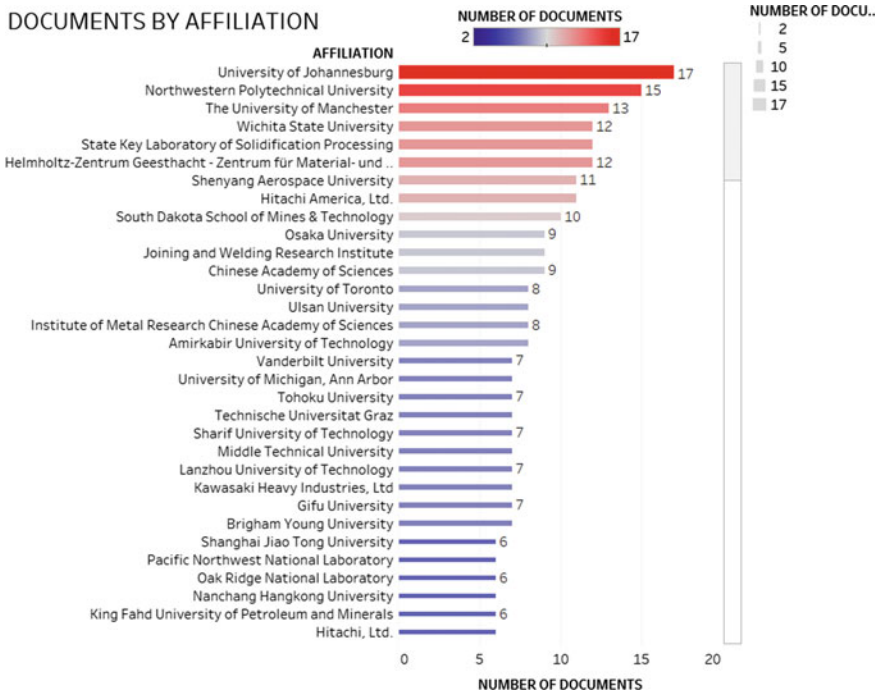


Fig. 8 Documents by affiliation

Table 3 Top 10 most productive authors with publishing documents in SCOPUS

S. No	Author	No. of documents
1	Akinlabi	17
2	Mubiayi	12
3	Badarinarayan	10
4	Li	10
5	Muci-Küchler	9
6	Yang	9
7	Chu	8
8	Hong	8
9	Makhatha	8
10	Okamoto	8

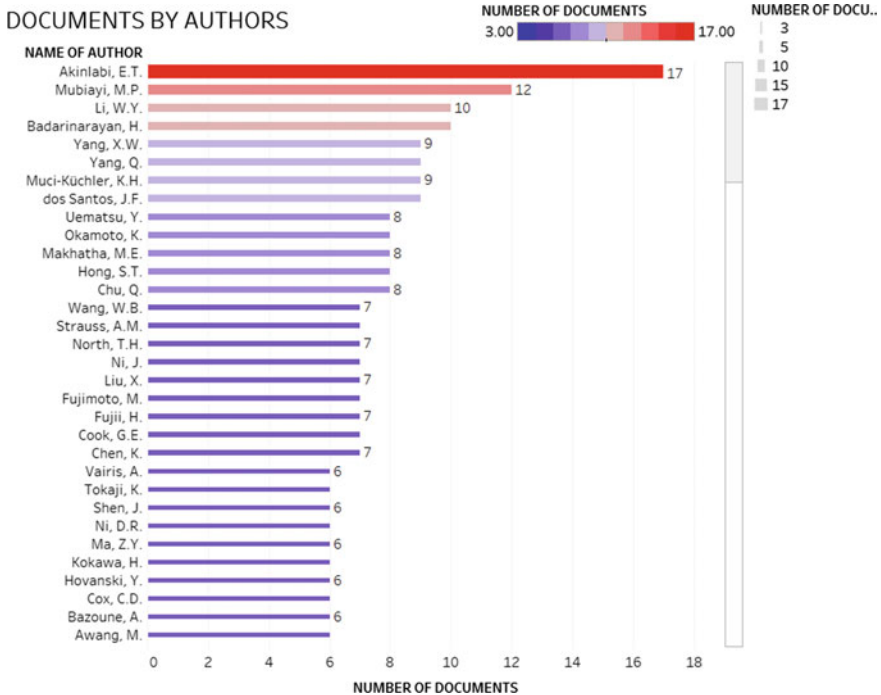


Fig. 9 Documents by authors

In this section, VOS viewer Software has been utilized, which is the most frequently used information visualization program, to pick the authors’ top keywords in their articles. Figure 11 includes a visualization of the most common SCOPUS keywords used by the authors. In the SCOPUS index database, almost all the keywords originating from “Friction Stir Spot Welding” are general. As SCOPUS

Table 4 Top 10 leading funding sponsors publishing on FSSW research field in SCOPUS

S. No	Funding sponsor	No. of documents
1	National natural science foundation of china	34
2	Engineering and physical sciences research council	11
3	National science foundation	11
4	National research foundation of Korea	9
5	Aeronautical science foundation of China	8
6	Fundamental research funds for the central universities	7
7	University of Johannesburg	6
8	Higher education discipline innovation project	5
9	Natural sciences and engineering research council of Canada	5
10	King Fahd university of petroleum and minerals	4

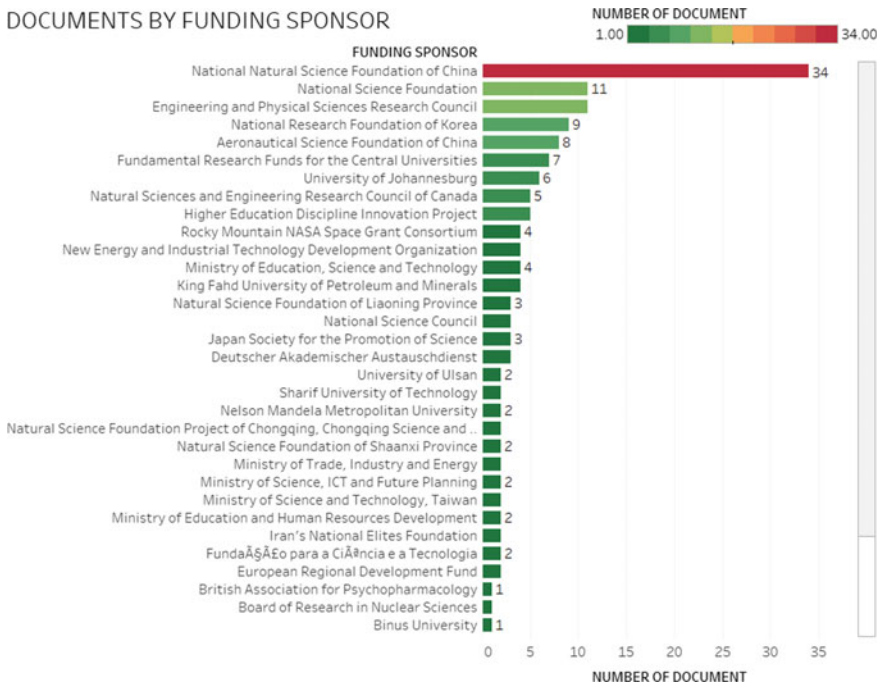


Fig. 10 Documents by funding sponsors

indexes papers from various and broader outlets, the strength of the keywords depicted by the circular node can be higher. In the top list of keywords, we will also find that one keyword, augmented reality, is distinct. As is visible from Fig. 11, “Friction Stir Spot Welding” is surrounded by keywords for “Friction Stir Welding” and “FSSW”.

5 Conclusion

This investigation has been progressed in a detailed bibliometric analysis has been done on FSSW for discovering the advancement in this area while the last phase consists of experimental analysis based on bibliometric investigation. SCOPUS, which is one of the broadly used repositories was employed for the bibliometric analysis of FSSW where about 461 publications were indexed. United States, China, Japan, and India countries contributed higher number of research documents than other countries or territories. Highest number of documents was put out in International Journal of Advanced Manufacturing Technology (Springer) and Science and Technology of Welding and Joining (Taylor and Francis) journals as indexed in SCOPUS repository. From University of Johannesburg institute, highest number of documents are published till 2020. Author named “Akinlabi” contributed highest number of documents in the field of FSSW research. The National Natural Science Foundation of China funder has sponsored highest as compared to other sponsored agencies in SCOPUS database. The bibliometric analysis in this investigation delivered the inherent arrangement of publications on FSSW which is truly necessary investigation for the arising field of FSSW. More investigation can be performed with the other indexing databases such as WoS (Web of Science), Science Direct, CrossRef, and Google Scholar as a prospect opportunity of this study.

References

1. Raheja GS, Singh S, Prakash C (2020) Processing and characterization of Al5086-Gr-SiC hybrid surface composite using friction stir technique. *Mater Today: Proc* 28:1350–1354
2. Mishra M, Prakash C, Shabadi R, Singh S (2020) Mechanical and microstructural characterization of magnesium/multi-walled carbon nanotubes composites fabricated via friction stir processing. In: *advances in materials science and engineering*, Springer, Singapore, pp 137–147
3. Kang AS, Prakash C, Singh J, Pramanik A (2020) Microstructural and mechanical properties of aa6061 aluminium alloy reinforced with nano-sic particles using FSP. In: *advances in materials science and engineering*, Springer, Singapore, pp 195–204
4. Khiste GP, Paithankar RR (2017) Analysis of Bibliometric term in SCOPUS. *Int J Libr Sci Inf Manag* 3(3):81–88
5. Tunga SK (2014) Doctoral dissertations on horticulture in agricultural sciences in West Bengal a bibliometric study 1991 2010. https://shodhganga.inflibnet.ac.in/bitstream/10603/102394/14/14_chapter%205.pdf
6. Saravanakumar R, *J Sci Dent* 5(1) <https://jsd.sbvjournals.com/doi/JSD/pdf/10.5005/jsd-5-1-1>
7. Muhuri PK, Shukla AK, Abraham A (2019) Industry 4.0: a bibliometric analysis and detailed overview. *Eng Appl Artif Intell* 78:218–235
8. Al-Roubaiy AO, Nabat SM, Batako AD (2014) Experimental and theoretical analysis of friction stir welding of Al–Cu joints. *Int J Adv Manuf Technol* 71(9–12):1631–1642
9. Ramanjaneyulu K, Reddy GM, Rao AV, Markandeya R (2013) Structure-property correlation of AA2014 friction stir welds: role of tool pin profile. *J Mater Eng Perform* 22(8):2224–2240
10. Abbass MK, Hussein SK, Khudhair AA (2016) Optimization of mechanical properties of friction stir spot welded joints for dissimilar aluminum alloys (AA2024–T3 and AA5754–H114). *Arab J Sci Eng* 41(11):4563–4572

11. Zhou L, Li G, Zhang R, Zhou W, He W, Huang Y, Song X (2019) Microstructure evolution and mechanical properties of friction stir spot welded dissimilar aluminum-copper joint. *J Alloy Compd* 775:372–382
12. Broadus RN (1987) Toward a definition of bibliometrics. *Scientometrics* 12(5):373–379. <https://doi.org/10.1007/BF02016680>
13. Tshivhase T, Kainuma Y (2019) Current carbon emission reduction trends for sustainability-a review. *J Sustain Dev* 12(4)
14. Maditati DR, Munim ZH, Schramm H-J, Kummer S (2018) A review of green supply chain management: from bibliometric analysis to a conceptual framework and future research directions. *Resour Conserv Recycl* 139:150–162. <https://doi.org/10.1016/j.resconrec.2018.08.004>
15. Badwelan A, Alsamhan A, Alatefi M, Anwar S, Ghaleb AM (2019) An overview of friction stir spot welding (FSSW) research with bibliometric indicators. Paper presented at the 72nd IIW annual assembly and international conference, Bratislava, Slovakia

Multi Parametric Optimization of Dry Turning of Titanium Alloy (Ti6Al4V Graded 5) using Coated Carbide Insert: A Novel Hybrid RSM-Artificial Gorilla Troop Optimization and Dingo Optimization Algorithm



Dilip Kumar Bagal, Siddharth Jeet, Abhishek Barua, Swastik Pradhan, Arati Rath, and Saujanya Kumar Sahu

Abstract The present research piloted dry turning of titanium alloys (Ti-6Al-4V Grade 5) utilizing modern titanium carbonitrides chemical vapor deposition (MT-CVD) coated carbide tool inserts. The impacts of cutting parameters such as feed rate, cutting speed, and depth of cut on output responses such as cutting forces, flank wear, and surface roughness were investigated using a Box-Behnken design based on response surface methodology (RSM). To find the optimum cutting condition, a newly developed hybrid optimization method, namely RSM-linked Artificial Gorilla Troop Optimization Algorithm and Dingo Optimization Algorithm, was utilized. The flank wear along with cutting force was recorded when the depth of cut was less while better surface finish was achieved with lower cutting speed. Additionally, analysis of variance was used to determine the most important component in each of the three responses, followed by a confirmatory test that revealed a high degree of agreement between anticipated and experimental results. As per the analysis of variance (ANOVA) results, the depth of cut was determined to be the most crucial component in attaining the lowest cutting force, flank wear, and surface

D. K. Bagal

Department of Mechanical Engineering, Government College of Engineering, Kalahandi, Bhawanipatna, Odisha, India

S. Jeet · A. Barua

Department of Mechanical Engineering, Centre for Advanced Post Graduate Studies, BPUT, Rourkela, Odisha, India

S. Pradhan (✉)

School of Mechanical Engineering, Lovely Professional University, Phagwara, Punjab, India
e-mail: swastik.22644@lpu.co.in

A. Rath

School of Computer Engineering, Kalinga Institute of Industrial Technology, Bhubaneswar, Odisha, India

S. K. Sahu

Department of Civil Engineering, Government College of Engineering, Kalahandi, Bhawanipatna, Odisha, India

roughness responses. The results obtained using the artificial gorilla optimization algorithm and the dingo optimization algorithm are found to be more precise than those obtained using the RSM-designed experimentation of dry turning operations, as cutting force, surface roughness, and flank wear have been minimized by utilizing the factor settings achieved using both the artificial gorilla optimization algorithm and the dingo optimization algorithm.

Keywords Artificial gorilla troop optimization algorithm · Dingo optimization algorithm · Dry turning · RSM · Titanium alloy

1 Introduction

Machining titanium alloys is a difficult job in the modern age. Titanium alloy's poor heat conductivity and strong reactivity contribute to a variety of delinquent behaviors. At a high machining speed, the chip heated up and attempted to cling to the machined surface, forming a weldment in the surface. This increased the machined surface and reduced the quality of the finished product, while at times, this characteristic resulted in product damage and waste. If coolant is applied to reduce the heat generation then separation of chip and the cutting fluid is a major concern. The disposal of the chip with those cutting fluid aggravate some skin diseases as the contamination of that fluid can cause itching and rashes formation in the skin. Ignorance about titanium alloy machining cannot be a good choice, since it offers a superior strength-to-weight ratio and corrosion resistance characteristics, and has largely replaced aluminum and iron metal components in the marine, automotive, medical, and aerospace industries. So, machining this alloy in an optimized way can solve some of those concern issues. If the machining is done by varying certain process parameters and after that machinability criteria are analyzed. Then based on that optimal cutting conditions is to be found which increased the machining performance of titanium alloy. Most of the researcher have worked in this direction by using various optimization techniques such as:

Maity et al. [1, 2] used response surface methodology and desirability function analysis to examine the responses like tool wear, surface roughness, and chip morphology during dry turning of Grade 5 titanium alloy utilizing coated carbide inserts. They found that cutting speed was the most influential factor. Additionally, they recreated the turning process in Deform 3D utilizing a micro groove cutting insert [3, 4]. Ramana et al. [5] studied the surface characteristics and tool wear of titanium alloy during turning under various machining and lubrication environments. It is found that the feed rate was the most important element in minimizing surface roughness, followed by the usage of CVD-coated tools [6, 7]. Gupta et al. [8, 9] investigated the surface characteristics of MQL-assisted turning of titanium alloy by means of RSM in conjunction with various meta-heuristic optimization techniques and concluded that lower values of turning parameters (cutting speed, feed rate, approach angle) in conjunction with graphite-based Nanofluids are optimal for

machining, as well as PSO, which provided optimal factor settings [10, 11]. Khan et al. [12] used the Taguchi approach and gray relational analysis to evaluate tool wear, energy consumption, and surface properties of titanium alloy turning under three different circumstances (dry, wet, and cryogenic). They identified feed rate as the most significant variable for surface roughness control while cutting speed was identified as the most significant parameter for tool wear and energy consumption management [13]. Singh et al. [14] used the Taguchi method to evaluate tool wear and surface properties of titanium alloys turned with textured tool profiles under dry and MQL conditions. They identified cutting speed as a critical component for regulating tool wear, whereas feed rate and cutting speed were the most important factors in regulating surface roughness [15]. Kumar and Misra [16] studied tool wear during dry turning of titanium alloy using ANN and RSM and concluded that cutting speed, along with machining time, was the most important factor in reducing tool flank wear. Chauhan and Dass [17] used response surface technique to study the roughness of the surface and force during CNC turning of Grade 5 titanium alloy. They discovered that surface roughness increases with cutting speed and feed rate and decreases with angle and depth of cut. Similarly, when the approach angle and cutting depth are increased while the cutting speed and feed rate are decreased, the tangential force increases. Chen et al. [18] investigated the Ti-6Al-4V turning job using the Taguchi method combined with kernel principal component analysis and found that feed rate was the most significant parameter for radial thrust force, while depth of cut was the most significant parameter for cutting power and coefficient of friction. Liu et al. [19] used coupling response surface technique to optimize the cutting parameters for titanium alloy turning under MQL conditions and identified feed rate as the most important element affecting surface roughness control. Shastri et al. [20] used Cohert intelligence to optimize MQL aided turning of grade-II titanium alloy and demonstrated the method's effectiveness in comparison to particle swarm optimization, experimental optimization, and desirability function optimization.

The turning operation of various grades of titanium alloy was studied by eminent experts from across the world. The majority of work has been carried out on grade 2 titanium alloy with little lubrication and various coated tool inserts. Additionally, a few studies have been conducted using Grade 5 titanium alloy in a low-lubrication condition. According to the experts, the most significant characteristic is cutting speed. There is a dearth of information on the relationship between cutting force decrease and tool wear and surface roughness. Though there is much opportunity for experimentation with Grade 5 titanium alloy, which can be dry turned with a variety of coated tool inserts and then optimized parametrically using some new nature-inspired meta-heuristic optimization techniques. Dry turning of Ti-6Al-4V titanium alloys with Grade 5 was performed in this research utilizing carbide cutting inserts covered with Modern Titanium carbonitrides chemical vapor deposition (MT-CVD). We investigated the impacts of cutting parameters such as cutting speed, feed rate, and depth of cut on cutting forces, flank wear, and surface roughness using a Box-Behnken design based on RSM. To find the optimum cutting condition, a hybrid optimization method was employed, consisting of an RSM-linked Artificial Gorilla Troop Optimization Algorithm and a Dingo Optimization Algorithm. Additionally,

analysis of variance was used to determine the most important component in each of the three responses, followed by a confirmatory test that revealed a high degree of agreement between anticipated and experimental results.

2 Material and the Experiment Setup

The workpiece used in this test was made of titanium alloy (Ti-6Al-4V) Grade 5. Machining was performed using the work piece's length and 50 mm diameter. The chemical composition of the workpiece and its mechanical properties are listed in Table 1. Inserts made of carbide (Model: WM25CT; Grade: SNMG120408) titanium alloy, chemical vapor deposition was fabricated using modern titanium carbonitrides (MT-CVD). CVD layering adheres very well to cemented carbides. WM25CT has an excellent balance of wear resistance and toughness. Tool holder cuts with approach angle of 75° for holding the cuts were employed (Grade: PSBNR2020K12, Make: Kennametal Inc.).

On the high-precision machine was the turning experiment is done (Model: NH 26; Made by: Hindustan Machine Tools Limited). The spindle power of the machine is 11 kW, and the spindle speed ranges from 20 to 1020 revolutions per minute. The cutting force, surface roughness, and flank wear of a titanium alloy (Grade 5) were studied during carbide insert processing. Figure 1 represents the experimental investigation flowchart. The cutting strength was evaluated using the dynamometer of the tool plate. The dynamometer was placed on the traveling roller to determine cutting forces. To determine cuts, the dynamometer was connected to the force indication device in the manner shown in Fig. 2. The surface roughness of the machined surface was determined using a Talysurf roughness meter. The tool manufacturer's microscope was used to determine the flank wear of inserts.

Table 1 Chemical and mechanical properties of titanium alloy (Grade 5)

Chemical properties		Mechanical properties	
Constituents	Content (%)	Property	Value
C	< 0.08	Density	4.42 g/cm ³
Fe	< 0.25	Melting range, $\pm 15^\circ\text{C}$	1649 $^\circ\text{C}$
N ₂	< 0.05	Specific heat	560 J/kg $^\circ\text{C}$
O ₂	< 0.2	Thermal conductivity	7.2 W/mK
Al	5.5–6.76	Tensile strength	1000 MPa
V	3.5–4.5	Elastic modulus	114 GPa
Ti	Balance	Hardness rockwell	36 $^\circ\text{C}$

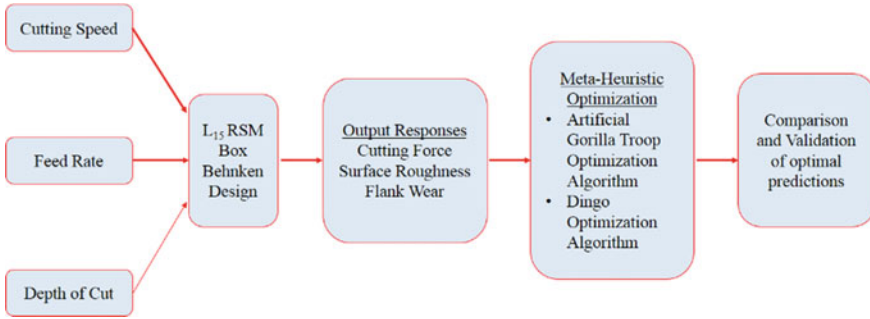


Fig. 1 Experimental investigation flowchart

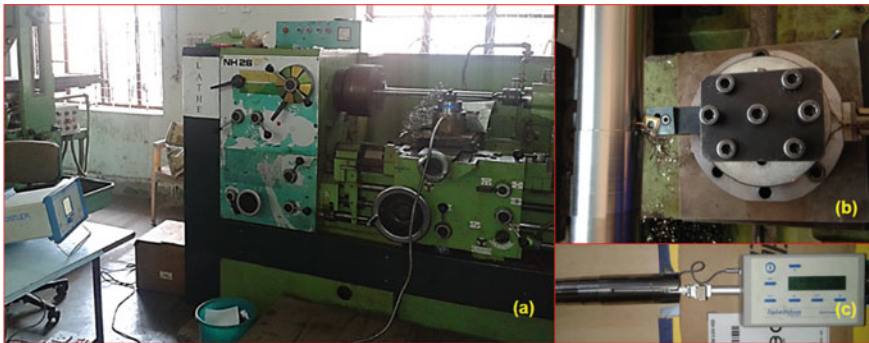


Fig. 2 a Experimental setup b turning of titanium alloy job using coated carbide tool insert c surface roughness measurement

3 Experimental Design Using Response Surface Methodology

The response surface takes a mathematical and statistical approach. By experimenting with the RSM design, it is possible to correlate process variables with output reactions. In mathematical models, a connection was established among the input variable and the output responses. Furthermore, the quadratic model for output with its regression coefficients is displayed as follows in the input parameters:

$$Z = \lambda_0 + \sum_{x=1}^k \lambda_x A_x + \sum_{x=1}^k \lambda_{xx} A_x^2 + \sum_{x,y=1,x \neq y}^k \lambda_{xy} A_x A_y + \mu \quad (1)$$

where Z is the output response, the quadratic, linear, and interaction terms, λ_0 , λ_x , λ_{xx} and λ_{xy} are regression coefficients. The process parameter is A_x , the

Table 2 Cutting parameters with their levels

Factors	Symbol	Levels		
		Low (-1)	Medium (0)	High (1)
Cutting speed (m/min)	<i>A</i>	75	100	125
Feed (mm/rev)	<i>B</i>	0.12	0.14	0.16
Depth of cut (mm)	<i>C</i>	0.5	0.75	1.0

process parameter is A_x^2 , the square of the process parameters respective $A_x A_y$ is the process parameter interactions terms.

Each test run was carried out via the response surface approach according to the arrangement. RSM has been deployed for reducing trail running and improving results quality by creating a mathematical model for all data. In this study, the machinery constraint and the preliminary study selected the cutting parameters to get better criteria for machinability. The layout was created with Minitab 18 software program. The layout incorporates the process variables and levels specified in Table 2. The experimental plan was created using the Box-Behnken (BBD) design in RSM.

4 Artificial Gorilla Troops Optimization Algorithm

Formulated by Benyamin Abdollahzadeh, Farhad Soleimanian Gharehchopogh, and Seyedali Mirjalili in 2021, Artificial Gorilla Troops optimization algorithm is one of the recently developed techniques inspired by gorillas' group behaviors [21].

During the exploration phase, three various operators have been used: migration to an unfamiliar location to enhance the optimization of Artificial Gorilla Troops. The second operator, a move toward the other gorillas, enhances the balance between exploration and development. The third operator in the exploration stage, i.e., migration to a known place, enhances Artificial Gorilla Troops' capacity to optimize search space substantially. In the operating phase, on the other hand, two operators are engaged which substantially enhances search performance. In the optimization of artificial gorillas, a novel method to phase change exploration and exploitation is used, as displayed in Fig. 3, which depicts an outline of the optimization process in the optimization algorithm for artificial gorillas troops. Figure 4 illustrates the optimization method for Artificial Gorilla Troops.

5 Dingo Optimization Algorithm (DOA)

The dingo optimization algorithm is formulated in 2021. The inspiration for the approach suggested is initially explored in this section. The mathematical model is then supplied [22, 23].

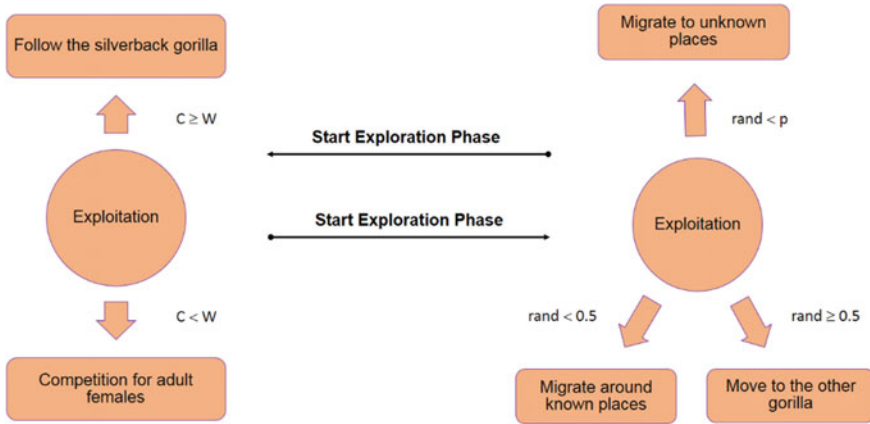


Fig. 3 Different phases of artificial gorilla troops optimizer [21]

5.1 Basics of Biology

The dingo is Australia’s largest carnivorous dog, scientifically known as *Canis lupus dingo*. Numerous studies on the feeding behavior and food of Dingoes have shown that these canines hunt on a variety of species, including mammals, birds, flora (seeds), reptiles, insects, and frogs, to name a few. They are opportunistic hunters, but they are also scavenging when they explore new areas and come upon unexpected dead. They usually chase their victim from behind and attack them. Group assault is their most often used hunting method by circling the victim inside a perimeter and chasing it to tiredness [22, 23].

5.2 Mathematical Model

This section begins with a mathematical model of Dingoes using a variety of hunting techniques. Then, it is suggested 0e DOA algorithm. 0e methods for hunting are assaulting, grouping, and compelling behavior. The chance of survival of Dingoes is also taken into account.

1st Strategy—Group Attack

Predators typically employ smart tactics of hunting. Dingoes generally seek small prey singly, for example, rabbits, but assemble in groups when they pursue large prey such as kangaroos. Dingoes may discover and surround the prey, for example, wolves, see Fig. 5. The following equation shows this behavior:

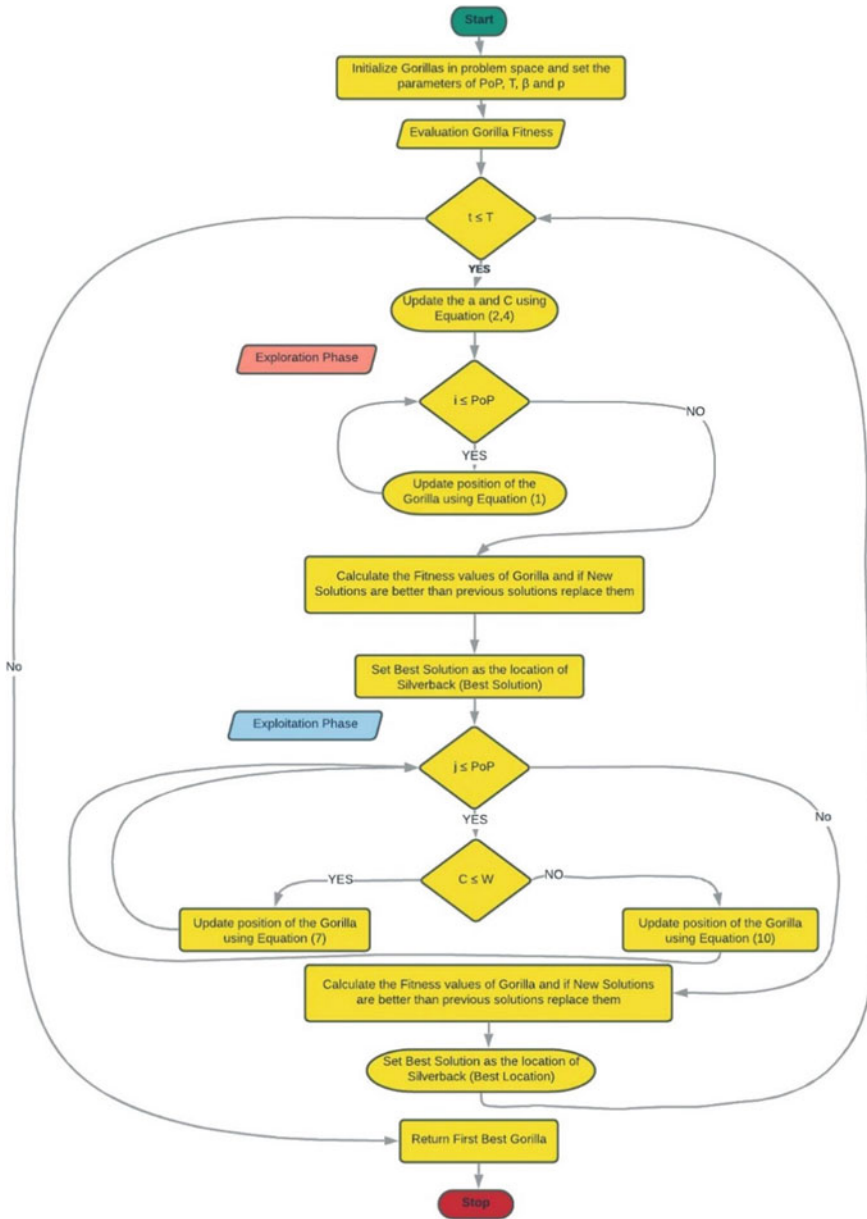


Fig. 4 Artificial gorilla troops optimization flowchart [21]

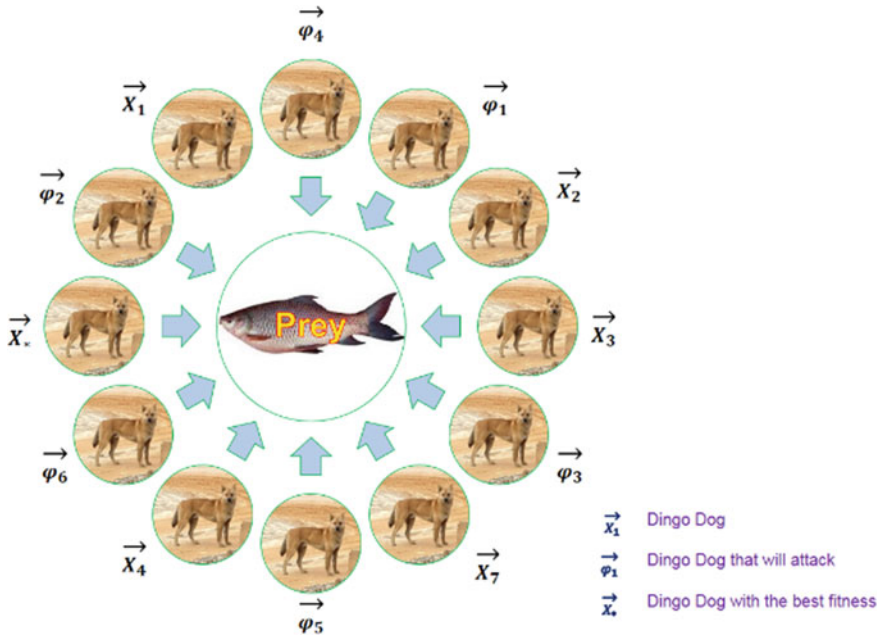


Fig. 5 Dingo dogs hunting strategy [22]

$$\vec{x}_i(t + 1) = \beta_1 \sum_{k=1}^{na} \frac{[\vec{\varphi}_k(t) - \vec{x}_i(t)]}{na} - \vec{x}_*(t) \tag{2}$$

In case $\vec{x}_i(t + 1)$ is an interval $(2, \text{sizepop}/2)$, where the new position is the whole population of Dingoes in size pop, and “na” is the interval random integer in the $[1, \text{sizepop}/2]$. β_1 is random, uniformly distributed random numbers within the interval of $[-2, 2]$; is a scale factor that alters the size and sensation of the Dingoes $\vec{\varphi}_k(t)$, the current search agent in the Dingoes (Dingoes to attack), where $\varphi \subset X, X$, the population of the Dingoes is random, and $\vec{x}_i(t)$ is the current search agent.

2nd Strategy—Persecution

Usually the Dingoes pursue tiny beasts that are hunted to get individually trapped. This comportment is shown in Eq. (3):

$$\vec{x}_i(t + 1) = \vec{x}_*(t) + \beta_1 * e^{\beta_2} * (\vec{x}_{r_1}(t) - \vec{x}_i(t)) \tag{3}$$

β_1 is the same as in Eq. (2), β_2 is a unitarily generated random number in the interval $[-1, 1]$, $\vec{x}_i(t + 1)$ represents the Dingoes’ motion, $\vec{x}_i(t)$ represents the current search agent, r_1 is a random number generated between 1 and the maximum number of search agents (Dingoes), and $\vec{x}_{r_1}(t)$ is the r_1^{th} search agent selected, where $i \neq r_1$.

3rd Strategy—Scavenger:

The scavenger tendency, when Dingoes locate carrots to eat, is termed as the action when they walk in their habitat. This behavior is modeled on Eq. (4).

$$\vec{x}_i(t+1) = 0.5 * [e^{\beta_2} * \vec{x}_{r_1}(t) - (-1)^\sigma * \vec{x}_i(t)] \quad (4)$$

where $\vec{x}_i(t+1)$ denotes the movement of the Dingoes, β_2 has the same value as in Eq. (3), r_1 is a random number generated between 1 and the maximum number of search agents (Dingoes), $\vec{x}_{r_1}(t)$ denotes the r_1^{th} search agent selected and $\vec{x}_i(t)$ denotes the current search agent, where $i \neq r_1$ and σ is a binary number randomly generated by Algorithm 2, where $\sigma \in \{0, 1\}$.

4th Strategy—Dingoes

Survival Rates. Dingo dog is in danger of being annihilated largely because of unlawful hunting. The DOA provides the following equation for the survival rate of Dingoes:

$$\text{Survival}_i = \frac{f_{\max} - f_i}{f_{\max} - f_{\min}} \quad (5)$$

where f_{\max} and f_{\min} are the worst and greatest values of today's generation, whereas f_i is the present search agent's fitness value. Equation surviving vector (5) includes the standardized fitness in the [1, 1] interval. For low-survival rates, e.g., those equal to or less than 0.3, Eq. (6) is used.

$$\vec{x}_i(t) = \vec{x}_*(t) + 0.5 * [\vec{x}_{r_1}(t) - (-1)^\sigma * \vec{x}_{r_2}(t)] \quad (6)$$

In this instance, $\vec{x}_i(t)$ is an updated low-survival search engine, (Dingoes) is a randomly generated number in the range of 1 to the maximum size of search agents, along r_1 and r_2 , $r_1 \neq r_2$, $\vec{x}_{r_1}(t)$ and $\vec{x}_{r_2}(t)$ are the r_1^{th} , r_2^{th} , chosen search agents, respectively. Also, $\vec{x}_*(t)$ is the most suitable search agent in previous iterations and σ .

6 Result and Discussions

Samples are processed using an experimental design based on RSM Box-Behnken [24–27] as indicated in Table 2. Total of 15 experimental runs is done in the turning machine according to the design of the experiment. Each experiment used a fresh cutting edge to assess the flank wear of the cutting inserts. Table 3 summarizes the results of the output responses, i.e., cutting force, surface roughness, and flank wear tests. In general, low cutting force, surface roughness, and flank wear values are required for superior quality and accuracy throughout the machining process.

Table 3 Experimental layout

Run No	A	B	C	Cutting force (N)	Surface roughness (μm)	Flank wear (mm)
1	75	0.12	0.75	235.88	1.91	0.62
2	125	0.12	0.75	101.10	2.06	0.40
3	75	0.16	0.75	91.63	1.17	0.35
4	125	0.16	0.75	147.13	1.57	0.45
5	75	0.14	0.5	173.88	1.98	0.56
6	125	0.14	0.5	104.38	1.70	0.45
7	75	0.14	1	338.63	1.88	0.66
8	125	0.14	1	263.13	1.91	0.61
9	100	0.12	0.5	58.87	1.90	0.26
10	100	0.16	0.5	50.10	1.91	0.17
11	100	0.12	1	182.50	2.06	0.49
12	100	0.16	1	183.75	1.17	0.35
13	100	0.14	0.75	74.67	1.57	0.35
14	100	0.14	0.75	70.61	1.98	0.38
15	100	0.14	0.75	71.15	1.70	0.37

6.1 Machining Parameter Effect on Cutting Force

Cutting force is monitored by RSM layout and evaluated by ANOVA during machining. The F ratio was computed with a 95% confidence interval and a P -value of less than 0.05 was considered. Table 4 is an ANOVA table for cutting force with 14 Degree of Freedom (DoF) which is also same for other responses. As shown in Table 4, the most important contributing factor is Depth of Cut (C), followed by Cutting Speed (A), and Feed Rate (B) is a non-significant component when cutting force reduction is desired during dry turning of titanium alloy (Grade 5). Additionally, the R -squared value of 97.92% was observed, indicating the importance of the experimental study.

Figure 6 illustrates the major effect map for cutting force. To minimize the cutting force, the smaller the better criteria were used and the graph's lower points were interpreted. As shown in Fig. 6, **A2B3C1**, i.e., 100 m/min cutting speed, 0.16 mm/rev feed rate, and 0.5 mm depth of cut results in the lowest value, which can be referred to as the optimal factor setting obtained using Response Surface Methodology for obtaining a lower cutting force while dry turning titanium alloy (Grade 5).

Table 4 ANOVA results for cutting force

Source	DoF	Adj. S.S	Contribution (%)	Adj. M.S	F-value	P-value
Model	9	100060	97.92	11117.8	26.15	0.001
Linear	3	49848	48.78	16616.2	39.08	0.001
A	1	6288	6.15	6287.7	14.79	0.012
B	1	1398	1.37	1397.6	3.29	0.130
C	1	42163	41.26	42163.2	99.16	0.000
Square	3	41126	40.25	13708.6	32.24	0.001
A ²	1	27624	27.03	27624.1	64.97	0.000
B ²	1	798	0.78	798.3	1.88	0.229
C ²	1	13904	13.61	13904.4	32.70	0.002
2-Way interaction	3	9086	8.89	3028.6	7.12	0.030
A × B	1	9052	8.86	9051.6	21.29	0.006
A × C	1	9	0.01	9.0	0.02	0.890
B × C	1	25	0.02	25.1	0.06	0.818
Error	5	2126	2.08	425.2		
Lack-of-fit	3	2116	2.07	705.4	145.13	0.007
Pure error	2	10	0.01	4.9		
Total	14	102186				

Main Effects Plot for Cutting Force
Data Means

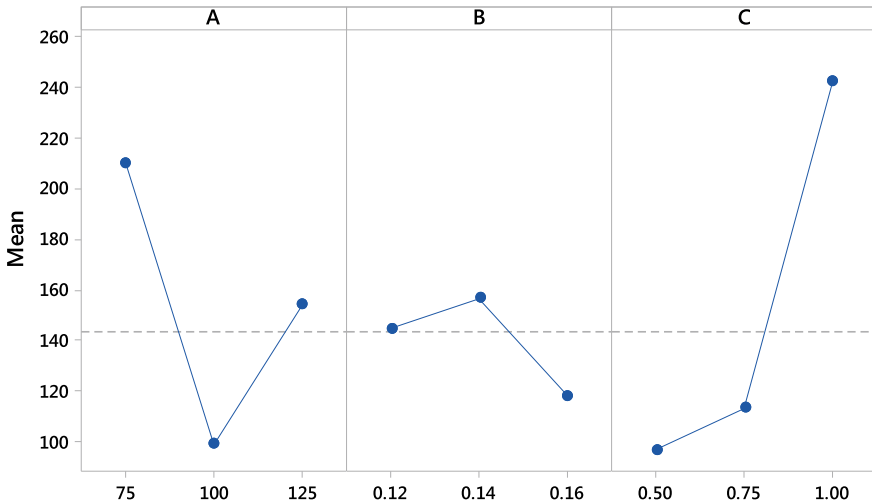


Fig. 6 Main effect plot for cutting force

6.2 Machining Parameter Effect on Surface Roughness

During machining, surface roughness is measured using RSM layout and analyzed using ANOVA. The F ratio was computed with a 95% confidence interval and a P -value of less than 0.05 was considered. Table 5 is an ANOVA table for cutting force. As shown in Table 5, the most important contributing factor is Depth of Cut (C), followed by Cutting Speed (A), and Feed Rate (B) is a non-significant component when minimizing surface roughness during dry turning of titanium alloy (Grade 5). Additionally, the R -squared value, i.e., 98.61% was observed, indicating the importance of the experimental study.

Figure 7 illustrates the major effect map for cutting force. To minimize the cutting force, the smaller the better criteria were used and the graph's lower points were interpreted. As shown in Fig. 7, A1B3C1, i.e., 75 m/min cutting speed, 0.16 mm/rev feed rate, and 0.5 mm depth of cut results in the lowest value, which can be referred to as the optimal factor setting obtained using RSM for achieving lower surface roughness while dry turning titanium alloy (Grade 5).

Table 5 ANOVA results for surface roughness

Source	DoF	Adj. S.S	Contribution (%)	Adj. M.S	F -value	P -value
Model	9	1.62479	98.61	0.180533	39.30	0.000
Linear	3	1.13530	68.90	0.378433	82.39	0.000
A	1	0.54080	32.82	0.540800	117.74	0.000
B	1	0.00045	0.03	0.000450	0.10	0.767
C	1	0.59405	36.05	0.594050	129.33	0.000
Square	3	0.16409	9.96	0.054698	11.91	0.010
A^2	1	0.00296	0.18	0.002964	0.65	0.458
B^2	1	0.03570	2.17	0.035703	7.77	0.039
C^2	1	0.13801	8.38	0.138010	30.05	0.003
2-Way interaction	3	0.32540	19.75	0.108467	23.61	0.002
$A \times B$	1	0.07290	4.42	0.072900	15.87	0.010
$A \times C$	1	0.13690	8.31	0.136900	29.80	0.003
$B \times C$	1	0.11560	7.02	0.115600	25.17	0.004
Error	5	0.02297	1.39	0.004593		
Lack-of-fit	3	0.02250	1.37	0.007500	32.14	0.030
Pure error	2	0.00047	0.03	0.000233		
Total	14	1.64776	98.61			

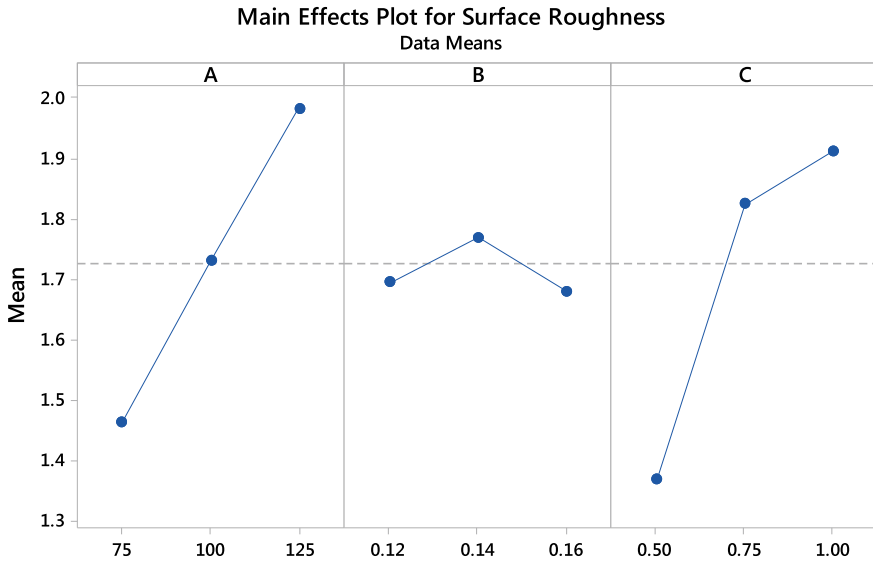


Fig. 7 Main effect plot for surface roughness

6.3 Machining Parameter Effect on Flank Wear

Flank wear is monitored by RSM layout and evaluated by ANOVA during machining. The F ratio was computed with a 95% confidence interval and a P-value of less than 0.05 was taken into consideration. Table 6 is an ANOVA table for cutting force. As shown in Table 6, if flank wear is minimized during dry turning of titanium alloy, the most important contributing component is the Depth of Cut (C), followed by the Feed Rate (B) and Cutting Speed (A). Additionally, the R-squared value of 98.68% was noticed, indicating the importance of the experimental study.

Figure 8 depicts the major effect plot for cutting force. To minimize the cutting force, the smaller the better criteria were used and the graph's lower points were interpreted. As shown in Fig. 8, A2B3C1, i.e., Cutting Speed of 100 m/min, Feed rate of 0.16 mm/rev, and Cut Depth of 0.5 mm, demonstrates the lowest value, which can be referred to as the optimal factor setting obtained using Response Surface Methodology for achieving lower flank wear while dry turning of titanium alloy.

6.4 Meta-Heuristic Optimization

For predicting better fitness value along with optimal factor setting, fitness functions need to be spawned. Thus, the three output responses were taken into consideration,

Table 6 ANOVA results for flank wear

Source	DoF	Adj. S.S	Contribution (%)	Adj. M.S	F-value	P-value
Model	9	0.261882	98.68	0.029098	41.67	0.000
Linear	3	0.091225	34.38	0.030408	43.54	0.001
A	1	0.009800	3.69	0.009800	14.03	0.013
B	1	0.025312	9.54	0.025312	36.25	0.002
C	1	0.056112	21.14	0.056112	80.35	0.000
Square	3	0.143532	54.09	0.047844	68.51	0.000
A ²	1	0.107231	40.41	0.107231	153.55	0.000
B ²	1	0.024878	9.37	0.024878	35.62	0.002
C ²	1	0.004001	1.51	0.004001	5.73	0.062
2-Way interaction	3	0.027125	10.22	0.009042	12.95	0.009
A × B	1	0.025600	9.65	0.025600	36.66	0.002
A × C	1	0.000900	0.34	0.000900	1.29	0.308
B × C	1	0.000625	0.24	0.000625	0.89	0.388
Error	5	0.003492	1.32	0.000698		
Lack-of-fit	3	0.003025	1.14	0.001008	4.32	0.194
Pure error	2	0.000467	0.18	0.000233		
Total	14	0.265373				

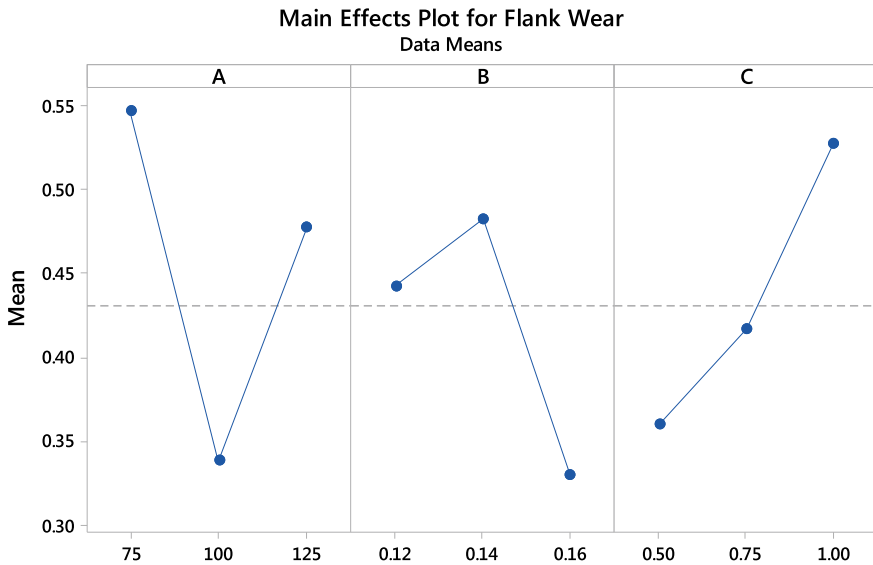


Fig. 8 Main effect plot for flank wear

namely cutting force, surface roughness, and flank wear values, and regression equations were developed in conjunction with the response surface methodology optimization procedure, which was piloted on the Minitab 18 platform. These regression equations will be used as the fitness function in the Artificial Gorilla and Dingo Optimization Algorithms, which were programmed and built using the Matlab R2018a platform:

Minimize:

$$\begin{aligned} \text{Cutting Force} = & 2641 - 41.94A - 258B - 1229C + 0.1384A^2 \\ & - 36760B^2 + 982C^2 + 95.1AB - 0.24AC + 501BC \end{aligned} \quad (7)$$

$$\begin{aligned} \text{Surface Roughness} = & -8.93 + 0.0039A + 67.0B + 13.45C \\ & - 0.000045A^2 - 245.8B^2 - 3.093C^2 + 0.2700AB \\ & - 0.02960AC - 34.00BC \end{aligned} \quad (8)$$

$$\begin{aligned} \text{Flank Wear} = & 1.808 - 0.08013A + 40.5B - 0.345C + 0.000273A^2 \\ & - 205.2B^2 + 0.527C^2 + 0.1600AB + 0.00240AC - 2.50BC \end{aligned} \quad (9)$$

Subject to:

$$75 \leq A \leq 125; \quad 0.12 \leq B \leq 0.16; \quad 0.5 \leq C \leq 1.0$$

As per the problem statement, cutting force, surface roughness, and flank wear responses must all be minimized in order to get a higher surface quality and less tool wear while dry turning titanium alloy (Grade 5). To get optimum turning parameters, the Artificial Gorilla Optimization Algorithm and the Dingo Optimization Algorithm methods have specified with certain pre-set parameters. In Artificial Gorilla Optimization Algorithm, “a troop of gorillas” population has been set to 100 with maximum iteration of 100. Similarly, in Dingo Optimization Algorithm method, “a pack of dogs (Dingo dogs)” population has been set to 100 with maximum iteration of 500. Both the codes have been set to minimization criteria for providing desired output. Figures 9, 10, and 11 illustrate the fitness convergence plot when the Artificial Gorilla Optimization method is used, whereas Figs. 12, 13, and 14 illustrate the fitness convergence plot when the Dingo Optimization algorithm is used. Table 7 summarizes the optimal factor setting together with projected fitness values. It can be noted that the prediction made by both Artificial Gorilla Optimization algorithm and Dingo Optimization algorithm are similar which also shows the efficiency of the algorithm.

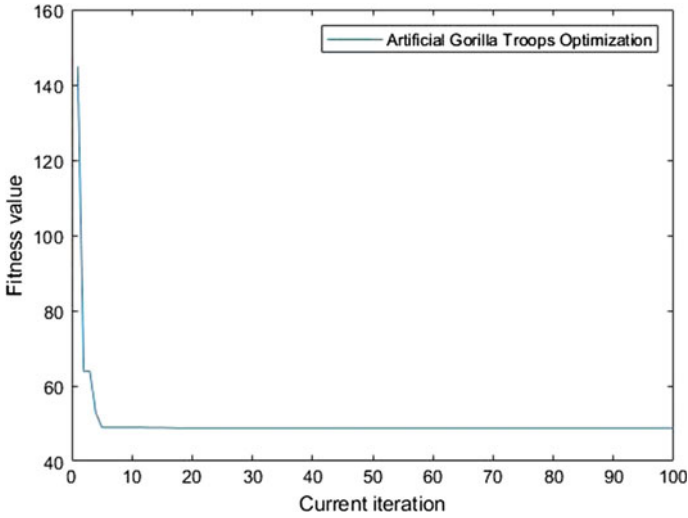


Fig. 9 Convergence plot for cutting force

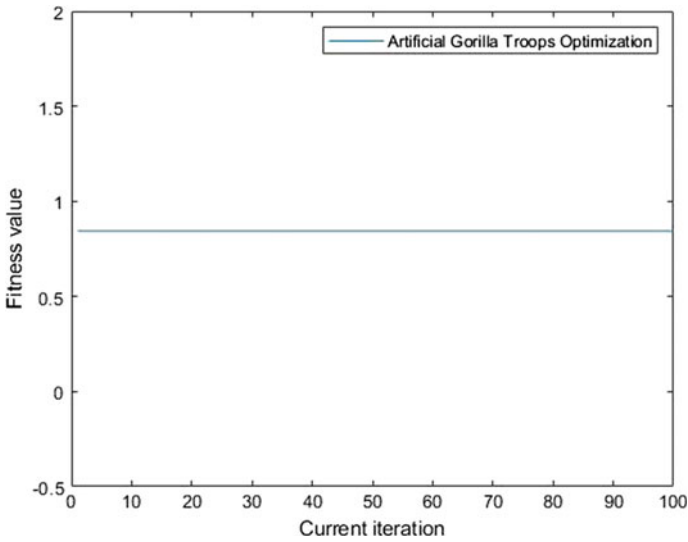


Fig. 10 Convergence plot for surface roughness

6.5 Confirmatory Test Results

In order to assess the importance of the projected value, unconfirmed optimization algorithms predictions were examined [28–38]. This information is critical for determining the optimal factor setting for cutting strength, surface ruggedness, and flank

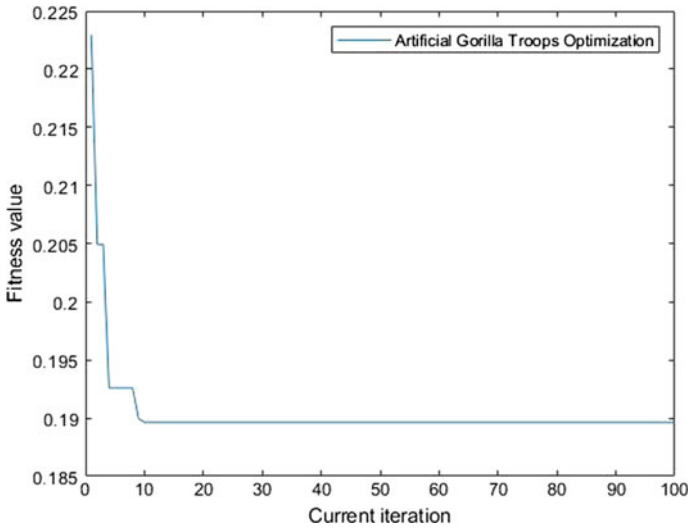


Fig. 11 Convergence plot for flank wear

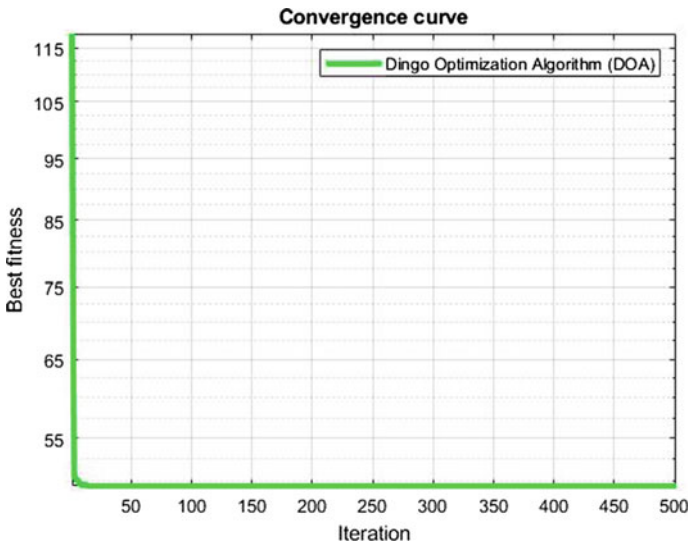


Fig. 12 Convergence plot for cutting force

wear reduction when dry turning titanium alloy with a coated carbide inserts. The results produced via the Artificial Gorilla Optimization algorithm and dingo optimization are more precise than those obtained through the RSM. Cutting forces, flank wear, and surface roughness have all been reduced, as shown by the Response Surface Factor settings for dry turning titanium alloys (Grade 5) with a coated carbide insert,

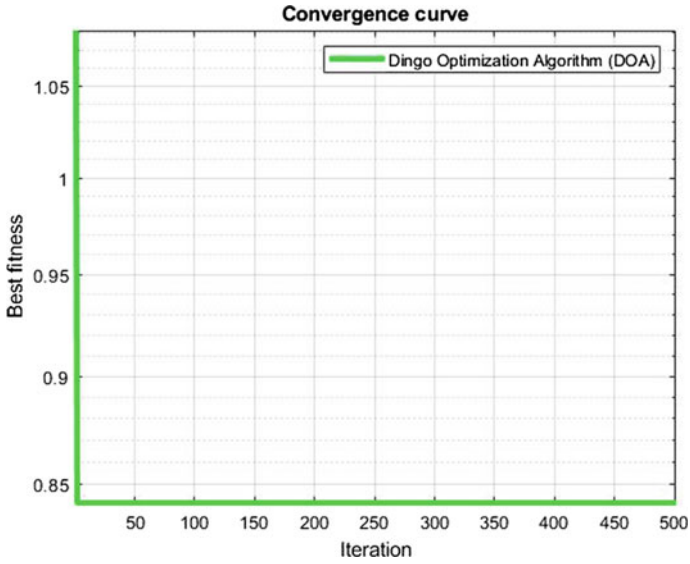


Fig. 13 Convergence plot for surface roughness

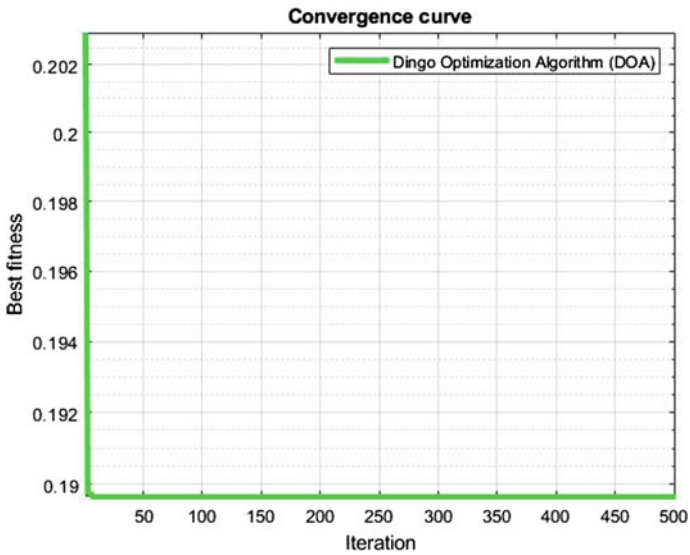


Fig. 14 Convergence plot for flank wear

Table 7 Confirmatory experiment

Responses	Applied approach	Cutting speed (<i>A</i>) (in m/min)	Feed rate (<i>B</i>) (in mm/rev)	Depth of cut (<i>C</i>) (in mm)	Predicted value	Experimental value
Cutting force	Response surface methodology	100	0.16	0.5	50.21 N	50.10 N
	Artificial gorilla troop optimization algorithm	100	0.16	0.5	50.15 N	50.10 N
	Dingo optimization algorithm	100	0.16	0.5	50.10 N	50.10 N
Surface roughness	Response surface methodology	75	0.16	0.5	0.88 μm	1.01 μm
	Artificial gorilla troop optimization algorithm	75	0.12	0.5	0.84 μm	0.84 μm
	Dingo optimization algorithm	75	0.12	0.5	0.84 μm	0.84 μm
Flank wear	Response surface methodology	100	0.16	0.5	0.19 mm	0.17 mm
	Artificial gorilla troop optimization algorithm	100	0.16	0.5	0.18 mm	0.17 mm
	Dingo optimization algorithm	100	0.16	0.5	0.18 mm	0.17 mm

utilizing factor values from both the Artificial Gorilla Optimization and Dingo Optimization algorithms and these values tabulated in Table 7. The findings of previous study [3] were very consistent, as they also suggested a significant component of depth of cut, in addition to other parameters, for reducing cutting force, surface roughness, and flank wear responses.

7 Conclusion

The impact of cutting parameters on the machinability of Ti6Al4V titanium alloy Grade 5 was investigated in this research by dry machining with coated carbide cutting inserts. And, the experiment is carried out by varying three cutting variables, namely cutting speed, feed rate, and depth of cut. The experiment was conducted using a Box-Behnken design based on RSM. The response surface technique was used to determine the impact of each process parameter. This study focused on minimizing cutting force, surface roughness, and flank wear. The optimum cutting condition and the influencing cutting parameter were studied by using different optimization methodologies. A comparative analysis has been carried out based on RSM approach using recently developed Artificial Gorilla optimization algorithm and Dingo optimization algorithm. Based on the experimental results implemented on dry turning operation the successive conclusions are prepared:

- The flank wear along with cutting force were recorded when the depth of cut was less while better surface roughness was achieved with lower cutting speed.
- The ANOVA analysis revealed that the depth of cut was the most important element in obtaining the lowest cutting force, flank wear, and surface roughness.
- A cutting speed of 100 m/min, a feed rate of 0.16 mm/rev, and a depth of cut of 0.5 mm were found to be the optimal factor settings for achieving the lowest cutting force and flank wear when dry turning titanium alloy (Grade 5) using coated carbide inserts, as stated by all three methods, namely Response Surface Methodology, Artificial Gorilla Troop Optimization Algorithm, and Dingo Optimization Algorithm.
- On the other hand, a cutting speed of 75 m/min, a feed rate of 0.12 mm/rev, and a depth of cut of 0.5 mm are the optimal factor settings for achieving the lowest possible surface roughness when dry turning titanium alloy (Grade 5) with coated carbide inserts, as determined by the Artificial Gorilla Troop and Dingo Optimization Algorithms.
- In general, the results obtained using the Artificial Gorilla Optimization and Dingo Optimization algorithms are more precise than the values obtained using the Response surface methodology, as cutting force, surface roughness, and flank wear responses have been minimized using the factor settings.

All meta-heuristic techniques provide the same factor configuration and projected value, thereby creating economic resolution for commercial Ti-6Al-4V alloy machining. This also opens scope for exploration of turning of titanium alloy (Grade 5) under hardening state, different Nano-lubricants MQL using different coated carbide insert both experimental and Finite Element Analysis platform. Also, different optimization techniques can be employed for comparative analysis.

References

1. Maity K, Pradhan S (2017) Study of chip morphology, flank wear on different machinability conditions of titanium Alloy (Ti-6Al-4V) using response surface methodology approach. *Int J Mater Form Mach Processes (IJMFMP)* 4(1):19–37. <https://doi.org/10.4018/IJMFMP.2017010102>
2. Maity K, Pradhan S (2017) Study of process parameter on mist lubrication of titanium (Grade 5) alloy. In: *IOP conference series: materials science and engineering*, 178(1):012030. <https://doi.org/10.1088/1757-899X/178/1/012030>
3. Maity K, Pradhan S (2018) Investigation of tool wear and surface roughness on machining of titanium alloy with MT-CVD cutting tool. *IOP Conf Ser Mater Sci Eng* 346(1):012053. <https://doi.org/10.1088/1757-899X/1033/1/012067>
4. Maity K, Pradhan S (2018) Investigation of FEM simulation of machining of titanium alloy using microgroove cutting insert. *Silicon* 10(5):1949–1959. <https://doi.org/10.1007/s12633-017-9707-x>
5. Ramana MV, Aditya YS (2017) Optimization and influence of process parameters on surface roughness in turning of titanium alloy. *Mater Today Proc* 4(2):1843–1851
6. Ramana MV (2017) Optimization and influence of process parameters on surface roughness in turning of titanium alloy under different lubricant conditions. *Mater Today Proc* 4(8):8328–8335
7. Ramana MV, Rao GKM, Rao DH (2014) Optimization and effect of process parameters on tool wear in turning of titanium alloy under different machining conditions. *Int J Mater Mech Manuf* 2(4):272
8. Gupta MK, Sood PK, Sharma VS (2016) Machining parameters optimization of titanium alloy using response surface methodology and particle swarm optimization under minimum–quantity lubrication environment. *Mater Manuf Processes* 31(13):1671–1682
9. Gupta MK, Sood PK, Sharma VS (2016) Optimization of machining parameters and cutting fluids during nano–fluid based minimum quantity lubrication turning of titanium alloy by using evolutionary techniques. *J Clean Prod* 135:1276–1288
10. Gupta MK, Sood PK, Singh G, Sharma VS (2018) Investigations of performance parameters in NFMQL assisted turning of titanium alloy using TOPSIS and particle swarm optimisation method. *Int J Mater Prod Technol* 57(4):299–321
11. Gupta MK, Mia M, Pruncu CI, Khan AM, Rahman MA, Jamil M, Sharma VS (2020) Modeling and performance evaluation of Al₂O₃, MoS₂ and graphite nanoparticle–assisted MQL in turning titanium alloy: an intelligent approach. *J Braz Soc Mech Sci Eng* 42(4):1–21
12. Khan MA, Jaffery SHI, Khan M, Younas M, Butt SI, Ahmad R, Warsi SS (2020) Multi-objective optimization of turning titanium-based alloy Ti-6Al-4V under dry, wet, and cryogenic conditions using gray relational analysis (GRA). *Int J Adv Manuf Technol* 106(9):3897–3911
13. Khan MA, Jaffery SHI, Khan M, Younas M, Butt SI, Ahmad R, Warsi SS (2019) Statistical analysis of energy consumption, tool wear and surface roughness in machining of titanium alloy (Ti-6Al-4V) under dry, wet and cryogenic conditions. *Mech Sci* 10(2):561–573
14. Singh R, Dureja JS, Dogra M (2021) Optimization of turning parameters during machining of Ti-6Al-4 V alloy with surface textured tools under dry/MQL environments. *Optimization methods in engineering*, Springer, Singapore, pp 605–619
15. Singh R, Dureja JS, Dogra M, Randhawa JS (2019) Optimization of machining parameters under MQL turning of Ti-6Al-4V alloy with textured tool using multi-attribute decision-making methods. *World J Eng*
16. Kumar P, Misra JP (2021) Process modeling and optimization using ANN and RSM during dry turning of Titanium alloy used in automotive industry. *Proc Inst Mech Eng Part D J Automob Eng* 235(7):2040–2050
17. Chauhan S, Dass K (2012) Optimization of machining parameters in turning of titanium (Grade-5) alloy using response surface methodology. *Mater Manuf Processes* 27(5):531–537

18. Li N, Chen YJ, Kong DD (2019) Multi-response optimization of Ti-6Al-4V turning operations using Taguchi-based grey relational analysis coupled with kernel principal component analysis. *Adv Manuf* 7(2):142–154
19. Liu Z, Xu J, Han S, Chen M (2013) A coupling method of response surfaces (CRSM) for cutting parameters optimization in machining titanium alloy under minimum quantity lubrication (MQL) condition. *Int J Precis Eng Manuf* 14(5):693–702
20. Shastri A, Nargundkar A, Kulkarni AJ, Benedicenti L (2021) Optimization of process parameters for turning of titanium alloy (Grade II) in MQL environment using multi-CI algorithm. *SN Applied Sciences* 3(2):1–12
21. Abdollahzadeh B, Soleimanian Gharehchopogh F, Mirjalili S (2021) Artificial gorilla troops optimizer: a new nature-inspired metaheuristic algorithm for global optimization problems. *Int J Intell Syst* 36(10):5887–5958
22. Bairwa AK, Joshi S, Singh D (2021) Dingo optimizer: a nature-inspired metaheuristic approach for engineering problems. *Math Probl Eng*
23. Peraza-Vázquez H, Peña-Delgado AF, Echavarría-Castillo G, Morales-Cepeda AB, Velasco-Álvarez J, Ruiz-Perez F (2021) A bio-inspired method for engineering design optimization inspired by dingoes hunting strategies. *Math Probl Eng*
24. Bagal DK, Barua A, Jeet S, Satapathy P, Patnaik D (2019) MCDM optimization of parameters for wire-EDM machined stainless steel using hybrid RSM-TOPSIS genetic algorithm and simulated annealing. *Int J Eng Adv Technol* 9(1):366–371. <https://doi.org/10.35940/ijeat.A9349.109119>
25. Bagal DK, Parida B, Barua A, Naik B, Jeet S, Singh SK, Pattanaik AK (2020) Mechanical characterization of hybrid polymer SiC nano composite using hybrid RSM-MOORA-Whale optimization algorithm. *IOP Conf Ser: Mater Sci Eng* 970(1):012017. <https://doi.org/10.1088/1757-899X/970/1/012017>
26. Pradhan DK, Sahu B, Bagal DK, Barua A, Jeet S, Pradhan S (2022) Application of progressive hybrid RSM-WASPAS-grey wolf method for parametric optimization of dissimilar metal welded joints in FSSW process. *Mater Today: Proc* 50(5):766–772. <https://doi.org/10.1016/j.matpr.2021.05.471>
27. Mangaraj SR, Bagal DK, Parhi N, Panda SN, Barua A, Jeet S (2022) Experimental study of a portable plasma arc cutting system using hybrid RSM-nature inspired optimization technique. *Mater Today: Proc* 50(5):867–878. <https://doi.org/10.1016/j.matpr.2021.06.138>
28. Kandi BP, Jeet S, Bagal DK, Barua A, Bhoi S, Mahapatra SS (2022) Mechanical characterization of quenched hardened chromoly steel using Taguchi coupled WASPAS method. *Mater Today: Proc* 50(5):2321–2327. <https://doi.org/10.1016/j.matpr.2021.10.224>
29. Sahoo AK, Jeet S, Bagal DK, Barua A, Pattanaik AK, Behera N (2022) Parametric optimization of CNC-drilling of Inconel 718 with cryogenically treated drill-bit using Taguchi-Whale optimization algorithm. *Mater Today: Proc* 50(5):1591–1598. <https://doi.org/10.1016/j.matpr.2021.09.121>
30. Sahoo UK, Jeet S, Bagal DK, Sahu MK, Kumari K, Barua A (2022) Optimization of industrial coatings tribological parameters by studying its application on mechanical components using Taguchi coupled WASPAS method. *Mater Today: Proc* 50(5):1405–1412. <https://doi.org/10.1016/j.matpr.2021.08.326>
31. Challan M, Jeet S, Bagal DK, Mishra L, Pattanaik AK, Barua A (2022) Fabrication and mechanical characterization of red mud based Al2025-T6 MMC using Lichtenberg optimization algorithm and Whale optimization algorithm. *Mater Today: Proc* 50(5):1346–1353. <https://doi.org/10.1016/j.matpr.2021.08.274>
32. Ravikiran B, Pradhan DK, Jeet S, Bagal DK, Barua A, Nayak S (2022) Parametric optimization of plastic injection moulding for FMCG polymer moulding (PMMA) using hybrid Taguchi-WASPAS-Ant Lion optimization algorithm. *Mater Today: Proc* 56(5):2411–2420. <https://doi.org/10.1016/j.matpr.2021.08.204>
33. Behera NC, Jeet S, Nayak CK, Bagal DK, Panda SN, Barua A (2022) Parametric appraisal of strength; hardness of resin compacted sand castings using hybrid Taguchi-WASPAS-Material Generation Algorithm. *Mater Today: Proc* 50(5):1226–1233. <https://doi.org/10.1016/j.matpr.2021.08.104>

34. Malik S, Jeet S, Bagal DK, Nayak RP, Barua A, Mahapatra SS (2022) Parametric appraisal of collapsibility and core shrinkage of phenol binded unbaked casting moulds using Taguchi-Sunflower optimization algorithm. *Mater Today: Proc* 50(5):1138–1144. <https://doi.org/10.1016/j.matpr.2021.08.031>
35. Jena S, Jeet S, Bagal DK, Baliarsingh AK, Nayak DR, Barua A (2022) Efficiency analysis of mechanical reducer equipment of material handling industry using Sunflower Optimization Algorithm and Material Generation Algorithm. *Mater Today: Proc* 50(5):1113–1122. <https://doi.org/10.1016/j.matpr.2021.08.005>
36. Mohanty A, Nag KS, Bagal DK, Barua A, Jeet S, Mahapatra SS, Cherkia H (2022) Parametric optimization of parameters affecting dimension precision of FDM printed part using hybrid Taguchi-MARCOS-nature inspired heuristic optimization technique. *Mater Today: Proc* 50(5):893–903. <https://doi.org/10.1016/j.matpr.2021.06.216>
37. Barua A, Jeet S, Bagal DK, Satapathy P, Agrawal PK (2019) Evaluation of mechanical behavior of hybrid natural fiber reinforced nano sic particles composite using Hybrid Taguchi-CoCoSo method. *Int J Innov Technol Explor Eng* 8(10):3341–3345. <https://doi.org/10.35940/ijitee.J1232.0881019>
38. Bagal DK, Naik B, Parida B, Barua A, Jeet S, Singh SK, Pattanaik AK (2020) Comparative mechanical characterization of M30 concrete grade by fractional replacement of Portland pozzolana cement with industrial waste using CoCoSo and CODAS methods. *IOP Conf Ser: Mater Sci Eng* 970(1):012015. <https://doi.org/10.1088/1757-899X/970/1/012015>

Retraction Note To: On Parametric Optimization of TSE for PVDF-Graphene-MnZnO Composite Based Filament Fabrication for 3D/4D Printing Applications



Vinay Kumar, Rupinder Singh, and Inderpreet Singh Ahuja

Retraction Note to:
Chapter “On Parametric Optimization of TSE for PVDF-Graphene-MnZnO Composite Based Filament Fabrication for 3D/4D Printing Applications” in: C. Prakash et al. (eds.), *Advances in Functional and Smart Materials*, Lecture Notes in Mechanical Engineering,
https://doi.org/10.1007/978-981-19-4147-4_5

The authors are retracting this chapter because it had been previously published by the same authors [1].

This article is therefore redundant. All authors agree to this retraction. [1] Kumar, V., Singh, R., Ahuja, I.S. (2022). On Parametric Optimization of TSE for PVDF-Graphene-MnZnO Composite Based Filament Fabrication for 3D/4D Printing Applications. In: Prakash, C., Singh, S., Basak, A., Davim, J. P. (eds) Numerical Modelling and Optimization in Advanced Manufacturing Processes. Materials Forming, Machining and Tribology. Springer, Cham. https://doi.org/10.1007/978-981-19-4147-4_5

The retracted version of this chapter can be found at
https://doi.org/10.1007/978-981-19-4147-4_5